Dissertation

Synthese, Charakterisierung und Anwendung poröser Aluminium-MOFs auf Basis schwefelhaltiger Linkermoleküle

Zur Erlangung des Doktorgrades

der Mathematisch-Naturwissenschaftlichen Fakultät der
Christian-Albrechts-Universität zu Kiel

vorgelegt von

Nele Reimer

Kiel, Mai 2015

Erster Gutachter: Prof. Dr. Norbert Stock
Zweiter Gutachter: Prof. Dr. Wolfgang Bensch

Tag der mündlichen Prüfung: 17.06.2015
Zum Druck genehmigt: 17.06.2015

Gez. Prof. Dr. Wolfgang J. Duschl
Der Dekan

Meinen Eltern

Synthese, Charakterisierung und Anwendung poröser Aluminium-MOFs auf Basis schwefelhaltiger Linkermoleküle

Diese Arbeit beschäftigt sich mit der Synthese, Charakterisierung und möglichen Anwendung neuer sowie isoretikulärer aluminiumhaltiger Metall-Organischer Gerüstverbindungen (Al-MOFs) basierend auf schwefelhaltigen Linkermolekülen. Verwendet wurden die Sulfone 4,4´-Sulfonyldibenzoesäure (H_2SDBA), 3,3´,4,4´-Diphenylsulfontetracarbonsäuredianhydrid (DPSDA) und 5,5-Dioxo-dibenzo[*b*,*d*]thiophen-3,7-Dicarbonsäure ($H_2BPDC-SO_2$), 2,5-Thiophendicarbonsäure (H_2TDC), das Lithiumsalz der 5-Sulfoisopthalsäure (m-$H_2BDC-SO_3H$) sowie 2,5-Dimercapto-1,4-Benzoldicarbonsäure (H_2DMBD). Zur Entdeckung und Syntheseoptimierung wurde auf Hochdurchsatzmethoden zurückgegriffen. Unter Verwendung der Linkermoleküle H_2SDBA und DPSDA konnten zwei neue sulfonfunktionalisierte mikroporöse Verbindungen CAU-11 $[Al(OH)(SDBA)]\cdot 0.25DMF$ und CAU-12 $[Al_2(OH)_2(DPSTC)(H_2O)_2]\cdot H_2O$ erhalten werden. Beide Verbindungen sind aus Ketten von *trans* eckenverknüpften AlO_6-Polyedern aufgebaut. Im Falle von CAU-11 werden die Ketten über die Linkermoleküle zu einer zweidimensionalen Schichtstruktur verknüpft. CAU-11 weist dabei eine äußerst selten vorkommende permanente Porosität innerhalb der Schichten auf. Das hydrophobe Sorptionsverhalten konnte, ausgehend von DPSDA, durch Herstellung der isoretikulären Verbindung CAU-11-COOH $[Al(OH)(H_2DPSTC)]\cdot 0.5H_2O$ in ein hydrophiles umgewandelt werden. Im Falle von CAU-12 $[Al_2(OH)_2(DPSTC)(H_2O)_2]\cdot H_2O$ werden die anorganischen Ketten zu einem dreidimensionalen Netzwerk verknüpft. Dabei koordinieren von den vier zur Verfügung stehenden Carbonsäuregruppen zwei vollständig und zwei nur mit einem Sauerstoffatom. Über thermische Aktivierung kommt es zu einer Phasenumwandlung indem die koordinierenden Wassermoleküle abgespalten werden und alle vier Carbonsäuregruppen vollständig koordinieren. Dadurch wird die Verbindung porös. Des Weiteren konnte unter Verwendung von $H_2BPDC-SO_2$ eine isoretikuläre Verbindung zu der bereits bekannten Verbindung DUT-5 $[Al(OH)(BPDC)]$ (BPDC = 4,4‘-Biphenyldicarboxylation) erhalten werden, die analog zu MIL-53 $[Al(OH)(BDC)]$ (BDC = 1,4-Benzoldicarboxylation) kristallisiert. DUT-5-SO_2 $[Al(OH)(BPDC-SO_2)]\cdot 2.5DMF$ basiert entsprechend ebenfalls auf Ketten von *trans* eckenverknüpften AlO_6-Polyedern, die über die Linkermoleküle zu einem dreidimensionalen Netzwerk mit eindimensionalen rautenförmigen Kanälen verknüpft wird. Durch die eingebrachten SO_2-Gruppen konnte eine deutlich erhöhte Aufnahme von gasförmigem CO_2 im Vergleich zum un- oder anders funktionalisierten DUT-5-Derivaten beobachtet werden. Eine zu MIL-53 analoge Struktur konnte ebenfalls ausgehend

von H_2TDC hergestellt werden. Al-MIL-53-TDC ist das erste Beispiel eines MIL-53 Derivats, das einen S-haltigen Heteroaromaten enthält. Das Material zeigt eine für ein MIL-53-Derivat hohe Aufnahmekapazität für H_2 Gas von 2.1 wt% (vgl. Al-MIL-53 1.66 wt%) und H_2O-Dampfsorptionsmessungen zeigen Potential für mögliche Anwendungen im Bereich von Wärmeaustauschprozessen. Die Einführung der sterisch sehr anspruchsvollen Sulfonsäuregruppen wurde über eine Synthese realisiert, in der Mischungen unterschiedlich funktionalisierter Linkermoleküle eingesetzt wurden. Dadurch konnten in den bereits bekannten Verbindungen CAU-10-H, -NO_2 und -OH die entsprechenden Isophthalationen partiell durch Sulfo-Isophthalationen ersetzt werden. Die Struktur von CAU-10 enthält im Gegensatz zu den bis hierhin angeführten Verbindungen Ketten aus *cis* eckenverknüpften AlO_6-Polyedern, wodurch sich eindimensionale Helices ausbilden. Der Einbau stark polarer -SO_3H Gruppen hat einen massiven Einfluss auf die Sorptionseigenschaften und die Hydrophilie der Materialien. Alle Verbindungen weisen eine für sulfonsäurefunktionalisierte Materialien außergewöhnlich hohe thermische Stabilität von bis zu 350 °C auf. Das große Potential diese Verbindungen als kapazitive Feuchtigkeitssensoren konnte aufgezeigt werden und die Verbindung CAU-10-H/-SO_3H wurde erfolgreich für die katalytische Dehydratisierung von Ethanol bei einer Reaktionstemperatur von 300 °C eingesetzt. Funktionelle Gruppen können auch nachträglich über post-synthetische Modifizierungen in ein Material eingebracht werden. Die Aminogruppe der Verbindung CAU-1 $[Al_4(OH)_2(OCH_3)_4(BDC\text{-}NH_2)_3]\cdot nH_2O$ (BDC-NH_2 = Aminotherephthalation) konnte erfolgreich unter Einsatz von Methyl- und 2-Pyridinylsulfonylchlorid zu den entsprechenden Sulfonamiden umgesetzt werden. Das Thiol-funktionalisierte Derivat CAU-1-SH $[Al_4(OH)_4(OCH_3)_2(DMBD)_3]\cdot 8H_2O$ konnte hingegen wieder über isoretikuläre Synthese unter Verwendung von H_2DMBD hergestellt werden.

Synthesis, Characterization and Application of porous Aluminum-MOFs based on Sulfur-containing Linker Molecules

This thesis deals with the synthesis, characterization and potential application of new and isoreticular aluminum based metal-organic frameworks (Al-MOFs) based on sulfur-containing linker molecules. Used were the sulfones 4,4’-sulfonyldibenzoic acid (H_2SDBA), 3,3´,4,4´-diphenylsulfonetetracarboxylic acid dianhydride (DPSDA) and 5,5-dioxo-dibenzo[*b*,*d*]thiophene-3,7-dicarboxylic acid (H_2BPDC-SO_2), 2,5-thiophenedicarboxylic acid (H_2TDC), 5-sulfoisophthalic acid monolithium salt (*m*-H_2BDC-SO_3H) as well as 2,5-dimercapto-1,4-benzenedicarboxylic acid (H_2DMBD). For the discovery as well as the optimization of reaction conditions high-throughput methods were employed. The use of the linker molecules H_2SDBA and DPSDA resulted in the formation of two new sulfone-functionalized microporous compounds, CAU-11 [Al(OH)(SDBA)]·0.25DMF and CAU-12 $[Al_2(OH)_2(DPSTC)(H_2O)_2]\cdot H_2O$, respectively. Both compounds are based on chains of *trans* corner-sharing AlO_6-polyhedra. In the case of CAU-11, the linker molecules connect these chains to build up a two-dimensional layered structure containing a very uncommon permanent interlayer porosity. The use of DPSDA also resulted in the isoreticular compound CAU-11-COOH $[Al(OH)(H_2DPSTC)]\cdot 0.5H_2O$. Therefore, the hydrophobic compound becomes hydrophilic. In CAU-12 $[Al_2(OH)_2(DPSTC)(H_2O)_2]\cdot H_2O$ the inorganic chains are connected to form a three-dimensional structure. Two of the four present carboxylic acid groups coordinate in a bidentate mode and the remaining two only in a monodentate mode. By thermal activation a phase transition is induced. Coordinating water molecules are removed and all carboxylic acid groups fully coordinate. Hence, the compound becomes porous. Furthermore, using H_2BPDC-SO_2 a compound isoreticular to the known material DUT-5 [Al(OH)(BPDC)] (BPDC = 4,4’-biphenyldicarboxylate) could be synthesized, which is structurally related to MIL-53 [Al(OH)(BDC)] (BDC = 1,4-benzenedicarboxylate). DUT-5-SO_2 is based on chains of *trans* corner-sharing AlO_6-polyhedra which are connected by the linker molecules to form a three-dimensional structure with one-dimensional pores. The additional SO_2-groups in this material lead to a strong increase in the sorption capacity for CO_2 compared to the unfunctionalized compound as well as derivatives containing other functionalities. Using H_2TDC another compound structurally related to MIL-53 could by synthesized. Al-MIL-53-TDC is the first example of a MIL-53 analogue based on a S-containing heteroaromatic dicarboxylate molecule. The material shows a higher uptake of hydrogen gas of 2.1 wt% (compared to 1.66 wt% for Al-MIL-53) and water vapor sorption measurement reveal potential for the application in the field

of heat-transformation processes. The incorporation of sterically challenging sulfonic acid groups could be realized by using mixtures of variably functionalized linker molecules. Hence, the respective isophthalate ions in the known compounds CAU-10-H, -NO_2 and -OH could partially be replaced by sulfoisophthalate ions. In contrast to the thitherto named compounds, CAU-10 is based on *cis* corner-sharing AlO_6-octahedra forming one-dimensional helices. The incorporation of such very polar groups has a strong influence on the sorption behavior and the hydrophilic properties of the resulting materials. All compounds show a very high thermal stability for -SO_3H functionalized materials up to 350 °C. The high potential of these materials as capacitive humidity sensors could be demonstrated and the compound CAU-10-H/SO_3H could successfully be used in the catalytic dehydration of ethanol at a reaction temperature of 300°C. To incorporate functional groups it is not always necessary to use the already pre-functionalized linker molecules. By post-synthetic modification reactions using methyl- and 2-pyridinylsulfonyl chloride the -NH_2 groups in CAU-1 $[Al_4(OH)_2(OCH_3)_4(BDC\text{-}NH_2)_3]\cdot nH_2O$ (BDC-NH_2 = aminotherephthalate) could be transformed into the respective sulfonamides. In contrast, the thiol-functionalized derivative CAU-1-SH $[Al_4(OH)_4(OCH_3)_2(DMBD)_3]\cdot 8H_2O$ was again obtained via isoreticular synthesis using H_2DMBD.

Danksagung

An erster Stelle möchte ich meinem Doktorvater Prof. Dr. Norbert Stock für die Betreuung dieser Arbeit meinen Dank aussprechen, für den überlassenen Freiraum, die Geduld und die stete Unterstützung.

Ich bedanke mich natürlich auch bei dem gesamten Arbeitskreis Stock mit all seinen aktuellen und ehemaligen Mitgliedern, die mich während meiner Zeit in wissenschaftlicher und nicht-wissenschaftlicher Weise begleitet haben. Besonderer Dank gilt hier an erster Stelle Selda Halis für neun Jahre gemeinsamen Studiums und den abwechslungsreichen Laboralltag, davon die letzte Zeit auf kleinstem Raum sowie Dr. Helge Reinsch für, was soll ich sagen…so vieles.

Das Gelingen dieser Arbeit war abhängig von vielen Menschen, die unterschiedlichste Beiträge geleistet haben. Gedankt sei an dieser Stelle den Damen der Spektroskopischen Abteilung der Anorganischen Chemie und der NMR-Abteilung in der Organischen Chemie für unzählige Messungen sowie der Werkstatt für ihr stetiges Bemühen, die Technik am Laufen zu halten. Den Mitgliedern des Arbeitskreises Bensch danke ich für die thermogravimetrischen Messungen und besonderer Dank gilt meiner Sorptionskollegin Jana Timm, für eine stets reibungslose und unkomplizierte Zusammenarbeit.

Mein Dank gilt in großem Maße auch meinen Kooperationspartnern für die durchgeführten Messungen und die fruchtbaren Diskussionen. Insbesondere sei hier Bart Bueken (KU Leuven, Belgien) gedankt, für die angenehme Kooperation sowie die freundliche Aufnahme und Betreuung während meiner kurzen Stippvisite im Bereich der Katalyse. Daran angelehnt bedanke ich mich auch bei allen Studenten, die in Form von F-Praktika oder Bachelorarbeiten an den Ergebnissen dieser Arbeit mitgewirkt haben.

Britta Bahn danke ich für ihr stets offenes Ohr für die Probleme, die der Universitätsalltag für Doktoranden so mit sich bringt und die große Stütze, die sie für den Arbeitskreis ist, indem sie einem stets mit Rat und vor allem Tat zur Seite steht.

Zuletzt möchte ich mich von ganzem Herzen bei meiner Familie und meinen Freunden bedanken, die gute und schlechte Zeiten mit mir durchgemacht und mich immer gestützt haben. Ohne Euch wäre diese Arbeit in dieser Form nicht entstanden.

Meinem Papa danke ich einfach für alles!

Inhaltsverzeichnis

Teil I.

Allgemeiner Teil

1 Einleitung

Poröse Materialien sind schon seit langem ein wichtiges Teilgebiet in der akademischen und industriellen Forschung. Da sie nicht nur mit ihrer äußeren, sondern auch mit ihrer (sehr hohen) inneren Oberfläche mit Atomen, Ionen oder Molekülen wechselwirken können liegen klassische Anwendungen im Bereich von Ionenaustausch, Sorption und Katalyse.[1] Man charakterisiert diese Materialien anhand ihrer Porendurchmesser als mikroporös (< 2 nm), mesoporös (2-50 nm) oder makroporös (> 50 nm).[2] Entscheidend für eine erfolgreiche Anwendung in oben angeführten Bereichen ist dabei eine enge Verteilung der Porengrößen und -volumina.

Ein klassischer Vertreter poröser Materialien sind Zeolithe. Dies sind mikroporöse, kristalline Alumosilicate, die aus SiO_4- und AlO_4-Tetraedern aufgebaut sind. Sie kommen natürlich vor, können aber auch in einer hohen strukturellen Vielfalt synthetisch hergestellt werden. Aufgrund ihrer gleichmäßigen Porenstruktur und ihrer hohen thermischen Stabilität haben sie sich in der industriellen Anwendung als Molekularsiebe und Trocknungsmittel sowie im Bereich der Katalyse schon seit langem etabliert. Sie werden ebenso als Ionentauscher eingesetzt, da durch den Austausch von Si^{4+} durch Al^{3+}-Ionen negative Ladungen in der Struktur entstehen, die über Kationen in den Poren ausgeglichen werden.[3]

Stetig neue Anwendungsgebiete stellen jedoch immer höhere Ansprüche an die benötigten Materialien. Eine neue Materialklasse, die sich in den letzten Jahren im Bereich der porösen Materialien entwickelt hat, sind die Metall-Organischen Gerüstverbindungen (MOFs = Metal-Organic Frameworks). Strukturell herausragendes Merkmal von MOFs ist ihr modularer Aufbau aus anorganischen und organischen Baueinheiten zu in der Regel dreidimensionalen Gerüsten. Als anorganische Einheiten können einzelne Metallatome oder Metall-Sauerstoff-Cluster fungieren, ebenso sind eindimensionale Metall-Sauerstoff-Ketten beobachtet worden. Als organische Linkermoleküle werden am häufigsten aromatische Polycarbonsäuren verwendet, welche deprotoniert die Verknüpfung der anorganischen Baueinheiten erwirken. Ebenso können Sulfonsäuren,[4] Phosphonsäuren,[5] oder leicht deprotonierbare Amine[6] als Linker fungieren. Aus diesem modularen Aufbau ergeben sich klar definierte Porengrößen und -eigenschaften, die gezielt auf mögliche Anwendungsbereiche abgestimmt werden können. Im Gegensatz zur Synthese von Zeolithen (tetraedrische

Baueinheiten) ist man bei der Synthese von MOFs aufgrund des modularen Aufbaus theoretisch keinerlei Beschränkungen unterworfen. Es ist eine Vielzahl an Kombinationsmöglichkeiten verschiedenster anorganischer und organischer Komponenten denkbar, die nur durch präparative Grenzen beschränkt wird. So sollten sich einzelne Baueinheiten durch geometrisch ähnliche Einheiten ersetzen lassen und in einer topologisch identischen Struktur resultieren. Dieses Prinzip wird isoretikuläre Synthese genannt.[7, 8] Durch Verwendung verlängerter oder verkürzter Linkermoleküle lassen sich so gezielt Porengrößen und durch Verwendung chemisch zusätzlich funktionalisierter Linker die Poreneigenschaften einstellen. Damit können Sorptionskapazitäten sowie Affinitäten gegenüber bestimmten Adsorptiven beeinflusst werden. Gezielt können auch Eigenschaften wie katalytische Aktivität oder Protonenleitfähigkeit in einem Material hervorgerufen werden, indem zusätzliche saure Gruppen wie z. B. Sulfonsäuren eigeführt werden.[9, 10] Eine weiterführende Synthesemethode zum feineren Einstellen bestimmter Eigenschaften beruht auf der Verwendung von Mischungen unterschiedlicher Linkermoleküle. Man unterscheidet dabei drei unterschiedliche Ansätze.[11] Im sogenannten „isostructural mixed linker“ (IML) Ansatz werden zwei oder mehr unterschiedlich funktionalisierte, aber geometrisch analoge, Linker in ein Gerüst eingebaut. Dieser Ansatz dient zur weiterführenden Funktionalisierung der Porenwände und kann Einfluss auf das Sorptionsverhalten[12, 13] oder die thermische Stabilität eines Materials[14, 15] haben. Der „heterostructural mixed linker“ (HML) Ansatz geht von der Verwendung von Linkermolekülen mit unterschiedlicher Geometrie aus und dient dem Erhalt neuer Gerüsttopologien. Verwendet man zwei Linkermoleküle, von denen eines eine geringere Anzahl an funktionellen Gruppen, die zur Koordination fähig sind, trägt, spricht man von „truncated mixed linker“ (TML) Ansatz. Hierbei dient das zweite Linkermolekül, je nach Kristallisationskinetik, entweder der Beeinflussung der Kristallmorphologie und Oberflächenchemie oder aktiviert die Funktionalisierung im Innern des Gerüstes. Gerade dieses hohe Maß an Modulierbarkeit der Eigenschaften macht die Metall-Organischen Gerüstverbindungen für ein Vielzahl potentieller Anwendungsmöglichkeiten wie z. B im Bereich der Gasspeicherung und -trennung, der Katalyse und Sensorik sowie als optische oder magnetische Materialien so interessant.[16-19]

Die thermische Stabilität von Metall-Organische Gerüstverbindungen ist im Vergleich zu Zeolithen aufgrund ihrer organischen Komponente deutlich niedriger. Innerhalb der MOFs zeichnen sich Al^{3+}-basierte MOFs, die Polycarboxylationen enthalten, jedoch durch eine vergleichsweise hohe thermische als auch chemische Stabilität aus. Die Ausgangsmaterialien zur Herstellung vieler Al-MOFs sind kostengünstig und Aluminium weist nur eine geringer Toxizität aus, was für industrielle Anwendung vorteilhaft ist.[20] Al-MOFs entstehen in der

Regel als mikrokristalline Pulver, was die Strukturaufklärung neuer Materialien erschwert. Die Verwendung hochauflösender Synchrotronstrahlung in Kombination mit immer sensibleren Detektoren führt jedoch zu immer besseren Datensätzen, welche mit leistungsfähigeren Computern und Programmen immer besser verarbeitet werden können. Zudem entwickeln sich immer neue Methoden und Strategien, was die Strukturlösung aus Pulverdaten zwar nicht trivial, aber dennoch möglich macht. Die Strukturchemie von Al^{3+}-Ionen im Wässrigen ist stark abhängig von pH-Wert. Dabei ist der amphotere Charakter der Sauerstoffverbindungen von Al^{3+} ebenfalls zu berücksichtigen. Leicht veränderte Synthesebedingungen können dazu führen, dass ausgehend von denselben Ausgangsmaterialien unterschiedliche Verbindungen entstehen.[21-23] Andersherum können sich bei der Herstellung isoretikulärer Verbindungen die Syntheseparameter so stark unterscheiden, dass diese erst explorativ ermittelt werden müssen.[24, 25] Daher haben sich die Hochdurchsatzmethoden zur Synthese neuer Verbindungen sowie zur isoretikulären Synthese etabliert.[26] Durch Parallelisierung der Reaktionen, Miniaturisierung der Reaktionsgefäße und Automatisierung einzelner Synthese- und Charakterisierungsschritte sind sie ein schnelles und kostengünstiges Werkzeug, um effizient große Parameterräume zu untersuchen und neue Verbindungen zu entdecken sowie Syntheseparameter zu optimieren.

In dieser Arbeit geht es um die Synthese, Charakterisierung und Anwendung aluminiumbasierter MOFs mit schwefelhaltigen Linkermolekülen. Mittels Hochdurchsatzmethoden sollten neue sowie isoretikuläre Verbindungen hergestellt werden. Der Einfluss der schwefelhaltigen Funktionalitäten auf die Eigenschaften der resultierenden Materialien sollte dabei eingehend charakterisiert werden. Zusätzlich zu Änderungen der Sorptionseigenschaften wurden in Kooperation mit anderen Arbeitsgruppen potentielle Anwendungsmöglichkeiten im Bereich der Katalyse, Protonenleitfähigkeit und der Sensorik sowie für Wärmeaustausch-Prozesse getestet.

2 Präparative Methoden

2.1. Solvothermalsynthese

Eine geeignete und wohl etablierte Methode zur Herstellung Metall-Organischer Gerüstverbindungen ist die Solvothermalsynthese. Hierbei werden die Edukte mit einem Lösungsmittel in einem abgeschlossenen Reaktionsgefäß auf Temperaturen oberhalb des Siedepunktes des verwendeten Lösungsmittels erhitzt. In Abhängigkeit der Temperatur und des verwendeten Lösungsmittels können im Reaktionsgefäß sehr hohe Drücke entstehen (autogener Druck), wodurch ein starker Einfluss auf die chemischen und physikalischen Eigenschaften des verwendeten Lösungsmittels ausgeübt wird.[27]

Das Verhalten von Wasser unter solvothermalen Bedingungen, man spricht hierbei von Hydrothermalsynthese, ist weitgehend verstanden. Die Erhöhung von Temperatur und Druck führt zu einer Erhöhung des Ionenprodukts. Man geht davon aus, dass Wasser bei 1000 °C und 150-200 kbar vollständig dissoziiert vorliegt. Mit steigendem Druck steigt die Dielektrizitätskonstante, wobei eine erhöhte Temperatur den gegenteiligen Effekt hervorruft, der auch überwiegt. Die Viskosität nimmt ab, wodurch die Mobilität der Ionen oder Moleküle zunimmt, weshalb sich unter solvothermalen Bedingungen auch schwer lösliche Komponenten zur Reaktion bringen lassen können. Die erhöhte Mobilität führt zusätzlich zu einer guten Durchmischung, weshalb man meist homogene Produkte erhält. Bei einer sehr niedrigen Löslichkeit (unter 2-5 %) der Reaktanden können Mineralisatoren wie Säuren, Basen oder Komplexbildner der Reaktionsmischung hinzugefügt werden.[27]

Die Vorteile der Solvothermalsynthese gegenüber der konventionellen Hochtemperatursynthese liegen darin, dass kinetisch stabile Produkte oder auch Produkte mit unkonventionellen Oxidationsstufen erhalten werden können. Die Reaktionszeit ist gegenüber einer Fest-Fest-Reaktion deutlich vermindert, ebenso die Reaktionstemperatur. Die erhaltenen Produkte sind meist homogen und oft können Einkristalle ausreichender Größe erhalten werden.[27]

Als Reaktionsgefäße wurden in dieser Arbeit Stahlautoklaven mit Einsätzen aus Teflon® verwendet (Abbildung 2.1).

Abbildung 2.1: Stahlautoklav mit Tefloneinsatz mit einem maximalen Füllvolumen von 30 mL.

2.1.1. Mikrowellengestützte Solvothermalsynthese

Seit etwa den 80er Jahren wird in der organischen Synthese neben der konventionellen Heizmethode, das Aufheizen unter Rückfluss mit Hilfe eines Ölbades, auch die mikrowellengestütze Heizmethode verwendet.[28] Hieraus ergaben sich deutlich verkürzte Reaktionszeiten sowie eine deutlich erhöhte Ausbeute und Reinheit der Reaktionsprodukte und eine erhöhte Reproduzierbarkeit.[29] Aufgrund dieser Vorteile, hat sich auch in der anorganischen Chemie die mikrowellengestützte Solvothermalsynthese zur Herstellung poröser Materialien[30-32] oder Nanopartikeln[33, 34] etabliert.

Mikrowellenstrahlung ist elektromagnetische Strahlung in einem Frequenzbereich von 0.3 bis 300 GHz. Haushaltsübliche Mikrowellenöfen arbeiten ebenso wie die Geräte, die in der Forschung eingesetzt werden, bei einer Frequenz von 2.45 GHz, um keinerlei Störungen in Telekommunikation oder Radar hervorzurufen. Die Energieübertragung beim Mikrowellenheizen beruht auf dem Prinzip des dielektrischen Heizens. Die elektrische Komponente des elektromagnetischen Feldes wechselwirkt mit dem Reaktionsgemisch durch dipolare Polarisierung und Ionenleitung. Die Moleküle oder Ionen richten sich gemäß dem angelegten Feld aus und wenn dieses zu oszillieren beginnt bewegen sich die Teilchen mit. Die Bewegung induziert Molekularreibung und Dielektrizitätsverlust, wodurch Energie in Form von Wärme freigesetzt wird. Die Reaktionsmischung wärmt sich in diesem Fall von innen auf, im Gegensatz zu konventionellen Heizmethoden, bei denen die Wärmezufuhr von außen stattfindet. Ob und wieviel Wärme durch Mikrowellenstrahlung erzeugt werden kann ist abhängig von den dielektrischen Eigenschaften eines Stoffes. Man definiert diese Eigenschaft über den Verlustfaktor tan δ. Dieser Faktor berechnet sich als der Quotient $\tan \delta = \varepsilon''/\varepsilon'$, wobei ε'' den Dielektrizitätsverlust, also die Effizient der Umwandlung von Mikrowellenstrahlung in

Wärme und ε´ die Dielektrizitätskonstante, also die Polarisierbarkeit im elektrischen Feld, beschreibt. Je größer der Verlustfaktor umso schneller lässt sich ein Stoff aufheizen.[29]

Gerade die starke Beschleunigung einer Mikrowellenreaktion gegenüber einer Reaktion mit konventionellem Heizen hat zu einer intensiven Diskussion eventueller nicht-thermischer Mikrowelleneffekte geführt. Dies konnte bis dato jedoch nicht eindeutig bestätigt werden. Das Problem beim Vergleich einer Reaktion mit mikrowellengestützem Heizen und konventionellem Heizen ist die Temperaturkontrolle. Die kommerziell erhältlichen Mikrowellenöfen besitzen meist einen IR-Sensor der von außen die Temperatur des Reaktionsgefäßes misst. Bei Synthesen in einem Ölbad beispielsweise, entspricht die im Ölbad gemessene Temperatur der Temperatur des Reaktionsgemisches im Inneren des Reaktionsgefäßes. Die tatsächliche Temperatur innerhalb eines Mikrowellenreaktors könnte viel höher sein, als die von außen gemessene und dadurch deutlich unterschätzt werden.[35]

Die in dieser Arbeit durchgeführten mikrowellengestützten Synthesen wurden mit einem Mikrowellofen Initiator® der Firma Biotage durchgeführt. Dabei wurden dickwandige Glasreaktoren verwendet, welche mit einem Teflonseptum und einer Bördelkappe aus Aluminium verschlossen wurden. Die einzelnen Komponenten sind in Abbildung 2.2 dargestellt. Das Gerät ist mit einem externen IR-Sensor ausgestattet und erlaubt Reaktionen bei Drücken bis zu 20 bar.

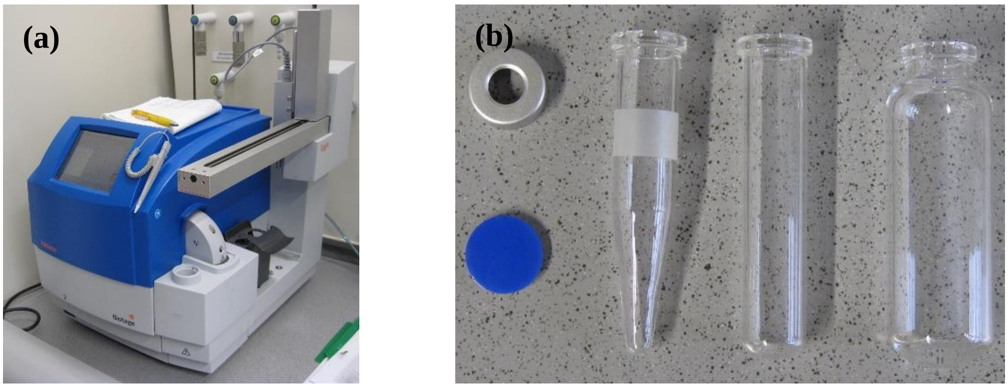

Abbildung 2.2: (a) Mikrowellenofen Initiator von Biotage. (b) Mikrowellengefäße aus Glas mit Septum und Bördelkappe. Die Reaktionsvolumina betragen 0.5-2 mL, 2-5 mL und 10-20 mL von links nach rechts.

2.1.2. Hochdurchsatzmethoden in der Solvothermalsynthese

Da eine Vielzahl chemischer sowie physikalischer Parameter Einfluss auf die Produktbildung bei einer Solvothermalsynthese nehmen kann, haben sich die Hochdurchsatzmethoden in diesem Bereich als ein effizientes Werkzeug etabliert. Das Prinzip der Hochdurchsatzmethodik beruht auf der Parallelisierung, Miniaturisierung und Automatisierung. Bezogen auf

Solvothermalsynthesen bedeutet dies die gleichzeitige Durchführung mehrere Einzelreaktionen, welche unter geringem Einsatz an Edukten durchgeführt wird, wobei versucht wird ein Großteil der Arbeitsschritte zu automatisieren.

Der typische Arbeitsablauf einer Hochduchsatzsynthese gliedert sich in verschiedene Abschnitte (Abbildung 2.3). Begonnen wird mit der ausführlichen Syntheseplanung. Auf diese folgt das Dosieren der Edukte, was unter Zuhilfenahme eines Pipettierroboters teilautomatisiert werden kann, in einen geeigneten Hochdurchsatzreaktor. Dieser sogenannte Multiklav wird dann verschlossen und einem definierten Temperatur-Zeit-Programm unterworfen. Die Produktisolierung kann mit Hilfe einer speziellen Filtriervorrichtung teilautomatisiert durchgeführt werden, um die einzelnen Proben im Anschluss mittels Röntgenpulverbeugung vollautomatisiert zu charakterisieren. Nach abschließender Datenevaluation kann dann ein neues Experiment geplant werden.

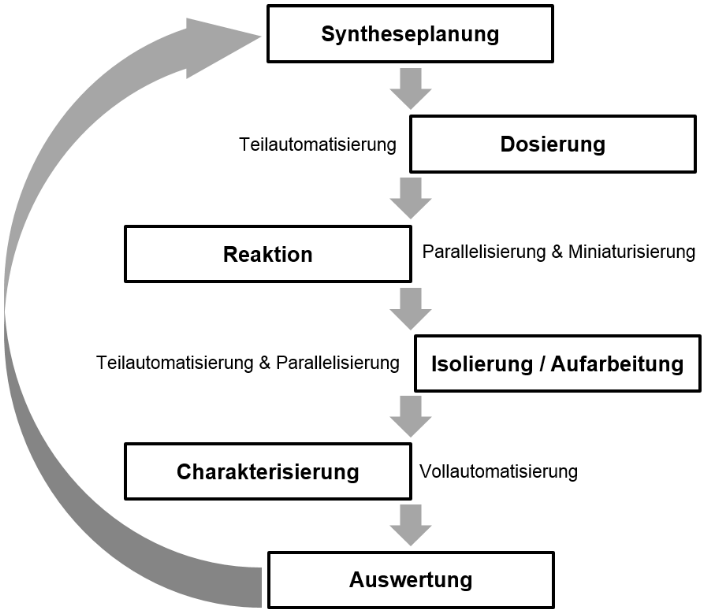

Abbildung 2.3: Schematische Darstellung des Arbeitsablaufes einer Hochdurchsatzuntersuchung.

Aus dieser Methodik ergeben sich zahlreiche Vorteile. Dadurch, dass pro Einzelreaktion nur eine minimale Menge an Chemikalien verbraucht wird, können systematische Untersuchungen auch unter Verwendung schwer zugänglicher oder teuer Edukte durchgeführt werden. Die Parallelisierung führt zu einer höheren Reproduzierbarkeit und einer erheblichen Zeitersparnis. Dies ergibt sich ebenso aus der Automatisierung, welche zusätzlich auch eine Verminderung menschlicher Fehler bewirkt. Nachteilig sind jedoch die hohen Anfangsinvestitionen, die getätigt werden müssen um die Methodik zu etablieren. Ebenso führt eine unüberlegte Syntheseplanung schnell zu unnötigen Mengen an „Datenmüll“. Abschließend ist zu erwähnen, dass sich nicht jede optimierte Synthese problemlos aufskalieren lässt, was bei den doch recht geringen Mengen an Probe zu Problemen bei der vollständigen Charakterisierung führen kann.[36]

Die in dieser Arbeit durchgeführten Hochdurchsatzsynthesen wurden zum einen unter konventionellem sowie unter mikrowellengestütztem Heizen durchgeführt. Für die konventionelle Synthese wurden speziell angefertigte 24er-Stahlmultiklaven verwendet. Diese Reaktoren besitzen Aussparungen für 24 Tefloneinsätze mit einem maximalen Füllvolumen von 2 mL. Die Einsätze werden mit Teflonfolie abgedeckt und zwischen zwei Stahlträgern mit Druckstempeln dicht verschlossen (Abbildung 2.4).

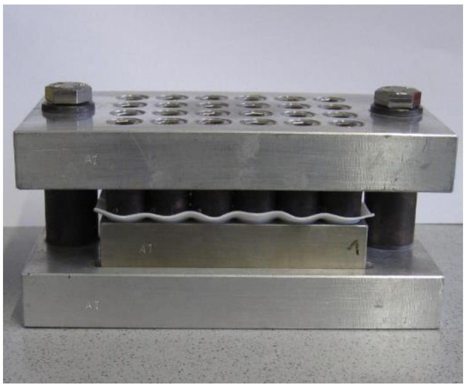

Abbildung 2.4: 24er-Stahlmultiklav für die Hochdurchsatzsynthese im Ofen.

Die mikrowellengestützten Synthesen wurden in einem Hochdurchsatz-Mikrowellenofen Synthos3000® der Firma Anton Paar durchgeführt. Für diesen Mikrowellenofen sind zwei verschiedene Reaktoren verfügbar. Für Reaktionen in Glasreaktoren stehen Siliciumcarbidblöcke mit 24 Aussparungen zur Verfügung. Die einzelnen Glasreaktoren weisen ein maximales Füllvolumen von 3 mL auf und werden einzeln mit Hilfe eines Teflonseptums und einer Schraupkappe verschlossen. Die einzelnen Komponenten sind in Abbildung 2.5 dargestellt.

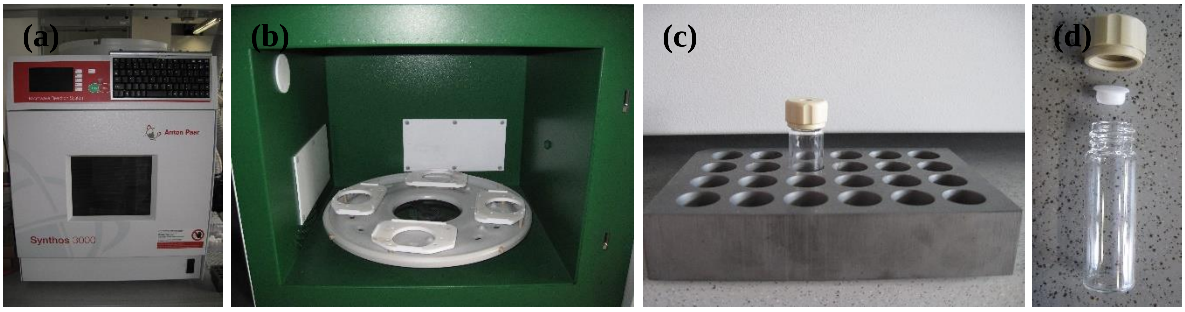

Abbildung 2.5: (a) HD-Mikrowellenofen Synthos3000 von Anton Paar. (b) Innenansicht mit Drehteller für die SiC-Blöcke. (c) SiC-Block mit einem verschlossenen Reaktionsgefäß. (d) Einzelne Bestandteile eines Reaktionsgefäßes.

Für Synthesen in Teflonreaktoren werden speziell angefertigte Tefloneinsätze mit einem maximalen Füllvolumen von 2.5 mL verwendet. Diese werden mit einer speziellen Halterung in die Siliciumcarbidblöcke gesetzt, mit Teflon- und Silikonfolien abgedichtet und zwischen zwei Platten festgeschraubt. Das Heizen der einzelnen Reaktoren erfolgt indirekt über die Siliciumcarbidblöcke (Abbildung 2.6). Die Temperaturkontrolle erfolgt über einen eingebauten IR-Sensor.

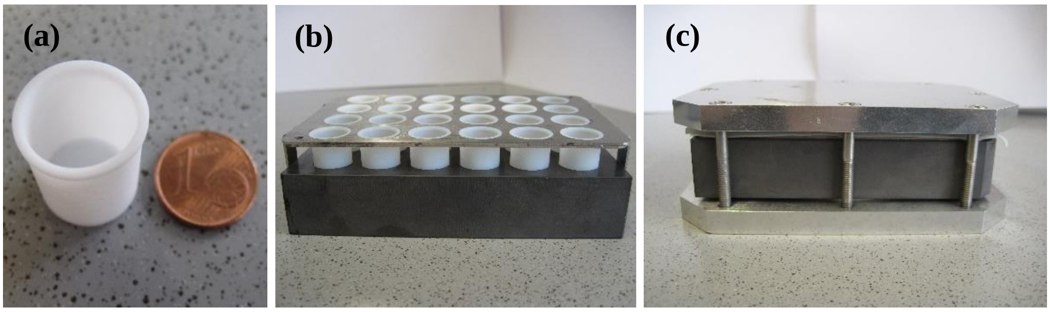

Abbildung 2.6: (a) Einzelner Tefloneinsatz für die HD-Mikrowelle. (b) SiC-Block bestückt mit 24 Tefloneinsätzen. (c) Kompletter Reaktorblock für die HD-Mikrowelle mit Tefloneinsätzen.

3 Charakterisierungsmethoden

In dieser Arbeit wurde eine Vielzahl unterschiedlichster Methoden zur detaillierten Charakterisierung der hergestellten Verbindungen verwendet. Eine Übersicht über die verwendeten Geräte mit entsprechenden Spezifikationen ist in Tabelle 3.1 aufgeführt. Im Detail soll im Folgenden nur die Röntgenpulverbeugung als Mittel der Strukturaufklärung besprochen werden. Die Verarbeitung der im Rahmen dieser Arbeit erhaltenen Daten wurde unter Zuhilfenahme verschiedener Computerprogramme durchgeführt, welche in Tabelle 3.2 aufgeführt sind. In der Regel wurden mehrere Programme kombiniert, um eine erfolgreiche Charakterisierung durchzuführen.

Tabelle 3.1: In dieser Arbeit am häufigsten verwendete Charakterisierungsmethoden.

Methode	Gerätetyp	Anmerkung
Pulverdiffraktometrie	STOE StadiP Kombi	$CuK_{\alpha 1}$-Strahlung, Transmissionsgeometrie, Image Plate Detektor, xy-Probentisch
	STOE StadiP	$CuK_{\alpha 1}$-Strahlung, Transmissionsgeometrie, Mythen Detektor
	MS-POWDER beamline (X04SA) EH1 at Swiss Light Source, PSI	Kapillarmessung, Transmissionsgeometrie, 1.000009 Å, Mythen II Detektor
Thermogravimetrie / Differenzthermoanalyse	NETSCH STA 409 CD	Korundtiegel, Luftatmosphäre (75 mL/min), Heizrate 4 K/min
CHNS Analyse	Eurovektor EuroEA	
FT-IR Spektroskopie	Bruker ALPHA-FT-IR A220/D-01	4000-450 cm^{-1}, ATR Einheit
Raman Spektroskopie	Bruker IFS 66 FRA 106	0-3300 cm^{-1}, Nd/YAG Laser
NMR Spektroskopie	Bruker DRX500	^1H-NMR Messungen in Lösung
Volumetrische Gasadsorption	BEL JAPAN INC. $Belsorp_{max}$	N_2, H_2, CO_2, CH_4 und H_2O Sorptionsmessungen bis 1 bar

Tabelle 3.2: In dieser Arbeit am häufigsten verwendete Computerprogramme.

Programm	**Verwendung**
Stoe WinXPow[37]	Graphische Darstellung von Pulverdiffraktogrammen, Konvertierung von Pulverdiffraktogrammen in andere Dateiformate
Topas Academics 4.1[38]	Indizierung, Verfeinerung von Zellparametern mit Pawley- und LeBail-Methoden, Strukturverfeinerung mit Rietveld-Methode
FOX[39, 40]	Strukturlösung mit Realraummethoden
Materials Studio 5.0[41]	Erstellen von Strukturmodellen, Geometrieoptimierung von Zellinhalten
Diamond[42]	Graphische Darstellung von Strukturen
Platon[43]	Berechnung theoretischer Porenvolumina, Konvertierung von Zellparametern

3.1. Röntgenbeugung

Ein Kristall ist ein homogener Festkörper, der dreidimensional translationsperiodisch aufgebaut ist. Wechselwirken Kristalle mit elektromagnetischer Strahlung so wirken sie wie ein optisches Gitter. Dabei wird die einfallende Strahlung an den Elektronenhüllen der Atome gebeugt. Die kleinste Wiederholeinheit im Kristall wird als Elementarzelle bezeichnet und ihre Geometrie wird über die Zellparameter a, b, c und α, β, γ definiert. Die Anordnung der in ihr befindlichen Atome wird modellhaft mit Hilfe von virtuellen Netzebenen dargestellt. Die Orientierung einer Netzebene im Kristall wird über die sogenannten Miller'sche Indices (*hkl*) angegeben. Zu jeder Ebene gibt es eine Schar paralleler Ebenen mit dem jeweiligen Netzebenenabstand d. Da sich dieser Abstand im Å-Bereich bewegt, wird für Beugungsexperimente an Kristallen Röntgenstrahlung verwendet. In Abbildung 3.1 ist schematisch dargestellt, wie zwei Röntgenstrahlen auf zwei parallele Netzebenen treffen und gebeugt werden.

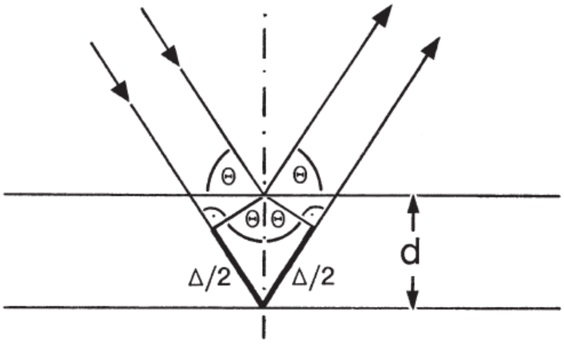

Abbildung 3.1: Beugung an zwei Netzebenen. Ableitung der Bragg'schen Gleichung.[44]

Es ist zu erkennen, dass beide Strahlen einen unterschiedlich langen Weg durch den Kristall zurücklegen (Gangunterschied Δ) und entsprechend miteinander interferieren. Über einfache trigonometrische Zusammenhänge lässt sich hieraus die Bragg'sche Gleichung (Gleichung 3.1) ableiten, welche den Zusammenhang zwischen der Wellenlänge λ, dem Beugungswinkel θ und dem Netzebenenabstand d wiedergibt.

$$n\lambda = 2d \sin\theta \tag{3.1}$$

Wenn der Gangunterschied Δ nun ein ganzzahliges Vielfaches der Wellenlänge λ ist, kommt es zu konstruktiver Interferenz und im Beugungsbild ist ein Reflex zu erkennen. Andernfalls kommt es zu destruktiver Interferenz. Die Intensität eines Reflexes kann durch

Integration aus einem Beugungsexperiment gewonnen werden und ist proportional zum Betragsquadrat der Strukturfaktors (3.2).

$$I \propto |F_{hkl}|^2 \tag{3.2}$$

Der Strukturfaktor wird über die Strukturfaktorgleichung definiert, welche die Intensität des gemessenen Reflexes einer bestimmten Netzebene (*hkl*) mit der Lage aller Atome (x, y, z) in der Elementarzelle relativ zum Nullpunkt verknüpft (3.3).

$$F_{hkl} = \sum_{hkl,i} f_i [\cos 2\pi(hx_i + ky_i + lz_i) + i \sin 2\pi(hx_i + ky_i + lz_i)] \tag{3.3}$$

Ebenfalls in der Strukturfaktorgleichung enthalten ist der Atomformfaktor f_i. Dieser berücksichtigt die Abhängigkeit der Streukraft von der Anzahl der Elektronen der streuenden Atomsorte sowie vom Beugungswinkel θ. Experimentell zugänglich sind aus Beugungsexperimenten nun lediglich die absoluten Werte der Strukturamplituden der einzelnen Reflexe. Das Vorzeichen und somit die Phasenbeziehung der gebeugten Röntgenstrahlung geht verloren, die jedoch benötigt wird, um die Elektronendichteverteilung (3.4) und somit die Lage der Atome zu beschreiben. Dies wird allgemein als das Phasenproblem bezeichnet.[44]

$$\rho_{hkl} = \frac{1}{V} \sum_{hkl} |F_{hkl}^{obs}| \cos[2\pi(hx + ky + lz) - \alpha_{hkl}] \tag{3.4}$$

V steht hierbei für das Volumen der Elementarzelle und α_{hkl} für die Phase.

3.2. Strukturlösung mittels Röntgenpulverbeugung

Bestrahlt man einen makroskopischen Einkristall mit Röntgenstrahlung und detektiert den gebeugten Strahl so werden diskrete Beugungsmaxima beobachtet. Bei der Röntgenpulverbeugung wird eine unendliche Anzahl mikrokristalliner Kristallite vermessen wodurch im Beugungsbild keine diskreten Reflexe beobachtet werden sondern so genannte Debye-Scherrer-Ringe, da jeder Kristall eigene Reflexe verursacht die anders zueinander im Raum orientiert sind (Abbildung 3.2).

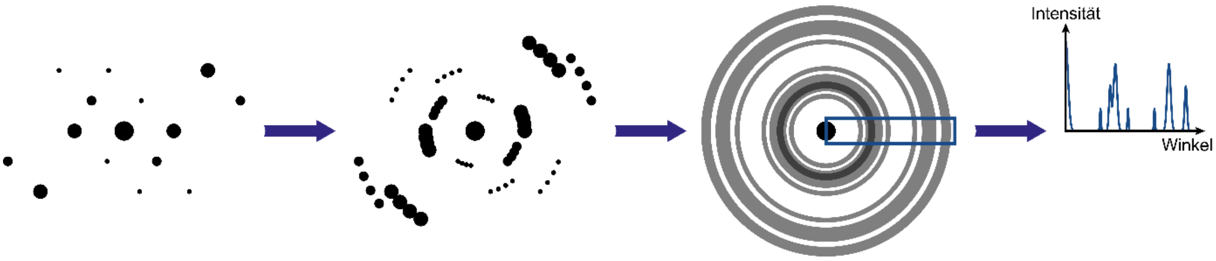

Abbildung 3.2: Überlagerung von Beugungsbildern einzelner Kristalle zu Debye-Scherrer-Ringen. Ein Pulverdiffraktogramm stellt dabei einen Schnitt durch diese Ringe dar.[45]

Das eigentliche Pulverdiffraktogramm ist ein Schnitt durch diese Ringe. Daraus resultierend kommt es zu einer Überlagerung vieler Reflexe, was den Informationsgehalt eines Pulverdiffraktogramms stark minimiert. Die Röntgenpulverdiffraktometrie ist eine Standardmethode zur Phasenidentifizierung und -analyse und trotz des geringen Informationsgehaltes ist es möglich Strukturen aus Röntgenpulverdaten zu ermitteln. Entscheidend ist hierbei die Qualität des gemessenen Pulverdiffraktogramms und im Folgenden sollen die einzelnen Schritte einer Strukturlösung aus Pulverdaten erläutert werden.

3.2.1. Indizierung und Zellverfeinerung

Der erste Schritt, um die Struktur einer unbekannten Verbindung zu lösen ist zunächst die Indizierung des gemessenen Pulverdiffraktogrammes. Indizierung bedeutet die Zuordnung der ermittelten *d*-Werte zu den *hkl*-Werten der entsprechenden Netzebenen. Dies geschieht mit Hilfe der quadratischen Bragg'schen Gleichung. Für eine kubische Elementarzelle gilt $a = b = c$ und $\alpha = \beta = \gamma = 90°$. Daraus ergibt sich für die quadratische Bragg'sche Gleichung folgender Ausdruck:

$$^1/_{d^2} = [h^2 + k^2 + l^2]/a^2 \tag{3.5}$$

Werden also nur Reflexe beobachtet, die Gleichung 3.5 erfüllen, so ist das Pulverdiffraktogramm kubisch indiziert. Zentrierungen sowie translatorische Symmetrieelemente, die eine Elementarzelle aufweist, führen zu systematische Auslöschungen in einem Pulverdiffraktogramm. Das heißt, bestimmte Reflexe, die laut Kristallsystem erlaubt sind, werden nicht beobachtet, weil sie keine Intensität aufweisen. Neben der Zellmetrik lassen sich hieraus nun erste Annahmen für eine mögliche Raumgruppe bzw. eine Auslöschungsgruppe aufstellen. Je niedriger die Symmetrie einer Elementarzelle umso schwieriger wird die Indizierung da immer mehr unbekannte Parameter auftauchen. Für eine monokline Zelle mit vier unbekannten Parametern (*a*, *b*, *c* und *β*) hat die quadratische Bragg’sche Gleichung bereits die Form:

$$1/_{d^2} = \frac{h^2}{a^2 \sin^2 \beta} + \frac{k^2}{b^2} + \frac{l^2}{c^2 \sin^2 \beta} - \frac{2hl \cos \beta}{ac \sin^2 \beta} \tag{3.6}$$

Daher wurden verschiedene Algorithmen entwickelt und in unterschiedliche Computerprogramme implementiert, um Indizierungen von Pulverdiffraktogrammen durchzuführen.[44]

Um die aus der Indizierung erhaltenen Zellparameter zu präzisieren, wird eine Verfeinerung auf Basis der Methode der kleinsten Fehlerquadrate durchgeführt. Dabei werden die Zellparameter iterativ verändert, bis die quadrierte Abweichung der beobachteten Werte im Vergleich zu den theoretisch Idealwerten ein Minimum erreicht (Gleichung 3.7).

$$\sum_i (d_i^{obs} - d_i^{calc})^2 = minimum \tag{3.7}$$

Die Pawley und LeBail-Methode berücksichtigen zusätzlich bei der Verfeinerung auch das Profil des gemessenen Pulverdiffraktogramms. Neben den Reflexlagen werden somit auch Nullpunktsverschiebungen, anisotrope Reflexformen sowie Textureffekte mit einbezogen. Man bezeichnet dies als „full pattern deconvolution“.[46] Während der Verfeinerung werden die Reflexintensitäten extrahiert und können für eine spätere Strukturlösung oder -verfeinerung verwendet werden. Die Qualität einer Verfeinerung kann optisch über den Vergleich des gemessenen und berechneten Diffraktogramms sowie über verschiedene Gütekriterien beurteilt werden. Ein gebräuchlicher Faktor für die Güte der Profilanpassung ist der R_{wp}-Wert:

$$R_{wp} = \left[\frac{\sum_{i=1}^{n} w_i (Y_i^{obs} - Y_i^{calc})^2}{\sum_{i=1}^{n} w_i (Y_i^{obs})^2}\right]^{1/2} \tag{3.8}$$

Dabei ist w_i ein Wichtungsfaktor, der die Genauigkeit der gemessenen Intensität angibt und Y_i^{obs} und Y_i^{calc} geben die gemessenen und berechneten Intensitäten am Punkt *i* an. Im Idealfall sollte dieser Wert somit gegen Null gehen.

Ein zweiter wichtiger Gütefaktor ist der *GoF* (*Goodness of Fit*). Dieser wird über Gleichung 3.9 berechnet und berücksichtigt die Anzahl der gemessenen Punkte *n* und die Anzahl der verfeinerten Parameter *p* (Zellparameter, Nullpunktsverschiebung etc.). Im Idealfall sollte dieser Wert gegen 1 gehen.[46]

$$GoF = \frac{\sum_{i=1}^{n} w_i (Y_i^{obs} - Y_i^{calc})^2}{n-p} \tag{3.9}$$

3.2.2. Strukturlösung und Strukturverfeinerung

Ein Beugungsbild lässt sich als Fouriertransformierte der Elektronendichte in einem Kristall verstehen. Über Gleichung 3.4 ließe sich theoretisch an jeden Punkt *xyz* in einem Kristall die Elektronendichte bestimmen, gäbe es nicht das sogenannte Phasenproblem. Die direkten Methoden versuchen dieses Problem zu lösen, indem sie die Tatsache ausnutzen, dass die Phasen bestimmter Reflexgruppen, sogenannte Reflextripletts, mit einer bestimmten Wahrscheinlichkeit voneinander abgeleitet werden können. Zusätzlich kommt bei Röntgenpulverbeugung das Problem der Reflexüberlappung zu tragen, da das Beugungsbild eines Pulvers eindimensional ist im Gegensatz zum dreidimensionalen Beugungsbild eines Einkristalls. Reflexe mit ähnlichen d-Werten überlappen und erschweren damit die Zuordnung der dazugehörigen Netzebenen.[44]

Einen anderen Ansatz verfolgen die sogenannten Realraummethoden. Sie umgehen das Problem der Reflexüberlappung, da für diesen Lösungsansatz keine Intensitäten der einzelnen Reflexe benötigt werden. Das experimentelle Pulverdiffraktogramm an sich ist hier die Zielvorgabe einer globalen Optimierung. Bei Kenntnis von Summenformel, Zellparametern und Raumgruppe generieren Computerprogramme wie FOX[39] eine zufällige Struktur. Die Lage der Atome wird schrittweise und zufällig so lange geändert, bis die Abweichung des korrespondierenden theoretischen Pulverdiffraktogramms minimalst vom experimentellen abweicht. Diese Methode erfordert einen hohen Rechenaufwand, daher ist die Kenntnis von Fragmenten die sich in einer Struktur befinden von Vorteil. Im Falle der MOFs wären dies die Linkermoleküle sowie die anorganischen Baueinheiten, die als starre Körper bewegt werden können.[47]

Mit Hilfe von Kraftfeldrechnungen lassen sich auch Strukturmodelle isoretikulärer Verbindungen basierend auf bereits bekannten Verbindungen erstellen.[48, 49] Durch den modularen Aufbau von MOFs lassen sich leicht einzelne Bauteile durch strukturell ähnliche ersetzen, ein Linkermolekül kann durch ein längeres oder kürzeres ausgetauscht werden oder eine zusätzliche funktionelle Gruppe wird eingefügt. Die erhaltene hypothetische Struktur kann dann mittels Kraftfeldrechnungen, die in Programmen wie Materials Studio[41] implementiert sind, geometrisch optimiert werden. Von Vorteil ist hier, wenn die Gitterparameter der isoretikulären Verbindung bereits aus einer Indizierung bekannt sind.

Die eben beschriebenen Methoden dienen allein der Erstellung eines geeigneten Strukturmodells. Eine Strukturaufklärung kann erst dann als abgeschlossen angesehen werden, wenn das ermittelte Strukturmodell mit ausreichender Übereinstimmung an die experimentell gewonnenen Messdaten angepasst wurde. Die am häufigsten Verwendete Methode ist die Rietveld-Methode. Hierbei werden wie bei der Pawley- oder LeBail-Methode die Profilvariablen und Gitterparameter gegen das experimentelle Pulverdiffraktogramm verfeinert. Zusätzlich werden aber auch noch die Positionen der Atome in der Elementarzelle, Besetzungsfaktoren und thermische Auslenkungsparameter angepasst. Neben dem bereits bekannten R_{wp}-Wert und dem *GoF* wir bei der Rietveld-Verfeinerung noch der R_{Bragg}-Wert als Gütefaktor bewertet (Gleichung 3.10). Dieser spiegelt den Grad der Übereinstimmung der experimentell ermittelten Intensitäten mit den theoretisch berechneten an jedem Messpunkt ($j = 1\text{-}m$) wieder.[46]

$$\mathrm{R}_{\mathrm{Bragg}} = \frac{\sum_{j=1}^{m}\left|I_j^{obs} - I_j^{calc}\right|}{\sum_{j=1}^{m} I_j^{obs}} \tag{3.10}$$

Teil II.

Kumulativer Hauptteil

4 Synthese, Charakterisierung und Anwendung poröser Aluminium-MOFs auf Basis schwefelhaltiger Linkermoleküle

In dieser Arbeit geht es zum einen um die Herstellung neuer poröser Al-MOFs, wobei der Einfluss der Geometrie des verwendeten Linkermoleküls auf die Strukturbildung untersucht werden sollte. Zum anderen wurden isoretikuläre Verbindungen zu bereits bekannten Strukturen hergestellt, um deren Eigenschaften gezielt zu beeinflussen. Allen in dieser Arbeit verwendeten Linkermolekülen ist gemein, dass sie eine schwefelhaltige funktionelle Gruppe tragen. Diese beeinflusst die Geometrie sowie die Eigenschaften der entsprechenden Linkermoleküle. Verwendet man anstelle von Terephthalsäure zum Beispiel 2,5-Thiophendiarbonsäure, verringert sich der Winkel, den die Carbonsäuregruppen zueinander einnehmen von 180° auf 148°, was Einfluss auf die Strukturbildung eines neuen MOFs nehmen kann. Zusätzlich ändert sich die Polarität des Linkermoleküls durch das zusätzliche Schwefelatom und kann damit die Eigenschaften des erhaltenen Materials beeinflussen. Im Folgenden soll daher zunächst ein Überblick über die bisher bekannte Strukturchemie poröser Al-MOFs und in einem zweiten Abschnitt ein Einblick in bereits bekannte MOFs mit schwefelhaltigen Linkermolekülen und deren Eigenschaften bzw. Anwendungsmöglichkeiten gegeben werden.

4.1. Poröse Aluminium-MOFs

Aluminium-MOFs haben in den letzten Jahren ein großes akademisches und industrielles Interesse geweckt. Dies ist bedingt durch ihre hohe chemische und thermische Stabilität, ihre Unempfindlichkeit gegenüber Hydrolyse und die geringen Kosten der meist kommerziell verfügbaren Ausgangsmaterialien. Zudem weisen die meisten Al-MOFs eine brauchbare permanente Porosität auf, die ihnen potentiell Anwendung in den Bereichen von Gasspeicherung und -trennung, Katalyse, Sensorik und Wärmeaustauschprozessen ermöglicht.

Obwohl die Strukturaufklärung neuer Verbindungen nicht einfach ist, da Al-MOFs in der Regel als mikrokristalline Pulver erhalten werden, sind bereits eine Vielzahl unterschiedlicher Strukturen bekannt. Diese konnten entweder aus Röntgenpulverdaten gelöst werden, oder aber mit Hilfe der Struktur bekannter isoretikulärer Verbindungen. In allen bisher beschriebenen Al-MOFs findet man AlO_6-Polyeder als kleinste Baueinheit, die sich in Abhängigkeit der gewählten Syntheseparameter und verwendeten Linkermolekülen zu unterschiedlichen anorganischen Strukturmotiven zusammensetzen können. Eine Übersicht über die bis dato bekannten anorganischen Baueinheiten ist in Abbildung 4.1 gegeben.

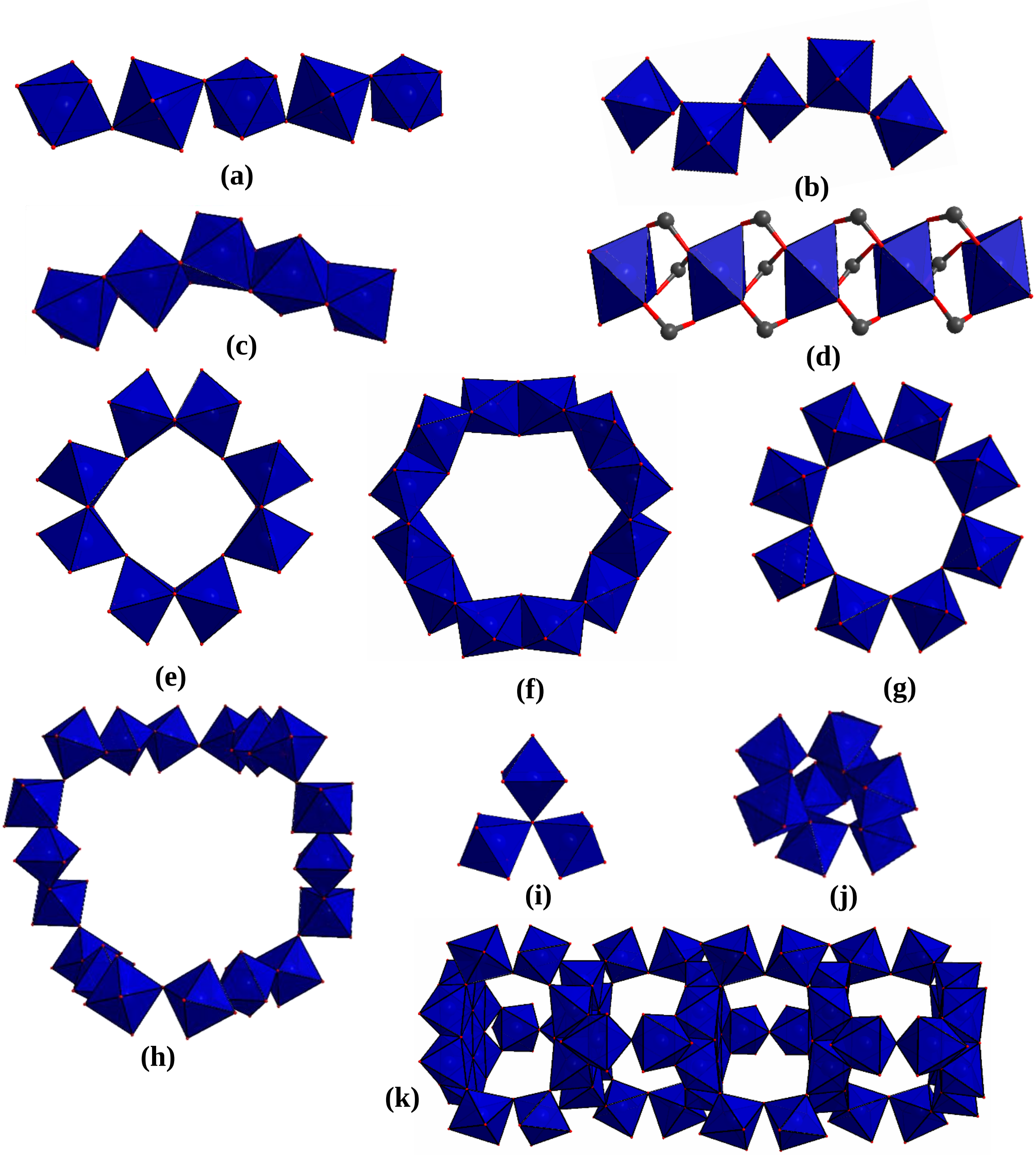

Abbildung 4.1: Anorganische Baueinheiten in Al-MOFs. (a) Zickzackketten *trans* eckenverknüpfter Oktaeder; (b) Helices *cis* eckenverknüpfter Oktaeder; (c) Ketten kantenverknüpfter Oktaeder; (d) Ketten isolierter Oktaeder; (e) Achterring aus eckenverknüpften Dimeren, (f) Zwölferring; (g) Achterring eckenverknüpfter Oktaeder; (h) 18-gliedriger Ring; (i) Trimer; (j) Cluster aus acht Okatedern; (k) Säule aus 13-kernigen Clustern.

In Kombination mit verschiedensten Di-, Tri und Tetracarbonsäuren ergibt sich daraus eine Vielzahl unterschiedlichster Gerüste, die in Tabelle 4.1 zusammengefasst sind.

Tabelle 4.1: Übersicht über die bis dato bekannten Al-MOFs.(Stand: März 2015)

Name	**Zusammensetzung des Gerüsts**	**Anorganische Baueinheit***
MIL-53[50]	[Al(OH)(BDC)]	(a)
MIL-121[51]	[Al(OH)(H_2BTEC)]	(a)
MIL-122[52]	[$Al_2(OH)_2$(1,4,5,8-NDC)]	(a)
MIL-118A[53]	[$Al_2(OH)_2(H_2O)_2$(BTEC)]	(a)
MIL-118B/C[53]	[$Al_2(OH)_2$(BTEC)]	(a)
Al-PMOF[54]	[$Al_2(OH)_2$(TCPP)]	(a)
Al-1,4-NDC[55]	[Al(OH)(1,4-NDC)]	(a)
MIL-69[56]	[Al(OH)(2,6-NDC)]	(a)
DUT-4[57]	[Al(OH)(2,6-NDC)]	(a)
DUT-5[57]	[Al(OH)(BPDC)]	(a)
CAU-8[58]	[Al(OH)(O_2C-C_6H_4-C(=O)-C_6H_4-CO_2]	(a)
MOF-253[59]	[Al(OH)(BiPyDC)]	(a)
MIL-129[60]	[Al(OH)(AzBDC)]	(a)
Al-*cis*-CDC[61]	[Al(OH)(*cis*-CDC)]	(a)
CAU-13[61]	[Al(OH)(*trans*-CDC)]	(a)
MIL-53-FA[62]	[Al(OH)(FUM)]	(a)
Basolite A520[62]	[Al(OH)(FUM)]	(a)
CAU-16[63]	[Al(OH)(AlPTC(OH)(H_2O))$_2$]	(a)
CYCU-3[64]	[Al(OH)(SDC)]	(a)
CAU-10[25]	[Al(OH)(1,3-BDC)]	(b)
NOTT-300[65]	[$Al_2(OH)_2$(BPTCA)]	(b)
MIL-120[66]	[$Al_4(OH)_8$(BTEC)]	(c)
CAU-15[67]	[$Al_4(OH)_8$(1,2-BDC)]	(c)
CAU-4[68]	[Al(BTB)]	(d)
CAU-1[69]	[$Al_4(OH)_2(OCH_3)_4$(BDC-NH_2)]	(e)
CAU-3[70]	[$Al_{12}(OCH_3)_{24}(BDC)_6$]	(f)
MOF-519[71]	[$Al_8(OH)_8(BTB)_4(H_2BTB)_4$]	(g)
MOF-520[71]	[$Al_8(OH)_8(BTB)_4(HCOO)_4$]	(g)
MIL-96[21]	[$Al_{12}O(OH)_{18}(H_2O)_3(Al_2(OH)_4)(BTC)_6$]	(h), (i)
MIL-100[22]	[$Al_3O(OH)(H_2O)_2(BTC)_2$]	(i)
MIL-101-NH_2[72]	[$Al_3O(H_2O)_2(OH)$(BDC-NH_2)$_3$]	(i)
MIL-110[23]	[$Al_8(OH)_{12}(OH)_3(H_2O)_3(BTC)_3$]	(j)
CAU-6[73]	[$Al_{13}(OH)_{27}(H_2O)_6$(BDC-NH_2)$_3Cl_6(C_3H_7H)_6$]	(k)

*** Gemäß Abbildung 4.1**

Mit der Entdeckung von MIL-53 wurde im Jahre 2004 der erste Al-MOF veröffentlicht (MIL = Matérieaux de l’Institut Lavoisier).[50] Die Struktur von MIL-53 basiert auf AlO_6-

Polyedern die über μ-OH Gruppen *trans* eckenverknüpft Ketten (Abbildung 4.1, (a)) ausbilden, welche über Terephthalationen zu einem dreidimensionalen Netzwerk, mit eindimensionalen rautenförmigen Kanälen, verknüpft werden. Herausragende Eigenschaft dieser Verbindung ist ihre Flexibilität. Man spricht in diesem Zusammenhang vom sogenannten ‚breathing effect‘, denn je nach Art der eingelagerten Gastmoleküle oder in Abhängigkeit der Temperatur[74] kann sich das Gerüst zusammenziehen oder aufweiten und damit die Porendurchmesser variieren (Abbildung 4.2).

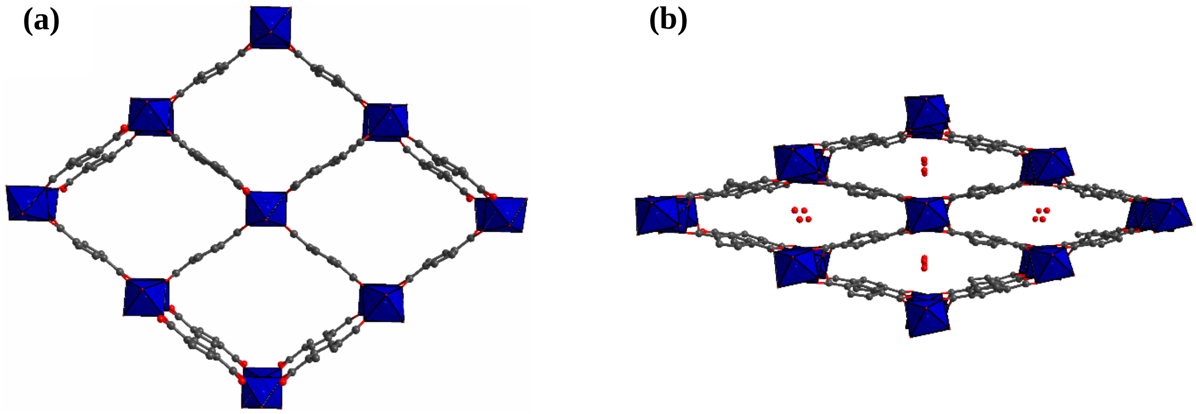

Abbildung 4.2: (a) Offene Form vom MIL-53, Blickrichtung entlang der *a*-Achse. (b) Geschlossene Form von MIL-53, Blickrichtung entlang der *c*-Achse. AlO_6-Polyeder sind in blau, Sauerstoffatome in rot und Kohlenstoffatome in grau dargestellt.[50]

Ausgehend von funktionalisierten Terephthalsäuren konnte eine Reihe von MIL-53 Derivaten hergestellt werden.[24, 55, 75-78] Die zusätzlichen funktionellen Gruppen haben dabei einen massiven Einfluss auf die Flexibilität, die thermische Stabilität sowie das Sorptionsverhalten des Materials. Zur Erweiterung der Porenradien wurde versucht, MIL-53 auch mit verlängerten aromatischen Dicarbonsäuren herzustellen. Unter Verwendung von 2,6-Naphthalindicarbonsäure gelang dies 2005 Loiseau et al. mit der Entdeckung von MIL-69.[56] MIL-69 kristallisiert in der geschlossenen Form von MIL-53, weist jedoch keinerlei Flexibilität auf und ist daher nicht porös. Durch die Verwendung von DMF an Stelle von Wasser als Lösungsmittel konnte jedoch 2009 eine offene, poröse Form von MIL-69, das DUT-4 (DUT = Dresden Universität of Technology) erhalten werden.[57] Im selben Zug konnte DUT-5,[57] die isoretikuläre Verbindung basierend auf 4,4‘-Biphenyldicarbonsäure erhalten werden, die eine weitere Vergrößerung der Porendurchmesser bewirkt. Beide Verbindungen weisen eine hohe permanente Porosität, jedoch keinerlei Flexibilität auf. In Anlehnung an DUT-5 konnte zusätzlich ein Derivat basierend auf 2,2´-Bipyridin-5,5´-Dicarbonsäure hergestellt werden, MOF-253.[59] In dem Versuch die Poren noch weiter zu vergrößern wurden Synthesen mit 4,4´-

Stilbendicarbonsäure durchgeführt. Hierbei wurde jedoch keine MIL-53 verwandte Struktur erhalten, sondern eine neue, das CYCU-3 (Chung Yuang Christian-University).[64] Diese Struktur basiert auf den gleichen Ketten wie MIL-53, jedoch werden diese über die Linkermoleküle so zu einem dreidimensionalem Netzwerk verknüpft, das mikroporöse trigonale und mesoporöse hexagonale Kanäle entstehen. Mit einem Durchmesser der hexagonalen Kanäle von 3 nm, einer spezifischen Oberfläche von $a_{s(BET)}$ = 2757 m^2/g und einem Mikroporenvolumen von V_{mic} = 1.39 cm^3/g weist CYCU-3 die bis dato mit höchsten Werte für einen Aluminium-MOF auf. Interessanterweise resultierten Synthesen mit 4,4´-Azobenzoldicarbonsäure als Linkermolekül in einer unporösen Schichtstruktur (MIL-129).[60]

Kürzlich konnte die MIL-53 Familie noch um zwei Verbindungen basierend auf aliphatischen Linkermolekülen erweitert werden. Im CAU-13 (CAU = Christian-Albrechts Universität) werden die Ketten *trans* eckenverknüpfter AlO_6-Polyeder über *trans* 1,4-Cyclohexandicarboxylationen verknüpft.[61] Der Cyclohexanring liegt hierbei abwechselnd in der e,e oder a,a Konformation vor. Das MIL-53-FA bzw. Basolite A520 enthält hingegen Fumarationen.[62] In Tabelle 4.2 sind, soweit in der Literatur angegeben, die spezifischen Oberflächen, Mikroporenvolumina und thermische Stabilitäten von den bis dato publizierten MIL-53-Analoga basierend auf Dicarbonsäuren zusammengefasst.

Tabelle 4.2: Übersicht über spezifische Oberflächen, Mikroporenvolumina und thermische Stabilität von bis dato bekannten MIL-53 Verbindungen, basierend auf Dicarbonsäuren.

Name	**$a_{s(BET)}$ [m^2/g]**	**V_{mic} [cm^3/g]**	**Stabilität [°C]**	**[Lit]**
MIL-53	1140	0.54	500	[24, 50]
MIL-69	-	-	450	[56]
DUT-4	1308	0.68	430	[57]
DUT-5	1613	0.81	430	[57]
MOF-253	2160	0.89	350	[59]
CAU-13	378	0.15	350	[61]
MIL-53-FA/Basolite A520	1080/1010	n.a.	450/400	[62]
CAU-16	-	-	330	[63]

Allen MIL-53 analogen Strukturen ist gemein, dass die koordinierenden Carboxylatgruppen einen Winkel von 180° zueinander einnehmen. Dies lässt sich nun nicht nur in Dicarbonsäuren vorfinden, sondern auch in Tetracarbonsäuren, sofern die gegenüberliegenden Gruppen koordinieren. Unter Verwendung von Pyromellitsäure (1,2,4,5-Benzoltetracarbonsäure) konnte MIL-121, ein MIL-53 Derivat mit zwei freien nicht koordinierenden Carbonsäuregruppen hergestellt werden.[51] Aufgrund des großen sterischen Anspruchs der freien Säuregruppen wird die Verbindung in der offenen Form erhalten und zeigt keinerlei Flexibilität sowie nur eine sehr geringe Porosität. Interessanterweise entsteht unter den gleichen Reaktionsbedingungen nur bei deutlich niedrigeren Konzentrationen an Al-Salz und Pyromellitsäure eine neue Verbindung, das MIL-118.[53] Die Struktur von MIL-118 basiert ebenfalls auf Ketten von *trans* eckenverknüpften AlO_6-Polyedern, jedoch ist die Koordination der Säuregruppen sehr ungewöhnlich. Im ‚as synthesized' (as) Produkt MIL-118A koordinieren zwei gegenüberliegende Carboxylationen mit beiden Sauerstoffatomen, die beiden anderen gegenüberliegenden jedoch nur mit einem Sauerstoffatom. Die oktaedrische Koordinationsumgebung der Aluminiumatome wird dabei durch Wassermoleküle vervollständigt (Abbildung 4.3 (a)). Erhitzt man diese Verbindung, kommt es zur Dehydratisierung und einer Phasenumwandung, MIL-118B entsteht. Die koordinierenden Wassermoleküle werden abgespalten und alle vier Carboxylatgruppen koordinieren vollständig (Abbildung 4.3 (b)). Es entstehen rautenförmige Kanäle, in die sich beim Abkühlen Wassermoleküle einlagern, was zu einer Verschiebung der anorganischen Ketten führt und die Kanäle bekommen eine eher rechteckige Form (MIL-118C) (Abbildung 4.3 (c)).

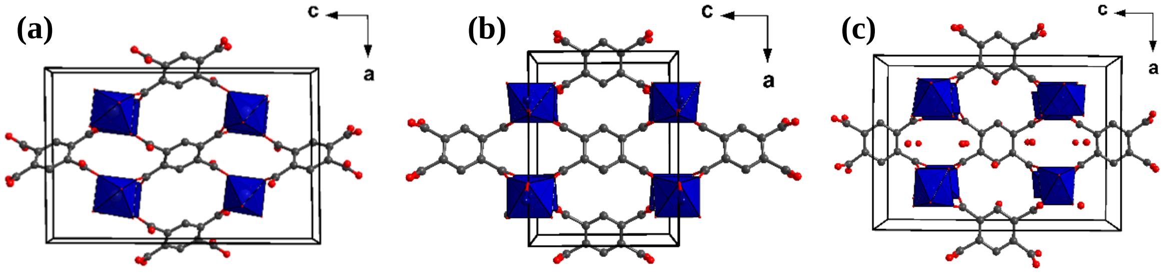

Abbildung 4.3: (a) Struktur von MIL-118A. (b) Struktur von MIL-118B. (c) Struktur von MIL-118C. AlO_6-Polyeder sind in blau, Kohlenstoffatome in grau und Sauerstoffatome in rot dargestellt.[53]

Die Synthese von MIL-121 und MIL-118 findet in reinem Wasser statt. Unter Zugabe von Natronlauge erhält man eine dritte Verbindung, MIL-120, deren Struktur Ketten aus kantenverknüpften AlO_6-Ployedern enthält (Abbildung 4.1, (c)).[66] Diese Art der Verknüpfung ist sehr selten und nur bei insgesamt zwei Al-MOFs bis dato beobachtet worden. Vier der Sauerstoffatome werden dabei von verbrückenden μ-OH Gruppen gestellt und nur zwei von koordinierenden Carboxylatgruppen des Pyromellitlinkers. Insgesamt entsteht aber wieder ein dreidimensionales Gerüst mit eindimensionalen hexagonalen Kanälen. Die Verwendung vergrößerter Tetracarbonsäuren führte ebenfalls zu Verbindungen mit Ketten aus *trans* eckenverknüpften AlO_6-Polyedern. So konnten das porphyrinbasierten Al-PMOF[54] und MIL-122[52] basierend auf 1,4,5,8-Naphthalintetracarbonsäure erhalten (Abbildung 4.4).

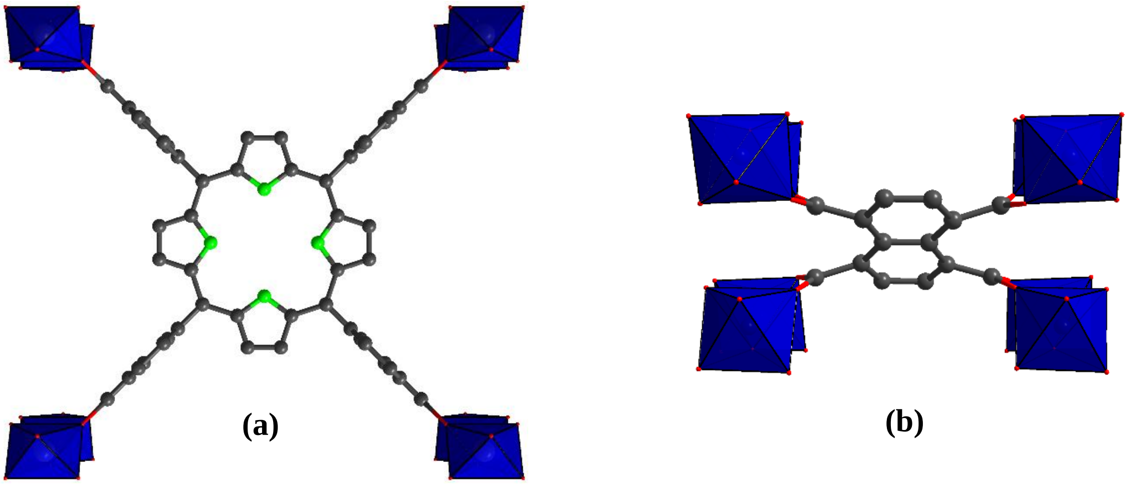

Abbildung 4.4: (a) Struktur von Al-PMOF, Blickrichtung entlang der *b*-Achse. (b) Struktur von MIL-122, Blickrichtung entlang der *c*-Achse. AlO_6-Polyeder sind in blau, Kohlenstoffatome in grau, Sauerstoffatome in rot und Stickstoffatome in grün dargestellt.[52, 54]

Erstaunlicherweise wurde kürzlich mit CAU-16[63] ein MIL-53 Derivat basierend auf Pyridin-2,4,6-Tricarbonsäure (H_3PTC) entdeckt, in der die Carbonsäuregruppen nicht mehr linear zueinander angeordnet sind, sondern einen Winkel von 120° zueinander einnehmen. Allerdings bildet sich in dieser Struktur ein zweikerniger Komplex ($[AlPTC(\mu\text{-}OH)(H_2O)]_2^{2-}$) als Linker aus, in dem die nicht-koordinierenden Carboxylatgruppen dann wieder einen Winkel von 180° zueinander einnehmen. CAU-16 tritt analog zu MIL-69 in einer geschlossenen Form auf und weist ebenso keinerlei Flexibilität auf (Abbildung 4.5). Es zeigt keinerlei Zugänglichkeit für N_2, jedoch konnte eine Aufnahme von gasförmigen CO_2 (1.76 mmol/g bei 196 K) beobachtet werden.

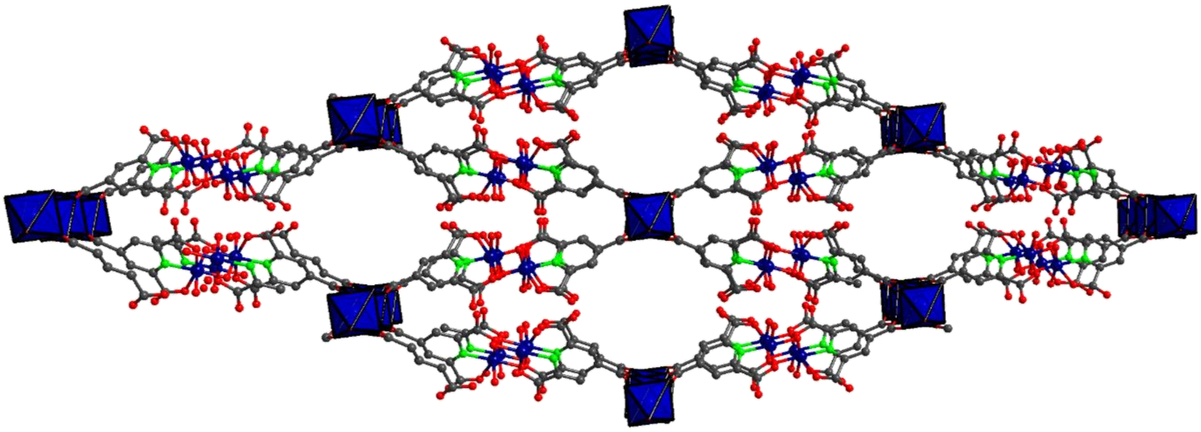

Abbildung 4.5: Struktur von CAU-16, Blickrichtung entlang der *c*-Achse. Die Polyeder innerhalb der zweikernigen ($[AlPTC(\mu\text{-}OH)(H_2O)]_2^{2-}$) Komplexe wurden der Übersicht halber weggelassen. AlO_6-Polyeder sind in blau, Kohlenstoffatome in grau, Sauerstoffatome in rot und Stickstoffatome in grün dargestellt.[63]

Einziges Beispiel einer Struktur mit Ketten *trans* eckenverknüpfter Oktaeder und einem gewinkelten Linkermolekül ist das CAU-8.[58] Hier bilden sich Schichten aus parallel verlaufenden Al-O-Ketten, wobei die räumliche Orientierung der Ketten in benachbarten Schichten abwechselnd um 90° zueinander verdreht ist. Die Schichten werden über 4,4´-Benzophenondicarboxylationen zu einem dreidimensionalem Netzwerk mit eindimensionalen Kanälen verknüpft. Verwendet man hingegen kleinere gewinkelte Linkermoleküle wie Isopthalsäure (1,3-Benzoldicabonsäure) oder Phthalsäure (1,2-Benzoldicarbonsäure) erhält man Strukturen mit anderen anorganischen Ketten. In der Phthalsäure beträgt der Winkel zwischen den Säuregruppen 60°. Die resultierende Verbindung CAU-15[67] weist Ketten aus kantenverknüpften AlO_6-Polyedern auf (Abbildung 4.1 (c)), die bereits im MIL-120 beobachtet werden konnten. Man erkennt hier eine Analogie, denn die Carboxylatgruppen des 1,2,4,5-Benzoltetracarboxylats, die im MIL-120 benachbarte Ketten miteinander verbinden, liegen ebenso in *otho*-Stellung zueinander vor wie die des Phthalats in CAU-15. Da hier aber nur zwei und nicht vier Carboxylate vorhanden sind, bildet sich nur eine Schichtstruktur aus (Abbildung 4.6).

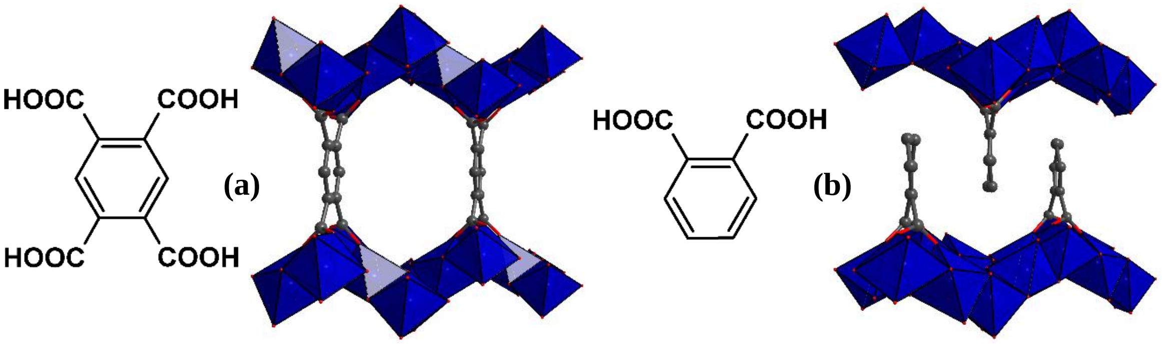

Abbildung 4.6: (a) 1,2,4,5-Benzoltetracarbonsäure und Struktur von MIL-120; Blickrichtung entlang der *c*-Achse. (b) 1,2-Benzoldicarbonsäure und Struktur von CAU-15; Blickrichtung entlang der *c*-Achse. AlO_6-Polyeder sind in blau, Kohlenstoffatome in grau und Sauerstoffatome in rot dargestellt.[66, 67]

Unter Verwendung von Isopthalsäure, in der die Säuregruppen in *meta*-Stellung zueinander orientiert sind, erhält man die Verbindung CAU-10.[25] Die Struktur von CAU-10 basiert auf Helices *cis* eckenverknüpfter AlO_6-Polyeder, die über die Isophthalationen zu einem dreidimensionalen Netzwerk mit quadratischen Kanälen verknüpft werden. Die Kanäle weisen dabei einen maximalen Durchmesser von 7 Å auf (Abbildung 4.7). Die Verbindung besitzt eine permanente Porosität mit einer spezifischen Oberfläche $a_{s(BET)} = 635\ m^2/g$ und einem Mikroporenvolumen von $V_{mic} = 0.25\ cm^3/g$.

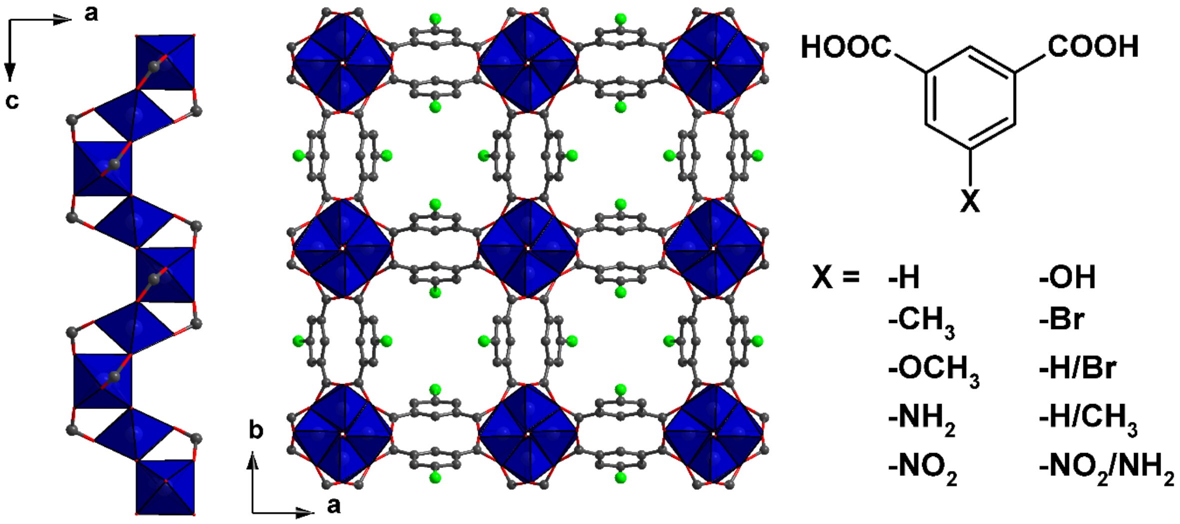

Abbildung 4.7: Struktur von CAU-10. AlO_6-Polyeder sind in blau, Kohlenstoffatome in grau, Sauerstoffatome in rot und die jeweilige funktionelle Gruppe in grün dargestellt.[13, 25]

Zur Modifizierung der Porenoberflächen wurde eine Reihe funktionalisierter CAU-10-X Derivate (X = CH_3, OCH_3, NH_2, NO_2, OH, Br) hergestellt. In Abhängigkeit der funktionellen Gruppe weisen die Verbindungen leichte Unterschiede in der Struktur auf, wodurch die optischen Eigenschaften des Materials beeinflusst werden. Zudem ergeben sich unterschiedliche Affinitäten und Kapazitäten gegenüber N_2, H_2, CO_2, und H_2O, die sich aus der Polarität und dem sterischen Anspruch der Funktionalität sowie den leichten strukturellen Unterschieden der einzelnen Materialien ergeben. Zur weiteren Feineinstellung der Sorptionseigenschaften konnten zudem Verbindungen unter Verwendung von Mischungen unterschiedlich funktionalisierter Linkermoleküle (X = -H/Br, -NO_2/NH_2, -H/CH_3) hergestellt werden.[13] Aufgrund der vorteilhaften Wassersorptionseigenschaften (S-förmige Isotherme, Porenfüllung bei ca. $p/p_0 = 0.18$, relativ hohe Kapazität von 382 cm^3/g) wird das unfunktionalisierte CAU-10-H aktuell als potentieller Kandidat für Anwendungen im Bereich von Wärmetauschprozessen gehandelt. Cyclische Wasserdampfmessungen zeigten eine außergewöhnlich hohe hydrothermale Stabilität des Materials[79] und zusätzlich gelang es, die Verbindung direkt auf γ-Aluminium bzw. metallischem Aluminium wachsen zu lassen, ohne dabei einen Verlust in der Sorptionsleistung zu beobachten.[80] Im NOTT-300 (NOTT = University of Nottingham), einem MOF der Biphenyl-3,3´,5,5´-Tetracarboxylationen enthält, liegen ebenfalls Helices aus *cis* eckenverknüpften AlO_6-Polyedern und somit eine strukturelle Verwandtschaft zu CAU-10 vor.[65] Die koordinierenden Carboxylatgruppen sind dabei in *meta*-Stellung zueinander orientiert, analog zu den Carboxylatgruppen der

Isophthalationen im CAU-10. Im Gegensatz zu CAU-10 zeigt NOTT-300 jedoch keine permanente Porosität gegenüber N_2 oder H_2, allerdings gegenüber CO_2 und SO_2.

Zusammenfassend kann man feststellen, dass in den Strukturen von Al-MOFs, die unter Verwendung von Dicarbonsäuren erhalten wurden, in denen die koordinierenden Säuregruppen in *ortho*-Stellung zueinander vorliegen die Bildung von Ketten kantenverknüpfter AlO_6-Polyeder favorisiert wird. Liegen die koordinierenden Säuregruppen in *meta*-Stellung vor wird die Bildung von Helices *cis* eckenverknüpfter und in *para*-Stellung die Bildung von Ketten *trans* eckenverknüpfter AlO_6-Polyeder bevorzugt. Dies gilt jedoch nur für Synthesen in Wasser und/oder DMF, wie es alle bis jetzt angeführten Verbindungen gemein haben. Verwendet man Methanol als Lösungsmittel so konnte mit Aminoterepthalsäure als Linkermolekül die Verbindung CAU-1 erhalten werden, die als anorganische Baueinheit Achterringe aus abwechselnd kanten- und eckenverknüpften AlO_6-Polyedern enthält (Abbildung 4.1 (e)).[69] Die Kantenverknüpfung wird dabei über Methoxygruppen und die Eckenverknüpfung über Hydroxygruppen realisiert. Jeder Achterring wird dann über zwölf Aminoterephthalationen, vier in der Ebene und jeweils vier oberhalb und unterhalb (Abbildung 4.8 (a)), mit zwölf weiteren Achterringen zu einem dreidimensionalem Netzwerk mit verzerrt oktaedrischen und tetraedrischen Poren verknüpft (Abbildung 4.8 (b)). Die Poren haben dabei einen Durchmesser von ca. 1 bzw. 0.45 nm woraus sich eine spezifische Oberfläche von $a_{s(BET)} = 1530\ m^2/g$ und ein Mikroporenvolumen von $V_{mic} = 0.64\ cm^3/g$ ergibt.

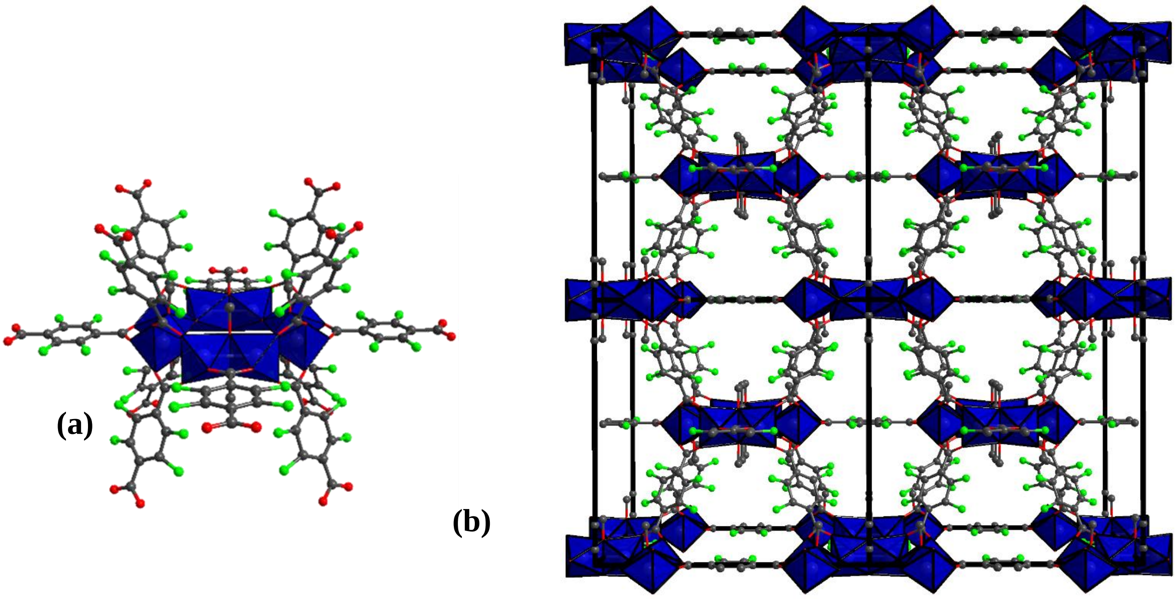

Abbildung 4.8: (a) Oktamere Baueinheit von CAU-1 mit koordinierenden Linkermolekülen. (b) 1x2x2 Super-Zelle von CAU-1 mit Blickrichtung entlang der *a*-Achse. AlO_6-Polyeder sind in blau, Kohlenstoffatome in grau, Sauerstoffatome in rot und Stickstoffatome in grün dargestellt.[69]

Da die Synthese in Methanol stattfindet, kann je nach gewählter Reaktionszeit und -temperatur, die Aminogruppe *in situ* methyliert werden. Des Weiteren lassen sich die Methoxygruppen der anorganischen Baueinheit durch thermische Aktivierung an Luft bei ca. 200 °C gegen Hydroxygruppen austauschen. Liegt die Aminogruppe unmethyliert vor, kann sie zusätzlich durch post-synthetischen Modifizierungsreaktion zum Amid umgesetzt werden, wodurch gezielt die Sorptionseigenschaften des Materials beeinflusst wurden.[81] Aufgrund der Aminogruppen besitzt CAU-1 eine hohe Affinität gegenüber CO_2 und wurde erfolgreich als Membranmaterial für die Trennung von CO_2 und N_2 eingesetzt.[82, 83] Des Weiteren konnte CAU-1, das leicht kolloidal hergestellt werden kann, als Sensormaterial für Bragg-Staggs eingesetzt werden.[84] Ein Derivat mit Dihydroxyterephthalsäure als Linkermolekül wurde ebenfalls erfolgreich hergestellt, die Syntheseversuche mit Terephthalsäure hingegen schlugen fehl.[85] CAU-3, welches auch aus Methanol synthetisiert wird, konnte hingegen mit Terephthalsäure (H_2BDC), Aminoterepthalsäure ($H_2BDC\text{-}NH_2$) sowie 2,6-Naphthalindicarbonsäure (2,6-H_2NDC) als Edukt erhalten werden.[70] Seine Struktur baut sich auf aus einem Zwölfring von kantenverknüpften AlO_6-Polyedern auf(Abbildung 4.1 (f)), wobei, im Gegensatz zum CAU-1, alle verbrückenden Sauerstoffatome, Teil von Methoxygruppen sind. Ein Ring ist zwölffach zu weiteren Ringen koordiniert, wobei sechs Linkermoleküle in der Ebene und jeweils drei abwechselnd ober- und unterhalb der Ebene des Ringes ausgerichtet sind. Dadurch entsteht ein dreidimensionales Netzwerk, ähnlich zu CAU-1, mit oktaedrischen und tetraedrischen Poren, mit Durchmesser von ca. 1.1 und 1.0 nm (Abbildung 4.9).

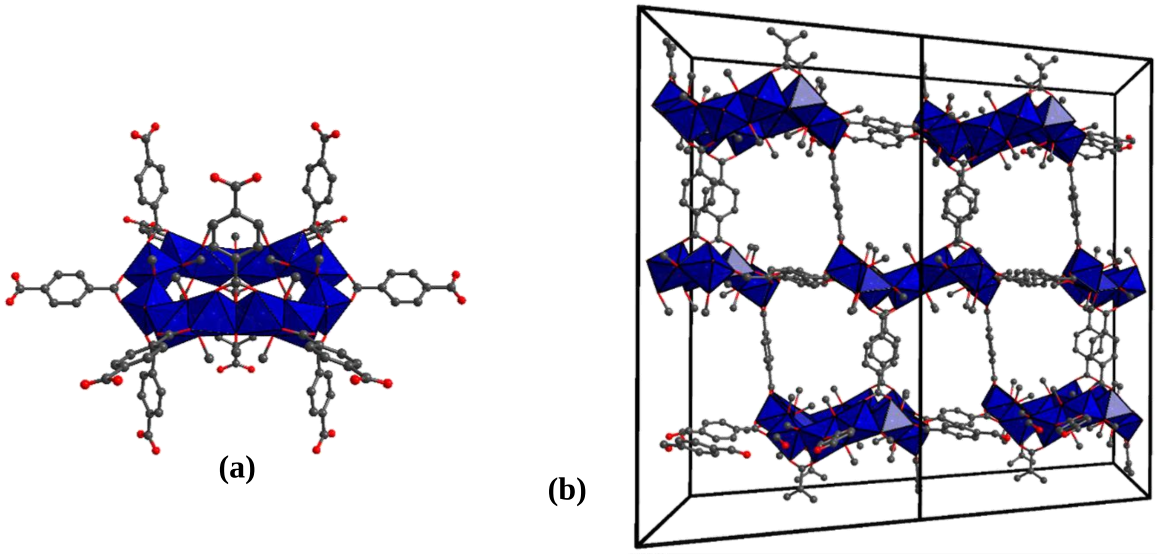

Abbildung 4.9: (a) Dodekamere Baueinheit von CAU-3-BDC mit koordinierenden Linkermolekülen. (b) Dreidimensionales Netzwerk, Blickrichtung entlang der *a*-Achse. AlO_6-Polyeder sind in blau, Sauerstoffatome in rot und Kohlenstoffatome in grau.[70]

Die resultierende spezifische Oberfläche von CAU-3-BDC-NH_2 liegt bei $a_{s(BET)}$ = 1250 m^2/g und das Mikroporenvolumen von V_{mic} = 0.53 cm^3/g und damit leicht unter den Werten von CAU-1. Die Derivate CAU-3-BDC und CAU-3-NDC weisen mit $a_{s(BET)}$ = 1550 bzw. 2320 m^2/g und V_{mic} = 0.64 bzw. 0.95 cm^3/g entsprechend höhere Werte auf.

Basierend auf Tricarbonsäuren wurden ebenfalls einige Al-MOFs synthetisiert. Mit 1,3,5-Benzoltricarbonsäuremethylester (Trimesinsäure) konnten ausgehend von den gleichen Edukten nur durch leichte Variation der Syntheseparameter drei verschiedene Strukturen erhalten werden.[86] MIL-110[23] wird nahe einem Wert von pH = 0 nach mehreren Tagen erhalten. Die Struktur besteht aus achtkernigen Aluminium-Oxo-Clustern (Abbildung 4.1 (j)) die über die Trimesatanionen zu einem Netzwerk mit eindimensionalen hexagonalen Kanälen mit einem Durchmesser von 1.6 nm verknüpft werden (Abbildung 4.10 (a)). MIL-100[22] entsteht hingegen nahe einem pH-Wert = 1 und bereits nach mehreren Stunden. Die Struktur beruht auf trimeren Baueinheiten μ_3-O-eckenverknüpfter AlO_6-Polyeder (Abbildung 4.1 (i)), zu einem sogenannten Supertetraeder verknüpft werden, wobei die Linkermoleküle auf den Polyederflächen liegen. Die Supertetraeder selber sind analog zu den tetraedrischen Knotenpunkten im zeotypen MTN-Netzwerk angeordnet. Diese übergeordnete Struktur findet sich ebenso im MIL-101-NH_2.[72] Hier werden die trimeren Einheiten über Aminoterephthalate verknüpft, die auf den Kanten der Supertetraeder liegen (Abbildung 4.10 (b)). Beide Verbindungen sind Beispiele für mesoporöse Strukturen mit spezifischen Oberflächen von ca. 2100 m^2/g. Das dritte Al-Trimesat, das bei einem pH-Wert > 1 entsteht, ist MIL-96.[21] Die Struktur basiert auf trimeren Einheiten und Ketten aus AlO_6-Oktaedern die eine Wabenstruktur mit 18-gliedrigen Ringen (Abbildung 4.1 (h)) ausbilden. Im Vergleich zu MIL-100 und MIL-110 weist MIL-96 die kleinsten Poren und geringste Sorptionskapazität auf. Die sehr ähnlichen Synthesebedingungen zeigen zum einen die Empfindlichkeit der Synthese zum anderen demonstrieren sie aber auch die große strukturelle Vielfalt.

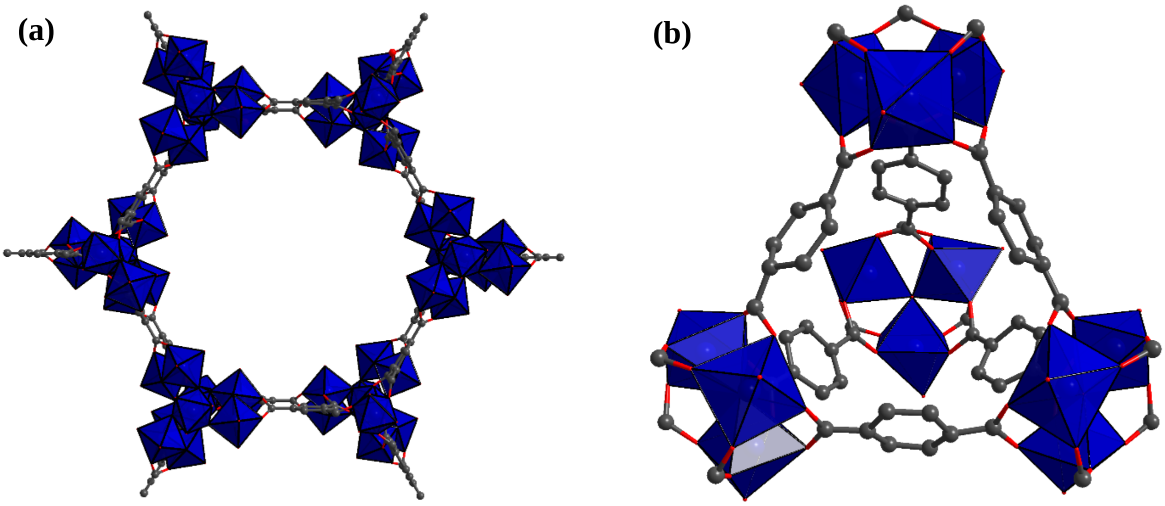

Abbildung 4.10: (a) Struktur von MIL-110, Blickrichtung entlang der *c*-Achse. (b) Supertetraeder in MIL-101-NH_2. Die NH_2-Gruppen wurden zur besseren Übersicht weggelassen. AlO_6-Polyeder sind in blau, Sauerstoffatome in rot und Kohlenstoffatome in grau.[23, 72]

Drei weitere Strukturen konnten ausgehend von 1,3,5-Benzoltribenzoesäure (H_3BTB) erhalten werden. CAU-4[68] basiert auf Ketten isolierter AlO_6-Polyeder (Abbildung 4.1 (d)), welche über die Linkermoleküle zu einem Netzwerk mit eindimensionalen hexagonalen Kanälen verknüpft werden. Der Durchmesser der Kanäle beträgt 9.6 Å und die Verbindung besitzt eine spezifische Oberfläche von $a_{s(BET)}$ = 1520 m^2/g und ein Mikroporenvolumen V_{mic} = 0.61 cm^3/g. MOF-519 und MOF-520 hingegen basieren auf Achterringen von eckenverknüpften AlO_6-Oktaedern (Abbildung 4.1 (g)).[71] An einem Ring koordinieren 16 BTB-Linker, wobei nur 12 davon zum Aufbau des Netzwerkes verwendet werden. MOF-520 hat die gleiche Struktur wie MOF-519 nur dass an Stelle der vier nicht verbrückenden H_2BTB-Linkern Formiationen sitzen. Dadurch sind die Poren im MOF-520 etwas größer als im MOF-519. Beide Verbindungen weisen hohe spezifische Oberflächen $a_{s(BET)}$ = 2400 bzw. 3290 m^2/g und Mikroporenvolumina V_{mic} = 0.94 bzw. 1.28 cm^3/g auf und besitzen zudem eine hohe Speicherkapazität für Methan (bei 80 bar 215 bzw. 288 cm^3/g).

Die größte anorganische Baueinheit findet man im CAU-6,[73] welches mit Isopropanol als Lösungsmittel hergestellt wird. Die Struktur basiert auf Säulen (Abbildung 4.1 (k)) aus geschichteten, eckenverknüpften, 13-kernigen Aluminium-Oxo-Clustern. Jede Säule ist über Aminoterephthalationen mit sechs weiteren Säulen verknüpft, so dass trigonale Kanäle mit einem Durchmesser von 5-10 Å entstehen.

4.2. Anwendung von MOFs basierend auf schwefelhaltigen Linkermolekülen

Zu Beginn dieser Arbeit waren im Bereich der Al-MOFs keinerlei Verbindungen bekannt, die auf Linkermolekülen mit schwefelhaltigen funktionellen Gruppen basierten. Auf Basis anderer Metalle waren zwar Verbindungen bekannt, allerdings wiesen diese keine herausragenden Eigenschaften auf. Erst im Laufe der letzten vier Jahre wurden verschiedene Materialien hergestellt und das hohe Anwendungspotential von MOFs mit schwefelhaltigen funktionellen Gruppen aufgezeigt. Hauptsächlich handelt es sich hierbei um Linkermoleküle mit Thiol- oder Thioether-, Sulfon- und Sulfonsäuregruppen sowie Thiophen, weshalb im Folgenden ein paar Beispiele aus der Literatur ausgeführt werden.

Thiol- bzw. Thioethergruppen haben nach dem HSAB-Prinzip den Charakter weicher Basen und zeichnen sich daher durch ihre hohe Affinität gegenüber weichen Säuren, z.B. Schwermetallen wie Quecksilber oder Palladium, aus. Um diese Eigenschaft nutzen zu können, muss bei der Synthese von MOFs mit thiolfunktionalisierten Linkermolekülen darauf geachtet werden, dass diese nicht an die Metallionen, die die anorganischen Baueinheiten aufbauen, koordinieren. Daher bieten sich hierfür Umsetzungen mit harten Metallen an. Unter Verwendung von 2,5-Bis(2-(methylthio)ethylthio)terephthalsäure (H_2L1) (Abbildung 4.11 (a)) gelang He et al. die Herstellung eines MOF-5 [$Zn_4O(BDC)_3$] Derivats. MOF-5 ist aus Zn_4O-Einheiten aufgebaut, die über die Terephthalationen zu einem kubischen Netzwerk verknüpft werden.

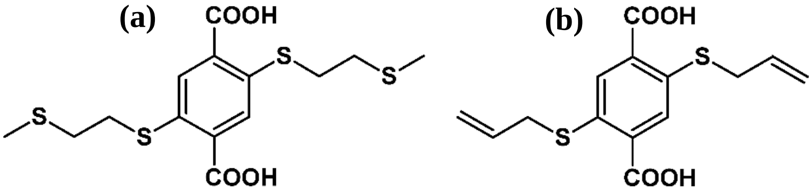

Abbildung 4.11: (a) 2,5-Bis(2-(methylthio)ethylthio)terephthalsäure (H_2L1). (b) 2,6-Bis(allylsulfanyl)-terephthalsäure (H_2L2).

Die $CH_3SCH_2CH_2S$-Seitenketten ragen in die Poren und führen zu einer effektiven Aufnahme (94 %) von $HgCl_2$ aus Ethanol (84 mg/L).[87] Im Jahre 2008 wurde die Synthese des Zr-MOFs UiO-66 (UiO = Universitetet i Oslo), [$Zr_6O_4(OH)_4(BDC)_{12}$] veröffentlicht.[88] Ähnliche Ergebnisse zur Adsorption von Palladium wurden mit einem UiO-66 Derivat basierend auf 2,6-Bis(allylsulfanyl)terephthalsäure (H_2L2) (Abbildung 4.11 (b)) erzielt.[89] UiO-66 basiert auf sechskernigen Zirkonium-Oxo-Clustern die über Terephthalationen zu einem dreidimensionalem Netzwerk mit oktaedrischen und tetraedrischen Poren verknüpft werden und eine hohe permanente Porosität von $a_{s(Langmuir)}$ = 1167 m^2/g aufweist. Isoretikuläre Synthesen unter Verwendung von 4,4´-Biphenyldicarbonsäure und *p*-Terphenyl-4,4″-dicarbonsäure resultierten in den respektiven Verbindungen UiO-67 und UiO-68 mit entsprechend größeren Poren und höheren Oberflächen ($a_{s(Langmuir)}$ = 3000 bzw. 4170 m^2/g). Mit 4,4´-Sulfonyldibenzoesäure (H_2SDBA)[90] und Dibenzo[*b,d*]thiophen-3,7-dicarbonsäure-5,5-dioxid (H_2BPDC-SO_2)[91] (Abbildung 4.12) konnten zwei funktionalisierte UiO-67 Derivate hergestellt werden, ersteres mit Hf^{4+} und Zr^{4+}, zweiteres nur mit Zr^{4+} .

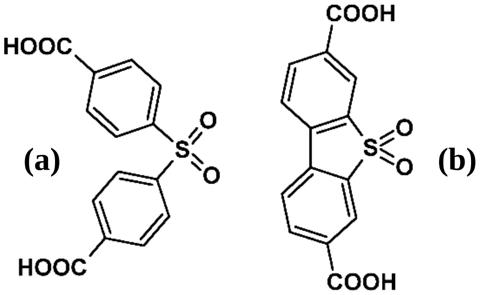

Abbildung 4.12: (a) 4,4´-Sulfonyldibenzoesäure (H_2SDBA). (b) Dibenzo[*b,d*]thiophen-3,7-dicarbonsäure-5,5-dioxid (H_2BPDC-SO_2).

Gegenüber dem unfunktionalisierten Material weisen die beiden Zr-Verbindungen durch die zusätzliche Sulfongruppe eine deutlich erhöhte Sorptionskapazität für CO_2 auf. Im Falle von UiO-67-SDBA konnte ein Anstieg um 145 % (1 bar und 298 K) beobachtet werden und die Sorptionsselektivität gegenüber CH_4 stieg um 100 % an.[90] Für UiO-67-BPDC-SO_2 beläuft sich die Zunahme der Kapazität auf 134 % und eine um das 3.3 bzw. 3.4fache gesteigerte Selektivität für CO_2/CH_4 und CO_2/N_2 gegenüber UiO-67 wird beobachtet. Die erhöhte Affinität zu CO_2 wurde zusätzlich durch Großkanonische Monte Carlo Simulationen belegt. Durch das Quadrupolmoment von CO_2 kann der positiv geladene Kohlenstoff im CO_2 mit den negativ geladenen Sauerstoffatomen der Sulfongruppen über zwei verschiedene Moden wechselwirken. Daher lagern sich die CO_2 Moleküle bevorzugt an den -SO_2-Gruppen an.[91] Ähnliche Ergebnisse wurden auch in Ca- und Cd-MOFs gefunden, die ebenfalls auf SDBA als Linker basieren.[92, 93]

Sulfonsäuren (R-SO_3H) zeichnen sich durch eine hohe Polarität und Acidität aus. Daher sollten sie Einfluss auf Sorptionseigenschaften, katalytische Aktivität und Protonenleitfähigkeit eines Materials haben. Gleichzeitig erschweren die hohe Polarität und Acidität in Kombination mit dem hohen sterischen Anspruch aber auch die Herstellung Sulfonsäure-funktionalisierter MOFs. 2011 wurde mit -SO_3H-funktionalisiertem Cr-MIL-101 (Cr-MIL-101-SO_3H), ein hochporöser und chemisch sowie thermisch sehr stabiler MOF hergestellt.[9] Die hohe Polarität der -SO_3H-Gruppen führte zu einer deutlich gesteigerten Affinität für Wasserdampf gegenüber dem unfunktionalisierten Material bei einer hohen Gesamtaufnahme von etwa 0.9 g/g. In Kombination mit der milden Bedingung für die Desorption (ca. 353 K bei Atmosphärendruck) kann dieses Material als vielversprechender Kandidat für Anwendungen im Bereich von Wärmetauschprozessen gehandelt werden.[94] Weitere Anwendungsmöglichkeiten für Cr-MIL-101-SO_3H könnten im Bereich der heterogenen Katalyse liegen. Das Material wurde als erstes in der Hydrolyse von Cellulose eingesetzt und zeigte im Vergleich zum unfunktionalisiertem Material eine deutlich gesteigerte Aktivität. Es wurde mehrfach recycelt, ohne dass ein Verlust der Aktivität beobachtet wurde. Zudem kam es nicht, wie unter Einsatz von Schwefelsäure für diese Reaktion, zur Bildung unerwünschter Nebenprodukten.[9] Weiterhin konnte Cr-MIL-101-SO_3H für die Acetylierung von Aldehyden mit Diolen erfolgreich eingesetzt werden. Für die Acetylierung von Benzaldehyd mit Glycol wurde Cr-MIL-101-SO_3H mit dem kommerziellen Katalysator Amberlyst-15 verglichen und zeigte nur eine leicht niedrigere Ausbeute an Aldehyd (97.3 % zu 99.9 % nach 3 h), allerdings eine deutlich höhere Umsatzfrequenz von 12.7 zu 7.8 $\text{mol/mol}_{\text{Säure}}\text{min}$. Zusätzlich lässt die katalytische Aktivität von Amberlyst-15 bei weiteren Durchläufen drastisch nach (70.1 und 55.0 % Ausbeute) im Gegensatz zu Cr-MIL-101-SO_3H, welches über fünf Durchläufe eine konstante Leistung aufweist.[95] Ähnliche Ergebnisse zeigten sich für die Veresterung verschiedener Säuren mit unterschiedlichen Alkoholen[96] sowie in der Alkoholyse verschiedener Epoxide.[97] Der starke Einfluss der Sulfonsäuregruppen auf die katalytische Aktivität eines MOFs wurde kürzlich noch einmal von Chen et al. demonstriert.[98] Über post-synthetische Modifizierung mit Chlorsulfonsäure wurden sulfonierte Cr-MIL-101, Zr-UiO-66 und Al-MIL-53 Verbindungen hergestellt. Dabei reichen die Anteile an eingeführten Sulfonsäuregruppen von max. 15 bis minimal 3 %. Alle Materialien wurden für die Umsetzung von Fructose in 5-Hydroxymethylfurfural eingesetzt. Die teilweise hohen Umsetzungsraten von über 99 % zeigten dabei nur eine Abhängigkeit vom Sulfonierungsgrad und waren unabhängig von der Struktur der jeweils eingesetzten Verbindung. Die Verbindung UiO-66 konnte nicht nur über post-synthetische Modifizierung sondern auch über direkte Synthese Sulfonsäure-funktionalisiert erhalten werden. Da es zunächst nicht möglich war eine stabile vollständig sulfonierte UiO-66 Verbindung herzustellen wurden unter Verwendung verschiedener Verhältnisse von Terephthalsäure und Sulfoterephthalsäure als Linkermoleküle drei Materialien mit unterschiedlichem -SO_3H-Gehalt hergestellt. Das Material mit dem geringsten Anteil (18 %) an eingebauten -SO_3H-Gruppen zeigte erstaunlicherweise eine höhere spezifische Oberfläche als das unfunktionalisierte ($a_{s(\text{Langmuir})}$ = 1436 vs. 1361 m^2/g), was vermutlich auf eine erhöhte Kristallinität zurückzuführen ist, und gleichzeitig auch eine gesteigerte Aufnahme von CO_2 (ca. 22.5 vs. 15 mL/g, 288 K, 1 bar). Die mit einhergehende erhöhte Adsorptionswärme (28-21 kJ/mol vs. 22-17 kJ/mol) lässt dabei auf verstärkte Wechselwirkungen mit den CO_2 Molekülen durch die Sulfonsäuregruppen schließen.[99] Später gelang in einer leicht abgewandelten Synthese auch die Herstellung von stabilem, vollständig sulfoniertem UiO-66-SO_3H. Zusätzlich wurden die -COOH und -I-funktionalisierten Derivate hergestellt, deren funktionelle Gruppen ähnliche Größen aber abfallende Polarität aufweisen. Alle drei Verbindungen wurden hinsichtlich der Sorptionsselektivität für CO_2 gegenüber CH_4 untersucht. Nur UiO-66-SO_3H zeigte im Vergleich zum unfunktionalisierten UiO-66 eine deutlich gesteigerte Selektivität[100] und bestätigt damit die Ergebnisse vorangegangener Großkanonischer Monte Carlo Simulationen.[101] Kürzlich konnte über post-synthetische Oxidation von UiO-66-$(SH)_2$ UiO-66-$(SO_3H)_2$ erhalten werden. Dieses Material zeigt mit $8.4x10^{-2}$ S/cm bei 80 °C und 90 % Luftfeuchtigkeit, die bis dato für einen MOF höchste gemessene Protonenleitfähigkeit und bewegt sich mit diesem Wert im Bereich von Nafion.[102]

Anstelle vom hydrophoben Benzol können auch hydrophilere Heteroaromaten als Basis für Linkermoleküle dienen. Im Falle von Schwefel kann man sich als einfachste Möglichkeit 2,5-Thiophendicarbonsäure (H_2TDC) vorstellen. Neben dem Einfluss auf die Sorptionseigenschaften durch die Polarität des Linkermoleküls kann der im Vergleich zu 180° im Falle von Terephthalsäure verringerte Winkel von 148°, den die Carbonsäuregruppen zueinander einnehmen zur Bildung neuer Strukturen beitragen. Die bereits mehrfach angesprochene Verbindung UiO-66 enthält Terephthalationen. Trotzdem konnte unter Verwendung von H_2TDC drei Verbindungen mit starker struktureller Ähnlichkeit zu UiO-66 hergestellt werden. DUT-67, DUT-68 und DUT-69 wurden ausgehend von und $ZrCl_4$ bzw. $HfCl_4$ durch leichte Abwandlungen der Syntheseparameter synthetisiert. Alle drei Verbindungen basieren auf leicht unterschiedlichen Zirkonium- bzw. Hafnium-Oxo-Clustern, die zu unterschiedlichen dreidimensionalen Netzwerken mit unterschiedlichen Porengeometrien verknüpft werden. Alle Verbindungen besitzen eine hohe permanente Porosität und einen hydrophilen Charakter.[103] Interessante Sorptionseigenschaften zeigen auch der Scandium-basierte MOF NOTT-401[104] und die Verbindung Cu-TDC.[105] Wasserstoffsorptionsmessungen zeigen Kapazitäten bei 77 K und 1 bar von entsprechend 2.3 wt% und 0.75 wt% mit Adsorptionswärmen von 6.7 und 9.2 kJ/mol. Die relativ hohen Adsorptionswärmen sind dabei auf die Polarisierbarkeit des Thiophens sowie die recht kleinen Porendurchmesser innerhalb der Strukturen zurückzuführen.

4.3. Ergebnisse

4.3.1. Effective Mercury Sorption by Thiol-Laced Metal–Organic Frameworks: in Strong Acid and the Vapor Phase

Der folgende Artikel wurde im Jahre 2013 in der Fachzeitschrift *Journal of the American Chemical Society*, *ACS* veröffentlicht.[106] Der Wiederabdruck erfolgte mit freundlicher Genehmigung der ACS. Reproduced with permission from:
K.-K. Yee, N. Reimer, J. Liu, S.-Y. Cheng, S.-M. Yiu, J. Weber, N. Stock, Z. Xu, *Journal of the American Chemical Society* **2013**, *135*, 7795-7798, DOI: 10.1021/ja400212k. Copyright 2013 American Chemical Society.
http://pubs.acs.org/doi/abs/10.1021/ja400212k

In diesem Artikel geht es um die Ausnutzung des HSAB-Prinzips zur Herstellung von MOFs mit freistehenden Thiol-Gruppen. Ausgehend von dem Linkermolekül 2,5-Dimercapto-1,4-Benzoldicarbonsäure (H_2DMBD) wurden zwei MOFs Zr-DMBD und Al-DMBD mit den Summenformeln $[Zr_6O_4(OH)_4(C_8H_4O_4S_2)_n(C_8H_2O_4S_2)_{n-x}]\cdot mDMF\cdot yH_2O$ und $[Al_4(OH)_{2+x}(OMe)_{4-x}(C_8H_4O_4S_2)_3]\cdot 8H_2O$ hergestellt, die isoretikulär zu UiO-66[88] bzw. CAU-1[69] sind. ($C_8H_4O_4S_2$ steht hierbei für den Anteil mit -SH Gruppen und $C_8H_2O_4S_2$ für den Anteil an dem durch Oxidation -S-S-Gruppen entstanden sind). Aufgrund des ‚harten‘ Charakters von Zirkonium- und Aluminiumionen koordinieren diese nur an die ‚harten‘ Carboxylatgruppen und nicht an die ‚weichen‘ Thiolgruppen, welche dadurch für eine weitergehende Funktionalisierung oder Anwendung verfügbar bleiben. In diesem Fall wurde das Zr-DMBD als geeignetes Adsorbens für die Entfernung von Quecksilberionen aus wässrigen Lösungen untersucht. Es zeigte sich, dass auf eine Formeleinheit 1.82 Atome Quecksilber aufgenommen werden können, was vermutlich darauf zurück zu führen ist, dass gegenüberstehende Thiolgruppe innerhalb der Poren teilweise zu Disulfidgruppen oxidiert sind, was die Aufnahmekapazität verringert. Die Oxidation der Thiolgruppen wurde für das Al-DMBD interessanterweise nicht beobachtet. Des Weiteren wurde gezeigt, wie die Photolumineszenz von Zr-DMBD durch die Adsorption von Quecksilberionen gequencht werden konnte.

JACS
JOURNAL OF THE AMERICAN CHEMICAL SOCIETY
Communication
pubs.acs.org/JACS

Effective Mercury Sorption by Thiol-Laced Metal−Organic Frameworks: in Strong Acid and the Vapor Phase

Ka-Kit Yee,[†] Nele Reimer,[‡] Jie Liu,[†] Sum-Yin Cheng,[†] Shek-Man Yiu,[†] Jens Weber,[§] Norbert Stock,*[,‡] and Zhengtao Xu*[,†]

[†]Department of Biology and Chemistry, City University of Hong Kong, 83 Tat Chee Avenue, Kowloon, Hong Kong, China
[‡]Institut für Anorganische Chemie, Christian-Albrechts Universität, Max-Eyth-Str. 2, 24118 Kiel, Germany
[§]Department of Colloid Chemistry, Max Planck Institute of Colloids and Interfaces, Research Campus Golm, 14476 Golm, Germany

Supporting Information

ABSTRACT: Free-standing, accessible thiol (−SH) functions have been installed in robust, porous coordination networks to provide wide-ranging reactivities and properties in the solid state. The frameworks were assembled by reacting $ZrCl_4$ or $AlCl_3$ with 2,5-dimercapto-1,4-benzenedicarboxylic acid (H_2DMBD), which features the hard carboxyl and soft thiol functions. The resultant Zr-DMBD and Al-DMBD frameworks exhibit the UiO-66 and CAU-1 topologies, respectively, with the carboxyl bonded to the hard Zr(IV) or Al(III) center and the thiol groups decorating the pores. The thiol-laced Zr-DMBD crystals lower the Hg(II) concentration in water below 0.01 ppm and effectively take up Hg from the vapor phase. The Zr-DMBD solid also features a nearly white photoluminescence that is distinctly quenched after Hg uptake. The carboxyl/thiol combination thus illustrates the wider applicability of the hard-and-soft strategy for functional frameworks.

The combination of carboxylic and sulfur (e.g., thioether or thiol) functions (see Figure 1 for an example)[1] represents a potentially powerful strategy for the molecular design of coordination networks [or metal−organic frameworks (MOFs)].[2] One potential advantage is derived from the distinct hard-and-soft characters of the carboxyl and sulfur groups: the ionic, chemically hard carboxyl group tends to bind metal ions for network formation, while the softer thioether or thiol groups could remain as free-standing, secondary donor groups. In this context, the thioether function has been actively explored, generating a series of porous networks with free-standing thioether groups that have proved to be useful for metal uptake and other applications. By comparison, efforts to incorporate thiol functions into coordination networks have been very limited, and porous coordination networks appended with free-standing thiol functions have yet to be made.

The advantages of incorporating the very reactive thiol group are obvious. First, the stronger-binding thiol groups would enable the uptake of diverse metal ions into MOF pores for effective removal of heavy metal ions and the creation of electroactive or catalytic sites (e.g., mimicking the iron−sulfur and copper−sulfur proteins). Second, the versatile organic transformations of thiols would also allow for convenient postcrystallization (postsynthetic) modifications,[3] such as covalent cross-linking inside the pores to synergize studies of organic polymers and solid-state frameworks. Unfortunately, it is their reactive nature that also complicates the synthesis of thiol-laced MOFs. For example, metal ions that are commonly used to build MOFs (e.g., Zn^{2+}, Cu^{2+}) often interact strongly with the thiol groups and disrupt crystallization. To suppress the thiol−metal interaction, it is helpful to choose chemically very hard (i.e., oxophilic) metal ions that more selectively bind to the carboxyl groups, such as Al(III),[4] Cr(III),[5] Eu(III),[1b] Zr(IV).[6]

Among these, Zr(IV)-based MOFs (Zr-MOFs) are attractive because of their stability and versatile modifiability.[6] For example, Zr-MOFs are largely stable toward water and even under mild acid/base conditions,[7] and they can be formed persistently with extensive functional and geometric modifications[8] on the organic linkers.[7b,9] In this work, we studied the reaction between $ZrCl_4$ and the bifunctional building block 2,5-dimercapto-1,4-benzenedicarboxylic acid (H_2DMBD) (Figure 1, synthesis known[10]) in order to construct a thiol-laced coordination network, Zr-DMBD, and explore the synergism between the thiol function and well-ordered porosity in the solid state. We discovered that this thiol-laced Zr-MOF is capable of effective mercury uptake from both aqueous solutions and the gas phase. In addition, we examined frameworks based on Al(III) and the DMBD linker to demonstrate the wider applicability of

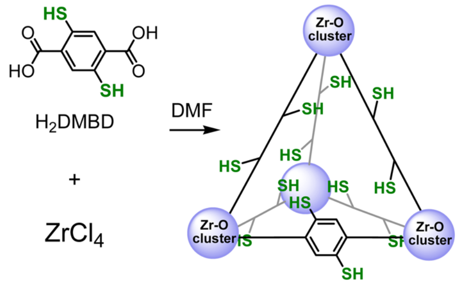

Figure 1. Synthetic scheme for the Zr-DMBD network. The topology is the same as for UiO-66 and is shown in simplified form as a tetrahedral cage.

Received: January 8, 2013
Published: May 7, 2013

dx.doi.org/10.1021/ja400212k | J. Am. Chem. Soc. 2013, 135, 7795−7798

the hard-and-soft strategy in achieving thiol-functionalized porous networks.

The Zr-DMBD framework was first revealed by the distinct powder X-ray diffraction (PXRD) pattern (Figure 2) to be isostructural with the reported UiO-66, which contains linear 1,4-benzenedicarboxylate struts and $Zr_6O_4(OH)_4$ clusters as 12-connected nodes.[11] The structure features a face-centered-cubic arrangement of the Zr−O clusters and thus consists of tetrahedral and octahedral cages in 2:1 ratio. Scanning electron microscopy (SEM) indicated that the solid product uniformly consists of regular-shaped octahedral crystallites on the scale of 200 nm [see the Figure 3 inset and Figure S1 in the Supporting Information (SI)]. The observed crystalline morphology is consistent with those of other reported isoreticular Zr-MOF crystals.[9a,e]

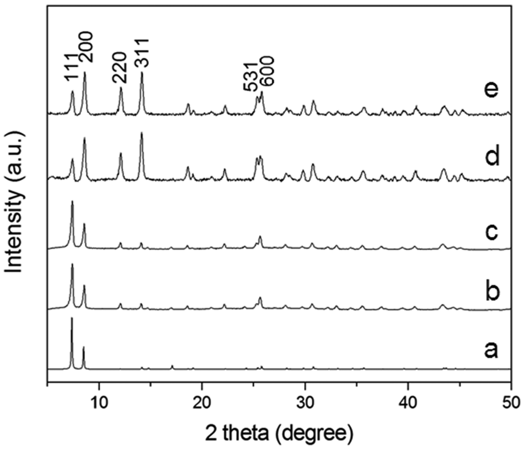

Figure 2. PXRD patterns (Cu Kα, λ = 1.5418 Å) for Zr-DMBD-related systems: (a) simulation from a structural model of Zr-DMBD (see the SI for the atomic coordinates); (b) as-made Zr-DMBD; (c) activated Zr-DMBD; (d) as-made Zr-DMBD after treatment with an aqueous solution of $HgCl_2$; (e) as-made Zr-DMBD after treatment with Hg(0) vapor.

The IR and Raman spectra of both as-made and activated (see the SI for the activation procedure) Zr-DMBD crystalline samples exhibit a peak at 2560 cm^{-1}, consistent with the S−H stretching frequency of free −SH groups (e.g., spectra a and b in Figures S2 and S3). The IR and Raman spectra also feature a distinct band at 501 cm^{-1} that can be assigned to the S−S stretch, indicating disulfide formation that is apparently due to air oxidation of the thiol groups (no measures were taken to exclude air in the crystallization and activation steps). The intensity of the S−S stretch at 501 cm^{-1} relative to that of the S−H stretch at 2560 cm^{-1} significantly increased in the activated sample (e.g., compare spectra a and b in Figure S3), suggesting that more of the −SH groups were oxidized to give disulfides under the heated conditions of the activation process. The elemental analysis and thermogravimetric analysis (TGA) data revealed the $[Zr_6O_4(OH)_4]$/DMBD linker ratio in the as-made Zr-DMBD sample to be 1:6 (see the SI).

The activated Zr-DMBD sample displayed typical type-I N_2 adsorption isotherms at 77.4 K with a BET surface area of 513 m^2/g and a micropore volume of 0.24 cm^3/g (Figure S5). The specific surface area is consistent with the results of CO_2 adsorption at 273 K (ca. 500 m^2/g; see the SI for details). Sorption tests at 273 and 283 K (Figure 3; also see the SI) indicated that the CO_2 adsorption could be fit to a dual-site Langmuir model, while the N_2 adsorption was fit using a single-site Langmuir approach. The calculated heat of adsorption for CO_2 was ca. 30 kJ/mol at low coverage and dropped to 25 kJ/mol at higher coverage. This finding agrees with calculations on other UiO-66 nets, in which functional groups giving rise to polar sites and pronounced interactions raised the low-coverage CO_2 heat of adsorption from 26 kJ/mol (for unmodified UiO-66) to 30−34 kJ/mol.[12] The interactions are also manifested in a distinct CO_2/N_2 selectivity of 187 at a gas composition of 0.15/0.85 (1 bar and 273 K), which is typical of microporous materials. Sorption of other gases (e.g., NH_3) would further unveil how the polar and acidic thiol groups impact the sorption behavior.

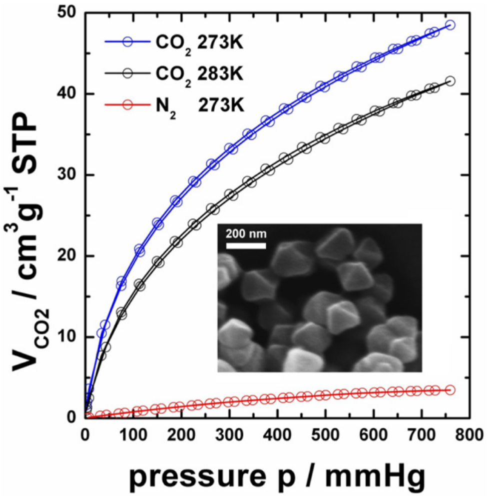

Figure 3. CO_2 (273 and 283 K) and N_2 (273 K) adsorption/desorption isotherms for activated Zr-DMBD. Inset: SEM image of an as-made sample of Zr-DMBD (grown with 160 equiv of acetic acid added as a modulator).

Sulfur-functionalized materials are often studied for mercury removal applications. Such materials include chalcogenide frameworks/aerogels,[13,14] thiol-functionalized mesoporous silica,[15] polymers appended with sulfur crown ethers,[16] and sulfurated mesoporous carbon.[17] Interestingly, MOFs, as a growing class of porous materials, have remained largely untapped in the important application of mercury removal, even though increasing efforts are being made to load metal species into the pores of MOFs.[3d,18]

To demonstrate the effective capture of mercury from water, an as-made Zr-DMBD sample (~10 mg) was placed in a dilute aqueous solution (10 mL) of $Hg(NO_3)_2$ containing 5% HNO_3 (concentration of Hg^{2+} ions, 10 ppm; total amount of Hg^{2+} ions, 0.1 mg). After the mixture wa stirred at room temperature for 12 h, the residual mercury concentration in the solution was smaller than 0.01 ppm, that is, over 99.9% of the mercury was removed by Zr-DMBD even when the initial Hg^{2+} concentration was as low as 10 ppm. Compared with an earlier MOF with a thioether function,[18] which lowered the Hg^{2+} concentration in an ethanol solution to 84 ppm, the improvement enabled by the stronger-binding thiol function in Zr-DMBD is dramatic. Also, Zr-DMBD is stable toward water, adding to the practical advantages.

To assess the mercury uptake capacity, an as-made sample of Zr-DMBD (20 mg) and 4.0 mL of a 3.5% w/w aqueous solution of $HgCl_2$ (140 mg total) were stirred at room temperature for 12 h. The solid was then isolated by centrifugation and further washed with methanol to remove residual $HgCl_2$ on the exterior of the Zr-DMBD powder. The solid sample thus obtained (denoted as Zr-DMBD-$HgCl_2$) was subjected to regular CHN and inductively coupled plasma (ICP) elemental analyses; ICP analysis determined the Zr/Hg ratio to be 6:1.82, leading to a composition of $Zr_6O_4(OH)_4\cdot(C_8H_2O_4S_2)_6\cdot(DMF)_{0.5}\cdot(H_2O)_{29}\cdot(HgCl_2)_{1.82}$. More notably, similar Hg uptake capacities (i.e., DMBD/Hg ratios of ca. 3:1) were observed over a wide range of Hg^{2+} concentrations (e.g., 100 ppm) and pH conditions (e.g., even in 2 M HNO_3), with the crystallinity of the Zr-DMBD host network being well-preserved (Figure S8). The Hg uptake capability was thus found to be substantial and robust. If measures are taken to minimize the formation of the weaker-binding S−S units (e.g., crystallizing Zr-DMBD under O_2-free conditions), one might access even higher uptake capacities that are closer to the stoichiometric DMBD/Hg ratio of 1:1 (each DMBD has two −SH groups, and we assume that each Hg^{2+} ion binds two thiolate S atoms).

The IR and Raman spectra and the PXRD pattern of the Zr-DMBD-$HgCl_2$ sample also indicate mercury uptake into the porous solid. In the IR and Raman spectra, the characteristic S−H stretch mode at 2560 cm^{-1} is absent in the Zr-DMBD-$HgCl_2$ sample (compare spectra a and b to spectrum c in Figures S2 and S3); moreover, a strong band at 355 cm^{-1} consistent with Hg−S stretching emerged for the $HgCl_2$-loaded sample. As shown in Figure 2, the lowest-angle peak (111) was greatly diminished after $HgCl_2$ treatment (pattern d), whereas the higher-angle peaks (e.g., 200, 220, 331, 600) generally became stronger. Such significant changes in diffraction intensity reflect the large increase in electron density in the channel region (i.e., the system becomes less porous) as a result of $HgCl_2$ uptake while indicating that the original crystal lattice remains intact in the process.

The facile mercury uptake from solutions prompted us to probe mercury vapor sorption, a property that bears closely on the industrial processes of flue gas detoxification.[14] On the basis of the setup for mercury vapor sorption recently reported by the Kanatzidis group,[14] an as-made crystalline sample of Zr-DMBD (20 mg) and elemental mercury (liquid, 300 mg) were placed in a sealed vial with spatial separation maintained to prevent the two from directly contacting each other. The vial was then immersed in a sand bath and heated at 140 °C for 24 h. The Zr-DMBD thus treated (i.e., Zr-DMBD-Hg) was found to have the composition $Zr_6O_4(OH)_4\cdot(C_8H_2O_4S_2)_6\cdot(DMF)_{0.25}\cdot(H_2O)_{34}\cdot(Hg)_{1.2}$ as jointly determined by ICP (indicating a Zr/Hg molar ratio of 6:1.2) and regular CHN elemental analyses (see the SI). The DMBD/Hg ratio of 4.6:1 indicates that the mercury vapor uptake was slightly lower than in the solution-treated sample (Zr-DMBD-$HgCl_2$) but still significant. In parallel to the solution treatment, the IR and Raman spectra and PXRD data for the vapor-treated sample also pointed to significant Hg uptake, as indicated by the absence of the S−H stretch mode at 2560 cm^{-1} (spectra d in Figures S2 and S3), the emergence of the Hg−S stretch at 355 cm^{-1} (spectrum d in Figure S3), and the weakening of the 111 peak in the PXRD pattern (Figure 2e).

The photoluminescence (PL) of the Zr-DMBD host network was also greatly impacted by the mercury uptake, be it from solution (e.g., $HgCl_2$/water) or Hg(0) vapor. As shown in Figure 4, the as-made sample features a broad emission centered around 500 nm (spectrum a), generating a distinct near-white emission. In the $HgCl_2$- and the Hg(0)-treated samples (Zr-DMBD-$HgCl_2$ and Zr-DMBD-Hg, respectively), the PL was largely suppressed, being less than $^1/_{10}$ of the intensity for the as-made sample (spectra b and c) and hardly visible to the eye (Figure 4 inset). Fluorescence quenching by heavy metal ions is well-documented and occurs via many intramolecular/intermolecular pathways, including spin−orbit coupling, energy transfer, and electron transfer.[19] Further studies of MOFs with combined PL, porosity, and thiol functions should better uncover the applicability in the uptake and monitoring of Hg^{2+} and other metal species.

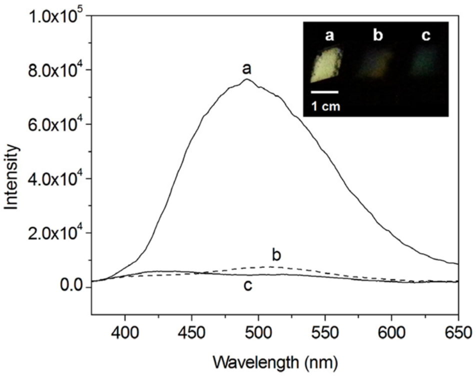

Figure 4. Room-temperature solid-state emission spectra (λ_{ex} = 355 nm) of Zr-DMBD samples: (a) as-made sample; (b) after treatment with an aqueous solution of $HgCl_2$; (c) after treatment with Hg(0) vapor. The inset shows photographs of samples a−c under 365 nm UV radiation.

The synthesis of thiol-functionalized MOFs is not limited to Zr(IV)-based systems. Our tests with Al(III) and H_2DMBD yielded a crystalline framework exhibiting the reported CAU-1 topology (discovered by Stock and co-workers[4b]). This thiol-laced Al-MOF (designated as CAU-1-SH; see Figures S9−S14 for the characterization and property studies) was made using very inexpensive starting material ($AlCl_3\cdot6H_2O$) and solvents (water or methanol), and the solid sample can be readily activated for porosity studies (e.g., the specific surface area for activated CAU-1-SH was 750 m^2/g; see Figure S12). The CAU-1-SH system thus offers significant advantages for large-scale production and applications. Further studies on these and other thiol-functionalized MOF systems are ongoing and will be published in due course.

■ ASSOCIATED CONTENT

Ⓢ Supporting Information

Experimental procedures; network synthesis and activation; SEM images; and elemental analysis, N_2/CO_2 sorption, TGA, IR/Raman, and PXRD data. This material is available free of charge via the Internet at http://pubs.acs.org.

■ AUTHOR INFORMATION

Corresponding Author

stock@ac.uni-kiel.de; zhengtao@cityu.edu.hk

Notes

The authors declare no competing financial interest.

■ ACKNOWLEDGMENTS

This work was supported by the City University of Hong Kong (Projects 7008095 and 7002590). Deutsche Forschungsgemeinschaft (DFG, SPP 1362 "Porous Metal-Organic Frameworks") and European Union (Seventh Framework Program FP7/2007-2013, grant agreement no. 228862) are also gratefully acknowledged for their financial support. Z.X. acknowledges the Alexander von Humboldt Foundation for a Humboldt Research Fellowship for Experienced Researchers (host: Prof. Markus Antonietti).

■ REFERENCES

(1) (a) Zhou, X.-P.; Xu, Z.; Zeller, M.; Hunter, A. D.; Chui, S. S.-Y.; Che, C.-M. *Inorg. Chem.* **2008**, *47*, 7459. (b) He, J.; Yang, C.; Xu, Z.; Zeller, M.; Hunter, A. D.; Lin, J. *J. Solid State Chem.* **2009**, *182*, 1821. (c) Burrows, A. D.; Frost, C. G.; Mahon, M. F.; Richardson, C. *Chem. Commun.* **2009**, 4218. (d) Zhou, X.-P.; Xu, Z.; Zeller, M.; Hunter, A. D. *Chem. Commun.* **2009**, 5439. (e) Zhou, X.-P.; Xu, Z.; He, J.; Zeller, M.; Hunter, A. D.; Clérac, R.; Mathonière, C.; Chui, S. S.-Y.; Che, C.-M. *Inorg. Chem.* **2010**, *49*, 10191. (f) Zhou, X.-P.; Xu, Z.; Zeller, M.; Hunter, A. D.; Chui, S. S.-Y.; Che, C.-M.; Lin, J. *Inorg. Chem.* **2010**, *49*, 7629. (g) He, J.; Yee, K.-K.; Xu, Z.; Zeller, M.; Hunter, A. D.; Chui, S. S.-Y.; Che, C.-M. *Chem. Mater.* **2011**, *23*, 2940. (h) Narayan, T. C.; Miyakai, T.; Seki, S.; Dincă, M. *J. Am. Chem. Soc.* **2012**, *134*, 12932. (i) Luo, T.-T.; Hsu, L.-Y.; Su, C.-C.; Ueng, C.-H.; Tsai, T.-C.; Lu, K.-L. *Inorg. Chem.* **2007**, *46*, 1532.

(2) Early examples and recent reviews: (a) Hoskins, B. F.; Robson, R. *J. Am. Chem. Soc.* **1989**, *111*, 5962. (b) Gardner, G. B.; Venkataraman, D.; Moore, J. S.; Lee, S. *Nature* **1995**, *374*, 792. (c) Yaghi, O. M.; Li, G. M.; Li, H. L. *Nature* **1995**, *378*, 703. (d) Thomas, K. M. *Dalton Trans.* **2009**, 1487. (e) Férey, G. *Chem. Soc. Rev.* **2008**, *37*, 191. (f) Robson, R. *Dalton Trans.* **2008**, 5113. (g) Kitagawa, S.; Matsuda, R. *Coord. Chem. Rev.* **2007**, *251*, 2490. (h) Bradshaw, D.; Claridge, J. B.; Cussen, E. J.; Prior, T. J.; Rosseinsky, M. J. *Acc. Chem. Res.* **2005**, *38*, 273. (i) Lee, S.; Mallik, A. B.; Xu, Z.; Lobkovsky, E. B.; Tran, L. *Acc. Chem. Res.* **2005**, *38*, 251. (j) Ockwig, N. W.; Delgado-Friedrichs, O.; O'Keeffe, M.; Yaghi, O. M. *Acc. Chem. Res.* **2005**, *38*, 176. (k) Suslick, K. S.; Bhyrappa, P.; Chou, J. H.; Kosal, M. E.; Nakagaki, S.; Smithenry, D. W.; Wilson, S. R. *Acc. Chem. Res.* **2005**, *38*, 283. (l) Xu, Z. *Coord. Chem. Rev.* **2006**, *250*, 2745. (m) Zhao, D.; Timmons, D. J.; Yuan, D.; Zhou, H.-C. *Acc. Chem. Res.* **2011**, *44*, 123. (n) Cohen, S. M. *Chem. Rev.* **2012**, *112*, 970.

(3) Selected examples: (a) Seo, J. S.; Whang, D.; Lee, H.; Jun, S. I.; Oh, J.; Jeon, Y. J.; Kim, K. *Nature* **2000**, *404*, 982. (b) Xu, Z.; Lee, S.; Kiang, Y.-H.; Mallik, A. B.; Tsomaia, N.; Mueller, K. T. *Adv. Mater.* **2001**, *13*, 637. (c) Brunet, P.; Demers, E.; Maris, T.; Enright, G. D.; Wuest, J. D. *Angew. Chem., Int. Ed.* **2003**, *42*, 5303. (d) Wu, C.-D.; Hu, A.; Zhang, L.; Lin, W. *J. Am. Chem. Soc.* **2005**, *127*, 8940. (e) Wang, Z.; Cohen, S. M. *J. Am. Chem. Soc.* **2007**, *129*, 12368.

(4) (a) Ahnfeldt, T.; Gunzelmann, D.; Loiseau, T.; Hirsemann, D.; Senker, J.; Férey, G.; Stock, N. *Inorg. Chem.* **2009**, *48*, 3057. (b) Ahnfeldt, T.; Guillou, N.; Gunzelmann, D.; Margiolaki, I.; Loiseau, T.; Férey, G.; Senker, J.; Stock, N. *Angew. Chem., Int. Ed.* **2009**, *48*, 5163. (c) Reinsch, H.; Marszalek, B.; Wack, J.; Senker, J.; Gil, B.; Stock, N. *Chem. Commun.* **2012**, *48*, 9486. (d) Reinsch, H.; Feyand, M.; Ahnfeldt, T.; Stock, N. *Dalton Trans.* **2012**, *41*, 4164.

(5) (a) Férey, G.; Mellot-Draznieks, C.; Serre, C.; Millange, F.; Dutour, J.; Surble, S.; Margiolaki, I. *Science* **2005**, *309*, 2040. (b) Hamon, L.; Serre, C.; Devic, T.; Loiseau, T.; Millange, F.; Férey, G.; De Weireld, G. *J. Am. Chem. Soc.* **2009**, *131*, 8775. (c) Serre, C.; Millange, F.; Thouvenot, C.; Nogues, M.; Marsolier, G.; Loueer, D.; Férey, G. *J. Am. Chem. Soc.* **2002**, *124*, 13519.

(6) Kim, M.; Cohen, S. M. *CrystEngComm* **2012**, *14*, 4096.

(7) (a) Silva, C. G.; Luz, I.; Llabrés i Xamena, F. X.; Corma, A.; García, H. *Chem.—Eur. J.* **2010**, *16*, 11133. (b) Kandiah, M.; Nilsen, M. H.; Usseglio, S.; Jakobsen, S.; Olsbye, U.; Tilset, M.; Larabi, C.; Quadrelli, E. A.; Bonino, F.; Lillerud, K. P. *Chem. Mater.* **2010**, *22*, 6632.

(8) (a) Morris, W.; Volosskiy, B.; Demir, S.; Gandara, F.; McGrier, P. L.; Furukawa, H.; Cascio, D.; Stoddart, J. F.; Yaghi, O. M. *Inorg. Chem.* **2012**, *51*, 6443. (b) Feng, D.; Gu, Z.-Y.; Li, J.-R.; Jiang, H.-L.; Wei, Z.; Zhou, H.-C. *Angew. Chem., Int. Ed.* **2012**, *51*, 10307. (c) Bon, V.; Senkovskyy, V.; Senkovska, I.; Kaskel, S. *Chem. Commun.* **2012**, *48*, 8407.

(9) (a) Schaate, A.; Roy, P.; Godt, A.; Lippke, J.; Waltz, F.; Wiebcke, M.; Behrens, P. *Chem.—Eur. J.* **2011**, *17*, 6643. (b) Schaate, A.; Roy, P.; Preusse, T.; Lohmeier, S. J.; Godt, A.; Behrens, P. *Chem.—Eur. J.* **2011**, *17*, 9320. (c) Garibay, S. J.; Cohen, S. M. *Chem. Commun.* **2010**, *46*, 7700. (d) Morris, W.; Doonan, C. J.; Yaghi, O. M. *Inorg. Chem.* **2011**, *50*, 6853. (e) Wang, C.; Xie, Z.; de Krafft, K. E.; Lin, W. *J. Am. Chem. Soc.* **2011**, *133*, 13445. (f) Jiang, H.-L.; Feng, D.; Liu, T.-F.; Li, J.-R.; Zhou, H.-C. *J. Am. Chem. Soc.* **2012**, *134*, 14690. (g) Guillerm, V.; Ragon, F.; Dan-Hardi, M.; Devic, T.; Vishnuvarthan, M.; Campo, B.; Vimont, A.; Clet, G.; Yang, Q.; Maurin, G.; Férey, G.; Vittadini, A.; Gross, S.; Serre, C. *Angew. Chem., Int. Ed.* **2012**, *51*, 9188. (h) Wang, C.; Wang, J.-L.; Lin, W. *J. Am. Chem. Soc.* **2012**, *134*, 19895.

(10) (a) Field, L.; Engelhardt, P. R. *J. Org. Chem.* **1970**, *35*, 3647. (b) Vial, L.; Ludlow, R. F.; Leclaire, J.; Perez-Fernandez, R.; Otto, S. *J. Am. Chem. Soc.* **2006**, *128*, 10253.

(11) Cavka, J. H.; Jakobsen, S.; Olsbye, U.; Guillou, N.; Lamberti, C.; Bordiga, S.; Lillerud, K. P. *J. Am. Chem. Soc.* **2008**, *130*, 13850.

(12) Yang, Q.; Wiersum, A. D.; Llewellyn, P. L.; Guillerm, V.; Serre, C.; Maurin, G. *Chem. Commun.* **2011**, *47*, 9603.

(13) Manos, M. J.; Malliakas, C. D.; Kanatzidis, M. G. *Chem.—Eur. J.* **2007**, *13*, 51.

(14) Oh, Y.; Morris, C. D.; Kanatzidis, M. G. *J. Am. Chem. Soc.* **2012**, *134*, 14604.

(15) Feng, X.; Fryxell, G. E.; Wang, L. Q.; Kim, A. Y.; Liu, J.; Kemner, K. M. *Science* **1997**, *276*, 923.

(16) Baumann, T. F.; Reynolds, J. G. *Chem. Commun.* **1998**, 1637.

(17) Shin, Y.; Fryxell, G. E.; Um, W.; Parker, K.; Mattigod, S. V.; Skaggs, R. *Adv. Funct. Mater.* **2007**, *17*, 2897.

(18) (a) Moon, H. R.; Kim, J. H.; Suh, M. P. *Angew. Chem., Int. Ed.* **2005**, *44*, 1261. (b) Ingleson, M. J.; Barrio, J. P.; Guilbaud, J.-B.; Khimyak, Y. Z.; Rosseinsky, M. J. *Chem. Commun.* **2008**, 2680. (c) Mulfort, K. L.; Farha, O. K.; Stern, C. L.; Sarjeant, A. A.; Hupp, J. T. *J. Am. Chem. Soc.* **2009**, *131*, 3866. (d) Chen, B.; Wang, L.; Xiao, Y.; Fronczek, F. R.; Xue, M.; Cui, Y.; Qian, G. *Angew. Chem., Int. Ed.* **2009**, *48*, 500. (e) Alkordi, M. H.; Liu, Y.; Larsen, R. W.; Eubank, J. F.; Eddaoudi, M. *J. Am. Chem. Soc.* **2008**, *130*, 12639. (f) Doonan, C. J.; Morris, W.; Furukawa, H.; Yaghi, O. M. *J. Am. Chem. Soc.* **2009**, *131*, 9492. (g) Tanabe, K. K.; Cohen, S. M. *Angew. Chem., Int. Ed.* **2009**, *48*, 7424. (h) Sabo, M.; Henschel, A.; Fröde, H.; Klemm, E.; Kaskel, S. *J. Mater. Chem.* **2007**, *17*, 3827. (i) Ishida, T.; Nagaoka, M.; Akita, T.; Haruta, M. *Chem.—Eur. J.* **2008**, *14*, 8456. (j) Uemura, T.; Hiramatsu, D.; Yoshida, K.; Isoda, S.; Kitagawa, S. *J. Am. Chem. Soc.* **2008**, *130*, 9216. (k) Schröder, F.; Esken, D.; Cokoja, M.; van den Berg, M. W. E.; Lebedev, O. I.; Van Tendeloo, G.; Walaszek, B.; Buntkowsky, G.; Limbach, H.-H.; Chaudret, B.; Fischer, R. A. *J. Am. Chem. Soc.* **2008**, *130*, 6119. (l) Meilikhov, M.; Yusenko, K.; Fischer, R. A. *Dalton Trans.* **2009**, 600. (m) Müller, M.; Zhang, X.; Wang, Y.; Fischer, R. A. *Chem. Commun.* **2009**, 119.

(19) (a) Masuhara, H.; Shioyama, H.; Saito, T.; Hamada, K.; Yasoshima, S.; Mataga, N. *J. Phys. Chem.* **1984**, *88*, 5868. (b) Nolan, E. M.; Lippard, S. J. *Chem. Rev.* **2008**, *108*, 3443. (c) Kasha, M. *J. Chem. Phys.* **1952**, *20*, 71.

4.3.3. Sulfonyl chlorides as an efficient tool for the postsynthetic modification of Cr-MIL-101-SO_3H and CAU-1-NH_2

Der folgende Artikel wurde im Jahre 2014 in der Fachzeitschrift *Chemical Communications, RSC* veröffentlicht. Der Wiederabdruck erfolgte mit freundlicher Genehmigung der Royal Society of Chemistry. Reproduced by permission of The Royal Society of Chemistry from:
A. Klinkebiel, N. Reimer, M. Lammert, N. Stock, U. Lüning, *Chemical Communications* **2014**, *50*, 9306-9308., DOI: 10.1039/C4CC03746D. Copyright 2014 The Royal Society of Chemistry.

Post-synthetische Modifizierungsreaktionen (PSM) sind ein effektives Werkzeug um zusätzliche funktionelle Gruppen in ein Material einzubringen, oder bereits vorhandene funktionelle Gruppen nachträglich zu modifizieren. In dieser Arbeit wurde eine neue Synthesestrategie entwickelt, die Sulfonylchloride als reaktive Zwischenstufen nutzt, um erstmalig Sulfonamidgruppen in Metall-Organischen Gerüstverbindungen einzubringen.

Sulfonamide besitzen aufgrund des starken elektronenziehenden Effektes der Sulfongruppe einen sauren Charakter und sind daher geeignete Verbindungen für katalytische Anwendungen. Sie werden aus einem Amin und Sulfonylchlorid hergestellt. Als Basismaterialien wurden Cr-MIL-101-SO_3H[9] und CAU-NH_2[69, 81] gewählt, so dass zwei unterschiedliche Orientierungen der gebildeten Sulfonamidgruppen resultieren, indem die Bindung einmal über das S-Atom und einmal über das N-Atom erfolgt.

Cr-MIL-101-SO_3H wurde zunächst unter Verwendung von Oxalylchlorid zum reaktiven Sulfonylchlorid umgesetzt und in einem zweiten Schritt zu verschiedenen *N*-alkyl, *N*-aryl sowie *N*-pyridin substituierten Sulfonamiden modifiziert. Der Umsetzungsgrad ist dabei abhängig von der Größe des verwendeten Amins und erreicht ein Maximum von 70 % für das kleinste (Methylamin).

CAU-1-NH_2 wurde zum Methyl- sowie Pyridinsulfonamide umgesetzt. Der Modifizierungsgrad für das Methylsulfonamid erreichte dabei 92 %, Dieser hohe Funktionalisierungsgrad lässt sich auf die Zugabe von Pyridin zurückführen, welches als Katalysator und Abfangreagenz für bei der Synthese entstandenes HCl fungierte. Dieser Effekt konnte bei den PSM-Reaktionen von Cr-MIL-101-SO_3H nicht beobachtet werden.

Die Kristallstrukturen sind in allen Fällen erhalten geblieben und auch die Porosität der Verbindungen blieb, in Abhängigkeit der Größe des hergestellten Sulfonamides sowie des Modifizierungsgrads vermindert, bestehen.

ChemComm

COMMUNICATION

View Article Online
View Journal | View Issue

Cite this: *Chem. Commun.*, 2014, 50, 9306

Received 16th May 2014,
Accepted 21st June 2014

DOI: 10.1039/c4cc03746d

www.rsc.org/chemcomm

Sulfonyl chlorides as an efficient tool for the postsynthetic modification of Cr-MIL-101-SO_3H and CAU-1-NH_2†

Arne Klinkebiel,[a] Nele Reimer,[b] Martin Lammert,[b] Norbert Stock[b] and Ulrich Lüning*[a]

Postsynthetic modification can be used to introduce sulfonamide functionalities into MOF frameworks. Using sulfonyl chlorides as reactive intermediates, Cr-MIL-SO_3H and CAU-1-NH_2 have been further modified to give hitherto unknown functionalized MOFs in which a sulfonamide group is bound to the framework either by its N or its S atom.

Among the classes of porous materials, metal–organic frameworks (MOFs) or porous coordination polymers (PCPs) represent a highly versatile group of compounds.[1] By varying the nature of the organic linker as well as the coordination environment of the constituting metal ions, these materials offer numerous opportunities to vary physical and chemical properties of the pore surface. They are promising materials for applications such as gas adsorption, separation, catalysis, chemical sensing, drug delivery.[2] Variation of the functionality of the organic linker molecules can be achieved by postsynthetic modification.[3] The introduction of already functionalized linkers is limited, due to the possible interference of the functional groups in the formation of the desired framework or their incompatibility with the reaction conditions. Nevertheless, numerous presynthetically modified MOFs have been described (*e.g.* amino,[4] hydroxyl,[5] formyl,[6] alkyne[7] and azide[8] containing structures). From these functionalized MOFs, postsynthetic modification opens a wide field of different derivatives like amides,[4f,9] imines,[10] ureas and triazoles.[7,8,11] To expand the available synthetic opportunities, it is of great importance to develop new synthetic strategies and methods for modifying functional groups which have not been successfully functionalized further until now. For example, the synthesis of frameworks containing non-coordinating acidic groups is difficult and therefore reports on postsynthetic modifications are rare.[12]

The class of sulfonamides, which is well-known for its antibacterial effects acting as antimetabolites[13] or their catalytical properties,[14] can be synthesized from sulfonic acids and amines. The chemical and electronic properties of the sulfonamide group are of great importance. Due to the strong electron-withdrawing effect of the sulfonyl group, the amide proton is acidic. Compared to carbonamides, a sulfonamide is more stable under basic aqueous conditions and the hydrogen-bond strength is enhanced.[15]

Here we show that the class of sulfonamides is accessible by tandem post-modification of the Cr-MIL-101-SO_3H using the corresponding sulfonyl chloride as a reactive intermediate. Extending our concept by treating an amino-containing network like CAU-1-NH_2[4f] with sulfonyl chlorides, it is possible to synthesize MOFs with a reversed orientation of the sulfonamide functionality as well.

The MIL-101 framework which is composed of chromium(III), 2-sulfoterephthalate and 2-sulfonate-terephthalate anions reported by Kitagawa and co-workers[16] is one of a few existing MOFs[17] containing a non-coordinating sulfonic acid. To the best of our knowledge, there has been no postsynthetic modification of this group described until now. We modified it to different *N*-alkyl and *N*-aryl substituted sulfonamides (**3a–f**) as well as an *N*-pyridine substituted one (**3g**) (Scheme 1).

PXRD data (ESI†) demonstrate that all structures are intact after the modification. Infrared spectra of compounds **3a–g** (ESI†) show characteristic bands for the introduced alkyl and aryl substituents as well as for sulfonamides. The N_2 adsorption isotherms (ESI†) of the functionalized Cr-MIL-101 **3a–g** samples exhibit the characteristic shape, while the sorption capacity slightly decreases as expected upon postsynthetic modification in comparison to starting material **1**. The decrease is only 20% for the methyl substituted sulfonamide **3a**, but 50% if benzyl substituted (**3f**). However for comparison of the different MOFs with one another, the varying degrees of post-synthetic modification (70% for **3a**, 50% for **3g**) have to be taken into consideration.

---

[a] *Otto-Diels-Institut für Organische Chemie, Olshausenstr. 40, 24098 Kiel, Germany. E-mail: luening@oc.uni-kiel.de*

[b] *Institut für Anorganische Chemie, Max-Eyth-Strasse 2, 24118 Kiel, Germany. E-mail: stock@ac.uni-kiel.de*

† Electronic supplementary information (ESI) available: Experimental details, ^{1}H-NMR spectroscopy, FT-IR spectroscopy, XRPD data, adsorption isotherms. See DOI: 10.1039/c4cc03746d

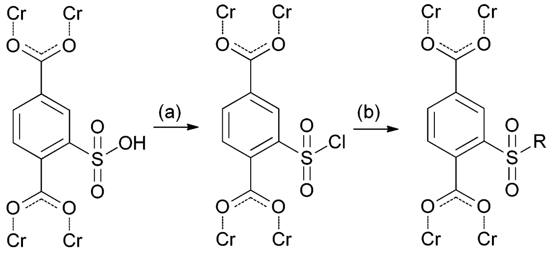

1 **2** **3 a-g**

a R = -NHMe (~ 70 %) **e** R = -NHPh (~ 60 %)
b R = -NHEt (~ 65 %) **f** R = -NHBn (~ 50 %)
c R = -NHPr (~ 65 %) **g** R = -NHPy (~ 45 %)
d R = -NMe$_2$ (~ 60 %)

Scheme 1 Two-step postsynthetic modification of Cr-MIL-101-SO$_3$H (**1**) *via* sulfonyl chloride **2** to produce sulfonamides **3a–g**. (a) Oxalyl chloride, cat. DMF, THF, 24 h, room temp. (b) Corresponding amine, THF, 24 h, room temp.

For further analysis, the MOFs were dissolved in sodium hydroxide, the insoluble chromium salts were removed, and the remaining solution was analyzed by ^{1}H-NMR data (ESI†). In Fig. 1, spectra for compound **3a** are shown as examples. They exhibit the aromatic signals for the desired sulfonamide **3a** and the corresponding unfunctionalized sulfoterephthalic acid of the starting material **1**. The ratio of the relative integrals allows us to determine the conversion, which is about 70% (Fig. 1(B)). Due to its water solubility, removal of the linker of starting material **1** (Fig. 1(A)) is possible by extracting the functionalized amide of **3a** with an organic solvent from an acidic solution, whereas the starting material stays mostly in the aqueous phase.

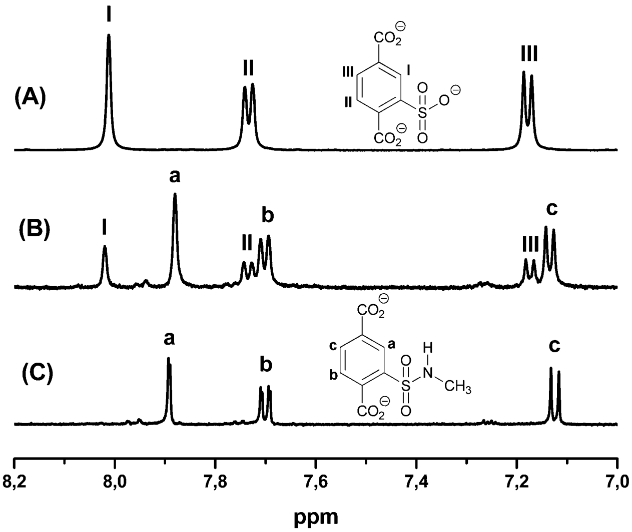

Fig. 1 ^{1}H-NMR spectra after dissolving the respective MOF in NaOD (aliphatic signals are not shown, see ESI† for details): (A) aromatic protons (I–III) of the unfunctionalized linker of starting material **1**, (B) mixture of functionalized amide **3a** (a–c) and unfunctionalized linker (I–III) after postsynthetic modification, (C) terephthalic protons (a–c) of the functionalized amide **3a** after extraction of the unfunctionalized linker.

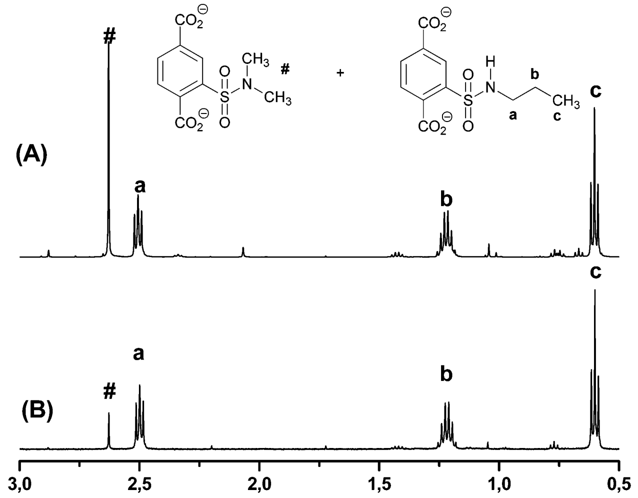

Fig. 2 ^{1}H-NMR spectra of the respective MOF in NaOD (aromatic signals are not shown, see ESI† for details): *N*-propyl sulfonamide **3c** (a–c) and side product *N*,*N*-dimethyl sulfonamide **3d** (#) after using (A) 15 μL and (B) 5 μL DMF as catalyst.

Comparison of conversion degrees (Scheme 1) shows a dependency on size of the introduced amine and an upper limit of about 70%. Addition of pyridine or triethylamine to scavenge the generated hydrochloric acid showed no improvement of conversion. Due to the instability of the sulfonyl chloride, the reaction temperature was not increased above 25 °C. The upper limit of conversion matches with the conclusion of Kitagawa[16] for one of three sulfonic acid groups to be deprotonated. The resulting charges are compensating the positive charges of the framework.

In all cases, dimethylsulfonamide **3d** is formed as a byproduct, which results from the reaction of sulfonyl chloride **2** and dimethylamine, which is formed as a sideproduct from the catalytical amount of dimethylformamide added during the reaction. For verification, we synthesized *N*,*N*-dimethylsulfonamide **3d** as reference. Variation of the catalytical amount of dimethylformamide from 15 μL to 5 μL showed a significant decrease of this sideproduct, which is shown exemplarily for sulfonamide **3c** in Fig. 2. The amount of sideproduct formed varies between 1–5% (see ESI† for details).

To extend our modification concept of using sulfonyl chlorides as intermediates, it was our next goal to invert the binding sequence of the sulfonamide by treating the amino containing framework CAU-1-NH$_2$[4f] (**5**) with sulfonyl chlorides in order to obtain related amides **4** and **6** (Scheme 2). The synthesis of sulfonamide **6** was carried out at room temperature due to the instability of 2-pyridinylsulfonyl chloride (ESI†), which was synthesized according to a literature procedure.[18] To obtain an *N*-alkyl substituted sulfonamide, we treated compound **5** with methyl sulfonyl chloride, which can withstand higher temperatures (see Table 1).

The ratio of the relative integrals of the desired sulfonamides and the corresponding amino terephthalic acid **5** in the ^{1}H-NMR spectra of the dissolved material (ESI†) allows an

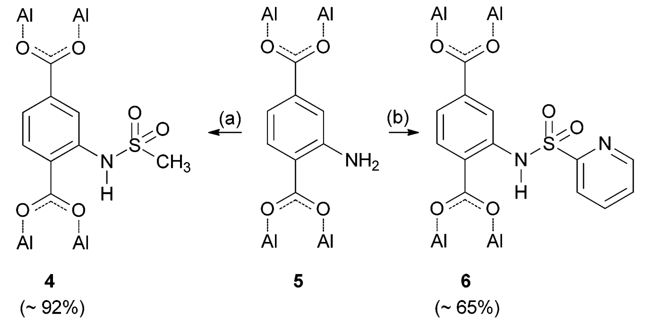

Scheme 2 Postsynthetic modification of CAU-1-NH_2 (**5**) using methyl and 2-pyridinylsulfonyl chloride giving the sulfonamides **4** and **6**. (a) For different reaction conditions see Table 1. (b) 2-Pyridinylsulfonyl chloride, pyridine, dichloromethane, 24 h, room temp.

Table 1 Optimization of the reaction conditions for the synthesis of sulfonamide **4**: 15 mg CAU-1-NH_2, 100 μL pyridine (if used), 2.0 mL methyl sulfonyl chloride (mw = microwave)

Catalyst	Temperature	Reaction time	Conversion (%)
—	60 °C	4 d	59
Pyridine	60 °C	24 h	92
—	90 °C (mw)	30 min	43
—	120 °C (mw)	30 min	64
—	120 °C (mw)	60 min	76
—	150 °C (mw)	30 min	82
—	180 °C (mw)	30 min	91
Pyridine	110 °C (mw)	10 min	92

approximation of the conversion of about 65% for pyridine-sulfonamide **6** and a conversion of 92% to methylsulfonamide **4**. In contrast to the previous approaches using Cr-MIL-101-SO_3H, the addition of pyridine as a catalyst and scavenger for the generated hydrochloric acid showed a significant improvement of conversion in both cases.

Due to the stability of methylsulfonyl chloride at higher temperatures, the reaction conditions for the synthesis of sulfonamide **4** were optimized by performing the reaction in a normal glass vessel as well as under microwave conditions.

In summary, we report a synthetic strategy for introducing the sulfonamide functionality into MOFs for the first time. Amino and sulfonic acid containing MOFs like CAU-1-NH_2 and Cr-MIL-101-SO_3H can be modified by using sulfonyl chlorides as reactive intermediates in two different routes. With the broad variation of substituents and the different orientations of the sulfonamide moiety to the framework, this method offers a promising tool for the postsynthetic modification of amino and sulfonic acid containing frameworks. Above all, the sulfonamide group is a powerful functionality with respect to catalysis and host–guest interactions. Their implementation into MOFs makes them promising materials for future developments.

Financial support of the Deutsche Forschungsgemeinschaft (SPP 1362) is gratefully acknowledged.

Notes and references

1 (*a*) O. M. Yaghi, M. O'Keeffe, N. W. Ockwig, H. K. Chae, M. Eddaoudi and J. Kim, *Nature*, 2003, **423**, 705; (*b*) S. Kitagawa, R. Kitaura and S. Noro, *Angew. Chem., Int. Ed.*, 2004, **43**, 2334 (*Angew. Chem.*, 2004, **116**, 2388); (*c*) G. Férey, *Chem. Soc. Rev.*, 2008, **37**, 191; (*d*) D. Farusseng, *Metal-Organic Frameworks*, Wiley-VCH, Weinheim, 2011.

2 (*a*) H.-C. Zhou, J. R. Long and O. M. Yaghi, (ed.) *Chem. Rev.*, 2012, **112**, 673; (*b*) J. R. Long and O. M. Yaghi, (ed.) *Chem. Soc. Rev.*, 2009, **38**, 1201; (*c*) C. Wang, D. Liu and W. Lin, *J. Am. Chem. Soc.*, 2013, **135**, 13222; (*d*) S. H. Jhung, N. A. Khan and Z. Hasan, *CrystEngComm*, 2012, **14**, 7099; (*e*) S. T. Meek, J. A. Greathouse and M. D. Allendorf, *Adv. Mater.*, 2011, **23**, 249; (*f*) B. Van de Voorde, B. Bueken, J. Denayer and D. De Vos, *Chem. Soc. Rev.*, 2014, DOI: 10.1039/c4cs00006d; (*g*) A. Dhakshinamoorthy and H. Garcia, *Chem. Soc. Rev.*, 2014, DOI: 10.1039/c3cs60442j; (*h*) E. Coronado and G. Mínguez Espallargas, *Chem. Soc. Rev.*, 2013, **42**, 1525.

3 S. M. Cohen, *Chem. Rev.*, 2012, **112**, 970.

4 (*a*) S. Bauer, C. Serre, T. Devic, P. Horcajada, J. Marrot, G. Férey and N. Stock, *Inorg. Chem.*, 2008, **47**, 7568; (*b*) J. S. Costa, P. Gamez, C. A. Black, O. Roubeau, S. J. Teat and J. Reedijk, *Eur. J. Inorg. Chem.*, 2008, 1551; (*c*) K. Koh, A. G. Wong-Foy and A. J. Matzger, *Angew. Chem., Int. Ed.*, 2008, **47**, 677 (*Angew. Chem.*, 2008, **120**, 689); (*d*) Z. Wang, K. K. Tanabe and S. M. Cohen, *Inorg. Chem.*, 2009, **48**, 296; (*e*) M. Eddaoudi, J. Kim, N. Rosi, D. Vodak, J. Wachter, M. O'Keeffe and O. M. Yaghi, *Science*, 2002, **295**, 469; (*f*) T. Ahnfeldt, N. Guillou, D. Gunzelmann, I. Margiolaki, T. Loiseau, G. Férey, J. Senker and N. Stock, *Angew. Chem., Int. Ed.*, 2009, **48**, 5163 (*Angew. Chem.*, 2009, **121**, 5265).

5 T. Ahnfeldt and N. Stock, *CrystEngComm*, 2012, **14**, 505.

6 W. Morris, C. J. Doonan, H. Furukawa, R. Banerjee and O. M. Yaghi, *J. Am. Chem. Soc.*, 2008, **130**, 12626.

7 T. Gadzikwa, G. Lu, C. L. Stern, S. R. Wilson, J. T. Hupp and S. T. Nguyen, *Chem. Commun.*, 2008, 5493.

8 Y. Goto, H. Sato, S. Shinkai and K. Sada, *J. Am. Chem. Soc.*, 2008, **130**, 14354.

9 (*a*) S. J. Garibay, Z. Wang, K. K. Tanabe and S. M. Cohen, *Inorg. Chem.*, 2009, **48**, 7341; (*b*) D. Britt, C. Lee, F. J. Uribe-Romo, H. Furukawa and O. M. Yaghi, *Inorg. Chem.*, 2010, **49**, 6387.

10 (*a*) M. J. Ingleson, J. P. Barrio, J.-B. Guilbaud, Y. Z. Khimyak and M. J. Rosseinsky, *Chem. Commun.*, 2008, 2680; (*b*) C. J. Doonan, W. Morris, H. Furukawa and O. M. Yaghi, *J. Am. Chem. Soc.*, 2009, **131**, 9492.

11 (*a*) T. Ahnfeldt, D. Gunzelmann, T. Loiseau, D. Hirsemann, J. Senker, G. Férey and N. Stock, *Inorg. Chem.*, 2009, **48**, 3057; (*b*) M. Savonnet, D. Bazer-Bachi, N. Bats, J. Perez-Pellitero, E. Jeanneau, V. Lecocq, C. Pinel and D. Farrusseng, *J. Am. Chem. Soc.*, 2010, **132**, 4518.

12 (*a*) N. Reimer, B. Gil, B. Marszalek and N. Stock, *CrystEngComm*, 2012, **14**, 4119; (*b*) M. I. H. Mohideen, B. Xiao, P. S. Wheatley, A. C. McKinlay, Y. Li, A. M. Z. Slawin, D. W. Aldous, N. F. Cessford, T. Düren, X. Zhao, R. Gill, K. M. Thomas, J. M. Griffin, S. E. Ashbrook and R. E. Morris, *Nat. Chem.*, 2011, **3**, 304.

13 G. L. Patrick, *An Introduction to Medicinal Chemistry*, Oxford University Press, 1995.

14 (*a*) T. Kano, R. Sakamoto, Y. Yamaguchi, K. Itoh and K. Maruoka, *Chem. Commun.*, 2013, **49**, 1118; (*b*) L. Zu, H. Xie, H. Li, J. Wang and W. Wang, *Org. Lett.*, 2008, **10**, 1211; (*c*) Z. Xu, R. Wang, J. Xu, C.-S. Da, W.-J. Yan and C. Chen, *Angew. Chem., Int. Ed.*, 2003, **42**, 5747 (*Angew. Chem.*, 2003, **115**, 5925).

15 C. S. Hunter, *Angew. Chem., Int. Ed.*, 2004, **43**, 5310 (*Angew. Chem.*, 2004, **116**, 5424).

16 G. Akiyama, R. Matsuda, H. Sato, M. Takata and S. Kitagawa, *Adv. Mater.*, 2011, **23**, 3294.

17 (*a*) S. Biswas, J. Zhang, Z. Li, Y.-Y. Liu, M. Grzywa, L. Sun, D. Volkmer and P. Van Der Voort, *Dalton Trans.*, 2013, **42**, 4730; (*b*) M. Lin Foo, S. Horike, T. Fukushima, Y. Hijikata, Y. Kubota, M. Takata and S. Kitagawa, *Dalton Trans.*, 2012, **41**, 13791; (*c*) Postsynthetic partial sulfatation: M. G. Goesten, J. Juan-Alcañiz, E. V. Ramos-Fernandez, K. B. S. S. Gupta, E. Stavitski, H. van Bekkum, J. Gascon and F. Kapteijn, *J. Catal.*, 2011, **281**, 177.

18 M. Kajino, A. Hasuoka and H. Nishida, *US Pat.*, US 20070060623A1, 2007.

4.3.4. New Al-MOFs Based on Sulfonyldibenzoate Ions: A Rare Example of Intralayer Porosity

Der folgende Artikel wurde im Jahre 2015 in der Fachzeitschrift *Inorganic Chemistry*, *ACS* veröffentlicht.[107] Der Wiederabdruck erfolgte mit freundlicher Genehmigung der ACS. Reproduced with permission from:

N. Reimer, H. Reinsch, A. K. Inge, N. Stock, *Inorganic Chemistry* **2014**, *54*, 492-501, DOI: 10.1021/ic502242j. Copyright 2015 American Chemical Society.
http://pubs.acs.org/doi/abs/10.1021/ic502242j

In dieser Arbeit wurden unter Verwendung V-förmiger sulfonfunktionalisierter Linkermoleküle vier neue Al-MOFs hergestellt und charakterisiert. Im Fokus standen hierbei der Einfluss der Linkergeometrie auf die Bildung der anorganischen Baueinheit sowie der Einfluss der funktionellen Gruppen auf die Sorptionseigenschaften der erhaltenen Materialien.

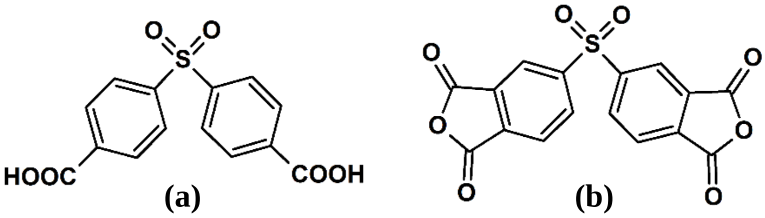

Abbildung 4.13: Für diese Studie verwendete Linkermoleküle. (a) 4,4‘-Sulfonyldibenzoesäure (H_2SDBA); (b) 3,3´,4,4´-Diphenylsulfontetracarbonsäuredianhydrid (DPSDA).

Es wurde eine Hochdurchsatzstudie durchgeführt, bei der zunächst das System Al^{3+}/4,4´-Sulfonyldibenzoesäure (H_2SDBA)/H_2O/NaOH untersucht wurde. Nach Aufreinigung mit DMF, wurde eine neue mikroporöse Verbindung [Al(OH)(SDBA)]·0.25DMF (CAU-11) erhalten, deren Struktur Ketten von *trans* eckenverknüpfter AlO_6-Polyedern enthält. Die Ketten werden so über die Carboxylatgruppen der Linkermoleküle verknüpft, dass sich Schichten mit eindimensionalen rautenförmigen Kanälen ausbilden. Hierbei weisen die Sulfongruppen in Richtung benachbarter Al-O-Ketten, was der Verbindung einen hydrophoben Charakter verleiht. Die anorganische Baueinheit ist interessanterweise analog zu der von MIL-53,[50] welches bis dato nur mit linearen Dicarbonsäuren als Linkermolekül hergestellt wurde. Erwartet wurde eigentlich eine Analogie zu Baueinheiten, die mit anderen V-förmigen Linkermolekülen wie Isophthalsäure in CAU-10[25] oder 4,4‘-Benzophenondicarbonsäure in CAU-8[58] erhalten wurden.

Unter der Verwendung des Linkermoleküls 3,3´,4,4´-Diphenylsulfontetracarbonsäuredianhydrid (DPSDA) wurde in einer zweiten Hochdurchsatzuntersuchung die zu CAU-11 isoretikuläre Verbindung $[Al(OH)(H_2DPSTC)]\cdot 0.5H_2O$ (CAU-11-COOH) hergestellt. Die zusätzliche nicht koordinierende Carboxylgruppe verleiht der vorher hydrophoben Verbindung einen hydrophilen Charakter.

Durch Veränderung des Verhältnisses von Al^{3+} zu DPSTA in der Synthese konnte in weiterführenden Hochdurchsatzsynthesen eine neue Verbindung $[Al_2(OH)_2(DPSTC)(H_2O)_2]\cdot H_2O$ (CAU-12) hergestellt werden. In der Struktur von CAU-12 koordinieren alle Carboxylatgruppen, zwei der vier Carboxylatgruppen koordinieren jedoch nur mit einem Sauerstoffatom. Durch thermische Aktivierung können die koordinierenden Wassermoleküle aus der Struktur entfernt werden und eine neue Verbindung $[Al_2(OH)_2(DPSTC)]\cdot nH_2O$ (CAU-12-dehy) resultiert, in deren Struktur die vier Carboxylatgruppen über alle Sauerstoffatome koordinieren. CAU-12 und CAU-12-dehy bilden dreidimensionale Gerüststrukturen aus und basieren ebenfalls auf Ketten von *trans* eckenverknüpften AlO_6-Polyedern. Sie weisen einen hydrophilen Charakter auf, da die Sulfongruppen in die vorhandenen Poren hinein weisen. Alle Strukturen wurden aus Röntgenpulverdaten gelöst und mittels Rietveldmethoden verfeinert.

Inorganic Chemistry
Article
pubs.acs.org/IC

New Al-MOFs Based on Sulfonyldibenzoate Ions: A Rare Example of Intralayer Porosity

Nele Reimer,[†] Helge Reinsch,[‡] A. Ken Inge,[†] and Norbert Stock*,[†]

[†]Institut für Anorganische Chemie, Christian-Albrechts-Universität zu Kiel, Max-Eyth-Strasse 2, D-24118 Kiel, Germany
[‡]INGAP Centre of Research-Based Innovation, Department of Chemistry, University of Oslo, Sem Saerlandsvei 26, N-0315 Oslo, Norway

Supporting Information

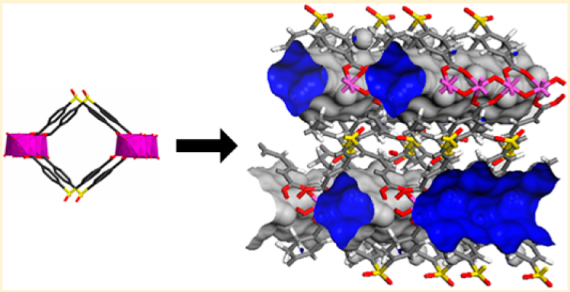

ABSTRACT: A new sulfone-functionalized metal−organic framework $[Al(OH)(SDBA)]\cdot 0.25DMF$, denoted CAU-11, was synthesized using a V-shaped linker molecule 4,4′-sulfonyldibenzoic acid (H_2SDBA). The crystal structure was solved from synchrotron X-ray powder diffraction data. Chains of trans corner-sharing AlO_6 octahedra are interconnected by the carboxylate groups to form layers (ABAB stacking). Within the layers, hydrophobic lozenge-shaped pores with a diameter of 6.4 × 7.1 Å^2 are present inducing permanent porosity (a_{BET} = 350 m^2 g^{-1} and V_{micro} = 0.17 cm^3 g^{-1}). With the application of HT-methods (HT = high throughput), the isoreticular carboxylate functionalized compound $[Al(OH)(H_2DPSTC)]\cdot 0.5H_2O$ (CAU-11-COOH) was synthesized using the linker molecule 3,3′,4,4′-diphenylsulfonetetracarboxylic dianhydride (DPSDA), which hydrolyzes under the reaction conditions. Due to the additional noncoordinating carboxylic acid groups the pores are hydrophilic. Changing the molar ratio of Al^{3+} to linker lead to the discovery of a second new compound $[Al_2(OH)_2(DPSTC)(H_2O)_2]\cdot 0.5H_2O$ (CAU-12). In CAU-12 the linker molecule is fully deprotonated which leads to different connectivity compared to the structure of CAU-11-COOH. Thermal activation of CAU-12 leads to dehydration and transformation of the structure to $[Al_2(OH)_2(DPSTC)]\cdot nH_2O$ (CAU-12-dehy). Coordinated water molecules were removed, and the coordination site is replaced by the previously noncoordinating O atom of the adjacent carboxylate group. The SO_2-groups point into the pores resulting in a highly hydrophobic three-dimensional framework. The compounds exhibit high thermal stability in air at least up to 420 °C. Synthesis of CAU-11 can be easily scaled up in very high yields (98%).

■ INTRODUCTION

In the field of porous materials, metal−organic frameworks (MOFs) have drawn much attention during the last two decades.[1−3] This is probably due to their modular assembly and their potential applications in the fields of gas storage and separation, catalysis, or drug delivery.[4−6] MOFs are built up from inorganic and organic building units. By variation of one of the building units by a chemically different but topologically equivalent unit, it is possible to modulate the properties of a compound. This approach is called isoreticular chemistry.[7] The synthesis of isoreticular compounds is not always easily accomplished since changing one component in the synthesis mixture often necessitates optimization of the reaction conditions of the desired compound. The reaction product of a solvothermal synthesis depends on many different reaction parameters, and systematic studies are therefore of great advantage. High-throughput (HT) methods have shown to be an important and efficient tool to accomplish this task.[8−10] We focused our work on MOFs based on Al^{3+} ions since these materials are known for their excellent thermal and chemical stability.[11,12] This makes them suitable for postsynthetic modification reactions and renders them as potential candidates for storage and separation or heat transformation processes.[4,13−15] In addition, aluminum is nontoxic, and the inorganic starting materials are in general inexpensive, which makes these compounds interesting for industrial applications.[16] Al-MIL-53 (MIL = Materiaux de l'Institute Lavoisier) is a very well-known Al-MOF that contains terephthalate ions.[17] Its structure is based on chains of trans corner-sharing AlO_6 octahedra which are interconnected by the carboxylate groups of the linker molecules, to build up a three-dimensional framework with lozenge-shaped pores. The inorganic building unit of MIL-53 is very common in other Al-MOFs based on linear linker molecules.[18−22] During the past two years we investigated the influence of the linker shape on the formation of the inorganic building unit and the resulting MOF structure.[20,23−27] V-shaped linkers were chosen for these studies (Figure 1).

The use of (functionalized) isophthalic acid (Figure 1, **1**) led to the porous compound $[Al(OH)(m\text{-}BDC)]\cdot$solvent (CAU-10).[25] Its structure is built of helices of cis corner-sharing AlO_6 octahedra, which are interconnected by the carboxylate groups of the linker molecule. Attempts to increase the pore size of

Received: September 16, 2014
Published: December 24, 2014

DOI: 10.1021/ic502242j
Inorg. Chem. 2015, 54, 492−501

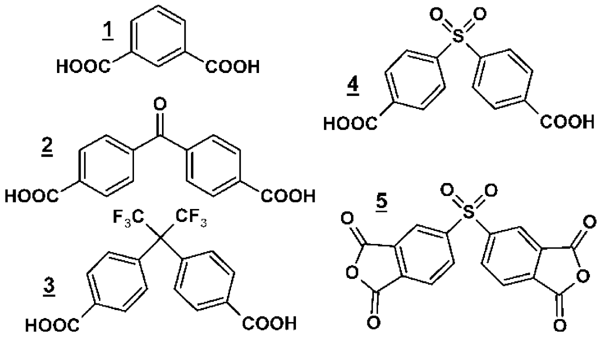

Figure 1. V-shaped linker molecules used for the synthesis of MOFs: Isophthalic acid (m-H_2BDC) (**1**), 4,4′-benzophenonedicarboxylic acid (**2**), 4,4′-(hexafluoroisopropylidene)bis(benzoic acid) (**3**), 4,4′-sulfonyldibenzoic acid (H_2SDBA) (**4**), and 3,3′,4,4′-diphenylsulfontetracarboxylic dianhydride (DPSDA) (**5**).

CAU-10 by replacing the isophthalic acid with the extended but more flexible linker 4,4′-benzophenonedicarboxylic acid (H_2BPDC, Figure 1, **2**) resulted in a new compound [Al(OH)(BPDC)]·solvent (CAU-8), which contains MIL-53 type inorganic building units.[26] Other larger V-shaped linkers have only sparsely been used in the synthesis of MOFs in combination with trivalent cations. Thus, only a few examples based on 4,4′-(hexafluoroisopropylidene)bis(benzoic acid) (Figure 1, **3**) and rare-earth metals[28,29] as well as one compound containing In^{3+} ions[30] are known. The geometry of 4,4′-sulfonyldibenzoic acid (H_2SDBA) is also very similar to that of H_2BPDC. This linker has been more extensively used (Supporting Information Table S1), but its reactions with trivalent cations have only resulted in three nonporous compounds so far based on neodymium, ytterbium, and erbium.[31] Several other compounds are known on the basis of mono- or bivalent cations with one-, two-, or three-dimensional structures. Among these, only a few of them, $[Cs_2Pb_2(SDBA)_3(DMF)]\cdot DMF$,[32] $[Ca(SDBA)]\cdot 0.45H_2O$,[33] and [Ca(SDBA)],[34] as well as $[Zn_3(OH)_2(SDBA)_2]\cdot EtOH$ and $[M_3(OH)_2(SDBA)_2(EtOH)(H_2O)_3]\cdot 3.5H_2O$ (M = Mg, Ni, Co),[35] exhibit permanent porosity (Supporting Information Table S1).

In this Article we present the results of our high-throughput investigation of the systems Al^{3+}/H_2SDBA/solvent/additive and Al^{3+}/DPSDA/solvent/additive based on the V-shaped ligands 4,4′-sulfonyldibenzoic acid (H_2SDBA, Figure 1, structure 4) and 3,3′,4,4′-diphenylsulfonetetracarboxylic dianhydride (DPSDA, Figure 1, structure 5). Four new compounds were obtained and characterized in detail by X-ray powder diffraction (PXRD), vibrational spectroscopy, thermogravimetric measurements and elemental analysis as well as temperature dependent X-ray powder diffraction and sorption measurements.

■ EXPERIMENTAL SECTION

Chemicals. All chemicals are commercially available and were employed without further purification.

Methods. Details of the HT studies for the discovery of CAU-11, CAU-11-COOH, and CAU-12 are described in the Supporting Information. HT-experiments under conventional heating were carried out in custom-made steel-multiclaves in Teflon-lined reaction vessels.[10] HT-experiments under microwave-assisted heating were performed in glass vials which were placed in a SiC block. Reactions were carried out in a microwave reaction system Synthos3000 by Anton Paar.[12] In order to scale-up the reactions, custom-made steel autoclaves containing Teflon-inlets with a volume of 30 mL were used. The initial characterization by means of PXRD was carried out on a STOE-Stadi-P combi diffractometer (Cu $K\alpha_1$ radiation) equipped with an xy-stage and an image plate detector system. The synchrotron PXRD data for the structure determination and refinement of CAU-11, [Al(OH)(SDBA)], and CAU-11-COOH, $[Al(OH)(H_2DPSTC)]\cdot 0.5H_2O$, were measured at the MS-POWDER beamline (X04SA), EH1 at the Swiss Light Source, Paul Scherrer Institute, Villigen, Switzerland. The wavelength was set to 1.000 009 Å, and the pattern was recorded on a MYTHEN II detector.[36] The data for structure determination and refinement of CAU-12, $[Al_2(OH)_2(DPSTC)(H_2O)_2]\cdot 0.5H_2O$, and CAU-12-dehy, $[Al_2(OH)_2(DPSTC)]\cdot nH_2O$, were collected on a STOE-Stadi-P diffractometer (Cu $K\alpha_1$-radiation) equipped with a PSD detector.

The temperature-dependent PXRD experiments were performed in Debye−Sherrer mode on a STOE Stadi-P diffractometer (Cu $K\alpha_1$, λ = 1.5406 Å) equipped with a STOE high temperature capillary furnace. Each powder pattern was recorded in the range 3−90° (2Θ). CAU-11 was investigated in the range from 20 °C up to 660 °C in steps of 40 °C. Each measurement was collected for 20 min, and the heating rate was 5 K min^{-1}. The patterns for CAU-11-COOH were recorded in the range 20 °C up to 660 °C in steps of 40 °C. Each measurement was collected for 15 min, and the heating rate was 10 K min^{-1}. CAU-12 was studied in the range from 30 °C up to 270 °C in steps of 20 °C and from 270 °C up to 620 °C in steps of 50 °C. Each measurement was collected for 15 min, and the heating rate was 5 and 10 K min^{-1}, respectively. IR spectra were recorded on a Bruker ALPHA-FT-IR A220/D-01 spectrometer equipped with an ATR-unit. The thermogravimetric (TG) analyses were carried out using a NETSCH STA 409 CD analyzer. The samples were heated in Al_2O_3 crucibles at a rate of 4 K min^{-1} under a flow of air (25 mL min^{-1}). The contents of carbon, hydrogen, nitrogen, and sulfur were determined by elemental chemical analysis on a Eurovektor EuroEA elemental analyzer. Gas sorption experiments were performed using a BEL JAPAN INC. Belsorpmax instrument. Nitrogen and hydrogen measurements were carried out at 77 K and carbon dioxide, methane, and water vapor measurements at 298 K.

HT-Experiments. CAU-11 ($[Al(OH)(SDBA)]\cdot 0.25DMF$) was discovered in the system $AlCl_3\cdot 6H_2O/H_2SDBA/H_2O/NaOH$. Reactions were carried out under solvothermal reaction conditions using our custom-made HT-reactors containing 24 Teflon inlets with a maximum volume of 2 mL.[10] First the solid starting materials ($AlCl_3\cdot 6H_2O$ and H_2SDBA) were placed in the inlets, followed by the addition of H_2O and then NaOH. Six different ratios of $AlCl_3\cdot 6H_2O$ to H_2SDBA (3:1−1:3, 1 equiv corresponds to 0.06 mmol) were chosen and repeated four times, with different amounts of NaOH as additive (0−4 equiv). Details of the exact chemical and physical parameters employed in the discovery of $[Al(OH)(SDBA)]\cdot 0.25DMF$ are listed in the Supporting Information (Table S2). For the optimization of the purity and crystallinity of the product, the following synthesis parameters were systematically varied: (1) the Al^{3+}-sources ($Al(NO_3)_3\cdot 9H_2O$, $AlCl_3\cdot 6H_2O$, $Al_2(SO_4)_3\cdot 18H_2O$, and $Al(ClO_4)_3\cdot 9H_2O$), (2) the overall concentrations (0.06−0.27 mol/L), and (3) the molar ratios of Al^{3+} to H_2SDBA (6:3−1:3 equiv). In addition the influence of additives (HCl and NaOH), the reaction temperature (120−170 °C), and the reaction time (12−36 h) was studied.

CAU-11-COOH ($[Al(OH)(H_2DPSTC)]\cdot 0.5H_2O$) was discovered in the system $Al^{3+}/DPSDA/H_2O/NaOH$. Reactions were carried out in analogy to the procedure described for CAU-11, but the HT-experiments were performed under microwave-assisted heating.[12] The solid starting materials were placed in glass vials with a maximum volume of 3 mL, followed by the addition of H_2O, aqueous Al^{3+} solution, and NaOH. The vials were closed with a Teflon seal and a screw cap and then placed in a SiC block, suitable for microwave heating. Details of the exact chemical and physical parameters employed for the discovery of $[Al(OH)(H_2DPSTC)]\cdot 0.5H_2O$ are listed in the Supporting Information (Table S3). For the optimization of the purity and crystallinity of the product, the following synthesis parameters were systematically varied: (1) Al^{3+} sources ($Al(NO_3)_3\cdot 9H_2O$, $AlCl_3\cdot 6H_2O$, $Al_2(SO_4)_3\cdot 18H_2O$, and $Al(ClO_4)_3\cdot 9H_2O$), (2) the

Table 1. Summary of the Crystallographic Parameters of the Rietveld Refinements of [Al(OH)(SDBA)], $[Al_2(OH)_2(DPSTC)(H_2O)_2]\cdot 0.5H_2O$, and $[Al_2(OH)_2(DPSTC)]\cdot nH_2O$, and the Parameters of $[Al(OH)(H_2DPSTC)]\cdot 0.5H_2O$ obtained from a Pawley Fit

	CAU-11 [Al(OH) (SDBA)][a]	CAU-11-COOH $[Al(OH)(H_2DPSTC)]$[a]	CAU-12 $[Al_2(OH)_2(DPSTC)(H_2O)_2]\cdot 0.5H_2O$	CAU-12-dehy $[Al_2(OH)_2(DPSTC)]\cdot nH_2O$
structure determined from	powder data		powder data	powder data
λ/Å	1.000 009	1.000 009	1.5406	1.5406
formula sum	$AlC_{14}H_9O_7S$	$AlC_{16}H_{11}O_{11}S$	$Al_2C_{16}H_{15}O_{14.5}S$	$Al_2C_{16}H_{10+2n}O_{12+n}S$
Z	4	4	1	1
cryst syst	orthorhombic	orthorhombic	triclinic	triclinic
a/Å	6.6111(5)	6.6551(3)	6.6872(4)	6.3521(6)
b/Å	12.888(1)	19.9428(12)	6.6878(6)	7.1524(9)
c/Å	20.020(1)	12.9656(7)	13.6148(11)	13.7010(15)
α/deg	90	90	84.698(8)	81.841(12)
β/deg	90	90	84.705(5)	88.967(7)
γ/deg	90	90	61.126(5)	64.2526(7)
V/Å^3	1705.9(2)	1720.5(2)	530.12(8)	544.41(11)
space group	$Pnma$	$Pna2_1$	$P\bar{1}$	$P\bar{1}$
solution method	real space method, FOX[37]		structural model from the literature[38]	structural model derived from CAU-12
refinement method	least-squares Rietveld method[39]	Pawley method[39]	least-squares Rietveld method[39]	least-squares Rietveld method[39]
R_{wp}	7.7	3.3	7.6	6.1
R_{Bragg}	1.4		1.4	1.0

[a] Samples were activated prior to the PXRD measurements to remove the solvent molecules.

overall concentration (0.067− 0.267 mol/L), and (3) the molar ratios of Al^{3+} and DPSDA (4:2−2:4 equiv). In addition the influences of reaction temperature (150−170 °C) and reaction time (3−5 h) were studied.

In the course of this systematic investigation the second phase $[Al_2(OH)_2(DPSTC)(H_2O)_2]\cdot 0.5H_2O$ (CAU-12) was discovered (Supporting Information Figure S2). Synthesis optimization was performed for CAU-12 as was for CAU-11-COOH. Details of the exact chemical and physical parameters employed for the synthesis of $[Al_2(OH)_2(DPSTC)(H_2O)_2]\cdot 0.5H_2O$ are listed in the Supporting Information (Table S4).

Optimized Reaction Conditions for $[Al(OH)(SDBA)]\cdot 0.25DMF$. The optimized synthesis parameters obtained from the HT-investigations were used for the synthesis scale up of CAU-11. CAU-11 is synthesized from a mixture of $AlCl_3\cdot 6H_2O$ (724 mg, 3 mmol), 4,4′-sulfonyldibenzoic acid (H_2SDBA) (268 mg, 1.2 mmol), 2 M aqueous solution of NaOH (1.8 mL, 3.6 mmol), and 18.2 mL of H_2O (no homogenization was necessary). The Teflon-liner was placed in a steel autoclave with a volume of 30 mL. The reaction was performed under conventional heating at 150 °C for 12 h, with 1 h heating up and 1 h cooling down. To remove free linker molecules as detected by IR spectroscopy, the resulting precipitate was filtered off and washed with DMF under microwave heating at 150 °C for 1 h. After being cooled to room temperature, the solid was filtered and dried in air. Yield ∼420 mg (∼98% based on H_2SDBA). Elemental analysis: N 0.82%, C 46.63%, H 2.70%, S 8.41%. Calculated values based on the molecular formula $[Al(OH)(SDBA)]\cdot 0.25DMF$: N 0.96%, C 48.33%, H 2.94%, S 8.74%.

Optimized Reaction Conditions for $[Al(OH)(H_2DPSTC)]\cdot 0.5H_2O$. CAU-11-COOH could only be obtained in the miniaturized reactors. CAU-11-COOH was synthesized in a 5 mL glass vial from a mixture of DPSDA (53.7 mg, 0.15 mmol), 1 M aqueous solution of $AlCl_3\cdot 6H_2O$ (75 μL, 0.15 mmol), and 1425 μL of H_2O (no homogenization was necessary). The reaction was carried out in a HT-microwave oven at 170 °C for 5 h. After cooling to room temperature, the precipitate was filtered off and dried in air. Yield ∼35 mg (∼50% based on DPSDA). Elemental analysis: C 43.23%, H 2.04%, S 7.46%. Calculated values based on the molecular formula $[Al(OH)(H_2DPSTC)]\cdot 0.5H_2O$: C 45.60%, H 2.88%, S 7.60%.

Optimized Reaction Conditions for $[Al_2(OH)_2(DPSTC)(H_2O)_2]\cdot 0.5H_2O$. CAU-12 was synthesized using a large excess of Al^{3+} ions in a mixture of DPSDA (17.9 mg, 0.05 mmol), 1000 μL of H_2O, and 1 M aqueous solution of $Al(NO_3)_3\cdot 9H_2O$ (500 μL, 0.5 mmol). The starting materials were placed in a 5 mL glass vial, and the reaction was carried out in a HT-microwave oven at 170 °C for 5 h. After cooling to room temperature, the precipitate was filtered off and dried in air. Upscaling of the reaction was not yet achieved. Yield ∼20 mg (∼85% based on DPSDA). Elemental analysis: C 37.32%, H 2.29%, S 5.84%. Calculated values based on the molecular formula $[Al_2(OH)_2(DPSTC)(H_2O)_2]\cdot 0.5H_2O$: C 36.72%, H 2.50%, S 6.13%.

Activation. Prior to the sorption measurements the samples were thermally activated. CAU-11 and CAU-11-COOH were heated overnight at 200 °C under vacuum ($p \leq 10^{-2}$ kPa), and CAU-12 was treated overnight at 250 °C under vacuum ($p \leq 10^{-2}$ kPa).

Structure Determination. All crystal data and the results of the refinement of $[Al(OH)(SDBA)]$, $[Al_2(OH)_2(DPSTC)(H_2O)_2]\cdot 0.5H_2O$, and $[Al_2(OH)_2(DPSTC)]\cdot nH_2O$, as well as the results of the Pawley-fit of $[Al(OH)(H_2DPSTC)]\cdot 0.5H_2O$, are summarized in Table 1. Bond lengths are provided in the Supporting Information (Tables S5−S7). The asymmetric units of CAU-11, CAU-12, and CAU-12-dehy are shown in Supporting Information Figures S3, S4, and S5, respectively.

Crystal Structure Determination of $[Al(OH)(SDBA)]$. The crystal structure of CAU-11 was determined from PXRD data obtained at the MS-POWDER beamline (X04SA), EH1 at the Swiss Light Source, Paul Scherrer Institut, Villigen, Switzerland. The wavelength was set to 1.000 009 Å, and the pattern was recorded on a MYTHEN II detector.[36] The sample, activated for 2 h at 200 °C, was measured in a 0.5 mm capillary. The powder pattern was indexed and refined using TOPAS Academic.[39] The structure was solved in the space group $Pna2_1$ by real space methods using the program FOX.[37] Fenske−Hall Z matrices of an AlO_6 octahedron and an SDBA linker without the oxygen atoms of the carboxylate groups were used as input. Rietveld refinement was performed using TOPAS Academic[39] in the higher symmetry space group *Pnma*. A Z matrix was used for bond restraints and constraints.

Pawley Refinement of $[Al(OH)(H_2DPSTC)]$. The high-resolution powder pattern of CAU-11-COOH was obtained at the synchrotron MS-POWDER beamline (X04SA), EH1 at the Swiss Light Source, Paul Scherrer Institut, Villigen, Switzerland, with a wavelength of λ = 1.000 009 Å and a MYTHEN II detector.[36] Prior to the measurement the compound was transferred into a 0.5 mm capillary and activated for 2 h at 200 °C under vacuum. The pattern was indexed with TOPAS Academic[39] in the space group $Pna2_1$, and a Pawley refinement resulted in very similar cell parameters to CAU-11 (Table 1). The final Pawley plot is shown in Figure 2.

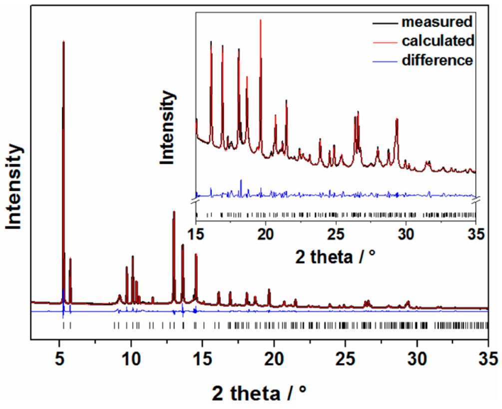

Figure 2. Pawley plot of the synchrotron high-resolution powder X-ray diffraction pattern of $[Al(OH)(H_2DPSTC)]$ using the program TOPAS Academics V4.1.[39] The inset shows the enlarged area of 15−35° (2θ).

Attempts to determine the structure were done by constructing a suitable starting model using force-field calculations as implemented in Materials Studio.[40] The structure of CAU-11 was taken as a starting model, and the noncoordinating carboxylate groups were added. The two additional −COOH groups per linker molecule are probably statistically distributed over four different crystallographic positions (see Supporting Information for details, Figures S6−S11), and hence, the space group $Pna2_1$ was retained. Possible structures with ordered −COOH groups were optimized by force field calculations using the forcite routine (Universal force field), keeping the experimentally determined lattice parameters constant (Supporting Information Figures S8−S11). The optimized structures were used to calculate the corresponding PXRD patterns (Supporting Information Figure S7). The relative reflection intensities in the simulated PXRD patterns deviate from the ones observed in the recorded PXRD pattern. Hence we conclude that the −COOH groups are statistically distributed in the structure of CAU-11-COOH.

Crystal Structure Determination of $[Al_2(OH)_2(DPSTC)(H_2O)_2]\cdot 0.5H_2O$. A structural model for the Rietveld refinement of CAU-12 was set up using a related crystal structure as starting point for force-field calculations. Indexing of the powder pattern indicated a possible triclinic cell [a = 6.6861(19) Å, b = 6.7921(16) Å, c = 13.5998(21) Å, α = 90.196(11)°, β = 84.653(14)°, γ = 59.474(13)°] which can be considered as an expanded structure of MIL-60,[38] a vanadium pyromellitate with the composition $[V(OH)_2((O_2C)_2\text{-}C_6H_2\text{-}(CO_2)_2)]\cdot 4H_2O$ which crystallizes in the space group $P\bar{1}$. In this structure the linker molecules also bear vicinal carboxylate groups at the benzene ring. Hence a structural model for CAU-12 was constructed using Materials Studio.[40] The vanadium atoms were replaced by aluminum atoms, and the experimental cell parameters were adapted. Subsequently the C_6H_2 unit of the pyromellitate ion was replaced by (C_6H_3–SO_2–C_6H_3), see Supporting Information Figure S12, and the whole structure was energetically minimized by force field calculations using the forcite routine (Universal force field). In this starting model, the SO_2 groups were statistically distributed over two symmetry equivalent positions, and therefore, their occupancy was set to 0.5. The resulting structure model was refined by Rietveld methods. The aromatic benzene rings were constrained as rigid bodies while all other atoms were freely refined. Residual electron density inside the channels was located by Fourier synthesis and attributed to water molecules represented by oxygen atoms.

It is worth mentioning that an Al-based analogue of MIL-60[38] exists, denoted MIL-118,[41] but this MOF crystallizes in a monoclinic space group.

Upon thermal activation at 250 °C, substantial changes of reflection positions and relative reflection intensities were observed in the PXRD pattern. The PXRD pattern was indexed in a triclinic unit cell which is related to the one determined for CAU-12 in its conventional setting [a = 6.2694(11) Å, b = 7.1684(9) Å, c = 13.7790(15) Å, α = 81.258(5)°, β = 89.360(9)°, γ = 64.732(8)°]. On the basis of the results reported for the thermal activation of MIL-118,[41] a corresponding structural transformation was anticipated for CAU-12, and a structural model was developed. In this model hydrogen bonded carboxylate groups (Al–OH_2···O_2C–) are replaced by coordinating Al–O_2C units. After structural optimization by force-field methods using the experimentally determined lattice parameters, the derived model was used for the Rietveld refinement. Residual electron density in proximity to the CO_2 and SO_2 groups was located by Fourier synthesis and attributed to partially occupied oxygen atoms representing water molecules which are present due to physisorptive rehydration. The refinement converged to reasonable values although some reflections are not perfectly described. This could be explained by the harsh thermal treatment which might induce stress/strain in the obtained framework structure.

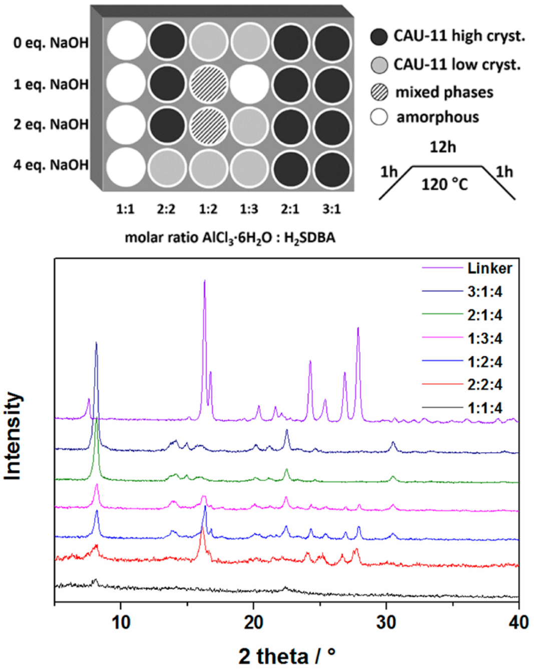

Figure 3. Top: Synthesis conditions and results of the high-throughput experiment that led to the discovery of CAU-11. Bottom: Selected powder patterns from the HT-experiment of the discovery of CAU-11. Molar ratios are given as $AlCl_3·6H_2O$:H_2DSBA:NaOH. The unit of 1 equiv corresponds to the amount of 0.06 mmol. Additional reflections in the red (2:2:4), blue (1:2:4), and magenta (1:3:4) powder patterns correspond to recrystallized linker molecules.

RESULTS AND DISCUSSION

HT-Experiments. [Al(OH)(SDBA)]·0.25DMF was discovered during the investigation of the system $AlCl_3·6H_2O$/H_2SDBA/H_2O/NaOH under solvothermal conditions. In the first experiment the amounts of $AlCl_3·6H_2O$ and H_2SDBA were varied in six steps (3:1–1:3), and the amount of NaOH as additive was varied in four steps (0–4). The different molar ratios used and the results obtained from PXRD measurements of the reaction products are shown in Figure 3, top. At low overall concentrations ($AlCl_3·6H_2O$:H_2SDBA = 1:1) only X-ray amorphous products were obtained, independent of the amount of NaOH added.

At higher overall concentrations ($AlCl_3·6H_2O$:H_2SDBA = 2:2) as well as with an excess of $AlCl_3·6H_2O$ over H_2SDBA, highly crystalline CAU-11 could be obtained with or without addition of NaOH. Reactions with an excess of linker resulted in poorly crystalline CAU-11 or CAU-11 with recrystallized linker molecules. This is also shown in Figure 3, bottom, where selected powder patterns are provided. Further HT-investigations varying the molar ratios of the reactants as well as the reaction time and temperature led to the optimized synthesis conditions. These were directly used in the synthesis scale-up employing a 30 mL reactor.

The investigation of the system Al^{3+}/DPSDA/H_2O/NaOH under microwave-assisted heating and solvothermal conditions resulted in the formation of two new compounds, [Al(OH)(H_2DPSTC)]·0.5H_2O (CAU-11-COOH) and [$Al_2(OH)_2$(DPSTC)$(H_2O)_2$]·0.5H_2O (CAU-12). In the first experiment the amounts of $AlCl_3·6H_2O$ with respect to DPSDA were varied in eight steps (4:2–2:4), and the amount of NaOH as additive was varied in three steps (0, 2, 4 equiv). The different molar ratios used and the results obtained from PXRD measurements of the reaction products are shown in Supporting Information Figure S1. CAU-11-COOH was obtained at all molar ratios without any addition of NaOH. Upon addition of NaOH a mixture of different products was found. Further HT-investigations optimizing the molar ratios of the reactants as well as the reaction time and temperature led to optimized synthesis conditions. Phase pure samples of highly crystalline CAU-12 were obtained while studying the influence of the overall concentration in the absence of NaOH as an additive (Supporting Information Figure S2). The overall concentration was varied, and different molar ratios of $AlCl_3·6H_2O$ to DPSDA, always with an excess of $AlCl_3·6H_2O$ (2:1 up to 10:1 and 3:2 up to 10:2; 1equiv = 0.05 mmol), were used. Pure CAU-12 was obtained only for the molar ratios 6:1, 5:2, and 6:2 of $AlCl_3·6H_2O$ to DPSDA. The other ratios resulted in mixtures of CAU-11-COOH and CAU-12 or pure CAU-11-COOH. Further HT-investigations optimizing the molar ratios of the reactants as well as the reaction time and temperature and the Al^{3+} source led to the optimized synthesis conditions.

Structure Description of [Al(OH)(SDBA)]. CAU-11 crystallizes as microsized particles (SEM micrograph, Supporting Information Figure S13). Hence, the structure was solved and refined from synchrotron PXRD data. The final Rietveld plot is shown in Figure 4. The structure of CAU-11 is built up from chains of trans corner-sharing AlO_6 octahedra (Figure 5, left). As observed in many other Al-MOFs, μ-OH groups are bridging adjacent Al^{3+} ions. The Al–O distances range from 1.85(4) to 1.97(2) Å, which is in good agreement with the values for recently published Al-MOFs based on the same inorganic building unit.[20,26] The chains are interconnected along the a-axis via the carboxylate groups of the linker molecules to form layers with lozenge-shaped pores (Figure 5,

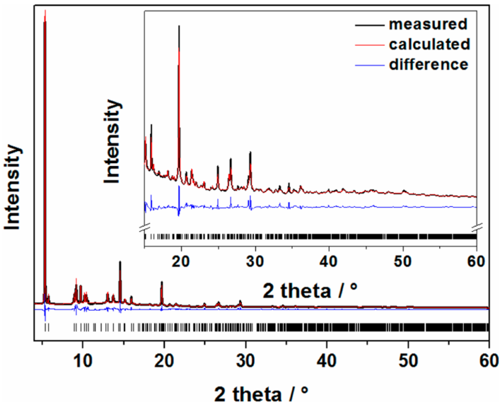

Figure 4. Final Rietveld plot of the structure refinement of [Al(OH)(SDBA)] (CAU-11). The observed powder pattern is shown in black, the calculated one is shown as an overlay in red, and the difference plot is shown in blue. The ticks mark the allowed Bragg peak positions. The inset shows the enlarged area of 15–60° (2*θ*).

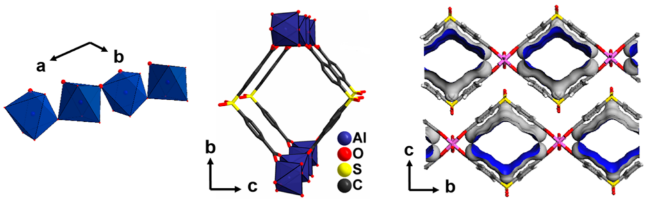

Figure 5. Structure of [Al(OH)(SDBA)]. Left: Inorganic building unit, chains of trans corner-sharing AlO_6 octahedra. Middle: Lozenge-shaped pore-channel built up by two Al–O-chains interconnected by the linker molecules. Right: Connolly surface modeled with Materials Studio.[40]

middle). These layers are stacked along the *c*-axis in an ABAB-fashion to form a layered structure (Figure 5, right) and further interact through weak hydrogen bonds (Supporting Information Figure S14). The sulfone groups do not point into the pore, but toward neighboring inorganic chains, suggesting a hydrophobic inner-pore surface. The bridging *μ*-OH groups are aligned along the *c*-axis pointing toward the SO_2 groups (O···O = 2.84 Å). The crystal structure of CAU-11 exhibits some relationship to $[In(OH)(C_{17}H_8F_6O_4)]$,[30] a material synthesized with 4,4′-(hexafluoroisopropylidene)bis(benzoic acid) as a V-shaped linker. The structure of $[In(OH)(C_{17}H_8F_6O_4)]$ also contains lozenge-shaped channels running through layers consisting of trans corner-sharing octahedra. However, the layers in the two structures have different topologies. The topology of CAU-11 can be described by a square lattice (4^4 net), while the net of $[In(OH)(C_{17}H_8F_6O_4)]$ cannot be flattened in a plane without crossing edges (Supporting Information Figure S15). The layers in $[In(OH)(C_{17}H_8F_6O_4)]$ exhibit ABCD type stacking.

Structure Description of $[Al_2(OH)_2(DPSTC)(H_2O)_2]\cdot 0.5H_2O$. The structure of CAU-12 was solved and refined from laboratory PXRD data. On the basis of the structure of MIL-60,[38] the structure model for CAU-12 was generated by force-field calculations using the program Materials Studio.[40] The final Rietveld plot is shown in Figure 6.

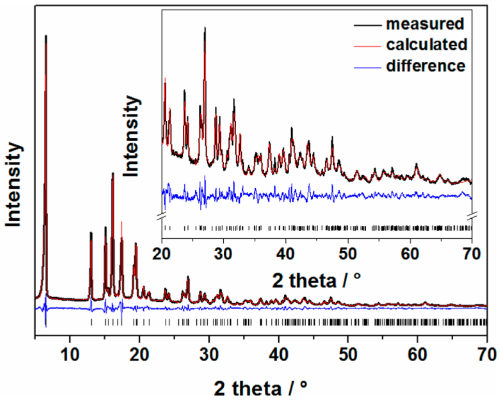

Figure 6. Final Rietveld plot of the structure refinement of $[Al_2(OH)_2(DPSTC)(H_2O)_2]\cdot 0.5H_2O$ (CAU-12). The observed powder pattern is shown in black, the calculated one is shown as an overlay in red, and the difference plot is shown in blue. The ticks mark the allowed Bragg peak positions. The inset shows the enlarged area of 20–70° (2*θ*).

The structure of CAU-12 is related to the one of MIL-60 and MIL-118A and consists of infinite chains of two types of trans corner-sharing AlO_6 octahedra which are connected in an alternating fashion. In the first type of AlO_6 octahedra, four oxygen atoms stem from the carboxylate groups of four linker molecules, and two are from bridging *μ*-OH groups. In the second type only two oxygen atoms stem from carboxylate groups of two linker molecules, two from the bridging *μ*-OH groups and two from coordinating water molecules (Figure 7, left). All of the Al–O distances range from 1.800(7) to 1.962(5) Å, which is in good agreement with the values of recently published Al-MOFs.[20,26] The structure achieves a three-dimensional framework through the connection of four inorganic chains with the carboxylate groups of the linker molecules (Figure 7, right). The linker molecules adopt a specific connection type since two of the four carboxylate groups are coordinated to two adjacent aluminum atoms in a bidentate bridging mode and the remaining two carboxylate groups are coordinated only to one aluminum atom in a monodentate manner (Figure 7, middle). The noncoordinating C–O bond is probably deprotonated, which is supported by the C2–O2 distance of 1.271(9) Å.[41] Furthermore, the IR spectrum does not contain a band around 1720–1700 cm^{-1}, which would be characteristic for the presence of –COOH groups. The noncoordinating oxygen atom of the $-CO_2$ group is in close contact to one coordinating water molecule of the neighboring AlO_6 octahedron suggesting possible hydrogen bonding (Figure 7, left). The sulfone group is distributed over two crystallographically equivalent positions which are each half occupied.

Structure Description of $[Al_2(OH)_2(DPSTC)]\cdot nH_2O$. The structure of CAU-12-dehy was refined from laboratory PXRD data. Using the structure of CAU-12, the structure model for CAU-12-dehy was set up by force-field calculations using the program Materials Studio.[40] The final Rietveld plot is shown in Figure 8.

The structure of CAU-12-dehy is closely related to that of CAU-12. It consists of the MIL-53 type inorganic building unit (Figure 9, left). The removal of the coordinated water molecules induce a rotation of the linker molecule (Figure 7, right, and Figure 9, middle), and the previously monodentate coordinating carboxylate groups now also bind via the second oxygen atom to adjacent Al atoms resulting in a bidentate coordination mode. The pores can be seen in Figure 9, right, where the view of the crystal structure along the *c*-axis is displayed.

DOI: 10.1021/ic502242j
Inorg. Chem. 2015, 54, 492–501

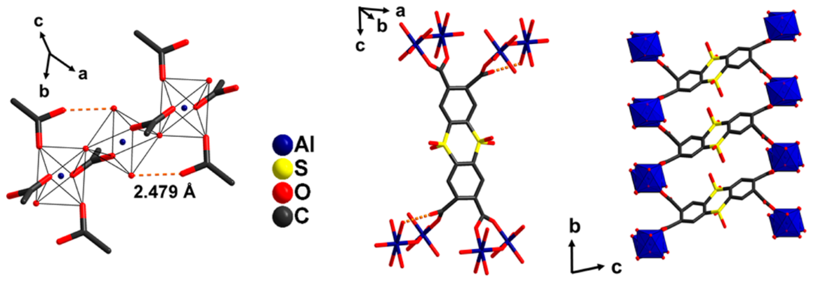

Figure 7. Structure of $[Al_2(OH)_2(DPSTC)(H_2O)_2]\cdot 0.5H_2O$ (CAU-12). Left: Inorganic building unit with two different types of AlO_6 octahedra. Middle: Coordination mode of one linker molecule. Right: View along the inorganic chains. Hydrogen bonds are shown as red dashed lines.

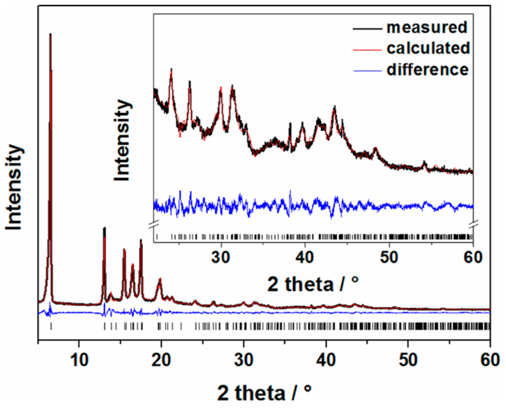

Figure 8. Final Rietveld plot of the structure refinement of $[Al_2(OH)_2(DPSTC)]\cdot nH_2O$. The observed powder pattern is shown in black, the calculated one is shown as an overlay in red, and the difference plot is shown in blue. The ticks mark the allowed Bragg peak positions. The inset shows the enlarged area of 22–60° (2θ).

Thermal Stability. All compounds were investigated concerning their thermal stability in air by thermogravimetric (TG) measurements (Supporting Information Figures S16, S19, and S22) and temperature dependent (TD) PXRD measurements (Figure 10 and Supporting Information Figures S17, S18, S20, and S21). The results of the TG measurements are summarized in Table 2.

The results obtained from the TG measurements for CAU-11 and CAU-11-COOH (Supporting Information Figures S16 and S19) are in good agreement with the deduced molecular formulas and reveal a high thermal stability for the two compounds. The thermal stability is additionally confirmed by TD-PXRD measurements (Supporting Information Figures S17 and S20).

The TG measurement of CAU-12 shows a two-step weight loss (Supporting Information Figure S22). From the molecular formula $[Al_2(OH)_2(DPSTC)(H_2O)_2]\cdot 0.5H_2O$ the first step (RT to 250 °C) can be attributed to the removal of coordinating and noncoordinating water molecules (measured 8.8%, calcd 8.6%) and the second (300–600 °C) to the decomposition of the framework (measrued 69.8%, calcd 71.9%) resulting in Al_2O_3 (measured 21.4%, calcd 19.5%). The TD-PXRD measurement (Figure 10, top) shows that the compound preserves its crystallinity up to 420 °C. As observed in the TG curve, the compound decomposes rapidly above 420 °C, and amorphous Al_2O_3 is formed. Above 270 °C a small shift of the first two reflections (001 and 002) toward lower diffraction angles is observed, and the remaining observable reflections shift to higher diffraction angles (Figure 10,

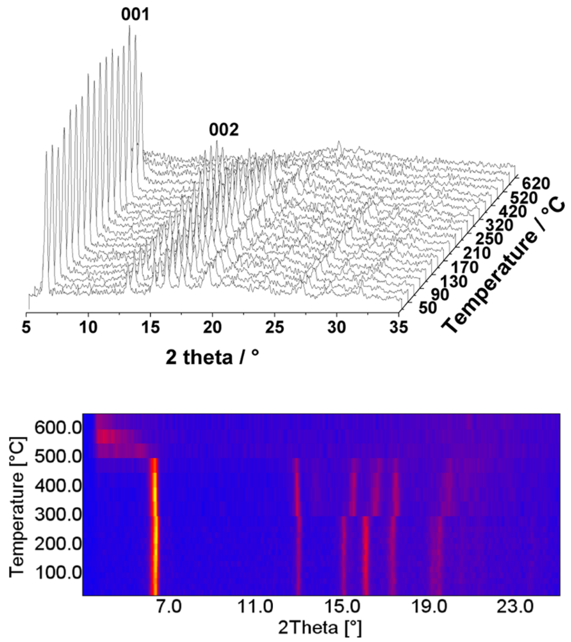

Figure 10. Top: TD-PXRD of CAU-12 in steps of 20 °C from 30 °C up to 270 °C and in steps of 50 °C from 270 °C up to 620 °C. Bottom: Top view corresponding to the TD-PXRD measurement of CAU-12.

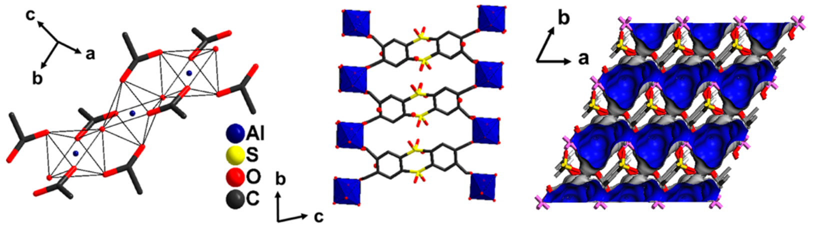

Figure 9. Structure of $[Al_2(OH)_2(DPSTC)]\cdot nH_2O$ (CAU-12-dehy). Left: Inorganic building unit, showing the full coordination of all carboxylate groups. Middle: View along the inorganic chains. Right: Connolly surface calculated with Materials Studio.[40]

Table 2. Summary of the Results of the TG Measurements of CAU-11, CAU-11-COOH, and CAU-12

temp range/ °C	fragment	mass fraction % measured	mass fraction % calcd
CAU-11			
RT-425	0.25 DMF	5.3	5.0
425–600	framework	80.6	81.1
>600	Al_2O_3	14.1	13.9
CAU-11-COOH			
RT-280	0.5 H_2O	2.2	2.1
350–650	framework	86.0	85.8
>650	Al_2O_3	11.8	12.1
CAU-12			
RT-250	2.5 H_2O	8.8	8.6
300–600	framework	69.8	71.9
>600	Al_2O_3	21.4	19.5

bottom). In accordance with the TG measurement, the removal of the coordinating water molecules should be completed at this temperature (~270 °C), and therefore, the conversion into the dehydrated form of CAU-12 has taken place.

Vibrational Spectroscopy. IR spectra were collected of the as-synthesized CAU-11, a sample washed in DMF, and a sample activated at 200 °C after the sorption measurements. In all spectra a sharp ν_{OH}-band at 3581 cm^{-1} due to μ-OH groups in the framework can be observed (Supporting Information Figure S23). Also, the characteristic signals of the asymmetric and symmetric stretching vibration of the coordinating carboxylate groups are clearly visible at ν_{as} = 1630 and ν_s = 1433 cm^{-1}. The as-synthesized sample shows a small $\nu_{C=O}$-band at 1704 cm^{-1} indicating the presence of minor residues of unreacted acid. This band disappears, when the sample is treated with DMF, but the $\nu_{C=O}$-band of the DMF molecules emerges at 1684 cm^{-1}. Thus, DMF is adsorbed in the pores of CAU-11. After the activation of the sample and the subsequent sorption measurement vibrations in this region were no longer observed, indicating total removal of unreacted acid and DMF. In all spectra the preservation of the sulfone groups is indicated by the ν_{SO2}-bands at 1303 and 1148 cm^{-1} which are due to the asymmetric and symmetric stretching vibrations as well as the δ_{SO2}-vibration at 543 cm^{-1}.[42]

The IR spectra of CAU-11-COOH, CAU-12, and CAU-12-dehy are shown in (Figure 11). In the IR-spectrum of CAU-11-COOH a ν_{OH}-band at 3588 cm^{-1} is visible showing the presence of μ-OH groups within the framework (Figure 11, black). Next to the characteristic bands of the asymmetric and symmetric stretching vibrations at 1625, 1437, and 1407 cm^{-1} due to the coordinating carboxylate groups a $\nu_{C=O}$-band at 1732 cm^{-1} is observed indicating the presence of free carboxylic acid groups. Since this vibration did not change during the sample treatment with different solvents, these groups are assigned to be the noncoordinating −COOH groups. The vibrations of the SO_2 groups are present at ν_{SO2} = 1322 and 1144 cm^{-1} and δ_{SO2} = 555 cm $^{-1}$.[42]

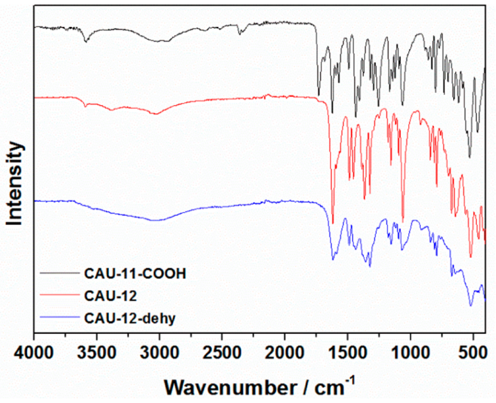

Figure 11. IR spectra of CAU-11-COOH (black), CAU-12 (red), and CAU-12-dehy (blue).

The IR-spectrum of CAU-12 also shows a small ν_{OH}-band at 3593 cm^{-1} due to μ-OH groups (Figure 11, red). The absence of a band around 1700 cm^{-1} indicates full deprotonation of the linker molecule and the presence of four $-COO^-$ groups in the product. The characteristic stretching vibrations of the carboxylate groups are observed at ν_{as} = 1620 cm^{-1} and ν_s = 1457 cm^{-1}, and also the vibrations of the SO_2 groups are present at ν_{SO2} = 1324 and 1156 cm^{-1} and δ_{SO2} = 561 cm^{-1}.[42] The IR spectrum of CAU-12-dehy exhibits broad overlapping bands at similar positions. Due to the adsorption of water from the atmosphere and the formation of hydrogen bonds, a very broad band from 2800–3600 cm^{-1} is observed.

Sorption Properties. To probe the sorption behavior of all compounds, measurements using different adsorptives were performed. Nitrogen as well as hydrogen sorption measurements were carried out at 77 K. Water vapor, carbon dioxide, as well as methane sorption measurements were performed at 298 K. Prior to each measurement, CAU-11 and CAU-11-COOH were activated at 200 °C (the total removal of DMF molecules from CAU-11 was verified by IR spectroscopy, Supporting Information Figure S23) and CAU-12 at 250 °C overnight under vacuum. In order to demonstrate the water stability of CAU-11 a second activation step using water (120 °C, 1 h, microwave irradiation) was carried out. No influence on the sorption properties was observed. The results of all measurements of all three samples are listed in Table 3.

Table 3. Results of the Sorption Measurements for CAU-11, CAU-11-COOH, and CAU-12 Using Various Adsorptives

	CAU-11	CAU-11-COOH	CAU-12-dehy
N_2 (a_{BET}, V_{mic}) (77 K)	350 m^2/g, 0.17 cm^3/g ($V_{mic,theor}$ = 0.18 cm^3/g)[43]		
H_2/wt % (77 K)	0.7	0.02	0.1
H_2O/wt % (298 K)	8.5	3.0	12.0
CO_2/wt % (298 K)	5.6	1.0	1.8
CH_4/wt % (298 K)	1.0		

The type I nitrogen isotherm of CAU-11 (Figure 12, top) demonstrates the microporosity of the compound. The specific surface area is about 350 m^2 g^{-1}, and the micropore volume is 0.17 cm^3 g^{-1} (p/p_0 = 0.5, theoretical volume calculated with Platon:[43] $V_{m(theor)}$ = 0.18 cm^3g^{-1}). Since the sulfone groups do not point into the pore channels but toward the inorganic chains, the water vapor isotherm is a type-III isotherm (Figure 12, bottom), showing the characteristic shape for a hydrophobic compound.

In Supporting Information Figure S24, sorption isotherms of the other gases are shown. At 100 kPa and 77 K, 0.7 wt % hydrogen is adsorbed, and 5.3 wt % of carbon dioxide is

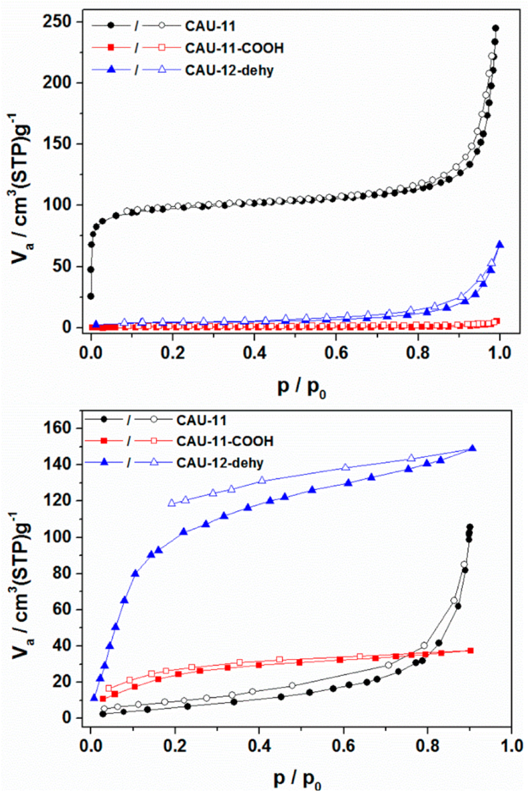

Figure 12. Results of the sorption measurements of CAU-11, CAU-11-COOH, and CAU-12-dehy. Top: Nitrogen gas sorption measurements (77 K). Bottom: Water vapor sorption measurements (298 K).

adsorbed at 100 kPa at 298 K. The uptake of 1.0 wt % of methane (100 kPa, 298 K) demonstrates the hydrophobic character of the compound.

Due to the additional carboxylic acid groups in the pores, CAU-11-COOH becomes nonporous toward nitrogen, but in contrast to CAU-11, uptake of H_2O is clearly observed at low p/p_0 values (Figure 12). The maximum uptake is only 3.0 wt %, but this is due to the small pores. The pore size and the hydrophilicity of the pores in CAU-11-COOH can also be used to explain the very low uptake of hydrogen, only 0.02 wt %, in contrast to a CO_2 uptake of 1.0 wt %, which has a bigger kinetic diameter but also a higher polarity than H_2, and can therefore be better adsorbed (see Supporting Information Figure S25).

CAU-12 shows a similar sorption behavior toward the adsorptives as observed for CAU-11-COOH. It is nonporous toward nitrogen, but it shows a strong affinity toward water vapor (uptake of 8.5 wt %), due to the incorporated and accessible sulfone groups (Figure 12). Accordingly, only a low uptake of 0.1 wt % of H_2 and yet a higher uptake of 1.8 wt % of CO_2 are observed, although H_2 has the smaller kinetic diameter but also lower polarity (see Supporting Information Figure S26).

■ CONCLUSION

In summary, we have discovered three new sulfone-functionalized Al-MOFs, using the high-throughput method. The syntheses were optimized, and the compounds were characterized in detail. The V-shape of the linker does not lead to the formation of a new inorganic building unit; instead, the very well-known inorganic building unit of trans corner-sharing AlO_6 polyhedra is observed. Interestingly, CAU-11 exhibits a layered structure, but nevertheless, it shows a high thermal stability up to 420 °C and a permanent porosity of 350 cm^3 g^{-1}. This is due to 1D channels within the 2D layers resulting in an intralayer porosity. With this linker molecule, only very few porous compounds have been previously reported. In addition, the sorption properties can be altered by introducing additional noncoordinating carboxylic acid groups which turn the hydrophobic compound into the hydrophilic CAU-11-COOH. The third compound CAU-12 exhibits a three-dimensional network with a very uncommon coordination mode of the linker molecule and a high thermal stability up to 420 °C. During thermal activation, the compound transforms to its dehydrated form CAU-12-dehy. Coordinating water molecules are removed, and the free coordination site is filled by the noncoordinating part of the carboxylate groups. Such a structural conversion has only once been reported for an Al-MOF and underlines the high stability of such frameworks. The highly hydrophilic character of this compound due to the incorporated sulfone groups is proven by detailed sorption measurements.

■ ASSOCIATED CONTENT

Ⓢ Supporting Information

Reported compounds in the literature based on 4,4′-sulfonyldicarboxylic acid; exact compositions of the reaction mixtures in the high-throughput experiments and distributions of the different products; simulated structures of CAU-11-COOH; SEM picture of CAU-12; the asymmetric units and bond lengths; topology of CAU-11; TG curves of all compounds; IR spectra of CAU-11; TD-PXRD measurements of CAU-11 and CAU-11-COOH; H_2, CO_2, and CH_4 sorption measurements of CAU-11, CAU-11-COOH, and CAU-12-dehy. This material is available free of charge via the Internet at http://pubs.acs.org.

■ AUTHOR INFORMATION

Corresponding Author

*E-mail: stock@ac.uni-kiel.de.

Notes

The authors declare no competing financial interest.

■ ACKNOWLEDGMENTS

This work has been supported by the DFG (SPP 1362). The research leading to these results has received funding from the Europeans Community's Seventh Framework Program (FP7/2007-2013) under grant agreement 228862. A.K.I. is supported by the Knut and Alice Wallenberg Foundation through the MAX IV postdoctoral scholarship. We thank Milan Köppen for assistance with the Rietveld refinement of CAU-11.

■ REFERENCES

(1) Themed issue on Metal-Organic Framework: *Chem. Soc. Rev.* **2009**, *38*, 1201−1508.

(2) Themed issue on Metal-Organic Framework: *Chem. Rev.* **2012**, *112*, 673−1268.

(3) Themed issue on Metal-Organic Frameworks: *Chem. Soc. Rev.* **2014**, *43*, 5415−6172.

(4) Goesten, M. G.; Juan-Alcañiz, J.; Ramos-Fernandez, E. V.; Sai Sankar Gupta, K. B.; Stavitski, E.; van Bekkum, H.; Gascon, J.; Kapteijn, F. *J. Catal.* **2011**, *281*, 177−187.

(5) Horcajada, P.; Chalati, T.; Serre, C.; Gillet, B.; Sebrie, C.; Baati, T.; Eubank, J. F.; Heurtaux, D.; Clayette, P.; Kreuz, C.; Chang, J.-S.;

Hwang, Y. K.; Marsaud, V.; Bories, P.-N.; Cynober, L.; Gil, S.; Férey, G.; Couvreur, P.; Gref, R. *Nat. Mater.* **2010**, *9*, 172−178.

(6) Couck, S.; Denayer, J. F. M.; Baron, G. V.; Remy, T.; Gascon, J.; Kapteijn, F. *J. Am. Chem. Soc.* **2009**, *131*, 6326.

(7) O'Keeffe, M. *Chem. Soc. Rev.* **2009**, *38*, 1215−1217.

(8) Reinsch, H.; Stock, N. *Microporous Mesoporous Mater.* **2013**, *171*, 156−165.

(9) Stock, N.; Biswas, S. *Chem. Rev.* **2012**, *112*, 933−969.

(10) Stock, N. *Microporous Mesoporous Mater.* **2010**, *129*, 287−295.

(11) Biswas, S.; Ahnfeldt, T.; Stock, N. *Inorg. Chem.* **2011**, *50*, 9518−9526.

(12) Reimer, N.; Gil, B.; Marszalek, B.; Stock, N. *CrystEngComm* **2012**, *14*, 4119−4125.

(13) Ahnfeldt, T.; Gunzelmann, D.; Wack, J.; Senker, J.; Stock, N. *CrystEngComm* **2012**, *14*, 4126−4136.

(14) Klinkebiel, A.; Reimer, N.; Lammert, M.; Stock, N.; Lüning, U. *Chem. Commun.* **2014**, *50*, 9306−9308.

(15) Ahnfeldt, T.; Gunzelmann, D.; Loiseau, T.; Hirsemann, D.; Senker, J.; Férey, G.; Stock, N. *Inorg. Chem.* **2009**, *48*, 3057−3064.

(16) Gaab, M.; Trukhan, N.; Maurer, S.; Gummaraju, R.; Müller, U. *Microporous Mesoporous Mater.* **2012**, *157*, 131−136.

(17) Loiseau, T.; Serre, C.; Huguenard, C.; Fink, G.; Taulelle, F.; Henry, M.; Bataille, T.; Férey, G. *Chem.—Eur. J.* **2004**, *10*, 1373−1382.

(18) Comotti, A.; Bracco, S.; Sozzani, P.; Horike, S.; Matsuda, R.; Chen, J.; Takata, M.; Kubota, Y.; Kitagawa, S. *J. Am. Chem. Soc.* **2008**, *130*, 13664−13672.

(19) Loiseau, T.; Mellot-Draznieks, C.; Muguerra, H.; Férey, G.; Haouas, M.; Taulelle, F. *C. R. Chim.* **2005**, *8*, 765−772.

(20) Niekiel, F.; Ackermann, M.; Guerrier, P.; Rothkirch, A.; Stock, N. *Inorg. Chem.* **2013**, *52*, 8699−8705.

(21) Senkovska, I.; Hoffmann, F.; Fröba, M.; Getzschmann, J.; Böhlmann, W.; Kaskel, S. *Microporous Mesoporous Mater.* **2009**, *122*, 93−98.

(22) Volkringer, C.; Loiseau, T.; Guillou, N.; Férey, G.; Haouas, M.; Taulelle, F.; Elkaim, E.; Stock, N. *Inorg. Chem.* **2010**, *49*, 9852−9862.

(23) Reinsch, H.; Krüger, M.; Wack, J.; Senker, J.; Salles, F.; Maurin, G.; Stock, N. *Microporous Mesoporous Mater.* **2012**, *157*, 50−55.

(24) Reinsch, H.; Marszalek, B.; Wack, J.; Senker, J.; Gil, B.; Stock, N. *Chem. Commun.* **2012**, *48*, 9486−9488.

(25) Reinsch, H.; van der Veen, M. A.; Gil, B.; Marszalek, B.; Verbiest, T.; de Vos, D.; Stock, N. *Chem. Mater.* **2013**, *25*, 17−26.

(26) Reinsch, H.; Krüger, M.; Marrot, J.; Stock, N. *Inorg. Chem.* **2013**, *52*, 1854−1859.

(27) Reinsch, H.; De Vos, D.; Stock, N. *Z. Anorg. Allg. Chem.* **2013**, *639*, 2785−2789.

(28) Gándara, F.; Andrés, A. d.; Gómez-Lor, B.; Gutiérrez-Puebla, E.; Iglesias, M.; Monge, M. A.; Proserpio, D. M.; Snejko, N. *Cryst. Growth Des.* **2008**, *8*, 378−380.

(29) Harbuzaru, B. V.; Corma, A.; Rey, F.; Atienzar, P.; Jordá, J. L.; García, H.; Ananias, D.; Carlos, L. D.; Rocha, J. *Angew. Chem.* **2008**, *120*, 1096−1099.

(30) Gándara, F.; Gomez-Lor, B.; Gutiérrez-Puebla, E.; Iglesias, M.; Monge, M. A.; Proserpio, D. M.; Snejko, N. *Chem. Mater.* **2008**, *20*, 72−76.

(31) Zhuang, W.-J.; Zheng, X.-J.; Sun, H.-L.; Jin, L.-P.; Xuebao, W. H. *Chin. J. Struct. Chem.* **2008**, *24*, 1305−1310.

(32) Li, H.; Shi, W.; Zhao, K.; Niu, Z.; Chen, X.; Cheng, P. *Chem.—Eur. J.* **2012**, *18*, 5715−5723.

(33) Yeh, C.-T.; Lin, W.-C.; Lo, S.-H.; Kao, C.-C.; Lin, C.-H.; Yang, C.-C. *CrystEngComm* **2012**, *14*, 1219−1222.

(34) Plonka, A. M.; Banerjee, D.; Woerner, W. R.; Zhang, Z.; Nijem, N.; Chabal, Y. J.; Li, J.; Parise, J. B. *Angew. Chem.* **2013**, *125*, 1736−1739.

(35) Wu, C.-Y.; Raja, D. S.; Yang, C.-C.; Yeh, C.-T.; Chen, Y.-R.; Li, C.-Y.; Ko, B.-T.; Lin, C.-H. *CrystEngComm* **2014**, *16*, 9308−9319.

(36) Willmott, P. R.; Meister, D.; Leake, S. J.; Lange, M.; Bergamaschi, A.; Boge, M.; Calvi, M.; Cancellieri, C.; Casati, N.; Cervellino, A.; Chen, Q.; David, C.; Flechsig, U.; Gozzo, F.; Henrich, B.; Jaggi-Spielmann, S.; Jakob, B.; Kalichava, I.; Karvinen, P.; Krempasky, J.; Ludeke, A.; Luscher, R.; Maag, S.; Quitmann, C.; Reinle-Schmitt, M. L.; Schmidt, T.; Schmitt, B.; Streun, A.; Vartiainen, I.; Vitins, M.; Wang, X.; Wullschleger, R. *J. Synchrotron Radiat.* **2013**, *20*, 667−682.

(37) Favre-Nicolin, V.; Cerny, R. *J. Appl. Crystallogr.* **2002**, *35*, 734−743.

(38) Barthelet, K.; Riou, D.; Nogues, M.; Férey, G. *Inorg. Chem.* **2003**, *42*, 1739−1743.

(39) *Topas Academics v4.1*; Coelho Software: Brisbane, Australia, 2007.

(40) *Materials Studio Version 5.0*; Accelrys Inc.: San Diego, CA, 2009.

(41) Volkringer, C.; Loiseau, T.; Guillou, N.; Ferey, G.; Haouas, M.; Taulelle, F.; Audebrand, N.; Margiolaki, I.; Popov, D.; Burghammer, M.; Riekel, C. *Cryst. Growth Des.* **2009**, *9*, 2927−2936.

(42) Socrates, G. *Infrared and Raman Characteristic Group Frequencies:* Tables and Charts, 3*rd ed.*; Wiley, 2004.

(43) Spek, A. L. P., Multipurpose, A.; Crystallographic Tool v 1.16, Utrecht Universität: Utrecht, Niederlande, 2011.

4.3.5. Four new Al-based microporous metal-organic framework compounds with MIL-53-type structure containing functionalized extended linker molecules

Der folgende Artikel wurde im Jahre 2015 in der *Fachzeitschrift Microporous and Mesoporous Materials, ELSEVIER GmbH* als Artikel zur Veröffentlichung akzeptiert. Der Wiederabdruck erfolgte mit freundlicher Genehmigung der ELSEVIER GmbH. Reproduced with permission from:
S. Halis, N. Reimer, A. Klinkebiel, U. Lüning, N. Stock, *Microporous and Mesoporous Materials* **2015**. DOI: 10.1016/j.micromeso.2015.01.030.

Al-MIL-53,[50] [Al(OH)(BDC)] mit BDC = 1,4-Benzoldicarboxylat, ist der bis dato am intensivsten untersuchteste Al-MOF. Die Struktur von Al-MIL-53 basiert auf Ketten von *trans* eckenverknüpften AlO_6-Oktaedern, die über Terephthalate zu einem dreidimensionalem Gerüst mit eindimensionalen rautenförmigen Kanälen verknüpft werden. Herausragende Eigenschaft dieser Verbindung ist ihre Flexibilität. In Abhängigkeit eingelagerter Gastmoleküle sowie Temperaturänderung kann sich die Struktur aufweiten oder zusammenziehen. Aktuell ist eine Vielzahl isoretikulärer Verbindungen bekannt, die zum einen auf funktionalisierten Terephthalateionen bzw verkürzten oder verlängerten Dicarboxylationen basieren, die alle unterschiedliche Flexibilitäten, thermische Stabilitäten und Sorptionseigenschaften aufweisen.[24, 56, 57, 59, 75-78, 108] MIL-53-Derivate wurden auch unter Verwendung von 2,6-Naphthalindicarbonsäure (2,6-H_2NDC), MIL-69[56] bzw. DUT-4,[57] und 4,4´-Biphenyldicarbonsäure, DUT-5,[57] erhalten und weisen ein komplett starres Gerüst auf. MIL-69 ist die unporöse Variante des DUT-4.

In dieser Arbeit wurden vier zu Al-MIL-53 isoretikuläre Verbindungen mit 1,5-Dinitro-3,7-Naphthalindicarbonsäure (H_2NDC-$(NO_2)_2$), 3-Nitro-4,4’-Biphenyldicarbonsäure (H_2BPDC-NO_2), 3-Amino-4,4’-Biphenyldicarbonsäure (H_2BPDC-NH_2) und 5,5-Dioxo-dibenzo[*b,d*]thiophen-3,7-Dicarbonsäure (H_2BPDC-SO_2) als Linkermoleküle hergestellt. Die resultierenden Verbindungen [Al(OH)(NDC-$(NO_2)_2$)]·DMF (**1**), [Al(OH)(BPDC-NO_2)]·1.7DMF ·0.8H_2O (**2**), [Al(OH)(BPDC-NH_2)]·1.7DMF·H_2O (**3**) und [Al(OH)(BPDC-SO_2)]·2.5DMF (**4**) sind isoretikulär zu MIL-69 bzw. DUT-5 und weisen ebenfalls keinerlei Gerüstflexibilität auf. Obwohl **1** strukturell ein MIL-69-Derivat ist, weist es eine permanente Porosität von $a_{s,BET}$ = 578 m^2g^{-1} und V_{mic} = 0.23 cm^3g^{-1} auf. Diese liegt deutlich unter den

Werten von DUT-4 ($a_{s,BET}$ = 1308 m^2g^{-1} und V_{mic} = 0.68 $cm^3g^{-1)}$, was aber auf die zusätzlichen funktionellen Gruppen und die nicht vollständig geöffnete Gerüststruktur zurückzuführen ist. Die DUT-5-Derivate **2**, **3**, und **4** weisen spezifische Oberflächen und Mikroporenvolumina im Bereich des unfunktionalisierten DUT-5 auf ($a_{s,BET}$: 1530-1966 vs 1613 m^2g^{-1} und V_{mic} = 0.66-0.79 vs 0.81 cm^3g^{-1}). Zusätzlich wurden Sorptionsmessung mit H_2, CO_2 und CH_4 durchgeführt und alle vier Materialien weisen eine Aufnahme der angeführten Gase auf. Besonderes Augenmerk gilt hierbei den CO_2 Sorptionsmessungen. Interessanterweise weist **1** die größte Affinität zu CO_2 auf, was vermutlich auf den deutlich geringeren Porendurchmesser im Vergleich zu den anderen Materialien, zurück zu führen ist. Vergleicht man die DUT-5-Derivate so zeigt die -NH_2-funktionalisierte Verbindung trotz größter spezifischer Oberfläche und der bisherigen Annahme, dass -NH_2-Gruppen die Adsorption von CO_2 in MOFs verbessern, die geringste Aufnahme.[109] Die -SO_2-funktionalisierte Verbindung weist die höchste Kapazität auf, was sich mit anderen Studien zu deckt, in denen -SO_2-funktionalisierte UiO-67-Derivate eine um bis zu 134 % erhöhte Aufnahmekapazität für CO_2 im Vergleich zum unfunktionalisierten Material besitzen.[90, 91]

Microporous and Mesoporous Materials xxx (2015) 1–7

Contents lists available at ScienceDirect

Microporous and Mesoporous Materials

journal homepage: www.elsevier.com/locate/micromeso

Four new Al-based microporous metal-organic framework compounds with MIL-53-type structure containing functionalized extended linker molecules

Selda Halis [a], Nele Reimer [a], Arne Klinkebiel [b], Ulrich Lüning [b], Norbert Stock [a], *

[a] *Institut für Anorganische Chemie, Christian-Albrechts-Universität, Max-Eyth-Straße 2, D-24118 Kiel, Germany*
[b] *Otto Diels-Institut für Organische Chemie, Christian-Albrechts-Universität, Otto-Hahn-Platz 4, D-24098 Kiel, Germany*

ARTICLE INFO

Article history:
Received 8 October 2014
Received in revised form
13 January 2015
Accepted 20 January 2015
Available online xxx

Keywords:
Metal organic framework
Functionalized extended linker molecules
Aluminum
Adsorption
Breathing behavior

ABSTRACT

Al-based metal-organic framework (MOF) compounds containing nitro- and amino-substituted and sulfone-bridged groups were synthesized: [Al(OH)(NDC-(NO$_2$)$_2$)] (**1**), [Al(OH)(BPDC-NO$_2$)] (**2**), [Al(OH)(BPDC-NH$_2$)] (**3**) and [Al(OH)(BPDC-SO$_2$)] (**4**), which are analogs of MIL-69/DUT-4 ([Al(OH)(NDC)]) or DUT-5 ([Al(OH)(BPDC)]) (NDC = 2,6-naphthalenedicarboxylate, BPDC = 4,4'-biphenyldicarboxylate). The compounds were synthesized under solvothermal conditions employing microwave-assisted heating and characterized by powder X-ray diffraction, thermogravimetric analysis and gas sorption measurements. They exhibit permanent porosity and are accessible to carbon dioxide, hydrogen and methane but do not show any framework flexibility like MIL-53. All compounds are highly stable as confirmed by temperature-dependent powder X-ray diffraction measurements (TD-PXRD) and framework decomposition takes place between 340 °C and 420 °C.

1. Introduction

In recent years, a large number of metal-organic-frameworks (MOFs) have attracted great attention due to the tunability of their chemical and physical properties, especially the pore surface functionality and the pore size [1–3]. Most of these porous compounds are built up from inorganic building units, *e.g.* metal ions, metal-oxide clusters or chains and organic linker molecules containing carboxylate, imidazolate or phosphonate groups [4,5] to interconnect the inorganic units. Once the optimal synthesis conditions for the formation of the inorganic building blocks are established, isoreticular compounds can be obtained to adjust the pore size [6,7] and the pore functionality [8,9]. Usually this necessitates the optimization of the synthesis conditions, which can efficiently be carried out using high-throughput methods.

MOFs based on trivalent metal cations are well-known and of special interest due to their desirable properties such as thermal and chemical stability [10]. Aluminum-based MOFs, which are light-weight and contain a non-toxic metal, are of particular importance because of their good chemical and high thermal stability. Especially Al-MIL-53, [Al(OH)(BDC)] (BDC = 1,4-benzenedicarboxylate) [11], and isoreticular compounds have been intensively investigated (MIL = Materials Institute Lavoisier) [6,12,13]. The parent material is stable up to 450 °C and exhibits a complex structural behavior, namely the reversible flexibility of the framework upon exchange or removal of guest molecules [11]. For the synthesis of MOFs with MIL-53-topology, the organic units can be replaced by a smaller linker molecule like fumaric acid [10], or larger ones like 2,6-naphthalenedicarboxylic acid (H$_2$NDC), 4,4′-biphenyldicarboxylic acid (H$_2$BPDC) or 2,2′bipyridine-5,5′-dicarboxylate acid (H$_2$BPyDC) obtaining the MIL-53 analogs MIL-69 [12], DUT-4, DUT-5 (DUT = Dresden University of Technology) [6] and MOF-253 [13]. In contrast to Al-MIL-53, the other MOFs exhibit no framework flexibility and MIL-69 is the non-porous version of DUT-4.

The introduction of functional groups into the frameworks is of substantial significance for tuning the pore properties of the resulting materials. In the case of Al-MIL-53, the introduction of functional groups, using differently functionalized terephthalate derivatives, resulted in the isoreticular compounds Al-MIL-53-COOH [9], Al-MIL-53-F [14], Al-MIL-53-NH$_2$ [15,16], Al-MIL-53-X (X = –Cl, –Br, –NO$_2$, –CH$_3$) [17], Al-MIL-53-OH [18]. They exhibit, depending on the nature of the functionalities, different

---

* Corresponding author.
E-mail address: stock@ac.uni-kiel.de (N. Stock).

http://dx.doi.org/10.1016/j.micromeso.2015.01.030

Please cite this article in press as: S. Halis, et al., Four new Al-based microporous metal-organic framework compounds with MIL-53-type structure containing functionalized extended linker molecules, Microporous and Mesoporous Materials (2015), http://dx.doi.org/10.1016/j.micromeso.2015.01.030

thermal stabilities as well as different sorption and breathing properties. For example, Al-MIL-53-NH_2 exhibits a high selectivity in the CO_2/CH_4 separation towards CO_2 [19]. Due to their stability, some of the compounds were used in post-synthetic modification (PSM) reactions. Thus, the introduction of functionalities, like amide, iso(thio)cyanate, (thio)carbamate and (thio)urea, was described [20]. Surprisingly, no reports have been published using functionalized extended linker molecules for the synthesis of Al-MIL-53 type structures.

Herein we report the investigation of the systems Al^{3+}/H_2NDC-$(NO_2)_2$/DMF, Al^{3+}/H_2BPDC-NO_2/DMF, Al^{3+}/H_2BPDC-NH_2/DMF and Al^{3+}/H_2BPDC-SO_2/DMF using our high-throughput (HT) set up incorporating microwave-assisted heating [9,21,22]. The resulting MIL-69/DUT-4 and DUT-5 analogs [Al(OH)(NDC-$(NO_2)_2$)]·DMF (**1**) and [Al(OH)(BPDC-NO_2)]·1.7DMF·0.8H_2O (**2**), [Al(OH)(BPDC-NH_2)]·1.7DMF·H_2O (**3**) [Al(OH)(BPDC-SO_2)]·2.5DMF (**4**), respectively, were characterized in detail and their sorption properties were determined using nitrogen, hydrogen, carbon dioxide and methane as adsorptive.

2. Experimental section

2.1. General information

Aluminum salts and solvents were purchased from commercial sources and were used without further purification. The synthesis procedure of the organic linker molecules are given in detail in the supporting information.

The high-throughput (HT) investigations were carried out in 5 mL glass vials with a maximum reaction volume of 3 mL, placed in a SiC-block using a high-throughput (HT) microwave oven Synthos 3000 from Anton Paar. The glass vials were equipped with a Teflon seal and a screw cap. The scale-up reactions were performed in a 5 mL or 20 mL microwave glass vials using a microwave oven Initiator from Biotage. Powder X-ray diffraction data were collected in transmission mode using a STOE STADI P diffractometer with Cu-$K_{\alpha1}$ ($\lambda = 1.5406$) radiation. Lattice parameters were determined and refined by Topas Academics 4.1 [23]. Thermogravimetric (TG) measurements were carried out with a heating rate of 2 K min^{-1} under a flow of air (75 cm^3 min^{-1}) using a NETSCH STA 409 CD analyzer. Elemental analyses (C, H, N, S) were performed on a EuroVector EuroEA Elemental Analyzer. Sorption measurements were carried out using a BELSORP-max instrument (BEL JAPAN INC.). Specific surface areas were calculated using the BET method as described in the literature [24] and micropore volumes were calculated from the N_2-adsorption isotherm at $p/p_0 = 0.5$. The N_2-sorption measurements were performed at 77 K. The samples were activated at 180 (compound **2** and **3**) and 250 °C (compound **1** and **4**) under dynamic vacuum (10^{-2} kPa) for 16 h. Mid-Infrared (MIR) spectra were recorded on a Bruker ALPHA-P FT-IR spectrometer in the spectral range 4000–400 cm^{-1} at room temperature.

2.2. Preparation

[Al(OH)(NDC-$(NO_2)_2$)] · DMF (**1**): The linker molecule 1,5-dinitro-3,7-naphthalenedicarboxylic acid H_2NDC-$(NO_2)_2$ was prepared according to the literature by nitration of 2,6-naphthalenedicarboxylic acid using nitric acid [25]. The raw product was purified by recrystallization from methanol. The functionalized linker and $AlCl_3 \cdot 6H_2O$ were used as starting materials and the molar ratio Al^{3+} : H_2NDC-$(NO_2)_2$: DMF of 1 : 1.8 : 217 results in highest crystallinity of the product **1**. The optimized reaction parameters could be used in scaled up reactions in a microwave oven, using a 5 mL microwave glass vial. A mixture of H_2NDC-$(NO_2)_2$ (0.54 mmol, 165.2 mg), $AlCl_3 \cdot 6H_2O$ (0.30 mmol, 72.4 mg) and 5 mL DMF were heated at 140 °C for 4 h. The microcrystalline product was dried in air. Elemental analysis, [Al(OH)(NDC-$(NO_2)_2$)]·DMF (**1**) found (%): C 42.5, H 2.6, N 9.5; calc (%): C 42.5, H 3.2, N 9.9.

[Al(OH)(BPDC-NO_2)]·1.7 DMF ·0.8 H_2O (**2**): 3-Nitro-4,4'-biphenyldicarboxylic acid (H_2BPDC-NO_2) was prepared by nitration of 4,4′-biphenyldicarboxylic acid varying a published synthesis procedure [26]. Details are given in the supporting information. For the optimized synthesis of compound **2**, a mixture of H_2BPDC-NO_2 (0.032 mmol, 9.2 mg), $AlCl_3 \cdot 6H_2O$ (0.02 mmol, 4.8 mg) and 0.5 mL DMF was heated at 150 °C for 3 h (molar ratio Al^{3+} : H_2BPDC-NO_2 : DMF of 1 : 1.6 : 318) in a microwave oven. The resulting microcrystalline product was dried in air. Elemental analysis, [Al(OH)(BPDC-NO_2)]·1.7DMF·0.8H_2O (**2**) found (%): C 51.6, H 4.8, N 8.0; calc (%): C 52.7, H 4.2, N 7.2.

[Al(OH)(BPDC-NH_2)]·1.7DMF·H_2O (**3**): The subsequent reduction of H_2BPDC-NO_2 using $SnCl_2$ led to 3-amino-4,4′-biphenyldicarboxylic acid (H_2BPDC-NH_2). Details are given in the supporting information. Compound **3** was prepared from a mixture of H_2BPDC-NH_2 (0.036 mmol, 9.3 mg), $AlCl_3 \cdot 6H_2O$ (0.02 mmol, 4.8 mg) and 0.5 mL DMF for 3 h at 150 °C under microwave heating (molar ratio Al^{3+} : H_2BPDC-NH_2 : DMF of 1 : 1.8 : 318). The resulting microcrystalline product was dried in air. Elemental analysis, [Al(OH)(BPDC-NH_2)]·1.7 DMF·H_2O (**3**) found (%): C 47.3, H 4.9, N 8.0; calc (%): C 46.7, H 5.7, N 8.7. The scale-up syntheses of product **2**

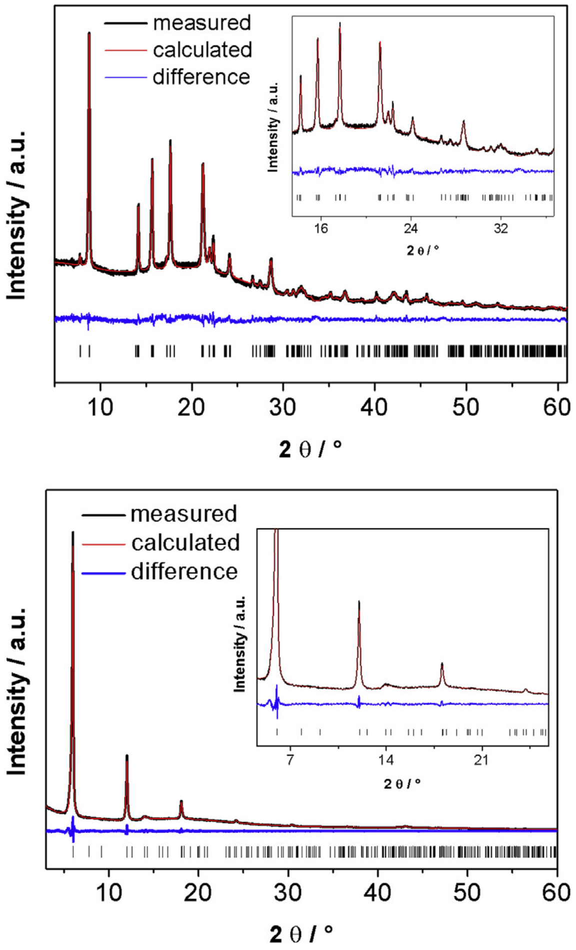

Fig. 1. Top: Pawley-Fit of [Al(OH)(NDC-$(NO_2)_2$)]·DMF (**1**) Bottom: Pawley-Fit of [Al(OH)(BPDC-NO_2)] (**2**) after activation.

Please cite this article in press as: S. Halis, et al., Four new Al-based microporous metal-organic framework compounds with MIL-53-type structure containing functionalized extended linker molecules, Microporous and Mesoporous Materials (2015), http://dx.doi.org/10.1016/j.micromeso.2015.01.030

and **3** proved to be not straightforward and resulted in products of lower crystallinity.

[Al(OH)(BPDC-SO$_2$)]·2.5DMF (**4**): The linker molecule 5,5-dioxo-dibenzo[*b*,*d*]thiophen-3,7-dicarboxylic acid (H$_2$BPDC-SO$_2$) was synthesized by sulfonation of dimethyl-4,4'-biphenyldicarboxylate using chorosulfonic acid according to a procedure reported in the literature [27]. The compound **4** was prepared from a mixture of H$_2$BPDC-SO$_2$ (0.6 mmol, 182.5 mg), Al(ClO$_4$)$_3$·9 H$_2$O in dimethylformamide (0.5 M) (0.6 mmol, 1.2 mL) and 8.8 mL DMF (molar ratio Al^{3+} : H$_2$BPDCSO$_2$: DMF = 1 : 1 : 187) in a 20 mL glass vial under microwave heating for 1 h at 160 °C. The precipitate was filtered off, dried in air and characterized by X-ray powder diffraction. Elemental analysis, [Al(OH)(BPDC-SO$_2$)]·2.5DMF (**4**) found (%): C 47.7 , N 5.5 , H 4.5 , S 6.0 ; calc (%): C 49.0 , N 6.6 , H 4.7 , S 6.1 .

3. Results and discussion

3.1. Structural characterization

Since all compounds were obtained as microcrystalline powders, X-ray powder diffraction (XRPD) measurements were carried out to demonstrate that the compounds are isostructural to MIL-69/DUT4 and DUT-5/MOF-253. As observed in the PXRD investigations of DUT-4, -5 and MOF-253, the PXRD patterns exhibit only few broad reflections which nevertheless allow the determination of the lattice parameters. The lattice parameters were refined using the Pawley method as implemented in the program Topas Academics 4.1 [23]. Starting values were taken from indexing (**1**) or the reported lattice parameters of DUT-5. In Fig. 1 and Fig. 2 the Pawley-Fits are shown. The obtained lattice parameters are given in Table 1 and are compared to MIL-69/DUT-4, DUT-5 and MOF-253. Based on these results we conclude that **1** adopts a MIL-69-type and **2**, **3**, and **4** a DUT-5-type structure.

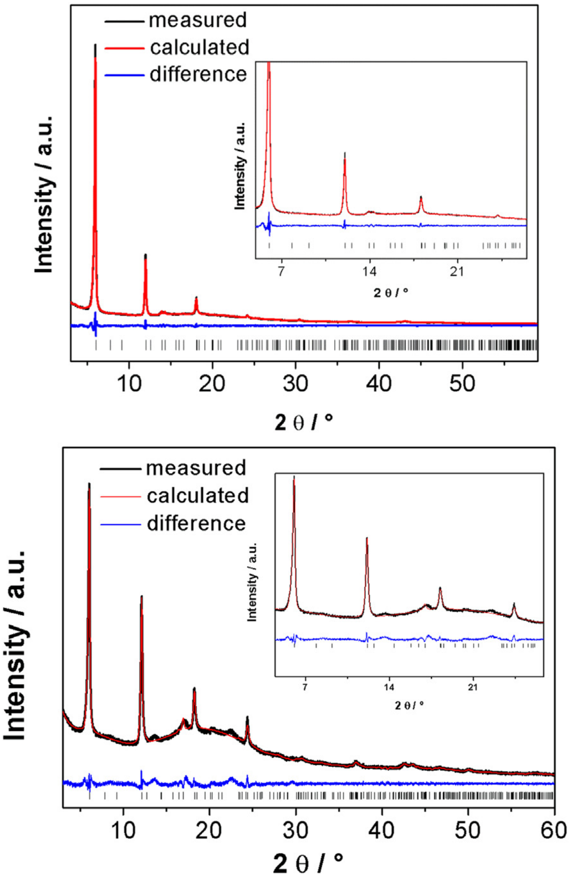

Fig. 2. Top: Pawley-Fit of [Al(OH)(BPDC-NH$_2$)] (**3**) after activation; Bottom: Pawley-Fit of Pawley-Fit of [Al(OH)(BPDC-SO$_2$)]·2.5DMF (**4**).

All described structures are isoreticular to MIL-53 and consist of chains of *trans* μ-OH corner sharing AlO$_6$-octahedra which are connected by the carboxylate groups of the functionalized extended linker molecules to form one-dimensional lozenge-shaped pores.

3.2. Structure simulations

The structural model of **1** was set-up using Materials Studio [28] starting from the crystal structure of Al-MIL-69 [12] since for both compounds a monoclinic *C*-centered cell was obtained. The naphthalenedicarboxylate molecules were modified by replacing H-atoms by nitro groups at the corresponding positions. Furthermore water molecules located in the pores were removed. The symmetry was changed to *P*1 to remove previous symmetry restrictions. Finally, the constructed structural model was optimized by full energy minimization using force field calculations [28] to give a plausible crystal structure in the space group *C*2/*c* (Fig. 3). Comparing the calculated PXRD pattern with the measured one, the reflection positions are in good agreement, deviations in the relative intensities are caused by the solvent molecules in the pores (see Figs. 4 and 5).

Concerning **2**, **3** and **4**, the structural models were simulated using the structure of Al-DUT-5 [6] as starting point. The cell parameters were replaced by the experimentally determined ones for **2**, **3** and **4** (as obtained by Pawley refinement) and the symmetry was set to *P*1. The biphenyldicarboxylate molecules were modified by nitro-, amino- and sulfone-groups at the corresponding positions, respectively. The constructed structural models were optimized by full energy minimization using force field calculations [28] to give a structural model with ordered functional groups. However, we assume that the functional groups are randomly distributed over the possible positions (Figs. S8 and S9).

Table 1
Lattice parameters of [Al(OH)(NDC-(NO$_2$)$_2$)] (**1**), [Al(OH)(BPDC-NO$_2$)] activated (**2**), [Al(OH)(BPDC-NH$_2$)] activated (**3**), [Al(OH)(BPDC-SO$_2$)] (**4**), MIL-69 ([Al(OH)(NDC)]) [11], as derived from the Pawley fits. The parameters of DUT-5 ([Al(OH)(BPDC)]) [6] and MOF-253 ([Al(OH)(BPyDC)]) [13] are given for comparison.

	MIL-69	DUT-4	[Al(OH)(NDC-(NO$_2$)$_2$)]	[Al(OH)(BPDC-NO$_2$)]
Space group/crystal system	*C*2/*c*	*Pnna*	*C*2/*c*	*orthorhombic*
a/Å	24.598(2)	18.825(3)	23.654(3)	22.62(1)
b/Å	7.5305(6)	6.7867(5)	11.176(2)	6.631(3)
c/Å	6.5472(5)	16.901(2)	6.592(1)	19.452(7)
β/°	106.863(8)	90	107.64(2)	90
V/Å^3	1660.6(2)	2159.3(9)	1660.8(5)	2918(2)
r$_{wp}$	–	10.6	4.0	3.5
	DUT-5	MOF-253	[Al(OH)(BPDC-NH$_2$)]	[Al(OH)(BPDC-SO$_2$)]
Space group/crystal system	*Imma*	*Imma*	*orthorhombic*	*orthorhombic*
a/Å	22.698(2)	23.59(10)	22.594(3)	22.442(16)
b/Å	6.60721(14)	6.911(29)	6.559(3)	6.494(3)
c/Å	19.2398(13)	19.84(8)	19.494(4)	19.169(9)
β/°	90	90	90	90
V/Å^3	2885.4(5)	–	2888(1)	2793.7(5)
r$_{wp}$	5.71	7.86	4.3	3.8

Please cite this article in press as: S. Halis, et al., Four new Al-based microporous metal-organic framework compounds with MIL-53-type structure containing functionalized extended linker molecules, Microporous and Mesoporous Materials (2015), http://dx.doi.org/10.1016/j.micromeso.2015.01.030

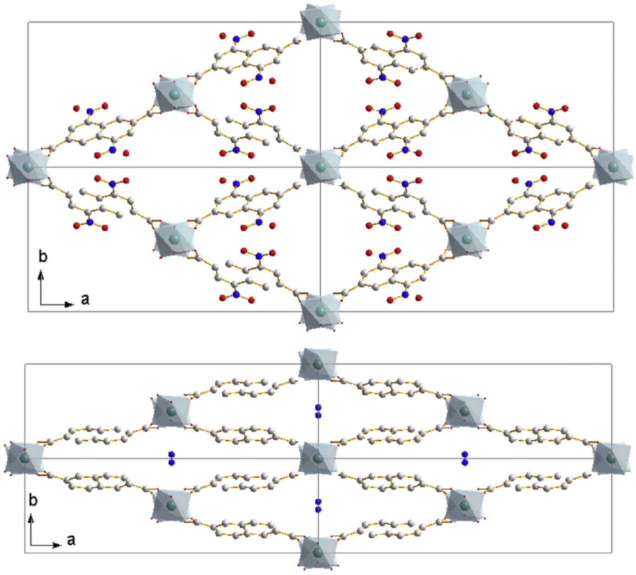

Fig. 3. Structural model of [Al(OH)(NDC-$(NO_2)_2$)] (top) and the structure of MIL-69 with encapsulated water molecules (bottom).

3.3. Thermal analysis

To investigate the thermal stability of the title compounds, thermogravimetric (TG) and temperature-dependent PXRD measurements were carried out (see Figs. 7–10).

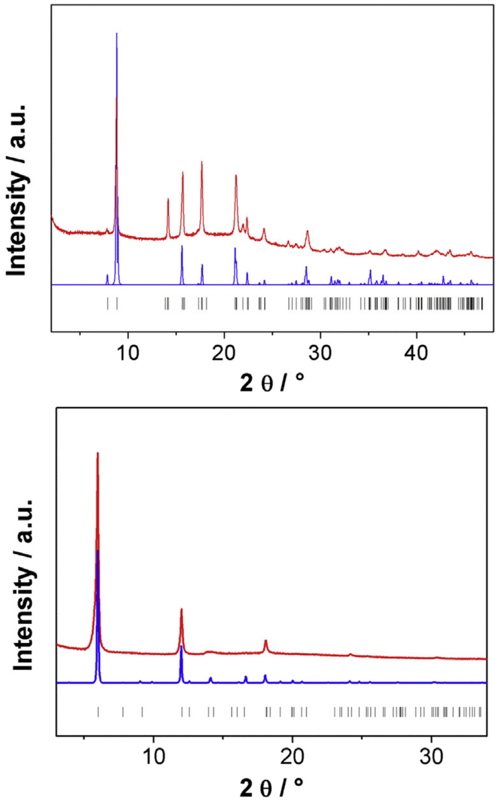

Fig. 4. Top: PXRD pattern of [Al(OH)(NDC-$(NO_2)_2$)]·DMF (**1**) (red), calculated PXRD pattern of **1** (blue); Bottom: PXRD pattern of [Al(OH)(BPDC-NO_2)]·DMF (**2**) (red), calculated PXRD pattern of **2** (blue); with the tics marking the allowed Bragg positions (black). (For interpretation of the references to colour in this figure legend, the reader is referred to the web version of this article.)

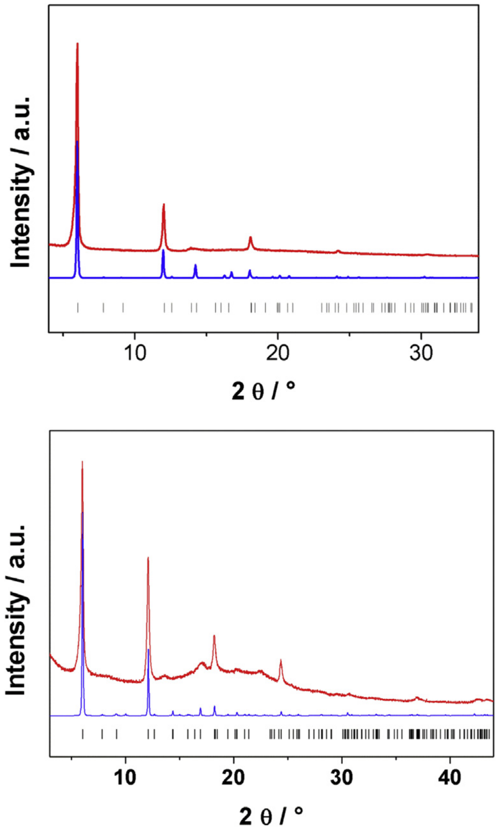

Fig. 5. Top: PXRD pattern of [Al(OH)(BPDC-NH_2)] (**3**) (red), calculated PXRD pattern of **3** (blue); Bottom: PXRD pattern of [Al(OH)(BPDC-SO_2)]·2.5DMF (**4**) (red), calculated PXRD pattern of **4** (blue); with the tics marking the allowed Bragg positions (black). (For interpretation of the references to colour in this figure legend, the reader is referred to the web version of this article.)

TG measurements were performed under air with a heating rate of 4 K m^{-1}. The results are given in Figs. 7 and 8 and Table 2. For compound **1** (Fig. 7, left), the first weight loss between 50 °C and 280 °C corresponds to the removal of incorporated one DMF molecule per formula units (obs. 17.7%; calc. 17.3%). The framework is stable up to 340 °C and decomposes under formation of Al_2O_3 (obs. 69.2%; calc. 69.9%). The first weight loss of 3.5% (cal. 3.5%) for compound **2** (Fig. 7, right) and 4.8% (calc. 4.8%) for compound **3** (Fig. 8, left) up to 100 °C correspond to the removal of 0.8 and 1 water molecule per formula unit, respectively. The second weight loss of 27.2% (calc. 27.0%) for **2** and 27.7% (calc. 27.7%) for **3** up to 260 °C can be attributed to the removal of 1.7 DMF molecules, respectively. The decomposition of the framework to Al_2O_3 of compound **2** occurs above 360 °C and of compound **3** above 400 °C (for **2**: obs. 49.5%; calc. 51.6%; for **3**: obs. 54.1%; calc. 55.1%). The TG curve of compound **4** (Fig. 8, right) shows a two-step weight loss. The first step up to 280 °C is due to the removal of incorporated DMF molecules (2.5 per formula unit, obs. 34.0%; calc. 34.6%) and the second step is related to the decomposition of the framework (obs. 55.8%; calc. 55.8%), resulting in Al_2O_3. The results of the TG measurements of all four compounds are in good agreement with the ones of the elemental analysis.

To prove the structural integrity during the removal of the guest molecules and to investigate a potential flexibility of the frameworks, TD-PXRD measurements of all four title compounds were performed. In the TD-PXRD pattern of **1** (Fig. 9, top) an increase of the reflection intensity for the 110 reflection at 8.82°(2θ) is observed up to 280 °C which can be explained by the removal of

Please cite this article in press as: S. Halis, et al., Four new Al-based microporous metal-organic framework compounds with MIL-53-type structure containing functionalized extended linker molecules, Microporous and Mesoporous Materials (2015), http://dx.doi.org/10.1016/j.micromeso.2015.01.030

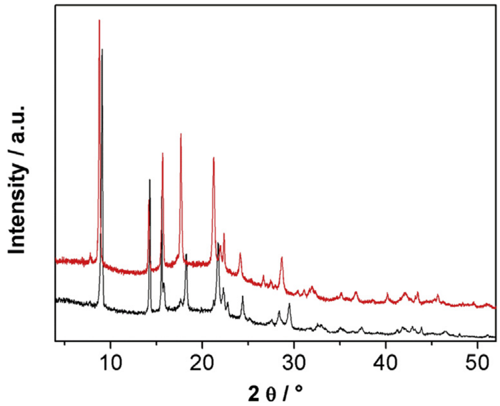

Fig. 6. PXRD pattern of the activated [Al(OH)(NDC-$(NO_2)_2$)] (black, bottom) and the as synthesized compound **1** (red, top). (For interpretation of the references to colour in this figure legend, the reader is referred to the web version of this article.)

adsorbed guest molecules. The compound exhibits a high thermal stability up to the decomposition of the framework above 340 °C. No further changes in the reflection positions and intensities are observed showing the rigidity of the framework. Compounds **2** and **3** (Fig. 9, bottom and Fig. 10, top) exhibit also a high thermal stability: for **2** at least up to 360 °C and for **3** up to 400 °C. The TD-PXRD patterns show a slight increase of the 101 reflection intensity up to 140 °C. Upon removal of DMF in the temperature range between 140 and 260 °C a strong increase of the reflection intensity is observed. The reflection intensities decrease starting around 360 and 400 °C, respectively. No changes of the reflection positions are detectable which hint at the rigidity of the framework. In the TD-PXRD pattern of **4** (Fig. 10, bottom) a strong increase of intensity of the first reflection is observed up to 280 °C corresponding to the removal of incorporated DMF molecules. Above 420 °C, the crystallinity decreases rapidly due to the decomposition of the framework. No shift of reflection positions upon thermal treatment is observed.

The observations from the TD-PXRD measurements are in good agreement with the results obtained from the TG-measurement. The removal of the water and DMF molecules is observed up to 280 °C and framework decomposition takes place between 340 °C and 420 °C.

3.4. IR spectroscopy

The IR-spectra of the as synthesized (black) and activated samples (blue) of all four title compounds are shown in the supporting information (Figs. S1–2). All spectra exhibit a weak band that can be assigned to the stretching vibrations of the hydroxyl groups bridging the Al ions (for the activated compounds at 3648 (**1**) and at 3706, 3704 and 3704 cm^{-1} for **2, 3** and **4** respectively. In all spectra the vibrations of the coordinating carboxylate groups are observed (ν_{as} at 1607–1599 cm^{-1} and ν_s at 1431–1496 cm^{-1}) [11]: The presence of DMF molecules in the as-synthesized products lead to characteristic bands (ν(C=O) at 1667–1662 cm^{-1}), which are not present in the spectra of the activated samples. Characteristic vibrations of the functional groups ($-NH_2$ (broad bands 3671–3064 cm^{-1}), $-NO_2$ (ν_{as} at 1535/1530 and ν_s at 1358/1347 cm^{-1}), $-SO_2$ (ν_{as} at 1300 and ν_s at 1137 cm^{-1}) are also observed in the IR-spectra. These are also present after activation of the compounds. A more detailed discussion of the individual bands is given in the supporting information.

3.5. Sorption properties

To determine the specific surface area and micropore volume of the four title compounds sorption experiments were carried out at 77 K using N_2. The values were calculated using the BET model and the uptake at $p/p_0 = 0.5$ (Table 3). These were compared to the ones reported for the unfunctionalized DUT-4, DUT-5 and MOF-253 (MIL-69 is non-porous). In addition to nitrogen sorption

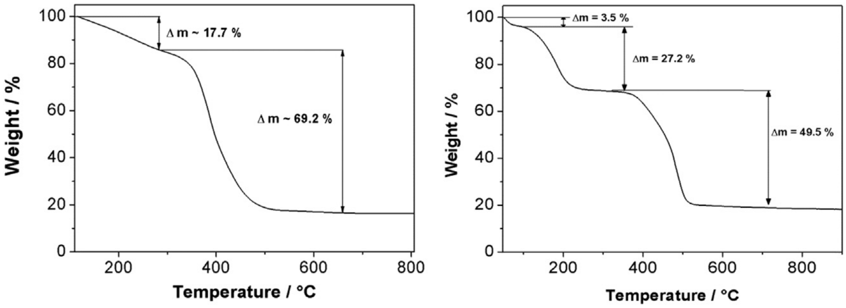

Fig. 7. TG curves of [Al(OH)(NDC-$(NO_2)_2$)]·DMF (**1**) (left);[Al(OH)(BPDC-NO_2)]·1.7DMF·0.8H_2O (**2**) (right).

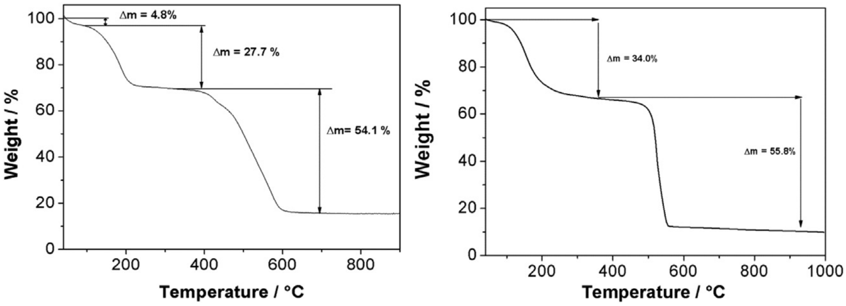

Fig. 8. TG curve of [Al(OH)(BPDC-NH_2)]·1.7DMF·H_2O (**3**) (left) and [Al(OH)(BPDC-SO_2)]·2.5DMF (**4**) (right).

Please cite this article in press as: S. Halis, et al., Four new Al-based microporous metal-organic framework compounds with MIL-53-type structure containing functionalized extended linker molecules, Microporous and Mesoporous Materials (2015), http://dx.doi.org/10.1016/j.micromeso.2015.01.030

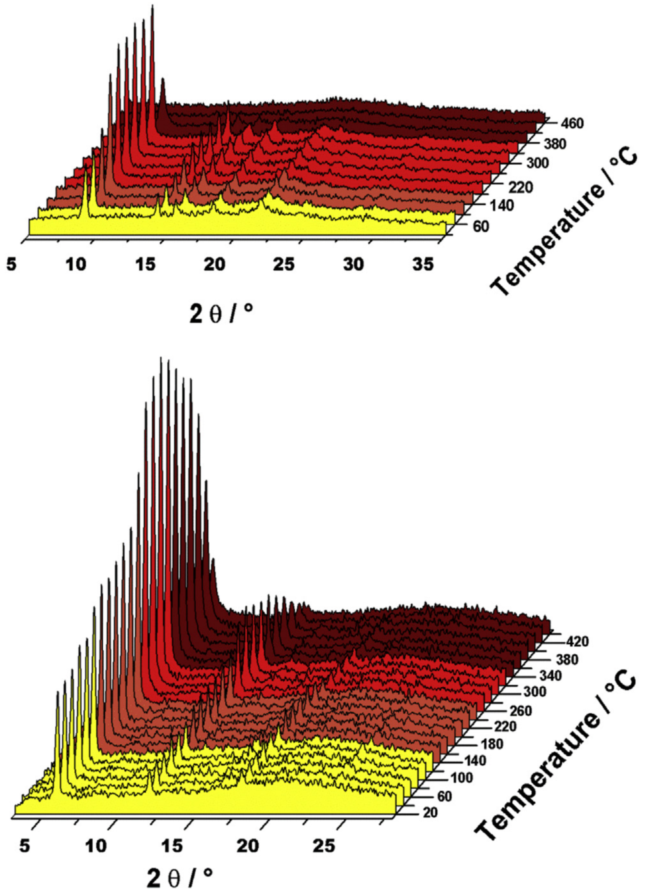

Fig. 9. TD-PXRD patterns of $[Al(OH)(NDC-(NO_2)_2)]\cdot DMF$ (**1**), top, and $[Al(OH)(BPDC-NO_2)]\cdot 1.7DMF\cdot 0.8\ H_2O$ (**2**), bottom, collected in air.

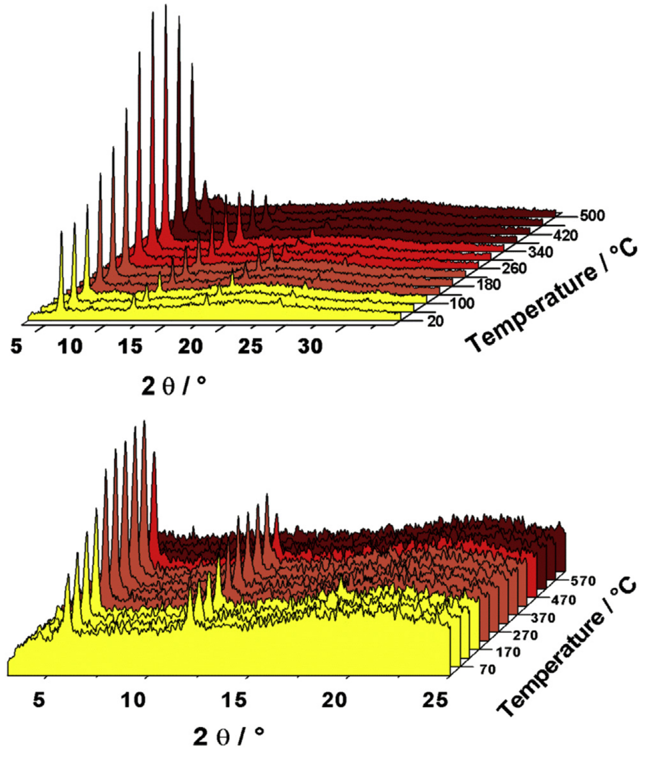

Fig. 10. TD-XRPD patterns of $[Al(OH)(BPDC-NH_2)]\cdot 1.7DMF\cdot H_2O$ (**3**), top, and $[Al(OH)(BPDC-SO_2)]\cdot 2.5DMF$ (**4**), bottom, collected in air.

Table 2
The summarized results of the TG measurements of compounds **1**, **2**, **3** and **4**.

Compound	Removal of H_2O	Removal of DMF	Framework decomposition
$[Al(OH)(NDC-(NO_2)_2)]\cdot DMF$ (**1**)	–	50–280 °C	above 340 °C
$[Al(OH)(BPDC-NO_2)]\cdot 1.7DMF\cdot 0.8H_2O$ (**2**)	50–100 °C	140–260 °C	above 360 °C
$[Al(OH)(BPDC)(NH_2)]\cdot 1.7DMF\cdot H_2O$ (**3**)	50–100 °C	140–260 °C	above 400 °C
$[Al(OH)(BPDC-SO_2)]\cdot 2.5DMF$ (**4**)	–	50–280 °C	above 420 °C

measurements, also sorption measurements using hydrogen (at 77 K), carbon dioxide (at 298 K) and methane (at 298 K) were performed (Table 3). The PXRD patterns of the title compounds after the sorption measurements (Fig. S3) show that the frameworks are stable after the removal of the guest molecules.

All four title compounds are permanently porous towards the four gases used in the study. Evaluation of the type-I N_2 sorption isotherms (Fig. 11) yields values of $a_{BET} = 578\ m^2\ g^{-1}$ and $V_{mic} = 0.23\ cm^3\ g^{-1}$ for **1**. As expected, these values are smaller than the ones observed for DUT-4, which can be explained by the presence of functional groups. The decrease is larger than expected since, in accordance with the results of the PXRD measurements, not the fully opened framework structure is formed as it is the case for DUT-4. In contrast, the a_{BET} and V_{mic} values of **2**, **3** and **4** are similar to the ones observed for DUT-5 (a_{BET}: 1530–1966 vs $1613\ m^2\ g^{-1}$ and $V_{mic} = 0.66$-0.79 vs $0.81\ cm^3\ g^{-1}$).

The results of the measurements using the other gases are also summarized in Table 3, the sorption isotherms are given in the supporting information (Figs. S4–S5). Based on the steeper uptake at low pressures we conclude that $[Al(OH)(NDC-(NO_2)_2)]$ (**1**) has the highest affinity towards H_2 and CH_4. This observation is due to the smaller pore diameter, which leads to stronger host guest interactions. In addition, it could be possible that NO_2-groups of adjacent linker molecules could interact with the gas molecules. While **1** shows the highest CH_4 uptake, compound **2** exhibits the lowest capacity at a pressure of 100 kPa (up to 1.5 wt%) probably due to the combination of the large surface area and the presence of the NO_2-groups.

Larger differences are observed in the CO_2 adsorption, which leads to values between 1.5 and 11.6 wt%. Due to the smaller pores, $[Al(OH)(NDC-(NO_2)_2)]$ (**1**) also shows the largest CO_2 uptake at small pressures (<50 kPa). Unexpectedly, the $-NH_2$ functionalized compound **3** with the highest specific surface area exhibits the smallest uptake. This observation is in contrast to previous reports,

Table 3
Apparent specific surface areas, micropore volumes values (derived from the N_2 sorption measurements) and maximum uptake of CO_2, H_2 and CH_4 (~ 100 kPa) of the four title compounds. For comparison, literature values for DUT-4 [6], DUT-5 [6] and MOF-253 [13] are also given (n.c. = not comparable since they were determined under different conditions).

Compound	a_{BET} $[m^2g^{-1}]$	V_{mic} $[cm^3g^{-1}]$	CO_2 [wt%]	H_2 [wt%]	CH_4 [wt%]
$[Al(OH)(NDC-(NO_2)_2)]$ (**1**)	578	0.23	10.0	1.0	1.2
DUT-4	1308	0.68	4.4[a]	n.c.	n.c.
$[Al(OH)(BPDC-NO_2)]$ (**2**)	1677	0.67	7.7	1.5	0.9
$[Al(OH)(BPDC)(NH_2)]$ (**3**)	1966	0.79	1.5	1.2	0.4
$[Al(OH)(BPDC-SO_2)]$ (**4**)	1530	0.66	11.6	0.6	0.5
DUT-5	1613	0.81	–	n.c.	n.c.
MOF-253	2160	0.89	4.3	–	–

[a] Estimated from the high pressure sorption curve reported in Ref. [6].

Please cite this article in press as: S. Halis, et al., Four new Al-based microporous metal-organic framework compounds with MIL-53-type structure containing functionalized extended linker molecules, Microporous and Mesoporous Materials (2015), http://dx.doi.org/10.1016/j.micromeso.2015.01.030

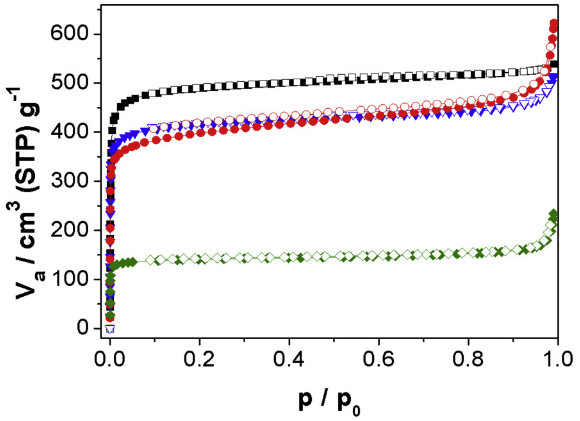

Fig. 11. N_2 adsorption–desorption isotherms (performed at 77 K) of [Al(OH)(NDC-$(NO_2)_2$)] (**1**) (olive, diamonds), [Al(OH)(BPDC-NO_2)] (**2**) (blue, triangles), [Al(OH)(BPDC-NH_2)] (**3**) (black, squares) and [Al(OH)(BPDC-SO_2) (4) (red, circles); after activation at 180 °C for 16 h (**2**, **3**) and at 250 °C for 16 h (**1**, **4**). Filled symbols mark the adsorption, while the empty symbols stand for the desorption. (For interpretation of the references to colour in this figure legend, the reader is referred to the web version of this article.)

which state that CO_2 adsorption is improved when the MOFs are functionalized with amino groups [29]. Comparing the three functionalized DUT-5 analogs, [Al(OH)(BPDC-SO_2)] shows the highest uptake at 100 kPa followed by [Al(OH)(BPDC-NO_2] and [Al(OH)(BPDC-NH_2] (11.6, 7.7 and 1.5 wt%, respectively) although the inverse trend was observed for the specific surface areas and micropore volumes.

4. Conclusion

Summarizing our results, we described four new functionalized aluminum based MOFs which exhibit permanent porosity: [Al(OH)(NDC-$(NO_2)_2$)] (**1**), [Al(OH)(BPDC-NO_2)] (**2**), [Al(OH)(BPDC-NH_2)] (**3**) and [Al(OH)(BPDC-SO_2)] (**4**) using dinitro-functionalized 2,6-naphthalenedicarboxylic acid, amino-, nitro- and sulfone-functionalized 4,4'-biphenyldicarboxylic acid, respectively, as linker molecules. The structures are analogs of MIL-69 (**1**) and DUT-5 (**2**, **3**, **4**) and exhibit any framework flexibility in their framework. In contrast to MIL-69, which is non-porous, the functionalized derivative is porous towards all studied gases. All described compounds are thermally stable up to at least 320 °C in air. For the DUT-5 based compounds the incorporation of functional groups has only a small influence on the specific surface area and microporosity as determined from the N_2 sorption curves. Large differences are observed in the low pressure adsorption of CO_2. Compound **1** containing two NO_2-groups shows a strong affinity towards CO_2.

Acknowledgment

The authors acknowledge the Deutsche Forschungsgemeinschaft (SPP1362) for funding and Dr. Helge Reinsch for fruitful discussions.

Appendix A. Supplementary data

Supplementary data related to this article can be found at http://dx.doi.org/10.1016/j.micromeso.2015.01.030.

References

[1] Themed issue on Metal-Organic Frameworks, Chem. Soc. Rev. (2009) 1201.
[2] Themed issue on Metal-Organic Frameworks, Chem. Rev. (2012) 673.
[3] Themed issue on Metal-Organic Frameworks, Chem. Soc. Rev. (2014) 5415.
[4] J.L.C. Rowsell, O.M. Yaghi, Microporous Mesoporous Mater. 73 (2004) 3.
[5] V. Colombo, S. Galli, H.J. Choi, G.D. Han, A. Maspero, G. Palmisano, N. Masciocchi, J.R. Long, Chem. Sci. 2 (2011) 1311.
[6] I. Senkovska, F. Hoffmann, M. Fröba, J. Getzschmann, W. Bohlmann, S. Kaskel, Microporous Mesoporous Mat. 122 (2009) 93.
[7] M. Eddaoudi, J. Kim, N. Rosi, D. Vodak, J. Wachter, M. O'Keeffe, O.M. Yaghi, Science 295 (2002) 469.
[8] A. Comotti, S. Bracco, P. Sozzani, S. Horike, R. Matsuda, J. Chen, M. Takata, Y. Kubota, S. Kitagawa, J. Am. Chem. Soc. 130 (2008) 13664.
[9] N. Reimer, B. Gil, B. Marszalek, N. Stock, CrystEngComm 14 (2012) 4119.
[10] C. Volkringer, T. Loiseau, N. Guillou, G. Férey, E. Elkaim, Solid State Sci. 11 (2009) 1507.
[11] T. Loiseau, C. Serre, C. Huguenard, G. Fink, F. Taulelle, M. Henry, T. Bataille, G. Férey, Eur. J. 10 (2004) 1373.
[12] T. Loiseau, C. Mellot-Draznieks, H. Muguerra, G. Férey, M. Haouas, F. Taulelle, C.R. Chim. 8 (2005) 765.
[13] E.D. Bloch, D. Britt, C. Lee, C.J. Doonan, F.J. Uribe-Romo, H. Furukawa, J.R. Long, O.M. Yaghi, J. Am. Chem. Soc. 132 (2010) 14382.
[14] S. Biswas, T. Rémy, S. Couck, D. Denysenko, G. Rampelberg, J.F.M. Denayer, D. Volkmer, C. Detavernier, P.V.D. Voort, Phys. Chem. Chem. Phys. 15 (2013) 3552.
[15] T. Ahnfeldt, D. Gunzelmann, T. Loiseau, D. Hirsemann, J. Senker, G. Ferey, N. Stock, Inorg. Chem. 48 (2009) 3057.
[16] J. Wack, R. Siegel, T. Ahnfeldt, N. Stock, L. Mafra, J. Senker, J. Phys. Chem. C 117 (2013) 19991.
[17] S. Biswas, T. Ahnfeldt, N. Stock, Inorg. Chem. 50 (2011) 9518.
[18] D. Himsl, D. Wallacher, M. Hartmann, Angew. Chem. 121 (2009) 4710.
[19] S. Couck, J.F.M. Denayer, G.V. Baron, T. Remy, J. Gascon, F. Kapteijn, J. Am. Chem. Soc. 131 (2009) 6326.
[20] S.M. Cohen, Chem. Rev. (2011) 970.
[21] N. Stock, Microporous Mesoporous Mat. 129 (2010) 287.
[22] H. Reinsch, N. Stock, Microporous Mesoporous Mat. 171 (2013) 50.
[23] Topas Academics 4.1, Coelho Software, 2007.
[24] J. Rouquerol, P. Llewellyn, P. Rouquerol, F. Rodriguez-Reinoso, N. Seaton, Elsevier, New York 160 (2007) 49.
[25] A.T. Nielsen, A.A. DeFusco, T.E. Browne, J. Org. Chem. 50 (1985) 4211.
[26] V.K. Olkhovik, A.A. Pap, V.A. Vasilevskii, N.A. Galinovskii, S.N. Tereshko, Russ. J. Org. Chem. 44 (2008) 1172.
[27] V.K. Olkhovik, D.A. Vasilevskii, A.A. Pap, G.V. Kalechyts, Y.V. Matveienko, A.G. Baran, N.A. Halinouski, V.G. Petushok, ARKIVOC (2008) xi.
[28] Materials Studio Version 5.0, Accelrys Inc, San Diego (, 2009.
[29] B. Arstad, H. Fjellvag, K. Kongshaug, O. Swang, R. Blom, Adsorption 14 (2008) 755.

Please cite this article in press as: S. Halis, et al., Four new Al-based microporous metal-organic framework compounds with MIL-53-type structure containing functionalized extended linker molecules, Microporous and Mesoporous Materials (2015), http://dx.doi.org/10.1016/j.micromeso.2015.01.030

4.3.5. Three series of sulfonic acid functionalized mixed-linker CAU-10 analogues: Sorption properties, proton conductivity and catalytic activity

Der folgende Artikel wurde im Jahre 2015 in der Fachzeitschrift *Chemistry - A European Journal, Wiley-VCH Verlag,* angenommen.

Das Einführen funktioneller Gruppen in Metall-Organische Gerüstverbindungen zur Modifizierung ihrer Eigenschaften erfolgt oft über die sogenannte isoretikuläre Synthese. Das Einbringen einer zweiten Funktionalität lässt sich über einen Reaktionsansatz realisieren, in dem zwei Linkermoleküle mit unterschiedlichen funktionellen Gruppen verwendet werden. Dieser Ansatz wurde in hier verfolgt, um in CAU-10-H, CAU-10-NO_2 und CAU-10-OH einen Teil der -H, -NO_2 bzw. -OH Gruppen durch Sulfonsäuregruppen zu ersetzen. Die Struktur von CAU-10 basiert auf Ketten aus *cis* kantenverknüpften AlO_6-Polyedern, die über Isophthalationen zu einem dreidimensionalen Netzwerk mit eindimensionalen Poren verknüpft werden. Die bereits bekannten Reaktionsbedingungen für die jeweiligen Materialien wurden übernommen und es konnten drei Serien von CAU-10 Derivaten $[Al(OH)(m\text{-BDC-H})_{1-y}(m\text{-BDC-SO}_3H)_y]$·Lösungsmittel (y = 0.08, 0.15, 0.205, 0.24; CAU-10-H/S1 bis CAU-10-H/S4), $[Al(OH)(m\text{-BDC-NO}_2)_{1-y}(m\text{-BDC-SO}_3H)_y]$·Lösungsmittel (y = 0.065, 0.10, 0.175, 0.215; CAU-10-N/S1 bis CAU-10-N/S4), und $[Al(OH)(m\text{-BDC-OH})_{1-y}(m\text{-BDC-SO}_3H)_y]$·Lösungsmittel (y = 0.08, 0.125; CAU-10-O/S1 und CAU-10-O/S2) erhalten werden.

Sorptionsmessungen mit verschiedenen Gasen (N_2, H_2, CO_2) sowie Wasserdampf zeigten einen deutlichen Einfluss der Sulfonsäuregruppen. Stickstoffmessungen ergaben verminderte Werte für spezifische Oberflächen und Mikroporenvolumina mit zunehmendem Gehalt an Sulfonsäuregruppen. Die Aufnahmekapazität für H_2 verminderte sich ebenso mit steigendem Dotierungsgrad für alle drei Serien. Für CO_2 Messungen bis 1 bar konnte in allen Fällen eine gesteigerte Affinität beobachtet werden und zusätzlich für die CAU-10-O/S Verbindungen eine gesteigerte Kapazität im Vergleich zum reinen CAU-10-OH. Das Einbringen der -SO_3H Gruppen hat offensichtlich einen stark polarisierenden Einfluss auf das Gerüst was zu verstärkten Wechselwirkungen mit dem polaren Gas führt. Bei Wasserdampfsorptionsmessungen wurde ebenfalls beobachtet, dass die Kapazität abnimmt, aber die Affinität mit zunehmendem Anteil an -SO_3H Gruppen deutlich ansteigt. Dies eröffnet eine potentielle Anwendung dieser Materialien im Bereich der Feuchtigkeitssensorik.

Aufgrund der hohen thermischen Stabilität sowie des durch die -SO_3H Gruppen sauren Charakters wurde CAU-10-H/S4 als heterogener Katalysator zur Dehydratisierung von Ethanol in der Gasphase eingesetzt. Im Gegensatz zum unfunktionalisierten CAU-10-H zeigte die Verbindung CAU-10-H/S4 eine deutlich höhere Umsetzung von Ethanol und bei Reaktionstemperaturen von 300°C eine hohe Selektivität für Ethen als Reaktionsprodukt. Die hohe Stabilität zeigt sich in konstanten Umsetzungsraten, dem Erhalt der Kristallinität des Materials nach sowie dem Ausbleiben von Desulfonierungsprozessen während der Reaktion. Zusätzlich wurden die Verbindungen CAU-10-H/S1, CAU-10-N/S2 und CAU-10-O/S2, die alle in etwa den gleichen Anteil an Sulfonsäuregruppen tragen, hinsichtlich ihrer Protonenleitfähigkeit untersucht. Die erhaltenen Werte für alle drei Materialien sind sehr niedrig und steigen in der Reihenfolge -H/S1 < -N/S2 < -O/S2 an (CAU-10-H/S1: $4.88 \cdot 10^{-7}$ S/cm bei 413 K; CAU-10-N/S2: $1.71 \cdot 10^{-8}$ S/cm bis $5.61 \cdot 10^{-7}$ S/cm zwischen 373 K und 413 K; CAU-10-O/S2: $2.74 \cdot 10^{-7}$ S/cm bis $8.61 \cdot 10^{-6}$ S/cm zwischen 333 bis 413 K). Hier ist deutlich der Einfluss der -H, -NO_2 und -OH Gruppen zu erkennen, denn letztere kann im Gegensatz zu den beiden ersteren durch Protonierung und Peprotonierung am Mechanismus der Protonenleitung teilnehmen.

Three series of sulfonic acid functionalized mixed-linker CAU-10 analogues: Sorption properties, proton conductivity and catalytic activity

Nele Reimer,[a] Bart Bueken,[b] Sebastian Leubner,[a] Christopher Seidler,[c] Michael Wark,[c] Dirk De Vos,[b] and Norbert Stock*[a]

Abstract: Ten mixed-linker metal-organic framework compounds [Al(OH)(*m*-BDC-X)$_{1-y}$(*m*-BDC-SO$_3$H)$_y$] (X = H, NO$_2$, OH) exhibiting the CAU-10-type structure were synthesized. The compounds can be grouped in three series depending on the mixtures of the ligands employed. The three series of compounds were obtained employing different ratios of *m*-H$_2$BDC-X and *m*-H$_2$BDC-SO$_3$Li. The resulting compounds are denoted CAU-10-H/S$_x$, -N/S$_x$ and -O/S$_x$ and show an exceptionable high thermal stability for sulfonated materials of up to 350 °C. A detailed characterization with special focus on the polarity and acidity was performed and the impact of the additional -SO$_3$H groups is clearly demonstrated by changes in the sorption affinities/capacities towards several gases and water vapor. In addition, selected samples were evaluated for proton conductivity and as catalysts for the gas-phase dehydration of ethanol to ethylene. While only very low proton conductivity values were observed a strong increase in catalytic activity was achieved. Although reactions were performed at temperatures of 250 and 300°C for more than 40 h, no desulphonation and no loss in crystallinity is observed, resulting in a stable ethanol conversion and demonstrating the high stability of this material.

Introduction

Metal-organic frameworks (MOFs) have attracted a lot of attention within the last years due to their potential applications in the fields of gas storage and separation, drug delivery or catalysis.[1] MOFs are built up from inorganic building units, for example metal ions or clusters, which are interconnected by organic linker molecules, forming, in general, three-dimensional porous structures. This modular assembly allows for properties tuning by chemical functionalization of the organic part or by replacement of the inorganic unit. This approach is called isoreticular chemistry[2] and has previously been applied to several well-known framework structures.[3] Recently, another concept to 'design' compounds with 'desired' properties has been established. In the so-called mixed linker approach, differently functionalized linker molecules are incorporated in one framework to selectively influence the characteristics of a compound.[4]

For example, Al-MIL-53, [Al(OH)(BDC-X)], is a flexible compound based on (functionalized) 1,4-benzenedicarboxylic acid (H$_2$BDC(-X)) and chains of *trans* corner-sharing AlO$_6$-octahedra.[3a, 5] Its flexibility as well as its thermal stability strongly depend on the nature of the functionalized linker molecule. By using a mixture of H$_2$BDC and H$_2$BDC-NH$_2$ it was possible to influence these properties depending on the fraction of the incorporated linker molecules.[6] In another recent study, mixed-linker MOFs based on the CAU-10, [Al(OH)(*m*-BDC-X)], structure were synthesized to fine-tune the sorption properties of this compound.[7] CAU-10 is built up from helical chains of *cis* corner-sharing AlO$_6$-octahedra interconnected by isophthalates. A series of isoreticular compounds has been synthesized with several functionalized isophthalates. Depending on the functional group of the linker molecule the structure of each derivative is slightly altered. This results in different uptake capacities, affinities and accessibilities of the pores of each compound towards different adsorbates.[3c]

The incorporation of sulfonic acid groups in MOFs is of great interest. Due to its strong acidic proton, compounds bearing these groups show potential for catalytic or proton conduction applications.[8] However, the sorption properties of such compounds can also be influenced. Recently, it was reported, that the introduction of sulfonic acid groups in the zirconium based compound UiO-66 led to a strong increase in the sorption selectivity for CO$_2$ over CH$_4$ compared to the unfunctionalized compound.[9] The synthesis of -SO$_3$H functionalized MOFs is not always easily accomplished. Only few examples are known in which the acid group was directly introduced into the framework by the use of an -SO$_3$H functionalized linker molecule.[8a, 10]

Another way to introduce sulfonic acid groups is through post-synthetic modification (PSM), which was demonstrated by Chen *et al.* using Cr-MIL-101, Zr-UiO-66 and Al-MIL-53.[8c, 11]

We focused our research on aluminum based MOFs, because these compounds are known for their high thermal and chemical stability.[3c, 12] In addition, starting materials are inexpensive and of low toxicity, which makes them interesting for industrial usage.[13]

The goal of the present study was to combine the properties of Al-MOFs and sulfonic acid functionalized compounds. Therefore, we chose CAU-10 as the parent structure and employed

---

[a] Dipl. chem. N. Reimer, B. Sc. S. Leubner, Prof. N. Stock
Institut für Anorganische Chemie
Christian-Albrechts-Universität zu Kiel
Max-Eyth-Straße 2, 24118 Kiel, Germany
E-mail: stock@ac.uni-kiel.de
[b] Ir. B. Bueken, Prof. D. De Vos
Centre for Surface Chemistry and Catalysis
University of Leuven
Kasteelpark Arenberg 23, 3001 Leuven, Belgium Department
[c] M. Sc. C. Seidler, Prof. M. Wark
Institut für Chemie
Carl von Ossietzky Universität Oldenburg
Carl-von-Ossietzky-Str. 9-11, 26129 Oldenburg, Germany

Supporting information for this article is given via a link at the end of the document isoreticular synthesis using 5-sulfo- isophthalic acid mono lithium salt (*m*-$H_2BDC-SO_3Li$). Pure *m*-$H_2BDC-SO_3Li$ as the organic linker does not lead to the CAU-10 analogue, hence mixtures of isotopic linkers were used. By adopting the synthesis conditions of the already known compounds CAU-10-H, -NO_2 and –OH, we were able to synthesize three series of mixed-linker compounds with the CAU-10 structure bearing different fractions of sulfonic acids incorporated into the framework. The obtained compounds were characterized in detail by IR-/NMR-spectroscopy, thermal and elemental analysis, X-ray powder diffraction (PXRD) and detailed sorption measurements. Selected samples were investigated concerning their proton conductivity and catalytic performance in the dehydration of ethanol.

Results and Discussion

PXRD investigations and Crystal Structure

The structure of the CAU-10 framework is built up from helical chains of *cis* corner-sharing AlO_6-octahedra.[3c] The three-dimensionality of the framework results from the connection of each helix to four adjacent helices with alternating rotational orientation via the carboxylate groups of (functionalized) isophthalate ions (Figure 1). Square-shaped channels are formed, with a maximum diameter of ~7Å. The pores can be modulated by the use of functionalized linker molecules[3c] or in a mixed-linker approach by the use of differently functionalized linker molecules.[7]

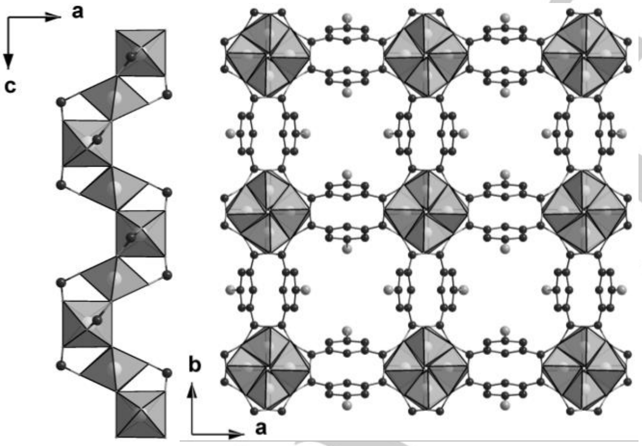

Figure 1. Structure of CAU-10. Al-atoms are displayed in very light grey, O-atoms in grey and C-atoms in dark grey. The light grey atoms represent possible functional groups.

All mixed-linker compounds in this study were obtained as microcrystalline powders. The SEM picture of CAU-10-H/S1 is given in Figure 2 (SEM images for CAU-10-H/S2-4 are shown in Figure S1-3). As an example, the PXRD patterns of the CAU-10-H/Sx samples compared to the pattern of CAU-10-H are shown in Figure 3. The mixed-linker compounds are also highly crystalline. Compared to the PXRD pattern of CAU-10-H only changes in the relative intensities of the reflections up to 20° (2θ) are observed, which are more pronounced with increasing amounts of -SO_3H groups. This can be explained by the additional electron density within the pores due to the incorporated sulfonic acid groups.

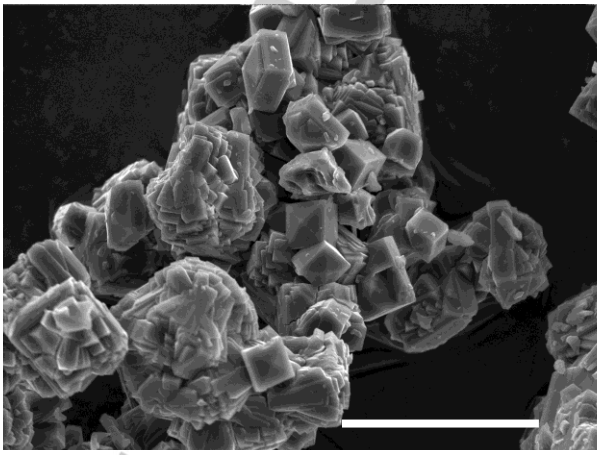

Figure 2. SEM micrograph of CAU-10-H/S1. The scale bar corresponds to a length of 10 µm.

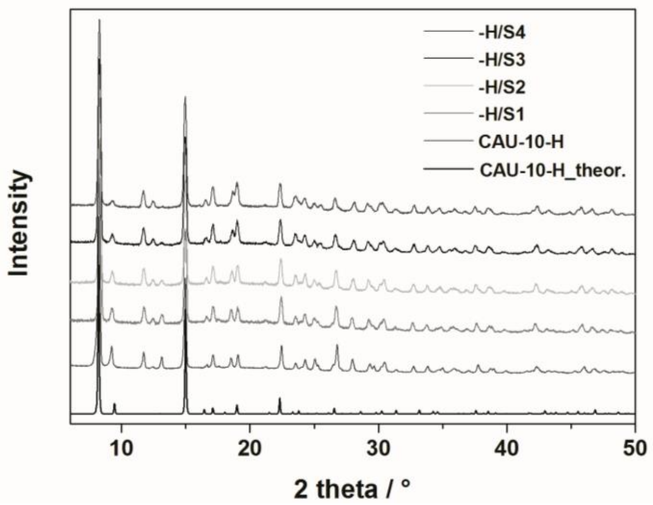

Figure 3. PXRD measurements for the mixed linker compounds CAU-10-H/Sx compared to the theoretical and experimental pattern of CAU-10-H.

The PXRD patterns of CAU-10-N/Sx and CAU-10-O/Sx compared to those of CAU-10-NO_2 and CAU-10-OH are given in Figure S4. The mixed-linker compounds are obtained with high crystallinity and the positions as well as the relative intensities of all reflections are in good accordance with those of CAU-10-NO_2 and CAU-10-OH. The high resolution PXRD patterns of all compounds were indexed using TOPAS Academics.[14] The resulting cell parameters were refined using the Pawley method[14] and only slight changes compared to those of the parent structures are observed (Table 1). The Pawley-fits are shown in Figure S5-14.

Table 1. Results of the Pawley Refinements.

Sample CAU-10-	Space Group	a = b / Å	c / Å	Rwp / %
H	$I4_1$	21.55(7)	10.38(3)	1.9
H/S1	$I4_1$	21.3846(6)	10.7424(5)	5.7
H/S2	$I4_1$	21.4262(8)	10.6918(6)	5.2
H/S3	$I4_1$	21.4786(6)	10.6635(5	4.4
H/S4	$I4_1$	21.4896(5)	10.6277(5)	4.8
NO_2	$P4_1$	21.4707(3)	10.3777(2)	3.2
N/S1	$P4_1$	21.532(1)	10.409(1)	4.0
N/S2	$P4_1$	21.539(1)	10.421(1)	3.3
N/S3	$P4_1$	21.525(1)	10.416(1)	3.6
N/S4	$P4_1$	21.514(2)	10.405(2)	3.2
OH	$P4$	21.3072(5)	38.6974(9)	4.8
O/S1	$P4$	21.325(1)	38.793(2)	4.2
O/S2	$P4$	21.285(2)	38.792(5)	5.5

Vibrational spectroscopy

IR spectra of all compounds were collected after washing the samples with water. As an example, the spectra of CAU-10-H/Sx, *m*-$H_2BDC-SO_3Li$ as well as CAU-10-H are shown in Figure 4. The red box marks the characteristic vibrations of the -SO_3H groups and it is clearly visible, that with rising amount of -SO_3H groups the intensities of the characteristic bands increase.

There are no indications for unreacted linker molecules, since no bands around 1700 cm^{-1} due to free carboxylic acid groups are observed. The characteristic stretching modes of the carboxylate groups of the mixed linker compounds are in accordance with those for the single linker compound. The presence of sulfonic acid groups is verified by the vibrations between 1250 and 1000 cm^{-1} (black box). The asymmetric and symmetric vibrations of the sulfonic acid groups are observed at $v_{O=S=O}$ = 1223 and 1160 cm^{-1}, respectively, and at v_{S-O} = 1044 cm^{-1}. The in-plane skeletal vibration of the sulfonic acid substituted benzene ring appears at v = 1080 cm^{-1} and the C-S vibration at v = 629 cm^{-1}. The C-H out-of-plane vibrations for the 1,3-substituted benzene rings are observed at v = 725 and 755 cm^{-1} and marked with red asterisks. For the 1,3,5-substituted benzene ring this vibration appears at v = 782 cm^{-1} and is marked with a black asterisk.[8b, 15] The IR spectra of CAU-10-N/Sx and CAU-10-O/Sx samples compared to the spectra of the linker molecule and the respective single linker compound are shown in Figure S15 and 16. Again, no unreacted linker molecules are observed in the spectra and the characteristic vibrations for the sulfonic acid groups are present.

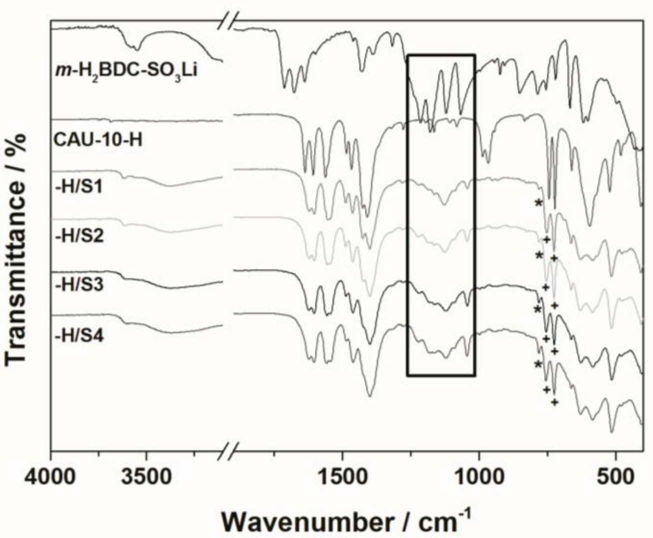

Figure 4. IR spectra of CAU-10-H/Sx compared to CAU-10-H and *m*-$H_2BDC-SO_3Li$. The asterisk marks the CH-out-of-plane vibration for the 1,3,5-substituted linker molecules and the plus the same vibration for the 1,3-substituted linker. The black box marks the area for the specific –SO_3H vibrations.

Thermal Analysis

To investigate the thermal stability, thermogravimetric (TG) measurements of all compounds were performed under air. The results for the CAU-10-H/Sx samples are shown in Figure 5.

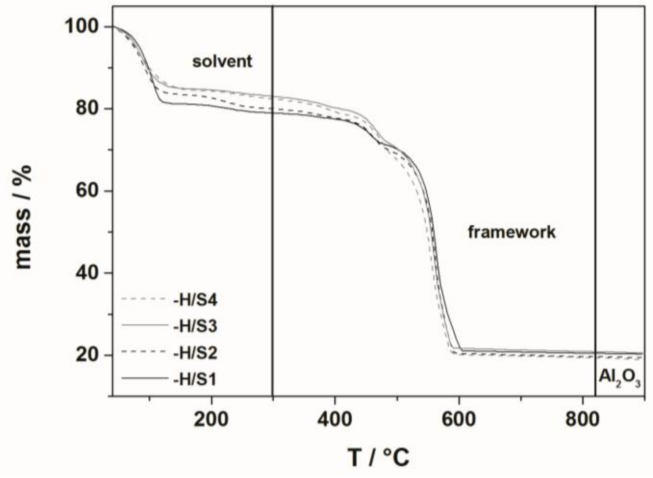

Figure 5. TG measurements of the CAU-10-H/Sx samples

All samples show a two-step weight loss. The first step up to around 300 °C can be attributed to the removal of incorporated H_2O and DMF molecules. At around 400 °C the frameworks start to decompose, resulting in X-ray amorphous Al_2O_3 at temperatures above 600 °C. The TG measurements of the CAU-10-N/Sx and –O/Sx samples are shown in Figure S17 and S18. Again, two-step weight losses are observed. For CAU-10-N/Sx the removal of incorporated solvent molecules is completed at around 250 °C and for CAU-10-O/Sx at around 230 °C. Above that temperature the frameworks slowly start to decompose resulting in X-ray amorphous Al_2O_3.

Sorption Properties

To investigate the influence of the partly incorporated sulfonic acid groups in the different functionalized CAU-10 analogues, sorption measurements with different adsorptives were performed. N_2 and H_2 (up to 1 bar) measurements were carried out at 77 K and CO_2 (up to 1 bar) and H_2O vapor measurements at 298 K.

For CAU-10-H/Sx it was only possible to record a N_2 isotherm for the compound with the lowest doping degree due to very long equilibration times (Figure S19). The pore volume is decreased to 0.21 cm^3/g and the specific surface area to 372 m^2/g compared to CAU-10-H (V_{mic} = 0.25 cm^3/g, a_S = 635 m^2/g). All CAU-10-N/Sx samples show a type-I isotherm characteristic for microporous materials (Figure S20). The specific surface area decreases with increasing amount of sulfonic acid groups incorporated into the framework. The single linker compound CAU-10-OH does not adsorb any nitrogen. However, for the mixed linker compounds a small uptake is observed (Figure S21). The incorporation of sulfonic acid groups perhaps leads to a more ordered orientation of the linker molecules due to interactions of the functional groups, so that the pores become accessible for the nitrogen molecules.

Water vapor measurements for all mixed-linker compounds compared to the parent ones are displayed in Figure 6.

In all cases it is clearly visible that with rising amount of incorporated -SO_3H groups the affinity at low humidity values strongly increases. For CAU-10-H/Sx the capacity decreases clearly due to the additional space required by the -SO_3H groups. For CAU-10-N/Sx only small changes in the sorption capacity are observed, since the replacement of a -NO_2 group by a -SO_3H group probably only slightly affects the pore volume. The same can be assumed for the CAU-10-O/S samples. The strong affinity towards water vapor suggests a potential application for these materials in the field of humidity sensing and therefore they are actually under investigation.

For the CO_2 measurements the same trend is observed. In all cases the affinity increases with rising amount of incorporated -SO_3H groups (Figure S22-24). The capacity for CAU-10-H/Sx (Figure S27) and -N/Sx (Figure S23) decreases but interestingly for CAU-10-O/Sx (Figure S24) it increases. Apparently, the presence of -OH and -SO_3H groups leads to strong interactions between the linker molecules which could lead to a polarizing effect of the pore surface to affect the affinity in a very strong way. This behavior has previously been observed for the mixed-linker compound CAU-10-NO_2/NH_2.[7]

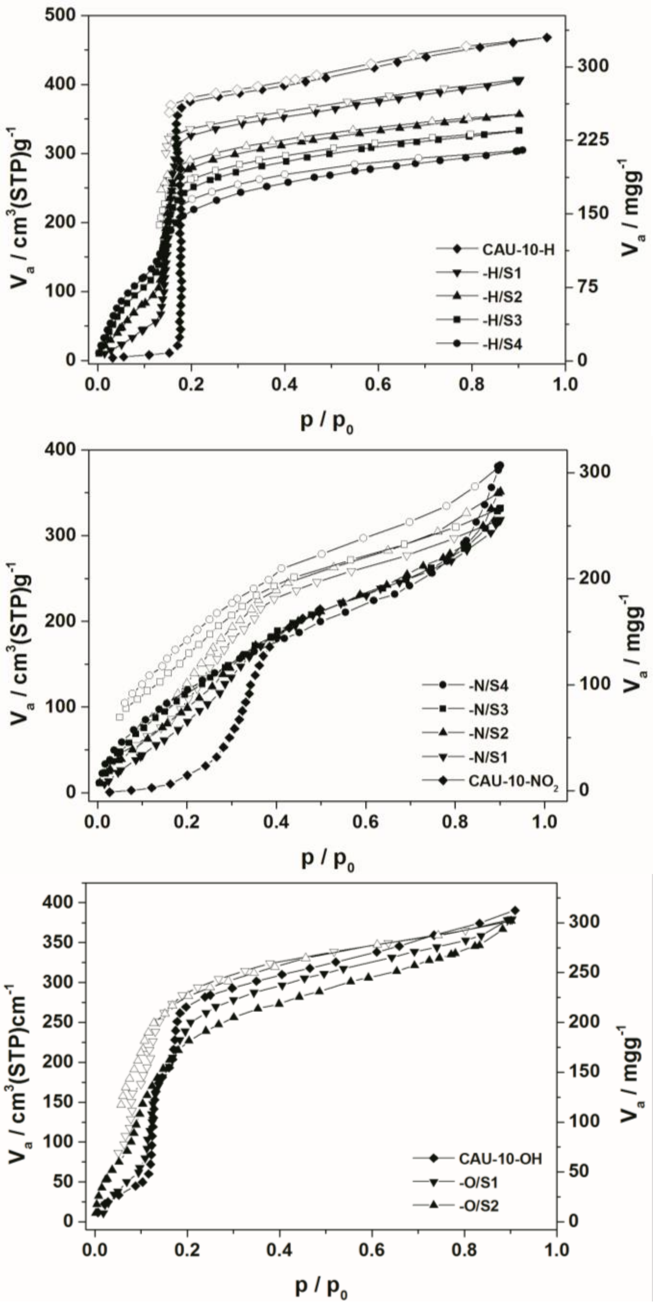

Figure 6. Water vapor sorption isotherms of the mixed-linker compounds compared to the single-linker ones. Top: CAU-10-H/Sx. Middle: CAU-10-N/Sx. Bottom: CAU-10-O/Sx.

Since hydrogen is a small non-polar molecule the polarity of the introduced sulfonic acid groups does not affect the affinity towards this gas and only the reduced pore volume influences the sorption behavior of the materials. Therefore, for all materials a reduced sorption capacity for H_2 is observed and no change in affinity (Figure S25-27). Trend graphs, which compare the affinities and capacities of all compounds towards H_2O vapor and CO_2 gas as well as the specific surface areas are shown in

Figure S28-30; Table 2 summarizes the results of all sorption measurements of all compounds.

Table 2. Results of the sorption measurements.

Sample CAU-10-	N_2 (77K) a_s [m^2/g] / V_{mic} [cm^3/g]	H_2 (77K) [wt%]	CO_2 (298K) [wt%]	H_2O (298K) [cm^3/g]
H	635 / 0.25	1.12	10.57	468
H/S1	372 / 0.21	1.03	10.52	407
H/S2	-	0.95	9.88	357
H/S3	-	0.91	9.44	329
H/S4	-	0.85	8.87	305
NO_2	440 / 0.18	1.01	8.71	215*
N/S1	324 / 0.15	0.91	8.61	318
N/S2	270 / 0.13	0.81	8.29	351
N/S3	242 / 0.12	0.69	7.72	332
N/S4	158 / 0.09	0.64	7.12	382
OH	-	0.79	5.57	390
O/S1	67 / 0.04	0.77	6.57	379
O/S2	74 / 0.05	0.69	8.04	377

* $p/p_0 = 0.5$

Proton conductivity

Due to the presence of $-SO_3H$ groups the proton conductivity of selected compounds, i.e. CAU-10-H/S1, CAU-10-N/S2 and CAU-10-O/S2 were determined. These samples contain roughly the same fraction of $-SO_3H$ groups. All investigated CAU-10 samples exhibited a low proton conductivity (Fig. S31). Only for CAU-10-O/S2 it was possible to determine proton conductivities in the whole temperature range. The obtained values were between $2.74 \cdot 10^{-7}$ S/cm and $8.61 \cdot 10^{-6}$ S/cm. For CAU-10-N/S2, sigma values from $1.71 \cdot 10^{-8}$ S/cm to $5.61 \cdot 10^{-7}$ S/cm were found in a temperature range of 373 K and 413 K. A proton conductivity of $4.88 \cdot 10^{-7}$ S/cm at 413K was determined for CAU-10-H/S1. Since the amount of $-SO_3H$ groups is similar in all three samples, the role of the -H, $-NO_2$ and -OH groups determines the proton conductivity. In combination with hydroxyl groups higher proton conductivity values could be determined over the whole temperature range. Observed values are one order of magnitude higher which could be due to the fact that both functional groups can be protonated and deprotonated and thus participate in the proton conducting mechanism. In contrast the amount of $-SO_3H$ groups in CAU-10-H/S1 and CAU-10-N/S2 does not lead to a sufficient density of functional groups for a constant proton conduction pathway. Only with increasing temperature, and therefore increasing mobility of the functional groups and the protons, proton conductivity can occur.

Catalytic experiments

The combination of well-defined pore spaces, the presence of strong acidic $-SO_3H$ groups and high thermal stabilities make the mixed-linker CAU-10 MOFs potentially interesting catalysts. Selected samples were evaluated as a catalyst for the gas-phase dehydration of ethanol to ethylene, the results of which are summarized in Table 3.

Table 3. Ethanol dehydration over mixed-linker CAU-10 samples.

Sample CAU-10-	X_{EtOH} [%]	$S_{C2=}$ [%]	S_{C2OC2} [%]	$S_{C2=O}$ [%]
H*	7	22	70	8
H/S2*	27	22	76	2
H/S4*	52	27	71	2
N/S4*	15	30	69	1
H†	56	52	42	6
H/S4†	91	79	20	1

* 250 °C; feed rate 6.9 mmol mmol·$g_{MOF}^{-1} \cdot h^{-1}$; 300 mg catalyst; †: 300 °C; X_{EtOH} = ethanol conversion; $S_{C2=}$ = ethylene selectivity, S_{C2OC2} = diethylether selectivity; $S_{C2=O}$ = acetaldehyde selectivity;

The presence of $-SO_3H$ groups in the mixed-linker CAU-10 materials clearly results in a strong increase in catalyst activity. The parent CAU-10-H shows only a very modest ethanol conversion of 7 % at 250 °C, mainly due to the presence of weakly acidic μ_2-OH groups decorating the inorganic chains, a situation similar to the one in MIL-53(Al) and the aluminum fumarate A520.[16] Under identical reaction conditions however, CAU-10-H/S2 and CAU-10-H/S4 achieve ethanol conversions of 27 % and 52 %, respectively, indicating that in these materials the more acidic protons of the $-SO_3H$ groups dominate as the Brønsted acidic active sites. Furthermore, a higher m-H_2BDC-SO_3H doping correlates to a higher activity. When comparing with CAU-10-N/S4 however, this material only reaches a conversion of 15 % (250 °C), in spite of its high $-SO_3H$-content. It is likely that the relatively bulky $-NO_2$ groups restrict diffusion through the one-dimensional pore system, resulting in lower conversions.

When the reaction temperature is increased to 300 °C, the reactivity differences between CAU-10-H and CAU-10-H/S4 become more pronounced, with ethanol conversions of 56 % and 91 %.

In order for this reaction to proceed selectively towards the olefin product, elevated reaction temperatures and relatively strong acidic sites are required.[17] While at 250 °C, the ethylene selectivity between CAU-10-H and the $-SO_3H$-bearing materials does not differ strongly, this picture changes drastically at 300 °C, where CAU-10-H/S4 achieves an ethylene selectivity of

79 %. In stark contrast to this, CAU-10-H only achieves a selectivity to ethylene of 52 %. Notably, both at 250 °C and 300 °C, a significant amount of acetaldehyde is formed over CAU-10-H. This dehydrogenation product is typically associated with the presence of basic sites. For instance, the carboxylate groups of isophthalic acid could act as proton acceptor sites. For the mixed-linker compounds, acetaldehyde formation is observed in a far lower yield, indicating that mainly the Brønsted acidic -SO_3H sites lining the pore interior are participating in the dehydration reaction. Furthermore, only trace amount of oligomerization products were observed (butenes < 0.2 %). For CAU-10-N/S4 however reaction at 300 °C, even for short reaction times, led to strong browning of the material and appearance of compounds of higher molecular weight in the gas chromatogram, indicating that this material does promote undesired condensation and oligomerization side-reactions.

The stability of the mixed-linker CAU-10 samples under the applied reaction conditions is confirmed by powder X-ray diffraction and the observation of stable conversion and selectivity profiles with extended reaction times, as is illustrated for CAU-10-H/S4 in Figure 7 and for CAU-10-H in Figure S32. This is further confirmed by the lack of desulphonation (Figure S33) of the used catalysts. The high thermal stability of the CAU-10-H/Sx materials is in stark contrast to many organic -SO_3H containing resins, which typically suffer from desulphonation starting at 150 °C.[18] In this sense, the mixed-linker MOFs could serve as attractive alternatives to these resins in more demanding applications such as catalysis at elevated temperatures.

Conclusions

In this contribution we present the synthesis of ten mixed-linker materials exhibiting the CAU-10 structure. The known compounds CAU-10-H, -NO_2 and -OH were chosen and the mixed-linker approach was used to introduce -SO_3H groups in different fractions up to a maximum amount of 24% for the CAU-10-H/S4 material. The -SO_3H groups do not affect the high thermal stability of the materials but the polarity of these groups strongly influences the sorption properties. Changes in sorption capacities and affinities towards several gases (N_2, H_2, CO_2) are observed and a strong increase in affinity towards water vapor reveal a potential application in the field of humidity sensing, which is currently under investigation. Due to the strong acidity of the -SO_3H groups, selected samples were evaluated for their proton conductivity and as a catalyst for the gas-phase dehydration of ethanol to ethylene. While only a low proton conductivity was observed, the presence of the -SO_3H groups clearly results in a strong increase in catalytic activity. Although reactions were performed at temperatures of 300°C a stable conversion of ethanol, no loss in crystallinity and no desulphonation is observed. This high stability is in contrast to many other -SO_3H containing resins so these compounds could be an alternative candidate for catalysis at elevated temperatures.

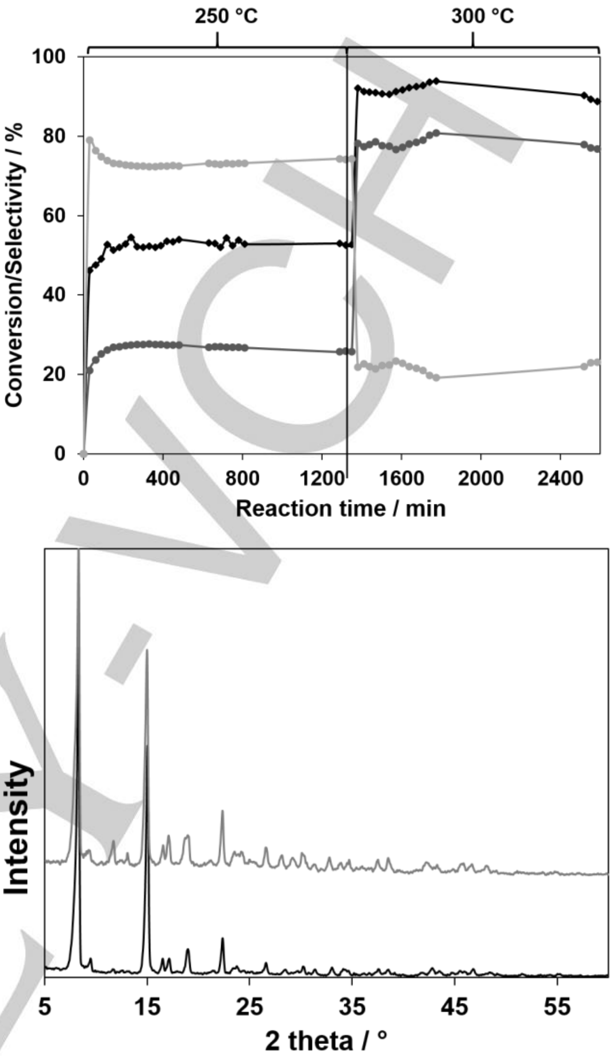

Figure 7. Top: Ethanol conversion (black) and selectivities to ethylene (grey) and diethylether (light grey) over CAU-10-H/S4 (feed rate 6.9 mmol·g_{MOF}^{-1}·h^{-1}. Bottom: Powder X-ray diffraction pattern of CAU-10-H/S4 before (black) and after reaction (light grey).

Experimental Section

Materials and Methods

All chemicals are commercially available and were used without further purification. For the synthesis, custom-made steel autoclaves with Teflon inlets with a volume of 30 mL or glass reactors with a volume of 100 mL for solvothermal reaction conditions were used. The initial characterization by means of PXRD methods was carried out on a STOE-Stadi-P Kombi diffractometer (Cu Kα_1 radiation) equipped with an xy stage and an image plate detector. The data for the indexing and Pawley refinements was collected on a STOE-Stadi-P diffractometer (Cu Kα_1 radiation) equipped with a Mythen detector. The software used for Pawley refinements was TOPAS Academics v4.1.[14] IR spectra were recorded on a Bruker ALPHA-FT-IR A220/D-01 spectrometer equipped with an ATR-unit. The thermogravimetric (TG) analyses were carried out using a NETSCH STA 409 CD analyzer. The samples were heated in

Table 4. Linker ratios used in the synthesis and for the final compounds with the resulting molecular formulae for all compounds.

Sample	Ratio used in synthesis		Ratio calc. by ^{1}H-NMR		Molecular formula calc. by ^{1}H-NMR and TG analysis
CAU-10-	*m*-H$_2$BDC-H	*m*-H$_2$BDC-SO$_3$Li	*m*-BDC-H	*m*-BDC-SO$_3$H	
H/S1	0.825	0.125	0.92	0.08	[Al(OH)(*m*-BDC-H)$_{0.92}$(*m*-BDC-SO$_3$H)$_{0.08}$]· 3.5H$_2$O·0.1DMF
H/S2	0.75	0.25	0.85	0.15	[Al(OH)(*m*-BDC-H)$_{0.85}$(*m*-BDC-SO$_3$H)$_{0.15}$]· 2.5H$_2$O·0.1DMF
H/S3	0.625	0.375	0.795	0.205	[Al(OH)(*m*-BDC-H)$_{0.795}$(*m*-BDC-SO$_3$H)$_{0.205}$]· 2H$_2$O·0.2DMF
H/S4	0.5	0.5	0.76	0.24	[Al(OH)(*m*-BDC-H)$_{0.76}$(*m*-BDC-SO$_3$H)$_{0.24}$]· 1.5H$_2$O·0.2DMF
CAU-10-	*m*-H$_2$BDC-NO$_2$	*m*-H$_2$BDC-SO$_3$Li	*m*-BDC-NO$_2$	*m*-BDC-SO$_3$H	
N/S1	0.825	0.125	0.935	0.065	[Al(OH)(*m*-BDC-NO$_2$)$_{0.935}$(*m*-BDC-SO$_3$H)$_{0.065}$]·2.23H$_2$O
N/S2	0.75	0.25	0.90	0.10	[Al(OH)(*m*-BDC-NO$_2$)$_{0.9}$(*m*-BDC-SO$_3$H)$_{0.1}$]·3.08H$_2$O
N/S3	0.625	0.375	0.825	0.175	[Al(OH)(*m*-BDC-NO$_2$)$_{0.825}$(*m*-BDC-SO$_3$H)$_{0.175}$]·2.97H$_2$O
N/S4	0.5	0.5	0.785	0.215	[Al(OH)(*m*-BDC-NO$_2$)$_{0.785}$(*m*-BDC-SO$_3$H)$_{0.215}$]·2.93H$_2$O
CAU-10-	*m*-H$_2$BDC-OH	*m*-H$_2$BDC-SO$_3$Li	m-BDC-OH	m-BDC-SO$_3$H	
O/S1	0.825	0.125	0.92	0.08	[Al(OH)(*m*-BDC-OH)$_{0.92}$(*m*-BDC-SO$_3$H)$_{0.08}$]·4.7H$_2$O
O/S2	0.75	0.25	0.875	0.125	[Al(OH)(*m*-BDC-NO$_2$)$_{0.875}$(*m*-BDC-SO$_3$H)$_{0.125}$]·4.68H$_2$O

Al_2O_3 crucibles at a rate of 4 °C min^{-1} under a flow of air (25 mL min^{-1}). The contents of carbon, hydrogen, nitrogen and sulfur were determined by elemental chemical analysis on a EuroVector EuroEA Elemental Analyzer. AAS for lithium were carried out using a Perking Elmer AAnalyst 300 spectrometer. Gas sorption experiments were performed using a BEL JAPAN INC. Belsorp$_{max}$ instrument. Measurements using N_2 and H_2 were performed at -196 °C and measurements using CO_2 and H_2O vapor at 28 °C. Prior to each measurement all samples were activated at 200 °C overnight at 10^{-2} kPa. Liquid-state ^{1}H-NMR spectroscopy was performed on a Bruker DRX500/Bruker Advance 200 spectrometer. Prior to the measurements 2-3 mg of the sample was dissolved in a mixture of NaOD (5%) and D_2O (95%). SEM pictures of gold sputtered samples were collected on a Philips XL30 FEG microscope. Catalytic investigations were performed on an in-house constructed continuous flow reactor (Figure S34). For each MOF, the reactor was loaded with a sample containing adsorbed atmospheric water, which was removed prior to reaction by outgassing the sample overnight at 150 °C under an N_2-flow (5 ml·min^{-1}). In each case, the resulting amount of dry material was 300 mg. An N_2-flow (10 ml·min^{-1}) was saturated with ethanol by passing through a bubbler containing pure ethanol (Fischer) which was kept thermostatically at 40 °C. This N_2-flow was allowed to equilibrate with ethanol for 4 hours prior to reaction. The resulting gas mixture was passed over the catalyst bed (feed rate 6.9 mmol·g_{MOF}^{-1}·h^{-1}) at different reaction temperatures (250 °C, 275 °C and 300 °C). Using a gas sample loop, samples were collected at 30 minute intervals (5s sampling time) and analyzed using an on-line GC (GC Shimadzu 2010 plus chromatograph with FID detector, GsBP-1 column; 100 m, 250 µm inner diameter). Data handling was performed using the GCsolution Analysis software (v 2.3). The proton conductivity was determined by electrochemical impedance spectroscopy (EIS),[19] in a 2 electrode cell setup using a Zahner Zennium workstation. Measurements were carried out between 1 Hz and 1 MHz (100mV) at temperatures ranging from 333-413 K at 100 % relative humidity (RH).[20] Further details are presented in the supporting information.

Synthesis

The exact amounts of starting materials for the synthesis of all compounds are listed in Table S1. According to the synthesis conditions of CAU-10-H,[3c] the syntheses of the CAU-10-H/Sx samples were carried out in custom-made steel autoclaves with Teflon inlets with a volume of 30 mL. In a typical experiment for CAU-10-H/S1, a mixture of 1M aqueous solution of $Al_2(SO_4)_3\cdot 18H_2O$ (920 µL, 1.38 mmol), *m*-H$_2$BDC (200.6 mg, 1.21 mmol), *m*-H$_2$BDC-SO$_3$Li (43.5 mg, 0.172 mmol), 1.15 mL DMF and 3.68 mL H_2O was placed in one of these vessels and the reaction was performed in an oven at 135°C for 12 h with 1 h heating and cooling ramp, respectively. The resulting precipitate was filtered off, intensively washed with water and dried in air at room temperature. The syntheses of the CAU-10-N/Sx and the CAU-10-O/Sx samples were carried out in 100 mL glass reactors equipped with a screw cap. In a typical experiment for CAU-10-N/S1, a mixture of a 2M aqueous solution of $AlCl_3\cdot 6H_2O$ (3400 µL, 6.8 mmol), *m*-H$_2$BDC-NO$_2$ (1260 mg, 5.97 mmol), *m*-H$_2$BDC-SO$_3$Li (214.9 mg, 0.853 mmol), 4.0 mL DMF and 12.6 mL H_2O was placed in one of the vessels. In a typical experiment for CAU-10-O/S1, a mixture of a 2M aqueous solution of $AlCl_3\cdot 6H_2O$ (2800 µL, 5.6 mmol), *m*-H$_2$BDC-OH (874.9 mg, 4.80 mmol), *m*-H$_2$BDC-SO$_3$Li (173.3mg, 0.686 mmol), 4.0 mL DMF and 13.2 mL H_2O was used. In both cases the reaction was performed in an oven at 120°C for 12 h with 2 h heating and cooling ramp, respectively. The resulting precipitate was filtered off, intensively washed with water and dried in air at room temperature. IR spectroscopy shows no residues of non-coordinating linker molecules. To determine the ratio of the incorporated linker molecules and thus to assign the molecular formula, liquid ^{1}H-NMR measurements were performed (Figure S35-37) on digested samples. Based on the integral ratios of the protons of the different linker molecules the actual ratios were calculated (Table 4). The results of the elemental analysis agree well with the compositions of all compounds determined from thermogravimetric (TG) and ^{1}H-NMR measurements (Table S2). As an example, the acidic character of the samples is verified by a simple indicator test. Upon addition of H_2O/methyl red a color change from yellow to pink is observed indicating an acidic pH-value (Figure S38). The exchange of the Li^+-ions against H^+-ions at the $-SO_3H$ groups was verified by atomic adsorption spectroscopy.

Acknowledgements

We acknowledge Dr. Helge Reinsch (CAU Kiel) for fruitful discussions. This work has been supported by the DFG (SPP 1362). B.B. and D.D.V. gratefully acknowledge the Research Foundation Flanders (FWO) for financial support (Aspirant grant).

Keywords: metal-organic frameworks, mixed-linker MOF, heterogeneous catalysis, proton conductivity, porous materials

[1] a) Themed issue on Metal-Organic Frameworks, *Chem. Soc. Rev.*, **2009**, *38*, 1201-1508; b) Themed issue on Metal-Organic Frameworks, *Chem. Rev.*, **2012**, *112*, 673-1268; c) Themed issue on Metal-Organic Frameworks, *Chem. Soc. Rev.*, **2014**, *43*, 5415-6172.

[2] O. M. Yaghi, M. O'Keeffe, N. W. Ockwig, H. K. Chae, M. Eddaoudi, J. Kim, *Nature* **2003**, *423*, 705-714.

[3] a) S. Biswas, T. Ahnfeldt, N. Stock, *Inorg. Chem.* **2011**, *50*, 9518–9526; b) M. Lammert, S. Bernt, F. Vermoortele, D. E. De Vos, N. Stock, *Inorg. Chem.* **2013**, *52*, 8521-8528; c) H. Reinsch, M. A. van der Veen, B. Gil, B. Marszalek, T. Verbiest, D. de Vos, N. Stock, *Chem. Mater.* **2013**, *25*, 17-26; d) H. Deng, S. Grunder, K. E. Cordova, C. Valente, H. Furukawa, M. Hmadeh, F. Gándara, A. C. Whalley, Z. Liu, S. Asahina, H. Kazumori, M. O'Keeffe, O. Terasaki, J. F. Stoddart, O. M. Yaghi, *Science* **2012**, *336*, 1018-1023; e) P. Horcajada, H. Chevreau, D. Heurtaux, F. Benyettou, F. Salles, T. Devic, A. Garcia-Marquez, C. Yu, H. Lavrard, C. L. Dutson, E. Magnier, G. Maurin, E. Elkaim, C. Serre, *Chem. Commun.* **2014**, *50*, 6872-6874; f) M. Eddaoudi, J. Kim, N. Rosi, D. Vodak, J. Wachter, M. O'Keeffe, O. M. Yaghi, *Science* **2002**, *295*, 469-472; g) S. J. Garibay, S. M. Cohen, *Chem. Commun.* **2010**, *46*, 7700-7702.

[4] a) A. D. Burrows, *CrystEngComm* **2011**, *13*, 3623-3642; b) W. Lu, Z. Wei, Z.-Y. Gu, T.-F. Liu, J. Park, J. Park, J. Tian, M. Zhang, Q. Zhang, T. Gentle Iii, M. Bosch, H.-C. Zhou, *Chem. Soc. Rev.* **2014**, *43*, 5561-5593; c) X. Kong, H. Deng, F. Yan, J. Kim, J. A. Swisher, B. Smit, O. M. Yaghi, J. A. Reimer, *Science* **2013**, *341*, 882-885.

[5] T. Loiseau, C. Serre, C. Huguenard, G. Fink, F. Taulelle, M. Henry, T. Bataille, G. Ferey, *Chem.-Eur. J.* **2004**, *10*, 1373-1382.

[6] a) S. Marx, W. Kleist, J. Huang, M. Maciejewski, A. Baiker, *Dalton Trans.* **2010**, *39*, 3795-3798; b) T. Lescouet, E. Kockrick, G. Bergeret, M. Pera-Titus, D. Farrusseng, *Dalton Trans.* **2011**, *40*, 11359-11361; c) T. Lescouet, E. Kockrick, G. Bergeret, M. Pera-Titus, S. Aguado, D. Farrusseng, *J. Mater. Chem.* **2012**, *22*, 10287-10293.

[7] H. Reinsch, S. Waitschat, N. Stock, *Dalton Trans.* **2013**, *42*, 4840-4847.

[8] a) G. Akiyama, R. Matsuda, H. Sato, M. Takata, S. Kitagawa, *Adv. Mater.* **2011**, *23*, 3294-3297; b) Y. Zang, J. Shi, F. Zhang, Y. Zhong, W. Zhu, *Catal. Sci. Technol.* **2013**, *3*, 2044-2049; c) J. Chen, K. Li, L. Chen, R. Liu, X. Huang, D. Ye, *Green Chem.* **2014**, *16*, 2490-2499; d) P. Ramaswamy, R. Matsuda, W. Kosaka, G. Akiyama, H. J. Jeon, S. Kitagawa, *Chem. Commun.* **2014**, *50*, 1144-1146; e) Z. Li, G. He, Y. Zhao, Y. Cao, H. Wu, Y. Li, Z. Jiang, *J. Power Sources* **2014**, *262*, 372-379.

[9] S. Biswas, J. Zhang, Z. Li, Y.-Y. Liu, M. Grzywa, L. Sun, D. Volkmer, P. Van Der Voort, *Dalton Trans.* **2013**, *42*, 4730-4737.

[10] a) Y. Jin, J. Shi, F. Zhang, Y. Zhong, W. Zhu, *J. Molec. Catal. A* **2014**, *383–384*, 167-171; b) M. Lin Foo, S. Horike, T. Fukushima, Y. Hijikata, Y. Kubota, M. Takata, S. Kitagawa, *Dalton Trans.* **2012**, *41*, 13791-13794.

[11] a) B. Li, Y. Zhang, D. Ma, L. Li, G. Li, G. Li, Z. Shi, S. Feng, *Chem. Commun.* **2012**, *48*, 6151-6153; b) W. J. Phang, H. Jo, W. R. Lee, J. H. Song, K. Yoo, B. Kim, C. S. Hong, *Angew. Chem.* **2015**, DOI: 10.1002/ange.201411703.

[12] a) T. Ahnfeldt, D. Gunzelmann, J. Wack, J. Senker, N. Stock, *CrystEngComm* **2012**, *14*, 4126-4136; b) N. Reimer, B. Gil, B. Marszalek, N. Stock, *CrystEngComm* **2012**, *14*, 4119-4125; c) S. Biswas, T. Ahnfeldt, N. Stock, *Inorg. Chem.* **2011**, *50*, 9518-9526.

[13] M. Gaab, N. Trukhan, S. Maurer, R. Gummaraju, U. Müller, *Microporous Mesoporous Mater.* **2012**, *157*, 131-136.

[14] A. A. Coelho, Coelho Software, Brisbane, Australia, **2007**.

[15] G. Socrates, *Infrared and Raman Characteristic Group Frequencies: Tables and Charts, 3rd Edition*, Wiley, **2004**.

[16] a) E. Alvarez, N. Guillou, C. Martineau, B. Bueken, B. Van de Voorde, C. Le Guillouzer, P. Fabry, F. Nouar, F. Taulelle, D. de Vos, J.-S. Chang, K. H. Cho, N. Ramsahye, T. Devic, M. Daturi, G. Maurin, C. Serre, *Angew. Chem.* **2015**, *127*, 3735–3739; b) U. Ravon, G. Chaplais, C. Chizallet, B. Seyyedi, F. Bonino, S. Bordiga, N. Bats, D. Farrusseng, *ChemCatChem* **2010**, *2*, 1235-1238.

[17] a) M. Zhang, Y. Yu, *Ind. Eng. Chem. Res.* **2013**, *52*, 9505-9514; b) A. Corma, J. Perez-Pariente, *Clay Minerals* **1987**, *22*, 423-433.

[18] P. F. Siril, H. E. Cross, D. R. Brown, *J. Mol. Cat. A: Chemical* **2008**, *279*, 63-68.

[19] a) E. Barsoukov, J. R. MacDonald, *Impedance spectroscopy*, 2. ed., Wiley&Sons, Hoboken, New Jersey, **2005**; b) J. Grehn, J. Krause, *Metzler Physik*, 3. ed., Schroedel Verlag, Hannover, **1998**.

[20] G. Alberti, M. Casciola, L. Massinelli, B. Bauer, *J. Membr. Sci.* **2001**, *185*, 73-81.

Entry for the Table of Contents (Please choose one layout)

Layout 1:

FULL PAPER

Mix-it: Introduction of sulfonic acid groups into CAU-10-H, -NO$_2$ and -OH by mixed-linker synthesis strongly influences the acidity and polarity of the resulting materials. Next to the impact on the sorption behavior also a high catalytic activity is observed in the gas-phase dehydration of ethanol to ethylene at a reaction temperature of 300°C.

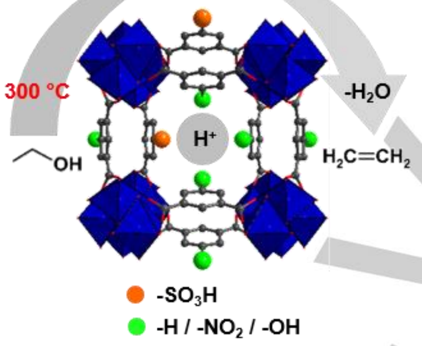

*Author(s), Corresponding Author(s)**

Page No. – Page No.

Title

4.3.8. Screening of Mixed-linker CAU-10 MOF Materials for Humidity Sensing by Impedance Spectroscopy

Der folgende Artikel wurde im Jahre 2015 in der Fachzeitschrift *Microporous and Mesoporous Materials, ELSEVIER GmbH*, zur Begutachtung eingereicht.

Das modulare Aufbauprinzip Metall-Organischer Gerüstverbindungen ermöglicht durch Verwendung funktionalisierter Linkermoleküle die gezielte Modulation der Porenoberfläche eines Materials. Durch Einbringen bestimmter Funktionalitäten lassen sich somit Sorptionsaffinitäten steuern. In den mikroporösen Verbindungen CAU-10-H, -NO_2 und -OH konnte über einen Reaktionsansatz, in dem zwei unterschiedlich funktionalisierte Linkermoleküle verwendet wurden, die vorhandenen funktionellen Gruppen (-H, -NO_2 und -OH) teilweise durch -SO_3H Gruppen ersetzt werden. Die resultierenden Verbindungen CAU-10-$H_{0.76}/(SO_3H)_{0.24}$, CAU-10-$(NO_2)_{0.79}/(SO_3H)_{0.21}$ und CAU-10-$(OH)_{0.89}/(SO_3H)_{0.11}$ weisen durch die eingebrachten stark polaren -SO_3H-Gruppen eine deutlich gesteigerte Affinität gegenüber Wasserdampf auf und wurden bezüglich ihres Sorptionsverhaltens gegenüber Wasserdampf und ihres Impedanzverhaltens untersucht. Dafür wurden sie in Form von Tabletten gepresst, mit einer dünnen Schicht Gold bedampft und als Dielektrikum in einen Plattenkondensator eingebaut. Über ein entsprechendes Dosiersystem wurden die Materialien definierten Atmosphären unterschiedlicher Feuchtigkeit ausgesetzt. In Abhängigkeit der Menge an physisorbiertem Wasser ändern die Proben dabei ihre elektrische Leitfähigkeit, was dem Funktionsprinzip eines kapazitiven Feuchtigkeitssensors entspricht. Die impedanzsspektrokopischen Messungen ergaben für alle drei Materialien eine Übereinstimmung der Änderung der elektrischen Parameter auf die unterschiedlichen Feuchtigkeiten mit den Ergebnissen der Wassersorptionsmessungen. Die Verbindungen zeigen eine hohe Sensitivität mit Werten bis zu fünf Größenordnungen über den gesamten Feuchtigkeitsbereich und weisen damit ein hohes Anwendungspotential für Raumluftkontrollsysteme auf.

Screening of Mixed-linker CAU-10 MOF Materials for Humidity Sensing by Impedance Spectroscopy

Alexander Weiss[a], Nele Reimer[b], Norbert Stock[b], Michael Tiemann[a], Thorsten Wagner[a,*]

[a]Department of Chemistry, University of Paderborn, Warburger Str. 100, D-33098 Paderborn, Germany, Fax: +49-5251-603423

[b]Institute of Inorganic Chemistry, Christian-Albrechts-University Kiel, Max-Eyth-Str. 2, D-24118 Kiel, Germany

Corresponding author: Thorsten Wagner, Tel: +49-5251-602486, thorsten.wagner@upb.de

Abstract

The sorption properties of mixed-linker CAU-10 type metal organic frameworks (MOFs), [Al(OH)(1,3-BDC-X)$_n$(1,3-BDC-SO$_3$H)$_m$] with 1,3-BDC = 1,3-benzenedicarboxyliate, X = H, NO_2 or OH, $0.76 \leq n \leq 0.89$ and $0.11 \leq m \leq 0.24$, can be varied by surface modification through variation of the respective linker molecules. It is thus possible to design surface-modified CAU-10 type MOFs with variable affinity and accessibility of the pores for water vapour. When used as a dielectric in a capacitor, the MOF material will change its permittivity depending on the amount of physisorbed water; this is the working principle of capacitive humidity sensors.

Three different mixed-linker compounds with CAU-10 structure are compared regarding their water sorption and impedance characteristics. A setup was developed allowing the characterization of the MOF samples under exposure to different relative humidity values in air by impedance spectroscopy. Interpretation of the results by means of standard models shows that the MOFs are qualified for functional layers of capacitive humidity sensors. Since the prepared MOFs are more temperature-stable than many commonly used polymers they offer the potential to build a new generation of high-temperature (up to 350 °C) humidity sensors.

Keywords: MOF, surface functionalization, humidity sensing, impedance, water sorption

(max. 5 keywords)

1. Introduction

Metal-organic frameworks (MOFs) are crystalline structures built up by metal clusters interconnected by organic linkers. The possibility to combine various clusters and linkers leads to a multiplicity of compositions with tuneable chemical and physical properties. Because of their high (micro)porosity and large surface area they are interesting for such applications as gas storage, separation, catalysis, drug delivery [1] or water procurement in dry regions [2]. Modified MOFs with semiconducting or ohmic properties are promising for conformal electronic devices and reconfigurable electronics [3]. Their highly ordered structure in combination with tuneable surface and porosity properties also provides a high potential for sensor applications. The spectrum of potential transducers reach from optical (e.g. luminescence [4,5]) over mechanical (e.g. coating of quartz-crystal microbalances [1] or microcantilevers [6]), to electronic mechanisms [7].

However, it was shown that the sensitivity of several MOFs is rather low when exposed to some common gases (Basolite® A100 (Al-BDC, [Al(OH)(1,4-BDC)] 1,4-BDC = 1,4-benzenedicarboxylate), Basolite® F300 (Fe-BTC), Basolite® C300 (Cu-BTC, [$Cu_3(H_2O)_3(BTC)_2$], BTC = 1,3,5-benzenetricarboxylate), 10% O_2, 10% CO_2, 1000 ppm C_3H_8, 1000 ppm NO, 1000 ppm H_2 [7]; Basolite® C300 (Cu-BTC), [$Cu_3(H_2O)_3(BTC)_2$], CO_2, O_2, CH_4 H_2 up to 2000 ppm [8]). Ethanol and methanol lead to a measurable reaction, whereas water causes the highest sensor response. Consequently MOFs are promising candidates for humidity sensing applications. Among all humidity sensing mechanisms resistive- and, particularly, capacitive-type sensors are the most frequent ones. With their variable affinity and pore accessibility for water vapour, MOFs can be utilized as sensitive layers. It is therefore worthwhile to investigate their conducting and dielectric properties in the presence of water vapour.

With CAU-10, [Al(OH)(1,3-BDC-H)], we chose a recent type of functionalized MOF, which was first described by Reinsch et al..[9] The structure of CAU-10 is built up by cis-corner-sharing AlO_6 octahedra to form a helix (Fig. 1). One helix is connected via the carboxylate groups of the isophthalate ions to four adjacent helices with alternating rotational orientation. Hence, a three-dimensional framework is formed with square-shaped one-dimensional channels with a maximum diameter of 7 Å. The single-linker compound CAU-10-H shows a permanent porosity of $a_{s,BET}$ = 635 m^2g^{-1} and a micropore volume of V_{mic} = 0.25 $cm^3g^{-1}$and is accessible for H_2 and CO_2 gas as well as H_2O vapour.[9] The characteristic S-shape of the water vapour isotherm as well as exceptional hydrothermal stability, which was shown by Fröhlich et al. by multi-cycle water vapour measurements open the possibility for an application in the field of heat transformation processes of this material. [10] In addition, it was possible to grow this compound directly on γ-alumina and metallic alumina without any loss of performance in repeated water vapour adsorption measurements, which is advantageous for industrial use.[11]

The isophthalate linker in CAU-10 can be functionalized in 5-position of the aromatic ring with CH_3, OCH_3, NO_2, NH_2, OH or Br groups. [9, 12] The additional functional group has a strong influence on the sorption properties of the respective material. Based on that fact, a fine-tuning of this property was performed using a mixed-linker approach. [12, 13] Recently Reimer et al. synthesized the mixed-linker compounds CAU-10-H/SO_3H, CAU-10-NO_2/SO_3H and CAU-10-OH/SO_3H containing different ratios of the two linker molecules, respectively. With increasing amounts of -SO_3H groups the hydrophobic/ hydrophilic character of these compounds could be varied. [13] The strong affinity towards water vapour in combination with a high thermal stability up to 350-400 °C, which is considerably higher than typical operating temperatures of commonly used polymer-based humidity sensor devices, turns these compounds into promising candidates even for high-temperature humidity sensing.

2. Experimental

2.1 MOF synthesis and characterization

Three samples are compared (CAU-10-H, CAU-10-NO_2, and CAU-10-OH), in which parts of the functional groups are replaced by sulfonic acid groups. The synthesis of CAU-10-$H_{0.76}$/$(SO_3H)_{0.24}$ was performed in a custom-made steel autoclave with a Teflon inset with a volume of 30 mL. The reaction was performed in an oven at 135 °C for 12 h with 1 h heating and cooling ramp, respectively. The resulting precipitate was filtered off, washed with water, and dried in air. Further synthesis details have been reported elsewhere (N. Reimer et al. [13]).

Synthesis of CAU-10-$(NO_2)_{0.79}/(SO_3H)_{0.21}$ and CAU-10-$(OH)_{0.89}/(SO_3H)_{0.11}$ was performed in a 100 mL glass reactor equipped with a screw cap in an oven at 120 °C for 12 h with 2 h heating and cooling ramp, respectively. The resulting precipitate was filtered off, washed with water and dried in air. The molar ratios of incorporated linker molecules were determined from ^{1}H-NMR measurements of the respective dissolved CAU-10 material using the peak integrals.

Water sorption isotherms were recorded using a BEL JAPAN INC. Belsorp$_{max}$ instrument. Prior to each measurement the samples were activated at 200 °C over night under vacuum (10^{-2} kPa).

2.2 Sample preparation

To measure the capacitance of the MOFs, a plate capacitor geometry was chosen. Powder samples were pressed to pellets with a diameter of 13 mm and 0.5 mm thickness and coated with layers of gold by thermal vapour deposition on both sides. A gold layer thickness of 80 nm provides conductivity on the rough pellet surface with sufficient gaps to allow gases to diffuse into the pellet. Conductivity of the electrodes was confirmed by measuring the surface resistance. The electrodes were connected utilizing a cylindrical custom-built sample holder, which allows gases to flow through the pellet in an advanced set-up developed from earlier work [14]. Details regarding sample preparation can be also found in a more comprehensive study on the impedance characteristics of the surface modified MOFs [15].

2.3 Measurement Setup

Defined atmospheres were provided by a gas mixing system consisting of two mass flow controllers. One stream delivered dry synthetic air, whereas the second one was humidified by flowing through a washing bottle with pure water. A mixing ratio of 0:1 (0% dry air, 100% humidified air) corresponds to an absolute humidity of ca. 26 g/m^3 at room temperature (27 °C). The mixture was transferred to a tube containing the sample holder. Impedance spectra were taken on a Solartron SI1260 frequency response analyser (FRA). A simple setup (Fig. 2) was used for the screening in the range from 10 Hz to 1 MHz; the sample was connected in a four-point arrangement to minimize effects from the connection lines. Measurements were conducted using a Sin-Signal with an amplitude of 500 mV. Details regarding the impedance spectroscopy setup and more detailed measurements and interpretations can be found in [15].

3. Results and Discussion

3.1 Water vapour sorption measurements

Water vapour sorption measurements were performed at 298 K. Comparison of the single-linker with the mixed-linker compounds CAU-10-$(OH)_{0.89}/(SO_3H)_{0.11}$ sample shows the smallest deviation. [9, 13]. This is explained by the considerably smaller sulfonate content of this sample. At pressures lower than $p/p_0 = 0.05$ all compounds show nearly the same affinity towards water vapour. In this region the slope of the isotherms is generally higher compared to the single-linker samples which exhibit a very flat increase below the step-like change in the region of $p/p_0 = 0.1 - 0.2$. This behaviour in water sorption is commonly attributed to a stronger adsorbate-adsorbent interaction, i.e. a higher water vapour affinity [16]. Canivet et al. observed that the slope of the adsorption branch in the low pressure region (Henri constant) basically depends on the surface chemistry. Hydrophilic modification of a given MOF structure leads to an increase in the Henry constant. According to Canivet et al., pores with diameters smaller than 2 nm are not filled by capillary condensation but by reversible, continuous filling. The pore filling pressure ρ (partial pressure at which half of the maximum water uptake is reached) is linked to the pore size. In addition, a correlation between these two indicators can be observed. High Henry constants are associated with low ρ values and vice versa. Hydrophilic modification leads to an increase in water adsorption affinity at low relative humidity values which in turn shifts pore filling to lower p/p_0 values [17]. This correlation is partly represented by the comparison of our sulfonic acid-modified samples with the unmodified samples [9, 13]. For all three title compounds the correlation holds with increasing Henry constant, which can be expected for stronger adsorbate-adsorbent interactions.

In addition to the change in the low pressure region, CAU-10-$(NO_2)_{0.79}/(SO_3H)_{0.21}$ shows some further effects. With increasing pressure its affinity is clearly lower than those of the other two compounds, indicating lower pore accessibility. This is still in good agreement with the behaviour of the unmodified samples. However, in the high-pressure region it exhibits a steeper slope. Taking the whole range into account, ρ shifts towards higher values.

In contrast to Canivet et al., Furukawa et al. found that the presence of hydroxyl functional groups has only a marginal effect on the water sorption isotherms [2]. Instead, the pore size of the MOF structure is presumed to play a primary role. According to Reinsch et al. we assume that the modification of the linker molecules has an effect on their steric orientation and thereby significantly alters the effective pore size and pore accessibility. Consequently, the influence of surface chemistry cannot clearly be differentiated from that of pore size and spatial aspects.

In a classical view hysteresis should only occur in mesoporous networks, due to non-equilibrium capillary condensation during adsorption. However, even for microporous MOFs a small hysteresis may be observed, which is frequently attributed to a slight structural flexibility of the network [17]. Reinsch et al. also stated that dehydration of the samples (at room temperature in vacuum) leads to minor structural changes [12]. Hence, we assume that the hysteresis is triggered by the water-MOF interaction, leading to network changes. This is particularly likely in our case because of the sulfonate modification. The relatively small hysteresis of CAU-10-$H_{0.76}/(SO_3H)_{0.24}$ compared to the others is explained by the weaker polarity of the residual hydrogen ligand.

3.2 Impedance Measurements

All three samples were measured over a frequency range from 10 Hz to 1 MHz. For every sweep the humidity was set to a fixed value for 20 minutes. This procedure was repeated consecutively 14 times with relative humidity values of 0%, 10%, 20%, … , 100%. All impedance spectra showed the behaviour of an RC element by first approximation. Hence, the capacitance was calculated from the impedance data by using Eq. (1):

$$Re(C) = \frac{-Im(Z)}{\omega(Re(Z)^2 + Im(Z)^2)} \qquad (1)$$

where Re(Z) and Im(Z) are the real and imaginary parts of the impedance, respectively. The real parts of the capacitance, Re(C), exhibit a clear frequency dependence which intensifies with increasing humidity, caused by an increasing dc conductivity of the MOFs (Fig. 4). A frequency of 1039 Hz was chosen from the spectrum to compare the samples to each other. (The signal-to-noise ratio is not sufficient at lower frequencies for the dry samples).

Figure 5 shows the sensor responses, defined here as $Re(C)/Re(C)_0$ (where $Re(C)_0$ corresponds to the value under dry conditions), at this frequency over the whole humidity range. The order of magnitude in the response of the different samples at high r.h. is in good agreement with the results of the water sorption measurements. CAU-10-$(OH)_{0.89}/(SO_3H)_{0.11}$ exhibits the highest response, while CAU-10-$(NO_2)_{0.79}/(SO_3H)_{0.21}$ has the lowest. In contrast, CAU-10-$(NO_2)_{0.79}/(SO_3H)_{0.21}$ has a higher response in the r.h. region from 30 % to 60 % than the other samples. This characteristic is not represented in the water sorption isotherms.

Desorption behaviour was analysed in consecutive measurements after the relative humidity was changed from 100 % to dry air in a single step (not shown). The recovery time increased in the order CAU-10-$H_{0.76}/(SO_3H)_{0.24}$, CAU-10-$(OH)_{0.89}/(SO_3H)_{0.11}$ and CAU-10-$(NO_2)_{0.79}/(SO_3H)_{0.21}$. This is very similar to the hysteresis behaviour in the desorption branches of the sorption isotherms. Taking into account that the hysteresis is attributed to water-triggered flexibility of the MOFs, as discussed above, it can be understood as the level of interaction strength. The stronger the interactions and thereby the changes in the framework are, the slower is the recovery time.

An accurate determination of the dynamic behaviour is difficult to achieve due to the slow characteristics of the gas mixing system which results in non-step-like changes of the atmosphere. The t_{90} time (i.e. the time for reaching 90 % of the equilibrium response) was ca. 12 minutes for a change from 30% to 40% r.h. (CAU-10-$(NO_2)_{0.79}/(SO_3H)_{0.21}$). This is too slow for fast studies but feasible in environmental applications (see next section). In general, the reproducibility of the measurements is high, but depends on the accuracy of gas dosage. Therefore it is very sensitive to changes in the environmental conditions, such as temperature.

3.3 Application test

To estimate the application potential in humidity sensing, CAU-10-$(NO_2)_{0.79}/(SO_3H)_{0.21}$, as an example, was further investigated in an ambient air control scenario for ca. 60 hours. Details regarding the choice of the sample can be found in [15]. Measurements were conducted using the frequency range between 1 Hz and 30 MHz and only basic data evaluation, given by Eq. (1), was performed. The sample holder was placed in a glass tube (length 20 cm) in the middle of a room, to avoid any potential influence of direct air flow in the ambience of the material. Additionally, a conventional temperature and humidity sensor was placed in the same tube as a reference (Sensirion SHT21). For the test one room window was kept slightly opened over the whole test duration to obtain a weak interchange between indoor and outdoor air. The trend of relative humidity is similar, but not equal to that of absolute humidity (a.h.), because of variations in the temperature. Among the number of possible electrical quantities, Re(Z) (not shown) as well as Re(C) (Fig. 6) correspond the best with the measured humidity at first view. A more detailed mathematical analysis reveals that Re(C) correlates better with relative humidity than Re(Z). This correlation between Re(C) and relative humidity was expected, since many commercially available sensors are based on this principle. Water with its high electrical permittivity changes the capacitance of a porous material proportionally to its amount adsorbed in the pores. This amount mainly depends on the relative humidity. The temperature dependence of this adsorption is only weak in the temperature range in which sensors are typical operated.

The capacitive sensitivity in the application test range between 40% rh and 60 rh is 0.13 pF/%rh. This is of the order of commercially available humidity sensors (IST MK33-W 0.45pF/%rh [18]; Michell Instruments H6000 0.86pF/%rh [19]). Since the prepared MOFs are temperature-stable up to 350°C they offer the potential to build a new class of high-temperature humidity sensors. Commonly used polymers have been improved with respect to temperature stability in the past but they are still limited below 200°C (Sensirion SHT21 up to 125°C [20], IST MK33-W up to 190°C [18], Michell Instruments H6000 up to 200°C [19]). The response time, which is approx. 12 minutes (see section 3.2), is larger than that of commercially available sensors (6s to 20 s), but it is still sufficient for application areas with slow dynamic characteristics.

4. Conclusion

CAU-10-type MOF materials were screened with respect to their water sorption behaviour and their potential application as sensor-active materials in humidity sensing. Samples with various types of chemical modification of the linker unit exhibit similar, but not identical behaviour. In particular, sulfonate groups increase the affinity towards water in the low pressure region. Assuming that the chemical modification has an effect on the steric orientation of the linker molecules and thereby on pore accessibility, the influence of surface chemistry cannot be clearly differentiated from that of pore size and spatial aspects. Sorption hysteresis may be explained by the water/MOF interaction leading to network changes.

Impedance spectroscopy is a powerful tool to analyse the electrical/dielectrical reaction of MOFs towards water. In general, the humidity response of the electrical parameters is in good agreement with the results from water sorption measurements; the recovery time is linked to hysteresis properties. The materials show high sensitivity with responses up to 5 orders of magnitude over the whole humidity range. The investigated MOF materials exhibit high application potential in ambient air control scenarios. They show distinct responses even for small changes in environmental conditions, although the reaction is relatively slow.

Acknowledgements

We acknowledge the financial support by the German Federal Ministry of Education and Research (BMBF, grant no. 13N12969) and the support of the project executing organization (VDI Technologiezentrum GmbH, Düsseldorf). This work has been supported by the DFG (SPP 1362).

References

[1] S.T. Meek, J.A. Greathouse, and M.D. Allendorf, Adv. Mater. 23, 249-267 (2011).

[2] H. Furukawa, F. Gandara, Y.-B. Zhang, J. Jiang, W.L. Queen, M.R. Hudson, and O.M. Yaghi, J. Am. Chem. Soc. 136, 4369-4381 (2014).

[3] A.A. Talin et al., Science 343, 66 (2014).

[4] S. Pramanik, C. Zheng. X. Zhang, T.J. Emge, and J. Li, J. Am. Chem. Soc. 133, 4153-4155 (2011).

[5] Z. Dou, J. Yu, Y. Cui, Y. Yang, Z. Wang, D. Yang, and G. Qian, J. Am. Chem. Soc. 136, 5527-5530 (2014).

[6] M.D. Allendorf, R.J.T. Houk, L. Andruszkiewicz, A.A. Talin, J. Pikarsky, A. Choudhury, K.A. Gall, and P.J. Hesketh, J. Am. Chem. Soc. 130, 14404-14405 (2008).

[7] S. Achmann, G. Hagen, J. Kita, I.M. Malkowsky, C. Kiener, and R. Moos, Sensors 9, 1574-1589 (2009).

[8] J. Liu, F. Sun, F. Zhang, Z. Wang, Rui. Zhang, C. Wang, and S. Qiu, J. Mater. Chem. 21, 3775 (2011).

[9] H. Reinsch, M.A. van der Veen, B. Gil, B. Marszalek, T. Verbiest, D. de Vos, and N. Stock, Chem. Mater. 25, 17-26 (2012)

[10] D. Fröhlich, S. K. Henninger, C. Janiak, Dalton Trans. 43, 15300-15304 (2014).

[11] M. F. de Lange, C. P. Ottevanger, M. Wiegman, T. J. H. Vlugt, J. Gascon and F. Kapteijna, CrystEngComm 17, 281-285(2015).

[12] H. Reinsch, S. Waitschat, N.Stock, Dalton Trans. 42, 4840-4847 (2013).

[13] N. Reimer, S. Leubner, B. Bueken, D. de Vos, N. Stock, Chemistry of Materials, in preparation.

[14] T. Wagner, S. Krotzky, A. Weiß, T. Sauerwald, C.-D. Kohl, J. Roggenbuck, and M. Tiemann, Sensors 11, 3135-3144 (2011).

[15] A. Weiss, N. Reimer, N. Stock, M. Tiemann, T. Wagner, Journal of Physical Chemistry C, in preparation

[16] K.S.W. Sing, et al., Reporting Physisorption Data for Gas/Solid Systems, Recommendations of IUPAC Commission on Colloid and Surface Chemistry Including Catalysis, Pure & Applied Chemistry., 57, 603-619 (1985).

[17] J. Canivet, J. Bonnefoy, C. Daniel, A. Legrand, B. Coasne, and D. Farrusseng, New J. Chem. 38, 3102 (2014).

[18] Innovative Sensor Technology IST AG, Data Sheet MK33-W capacitive humidity sensor, www.ist-ag.de, downloaded 11 Feb. 2015.

[19] Michell Instruments, Data Sheet H6000 capacitive humidity sensor, www.michell.com, downloaded 11. Feb. 2015.

[20] Sensirion AG, Data Sheet SHT25 Humidty and Temperature Sensor IC, www.sensirion.com, downloaded 11. Feb 2015.

Figure captions

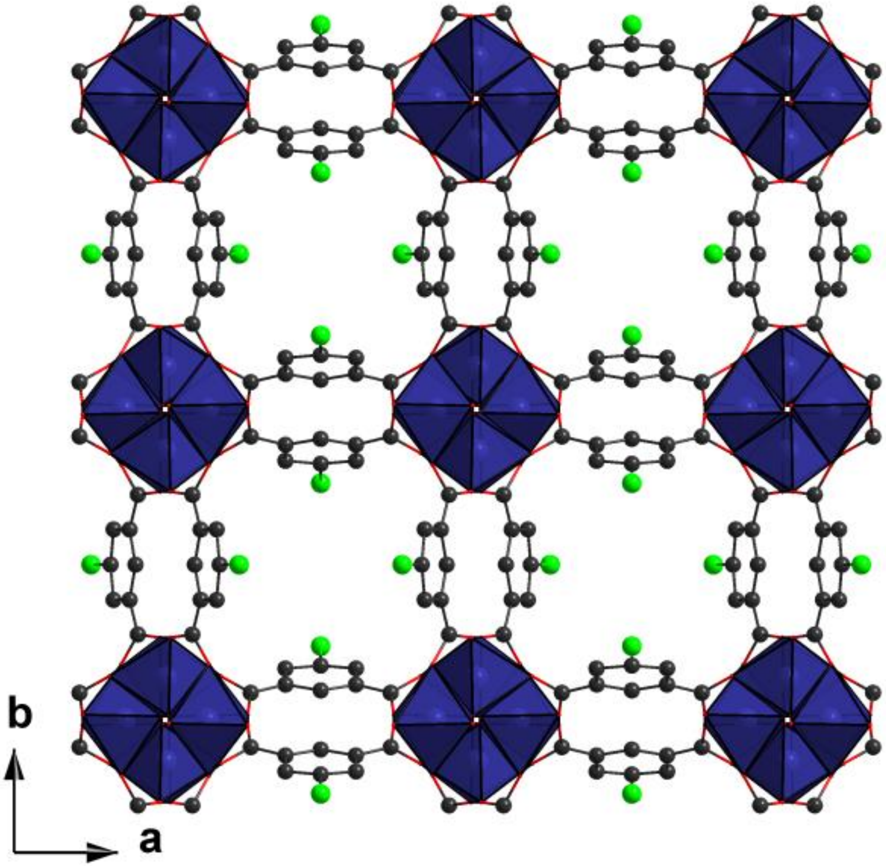

Figure 1. Structure of the CAU-10 MOF with AlO_6 octahedra helices (blue), isophthalate linkers (black), and position of the functional groups (green)[CIF file from Ref. Reinsch2013].

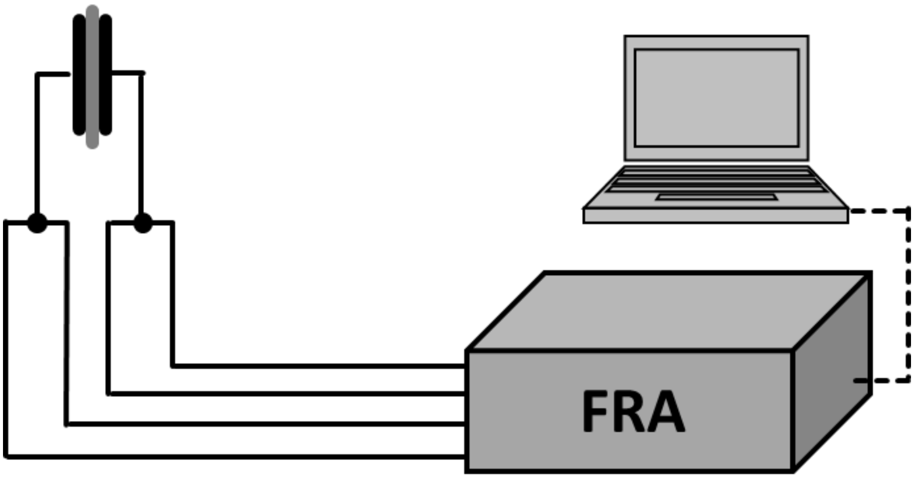

Figure 2. Measuring set-up consisting of the FRA in4-point-arrangement for low Ohmic sample behaviour.

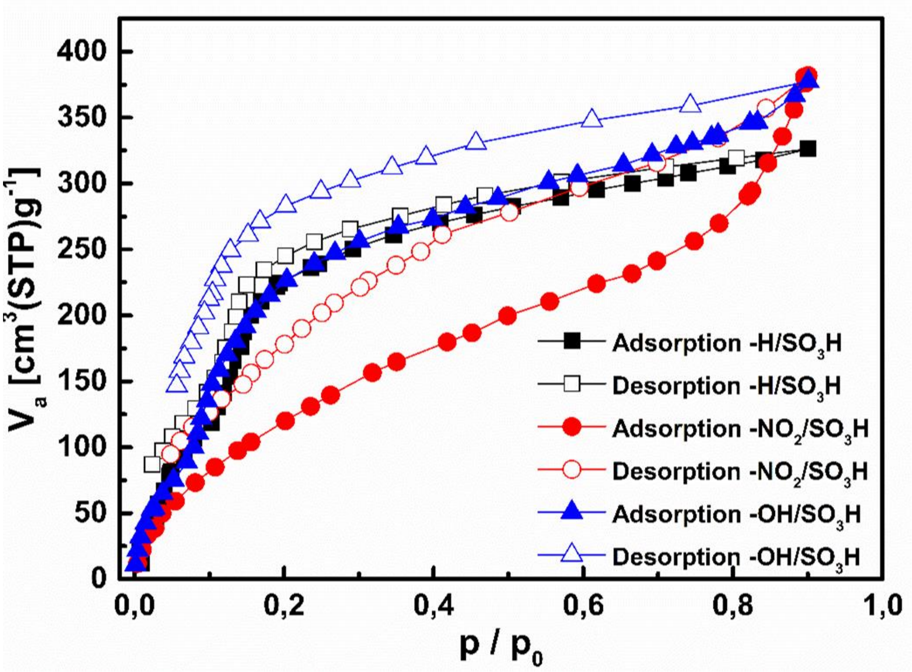

Figure 3. Water sorption isotherms at 298 K.

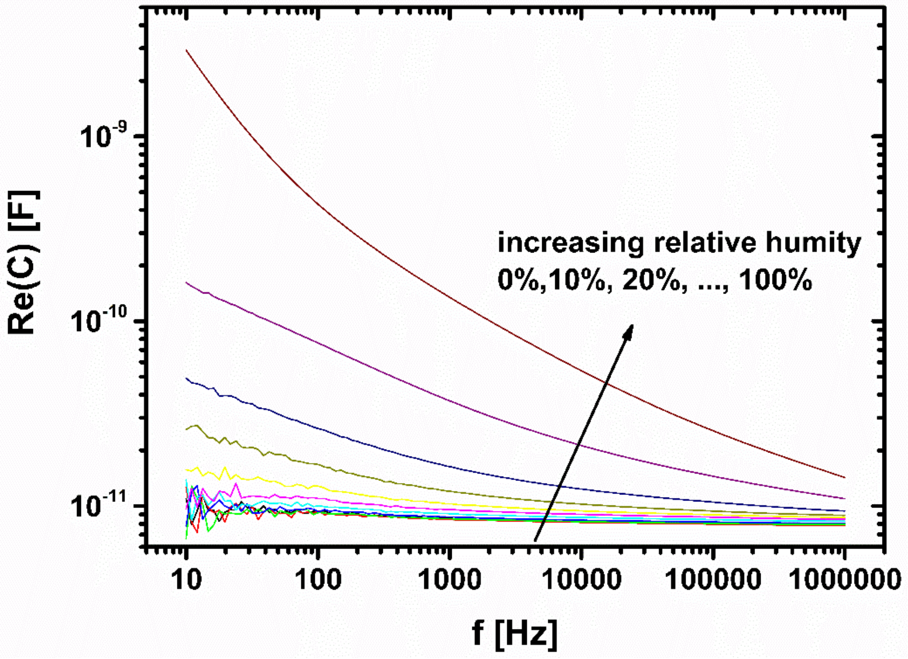

Figure 4. Exemplary plots of Re(C) over the frequency range for the CAU-10-H/SO$_3$H sample.

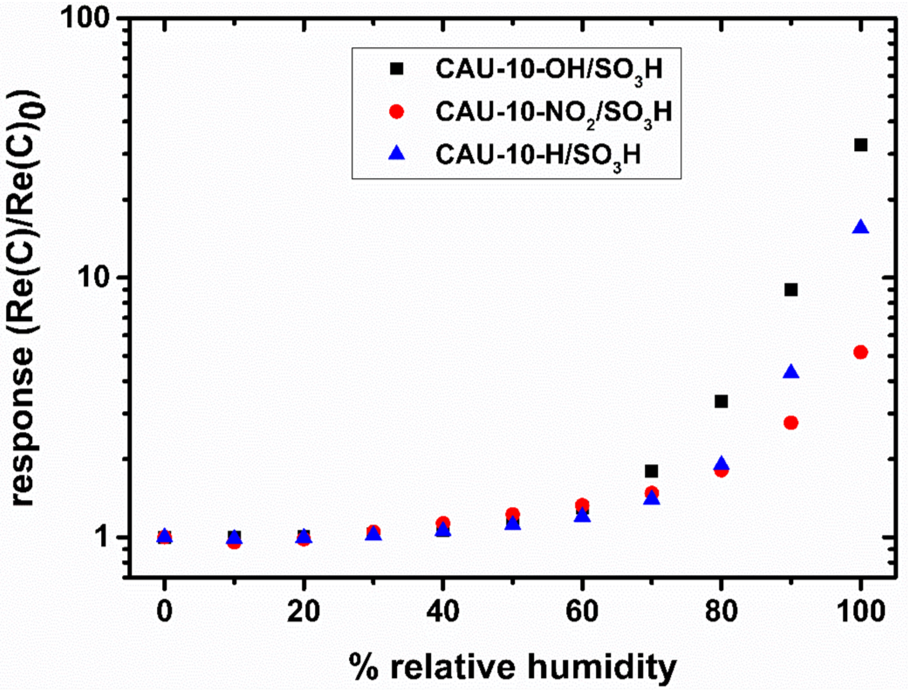

Figure 5. Response Re(C)/Re(C)0 at 1039 Hz of all three samples when exposed to different humidity levels.

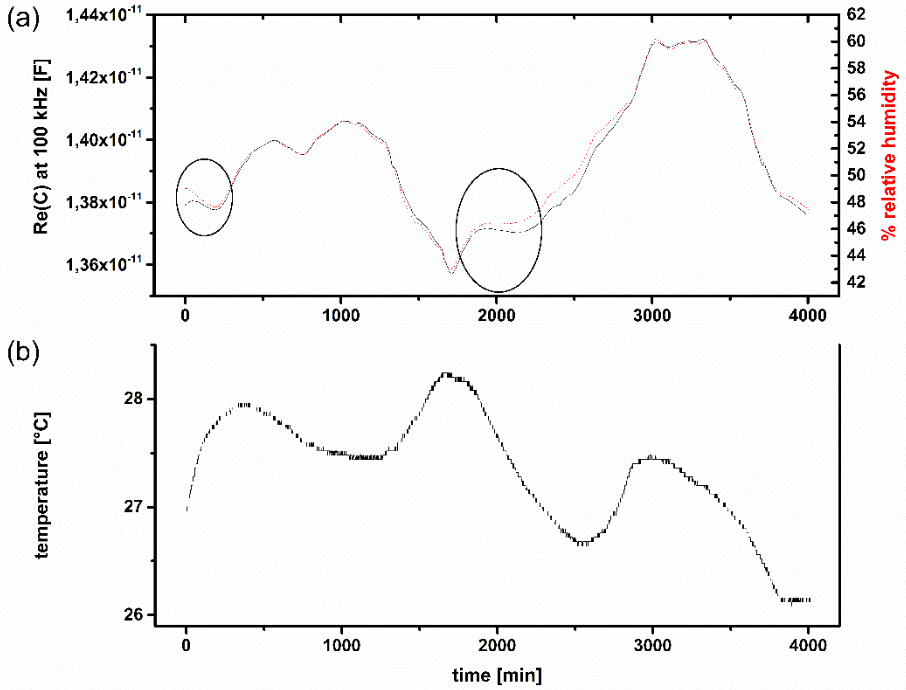

Figure 6. Application test of CAU-10-$(NO_2)_{0.79}/(SO_3H)_{0.21}$. Re(C) at 100 kHz compared to relative humidity (top) and temperature (bottom); (Reference humidity measurements in dashed lines).

4.3.9. Surface-modified CAU-10 MOF Materials as Humidity Sensors: Impedance Spectroscopic Study on Water Uptake

Der folgende Artikel wurde im Jahre 2015 in der Fachzeitschrift *Physical Chemistry Chemical Physics*, *RSC* zur Begutachtung eingereicht.

Ausgehend von der Studie aus 1.1.1 wurden in dieser Arbeit für ein tiefergehendes Verständnis das Sorptionsverhalten der Verbindungen CAU-10-$H_{0.76}/(SO_3H)_{0.24}$, CAU-10-$(NO_2)_{0.79}/(SO_3H)_{0.21}$ und CAU-10-$(OH)_{0.89}/(SO_3H)_{0.11}$ gegenüber Wasserdampf mit deren konduktiven und dielektrischen Eigenschaften, die über impedanzspektroskopische Messungen bestimmt wurden, korreliert. Dafür wurden die Materialien in Form von Tabletten gepresst, mit einer dünnen Schicht Gold bedampft und als Dielektrikum in einen Plattenkondensator eingebaut. Über ein entsprechendes Dosiersystem wurden die Materialien definierten Atmosphären unterschiedlicher Feuchtigkeit ausgesetzt. In Abhängigkeit der Menge an physisorbiertem Wasser ändern die Proben dabei ihre elektrische Leitfähigkeit, was dem Funktionsprinzip eines kapazitiven Feuchtigkeitssensors entspricht. Die Impedanzspektren wurden in einem Frequenzbereich von 1 mHz bis 1 mHz aufgenommen und mit dem Havriliak-Negami Modell ausgewertet. Erstmals wurden Messungen im Bereich von 1 bis 10 mHz an solchen Materialien durchgeführt. Für CAU-10-$(NO_2)_{0.79}/(SO_3H)_{0.21}$ und CAU-10-$(OH)_{0.89}/(SO_3H)_{0.11}$ wurde unter trockenen Bedingungen Leitfähigkeiten im Bereich von 10^{-14} bis 10^{-13} S/m gemessen. Mit steigender Luftfeuchtigkeit wurde ein exponentieller Abfall des Wiederstandes beobachtet. Die hohe Sensitivität der Materialien zeigt sich darin, dass der Widerstand über den gesamten Feuchtigkeitsbereich über fünf Größenordnungen absinkt. Umgekehrt zeigt sich für die Kapazität ein exponentieller Anstieg mit linear ansteigender Luftfeuchtigkeit. Des Weiteren ist eine deutliche Korrelation zwischen der Impedanz und der absoluten Feuchtigkeit zu beobachten. Insgesamt weisen die untersuchten Materialien ein hohes Anwendungspotential auf, zeigen sie doch selbst bei sehr kleinen Änderungen in der Atmosphäre eindeutige Signaländerungen, auch wenn diese relativ langsam vollzogen werden.

Surface-modified CAU-10 MOF Materials as Humidity Sensors: Impedance Spectroscopic Study on Water Uptake

Alexander Weiss[1], Nele Reimer[2], Norbert Stock[2], Michael Tiemann[1] and Thorsten Wagner[,1]*

[1]University of Paderborn, Faculty of Science, Department Chemistry,
Warburger Str. 100, 33098 Paderborn, Germany

[2]Christian Albrechts University Kiel, Institute of Inorganic Chemistry,
Max-Eyth-Straße 2, 24118 Kiel, Germany

Keywords: MOF, surface functionalization, humidity sensing, impedance, water sorption

Abstract

Metal-organic frameworks (MOFs) are crystalline microporous materials with tunable chemical and physical properties. By combining various metal clusters with different interconnecting organic linkers, the pore structure, crystallinity, as well as the surface properties can be modified. In the presented work modification of the organic linker molecules is utilized to synthesize CAU-10 type MOFs with variable affinity of the pore surface to water. In principle, this should influence the accessibility of the pores for water vapor and therefore offer a tool to control its sorption properties. For a deeper understanding we studied the water sorption characteristics and compared the results to the conductive and dielectric properties measured by impedance spectroscopy. Spectra in a wide frequency range from 1 mHz to 1 MHz were recorded. Data analysis is performed using the Havriliak-Negami model. The MOFs are also tested as sensitive layers for capacitive humidity sensing by correlating the change in permittivity of the materials with the amount of physisorbed water. Such a MOF-based sensor was tested with respect to environmental monitoring and compared to a commonly used commercial humidity sensor.

Introduction

Metal organic frameworks (MOF) are highly porous structures whose surface areas can achieve values up to 7000 m²/g [1]. MOFs consist of metal ions clusters that act as knots and interconnecting organic linkers. One of their main advantages is the high tunability by combining various metals with different linkers. More than 10,000 structures with different properties are known up to now. This fact makes them a promising class of materials for various applications such as gas storage, heat exchange, separation, catalysis, and sensing. The latter one can be realized by a wide range of transducer mechanisms reaching from optical, (e.g., luminescence [2,3] or colour change [4]) over mechanical (e.g., coating of quartz-crystal microbalances [5]) or microcantilevers [6]), to electronic mechanisms.

Due to the multiplicity of sensing mechanisms and target gases there are only a few reports concerning the conducting and dielectric properties of MOFs in the presence of water vapour [7,8]. Although low frequencies are less suitable for fast sensing devices, both groups show that lower frequencies enhance the response to humidity. To our knowledge this is the first work covering the range below 1 Hz, which is promising for a better analysis of MOF impedance spectra.

The understanding of electric system response in combination with water sorption measurements is a crucial factor on the way to resistive-type or capacitive-type humidity sensors, which represent the most popular among all humidity sensing mechanisms. The polymers that are commonly used for this purpose cannot be operated at high temperatures (<200°C [9]) und have the disadvantage of possible damage at very high relative humidity.

Experimental Methods

Synthesis and Characterization

In the present study three modifications of the CAU-10 MOF are compared (CAU-10-H, CAU-10-NO_2, and CAU-10-OH). Parts of the functional groups are replaced by sulfonic acid groups. Synthesis was performed according to literature [10]. For the CAU-10-$H_{0.76}/(SO_3H)_{0.24}$ samples (further denoted as CAU-10-H/S) the reaction temperature in the steel autoclave with a Teflon inset was chosen 135°C for 12 h with 1 h heating and cooling ramp, respectively. The syntheses of CAU-10-$(NO_2)_{0.79}/(SO_3H)_{0.21}$ and the CAU-10-$(OH)_{0.89}/(SO_3H)_{0.11}$ (further denoted as CAU-10-O/S and CAU-10-N/S) were performed in a glass reactor equipped with a screw cap and a volume of 100 mL. The reactions were performed in an oven at 120 °C for 12 h with 2 h heating and cooling ramp, respectively. The resulting precipitates were filtered off, washed with water and dried in air.

To determine the ratio of incorporated linker molecules, liquid ^{1}H-NMR spectroscopy measurements were performed. The resulting compounds exhibit doping degrees of sulfonic acid groups of 23.5 %, 21.3 % and 10.9 %, respectively, as calculated from the peak integrals.

Water sorption isotherms were recorded using a BEL JAPAN INC. Belsorp$_{max}$ instrument. Prior to each measurement the samples were activated at 200 °C over night under vacuum (10^{-2} kPa).

Sample Preparation

To measure the capacitance of the MOFs, a plate capacitor geometry was chosen. 100 mg of the powder samples were pressed to pellets with a diameter of 13 mm and 0.5 mm thickness. The pressure was 35.8 MPa for CAU-10-H/S and CAU-10-O/S, and 57.2 MPa for CAU-10-N/S. In order to create mechanically stable electrodes which are permeable to gases and vapor, the pellets were coated with layers of gold by thermal vapor deposition on both sides. The size of these electrodes was chosen as 11 mm to prevent short-circuits at the edges (Figure 1). This setup avoids capacitance changes due to electrode displacement, as occasionally observed when inelastic metal electrodes are only pressed on top of the pellet. The gold layer thickness was adjusted to 80 nm utilizing a quartz crystal microbalance. This thickness guarantees sufficient conductivity on the rough pellet surface and provides gaps and cracks to allow gases to diffuse through the system at the same time. Conductivity of the electrodes was confirmed by measuring the surface resistance. The electrodes were connected utilizing a cylindrical custom-built sample holder, which allows gases to flow through the pellet and is an advanced development of earlier works [11] (Figure 2).

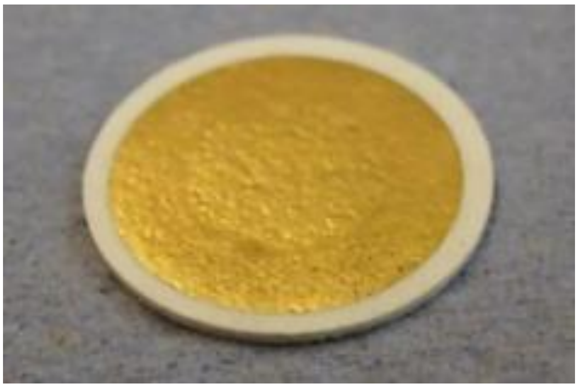

Figure 1. Pressed MOF pellet with 80 nm gold layer.

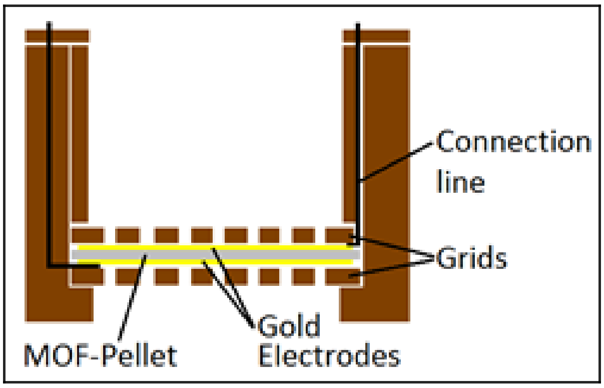

Figure 2. Cross section schema of the sample holder.

Measurement System

Defined atmospheres were provided by a gas mixing system consisting of two mass flow controllers. One stream delivered dry synthetic air, whereas the second one was humidified by flowing through a washing bottle with pure water. A mixing ratio of 0:1 (0% dry air, 100% humidified air) corresponds to an absolute humidity of ca. 26 g/m^3 at room temperature (27 °C). The mixture was led to a tube containing the sample holder. Impedance spectra were taken on a Solartron SI1260 frequency response analyzer (FRA). A simple setup was used for the first screening in the range from 10 Hz to 1 MHz (Figure 3a, details see also [12]). Therefore the sample was connected in a 4-point-arrangement to minimize effects from the connection lines. The screening measurements showed that the samples exhibited highly ohmic behavior at low frequencies when exposed to air with r.h. values between 0% and 30% [12]. To overcome the induced low signal-to-noise ratio the system was enhanced by a 'Chelsea Dielectric Interface', the function of which is two-fold. It acts as a high-impedance buffer between the sample and the FRA. Additionally, it facilitates the measurement of small currents flowing through the dielectric sample (pA). It also acts as a wide band-width current-to-voltage converter so the FRA is set to voltage measurement in this setup (Figure 3b). Thus, the measurement frequencies can be reduced down to the mHz order even for small capacitance.

Measurements were conducted using a Sin-Signal with an amplitude of 500 mV. A Sensirion SHT21 served as reference humidity and temperature sensor for the application survey. In these measurements the absolute humidity (a.h.) is calculated according to Equation (1)

$$a.h. = \frac{13.233 * r.h. * 10^{\left(\frac{a*T}{b+T}\right)}}{273,15+T} \tag{1}$$

with r.h. being the relative humidity, T the temperature in °C and the parameters a = 7.5 and b = 237.3.

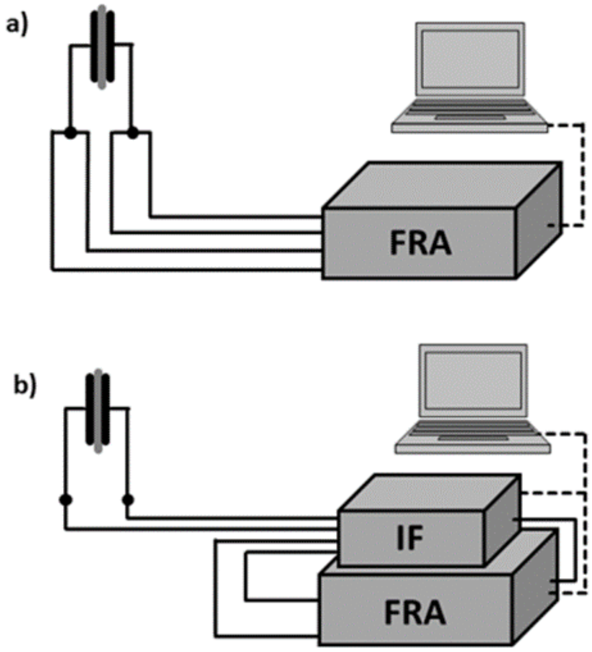

Figure 3. Set-up a) in 4-point-arrangement with only the FRA and b) enhanced with dielectric interface for highly ohmic sample conditions.

Results and Discussion

Water vapor sorption measurements

In the following a short summary of the water sorption results is given. A more detailed interpretation has been provided in another work by this group focused on the synthesis and screening measurements of the presented samples for humidity sensing application [12].

Water vapor sorption measurements were performed at 298 K (plot see supporting information, SI Fig. S1). Compared to un-modified samples by Reinsch et al. [13] the CAU-10-O/S sample shows the smallest change in water sorption. This result is attributed to the considerably smaller sulfonate content of this sample.

The affinity towards water is nearly the same at a pressure range lower than $p/p_0 = 0.05$ for all samples. The slope of the isotherms is generally higher compared to the unmodified samples in this region. This behavior in water sorption is commonly attributed to a stronger adsorbate-adsorbent interaction, i.e. a higher water vapor affinity [14]. Hydrophilic modification of the surface groups leads to an increasing affinity in water adsorption and therefore pore filling shifts to lower p/p_0 values [15]. The unmodified samples exhibit a very flat increase below the step-like change in the region of $p/p_0 = 0.1 - 0.2$.

CAU-10-N/S shows some further effects in the pressure region above p/p0 = 0.1 - 0.2. In good agreement with the behavior of the unmodified samples with increasing pressure its affinity towards water is clearly lower than those of the other two compounds. However, in the high-pressure region (0.8 – 1.0) it exhibits a steeper slope. Taking the whole range into account, the partial pressure at which half of the maximum water uptake is reached, shifts towards higher values.

Since, according to Reinsch et al., the modification of the linker molecules has an effect on their steric orientation and thereby significantly alters the effective pore size and pore accessibility, the influence of surface chemistry cannot clearly be differentiated from that of pore size and spatial aspects. The observed hysteresis is attributed to water-MOF interaction, leading to network changes. This is particularly likely in our case because of the sulfonate modification. The relatively small hysteresis of CAU-10-H/S compared to the others is explained by the weaker polarity of the framework.

Impedance Measurements

Screening

As already described in [12] all three samples were measured over a frequency range from 10 Hz to 1 MHz for a first screening. The impedance spectra showed RC-type behavior at first glance. Results of these measurements and the calculated capacitance can be found in the supporting information (Fig. S2). To summarize the result it can be stated that in this frequency range the order of magnitude in the response (defined here as $Re(C)/Re(C)_0$ where $Re(C)_0$ corresponds to the value under dry conditions) at high r.h. is in good agreement with the results of the water sorption measurements. However, the relative response of the different samples is not represented in the water sorption isotherms, especially the behavior in the r.h. region from 30 % to 60 % (SI, Fig. S3).

The recovery time for the water desorption (change from 100 % r.h. to dry air) increased in the order CAU-10-H/S, CAU-10-O/S and CAU-10-N/S. This is very similar to the hysteresis behavior in the desorption branches of the sorption isotherms.

The dynamic behavior of CAU-10-N/S was analyzed by fast changes of the atmosphere from 30% to 40% r.h.. However, the response time is limited by the inertia of the gas mixing system, leading to non-step-like atmosphere changes. Consequently the t_{90}-time can only by estimated and add up to approximately 12 minutes.

Extended Frequency Range

The non-constant behavior of Re(C) over the frequency range observed in the screening measurements (SI, Fig. S2) indicates a more complex system than assumed so far. Therefore, further investigation and extended models are required which will be presented in the following. For this purpose only the samples CAU-10-O/S and CAU-10-N/S are taken into account, which show the strongest, respectively the weakest response in the first screening. The characteristic time constants of the relaxation processes at low humidity are in the region of 1 Hz and below. Consequently, the frequency range was extended down to 1 mHz utilizing the dielectric interface (Figure 3, setup b). As apparent from Figure 4 and 5, the low frequency range is necessary to obtain significant data for the impedance characterization of the sample. The frequency cycles for high humidity values are cut off at the low frequency tail because the small DC resistance exceeds the measuring range in this setup. The spectra do not show any multiple steps attributable to different contributions (bulk, boundaries, etc.), as previously observed in the same frequency range for other MOFs containing sulfonic acid groups (β-PCMOF2) [16].

Achmann et al. also showed frequency spectra of Basolite® A100 (Al-BDC, [Al(OH)(1,4-BDC)] 1,4-BDC = 1,4-benzenedicarboxylate) at 120°C in dry and wet N_2 carrier gas which did not exhibit any RC-like behavior, potentially due to the limited frequency range (> 1 Hz). They obtained responses at 1 Hz for all impedance measurement parameters (Z, Re(C), Im(Z)) that are smaller than 50% [7]. Our samples, in contrast, show responses of up to 4 orders of magnitude. The measurements cover the same range of relative humidity, but were carried out at room temperature.

Due to this strong response on humidity, the measurement is very sensitive to changes in environmental conditions, such as temperature (see also section 'application test'). This is the limiting factor with respect to reproducibility, which is high concerning only the impedance measurements.

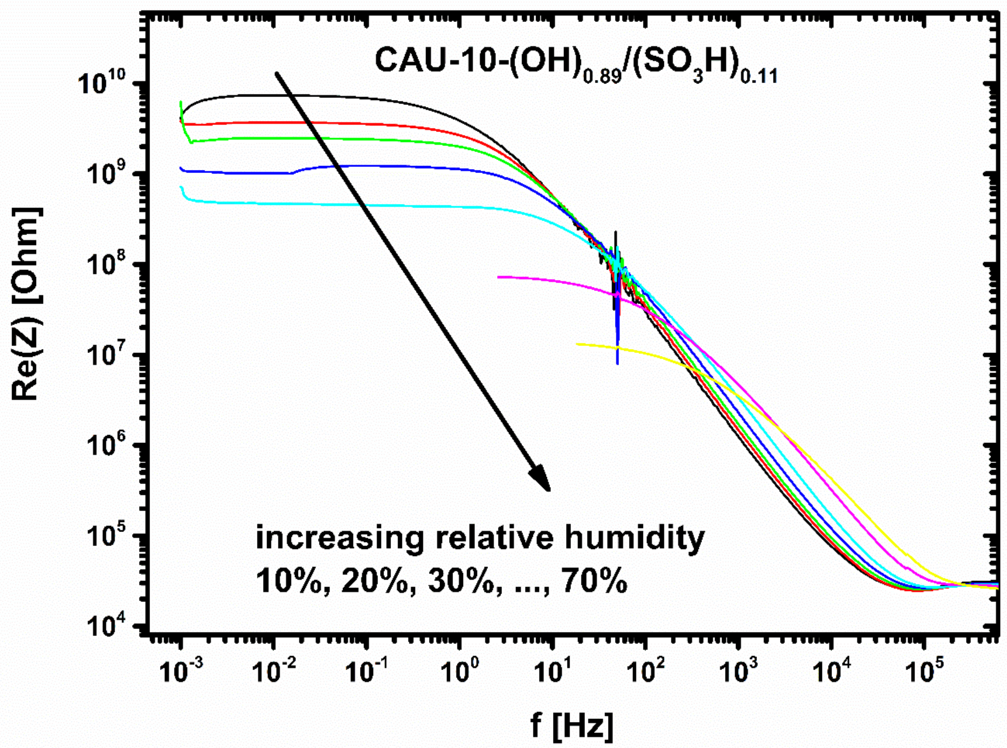

Figure 4. Re(Z) of CAU-10-O/S at different relative humidity.

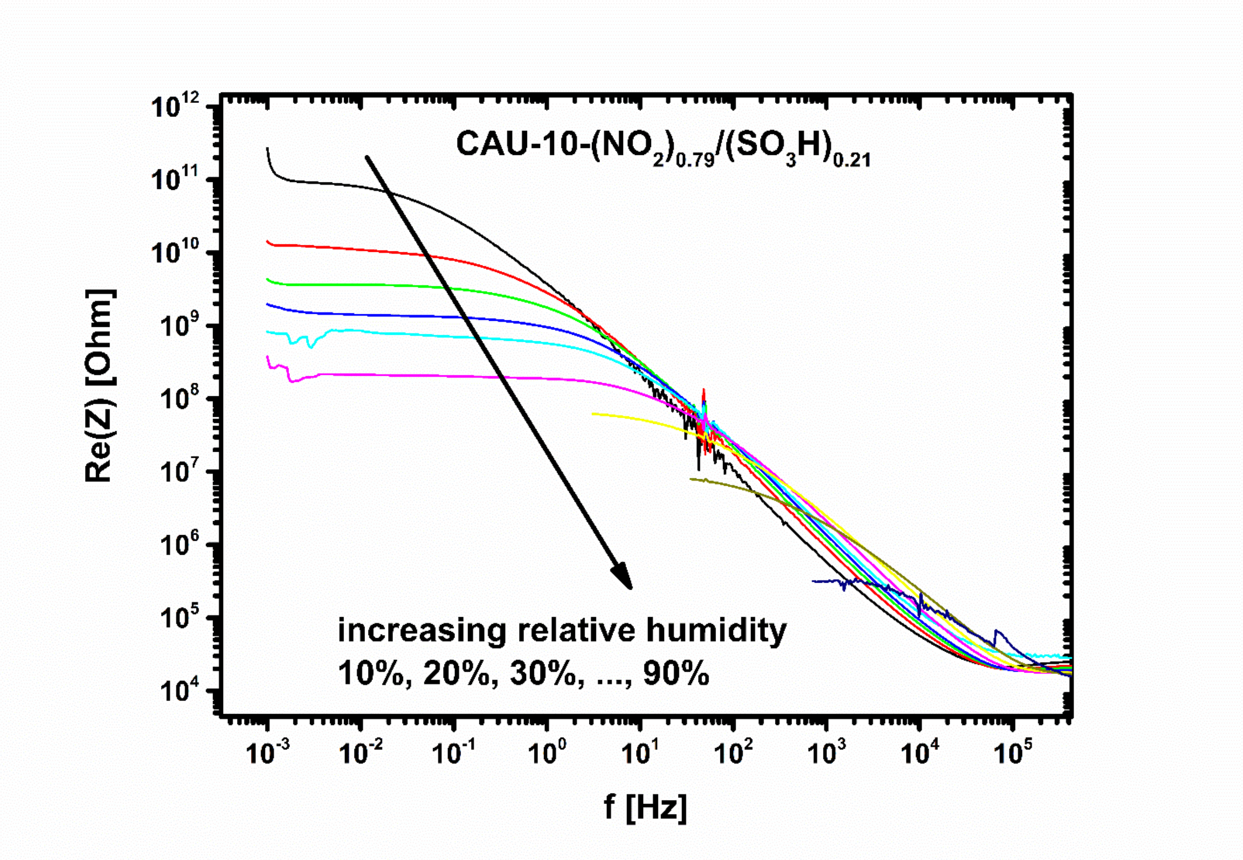

Figure 5. Re(Z) of CAU-10-N/S at different relative humidity.

Data Fitting

Closer inspection of the real and imaginary parts of the impedance Z(ω) reveals that a simple RC element is not sufficient to fit the data. Experimental systems always exhibit imperfections (e.g. electrode roughness, polycrystallinity) which lead to a distribution in relaxation time. This behavior can be modelled by using a constant-phase element (CPE) in parallel with a resistor. According to the Cole-Cole model this equivalent circuit, also referred to as 'ZARC-element', can be described by Equation 3 with the resistor R and the CPE parameter Q. The parameter α represents the width of the relaxation time distribution and reaches from 1 for perfect capacitors to 0 for ohmic resistor behavior [17].

$$Z(\omega) = \frac{R}{1+RQ(i\omega)^{\alpha}} \qquad (3)$$

As can be seen in the Nyquist plot of an exemplary data set (Figure 6) this Cole-Cole model approach still differs from the measured data points which show a distorted arc. Taking this asymmetry into account the data was fitted applying the Havriliak-Negami (HN) model, which represents an overlap of several semicircles with similar but not equal time constants [18]. This 'universal' character of the HN model allows an easy comparison of measurements even with different numbers of involved processes.

$$Z(\omega) = \frac{R}{(1+RQ(i\omega)^{\alpha})^{\beta}} \qquad (4)$$

Equation 4 reduces to the Cole-Cole model if $\beta = 1$ and to the Cole-Davidson model[19] if $\alpha = 1$. To fit the present data it is important to notice that β is not restricted to $0 < \beta < 1$ as mentioned in some publications [20,21]. The right restriction is obtained from Havriliak and Negami [18] by setting the maximum angle between the arc and the real-part axis to 90°, leading to the expression $\beta < 1/\alpha$. This constraint allows values of $\beta > 1$ which are necessary to fit arcs with maxima shifted to higher frequencies (lower real part).

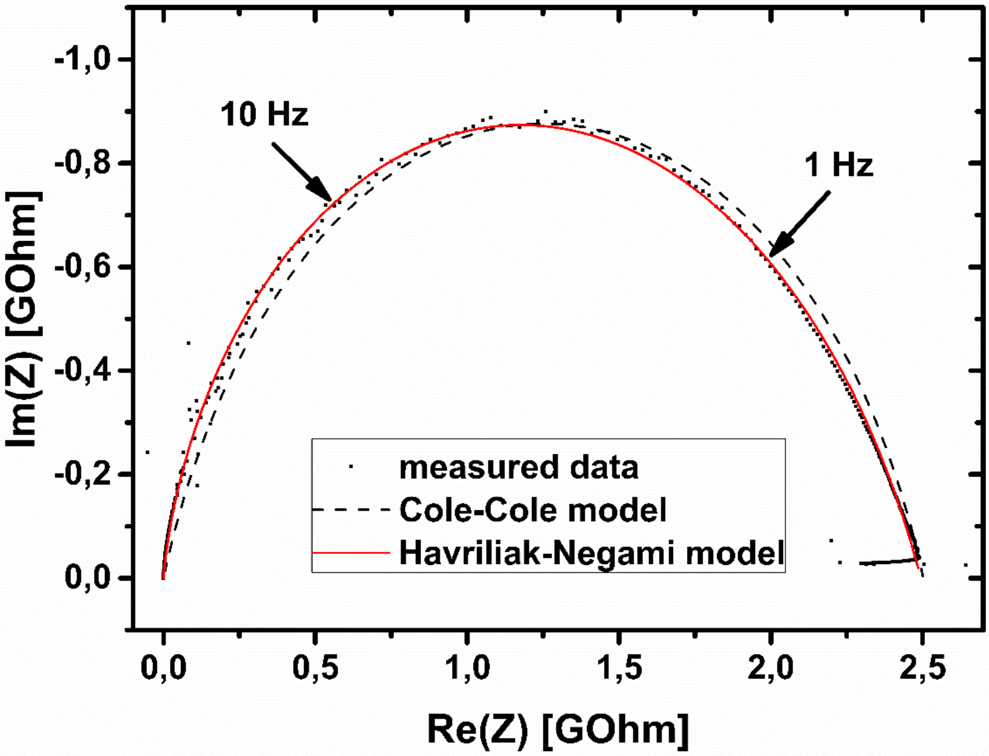

Figure 6. Measured data for CAU-10-O/S at 30% r.h. (dots), fitted with Cole-Cole model (black, dashed line) and fitted with Havriliak-Negami model (red line).

Applying the HN-model to all wide frequency range data sets yield the parameters R, Q, α and β of the MOFs for humidity between 10 % and 90 % r.h.. As can be seen from Figure 7 the resistance R decreases approximately exponentially with increasing humidity. This relation holds better for CAU-10-N/S, whereas CAU-10-O/S still shows a slight curvature in the logarithmic plot.

Sakai et al. report on resistive-type humidity sensors consisting of a microporous matrix impregnated with a hydrophilic polymer containing a sulfonate function. The shape of the logarithmic impedance vs. humidity graph varied with the degree of sulfonation. It changes from convex for low sulfonation over linear to concave for high sulfonation [22]. This is in good agreement with our results that show a more convex form for CAU-10-O/S, which has a two times lower sulfonate content than the CAU-10-N/S sample. Even though the two samples are different from each other with respect to their additional functionalities, this may be an indication of the special impact of the sulfonate group due to its high polarity.

The conductivity in “dry” conditions is determined from the parameter R at 10 % r.h.. (Fig. 7. At 0 % r.h. no distinct plateau is observed, and the data cannot be fitted by this model). Taking the geometrical factors into account conductivities of 4.870×10^{-13} S/cm for the CAU-10-N/S and 6.922×10^{-12} S/cm for the CAU-10-O/S sample are obtained. Extrapolation of the R/r.h. plot to 0 % r.h. delivers values which are smaller by up to one order of magnitude.

So far no other conductivity investigations for this particular kind of MOF can be found in the literature. However, comparing the conductivity of our samples to other MOFs reveals that it is lower by several orders of magnitude. For example, Koboyashi et al. determined values of 10^{-8} S/cm for Cu[Ni(pdt)$_2$] (pdt^{2-} = pyrazine-2,3-dithiolate)[23]. Talin et al. modified the conductivity of Cu$_3$-(BTC)$_2$ (also known as HKUST-1; BTC, benzene-1,3,5-tricarboxylic acid) by infiltrating a guest molecule into the pores, resulting in ohmic conductivities around 10^{-2} S/cm for an otherwise insulating MOF. The charge transport is explained by the interaction of the TCNQ guest molecule with the accessible metal sites [24].

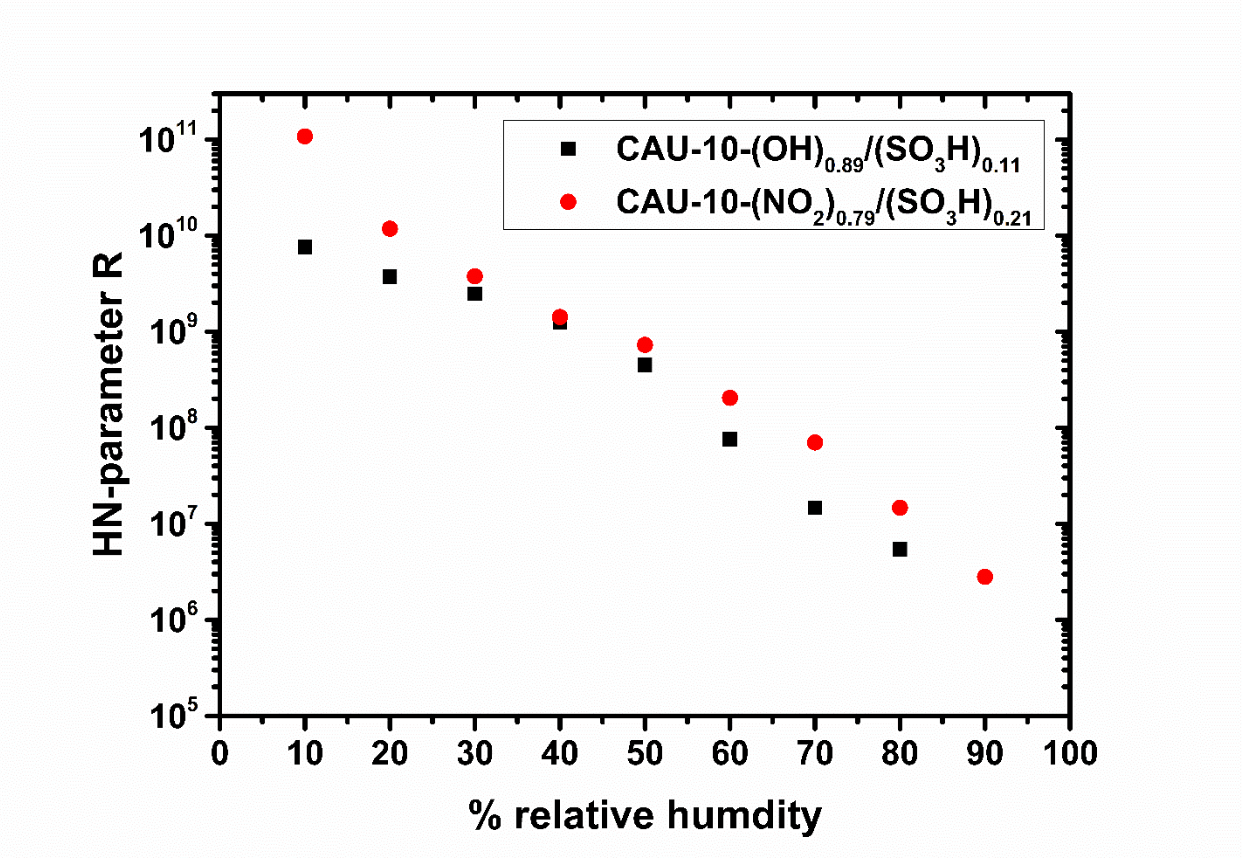

Figure 7. Dependence of the HN-parameter R on the relative humidity for the samples CAU-10-O/S and CAU-10-N/S.

The CPE parameter Q shows a behavior similar to that of R, but in opposite direction, i.e. it increases with humidity (Figure 8). For the CAU-10-N/S the trend is approximately exponential, whereas for the CAU-10-O/S the increase is a bit stronger (as opposed to the behavior which the samples show in the water sorption measurements). However, correlation of Q with the parameter R confirms that they are widely linearly independent (-0.51 for CAU-10-O/S, -0.25 for CAU-10-N/S). Therefore the selected model is not over-determined. Compared to the capacitance determined without the HN-model, the parameter Q approaches a more linear shape in the logarithmic plot, i.e. shows an exponential humidity dependence. Liu et al. specify a linear response of capacitance to changes in relative humidity for Cu-BTC, but this only applies to the special case of high frequencies (1 MHz). In principle, the dependence in that study seems to be rather exponential, as is apparent from their SI; frequency spectra to estimate more details are not shown [25].

Taking a closer look at CAU-10-N/S, a nearly linear trend in water sorption measurements at relative pressure between 0.1 and 0.8 is apparent, which is accompanied by an exponential trend in capacitance in the same range. This may be explained by a spacial dependence of the water permittivity. In the vicinity of the pore walls water molecules are stronger attached to the surface groups, which reduces their permittivity. Paul and Paddison calculated that influence in hydrated, sulfonic acid-decorated micropores of various polymers finding a steep reduction of the permittivity. For pore wall distances smaller than ca. 0.8 - 0.9 nm it starts to drop from values of ca. 80 (bulk permittivity) to ca. 10. [26]. Taking into account that pore filling starts at the pore walls, an overlap of adsorption curve and permittivity curve may be a reason for the resulting exponential-like dependence of Q (capacitance).

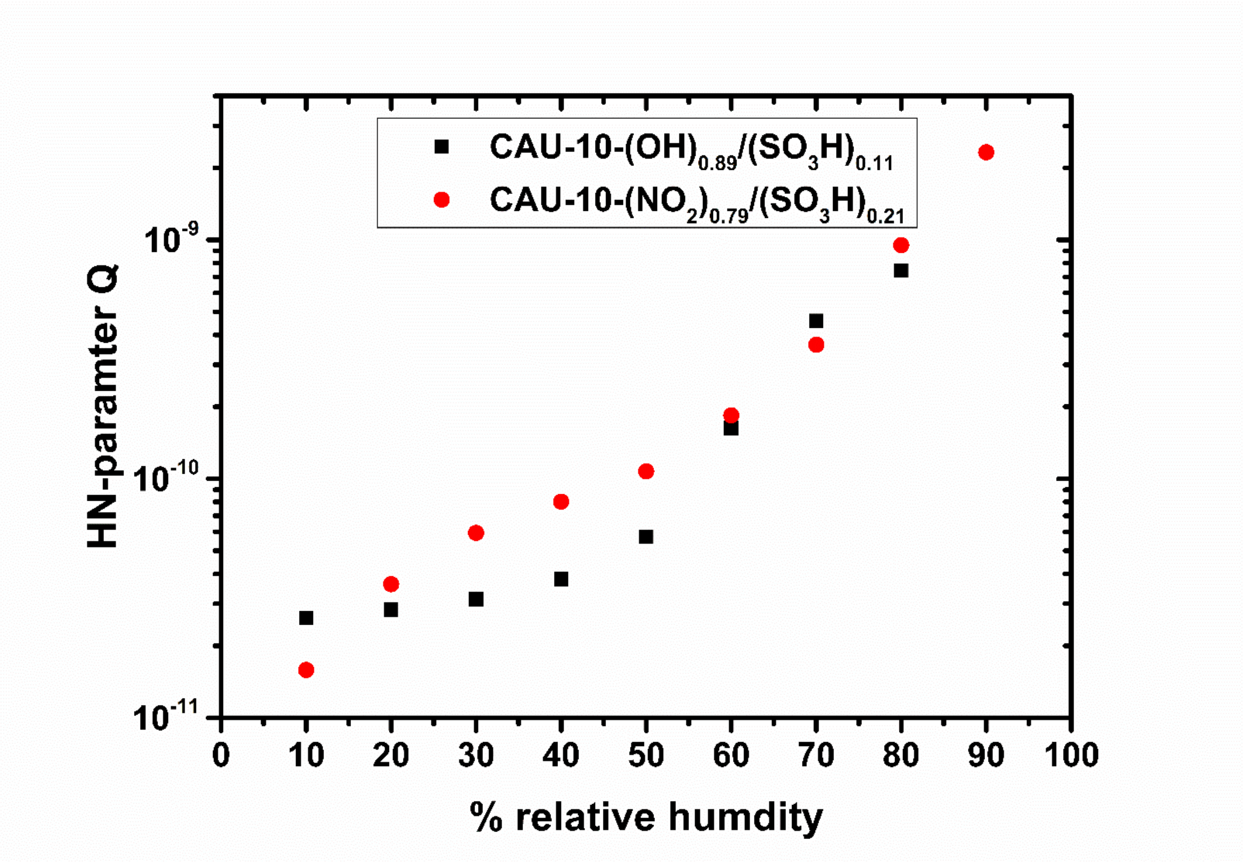

Figure 8. Dependence of the HN-parameter Q on the relative humidity for the samples CAU-10-O/S and CAU-10-N/S.

The humidity dependence of the HN parameters α and β is shown in Figure 9. For both samples the parameters are clearly correlated to each other with a Pearson product-moment correlation coefficients (PPMCC) of -0.87 for the CAU-10-O/S and -0.78 for the CAU-10-N/S sample. This may be attributable to the fact that fitting of left-skewed arcs (compare Fig. 6) requires values of $\beta > 1$ and therefore very close to the constraint $\beta < 1/\alpha$. Both samples show qualitatively nearly the same trend, but the parameters for CAU-10-N/S deviate stronger from 1 than those of CAU-10-O/S. This indicates a broader relaxation time distribution and/or further involved processes. It cannot be clearly determined whether this is due to the higher sulfonate content of CAU-10-N/S or due to the stronger influence of the NO_2 residual group, or a combination of both effects.

In the low humidity region the trends of α and β show a narrowing of the relaxation time distribution with increasing humidity. At 50 % or 60 % r.h., depending on the sample, the trend develops in opposite direction, which suggests a gradual change in conduction mechanisms. Hurd et al. reported on the conductivity change of β-PCMOF2 with dehydration. They compared their findings to the loss of proton conduction in sulfonated ionomers, because water is crucial for the Grotthus as well as for the vehicle mechanisms [16]. We suggest that the critical H_2O concentration for the samples investigated can be read from maxima and minima in parameter α and β, respectively.

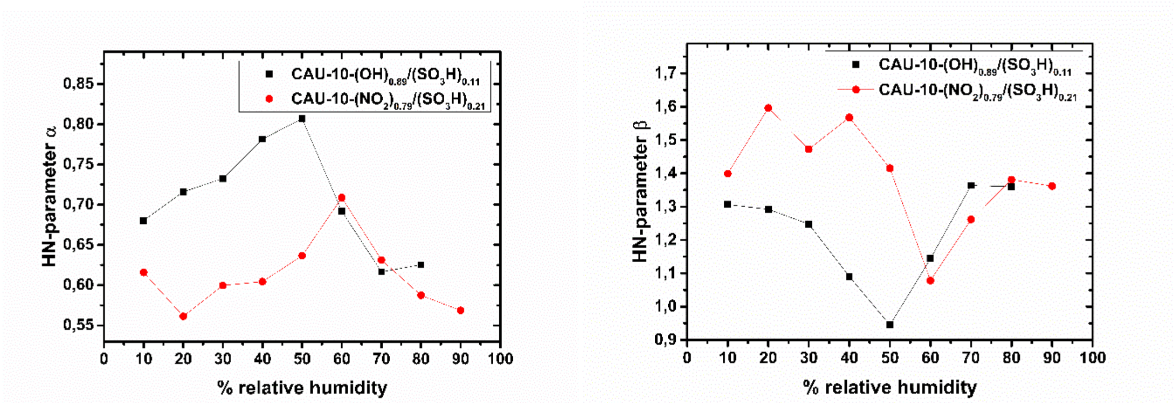

Figure 9. Dependence of the HN-parameter α (left) and β (right) on the relative humidity for the samples CAU-10-O/S and CAU-10-N/S.

Application test

To estimate the application potential in humidity sensing, CAU-10-N/S was further investigated in an ambient air control scenario for ca. 60 hours. CAU-10-N/S was chosen because it showed a more linear trend in the HN parameters R and Q than CAU-10-O/S. The low frequency tail of the spectrum is not suitable for this kind of application, because mHz measurement cycles require too much time. Consequently, one cannot perform adequate data fitting, as carried out in the previous section. Therefore, measurements were conducted using the frequency range between 1 Hz and 30 MHz (Fig 3, setup b) and only basic data evaluation (compare Eq (1) in Ref. [12]). The sample holder was placed in a glass tube (length 20 cm) in the middle of a room, to avoid any potential influence of direct air flow close to the material.

Additionally, a conventional temperature and humidity sensor was placed in the same tube as a reference (Sensirion SHT21).

For test No.1, which was partially already presented in [12], one room window was kept slightly opened during the whole measurement to obtain a weak interchange between indoor and outdoor air. The trend of relative humidity is similar, but not equal to that of absolute humidity (a.h.), because of variations in the temperature (Fig. 10 c). Among the number of possible electrical quantities, Re(Z) as well as Re(C) correspond the best with the measured humidity at first view. At points where one quantity differs from the reference measurements, the other can be utilized (Figure 10). To obtain general statements for the correlation of humidity and electrical quantities the Pearson product-moment correlation coefficients (PPMCC) were calculated at several frequencies (1 Hz, 10 Hz, 10^3 Hz, 10^4 Hz, 10^5 Hz). The results can be summarized by the following statements: (i) Re(C) correlates better with relative humidity than with absolute humidity values; (ii) Re(Z) correlates better with absolute humidity than with relative humidity values; (iii) absolute humidity correlations for both quantities are better at low frequencies; (iv) relative humidity correlations for both quantities are better at high frequencies. The correlation coefficients of Re(Z) are negative and only considered as absolute values and the first two statements are stronger than the last ones, i.e. their influence on the correlation coefficient is almost 1 order of magnitude larger.

The correlation between Re(C) and relative humidity was expected, since many commercially available sensors are based on this principle. Water with its high electrical permittivity changes the capacitance of a porous material proportionally to its amount adsorbed in the pores. This amount mainly depends on the relative humidity. The temperature dependence of this adsorption is only weak in the temperature range in which sensors are typical operated. However, in the intervals 0-100 min and 1900-2200 min the Re(Z) correlates better with the absolute humidity a.h. (Figure 10). A more detailed analysis of the temperature reveals that these two time intervals show the strongest temperature change (+0.00661 °C/min and -0.00273

°C/min, respectively). This suggests that non-equilibrium conditions account for the effect. A potentially higher heat capacity of the MOF material would be insufficient as the only explanation, as it would act in the opposite direction for opposite temperature changes, which is not the case (not shown).

The impedance, in contrast to the capacitance, depends not only on the amount of water adsorbed, but mainly on the interconnection of water molecules to the surface and between water clusters and layers themselves. Percolation effects or changes in mechanism as mentioned in the previous section may play a role.

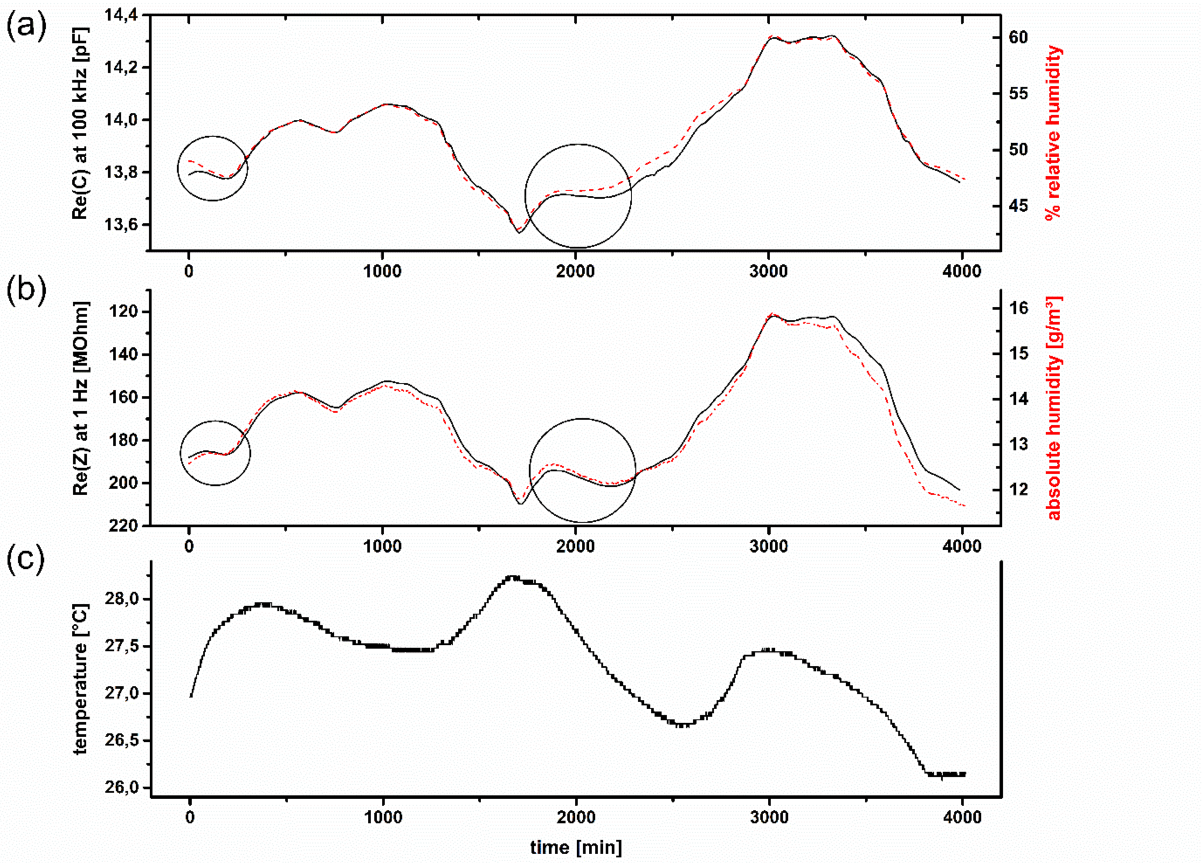

Figure 10. Application test No.1 for CAU-10-N/S. Re(C) at 100 kHz compared to relative humidity (a); Re(Z) at 1 Hz (reversed scale) compared to absolute humidity (b); and temperature (c); (Humidity measurands in dashed lines).(a and c are already shown in [12])

The sensor response at drastic atmosphere changes was further analyzed in test No.2. In this case both the temperature and the humidity in the room were approximately kept constant for

270 min, followed by opening a window for 30 minutes. Figure 11 (c) shows that the temperature drops until t = 360 min at a rate of -0.0457 °C/min during the first few minutes. The humidity trends shown on the right scales in Figure 11 (a) and (b) change soon after the window is closed at t = 300 min. The electrical quantities (left scale in Figure 11 (a) and (b)) reveal a weak correlation with relative humidity. A better correlation is observed for the absolute humidity, especially that in case of Re(Z), which is in good agreement with the results from test No.1.

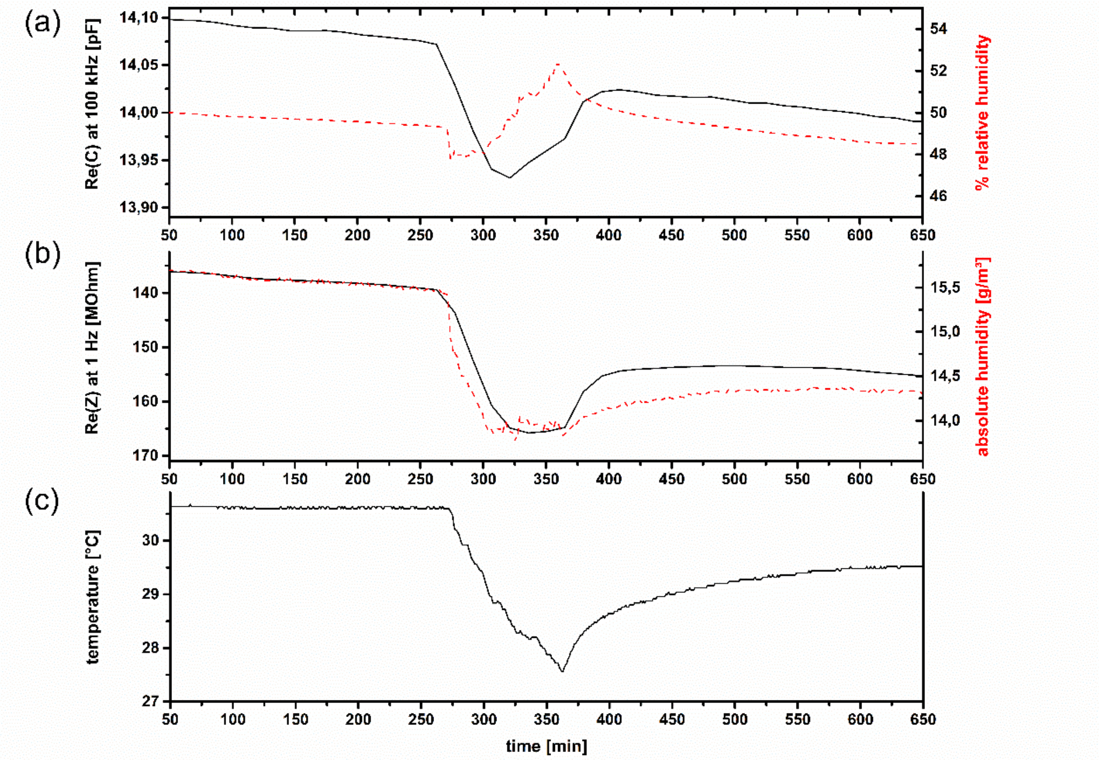

Figure 11. Application test No.2 of CAU-10-N/S during the opening of a window from minute 270 to 300. Re(C) at 100 kHz compared to relative humidity (a); Re(Z) at 1 Hz (reversed scale) compared to absolute humidity (b); and temperature (c); (Humidity in dashed lines).

Conclusion

CAU-10-type MOF materials with different linker molecules were investigated with respect to their electrical and dielectrical response to humidity. Frequency ranges down to 1-10 mHz are necessary to obtain reliable data for this kind of material. Data fitting is accomplished by the Havriliak-Negami (HN) model, which is not over-determined. It is worth mentioning that the HN parameter β is only restricted by the expression $\beta < 1/\alpha$. Values of $\beta > 1$ are necessary to fit arcs with left shifted maxima in Nyquist plots.

The DC resistance (represented by the HN parameter R) under dry conditions is significantly higher than for other reported types of MOFs. It decreases approximately exponentially with increasing humidity. The deviation from this relation may be correlated with the sulfonic acid content. R shows high sensitivity with responses up to 5 orders of magnitude over the whole humidity range

The exponential humidity dependence of HN parameter Q in comparison to a linear trend of the water sorption isotherms is explained by an overlap of the adsorption curve with the variation of the water permittivity near the pore wall. The HN-parameters α and β are correlated to each other to some extend and may be indicators for a change in conduction mechanism along the pore channels caused by hydration/dehydration of the sample.

Due to their thermal stability the investigated MOF materials exhibit the potential for high temperature applications. It is shown that they already exhibit distinct responses even for small condition changes in an ambient air control scenario, although the reaction is relatively slow. Beside the expected correlation of electrical measurement parameters to relative humidity, a good correlation of Re(Z) to absolute humidity is also observed in intervals with the strongest relative change in temperature. We suggest that non-equilibrium conditions and maybe percolation effects account for this correlation.

Frequency ranges down to 1-10 mHz are necessary to obtain reliable data for this kind of materials; data fitting is accomplished by the Havriliak-Negami (HN) model. The DC conductivity (represented by the HN parameter R) under dry conditions is in the range of 10^{-14} to10^{-13} S/cm, and thus significantly lower than for other types of MOFs (10^{-8} S/cm). The parameters α and β from the HN model may be indicators for a change in conduction mechanism along the pore channels caused by hydration/dehydration of the sample.

Acknowledgement

We acknowledge the financial support by the German Federal Ministry of Education and Research (BMBF, grant no. 13N12969) and the support of the project executing organization (VDI Technologiezentrum GmbH, Düsseldorf).

This work has been supported by the DFG (SPP 1362).

Supporting Information Available: Watersorption data and results from the screening measurements. This material is available free of charge via the Internet at http://pubs.acs.org.

Corresponding Author

Dr. Thorsten Wagner

Universität Paderborn

Naturwissenschaftliche Fakultät

Department Chemie

Warburger Straße 100

D-33098 Paderborn

Phone. (05251) 60 2486

Fax. (05251) 60 3423

thorsten.wagner@upb.de

Author Contributions

The manuscript was written through contributions of all authors. All authors have given approval to the final version of the manuscript.

References

[1] Senkovska, I.; Kaskel, S.; Ultrahigh porosity in mesoporous MOFs: promises and limitations. *Chem Commun.* **2014**, 50, 7089-7098.

[2] Pramanik, S.; Zheng, C.; Zhang, X.; Emge, T.J.; Li, J. New Microporous Metal-Organic Framework Demonstrating Unique Selectivity for Detection of High Explosives and Aromatic Compounds. *J. Am. Chem. Soc.* **2011**, 133, 4153-4155.

[3] Dou, Z.; Yu, J.; Cui, Y.; Yang, Y.; Wang, Z.; Yang, D.; Qian, G.; Luminescent Metal−Organic Framework Films As Highly Sensitive and Fast-Response Oxygen Sensors. *J. Am. Chem. Soc.* **2014**, 136, 5527-5530.

[4] Schlechte, L.; Wehring, B.; Klein, N.; Beese, H.; Grählert, W.; Kaskel, S. Metal-Organic Frameworks as humidity sensor. *Proceedings of the 17th ITG/GMA symposium on sensors and measurement systems*, *Nuremberg, 3-4 June 2014*. VDE Verlag GMBH: Berlin Offenbach, Germany, 2014.

[5] Meek, S.T.; Greathouse, J.A.; Allendorf, M.D. Metal-Organic Frameworks: A Rapidly Growing Class of Versatile Nanoporous Materials. *Adv. Mater.* **2011**, 23, 249-267.

[6] Allendorf, M.D.; Houk, R.J.T.; Andruszkiewicz, L.; Talin, A.A.; Pikarsky, J.; Choudhury, A.; Gall, K.A.; Hesketh, P.J. Stress-Induced Chemical Detection Using Flexible Metal-Organic Frameworks. *J. Am. Chem. Soc.* **2008**, 130, 14404-14405.

[7] Achmann, S.; Hagen, G.; Kita, J.; Malkowsky, I.M.; Kiener, C.; Moos, R. Metal-Organic Frameworks for Sensing Applications in the Gas Phase. *Sensors* **2009**, 9, 1574-1589.

[8] Y. Zhang, Y. Chen, Y. Zhang, H. Cong, B. Fu, S. Wen, S. Ruan, A novel humidity sensor based on NH2-MIL-125(Ti) metal organic framework with high responsiveness. *J. Nanopart. Res.* **2013**, 15:2014.

[9] Michell Instruments. Data Sheet H6000 capacitive humidity sensor, www.michell.com, downloaded 11. Feb. 2015.

[10] Reimer, N.; Leubner, S.; Bueken, B.; de Vos, D.; Stock, N. Chemistry of Materials, in preparation.

[11] Wagner, T.; Krotzky, S.; Weiß, A.; Sauerwald, T.; Kohl, C.-D.; Roggenbuck, J.; Tiemann, M. A High Temperature Capacitive Humidity Sensor Based on Mesoporous Silica. *Sensors* **2011**, 11, 3135-3144.

[12] Weiss, A.; Reimer, N.; Stock, N.; Tiemann, M.; Wagner, T. Screening of Mixed-linker CAU-10 MOF Materials for humidity Sensing by Impedance Spectroscopy. *Microporous and Mesoporous Materials*, submitted 2015.

[13] Reinsch, H.; van der Veen, M.A.; Gil, B.; Marszalek, B.; Verbiest, T.; de Vos, D.; Stock, N. Structures, Sorption Characteristics, and Nonlinear Optical Properties of a New Series of Highly Stable Aluminum MOFs. *Chem. Mater.* **2012**, 25, 17-26.

[14] Sing, K.S.W.; Everett D.H.; Haul, R.A.W.; Moscou, L.; Perotti, R.A.; Rouquerol, J.; Siemieniewska, T. Reporting Physisorption Data for Gas/Solid Systems with special Reference to the Determination of Surface Area and Porosity. Recommendations of IUPAC Commission on Colloid and Surface Chemistry Including Catalysis. *Pure & Appl Chem.* **1985**, 57, 603-619.

[15] Canivet, J.; Bonnefoy, J.; Daniel, C.; Legrand, A.; Coasne, B.; Farrusseng, D. Structure–property relationships of water adsorption in metal–organic frameworks. *New J. Chem.* **2014**, 38, 3102.

[16] Hurd, J.A.; Vaidhyanathan, R.; Thangadurai, V.; Ratcliffe, C.L.; Moudrakovski, I.L.; Shimizu, G.K.H. Anhydrous proton conduction at 150°C in a crystalline metal–organic framework. *Nature Chem.* **2009**, 1, 705-710.

[17] Barsoukov, E.; Macdonald, J.R. *Impedance Spectroscopy, Theory, Experiment, and Application, Second Edition*, Wiley-Interscience, Hoboken, U.S.A, 2005.

[18] Havriliak, S.; Negami, S. A Complex Plane Analysis of or-Dispersions in Some Polymer Systems, *J. Polym. Sci., C Polym. Symp.* **1966**, 14, 99-117.

[19] Davidson, D.W.; Cole, R.H. Dielectric Relaxation in Glycerol, Propylene Glycol, and n-propanol*, J. Chem. Phys.* **1951**, 19, 1484–1490.

[20] Alvarez, F.; Alegria, A.; Colmenero, J. Relationship between the time-domain Kohlrausch-Williams-Watts and frequency-domain Havriliak-Negami relaxation functions. *Phys. Rev. B* **1991**, 44, 7306-7312.

[21] Weron, K. Havriliak-Negami Response in the Framework of the continuous-time random walk*. *Acta Phys. Pol B*. **2005**, 36, 1855-1868.

[22] Sakai, Y.; Sadaoka, Y.; Matsuguchi, M. Humidity sensors based on polymer thin films. **1966**, 35-36, 85-90.

[23] Koboyashi, Y.; Jacobs, B.; Allendorf, M.D.; Long, J.R. Conductivity, Doping, and Redox Chemistry of a Microporous Dithiolene-Based Metal-Organic Framework. *Chem. Mater.* **2010**, 22, 4120-4122.

[24] Talin, A.A.; et al., Tunable Electrical Conductivity in Metal-Organic Framework Thin-Film Devices, *Science* **2014**, 343, 66.

[25] Liu, J.; Sun, F.; Zhang, F.; Wang, Z.; Rui. Zhang, R.; Wang, C.; Qiu, S. In situ growth of continuous thin metal–organic framework film for capacitive humidity sensing. *J. Mater. Chem.* **2011**, 21, 3775.

[26] Paul, R.; Paddison, S.J. A statistical mechanical model for the calculation of the permittivity of water in hydrated polymer electrolyte membrane pores. *J. Chem. Phys.* **2011**, 115, 7762.

4.3.8. New group 13 MIL-53 derivatives based on 2,5-thiophenedicarboxylic acid

Der folgende Artikel wurde im Jahre 2015 in der Fachzeitschrift *Journal of Materials Chemistry A*, *RSC* zur Begutachtung eingereicht.

Im Rahmen dieser Arbeit wurden drei isoretikuläre Verbindungen [M(OH)(TDC)]·Lösungsmittel (M-MIL-53-TDC) basierend auf 2,5-Thiophendicarbonsäure (H_2TDC) und dreiwertigen Kationen (M = Al^{3+}, Ga^{3+}, In^{3+}) hergestellt und charakterisiert. Bei der 2,5-Thiophendicarbonsäure handelt es sich um eine Dicarbonsäure, bei der die Säuregruppen einen Winkel von 148° zueinander einnehmen. Daher wurde eine strukturelle Analogie zu anderen bereits bekannten, auf gewinkelten Linkermolekülen basierenden Al-MOFs wie CAU-10[25] (Isophthalsäure, Winkel zwischen Carbonsäuregruppen 120°) oder CAU-15[67] (Phthalsäure, Winkel zwischen Carbonsäuregruppen 60°) erwartet. In diesem Fall bildeten sich jedoch Analoga zu Al-MIL-53, welches bis dato nur mit linearen Dicarbonsäuren hergestellt wurde. Zusätzlich sind diese Verbindungen die ersten MIL-53 Derivate die ein S-haltigen Heteroaromatmolekül enthalten. Die Strukturbestimmung von Al-MIL-53-TDC erfolgte aus Röntgenpulverdaten in Kombination mit Kraftfeldrechnungen und wurde mittels Festkörper-NMR Messungen (^1H, ^{13}C, ^{27}Al) verifiziert.

Alle drei Materialien weisen eine permanente Porosität auf, wobei Al-MIL-53-TDC mit einer spezifischen Oberfläche von 1151 m^2g^{-1} und einem Mikroporenvolumen von 0.48 cm^3g^{-1} heraussticht. Auch gegenüber anderen Gasen sowie Wasserdampf zeigt Al-MIL-53-TDC die höchste Aufnahmekapazität. Ga- und In-MIL-53-TDC sind gegenüber Wasserdampf hingegen nicht stabil. Mit 5.5 Wassermolekülen pro Formeleinheit liegt Al-MIL-53-TDC dabei nur knapp unter dem Wert für Al-MIL-53-OH, welches mit 6 Molekülen H_2O pro Formeleinheit die höchste Kapazität der funktionalisierten Al-MIL-53 Derivate aufweist. Dabei zeigt die Isotherme von Al-MIL-53-TDC eine sogenannte S-Form, mit einem sprunghaften Anstieg im Bereich von etwa $p/p_0 = 0.35$, was, in Kombination mit der hohen thermischen Stabilität bis 420 °C, eine potentielle Anwendung im Bereich von Wärmeaustausch-Prozessen ermöglicht. Cyclische Messungen bestätigen zudem die Stabilität des Materials. Die Kapazität für H_2 liegt mit 2.1 wt% deutlich oberhalb der Werte für unfunktionalisiertes Al-MIL-53 sowie Al-MIL-53 dotiert mit Alkali- oder Erdalkalimetallen.

Journal Name

RSCPublishing

ARTICLE

Cite this: DOI: 10.1039/x0xx00000x

New group 13 MIL-53 derivatives based on 2,5-thiophenedicarboxylic acid

N. Reimer,[a] C.-W. Hsu,[b] H. Reinsch,[a] R. Siegel,[c] J.-J. Chen,[d] C.-H. Lin,[b] A. Cadiau,[e] C. Serre,[e] J. Senker [c] and N. Stock*[a]

Received 00th January 2012,
Accepted 00th January 2012

DOI: 10.1039/x0xx00000x

www.rsc.org/

New rigid M^{3+}-based (M = Al, Ga, In) metal-organic frameworks (MOFs) of the composition [M(OH)(TDC)]·solvent, (M-TDC), TDC = 2,5-thiophenedicarboxylate were synthesized and characterized in detail. Due to the poor quality of the PXRD measurements of all compounds, only structural models could be obtained by a combination of force-field calculations and ^1H, ^{13}C and ^{27}Al solid-state-NMR measurement. The structure of these compounds is related to the MIL-53-type structure, containing chains of *trans* corner-sharing AlO_6-octahedra, connected by the linker molecules to form square-shaped 1-D channels. These compounds are the first example of MIL-53 analogues based on a sulfur-containing linker molecule. Their synthesis is easily scaled-up using microwave assisted solvothermal conditions and high yields (84 %) are obtained. All materials possess high thermal stability up to 420 °C in air and show permanent porosity towards N_2, H_2, CO_2, and CH_4. The specific surface area of the Al-based compound is determined as $a_{s,BET} = 1150\ m^2g^{-1}$ and the micropore volume at $p/p_0 = 0.5$ is $V_{mic} = 0.48\ cm^3g^{-1}$. The water vapor measurement reveals an uptake of 5.5 H_2O molecules per sum formula (469 mg/g) and shows a characteristic S-shape. The adsorbed amount of H_2 up to 1 bar is 2.1 wt% and lies above other Al-MIL-53 compounds based on linear functionalized terephthalates.

1. Introduction

Within the last years, metal-organic frameworks (MOFs) have drawn much attention in the field of porous materials.[1-3] MOFs are constructed in a modular way from inorganic and organic building units. By replacing one of the building units by a chemically different but topologically equivalent unit, it is possible to modulate the properties of a compound. This so-called isoreticular chemistry[4] enables a broad field of potential applications for this compounds, such as gas storage and separation, catalysis or drug delivery.[5-7] For the synthesis of isoreticular compounds high-throughput (HT) methods have proven to be an important and efficient tool, since the replacement of one component in a reaction mixture often necessitates to optimize the reaction conditions.[8-10]

The focus of our work is on MOFs based on trivalent cations, in particular on aluminum, since these materials are known for their excellent thermal and chemical stability.[11, 12] These properties distinguish Al-MOFs as potential candidates for gas storage and separation or heat transformation processes.[13-16] Beneficial for industrial applications are the facts, that the Al sources are generally inexpensive, that aluminum is a light metal and of low toxicity.[17]

A very well-known Al-MOF based on terephthalic acid is Al-MIL-53 (MIL = Materiaux de l'Institut Lavoisier).[18] Its framework is constructed from chains of *trans* corner-sharing AlO_6-octahedra with adjacent Al^{3+}-ions bridged by μ-OH groups. The chains are interconnected by the carboxylate groups of the linker molecules to form a 3D-network with lozenge-shaped pores. The characteristic for MIL-53 is its breathing behavior. Indeed, depending on the incorporated guest molecules, the temperature or the mechanical pressure, the framework can be open and close.[19-24] To tune the properties concerning flexibility, thermal stability as well as sorption behavior, MIL-53 derivatives based on functionalized terephthalates,[11, 12, 25-27] aliphatic linker molecules like cyclohexenedicarboxylic acid or fumaric acid[28-30] or even extended aromatic linker molecules, have been synthesized.[31-34] Interestingly, the extended frameworks seem less flexible than the parent material. For all published compounds, the carboxylate groups are in a linear arrangement. To investigate the influence of the linker shape on the formation of the inorganic unit we recently expanded our research on V-shaped linkers. Based on (functionalized) isophthtalates some of us obtained the new compound CAU-10 (CAU stands for Christian Albrecht University), [Al(OH)(*m*-BDC-X)], (X = -H, $-CH_3$, $-OCH_3$, $-NO_2$, $-NH_2$, -OH), with chains of *cis* corner-sharing AlO_6-octahedra.[35] With an exocyclic bond angle of 148°, 2,5-thiophenedicarboxylic acid H_2TDC lies nearly in the middle between the bond angles of isophthalic acid (120°) and terephthalic acid (180°).[36] Hence, the upcoming question is, if a structure based on thiophenedicarboxylates will favor the formation of chains of *trans* or *cis* corner-sharing AlO_6-octahedra. To the best of our knowledge, up to now, no Al-MIL-53 derivative based on a 'small' bended linker molecule or a heterocyclic linker molecule has been published. Only one example is known for Ga-MIL-53, based on camphoric acid.[37] Interestingly, extended V-shaped linker molecules already resulted in structures based on chains of *trans* corner-sharing AlO_6-octahedra. [38] [39]

H_2TDC is quite common in the synthesis of MOFs (Table S1). So far, several compounds have been published based on di-, tri- and tetravalent cations. Among these, only a few porous compounds with the metal ions Zn^{2+}, Cu^{2+}, Sc^{3+}, In^{3+}, La^{3+}, Zr^{4+} and Hf^{4+} have been reported.[36, 40-44] The structure of NOTT-401 is based on chains of *cis* corner-sharing ScO_6-octahedra,[41] similar to CAU-10,[35] which are interconnected by the linker molecules to form square-shaped channels with a diameter of 6.3 Å. This compound is thermally highly stable and shows a high uptake of 2.3 wt% of hydrogen up to 1 bar at 77 K. In addition, Yang et al very recently reported a copper-based compound with a high isosteric heat (7.5 - 9.2 kJ mol^{-1}) of adsorption for hydrogen .[36] The authors concluded, that this is the result of the quite narrow pore size (5.4 - 8 Å) as well as the polarizability of the thiophenedicaboxylate ion. Therefore, we tried to combine the properties of Al-based MOFs with the ones of the (porous) H_2TDC-based MOFs.

In this contribution we wanted to investigated the influence of the exocyclic bond angle of H_2TDC on the formation of the inorganic building unit of the resulting structure and its possible framework flexibility. In addition, the influence of the sulfur atom within the aromatic system on the sorption properties should be studied in detail. Therefore we present the result of our microwave assisted high-throughput investigation of the system Al^{3+}/H_2TDC/solvent. The new compound Al-MIL-53-TDC was obtained and characterized in detail by X-ray powder diffraction (PXRD), vibrational as well as solid-state NMR spectroscopy, thermogravimetric measurements and elemental analysis as well as temperature dependent X-ray powder diffraction and sorption measurements. Isoreticular compounds based on Ga^{3+} and In^{3+} were also synthesized and characterized in detail.

2. Experimental section

2.1 Materials and methods

All chemicals are commercially available and were used without further purification. HT-experiments were performed in Teflon vessels with a maximum volume of 2.5 mL which were placed in a SiC block. The block was covered with a thin Teflon foil and a silicon mat and placed between two tiles which were screwed together. This whole set-up was then placed in a microwave reaction system Synthos3000 by Anton Paar (Figure S1).[12, 45, 46] In order to scale-up the reactions, glass vials with a maximum volume of 20 mL were used and the reaction was performed in a microwave oven Initiator from Biotage.

The initial characterization by means of Powder X-Ray Diffraction (PXRD) methods was carried out on a STOE-Stadi-P Kombi diffractometer (CuKα_1 radiation) equipped with a xy stage and an image plate detector. The PXRD data for the structure determination and refinement was collected on a STOE-Stadi-P diffractometer (CuKα_1 radiation) equipped with a mythen detector. Force-field calculations for structural optimization were performed using Materials Studio[47] and all processing of PXRD data was carried out using TOPAS Academics.[48] IR spectra were recorded on a Bruker ALPHA-FT-IR A220/D-01 spectrometer equipped with an ATR-unit. The thermogravimetric (TG) analysis was carried out using a NETSCH STA 409 CD analyzer. The sample was heated in Al_2O_3 crucibles at a rate of 4 K min^{-1} under a flow of air (25 mL min^{-1}). The temperature-dependent PXRD experiment was performed in Debye–Sherrer mode on a STOE Stadi-P diffractometer (Cu-Kα_1, λ = 1.5406 Å) equipped with a STOE high temperature capillary furnace. Each powder pattern was recorded in the range of 3 to 90° (2Θ). Al-MIL-53-TDC was investigated in the range of 20 °C up to 580 °C in steps of 40 °C. Each measurement was collected for 15 minutes and the heating rate was 20 Kmin^{-1}. SEM pictures were collected on a JEOL JSM 7600F microscope. The contents of carbon, hydrogen, nitrogen and sulfur were determined by elemental chemical analysis on a EuroVector EuroEA Elemental Analyzer. Gas sorption experiments were performed using a BEL JAPAN INC. Belsorp$_{max}$ instrument. Measurements using N_2 and H_2 were performed at 77 K and measurements using CH_4, CO_2 and H_2O vapor at 298 K. Prior to each measurement Al-MIL-53-TDC was activated at 250 °C over night at 10^{-2} kPa. All solid-state NMR experiments were acquired on Bruker Avance-III HD spectrometers operating at a B_0 field of 14.1 T (^{1}H and ^{27}Al) and 9.4T (^{13}C). ^{1}H (600.15 MHz) high-resolution spectra were acquired after a 90^0 pulse of 1.4 μs with a spinning speed of 62.5 kHz using a commercial 1.3mm MAS double resonance probe (Bruker). ^{13}C (100.6 MHz) MAS spectra were obtained with a ramped cross-polarization (CP)[49] experiment where the nutation frequency ν_{nut} on the proton channel was varied linearly by 30%. The samples were spun at 12.5 kHz in 3.2mm MAS triple resonance probe (Bruker). The corresponding ν_{nut} on the ^{13}C channel and the contact time were adjusted to 70 kHz and 3.0 ms, respectively. Proton broadband decoupling with spinal-64[50] was applied during acquisition. Both the ^{1}H and ^{13}C spectra are referenced with respect to TMS (tetramethylsilane) using the secondary standard adamantane. Finally, the ^{27}Al (156.4 MHz) 1D experiments were acquired after a 3^0 flip angle of 0.5 μs with a spinning speed of 40 kHz (1.9mm probe). The reference was set using a solution of $AlCl_3$ adjusted to pH of one with hydrochloric acid. The ^{27}Al STMAS spectrum was acquired with a spinning rate of 40 kHz using the

DQF-STMAS-split-t1 pulse sequence.[51] The ^{27}Al 1D NMR spectra were simulated using the program DMFIT.[52]

The materials and methods for the synthesis and characterization of Ga-MIL-53-TDC and In-MIL-53-TDC can be found in the Supporting Information.

2.2 Synthesis

High-throughput methods are a powerful tool to systematically screen reaction systems with multiple parameters. Reaction trends are easily investigated and reaction conditions for newly discovered compounds can efficiently be optimized.[10, 53] During the HT-MW investigation of the system Al^{3+}/H_2TDC/solvent the compound Al-MIL-53-TDC was discovered. For the optimization of the crystallinity and phase purity several parameters were varied. The syntheses were performed in the temperature range of 100-140 °C and the reaction time was varied from 2-5 h. As Al^{3+}-sources $AlCl_3·6H_2O$, $Al(NO_3)_3·9H_2O$, $Al_2(SO_4)_3·18H_2O$ and $Al(ClO_4)_3·9H_2O$ were used. Different solvents (H_2O, DMF, ethanol and methanol) as well as solvent mixtures (H_2O/DMF) were tested.

The optimized reaction conditions for the HT-MW-set-up are as follows: A mixture of $AlCl_3·6H_20$ (57.9 mg, 0.24 mmol), 2,5-thiophenedicarboxlic acid (31.0 mg, 0.18 mmol), 900 µL DMF and 100 µL H_2O was placed in the Teflon vessels and the reaction was performed at 100 °C for 5 h. The initial heating power was 800 W, which was reached within 2 min and was held for 4 min. After reaching 100 °C the power was automatically set to keep the temperature constant. Upscaling was possible to the twentyfold amount using glass vials and the Initiator microwave oven by Biotage. The reaction conditions are as follows: A mixture of $AlCl_3·6H_20$ (1158 mg, 4.8 mmol), 2,5-thiophenedicarboxlic acid (620.0 mg, 3.6 mmol), 18 mL DMF and 2 mL H_2O was placed in the glass vials and the reaction was performed at 100 °C for 5 h. To remove residues of unreacted linker molecules the as synthesized compound was washed with an excess of DMF for 1 h at 150 °C under microwave heating resulting in 880 mg (3.0 mmol) $[Al(OH)(TDC)]·1.5H_2O·0.7DMF$ (Al-MIL-53-TDC). Yield: 84 % related to the amount of H_2TDC. Elemental analysis: calc. C: 33.3 %, H: 2.7 %, N: 3.4 %, S: 11.0 %; meas. C: 34.4 %, H: 2.9 %, N: 3.6 %, S: 11.6 %. These results are in good agreement with the thermogravimetric analysis.

Details of the synthesis of $[Ga(OH)(TDC)]·0.5H_2O·1DMF$ (Ga-MIL-53-TDC) and $[In(OH)(TDC)]·0.25MeOH·1DMF$ (In-MIL-53-TDC) can be found in the Supporting Information.

3. Results and discussion

3.1 Structural characterization

Structure modelling All three compounds were obtained as microcrystalline powders (Fig. S2 and S3). In order to set up structural models, the PXRD patterns were indexed using TOPAS academics.[48] Due to the low number of resolved reflections in all cases, the suggested solutions were not unique. Based on these results a plausible unit cell with primitive orthorhombic symmetry could be developed for Al-MIL-53-TDC. The cell parameters obtained from Pawley fitting (a = 13.276(2) , b = 14.605(3) and c = 14.712(3) Å) were taken as benchmarks for the further modelling by force-field calculations, employing Materials Studio.[47] The cell parameter a is nearly a multiple of 6.6 Å, which is the commonly observed cell dimension of Al-MOFs with MIL-53-structure. The value corresponds to the periodicity along the chains of *trans*-connected AlO_6-polyhedra. We attributed the apparent doubling of this cell axis to a lowered symmetry of the linker molecules. Taking the structure of Al-MIL-53-*as* (primitive orthorhombic symmetry) as a starting point, we generated a supercell with doubled size along the AlO-chains and alternating orientation of the thiophene-rings. The deduced cell parameters were fixed and full energetic minimization in the space group P1 using the Universal force field yielded a preliminary model with the space group symmetry P*nna*. However, in disagreement with this structure the solid-state NMR data indicated two crystallographically independent linker molecules (3.2). This suggested a slightly lower symmetry, e.g. in $Pna2_1$, which is a direct subgroup of P*nna*. A starting model in $Pna2_1$ was therefore generated using Powdercell and this model was again energetically minimized using the universal force field. The cell parameters of Ga-MIL-53-TDC and In-MIL-53-TDC were also deduced from Pawley-Fits of their respective PXRD patterns and models of identical $Pna2_1$ symmetry were generated using these values. The figures of merit and the unit cell parameters are displayed in Table 1 and the Pawley Fits are shown in Fig. S4-6.

Table 1 Crystallographic data of all three compounds resulting from Pawley refinements.

	Al-MIL-53-TDC	Ga-MIL-53-TDC	In-MIL-53-TDC
a / Å	13.276(2)	13.436(4)	14.066(8)
b / Å	14.605(3)	14.810(3)	15.059(4)
c / Å	14.712(3)	14.972(3)	15.422(5)
$\alpha = \beta = \gamma$ / °	90	90	90
R_{WP} / %	3.0	3.1	4.5
Goodness of Fit	1.4	2.0	2.7

Comparisons of the theoretical powder patterns generated from the calculated model with the experimental ones of all three compounds can be found in Fig. S7-9. The relative intensities differ partially due to possible disorder or defects within the frameworks and residues of incorporated solvent molecules in the pores.

Structure description. As an example, the structural model of Al-MIL-53-TDC is shown in Fig. 2. The structure is based on chains of *trans* corner-sharing AlO_6-octahedra with μ-OH groups bridging adjacent Al^{3+} ions (Fig. 2, left). The chains are interconnected by the carboxylate groups of the linker molecules to build square-shaped 1D channels along the a-axis (Fig. 2, right). These channels have a diameter of approximately 8 x 8.2 Å, which is only slightly smaller than the pores of the open form of Al-MIL-53 (~8.5 x 8.5 Å). The thiophene units are arranged in an alternating orientation

(Fig. 2, left), which results in a doubling the *a*-axis compared to the one observed for Al-MIL-53.[18]

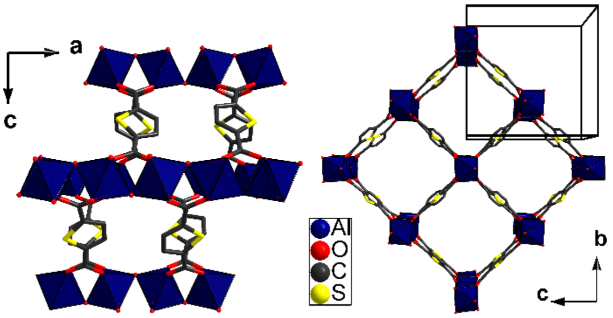

Fig. 1 Structure of Al-MIL-53-TDC. Left: Chains of trans corner-sharing AlO_6 octahedra and the alternating orientation of the thiophene units. Right: View along the *a*-axis into the lozenge-shaped pores. The black box marks the unit cell.

3.2 Solid-State NMR spectroscopy

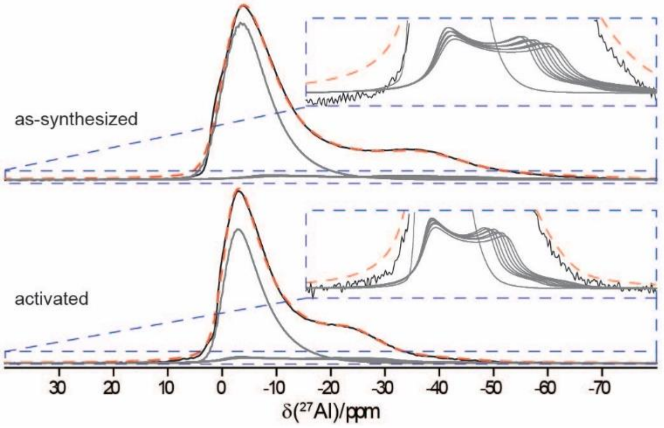

Fig. 2: ^{27}Al MAS spectra of the as-synthesized (top) and activated (bottom) Al-MIL-53-TDC together with the deconvolution (sub-spectra in grey and sum in dashed red lines) taking into account the isotropic chemical shift and a second-order quadrupolar broadening. A zoom oon the sub-spectra is shown in the insets

The ^{27}Al NMR spectra of the as-synthesized and activated Al-MIL-53-TDC (Fig. 2) both show the presence of two different Al sites with a ratio of roughly 1:1 in agreement with the crystallographic structure. Both sites exhibit significant broadening due to some chemical shift and quadrupolar interactions distribution. Indeed, the STMAS spectrum of the activated sample (Fig. 3) shows that the right side of the peaks slowly moves towards lower chemical shift values (blue dashed line in Fig. 3) indicating a distribution of the quadrupolar interaction. While the left side, stays more or lesss constant (red dashed line) indicating that the isotropic shift is changing to compensate the second-order quadrupolar shift. This distribution is more pronounced for peak 1. To correctly mimick the distribution, the ^{27}Al spectra were deconvoluted using the program dmfit[54] using two different models. The the Cz-simple model for peak 1 allows the simulation of large distribution for both the chemical shift and the quadrupolar interaction. While peak 2 was simulated using only9 (as-synthesized) and 7 (activated) subspectra since it is less distributed. For peak 1, the average isotropic shift (δ_{iso}) are -0.1 (as-synthesized) and 0.1 ppm (activated) and the average quadrupolar coupling (C_Q) are 2.1 (as-synthesized) and 2.0 MHz (activated). For peak 2 the average values are δ_{iso} = 3.6 and 5.8 ppm and C_Q = 10.8 and 9.2 MHz with η_Q = 0 for the as-synthesized and activated Al-MIL-53-TDC, respectively. Additional details are given in Table S2. This distribution is assigned to local distortions and/or small rearrangements of the framework. Finally, the larger C_Q for the as-synthesized sample is probably due to an increased distortion of the AlO_6 octahedra in the framework caused by the presence of DMF. Such changes in the C_Q were previously observed for different guest molecules in the MIL-53.[55]

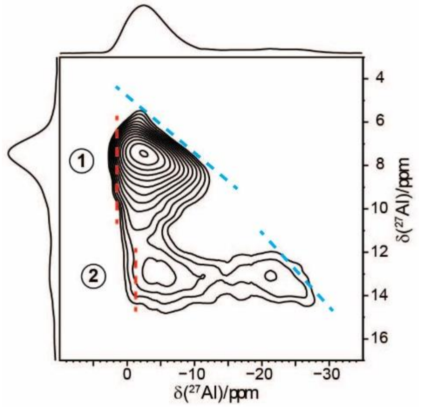

Fig. 3: ^{27}Al MAS spectra of the activated Al-MIL-53-TDC. The blue and red dashed line highlight the effect of the distribution.

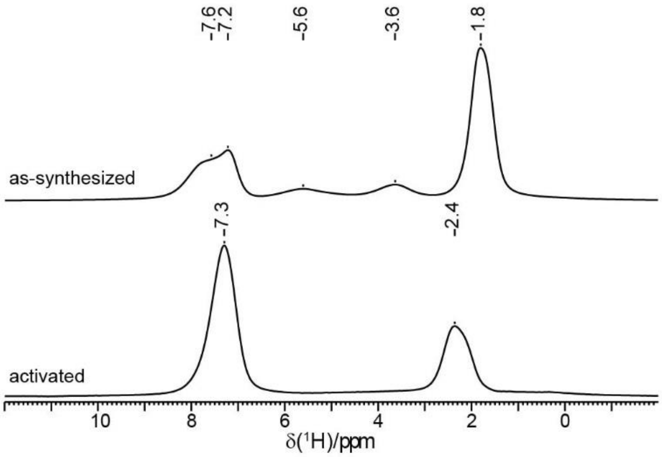

Fig. 4: ^{1}H MAS spectra of the as-synthesized (top) and activated (bottom) Al-MIL-53-TDC.

The ^{1}H NMR spectra (Fig. 4) exhibit five and two well-resolved peaks for the as-synthesid and activated sample, respectively. The signals characteristic for DMF are clearly visible at 1.8 ppm typical for the methyl protons and at 7.2 ppm assigned to the proton attached to the carboxyl group. An analysis of the relative intensities leads to approximately 0.7 DMF molecules per formula unit which matches well to the results of the TG data. The peak at 7.6 and 7.3 ppm is attributed to the ^1H of the thiophene ring. Finally, for the as-synthesized sample, the peak at 3.6 and 5.6 ppm are attributed to the adsorbed water and μ-OH, respectively. The amount of water in this sample is on the same order as the μ-OH, but hard to correctly estimate as the peak are relatively broad and almost in the baseline. Note that for the as-synthesized material the incorporation of DMF molecules leads to a downfield shift of about 3.2 ppm for the OH resonances which is probably due to hydrogen bond interactions between OH and DMF. Such chemical shifts are similar to the ones previously observed in the case of MIL-53.[55]

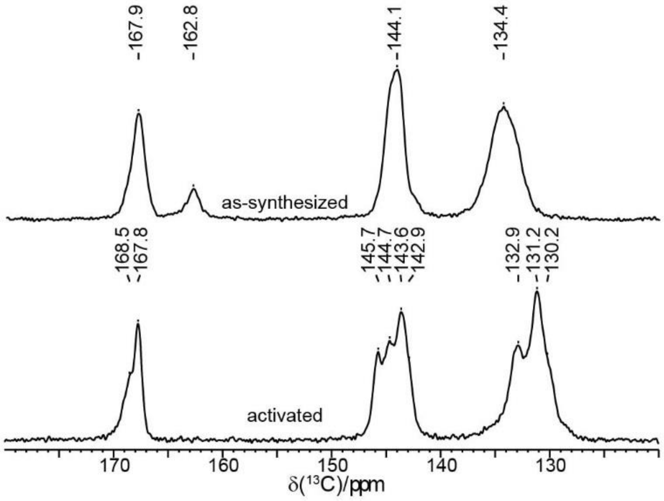

Fig. 5: ^{13}C CP-MAS spectra of the as-synthesized (top) and activated (bottom) Al-MIL-53-TDC.

The ^{13}C spectra (Fig. 5 and S10) exhibit three different regions: the carboxylic group (~ 168 ppm), the thiophene ring carbons bonded to the sulfur (~ 144 ppm) and the other carbon of the ring (~ 131 ppm). Additionaly a peak at 162.8 ppm attributed to DMF is observed for the as-synthesized MIL. As opposed to the as-synthesized sample, The activated MIL allows to differentiate several peaks in each of those regions. One can discern at least two resonances for the carboxylic groups, four different shifts for the carbons bonded to the sulfur and at least three peaks for the last carbon type. This did suggest a lower symmetry as initially proposed (P*na*2$_1$, intead of P*nna*). Finally, note that one of the carboxylic carbon (at 168.5 ppm) exhibit more distribution than the other one (at 167.5 ppm) which can be correlated to the difference of distribution observed in ^{27}Al NMR spectra.

^{27}Al, ^1H, and ^{13}C NMR spectra present noticeable differences between the as-synthesized and activated Al-MIL-53-TDC. These changes in the spectra are attributed to a rearrangement of the framework after DMF is removed upon activation. Additionanly, a large distribution is observed around the Al,which could be assigned to local distortions and/or small rearrangements of the framework. The activated sample presented two different ^{27}Al sites and two times four carbons for the thiophene ring. These are in good agreement with the P*na*2$_1$ symmetry. However, due to lower resolution, only one ^1H resonance for the thiophene ring and one for the carboxyle group were observed.

3.3 Spectroscopic analysis

IR spectroscopy. IR spectra of the as-synthesized Al-MIL-53-TDC, as well a sample washed in DMF, and a sample activated at 250 °C after the sorption measurement were collected (Fig. 3).

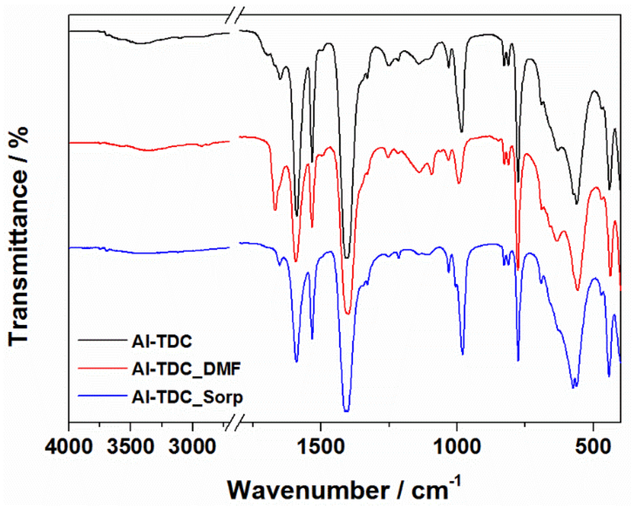

Fig. 2 IR spectra of the as synthesized compound (black), Al-MIL-53-TDC solvothermally washed with DMF (red) and Al-MIL-53-TDC after nitrogen sorption measurement (blue).

In all spectra a very small ν_{OH}-band at 3685 cm^{-1} due to µ-OH-groups in the framework is observed. A broad band at around 3390 cm^{-1} is visible, indicating H-bonds of incorporated water molecules. The characteristic signals of the asymmetric and symmetric stretching vibration of the coordinating carboxylate groups are clearly present at 1589 and 1408 cm^{-1}, respectively. The as-synthesized sample shows a small $\nu_{C=O}$-band at 1702 cm^{-1} suggesting the presence of minor residues of unreacted acid. This band disappears when the sample is treated with DMF, but the $\nu_{C=O}$-band of the DMF molecules arises at 1668 cm^{-1} due to the incorporation of DMF molecules within the pores of Al-MIL-53-TDC. After activation of the sample and the following sorption measurement no vibrations in this region are observed any longer, indicating the total removal of unreacted acid and DMF. Stretching vibrations of the aromatic ring are clearly visible at $\nu_{C=C}$ = 1651, $\nu_{C=C}$ = 1531 and ν_{C-S} = 690 cm^{-1} in all spectra.

IR spectra of Ga-MIL-53-TDC and In-MIL-53-TDC showing the same characteristic vibrations can be found in the Supporting Information (Fig. S10).

3.4 Thermal analysis

The thermal stability of Al-MIL-53-TDC under air was investigated by thermogravimetric (TG) analysis and temperature dependent powder X-ray diffraction (TD-PXRD). The result of the TG measurement is shown in Fig. 4.

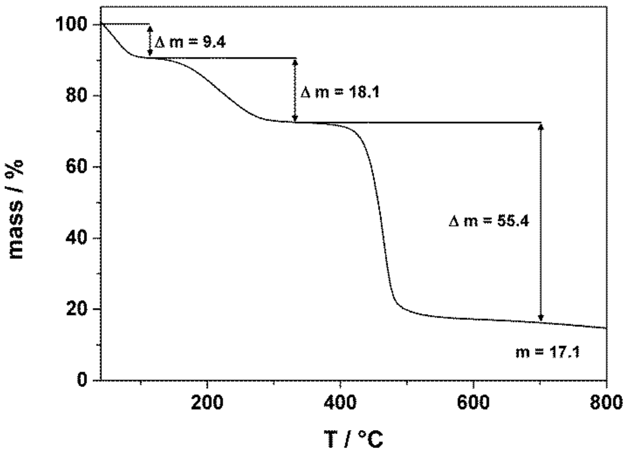

Fig. 3 Thermogravimetric measurement of Al-MIL-53-TDC.

Upon heating, the sample shows a three-step weight loss. The first step up to around 120 °C can be attributed to the removal of incorporated water molecules (meas. 9.4 %, calc. 9.3%), followed by a second step up to around 300 °C due to the removal of DMF molecules (meas. 18.1 %, calc. 17.5 %). Above temperatures of 400 °C the framework decomposes (meas. 55.4 %, calc. 55.8 %) resulting in X-ray amorphous Al_2O_3 (meas. 17.1 %, calc. 17.4 %). These results are in good accordance to the result of the TD-PXRD measurement Fig. 5. A TG curve of the activated compound is shown in Fig. S11.

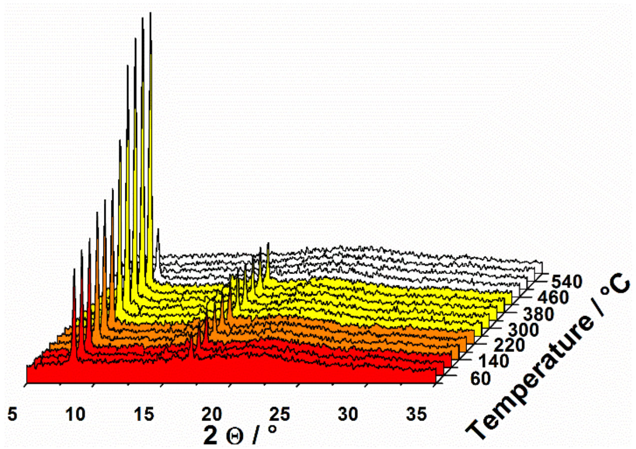

Fig. 4 TDPXRD measurement of $[Al(OH)(TDC)]\cdot 1.5H_2O\cdot 0.7DMF$ from 20 °C up to 580 °C in steps of 40 °C (Cu-Kα_1 radiation).

Up to 100 °C no change in the relative reflection intensities is observed. Above that temperature a small increase in intensity of the first reflection is observed due to the removal of incorporated water molecules, followed by a second increase in intensity starting at 220 °C due to the removal of DMF molecules. Above 340 °C no more changes are observed and above 420 °C the compound decomposes. Over the whole range no shift of any reflection is observed, revealing the rigidity of the structure.

The two other MOFs Ga- and In-MIL-53-TDC show a similar TG curve as Al-MIL-53-TDC (Fig. S12/13 and Table S3/S4). Up to 250 °C incorporated guest molecules are removed and above temperatures of 300 °C both compounds start to decompose. TD-XRPD measurements of Ga-MIL-53-TDC underline these results (Fig. S14).

3.5 Sorption properties

To probe the sorption behavior of $[Al(OH)(TDC)]\cdot 1.5H_2O\cdot 0.7DMF$, measurements using different adsorptives were performed. Nitrogen as well as hydrogen sorption measurements were carried out at 77 K. Water vapor, carbon dioxide as well as methane sorption measurements were performed at 298 K. Prior to each measurement, Al-MIL-53-TDC was activated at 250 °C over night under vacuum. The total removal of DMF molecules from Al-MIL-53-TDC was verified by IR spectroscopy (Fig. 2) and elemental analysis (meas. C: 33.4 %, H: 2.5 %, N: 0 %, S: 14.6 %; calc. C: 34.0 %, H: 1.7 %, N: 0 %, S: 15.1 %). The isotherms of the nitrogen and water vapor measurements are shown in Fig. 6. For nitrogen, Al-MIL-53-TDC shows a type-I isotherm, characteristic for microporous materials. The specific surface area is $a_{s,BET}$ = 1150 m^2g^{-1} and the micropore volume at p/p_0 = 0.5 is V_{mic} = 0.48 cm^3g^{-1} (theor. 0.56 cm^3g^{-1})[56], which is slightly lower than the value reported for Al-MIL-53 (0.54 cm^3g^{-1}).[18]

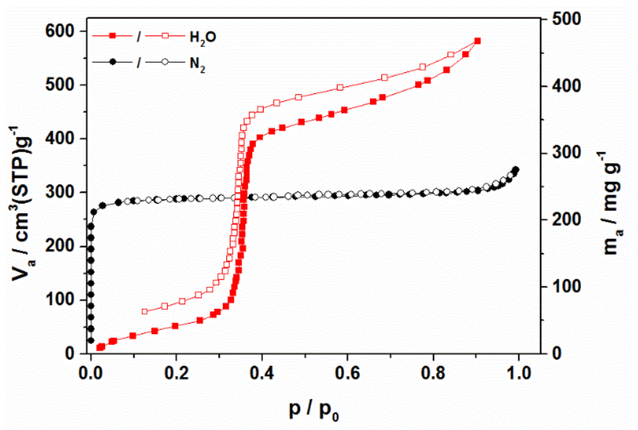

Fig. 5 Nitrogen (77 K) and water vapor (298 K) sorption measurements of Al-MIL-53-TDC.

The water vapor measurement shows an S-shaped isotherm with a maximum uptake of 469 mg g^{-1}. This value corresponds to 5.5 molecules per formula unit and is in the range of the uptake observed for Al-MIL-53-$(OH)_2$.[11] For MIL-53-$(OH)_2$ water adsorption however occurs in two steps (at p/p_0 = 0.02 and 0.4), due to the flexibility of the framework. Pore filling takes place at the second step. The desorption shows a large hysteresis, which is also explained by the framework flexibility. In contrast, for Al-MIL-53-TDC a S-shaped isotherm is observed with pore filling occuring at around p/p_0 = 0.35. A very small hysteresis is observed, which can be a result of kinetic effects due to non-equilibrium during the measurement. This measurement coinsides more with the result obtained for CAU-10-H. This compound also shows a S-shaped isotherm and is actually under investigation for applications in heat-transformation processes. [16, 57]Therefore, a first experiment of cyclic H_2O measurements was perfomed for Al-MIL-53-TDC, showing promising results (Fig. S15). No hysteresis is observed, the sorption capacity as well as the point of pore filling stay constant over two cycles and no loss in crystallinity is observed (Fig. S16). Further experiments are part of ongoing studies, but the shape of the isotherm and the relative high uptake in combination with the high thermal stability of the compound suggest a potential application in the field of heat transformation processes.

The isotherms of the hydrogen, carbon dioxide and methane sorption measurements are shown in Fig. 7. The maximum uptake of H_2 up to 1 bar is 2.1 wt%. This value is higher than for Al-MIL-53 with an uptake of 1.7 wt% and even for Al-MIL-53 doped with alkaline and alkaline earth metals (1.69-1.84 wt%).[58] The uptake for the scandium based compound [Sc(OH)(TDC)] (NOTT-401) is 2.3 wt% up to 1 bar, which is only slightly higher due to the higher specific surface area and micropore volume (1514 m^2g^{-1}/0.66 cm^3g^{-1}).[41] These results suggest, that due to the heterocyclic linker molecule stronger interactions between the framework and the hydrogen molecules are present. Similar observations on copper-based MOFs were recently made by Yang et al.[36]

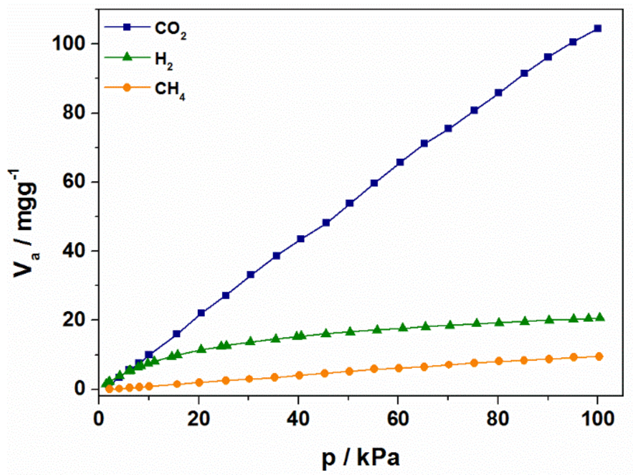

Fig. 6 Carbon dioxide (298 K), hydrogen (77 K) and methane (298 K) sorption measurements of of Al-MIL-53-TDC.up to 1 bar.

The CO_2 uptake of Al-MIL-53-TDC up to 100 kPa is 10.5 wt%. For comparison, for Al-MIL-53-NH_2 and MIL-53-NO_2 an uptake of close to 8 and 10.8 wt% was determined at this pressure.[11] The adsorbed amount of CH_4, 0.95 wt%, is in the same order than the value for Al-MIL-53 (estimated from high pressure measurement: ~1 wt% at 1 bar at 298 K).[59]

Results of the sorption measurements for Ga- and In-MIL-53-TDC can be found in the Supporting Information. For all gases the corresponding uptakes are lower with regard to the higher molecular weight of the materials (Table S5 and Fig. S17-S20). Water vapor measurements were performed but resulted in a strong decrease of crystallinity for both samples demonstrating a low stability towards moisture (Fig. S21).

4. Conclusion

In this contribution we describe the synthesis and characterization including a structural approach of compounds with the composition [M(OH)(TDC)]·solvent (M = Al, Ga, In), a new series of MIL-53 analogues. One focus of our research was the shape of the linker molecule. The exocyclic bond angle of H_2TDC is set nearly in the middle between terephthalic acid and isophthalic acid. We resulted in a structure related to MIL-53 which is based on the former one, so further investigations using 2,5-furandicarboxylic acid, with a smaller exocyclic bond angle of 125° would be interesting, to see if a structure related to CAU-10 is obtained. M-TDC is the first example of a MIL-53-type compound based on a heterocyclic linker molecule and in contrast to the MIL-53 compounds based on terephthalic acid, M-TDC shows no breathing behavior. It is exclusively obtained in an open pore form revealing a permanent porosity towards several gases and in case for Al-MIL-53-TDC also water vapor. The incorporation of a sulfur atom within the aromatic system leads to a strong polarizability of the framework which results in high uptakes of hydrogen gas and water vapor for the aluminum based material. In combination with the high thermal stability for the this compound the possibility of potential applications in the field of heat transformation processes should be taken into account. Therefore, multi-cyclic water vapor measurements are part of ongoing investigations. In addition, we have demonstrated, that with a combination of theoretical and experimental techniques, namely force-field calculations and solid-state NMR spectroscopy, it is possible to derive structural models from PXRD data with even moderate quality.

Acknowledgements

This work has been supported by the DFG (SPP 1362 and SE 1417/3-2).

Notes and references

[a] *Institut für Anorganische Chemie, Christian-Albrechts-Universität zu Kiel, Max-Eyth-Straße 2, D-24118 Kiel, Germany. E-mail: stock@ac.uni-kiel.de*

[b] *Department of Chemistry, Professor Chung Yuan Christian University, Chung-Li 320, Taoyuan, Taiwan.*

[c] *Department for Inorganic Chemistry III, University of Bayreuth, Universitätsstraße 30, D-95440 Bayreuth, Germany.*

[d] *Green Energy & Environment Research Laboratories, Industrial Technology Research Institute, Hsinchu 310, Taiwan*

[e] *Institut Lavoisier de Versailles, UMR CNRS 8180, Université de Versailles St Quentin, 78035 Versailles, France*

†

Electronic Supplementary Information (ESI) available: [Al-MIL-53-TDC: SEM micrograph , Pawle-Fit, TG of activated sample, XRD data of samples after sorption measurements, repeated water vapour measurements; Ga-/In-MIL-53-TDC: synthesis and characterization (SEM micrographs, Pawley-Fits, IR data, TG, elemental analysis, N_2, CO_2, H_2 and CH_4 sorption measurements and XRD data after sorption measurements); Ga-MIL-53-TDC: TD-PXRD data]. See DOI: 10.1039/b000000x/

1. Themed issue on Metal-Organic Frameworks, *Chem. Soc. Rev.*, 2009, **38**, 1201-1508.
2. Themed issue on Metal-Organic Frameworks, *Chem. Rev.*, 2012, **112**, 673-1268.
3. Themed issue on Metal-Organic Frameworks, *Chem. Soc. Rev.*, 2014, **43**, 5415-6172.
4. M. O'Keeffe, *Chem. Soc. Rev.*, 2009, **38**, 1215-1217.
5. M. G. Goesten, J. Juan-Alcañiz, E. V. Ramos-Fernandez, K. B. Sai Sankar Gupta, E. Stavitski, H. van Bekkum, J. Gascon and F. Kapteijn, *J. Catal.*, 2011, **281**, 177-187.
6. P. Horcajada, T. Chalati, C. Serre, B. Gillet, C. Sebrie, T. Baati, J. F. Eubank, D. Heurtaux, P. Clayette, C. Kreuz, J.-S. Chang, Y. K. Hwang, V. Marsaud, P.-N. Bories, L. Cynober, S. Gil, G. Férey, P. Couvreur and R. Gref, *Nat. Mater.*, 2010, **9**, 172-178.
7. S. Couck, J. F. M. Denayer, G. V. Baron, T. Remy, J. Gascon and F. Kapteijn, *J. Am. Chem. Soc.*, 2009, **131**, 6326-+.
8. H. Reinsch and N. Stock, *Microporous Mesoporous Mater.*, 2013, **171**, 156-165.
9. N. Stock and S. Biswas, *Chem. Rev.*, 2012, **112**, 933-969.
10. N. Stock, *Microporous Mesoporous Mater.*, 2010, **129**, 287-295.
11. S. Biswas, T. Ahnfeldt and N. Stock, *Inorg. Chem.*, 2011, **50**, 9518-9526.
12. N. Reimer, B. Gil, B. Marszalek and N. Stock, *CrystEngComm*, 2012, **14**, 4119-4125.
13. F. Jeremias, A. Khutia, S. K. Henninger and C. Janiak, *J. Mater. Chem.*, 2012, **22**, 10148-10151.
14. H. Yin, J. Wang, Z. Xie, J. Yang, J. Bai, J. Lu, Y. Zhang, D. Yin and J. Y. S. Lin, *Chem. Commun.*, 2014, **50**, 3699-3701.
15. F. Gándara, H. Furukawa, S. Lee and O. M. Yaghi, *J. Am. Chem. Soc.*, 2014.
16. D. Fröhlich, S. K. Henninger and C. Janiak, *Dalton Trans.*, 2014, **43**, 15300-15304.
17. M. Gaab, N. Trukhan, S. Maurer, R. Gummaraju and U. Müller, *Microporous Mesoporous Mater.*, 2012, **157**, 131-136.
18. T. Loiseau, C. Serre, C. Huguenard, G. Fink, F. Taulelle, M. Henry, T. Bataille and G. Férey, *Chem. – Eur. J.*, 2004, **10**, 1373-1382.
19. Y. Liu, J. H. Her, A. Dailly, A. J. Ramirez-Cuesta, D. A. Neumann and C. M. Brown, *J. Am. Chem. Soc.*, 2008, **130**, 11813-11818.
20. M. A. Springuel-Huet, A. Nossov, Z. Adem, F. Guenneau, C. Volkringer, T. Loiseau, G. Ferey and A. Gedeon, *J. Am. Chem. Soc.*, 2010, **132**, 11599-11607.
21. T. K. Trung, P. Trens, N. Tanchoux, S. Bourrelly, P. L. Llewellyn, S. Loera-Serna, C. Serre, T. Loiseau, F. Fajula and G. Férey, *J. Am. Chem. Soc.*, 2008, **130**, 16926-16932.
22. L. Alaerts, M. Maes, L. Giebeler, P. A. Jacobs, J. A. Martens, J. F. M. Denayer, C. E. A. Kirschhock and D. E. De Vos, *J. Am. Chem. Soc.*, 2008, **130**, 14170-14178.
23. P. Serra-Crespo, E. Stavitski, F. Kapteijn and J. Gascon, *RSC Advances*, 2012, **2**, 5051-5053.
24. P. Serra-Crespo, A. Dikhtiarenko, E. Stavitski, J. Juan-Alcaniz, F. Kapteijn, F.-X. Coudert and J. Gascon, *CrystEngComm*, 2015, **17**, 276-280.
25. T. Ahnfeldt, D. Gunzelmann, T. Loiseau, D. Hirsemann, J. Senker, G. Férey and N. Stock, *Inorg. Chem.*, 2009, **48**, 3057-3064.
26. D. Himsl, D. Wallacher and M. Hartmann, *Angew. Chem.*, 2009, **121**, 4710-4714.
27. S. Biswas, T. Remy, S. Couck, D. Denysenko, G. Rampelberg, J. F. M. Denayer, D. Volkmer, C. Detavernier and P. Van Der Voort, *Phys. Chem. Chem. Phys.*, 2013, **15**, 3552-3561.
28. F. Niekiel, M. Ackermann, P. Guerrier, A. Rothkirch and N. Stock, *Inorg. Chem.*, 2013, **52**, 8699–8705.
29. F. Jeremias, D. Frohlich, C. Janiak and S. K. Henninger, *RSC Advances*, 2014, **4**, 24073-24082.
30. E. Alvarez, N. Guillou, C. Martineau, B. Bueken, B. Van de Voorde, C. Le Guillouzer, P. Fabry, F. Nouar, F. Taulelle, D. de Vos, J.-S. Chang, K. H. Cho, N. Ramsahye, T. Devic, M. Daturi, G. Maurin and C. Serre, *Angew. Chem.*, 2015, **127**, 3735–3739.
31. I. Senkovska, F. Hoffmann, M. Froba, J. Getzschmann, W. Bohlmann and S. Kaskel, *Microporous Mesoporous Mater.*, 2009, **122**, 93-98.
32. T. Loiseau, C. Mellot-Draznieks, H. Muguerra, G. Férey, M. Haouas and F. Taulelle, *C. R. Chim.*, 2005, **8**, 765-772.
33. A. Comotti, S. Bracco, P. Sozzani, S. Horike, R. Matsuda, J. Chen, M. Takata, Y. Kubota and S. Kitagawa, *J. Am. Chem. Soc.*, 2008, **130**, 13664-13672.
34. E. D. Bloch, D. Britt, C. Lee, C. J. Doonan, F. J. Uribe-Romo, H. Furukawa, J. R. Long and O. M. Yaghi, *J. Am. Chem. Soc.*, 2010, **132**, 14382-14384.
35. H. Reinsch, M. A. van der Veen, B. Gil, B. Marszalek, T. Verbiest, D. de Vos and N. Stock, *Chem. Mater.*, 2013, **25**, 17-26.
36. J. Yang, M. Lutz, A. Grzech, F. M. Mulder and T. J. Dingemans, *CrystEngComm*, 2014, **16**, 5121-5127.
37. H. Reinsch and D. De Vos, *Microporous Mesoporous Mater.*, 2014, **200**, 311-316.
38. H. Reinsch, M. Krüger, J. Marrot and N. Stock, *Inorg. Chem.*, 2013, **52**, 1854-1859.
39. N. Reimer, H. Reinsch, A. K. Inge and N. Stock, *Inorg. Chem.*, 2014, **54**, 492-501.
40. V. Bon, I. Senkovska, I. A. Baburin and S. Kaskel, *Cryst. Growth Des.*, 2013, **13**, 1231-1237.
41. I. A. Ibarra, S. Yang, X. Lin, A. J. Blake, P. J. Rizkallah, H. Nowell, D. R. Allan, N. R. Champness, P. Hubberstey and M. Schröder, *Chem. Commun.*, 2011, **47**, 8304-8306.
42. Y. Takashima, C. Bonneau, S. Furukawa, M. Kondo, R. Matsuda and S. Kitagawa, *Chem. Commun.*, 2010, **46**, 4142-4144.
43. C.-H. Zhan, F. Wang, Y. Kang and J. Zhang, *Inorg. Chem.*, 2011, **51**, 523-530.
44. Y.-X. Tan, Y.-P. He and J. Zhang, *Chem. Commun.*, 2014, **50**, 6153-6156.
45. P. Maniam and N. Stock, *Inorg. Chem.*, 2011, **50**, 5085-5097.
46. M. Feyand, C. F. Seidler, C. Deiter, A. Rothkirch, A. Lieb, M. Wark and N. Stock, *Dalton Trans.*, 2013, **42**, 8761-8770.
47. *Materials Studio Version 5.0*, Accelrys Inc, San Diego, CA, USA, **2009**.
48. A. A. Coelho, *Topas Academics v4.1*, Coelho Software, Brisbane, Australia, **2007**.
49. A. Pines, M. G. Gibby and J. S. Waugh, *J. Chem. Phys.*, 1973, **59**, 569-590.
50. B. M. Fung, A. K. Khitrin and K. Ermolaev, *J. Magn. Reson.*, 2000, **142**, 97-101.
51. R. Siegel, J. Rocha and L. Mafra, *Chem. Phys. Lett.*, 2009, **470**, 337-341.
52. D. Massiot, F. Fayon, M. Capron, I. King, S. Le Calvé, B. Alonso, J.-O. Durand, B. Bujoli, Z. Gan and G. Hoatson, *Magnetic Resonance in Chemistry*, 2002, **40**, 70-76.
53. H. Reinsch and N. Stock, *Microporous Mesoporous Mater.*, 2013, **171**, 156-165.
54. D. R. Neuville, L. Cormier and D. Massiot, *Geochimica et Cosmochimica Acta*, 2004, **68**, 5071-5079.
55. J. Wack, R. Siegel, T. Ahnfeldt, N. Stock, L. Mafra and J. Senker, *J. Phys. Chem. C*, 2013, **117**, 19991-20001.
56. A. L. Spek, *PLATON, A Multipurpose Crystallographic Tool v 1.16*, Utrecht Universität, Utrecht, Niederlande, **2011**.
57. M. F. de Lange, C. P. Ottevanger, M. Wiegman, T. J. H. Vlugt, J. Gascon and F. Kapteijn, *CrystEngComm*, 2015, **17**, 281-285.
58. M. Kubo, A. Shimojima and T. Okubo, *J. Phys. Chem. C*, 2012, **116**, 10260-10265.
59. A. Boutin, F.-X. Coudert, M.-A. Springuel-Huet, A. V. Neimark, G. Férey and A. H. Fuchs, *J. Phys. Chem. C*, 2010, **114**, 22237-22244.

4.4. Zusätzliche Arbeit

4.4.1. Thermal post-synthetic modification of Al-MIL-53–COOH: systematic investigation of the decarboxylation and condensation reaction

Der folgende Artikel wurde im Jahre 2012 in der Fachzeitschrift *CrystEngComm*, *RSC* veröffentlicht.[77] Der Wiederabdruck erfolgte mit freundlicher Genehmigung der RSC. Reproduced by permission of The Royal Society of Chemistry from:
N. Reimer, B. Gil, B. Marszalek, N. Stock, *CrystEngComm* **2012**, *14*, 4119-4125, DOI: 10.1039/C2CE06649A. Copyright 2012 The Royal Society of Chemistry.
http://pubs.rsc.org/en/Content/ArticleLanding/2012/CE/c2ce06649a#!divAbstract

Al-MIL-53 ist der bis dato am intensivsten untersuchteste aluminiumbasierte MOF. Seine Struktur basiert auf Ketten aus *trans* eckenverknüpften AlO_6-Polyedern, die über Terephthalationen zu einem dreidimensionalem Netzwerk mit eindimensionalen rautenförmigen Kanälen verknüpft werden. Herausragende Eigenschaft von MIL-53 ist seine Flexibilität. Je nach eingelagerten Gastmolekülen oder Temperatur kann sich die Struktur aufweiten oder zusammenziehen. Dieser so genannte „*breathing effect*“ kann durch zusätzliche funktionelle Gruppen am Linkermolekül beeinflusst werden. Des Weiteren können die thermische Stabilität sowie die Sorptionseigenschaften des entsprechend funktionalisierten Materials beeinflusst werden.

Die Hochdurchsatzuntersuchung des Systems Al^{3+}/Trimellitsäure (H_2BDC-COOH)/H_2O führte zu der Synthese von Al-MIL-53-COOH mit der Summenformel $[Al(OH)(BDC\text{-}COOH)]\cdot 0.9H_2O$. Die Struktur der Verbindung liegt in der geschlossenen Form vor und kann durch solvothermale Behandlung mit DMF oder durch Behandlung mit einem Überschuss an H_2O in die offene Form umgewandelt werden. Durch die zusätzliche nicht koordinierende -COOH-Gruppe zeigt die Verbindung ein stark selektives Sorptionsverhalten gegenüber polaren Gasen/Dämpfen.

Mittels *in situ* IR Spektroskopie und ^{1}H-NMR Spektroskopie konnte eine thermisch induzierte post-synthetische Modifizierung nachgewiesen werden. Bei erhöhten Aktivierungstemperaturen finden gleichzeitig zwei Prozesse statt. Zum einen kommt es zur partiellen Decarboxylierung einiger -COOH-Gruppen und zum anderen wird eine

Kondensationsreaktion von sich in den Poren gegenüberstehende -COOH-Gruppen unter Ausbildung von Anhydridfunktionalitäten beobachtet. Diese Prozesse beeinflussen die Sorptionseigenschaften des Materials. Ab einem Decarboxylierungsgrad von etwa 30 % scheint genug Platz in den Poren vorzuliegen, so dass die vormals für Stickstoff unporöse Verbindung nun zugänglich für Stickstoff wird.

This paper is published as part of a *CrystEngComm* Collection entitled:

Post-synthetic modification of coordination networks

Guest Editors: Andy Burrows and Seth Cohen

Published in issue 12, 2012 of *CrystEngComm*

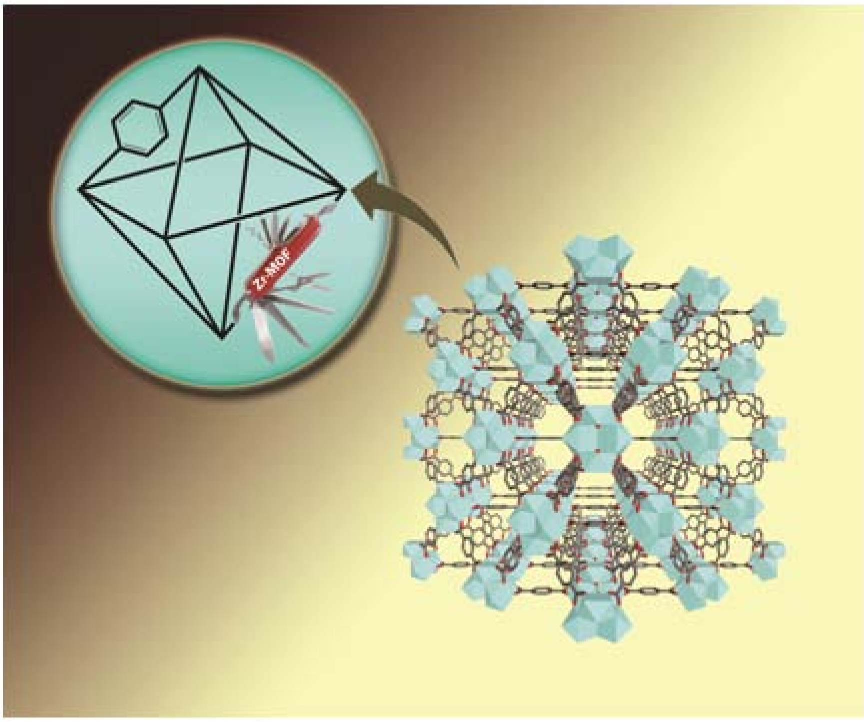

Image reproduced with permission of Seth M Cohen

Articles published in this issue include:

Discovery, development, and functionalization of Zr(IV)-based metal–organic frameworks
Min Kim and Seth M. Cohen
CrystEngComm, 2012, DOI: 10.1039/C2CE06491J

Controlled modification of the inorganic and organic bricks in an Al-based MOF by direct and post-synthetic synthesis routes
Tim Ahnfeldt, Daniel Gunzelmann, Julia Wack, Jürgen Senker and Norbert Stock
CrystEngComm, 2012, DOI: 10.1039/C2CE06620C

Conversion of primary amines into secondary amines on a metal–organic framework using a tandem post-synthetic modification
Andrew D. Burrows and Luke L. Keenan
CrystEngComm, 2012, DOI: 10.1039/C2CE25131K

Visit the *CrystEngComm* website for more cutting-edge crystal engineering research
www.rsc.org/crystengcomm

CrystEngComm

www.rsc.org/crystengcomm

Volume 14 | Number 12 | 21 June 2012 | Pages 4083–4224

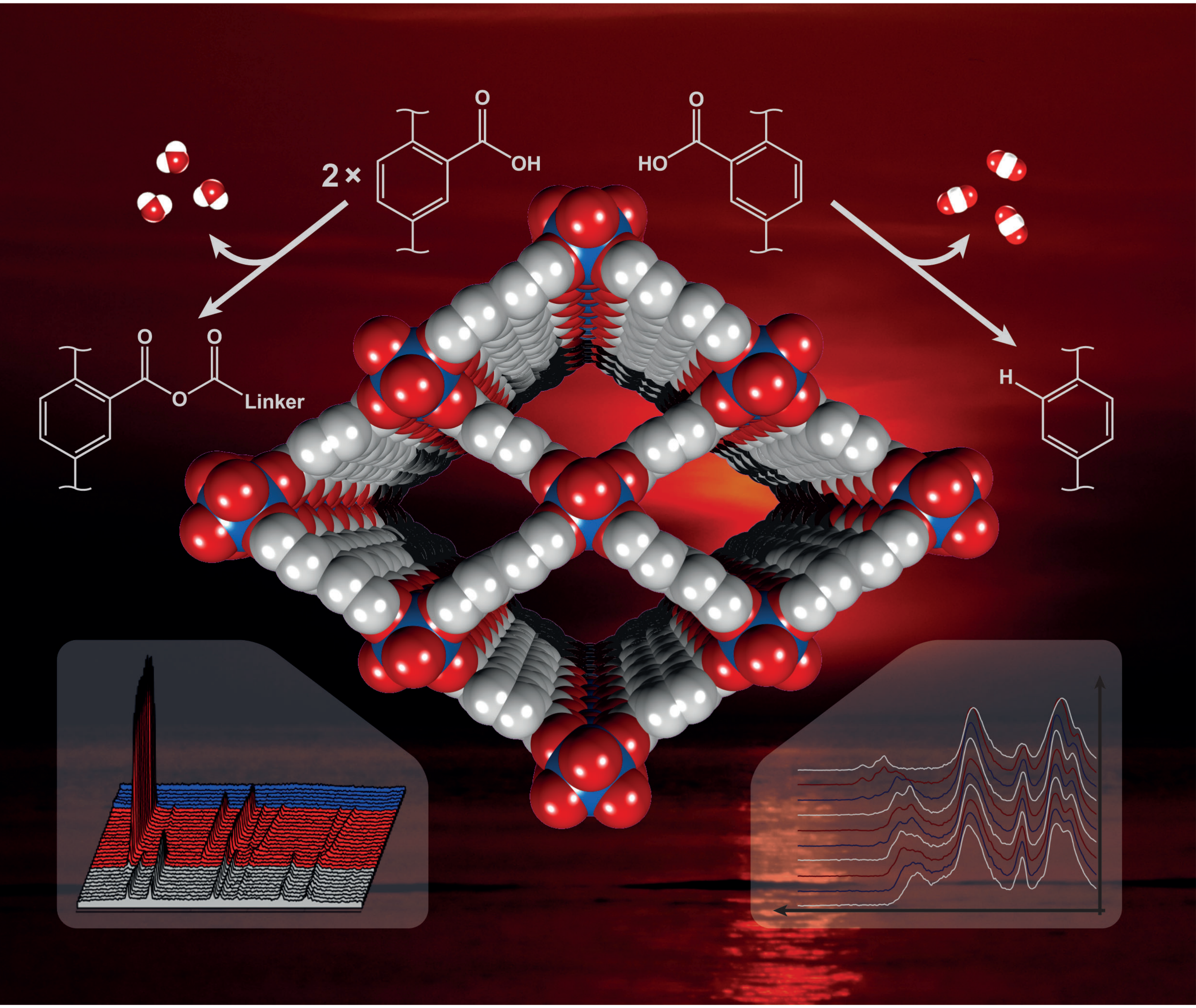

COVER ARTICLE
Stock *et al.*
Thermal post-synthetic modification of Al-MIL-53–COOH: systematic investigation of the decarboxylation and condensation reaction

RSC Publishing

CrystEngComm

Dynamic Article Links

Cite this: *CrystEngComm*, 2012, **14**, 4119–4125

www.rsc.org/crystengcomm

PAPER

Thermal post-synthetic modification of Al-MIL-53–COOH: systematic investigation of the decarboxylation and condensation reaction†

Nele Reimer,[a] Barbara Gil,[b] Bartosz Marszalek[b] and Norbert Stock*[a]

Received 9th December 2011, Accepted 27th January 2012
DOI: 10.1039/c2ce06649a

Aluminium trimellitate [Al(OH)(BDC–COOH)]·0.9H_2O (**1**), the Al-MIL-53–COOH derivative, was discovered under solvothermal conditions using a high-throughput set-up suitable for microwave (MW)-assisted heating. The compound shows high structural flexibility. The large-pore (lp) form of the framework is obtained under large excess of H_2O or after solvothermal treatment with *N*,*N*-dimethylformamide upon which [Al(OH)(BDC–COOH)]·0.7DMF (**2**) is obtained. Exposure of the water rich lp form of **1** to ambient conditions leads to the transformation to the narrow-pore (np) form. Thermal activation of both compounds results in the formation of the empty lp form and the activation of **1** was studied in detail by *in situ* IR-spectroscopy. Depending on the activation temperature and time two post-synthetic modification (PSM) processes are observed: the partial decarboxylation and the formation of acid anhydride groups. Thus at high temperatures and long activation times [Al(OH)(BDC–OCOCO–BDC)$_{x/2}$(BDC)$_y$] ($x + y = 1$) is formed. Upon cooling in air the anhydride functionality still remains intact, but the np form is obtained in air due to the adsorption of H_2O molecules. Sorption measurements of **1** confirm a preference for polar gases like H_2O and CO_2 in comparison to N_2, H_2, and CH_4. The N_2 capacity depends strongly on the degree of decarboxylation.

Introduction

In the last decade, metal–organic frameworks (MOFs) have developed into an important class in the field of crystalline and porous materials,[1–3] due to their potential applications in gas storage and separation,[4] catalysis[5] and drug delivery.[6] They are built up from inorganic building units such as metal ions or metal-oxide clusters, which are interconnected by organic linker molecules, usually containing carboxylate or nitrogen containing or phosphonate functionalities.[7,8]

Once the optimal reaction conditions for the formation of the inorganic units are found, isoreticular synthesis can be adopted to modulate the pore size and the pore functionality and thus tune the properties of the resulting materials.[7,9–12]

Based on trivalent cations, MOFs with highly desirable properties have been reported.[9,11,13] In the case of aluminium, the resulting MOFs are known to show high thermal stability. A well investigated compound is Al-MIL-53,[14] which is stable up to 450 °C and belongs to the group of flexible framework materials (MIL = Material Institute Lavoisier). The compound is based on terephthalic acid (H_2BDC) and isoreticular synthesis has been performed using the extended linker molecules 1,4- and 2,6-naphthalenedicarboxylic acid (H_2NDC), 4,4-biphenyldicarboxylic acid and 2,2′-bipyridine-4,4′-dicarboxylic acid resulting in the rigid MIL-53 analogues Al(OH)(1,4-NDC)·2H_2O,[15] DUT-4, DUT-5 (ref. 16) and MOF-253 (ref. 17) (DUT = Dresden University of Technology). The introduction of functional groups was also performed using different functionalized terephthalate derivatives resulting in the polar Al-MIL-53–X (X = –Cl, –Br, –NO_2),[18] the unpolar Al-MIL-53–CH_3,[18] the basic Al-MIL-53–NH_2 (ref. 18 and 19) and the slightly acidic materials Al-MIL-53–X (X –OH,[20] –$(OH)_2$ (ref. 18)) and therefore all frameworks show different breathing behaviour. The amino-functionalized compound was intensively investigated concerning gas adsorption/separation and a high selectivity of CO_2 towards CH_4 was observed.[4] Also a series of iso(thio)cyanate, (thio)carbamate and (thio)urea was synthesized by post-synthetic modification (PSM) showing significant changes in the sorption properties of these materials depending on the incorporated functional group.[21] The hydroxyl-functionalized material showed also interesting sorption properties. By post-synthetic hydrogen lithium exchange at the hydroxyl groups, an increase in the adsorption capacity for hydrogen was observed.[20]

Based on DFT (Density Functional Theory) and GCMC (Grand Canonical Monte Carlo) calculations the lp form of Al-MIL-53–COOH containing non-coordinating carboxylic acid groups was proposed to be a promising candidate for CO_2

---

[a] *Institut für Anorganische Chemie, Christian-Albrechts Universität, Max-Eyth-Str. 2, 24118 Kiel, Germany. E-mail: stock@ac.uni-kiel.de; Fax: +49 0431 880 1775; Tel: +49 0431 8801675*
[b] *Faculty of Chemistry, Jagiellonian University, ul. Ingardena 3, 30-060 Kraków, Poland. E-mail: gil@chemia.uj.edu.pl; Fax: +48 12 634 05 15; Tel: +48 12 663 20 16*

† Electronic supplementary information (ESI) available. See DOI: 10.1039/c2ce06649a

capture applications.[22] In addition, the carboxylic acid group could open the possibility for post-synthetic modification reactions or cation exchange. Until now, there have been only few examples of MOFs containing non-coordinating carboxylic acid groups. Based on the MIL-53 structure Fe and Al-MIL-53(COOH)$_2$ (ref. 9 and 23) have been reported, which are built up from pyromellitic acid, resulting in materials with two non-coordinating carboxylic acid sites. Both compounds are rigid and show no or only low porosity.

The discovery and synthesis optimization of MOFs can be efficiently carried out using high-throughput (HT) methods.[24–26] Conventional heating was used in these studies and also a temperature-gradient reactor system has been successfully integrated into the work flow.[24,27,28] Recently we were able to incorporate microwave (MW)-assisted heating into our HT methodology, which is usually employed in organic synthesis.[29–31]

Here, we report the systematic investigation of the system $Al^{3+}/H_2BDC–COOH$ (trimellitic acid)/H_2O by using MW-assisted heating in a HT setup. Al-MIL-53–COOH, a new flexible and porous member of the family of Al-MIL-53 containing free carboxylic acid sites was discovered. In addition, the detailed PSM by thermal activation is reported.

Experimental

Materials

All chemicals were purchased from commercial sources and used without further purification unless otherwise noted. $AlCl_3·6H_2O$ and trimellitic acid (1,2,4-benzenetricarboxylic acid) were purchased from Fluka and DMF from Grüssing.

Synthesis and activation of Al-MIL-53–COOH

The discovery as well as the synthesis optimization under hydrothermal conditions was carried out using high-throughput (HT) methods.[24,27] Recently, we were able to integrate a HT-microwave reactor system into our workflow.[19] The Anton Paar Synthos 3000 microwave oven (Fig. S1a†) with a 96 position rotor (Fig. S1b†) was used. This rotor offers four positions for silicon carbide (SiC) blocks each with a 4 × 6 array (Fig. S1c†). 5 mL glass vials, with a maximum reaction volume of 3 mL, are equipped with a Teflon seal and a screw cap (Fig. S1d†) and placed into the 4 × 6 array. These glass vials are suitable for temperatures up to 200 °C and pressures up to 20 bar. The temperature control is accomplished using an IR sensor.

The syntheses were performed in the range of 125–200 °C and the following aluminium salts were used: $AlCl_3·6H_2O$, $Al(NO_3)_3·9H_2O$, $Al_2(SO_4)_3·8H_2O$ and $AlNH_4(SO_4)_2·12H_2O$. From the large number of experiments (*ca.* 250) the following optimal reaction conditions were extracted: (1) $AlCl_3·6H_2O$ is the optimal aluminium source; (2) the molar ratio Al^{3+} : $H_2BDC–COOH$ of 1 : 1 results in highest crystallinity of the product; (3) the reaction temperature should be around 170 °C since lower temperatures lead to less crystalline products; (4) a reaction time for 5 h is sufficient to get fully crystalline products.

The optimized reaction parameters were used for the scale-up reaction, which was performed in a conventional oven using a Teflon lined steel autoclave. 301.6 mg (1.44 mmol) 1,2,4-benzenetricarboxylic acid (trimellitic acid), 344 mg (1.43 mmol) $AlCl_3·6H_2O$ and 15.344 mL (0.85 mol) H_2O were heated at 170 °C for 12 h. The resulting microcrystalline product was dried in air and identified by X-ray powder diffraction (XRPD) and elemental analysis as $[Al(OH)(BDC–COOH)]·0.9H_2O$ crystallising in the narrow-pore form (np) of Al-MIL-53–COOH. Elemental analysis, found: C, 39.9; H, 2.6; calc. C, 40.3; H, 2.2%.

$[Al(OH)(BDC–COOH)]·0.9H_2O$ (100 mg, 0.33 mmol) was treated with 20 mL DMF (1 h, 170 °C) using MW-assisted heating. The formed product was identified by X-ray powder diffraction and elemental analysis as $[Al(OH)(BDC–COOH)]·0.7DMF$ crystallizing in the large-pore form (lp) of Al-MIL-53–COOH. Elemental analysis, found: C, 42.9; H, 3.6; N, 3.8; calc. C, 43.9; H, 3.3; N, 3.2%. This form is stable up to at least eight days under ambient conditions, then it transforms partially back into the closed-pore form through the exchange of the DMF by water molecules from the atmosphere (Fig. S2†).

Physical measurements

X-Ray powder diffraction patterns were collected in transmission mode using a STOE STADI P diffractometer equipped with a linear position sensitive detector using monochromated Cu-Kα_1 (λ = 1.5406 Å) radiation. Lattice parameters were determined and refined using TOPAS-Academic V4.1.[32] The temperature-dependant X-ray diffraction experiments were performed in Debye–Sherrer mode on a STOE Stadi-P diffractometer (Cu-Kα_1, λ = 1.5406 Å) equipped with a STOE high temperature capillary furnace. Each powder pattern was recorded (IPSD detector) in the full range −8 to 127° (2Θ) at intervals of 20 °C up to 620 °C with 20 min per step scan. The temperature ramp between two samples was 25 °C min^{-1}. Thermogravimetric (TG) measurements were carried out under a flow of air (75 cm^3 min^{-1}) with a heating rate of 4 K min^{-1} using a Netzsch STA 409 CD analyzer. The contents of carbon, hydrogen and nitrogen were determined by elemental chemical analysis on a Eurovektor EuroEA Elemental Analyzer. Sorption measurements were carried out using a Belsorp-max instrument (BEL JAPAN INC.). For the sorption experiments, the samples were activated at 200 °C under vacuum (10^{-2} kPa) for 12 h, unless otherwise noted. Liquid-state NMR spectroscopy was performed on a Bruker DRX500/Bruker Advance 200 spectrometer. FTIR spectra were recorded with a Bruker Tensor 27 spectrometer equipped with an MCT detector and working with the spectral resolution of 2 cm^{-1}. For the IR experiment a silicon wafer was covered by a thin layer of the material by evaporating on its surface a few drops of the corresponding dispersion in methanol.

Results and discussion

Structure description

The XRPD patterns of both compounds were indexed and refined using the Pawley method (see ESI, Fig. S3 and S4†). Table 1 gives an overview of the obtained lattice parameters compared to the ones reported for Al-MIL-53.

Based on the results of the refined parameters, the structures of the different forms of Al-MIL-53–COOH were found to correspond to the ones of the unfunctionalized system Al-MIL-53

Table 1 Lattice parameters of Al-MIL-53(lp) and Al-MIL-53(np)[14] compared with the ones obtained in this work

	Al-MIL-53–COOH(H_2O)	Al-MIL-53–COOH(DMF)	Al-MIL-53(np)	Al-MIL-53(lp)
Space group	*Cc*	*Imma*	*Cc*	*Imma*
a/Å	19.608(1)	6.6411(2)	19.513(2)	6.6085(1)
b/Å	8.4537(4)	16.6007(5)	7.612(1)	16.675(3)
c/Å	6.6531(3)	12.9450(6)	6.576(1)	12.813(2)
β/°	106.86(5)	90	104.24(1)	90

(Fig. 1). Accordingly the structure is built up from chains of trans μ–OH corner-sharing AlO_6-octahedra which are interconnected by trimellitic acid molecules to form one-dimensional lozenge-shaped pores.

In contrast to other MIL-53 compounds, the as synthesized compound **1** only contains water molecules inside the pores. The size of the trimellitic acid molecules probably hinders them entering the pores. The np form is observed since hydrogen bonds between water molecules and the non-coordinating carboxylic acid and μ-OH groups are formed (see IR spectroscopy). In case the dry sample is treated with a few drops of water, the XRPD measurement shows a different powder pattern (Fig. S5†), corresponding to the lp form of Al-MIL-53. The lp form transforms back into the np form upon drying under ambient conditions. A similar behaviour has also been recently reported for Al-MIL-53–$(OH)_2$ and Cr-MIL-53.[18,33]

The water molecules in **1** can be exchanged by DMF molecules and **2** is obtained. The solvent exchange is reversible and leads to a drastic change of the cell parameters. In analogy to Al-MIL-53 the lp form is formed.

Infrared spectroscopy

In the region above 2000 cm^{-1} the IR-spectrum of Al-MIL-53–COOH(H_2O) (Fig. 2) shows the presence of hydrogen-bonded water molecules (width maximum at 3400 cm^{-1}) together with the bending vibrations of water at 1705 cm^{-1}. Bands of the non-coordinating carboxylic acid groups (symmetric stretching vibration at 1722 and 1750 cm^{-1}) start to be visible when the majority of water is removed (treatment at 250 °C). Further, characteristic stretching vibrations of the coordinating carboxylate groups can be observed, ν_{as} at 1597 and ν_s at 1430 and 1409 cm^{-1}. The absorption at 1499 cm^{-1} can be attributed to the symmetric ring-stretching vibration, whereas the C–C deformation vibrations of the 1,2,4-substituted aromatic ring appear at 589 and 474 cm^{-1}. The C–H deformation vibrations of the aromatic ring absorb at 1160 and 762 cm^{-1}.

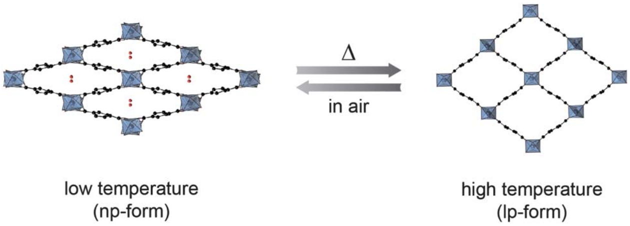

Fig. 1 Structural transition between the low-temperature (np) and the high-temperature (lp) form of Al-MIL-53. One water molecule is located in the centre of the pore of the lt-form. The figure was drawn using structural data taken from ref. 14.

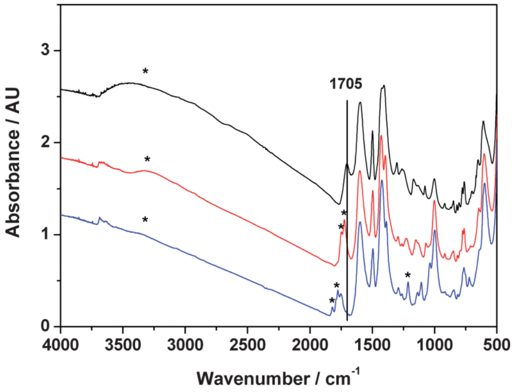

Fig. 2 IR-spectra of [Al(OH)(BDC–COOH)]·0.9H_2O (black), **1** treated at 250 °C (red) and at 410 °C (blue), respectively. The characteristic bands are marked with an asterisk.

In addition to the loss of water molecules, the thermal activation at higher temperatures (*e.g.* 410 °C) leads to a condensation of neighboring carboxylic acid groups to form anhydride functionalities (Fig. 2), which are confirmed by characteristic absorptions bands in the IR-spectrum.

The absorptions at 1821 and 1775 cm^{-1} are due to the asymmetric and symmetric C=O stretching vibrations and at 1210 cm^{-1} due to the C–O stretching vibration of the OCOCO-moiety.

Thermal analysis and stability

The thermogravimetric measurement of **1** (Fig. 3 top) was performed under air with a heating rate of 4 K min^{-1}. The first weight loss up to 240 °C corresponds to the removal of incorporated water molecules (calc. 6.0%; obs. 6.1%). Above 240 °C a small gradual weight loss is observed due to condensation of neighboring carboxylic acid groups to form acid anhydrides and

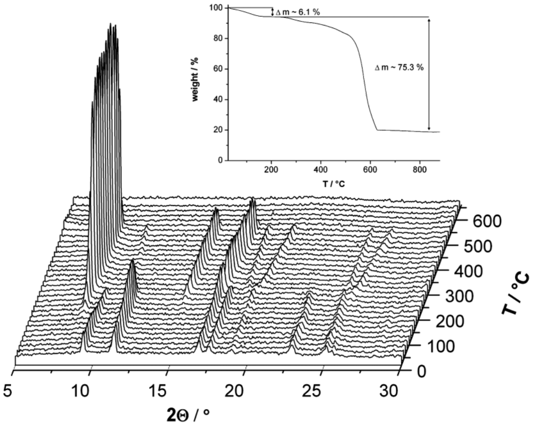

Fig. 3 Top: TGA curve of Al-MIL-53–COOH(H_2O). Bottom: TD-XRPD patterns of Al-MIL-53–COOH(H_2O) from 20–620 °C in steps of 20 °C, showing the phase transition between the np and the lp form.

partial decarboxylation. This process is followed by the decomposition of the framework above 450 °C forming X-ray amorphous Al_2O_3 (in total: calc. 74.6%; obs. 75.3%). The observed weight losses are in good agreement with the results obtained by the elemental analysis. The composition of the title compound **1** is therefore confirmed to be [Al(OH)(BDC–COOH)]·0.9H_2O.

In comparison the TG analysis of **2** (Fig. 4 top), also performed under air with a heating rate of 4 K min^{-1}, shows a larger first weight loss up to 270 °C due to the removal of the incorporated DMF molecules (calc. 16.9%; obs. 16.9%).

Above 270 °C an almost identical decomposition process as observed for **1** is found (calc. 66.0%; obs. 65.5%). The weight losses are in good agreement with the results obtained by elemental analysis. The composition of the compound **2** is confirmed to be [Al(OH)(BDC–COOH)]·0.7 DMF.

In addition to the TG analysis, temperature dependent X-ray powder diffraction (TD-XRPD) measurements were performed. Both samples were heated from room temperature up to 620 °C in steps of 20 °C. The TD-XRPD data of **1** (Fig. 3 bottom) shows a phase transition starting at 200 °C, the intensity of the reflections of the narrow-pore form decreases and new reflections belonging to the large-pore form appear. This transformation is completed at 280 °C and the large-pore form exists up to 480 °C. Above this temperature the intensity of the reflections decreases rapidly due to the decomposition of the framework resulting in the formation of amorphous Al_2O_3. The measurement shows a slight shift of the reflections of the large-pore form towards higher 2θ angles with increasing temperature. This could be explained by the partial decarboxylation and the condensation of neighboring carboxylic acid groups, which influences the geometry of the flexible framework.

The TD-XRPD measurement of Al-MIL-53–COOH(DMF) (Fig. 4 bottom) shows a slightly different progression. Already starting with a large-pore form, above 120 °C a shift of the reflections to higher 2θ angles up to 240 °C is observed (exception reflection at 10.6° 2θ). This can be explained by the removal of incorporated DMF molecules, which leads to a distortion of the framework. Between 240 °C and 300 °C the first reflection shifts nearly back to its original position, but a slight shift to higher angles is observed. This shift increases up to 400 °C, again due to partial decarboxylation and condensation of neighboring carboxylic acid groups. Above 440 °C the structure decomposes.

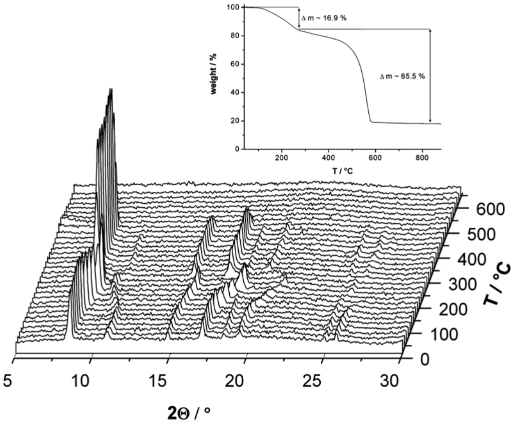

Fig. 4 Top: TGA curves of Al-MIL-53–COOH(DMF). Bottom: TD-XRPD patterns of Al-MIL-53–COOH(DMF) from 20–620 °C in steps of 20 °C.

Sorption properties

The sorption behavior of **1** was investigated using different gases/vapors. The measurements using N_2 and H_2 were performed at 77 K and using CO_2, H_2O and CH_4 at 298 K. All samples were activated at 200 °C for 12 h under vacuum. The sorption isotherms are shown in Fig. 5 and 6.

The sorption measurements show no or only poor porosity towards nitrogen (Fig. 5), methane (Fig. 6) and hydrogen (Fig. 6) probably due to their large kinetic diameter, in case of nitrogen and methane, and their non-polar character respectively.

Concerning carbon dioxide (Fig. 6), a molecule with a higher polarizability and stronger quadrupole moment compared to nitrogen, an adsorption is observed.

Finally, the compound shows high affinity to H_2O vapor (Fig. 5) due to the very strong interactions with the functional group. The isotherm of Al-MIL-53–COOH shows a two step adsorption. In the first step up to $p/p_0 = 0.5$, the pores are filled with one water molecule to obtain again the hydrated 'lt' form and with increasing pressure the framework opens and a second water molecule can enter the pores.

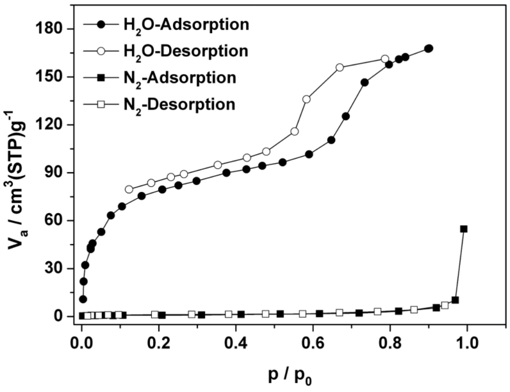

Fig. 5 Sorption behaviour of Al-MIL-53–COOH(H_2O) activated at 200 °C for 12 h towards N_2, and H_2O.

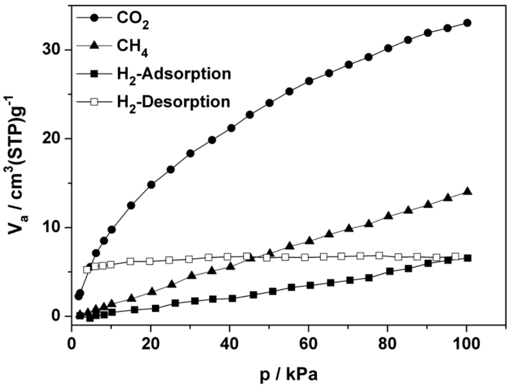

Fig. 6 Sorption behaviour of Al-MIL-53–COOH(H_2O) activated at 200 °C for 12 h towards CO_2, CH_4, and H_2.

Systematic investigation of the activation procedure

To investigate the thermal stability of the functional group and the ongoing processes during thermal activation, *in situ* infrared spectroscopy was performed (Fig. 7).

The sample was gradually heated at the rate of 5 °C min^{-1} under vacuum in the temperature range between 25 and 450 °C. At the lower temperatures the disappearance of the band at 1705 cm^{-1} indicates removal of water from the Al-MIL-53–COOH channels. At higher temperatures, gradual condensation of the free –COOH groups was observed. The intensities of the bands of free –COOH groups (1722 and 1750 cm^{-1}) decrease and at the same time the bands characteristic of trimellitic anhydride appear and increase in intensity. The new bands are characteristic of cyclic, five ring anhydride vibrations at 1775 cm^{-1}, 1791 cm^{-1} and 1821 cm^{-1} (due to the C=O symmetric and asymmetric stretching vibrations and C–O–C stretching) together with the bands at 1210 cm^{-1}, 1108 cm^{-1} and 1104 cm^{-1} (O=C–O–C=O stretching also for five ring anhydrides). The transformation of the free –COOH groups was completed at 400 °C. It is worthy to note that the bands characteristic of the stretching vibrations of the coordinating carboxylate groups (in between 1650 and 1320 cm^{-1}) have not changed indicating that condensation affected only the free carboxylic groups of the trimellitic linker. Above 450 °C the structure rapidly collapses. The formation of acid anhydride functionalities is also confirmed by solid-state NMR measurements, showing an additional signal at 163.51 ppm for the activated sample of Al-MIL-53–COOH at 410 °C (Fig. S6†). The position of this signal is characteristic for cyclic anhydride functionalities.

In addition the post-synthetic modification was systematically studied using liquid-state NMR-spectroscopy. Therefore, thermal treatment of a sample of Al-MIL-53–COOH for varying activation times (12–48 h) and temperatures (210–410 °C) under vacuum was performed. Interestingly a partial decarboxylation of the linker molecule was found to take place simultaneously (Fig. 8).

The activated samples were dissolved in a mixture of NaOD/D_2O. This leads to the hydrolysis of the anhydride functionality. In addition to the expected signals of the trimellitic acid (7.78, 7.70 and 7.33 ppm) a signal at 7.73 ppm in the spectrum is observed. This can only be explained, by a partial decarboxylation of acid groups to form terephthalate units in the framework. To calculate the degree of decarboxylation the integral of the terephthalate protons was compared with the sum of the integrals of the aromatic H atoms of the trimellitic acid. Thus, with increasing activation temperature and time the degree of decarboxylation increases (Table 2).

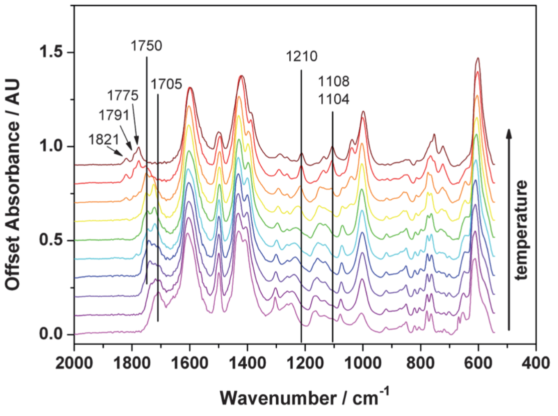

Fig. 7 Results of the *in situ* IR-spectroscopic of the thermal activation (25–450 °C) of [Al(OH)(BDC–COOH)]·0.9H_2O.

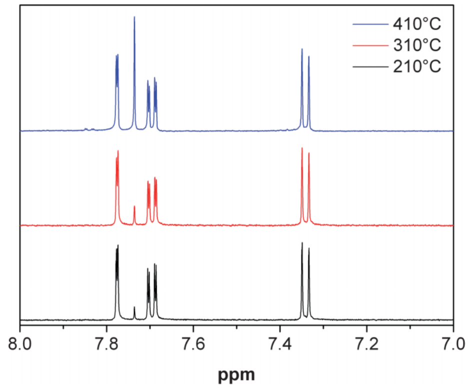

Fig. 8 Liquid-state NMR spectra of Al-MIL-53–COOH(H_2O) samples, thermally treated at different temperatures.

The main increase of decarboxylation is observed above 350 °C. This is in good agreement with the *in situ* IR measurements. The influence of the activation time was also investigated at 410 °C, demonstrating an additional increase in the degree of decarboxylation up to 40.7% for an activation time of 48 h. The chemical modification by thermal treatment has previously been reported as the so-called post-synthetic deprotection (PSD). This type of PSM was used as an approach to thermally remove protective groups.[34–36]

The activation procedure has a direct effect on the sorption behaviour. Only at a degree of decarboxylation of approximately 30% the pores become accessible to nitrogen (Fig. 5, Fig. 9). This phenomenon must be due to a decrease of intraframework interactions in the activated samples. After the thermal treatment all samples still show high crystallinity (Fig. S7†). In the XRPD patterns of the samples activated at 410 °C for 24, 36 and 48 h an

Table 2 Influence of activation temperature (top) and time (bottom) on the degree of decarboxylation

Temperature/°C	Time/h	Degree of decarboxylation (%)
210	12	2.0
230	12	2.3
250	12	2.4
270	12	2.7
290	12	3.3
310	12	3.4
330	12	4.0
350	12	6.2
370	12	10.8
390	12	14.0
410	12	16.7
410	12	16.7
410	24	33.3
410	36	40.7
410	48	40.7

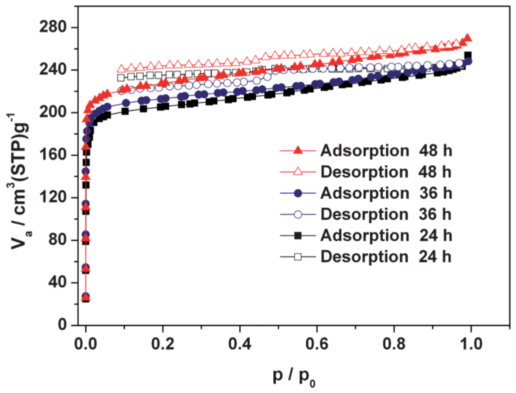

Fig. 9 N_2-sorption isotherms of Al-MIL-53–COOH(H_2O) activated in a vacuum at 410 °C for 24, 36 and 48 h.

additional reflection that can be attributed to the lp form of the Al-MIL-53 occurs (Fig. S8†). After several days of exposure to the atmosphere, this reflection decreases in intensity and therefore the np form of Al-MIL-53 is regenerated. Up to now we have no explanation for this behaviour since non-functionalized Al-MIL-53 in air exhibits the np form. Table 3 shows the values for the specific surface areas and micropore volumes according to the activation time at 410 °C.

Conclusion

In this contribution we describe the synthesis and detailed characterization of a new member of the family of Al-MIL-53 compounds, containing one free carboxylic acid site per ligand. In contrast to other MIL-53 materials the as synthesized compound appears already without unreacted linker molecules inside the pores, so it exists in a narrow-pore form containing only water molecules. These can be exchanged by DMF molecules resulting in a large-pore form. The water-containing compound shows selective sorption behavior, *i.e.*, a much higher affinity to polar gases compared to unpolar gases.

Additionally, post-synthetic modification induced by thermal treatment was performed. This resulted in the condensation of neighboring non-coordinating carboxylic acid groups to form anhydride functionalities and a partial decarboxylation. Depending on the degree of decarboxylation the compound shows no or good porosity towards nitrogen gas.

We have demonstrated that a detailed characterization of the activated MOFs, including dissolution and NMR-spectroscopic investigations, is mandatory to fully understand their properties and to detect unexpected processes taking place during the activation.

Table 3 Specific surface area and micropore volume according to the activation time at 410 °C

Temperature/°C	Time/h	a_s/m^2 g^{-1}	V_m/cm^3 g^{-1}
410	24	801	0.34
410	36	849	0.35
410	48	900	0.37

Acknowledgements

The authors would like to thank Tim Ahnfeldt for the support at the start of this research project. This work has been financially supported by the DFG (SPP 1362, STO-643/5-1). The research leading to these results has also received funding from the European Community's Seventh Framework Programme (FP7/2007-20013) under grant agreement no. 228862. The IR studies (BG and BM) were carried out with the equipment purchased thanks to the financial support of the European Regional Development Fund in the framework of the Polish Innovation Economy Operational Program (contract no. POIG.02.01.00-12-023/08).

Notes and references

1 C. Janiak and J. K. Vieth, *New J. Chem.*, 2010, **34**, 2366–2388.
2 A. K. Cheetham, C. N. R. Rao and R. K. Feller, *Chem. Commun.*, 2006, 4780–4795.
3 J. L. C. Rowsell and O. M. Yaghi, *Microporous Mesoporous Mater.*, 2004, **73**, 3–14.
4 S. Couck, J. F. M. Denayer, G. V. Baron, T. Remy, J. Gascon and F. Kapteijn, *J. Am. Chem. Soc.*, 2009, **131**, 6326–6327.
5 M. G. Goesten, J. Juan-Alcañiz, E. V. Ramos-Fernandez, K. B. Sai Sankar Gupta, E. Stavitski, H. van Bekkum, J. Gascon and F. Kapteijn, *J. Catal.*, 2011, **281**, 177–187.
6 P. Horcajada, C. Serre, G. Maurin, N. A. Ramsahye, F. Balas, M. Vallet-Regí, M. Sebban, F. Taulelle and G. Férey, *J. Am. Chem. Soc.*, 2008, **130**, 6774–6780.
7 M. Eddaoudi, J. Kim, N. Rosi, D. Vodak, J. Wachter, M. O'Keeffe and O. M. Yaghi, *Science*, 2002, **295**, 469–472.
8 V. Colombo, S. Galli, H. J. Choi, G. D. Han, A. Maspero, G. Palmisano, N. Masciocchi and J. R. Long, *Chem. Sci.*, 2011, **2**, 1311–1319.
9 T. Devic, P. Horcajada, C. Serre, F. Salles, G. Maurin, B. Moulin, D. Heurtaux, G. Clet, A. Vimont, J.-M. Grenèche, B. L. Ouay, F. Moreau, E. Magnier, Y. Filinchuk, J. Marrot, J.-C. Lavalley, M. Daturi and G. Férey, *J. Am. Chem. Soc.*, 2010, **132**, 1127–1136.
10 J. H. Cavka, S. Jakobsen, U. Olsbye, N. Guillou, C. Lamberti, S. Bordiga and K. P. Lillerud, *J. Am. Chem. Soc.*, 2008, **130**, 13850–13851.
11 C. Serre, C. Mellot-Draznieks, S. Surblé, N. Audebrand, Y. Filinchuk and G. Férey, *Science*, 2007, **315**, 1828–1831.
12 A. Sonnauer, F. Hoffmann, M. Fröba, L. Kienle, V. Duppel, M. Thommes, C. Serre, G. Férey and N. Stock, *Angew. Chem.*, 2009, **121**, 3849–3852.
13 G. Férey, C. Mellot-Draznieks, C. Serre, F. Millange, J. Dutour, S. Surblé and I. Margiolaki, *Science*, 2005, **309**, 2040–2042.
14 T. Loiseau, C. Serre, C. Huguenard, G. Fink, F. Taulelle, M. Henry, T. Bataille and G. Férey, *Chem.–Eur. J.*, 2004, **10**, 1373–1382.
15 A. Comotti, S. Bracco, P. Sozzani, S. Horike, R. Matsuda, J. Chen, M. Takata, Y. Kubota and S. Kitagawa, *J. Am. Chem. Soc.*, 2008, **130**, 13664–13672.
16 I. Senkovska, F. Hoffmann, M. Fröba, J. Getzschmann, W. Bohlmann and S. Kaskel, *MicroporousMesoporous Mater.*, 2009, **122**, 93–98.
17 E. D. Bloch, D. Britt, C. Lee, C. J. Doonan, F. J. Uribe-Romo, H. Furukawa, J. R. Long and O. M. Yaghi, *J. Am. Chem. Soc.*, 2010, **132**, 14382–14384.
18 S. Biswas, T. Ahnfeldt and N. Stock, *Inorg. Chem.*, 2011, **50**, 9518–9526.
19 T. Ahnfeldt, D. Gunzelmann, T. Loiseau, D. Hirsemann, J. Senker, G. Ferey and N. Stock, *Inorg. Chem.*, 2009, **48**, 3057–3064.
20 D. Himsl, D. Wallacher and M. Hartmann, *Angew. Chem.*, 2009, **121**, 4710–4714.
21 C. Volkringer and S. M. Cohen, *Angew. Chem., Int. Ed.*, 2010, **49**, 4644–4648.
22 A. Torrisi, R. G. Bell and C. Mellot-Draznieks, *Cryst. Growth Des.*, 2010, **10**, 2839–2841.
23 C. Volkringer, T. Loiseau, N. Guillou, G. Férey, M. Haouas, F. Taulelle, E. Elkaim and N. Stock, *Inorg. Chem.*, 2010, **49**, 9852–9862.
24 N. Stock, *Microporous Mesoporous Mater.*, 2010, **129**, 287–295.

25 R. Banerjee, A. Phan, B. Wang, C. Knobler, H. Furukawa, M. O'Keeffe and O. M. Yaghi, *Science*, 2008, **319**, 939–943.
26 K. Sumida, S. Horike, S. S. Kaye, Z. R. Herm, W. L. Queen, C. M. Brown, F. Grandjean, G. J. Long, A. Dailly and J. R. Long, *Chem. Sci.*, 2010, **1**, 184–191.
27 S. Bauer and N. Stock, *Chem. Unserer Zeit*, 2007, **41**, 390–398.
28 S. Bauer and N. Stock, *Angew. Chem.*, 2007, **119**, 6981–6984.
29 M. A. Herrero, J. M. Kremsner and C. O. Kappe, *J. Org. Chem.*, 2008, **73**, 36–47.
30 A. Sonnauer and N. Stock, *J. Solid State Chem.*, 2008, **181**, 3065–3070.
31 P. Maniam and N. Stock, *Inorg. Chem.*, 2011, **50**, 5085–5097.
32 A. Coelho, in *TOAPS Academic v4.1, ed.*, Coelho Software, Brisbane, 2007.
33 N. Guillou, F. Millange and R. I. Walton, *Chem. Commun.*, 2011, **47**, 713–715.
34 T. Yamada and H. Kitagawa, *J. Am. Chem. Soc.*, 2009, **131**, 6312–6313.
35 R. K. Deshpande, J. L. Minnaar and S. G. Telfer, *Angew. Chem.*, 2010, **122**, 4702–4706.
36 D. J. Lun, G. I. N. Waterhouse and S. G. Telfer, *J. Am. Chem. Soc.*, 2011, **133**, 5806–5809.

5 Zusammenfassung

Die Ergebnisse dieser Arbeit lassen sich thematisch in drei Themenbereiche unterteilen:

1. Synthese und Charakterisierung neuer Al-MOFs
2. Synthese und Charakterisierung isoretikulärer Al-MOFs
3. Anwendungsmöglichkeiten poröser Al-MOFs, die schwefelhaltige Linkermoleküle enthalten

In dieser Arbeit wurde eine Vielzahl neuer Verbindungen ausgehend von schwefelhaltigen Linkermolekülen hergestellt (Abbildung 5.1). Unter Verwendung von sulfonfunktionalisierten Linkermolekülen konnten drei Verbindungen CAU-11, CAU-12 und CAU-12-dehy mit bis dato unbekannten Strukturen erhalten werden. Zusätzlich konnte die Verbindung CAU-11-COOH, synthetisiert werden. Neben den isoretikulären Verbindungen CAU-1-SH, DUT-5-SO_2 und Al-MIL-53-TDC konnten, ausgehend von Mischungen unterschiedlich funktionalisierter Linkermoleküle, zehn sulfonierte isoretikuläre CAU-10-Verbindungen hergestellt werden. Zusätzlich konnten über post-synthetische Modifizierungsreaktionen zwei CAU-1-Sulfonamide erhalten werden. Eine Übersicht über alle Verbindungen ist in Tabelle 5.1 gegeben. Einige der Verbindungen zeigen dabei Anwendungsmöglichkeiten in Bereichen der heterogenen Katalyse, Feuchtigkeitssensorik, Protonenleitfähigkeit und Wärmetauschprozesse.

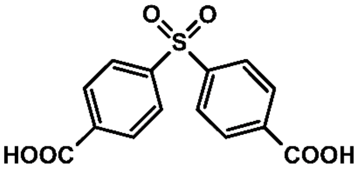

H_2SDBA

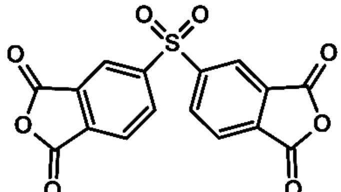

DPSDA

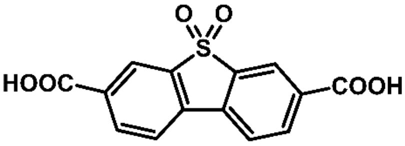

H_2BPDC-SO_2

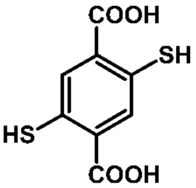

H_2DMBD

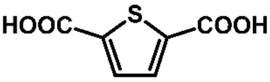

H_2TDC

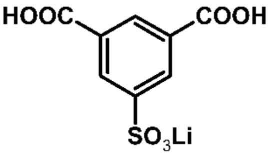

***m*-H_2BDC-SO_3Li**

Abbildung 5.1: Übersicht über die in dieser Arbeit verwendeten schwefelhaltigen Linkermoleküle.

Tabelle 5.1: Übersicht über die in dieser Arbeit hergestellten Verbindungen.

Name	**Zusammensetzung des Gerüsts**	**Synthese aus / über**	**thermische Stabilität [°C]**
CAU-11	[Al(OH)(SDBA)]	H_2O	420
CAU-11-COOH	[Al(OH)(H$_2$DPSTC)]	H_2O	350
CAU-12	[Al$_2$(OH)$_2$(DPSTC)(H$_2$O)$_2$]	H_2O	250
CAU-12-dehy	[Al$_2$(OH)$_2$(H$_2$DPSTC)]	thermische Aktivierung von CAU-12	420
DUT-5-SO$_2$	[Al(OH)(BPDC-SO$_2$)]	DMF	420
CAU-1-NHSO$_2$Me	[Al$_4$(OH)$_2$(OCH$_3$)$_{1.69}$(BDC-NH$_2$)$_{0.23}$ (BDC-NHSO$_2$Me)$_{2.66}$(BDC-NHCH$_3$)$_{0.11}$]	post-synthetische Modifizierung von CAU-1	n.a.
CAU-1-NHSO$_2$Py	[Al$_4$(OH)$_2$(OCH$_3$)$_{1.69}$(BDC-NH$_2$)$_{1.01}$ (BDC-NHSO$_2$Py)$_{1.88}$(BDC-NHCH$_3$)$_{0.11}$]	post-synthetische Modifizierung von CAU-1	n.a.
CAU-1-SH	[Al$_4$(OH)$_{2+x}$(OMe)$_{4-x}$(DMBD)$_3$]	Methanol	200
Al-MIL-53-TDC	[Al(OH)(TDC)]	DMF	420
CAU-10-H/S1	[Al(OH)(*m*-BDC-H)$_{0.92}$(*m*-BDC-SO$_3$H)$_{0.08}$]	H_2O/DMF	400
CAU-10-H/S2	[Al(OH)(*m*-BDC-H)$_{0.85}$(*m*-BDC-SO$_3$H)$_{0.15}$]	H_2O/DMF	400
CAU-10-H/S3	[Al(OH)(*m*-BDC-H)$_{0.795}$(*m*-BDC-SO$_3$H)$_{0.205}$]	H_2O/DMF	400
CAU-10-H/S4	[Al(OH)(*m*-BDC-H)$_{0.76}$(*m*-BDC-SO$_3$H)$_{0.24}$]	H_2O/DMF	400
CAU-10-N/S1	[Al(OH)(*m*-BDC-NO$_2$)$_{0.935}$(*m*-BDC-SO$_3$H)$_{0.065}$]	H_2O/DMF	250
CAU-10-N/S2	[Al(OH)(*m*-BDC-NO$_2$)$_{0.9}$(*m*-BDC-SO$_3$H)$_{0.1}$]	H_2O/DMF	250
CAU-10-N/S3	[Al(OH)(*m*-BDC-NO$_2$)$_{0.825}$(*m*-BDC-SO$_3$H)$_{0.175}$]	H_2O/DMF	250
CAU-10-N/S4	[Al(OH)(*m*-BDC-NO$_2$)$_{0.785}$(*m*-BDC-SO$_3$H)$_{0.215}$]	H_2O/DMF	250
CAU-10-O/S1	[Al(OH)(*m*-BDC-OH)$_{0.92}$(*m*-BDC-SO$_3$H)$_{0.08}$]	H_2O/DMF	230
CAU-10-O/S2	[Al(OH)(*m*-BDC-NO$_2$)$_{0.875}$(*m*-BDC-SO$_3$H)$_{0.125}$]	H_2O/DMF	230

5.1. Synthese und Charakterisierung neuer Al-MOFs

Unter Verwendung der V-förmigen Linkermoleküle 4,4‘-Sulfonyldibenzoesäure (H_2SDBA) und 3,3´,4,4´-Diphenylsulfontetracarbonsäuredianhydrid (DPSDA) konnten die MOFs CAU-11, CAU-11-COOH, CAU-12 und CAU-12-dehy hergestellt und charakterisiert werden. Im Fokus der Untersuchungen standen hierbei der Einfluss der Linkergeometrie auf die Bildung der anorganischen Baueinheit sowie der Einfluss der funktionellen Gruppen auf die Sorptionseigenschaften der erhaltenen Materialien. Ein Überblick über die kristallographischen Daten ist in Tabelle 5.2 gegeben.

Tabelle 5.2: Überblick über die kristallographischen Daten von CAU-11, CAU-11-COOH, CAU-12 und CAU-12-dehy.

	CAU-11	**CAU-11-COOH**	**CAU-12**	**CAU-12-dehy**
λ [Å]	1.000009	1.000009	1.5406	1.5406
Summenformel	$AlC_{14}H_9O_7S$	$AlC_{16}H_{11}O_{11}S$	$Al_2C_{16}H_{15}O_{14.5}S$	$Al_2C_{16}H_{10+2n}O_{12+n}S$
Z	4	4	1	1
Kristallsystem	orthorhombisch	orthorhombisch	triklin	triklin
a [Å]	6.6111(5)	6.6551(3)	6.6872(4)	6.3521(6)
b [Å]	12.888(1)	19.9428(12)	6.6878(6)	7.1524(9)
c [Å]	20.020(1)	12.9656(7)	13.6148(11)	13.7010(15)
α [°]	90	90	84.698(8)	81.841(12)
β [°]	90	90	84.705(5)	88.967(7)
γ [°]	90	90	61.126(5)	64.2526(7)
V [Å^3]	1705.9(2)	1720.5(2)	530.12(8)	544.41(11)
Raumgruppe	*Pnma*	*Pna*2_1	*P*-1	*P*-1
Methode der Strukturlösung	Realraum-Methode, FOX[40]		Strukturmodell aus Literatur[110]	Strukturmodell ausgehend von CAU-12
Methode der Verfeinerung	Rietveld-Methode[38]	Pawley-Methode[38]	Rietveld-Methode[38]	Rietveld-Methode[38]
R_{wp}	7.7	3.3	7.6	6.1
R_{Bragg}	1.4		1.4	1.0

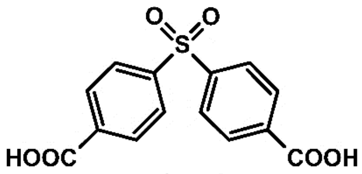

H_2SDBA

1. Die Untersuchung des Systems $Al^{3+}/H_2SDBA/H_2O/NaOH$ unter solvothermalen Bedingungen mittels konventioneller Hochdurchsatzmethoden führte zur Entdeckung der neuen Struktur CAU-11. Nach Aufreinigung des Materials mit DMF konnte aus einer Kombination von thermogravimetrischen Messungen sowie Elementaranalyse die Summenformel als $[Al(OH)(SDBA)]\cdot 0.25DMF$ bestimmt werden.
2. Die Struktur von CAU-11 wurde aus Synchrotron-Röntgenpulverdaten mit Hilfe von Realraum-Methoden gelöst und mittels Rietveld-Methoden verfeinert. Sie basiert auf Ketten von *trans* eckenverknüpfter AlO_6-Polyedern. Diese werde so über die Carboxylatgruppen der Linkermoleküle verknüpft, dass sich Schichten mit rautenförmigen Kanälen mit einem Durchmesser von 6.4×7.1 Å^2 ausbilden. Die Schichten werden über Wasserstoffbrückenbindungen zwischen den Sulfongruppen und den verbrückenden μ-OH-Gruppen benachbarter Al-O-Ketten zusammengehalten.
3. CAU-11 ist stabil bis 420 °C und besitzt eine permanente Porosität mit einer spezifischen Oberfläche von $a_{s(BET)} = 350$ m^2/g und einem Mikroporenvolumen von $V_{mic} = 0.17$ cm^3/g. Die Sulfongruppen weisen in den Zwischenschichtraum in Richtung benachbarter Al-O-Ketten, was der Verbindung einen hydrophoben Charakter verleiht und sich in den Sorptionseigenschaften wiederspiegelt. Die Verbindung ist zugänglich für H_2, CO_2 und CH_4. H_2O-Dampf wird ebenfalls aufgenommen, jedoch zeigt die Isotherme den charakteristischen Verlauf eines hydrophoben Materials. Die Sorptionseigenschaften sind in Tabelle 5.3 zusammengefasst.

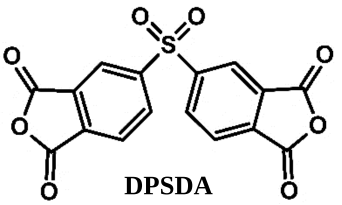

DPSDA

4. Die Untersuchung des Systems $Al^{3+}/DPSDA/H_2O$ unter solvothermalen Bedingungen mittels mikrowellengestützter Hochdurchsatzsynthesen führte zur Entdeckung von zwei Verbindungen. Unter Verwendung von $AlCl_3\cdot 6H_2O$ als Aluminiumquelle und äquimolaren Mengen an Al-Salz und Linkermolekül konnte CAU-11-COOH erhalten werden. Wurde $Al(NO_3)_3\cdot 9H_2O$ als Aluminiumquelle in hohem Überschuss verwendet, erhielt man die Verbindung CAU-12.
5. Aus einer Kombination von IR spektroskopischen und thermogravimetrischen Messungen sowie Elementaranalyse ließ sich die Summenformel Von CAU-11-COOH als $[Al(OH)(H_2DPSTC)]\cdot 0.5H_2O$ bestimmen. Röntgenpulverdaten konnten indiziert und die erhaltenen Zellparameter mit Pawley-Methoden verfeinert werden. Kraftfeld-Methoden wurden eingesetzt, um ein Strukturmodell aufzustellen und die strukturelle Verwandtschaft zu CAU-11 zu verifizieren.

6. In CAU-11-COOH zeigen die zusätzlichen nicht koordinierenden -COOH-Gruppen in die Poren, wodurch die Verbindung hydrophil wird. Dies zeigt sich experimentell in einer deutlich gesteigerten Affinität gegenüber Wasserdampf. Für Stickstoff ist die Verbindung nicht zugänglich, H_2 und CO_2 werden hingegen aufgenommen. Die Sorptionseigenschaften sind in Tabelle 5.3 zusammengefasst.
7. Die Summenformel von CAU-12 konnte als $[Al_2(OH)_2(DPSTC)(H_2O)_2]\cdot H_2O$ bestimmt werden. Die Struktur wurde aus Röntgenpulverdaten gelöst und mittels Rietveld-Methoden verfeinert. Sie basiert ebenfalls auf Ketten *trans* eckenverknüpfter AlO_6-Polyeder und es koordinieren alle vier Carboxylatgruppen des Linkers, allerdings zwei der vier Gruppen nur mit einem Sauerstoffatom. Die oktaedrische Koordination der Aluminiumatome wird durch zusätzliche Wassermoleküle abgesättigt. Erhitzt man CAU-12 werden die koordinierenden Wassermoleküle abgespalten und die Carboxylgruppen koordinieren vollständig, CAU-12-dehy, $[Al_2(OH)_2(DPSTC)]\cdot nH_2O$, entsteht.
8. Da die Sulfongruppen in CAU-12-dehy in die Poren hineinzeigen, weist dieses Material ebenfalls einen hydrophilen Charakter auf und ist zugänglich für H_2, CO_2 und H_2O. Die Sorptionseigenschaften sind in Tabelle 5.3 zusammengefasst.

Tabelle 5.3: Übersicht über die Sorptionseigenschaften von CAU-11, CAU-11-COOH und CAU-12-dehy.

	CAU-11	**CAU-11-COOH**	**CAU-12-dehy**
N_2 (a_{BET}, V_{mic}) (77 K)	350 m^2/g, 0.17 cm^3/g ($V_{mic,theor.}$ = 0.18 cm^3/g)	-	-
H_2 [wt%] (77 K)	0.7	0.02	0.1
H_2O [wt%] (298 K)	8.5	3.0	12.0
CO_2 [wt%] (298 K)	5.6	1.0	1.8
CH_4 [wt%] (298 K)	1.0	-	-
	hydrophob	hydrophil	hydrophil

5.2. Synthese und Charakterisierung isoretikulärer Al-MOFs

Insgesamt wurden 15 isoretikuläre Verbindungen hergestellt. Dazu wurden drei verschiedene Syntheseansätze verwendet. Drei Verbindungen wurden über isoretikuläre Synthese unter Verwendung funktionalisierter Linkermoleküle erhalten. Die kristallographischen Daten sind in Tabelle 5.4 zusammengefasst. Mittels post-synthetische Modifizierungsreaktionen konnten zwei Verbindungen hergestellt werden und unter Verwendung von Mischungen unterschiedlich funktionalisierter Linkermoleküle konnten zehn Verbindungen synthetisiert werden.

Tabelle 5.4: Übersicht über die kristallographischen Daten von CAU-1-SH, DUT-5-SO$_2$ und Al-MIL-53-TDC.

	CAU-1-SH	**DUT-5-SO$_2$**	**Al-MIL-53-TDC**
λ [Å]	1.5406	1.5406	1.5406
Kristallsystem	tetragonal	orthorhombisch	orthorhombisch
a [Å]	18.361(22)	22.442(16)	13.276(2)
b [Å]	18.361(22)	6.494(3)	14.605(3)
c [Å]	17.827(23)	19.169(9)	14.712(3)
$\alpha = \beta = \gamma$ [°]	90	90	90
Raumgruppe	*I4/mmm*	-	$Pna2_1$
Strukturbestimmung	Pawley-Methode	Pawley-Methode	Pawley-Methode
R_{wp}	3.6	3.8	3.0

1. Unter Verwendung von 2,5-Dimercapto-1,4-benzoldicarbonsäure (H_2DMBD) konnte in Anlehnung an die literaturbekannte Synthese von CAU-1 die Verbindung CAU-1-SH $[Al_4(OH)_{2+x}(OMe)_{4-x}(DMBD)_3]\cdot 8H_2O$ hergestellt werden. Die strukturelle Analogie zu CAU-1 wurde mittels Pawley-Methoden verifiziert. Der Erhalt der Thiolgruppen wurde mittels Raman spektroskopischen Messungen bestätigt und die Verbindung ist stabil bis 250 °C. N_2 Sorptionsmessungen ergaben eine spezifische Oberfläche von $a_{s(BET)} = 750$ m^2/g und ein Mikroporenvolumen von $V_{mic} = 0.32$ cm^3/g.

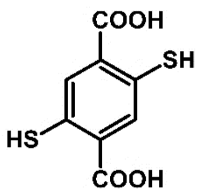

H_2DMBD

2. Die Untersuchung des Systems Al^{3+}/H_2BPDC-SO$_2$/DMF (H_2BPDC-SO$_2$ = 5,5-Dioxo-dibenzo[*b*,*d*]thiophen-3,7-dicarbonsäure) unter solvothermalen Bedingungen mittels mikrowellengestützter Hochdurchsatzsynthese führte zur Entdeckung der isoretikulären

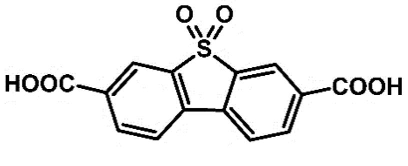

H_2BPDC-SO$_2$

Verbindung DUT-5-SO_2, [Al(OH)(BPDC-SO_2)]·2.5DMF. Die strukturelle Analogie wurde mittels Pawley-Methoden verifiziert. Die Verbindung ist bis 420 °C stabil und weist eine permanente Porosität mit einer spezifischen Oberfläche von $a_{s(BET)}$ = 1530 m^2/g und einem Mikroporenvolumen von V_{mic} = 0.66 cm^3/g auf. Zusätzlich ist die Verbindung zugänglich für CO_2, H_2 und CH_4 Moleküle, wobei die CO_2 Kapazität von 11.6 wt% bis 1 bar besonders hervorzuheben ist (Tabelle 5.5). Sie liegt deutlich oberhalb anderer funktionalisierter DUT-5 Derivate wie DUT-5-NO_2 (7.7 wt%) oder DUT-5-NH_2 (1.5 wt%).

3. Die mikrowellengestützte Hochdurchsatzuntersuchung des Systems Al^{3+}/H_2TDC/DMF (H_2TDC = 2,5-Thiophendicarbonsäure) resultierte in der Entdeckung der Verbindung Al-MIL-53-TDC, [Al(OH)(TDC)]·1.5H_2O·0.7DMF. Da die Qualität der Röntgenpulverdaten nur moderat war wurde über Kraftfeld-Methoden ein Strukturmodell ausgehend von der Struktur von Al-MIL-53 generiert. Zusätzlich wurden Festkörper-NMR-Messungen (^{1}H, ^{13}C und ^{27}Al) durchgeführt um das Strukturmodell zu bestätigen. Al-MIL-53-TDC enthält wie Al-MIL-53 Ketten *trans* eckenverknüpfter AlO_6-Polyeder. Diese werden über die Carboxylatgruppen der Linkermoleküle zu einem dreidimensionalen Netzwerk mit quadratischen Kanälen mit einem Durchmesser von ca. 8.2 x 8.2 Å^2 verknüpft. Die Thiopheneinheiten sind dabei in ihrer Orientierung alternierend ausgerichtet. Thermogravimetrische sowie temperaturabhängige Röntgenpulverdaten ergeben für Al-MIL-53-TDC eine thermische Stabilität bis zu 420°C. Die Verbindung weist eine permanente Porosität mit einer spezifischen Oberfläche von $a_{s(BET)}$ = 1151 m^2/g und einem Mikroporenvolumen von V_{mic} = 0.48 cm^3/g auf. Die Poren sind zugänglich für H_2, CO_2, CH_4 und H_2O (Tabelle 5.5), wobei die Wasserdampfmessung einen charakteristischen S-förmigen Kurvenverlauf zeigt mit einer Aufnahmekapazität von 469 mg/g. Erste cyclische Messungen bestätigen die hohe Stabilität des Materials, da kein Verlust in der Kapazität beobachtet wird.

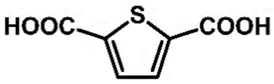

H_2TDC

4. Über post-synthetische Modifizierungsreaktionen konnten zwei verschiedene Sulfonamide ausgehend von CAU-1-NH_2 hergestellt werden. Unter Verwendung von Methyl- bzw. 2-Pyrdinylsulfonylchlorid konnten die entsprechenden Verbindungen CAU-1-NHSO_2Me und CAU-1-NHSO_2Py erhalten werden. Der Modifizierungsgrad für das Methylsulfonamid erreichte dabei 92 %. Diese hohe Umsetzung lässt sich auf die Zugabe von Pyridin zurückführen, welches als Katalysator und Abfangreagenz für bei der Synthese entstandenes HCl fungierte. Die Porosität der Verbindungen ist trotz der Modifizierung

erhalten geblieben, allerdings haben sich die Werte für die spezifischen Oberflächen und das Mikroporenvolumen entsprechend verringert (Tabelle 5.5).

Tabelle 5.5: Übersicht über die Sorptionseigenschaften von CAU-1-SH, DUT-5-SO_2, Al-MIL-53-TDC und CAU-1-$NHSO_2Me$ bzw. -$NHSO_2Py$.

Verbindung	**N_2 (77K) a_s [m^2/g] / V_{mic} [cm^3/g]**	**H_2 (77K) [wt%]**	**CO_2 (298K) [wt%]**	**H_2O (298K) [mg/g]**	**CH_4 (298K) (wt%)**
CAU-1-SH	755 / 0.32	-	-	-	-
DUT-5-SO_2	1530 / 0.66	0.6	11.6	-	0.5
Al-MIL-53-TDC	1151 / 0.48	2.1	10.5	469	1.0
CAU-1-$NHSO_2Me$	900 / 0.37	-	-	-	-
CAU-1-$NHSO_2Py$	720 / 0.29	-	-	-	-

5. Mischungen unterschiedlich funktionalisierter Linkermoleküle wurden verwendet um in CAU-10-H, CAU-10-NO_2 und CAU-10-OH die -H, -NO_2 und -OH Gruppen teilweise durch -SO_3H Gruppen zu ersetzen. Die bereits bekannten Reaktionsbedingungen für die jeweiligen Materialien wurden übernommen und es resultierten drei Serien von sulfonierten Analoga [Al(OH)(*m*-BDC-H)$_{1-y}$(*m*-BDC-SO_3H)$_y$]·Lösungsmittel (y = 0.08, 0.15, 0.205, 0.24; CAU-10-H/S1 bis CAU-10-H/S4), [Al(OH)(*m*-BDC-NO_2)$_{1-y}$(*m*-BDC-SO_3H)$_y$]·Lösungsmittel (y = 0.065, 0.10, 0.175, 0.215; CAU-10-N/S1 bis CAU-10-N/S4) und [Al(OH)(*m*-BDC-OH)$_{1-y}$(*m*-BDC-SO_3H)$_y$]·Lösungsmittel (y = 0.08, 0.125; CAU-10-O/S1 und CAU-10-O/S2). Die strukturelle Analogie zu CAU-10 wurde mit Pawley-Methoden verifiziert (Tabelle 5.6).

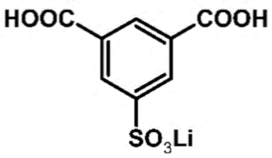

_m_-H_2BDC-SO_3Li

Tabelle 5.6: Übersicht über die kristallographischen Daten der sulfonierten CAU-10 Verbindungen.

Verbindung CAU-10-	**Raumgruppe**	***a* = *b* [Å]**	***c* [Å]**	**R_{wp} [%]**
H	$I4_1$	21.55(7)	10.38(3)	1.9
H/S1	$I4_1$	21.3846(6)	10.7424(5)	5.7
H/S2	$I4_1$	21.4262(8)	10.6918(6)	5.2
H/S3	$I4_1$	21.4786(6)	10.6635(5	4.4
H/S4	$I4_1$	21.4896(5)	10.6277(5)	4.8
NO_2	$P4_1$	21.4707(3)	10.3777(2)	3.2
N/S1	$P4_1$	21.532(1)	10.409(1)	4.0
N/S2	$P4_1$	21.539(1)	10.421(1)	3.3
N/S3	$P4_1$	21.525(1)	10.416(1)	3.6
N/S4	$P4_1$	21.514(2)	10.405(2)	3.2
OH	$P4$	21.3072(5)	38.6974(9)	4.8
O/S1	$P4$	21.325(1)	38.793(2)	4.2
O/S2	$P4$	21.285(2)	38.792(5)	5.5

Der Dotierungsgrad der einzelnen Verbindungen wurde mit ^{1}H-NMR spektroskopischen Messungen ermittelt und über thermogravimetrische (TG) Messungen und Elementaranalyse bestätigt. Die TG Messungen bestätigten zusätzlich für alle Materialien eine hohe thermische Stabilität bis 350 °C. Sorptionsmessungen mit verschiedenen Gasen (N_2, H_2, CO_2) sowie Wasserdampf zeigten einen deutlichen Einfluss der zusätzlichen Sulfonsäuregruppen (Tabelle 5.7). Stickstoffmessungen ergaben verminderte Werte für spezifische Oberflächen und Mikroporenvolumina mit zunehmendem Gehalt an Sulfonsäuregruppen. Die Aufnahmekapazität für H_2 verminderte sich ebenso mit steigendem Dotierungsgrad für alle drei Serien. Für CO_2 konnte in allen Fällen eine gesteigerte Affinität beobachtet werden und zusätzlich für die CAU-10-OH/SO_3H Verbindungen eine gesteigerte Kapazität. Das Einbringen der -SO_3H Gruppen hat offensichtlich einen stark polarisierenden Einfluss auf das Gerüst was zu verstärkten Wechselwirkungen mit dem polaren Gas führt. Wasserdampfmessungen zeigen ebenfalls eine verringerte Kapazität und steigende Affinität mit zunehmendem Anteil an -SO_3H Gruppen. Die gesamten Sorptionsdaten sind in Tabelle 5.7 zusammengefasst.

Tabelle 5.7: Übersicht über die Sorptionsdaten der sulfonierten CAU-10 Verbindungen (* $p/p_0 = 0.5$).

Verbindung CAU-10-	**N_2 (77K) a_s [m²/g] / V_{mic} [cm³/g]**	**H_2 (77K) [wt%]**	**CO_2 (298K) [wt%]**	**H_2O (298K) [cm³/g]**
H	635 / 0.25	1.12	10.57	468
H/S1	372 / 0.21	1.03	10.52	407
H/S2	-	0.95	9.88	357
H/S3	-	0.91	9.44	329
H/S4	-	0.85	8.87	305
NO_2	440 / 0.18	1.01	8.71	215*
N/S1	324 / 0.15	0.91	8.61	318
N/S2	270 / 0.13	0.81	8.29	351
N/S3	242 / 0.12	0.69	7.72	332
N/S4	158 / 0.09	0.64	7.12	382
OH	-	0.79	5.57	390
O/S1	67 / 0.04	0.77	6.57	379
O/S2	74 / 0.05	0.69	8.04	377

5.3. Anwendungsmöglichkeiten poröser Al-MOFs die schwefelhaltige Linkermoleküle enthalten

Verschiedene in dieser Arbeit hergestellte Verbindungen weisen ein hohes Potential für bestimmte Anwendungen auf. Im Folgenden sollen diese einmal zusammenfasst werden.

1. Al-MIL-53-TDC zeigt Charakteristika, die für Anwendungen im Bereich von Wärmetauschprozessen vorteilhaft sind. Die Verbindung ist thermisch stabil bis 420 °C und weist eine Aufnahmekapazität für Wasserdampf von 469 mg/g auf, was 5.5 Wassermolekülen pro Formeleinheit entspricht. Die Isotherme hat einen charakteristisch S-förmigen Verlauf, wobei die Porenbefüllung bei ca. $p/p_0 = 0.35$ stattfindet. Erste cyclische Testmessungen zeigen eine hohe hydrothermale Stabilität der Verbindung. Es wird kein Verlust in der Kapazität beobachtet und der Relativdruck an dem die Porenbefüllung stattfindet bleibt konstant. Die Abwesenheit einer Hysterese belegt, dass die adsorbierten Wassermoleküle leicht wieder zu desorbieren sind.
2. CAU-10-H/S4 (ca. 24 % -SO_3H-Gruppen) wurde als heterogener Katalysator für die Dehydratisierung von Ethanol zu Ethen in der Gasphase eingesetzt. Die Reaktion wurde bei 250 und 300 °C für insgesamt über 40 h durchgeführt. Bei einer Reaktionstemperatur von 250°C liegen die Werte für die Umsetzung von Ethanol für CAU-10-H und CAU-10-H/S4 bei 7 bzw. 52 % und die Selektivität für Ethen bei 22 bzw. 27 %. Wird die Reaktionstemperatur auf 300 °C erhöht, so steigern sich die Umsetzung von Ethanol und die Selektivität für Ethen auf 56 bzw. 91 % und 52 bzw. 79 %. Die zusätzlichen -SO_3H-Gruppen in CAU-10-H/S4 führen somit zu einer deutlich gesteigerten katalytischen Aktivität im Vergleich zu CAU-10-H. Bei beiden Reaktionstemperaturen wurden für CAU-10-H signifikante Mengen von Acetaldehyd (8 bzw. 6 %), einem unerwünschten Nebenprodukt charakteristisch für basische Stellen in einem Katalysator (hier Carboxylatgruppen der Isopthtalationen), detektiert. Für CAU-10-H/S4 vielen diese Werte deutlich niedriger aus (2 bzw. 1 %), man kann also davon ausgehen, dass nur die Brønsted-sauren SO_3H-Gruppen die Dehydratisierung katalysieren. Trotz der extremen Reaktionsbedingungen zeigen sich stabile Umsetzungsraten. Die Kristallinität von CAU-10-H/S4 bleibt erhalten und es finden keine Desulfonierungsprozesse statt. Diese Ergebnisse sind herausragend, da bei den meisten -SO_3H-funktionalisierte Materialien für solche Reaktionen diese Prozesse bereits ab Temperaturen von 150 °C stattfinden.

3. Die Materialien CAU-10-H/S4, CAU-10-N/S4 und CAU-10-O/S2 weisen durch die vorhandenen -SO_3H-Gruppen eine hohe Sensitivität gegenüber Wasserdampf auf. Zur Untersuchung ihres Impedanzverhaltens wurden sie in Form von Tabletten gepresst, mit einer dünnen Schicht Gold bedampft und als Dielektrikum in einen Plattenkondensator eingebaut. Über ein entsprechendes Dosiersystem wurden die Materialien definierten Atmosphären unterschiedlicher Feuchtigkeit ausgesetzt. In Abhängigkeit der Menge an physisorbiertem Wasser ändern die Proben dabei ihre elektrische Leitfähigkeit, was dem Funktionsprinzip eines kapazitiven Feuchtigkeitssensors entspricht. Für CAU-10-$(NO_2)_{0.79}/(SO_3H)_{0.21}$ und CAU-10-$(OH)_{0.89}/(SO_3H)_{0.11}$ wurde unter trockenen Bedingungen Leitfähigkeiten im Bereich von 10^{-14} bis 10^{-13} S/m gemessen. Mit steigender Luftfeuchtigkeit wurde ein exponentieller Abfall des Wiederstandes beobachtet. Die hohe Sensitivität der Materialien zeigt sich darin, dass der Widerstand über den gesamten Feuchtigkeitsbereich über fünf Größenordnungen absinkt. Umgekehrt zeigt sich für die Kapazität ein exponentieller Anstieg mit linear ansteigender Luftfeuchtigkeit. Des Weiteren ist eine deutliche Korrelation zwischen der Impedanz und der absoluten Feuchtigkeit zu beobachten. Insgesamt weisen die untersuchten Materialien ein hohes Anwendungspotential auf, zeigen sie doch selbst bei sehr kleinen Änderungen in der Atmosphäre eindeutige Signaländerungen.
4. Mittels elektrochemischer Impedanzspektroskopie konnte Protonenleitfähigkeit für die Verbindungen CAU-10-H/S1, -N/S2 und -O/S2 (ca. 8, 10 bzw. 12.5 % -SO_3H-Gruppen) über einen Temperaturbereich von 333 bis 413 K bei 100 % Luftfeuchtigkeit nachgewiesen werden. Für CAU-10-H/S1 konnte dabei lediglich bei 413 K ein Wert von $4.88 \cdot 10^{-7}$ S/cm ermittelt werden. Für CAU-10-N/S2 konnten im Bereich von 373 und 413 K Werte zwischen $1.71 \cdot 10^{-8}$ und $5.61 \cdot 10^{-7}$ S/cm erhalten werden und nur für CAU-10-O/S konnte über den gesamten Temperaturbereich Protonenleitfähigkeit zwischen $2.74 \cdot 10^{-7}$ und $8.61 \cdot 10^{-6}$ S/cm gemessen werden. CAU-10-O/S2 liegt damit eine Größenordnung über den anderen beiden Verbindungen, was sich darauf zurückzuführen lässt, dass die -OH-Gruppen, im Gegensatz zu -NO_2 und -H, im Gerüst ebenfalls leicht protoniert und deprotoniert werden können und damit der Leitweg der Protonen innerhalb des Gerüsts nicht unterbrochen wird.

6 Ausblick

Aus den Ergebnissen dieser Arbeit wird ersichtlich, dass Sulfonsäuregruppen in einem MOF ein breites Anwendungsspektrum eröffnen. Obwohl die hier vorgestellten Verbindungen nur partiell mit Sulfonsäuren funktionalisiert waren, zeigten sich teilweise herausragende Eigenschaften. Daher sollten weitere sulfonierte Linkermoleküle zur Herstellung von Al-MOFs untersucht werden. Aktuelle Arbeiten im Arbeitskreis beschäftigen sich mit der Herstellung von Al-MIL-53-SO_3H ausgehend von 2-Sulfoterepthalsäure (Abbildung 6.1 (a)). Hier ist besonderes Augenmerk auf die Flexibilität und thermische Stabilität der Struktur zu legen. Die Geometrie der rautenförmigen Kanäle in der Struktur von MIL-53 könnte sich dabei unterstützend auf mögliche Protonenleitfähigkeit auswirken. 2,5-Disulfoterephthalsäure könnte über Oxidation aus 2,5-Dimercaptoterephthalsäure (Abbildung 6.1 (b)) hergestellt werden und stellt ein ebenfalls mögliches Linkermolekül dar. Des Weiteren könnte der Einsatz von 4,8-Disulfo-2,6-naphthalindicarbonsäure (Abbildung 6.1 (c)) interessant sein. Dieser Linker lässt sich sehr einfach über die Sulfonierung von 2,6-Naphthalindicarbonsäure mit rauchender Schwefelsäure erhalten.[111] Aktuelle Arbeiten führten bis jetzt nur zu einem an Luft instabilen Al-MOF, aber vielleicht könnten hier der Einsatz von Mischungen aus Disulfo-2,6-naphthalindicarbonsäure und der unfunktionalisierten 2,6-Naphthalindicarbonsäure zu einer stabilen Verbindung führen.

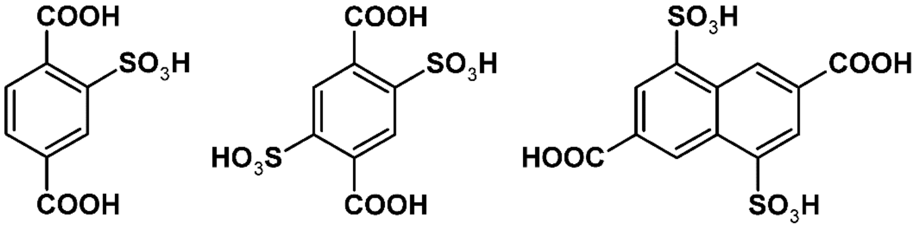

(a) (b) (c)

Abbildung 6.1: Mögliche sulfonierte Linkermoleküle. (a) 2-Sulfoterephthalsäure. (b) 2,5-Disulfotereph-thalsäure. (c) 4,8-Disulfo-2,6-naphthalindicarbonsäure.

Eine andere Möglichkeit sulfonierten MOFs herzustellen wären die post-synthetischen Modifizierungsreaktionen. Ausgehend von thiolfunktionalisierten Verbindungen könnten diese oxidativ umgewandelt werden. Erste Versuche wurden hierzu bereits mit der in dieser Arbeit vorgestellten Verbindung CAU-1-SH gemacht, führten aber noch nicht zu einem Material mit zufriedenstellender Kristallinität. Die Bandbreite organischer Oxidationsreaktionen ist jedoch groß und lässt sicherlich noch die eine oder andere Möglichkeit offen. Für das kürzlich publizierte UiO-66-(SH)$_2$ konnte diese Modifizierungsreaktion unter Verwendung von H_2O_2 (30 %) zumindest erfolgreich durchgeführt werden.[102]

Al-MIL-53-TDC ist die erste MIL-53 Struktur ausgehend von einem gewinkelten fünfgliedrigen Heteroaromaten mit sehr interessanten Wasserstoff- und Wassersorptionseigenschaften. Ausführliche cyclische Wasserdampfmessungen hinsichtlich der hydrothermalen Stabilität der Verbindung sind Gegenstand weiterführender Untersuchungen und sollten das Potential dieses Materials für Anwendungen im Bereich von Wärmetauschprozessen erfassen. Ebenso wie Derivate verlängerter Linkermoleküle auf Basis von Phenylbausteinen für MIL-53 bekannt sind, könnte man sich ähnliche Linkermoleküle aus Thiopheneinheiten aufgebaut vorstellen (Abbildung 6.2).

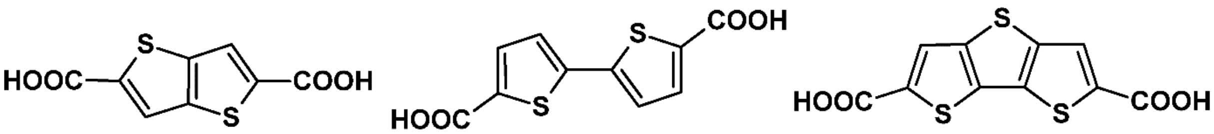

(a) (b) (c)

Abbildung 6.2: Verlängerte Dicarbonsäuren aus Thiopheneinheiten aufgebaut. (a) Thieno(3,2)-thiophen-2,5-dicarbonsäure. (b) [2,2'-Bithiophen]-5,5'-dicarbonsäure. (c) Dithieno[3,2-*b*:2',3'-*d*]-thiophen-2,6-dicarbonsäure.

Diese Linkermoleküle sind kommerziell zwar nicht erhältlich, aber ihre Herstellung wurde bereits in der Literatur beschrieben. Die Herstellung ist mit einem größeren synthetischen Aufwand verbunden, jedoch könnten resultierende MOFs interessante Sorptionseigenschaften sowie neue Strukturen aufweisen. Eine weitere interessante Tricarbonsäure ist in Abbildung 6.3 dargestellt.

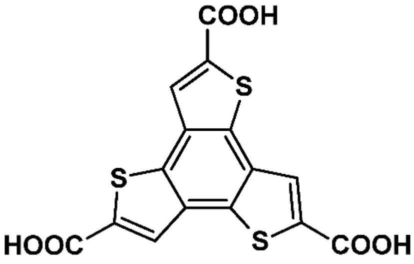

Abbildung 6.3: Struktur von Benzo-(1,2;3,4;5,6)-tris(thiophen-2'-carbonsäure) (H_3BTTC).

H_3BTTC wurde bereits zur Synthese eines mikroporösen Cd-MOFs eingesetzt. Durch thermische Aktivierung der Verbindung konnte der Linker schrittweise entfernen werden, und so Mesoporen erzeugt werden.[112] Ebenso konnte eine mesoporöse Struktur mit trimeren, gemischtvalenten, Fe-O-Einheiten analog zu MIL-100 erhalten werden, allerdings ohne die Ausbildung von Supertetraedern.[113] Ebenso vorstellbar wäre aber auch der Einsatz von Tetracarbonsäuren zum Erhalt neuer Strukturen, wie mit einem Beispiel in Abbildung 6.4 gezeigt. Dieses Linkermolekül ist ebenfalls kommerziell nicht erhältlich, aber die Herstellung bereits in der Literatur beschrieben.

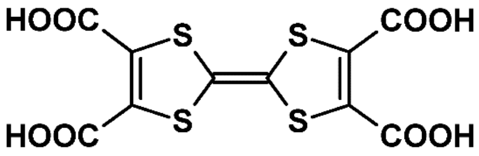

Abbildung 6.4: Struktur von Tetrathiofulvalentetracarbonsäure.

Ausgehend von den in dieser Arbeit verwendeten $-SO_2$-funktionalisierten Linkermoleküle, könnte man sich als weitere funktionelle Gruppen Thioketone oder Sulfoxide vorstellen (Abbildung (a) und (b)). Der Einfluss der Geometrie möglicher Linkermoleküle auf die gebildeten Strukturen kann hierbei im Fokus stehen, ebenso wie die resultierenden Sorptionseigenschaften. Anstelle von den weiter verbreiteten Sulfonsäuregruppen, könnte man sich auch vorstellen Thiocarbonsäuren als funktionelle Gruppen einzubringen (Abbildung 6.5 (c) bis (e)).

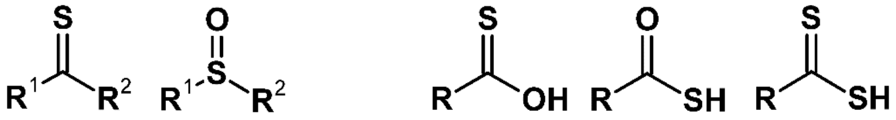

(a) (b) (c) (d) (e)

Abbildung 6.5: Strukturen von (a) Thioketon, (b) Sulfoxid, (c) Monothiocarbonsäure (Thionsäure), (d) Monothiocarbonsäure (Thiolsäure) und (e) Dithiocarbonsäure.

Thiocarbonsäuren könnten allerdings auch selbst an Metalle koordinieren und damit am Aufbau eines Netzwerkes beteiligt sein. Unter Berücksichtigung des HSAB-Konzeptes müsste man hier allerdings wohl vom Aluminium weg auf andere, weichere Metallen zurückgreifen.

7 Literaturverzeichnis

[1] M.E. Davis, *Nature* **2002**, *417*, 813-821.

[2] K.S.W. Sing, *Pure Appl. Chem.* **1982**, *54*, 2201-2218.

[3] L. Puppe, *Chemie in unserer Zeit* **1986**, *20*, 117-127.

[4] G.K.H. Shimizu, R. Vaidhyanathan, J.M. Taylor, *Chem. Soc. Rev.* **2009**, *38*, 1430-1449.

[5] K.J. Gagnon, H.P. Perry, A. Clearfield, *Chem. Rev.* **2012**, *112*, 1034-1054.

[6] J.-P. Zhang, Y.-B. Zhang, J.-B. Lin, X.-M. Chen, *Chem. Rev.* **2011**, *112*, 1001-1033.

[7] O.M. Yaghi, M. O'Keeffe, N.W. Ockwig, H.K. Chae, M. Eddaoudi, J. Kim, *Nature* **2003**, *423*, 705-714.

[8] H. Furukawa, J. Kim, N.W. Ockwig, M. O’Keeffe, O.M. Yaghi, *J. Am. Chem. Soc.* **2008**, *130*, 11650-11661.

[9] G. Akiyama, R. Matsuda, H. Sato, M. Takata, S. Kitagawa, *Adv. Mater.* **2011**, *23*, 3294-3297.

[10] S.-N. Zhao, X.-Z. Song, M. Zhu, X. Meng, L.-L. Wu, S.-Y. Song, C. Wang, H.-J. Zhang, *Dalton Trans.* **2015**, *44*, 948-954.

[11] D.N. Bunck, W.R. Dichtel, *Chem. - Eur. J.* **2013**, *19*, 818-827.

[12] S.M. Chavan, G.C. Shearer, S. Svelle, U. Olsbye, F. Bonino, J. Ethiraj, K.P. Lillerud, S. Bordiga, *Inorg. Chem.* **2014**.

[13] H. Reinsch, S. Waitschat, N. Stock, *Dalton Trans.* **2013**, *42*, 4840-4847.

[14] W. Kleist, M. Maciejewski, A. Baiker, *Thermochim. Acta* **2010**, *499*, 71-78.

[15] S. Marx, W. Kleist, J. Huang, M. Maciejewski, A. Baiker, *Dalton Trans.* **2010**, *39*, 3795-3798.

[16] Themed issue on Metal-Organic Frameworks, Chem. Soc. Rev. **2009**, *38*, 1201-1508.

[17] Themed issue on Metal-Organic Frameworks, Chem. Rev. **2012**, *112*, 673-1268.

[18] Themed issue on Metal-Organic Frameworks, Chem. Soc. Rev. **2014**, *43*, 5415-6172.

[19] Themed issue on Metal-Organic Frameworks, CrystEngComm **2015**, *17*, 185-472.

[20] M. Gaab, N. Trukhan, S. Maurer, R. Gummaraju, U. Müller, *Microporous Mesoporous Mater.* **2012**, *157*, 131-136.

[21] T. Loiseau, L. Lecroq, C. Volkringer, J. Marrot, G. Férey, M. Haouas, F. Taulelle, S. Bourrelly, P.L. Llewellyn, M. Latroche, *J. Am. Chem. Soc.* **2006**, *128*, 10223-10230.

[22] C. Volkringer, D. Popov, T. Loiseau, G.r. Férey, M. Burghammer, C. Riekel, M. Haouas, F. Taulelle, *Chem. Mater.* **2009**, *21*, 5695-5697.

[23] C. Volkringer, D. Popov, T. Loiseau, N. Guillou, G. Ferey, M. Haouas, F. Taulelle, C. Mellot-Draznieks, M. Burghammer, C. Riekel, *Nat. Mater.* **2007**, *6*, 760-764.

[24] S. Biswas, T. Ahnfeldt, N. Stock, *Inorg. Chem.* **2011**, *50*, 9518-9526.

[25] H. Reinsch, M.A. van der Veen, B. Gil, B. Marszalek, T. Verbiest, D. de Vos, N. Stock, *Chem. Mater.* **2013**, *25*, 17-26.

[26] H. Reinsch, N. Stock, *Microporous Mesoporous Mater.* **2013**, *171*, 156-165.

[27] A. Rabenau, *Angew. Chem.* **1985**, *97*, 1017-1032.

[28] P. Lidström, J. Tierney, B. Wathey, J. Westman, *Tetrahedron* **2001**, *57*, 9225-9283.

[29] C.O. Kappe, *Angew. Chem.* **2004**, *116*, 6408-6443.

[30] S.H. Jhung, J.-H. Lee, P.M. Forster, G. Férey, A.K. Cheetham, J.-S. Chang, *Chem. - Eur. J.* **2006**, *12*, 7899-7905.

[31] S.H. Jhung, J.H. Lee, J.W. Yoon, C. Serre, G. Férey, J.S. Chang, *Adv. Mater.* **2007**, *19*, 121-124.

[32] J. Klinowski, F.A. Almeida Paz, P. Silva, J. Rocha, *Dalton Trans.* **2011**, *40*, 321-330.

[33] S. Yoon, E.-S. Lee, A. Manthiram, *Inorg. Chem.* **2012**, *51*, 3505-3512.

[34] R. Tripathi, G. Popov, X. Sun, D.H. Ryan, L.F. Nazar, *J. Mater. Chem. A* **2013**, *1*, 2990-2994.

[35] C.O. Kappe, B. Pieber, D. Dallinger, *Angew. Chem.* **2013**, *125*, 1124-1130.

[36] S. Bauer, N. Stock, *Chemie in unserer Zeit* **2007**, *41*, 390-398.

[37] *WinXPow*, Stoe & Cie GmbH, Darmstadt, **1999**.

[38] A.A. Coelho, *Topas Academics v4.1*, Coelho Software, Brisbane, Australia, **2007**.

[39] V. Favre-Nicolin, R. Cerny, J. Rohlicek, M. Husak, *FOX - Free Objects for Crystallography, Version 1.9.7*, **2000-2011**.

[40] V. Favre-Nicolin, R. Cerny, *J. Appl. Cryst.* **2002**, *35*, 734-743.

[41] *Materials Studio Version 5.0*, Accelrys Inc, San Diego, CA, USA, **2009**.

[42] K. Brandenburg, *Diamond 3.2f*, Crystal Impact GbR, Bonn, Deutschland, **2007-2010**.

[43] A.L. Spek, *PLATON, A Multipurpose Crystallographic Tool v 1.16*, Utrecht Universität, Utrecht, Niederlande, **2011**.

[44] W. Massa, *Kristallstrukturbestimmung*, 5. Aufl., Teubner, Wiesbaden, **2007**.

[45] L.-H. Schilling, *Dissertation*, CAU Kiel, Kiel, **2014**.

[46] Vitalij K. Pecharsky, P.Y. Zavalij, *Fundamentals of Powder Diffraction and Structural Characterization of Materials*, Springer Science+Business Media, Inc., New York, NY 10013, USA, **2005**.

[47] K.D.M. Harris, M. Tremayne, B.M. Kariuki, *Angew. Chem.* **2001**, *113*, 1674-1700.

[48] M.A. Addicoat, N. Vankova, I.F. Akter, T. Heine, *J. Chem. Theory Comput.* **2014**, *10*, 880-891.

[49] J.K. Bristow, D. Tiana, A. Walsh, *J. Chem. Theory Comput.* **2014**, *10*, 4644-4652.

[50] T. Loiseau, C. Serre, C. Huguenard, G. Fink, F. Taulelle, M. Henry, T. Bataille, G. Férey, *Chem. – Eur. J.* **2004**, *10*, 1373-1382.

[51] C. Volkringer, T. Loiseau, N. Guillou, G. Férey, M. Haouas, F. Taulelle, E. Elkaim, N. Stock, *Inorg. Chem.* **2010**, *49*, 9852–9862.

[52] C. Volkringer, T. Loiseau, N. Guillou, G. Ferey, E. Elkaim, *Solid State Sci.* **2009**, *11*, 1507-1512.

[53] C. Volkringer, T. Loiseau, N. Guillou, G. Férey, M. Haouas, F. Taulelle, N. Audebrand, I. Margiolaki, D. Popov, M. Burghammer, C. Riekel, *Cryst. Growth Des.* **2009**, *9*, 2927-2936.

[54] A. Fateeva, P.A. Chater, C.P. Ireland, A.A. Tahir, Y.Z. Khimyak, P.V. Wiper, J.R. Darwent, M.J. Rosseinsky, *Angew. Chem.* **2012**, *124*, 7558-7562.

[55] A. Comotti, S. Bracco, P. Sozzani, S. Horike, R. Matsuda, J. Chen, M. Takata, Y. Kubota, S. Kitagawa, *J. Am. Chem. Soc.* **2008**, *130*, 13664-13672.

[56] T. Loiseau, C. Mellot-Draznieks, H. Muguerra, G. Férey, M. Haouas, F. Taulelle, *C. R. Chim.* **2005**, *8*, 765-772.

[57] I. Senkovska, F. Hoffmann, M. Froba, J. Getzschmann, W. Bohlmann, S. Kaskel, *Microporous Mesoporous Mater.* **2009**, *122*, 93-98.

[58] H. Reinsch, M. Krüger, J. Marrot, N. Stock, *Inorg. Chem.* **2013**, *52*, 1854-1859.

[59] E.D. Bloch, D. Britt, C. Lee, C.J. Doonan, F.J. Uribe-Romo, H. Furukawa, J.R. Long, O.M. Yaghi, *J. Am. Chem. Soc.* **2010**, *132*, 14382-14384.

[60] C. Volkringer, T. Loiseau, T. Devic, G. Férey, D. Popov, M. Burghammer, C. Riekel, *CrystEngComm* **2010**, *12*, 3225-3228.

[61] F. Niekiel, M. Ackermann, P. Guerrier, A. Rothkirch, N. Stock, *Inorg. Chem.* **2013**, *52*, 8699–8705.

[62] E. Alvarez, N. Guillou, C. Martineau, B. Bueken, B. Van de Voorde, C. Le Guillouzer, P. Fabry, F. Nouar, F. Taulelle, D. de Vos, J.-S. Chang, K.H. Cho, N. Ramsahye, T. Devic, M. Daturi, G. Maurin, C. Serre, *Angew. Chem.* **2015**, *127*, 3735–3739.

[63] M.T. Wharmby, M. Snoyek, T. Rhauderwiek, K. Ritter, N. Stock, *Cryst. Growth Des.* **2014**, *14*, 5310-5317.

[64] S.H. Lo, C.H. Chien, Y.L. Lai, C.C. Yang, J.J. Lee, D.S. Raja, C.H. Lin, *J. Mater. Chem. A* **2013**, *1*, 324-329.

[65] S. Yang, J. Sun, A.J. Ramirez-Cuesta, S.K. Callear, I.F. DavidWilliam, D.P. Anderson, R. Newby, A.J. Blake, J.E. Parker, C.C. Tang, M. Schröder, *Nat. Chem.* **2012**, *4*, 887-894.

[66] C. Volkringer, T. Loiseau, M. Haouas, F. Taulelle, D. Popov, M. Burghammer, C. Riekel, C. Zlotea, F. Cuevas, M. Latroche, D. Phanon, C. Knöfelv, P.L. Llewellyn, G. Férey, *Chem. Mater.* **2009**, *21*, 5783-5791.

[67] H. Reinsch, D. De Vos, N. Stock, *ZAAC* **2013**, *639*, 2785-2789.

[68] H. Reinsch, M. Krüger, J. Wack, J. Senker, F. Salles, G. Maurin, N. Stock, *Microporous Mesoporous Mater.* **2012**, *157*, 50-55.

[69] T. Ahnfeldt, N. Guillou, D. Gunzelmann, I. Margiolaki, T. Loiseau, G. Férey, J. Senker, N. Stock, *Angew. Chem.* **2009**, *121*, 5265-5268.

[70] H. Reinsch, M. Feyand, T. Ahnfeldt, N. Stock, *Dalton Trans.* **2012**, *41*, 4164-4171.

[71] F. Gándara, H. Furukawa, S. Lee, O.M. Yaghi, *J. Am. Chem. Soc.* **2014**.

[72] M. Hartmann, M. Fischer, *Microporous Mesoporous Mater.* **2012**, *164*, 38-43.

[73] H. Reinsch, B. Marszalek, J. Wack, J. Senker, B. Gil, N. Stock, *Chem. Commun.* **2012**, *48*, 9486-9488.

[74] M. Mendt, B. Jee, N. Stock, T. Ahnfeldt, M. Hartmann, D. Himsl, A. Pöppl, *J. Phys. Chem. C* **2010**, *114*, 19443-19451.

[75] T. Ahnfeldt, D. Gunzelmann, T. Loiseau, D. Hirsemann, J. Senker, G. Férey, N. Stock, *Inorg. Chem.* **2009**, *48*, 3057-3064.

[76] D. Himsl, D. Wallacher, M. Hartmann, *Angew. Chem.* **2009**, *121*, 4710-4714.

[77] N. Reimer, B. Gil, B. Marszalek, N. Stock, *CrystEngComm* **2012**, *14*, 4119-4125.

[78] S. Biswas, T. Remy, S. Couck, D. Denysenko, G. Rampelberg, J.F.M. Denayer, D. Volkmer, C. Detavernier, P. Van Der Voort, *Phys. Chem. Chem. Phys.* **2013**, *15*, 3552-3561.

[79] D. Fröhlich, S.K. Henninger, C. Janiak, *Dalton Trans.* **2014**, *43*, 15300-15304.

[80] M.F. de Lange, C.P. Ottevanger, M. Wiegman, T.J.H. Vlugt, J. Gascon, F. Kapteijn, *CrystEngComm* **2015**, *17*, 281-285.

[81] T. Ahnfeldt, D. Gunzelmann, J. Wack, J. Senker, N. Stock, *CrystEngComm* **2012**, *14*, 4126-4136.

[82] X. Si, C. Jiao, F. Li, J. Zhang, S. Wang, S. Liu, Z. Li, L. Sun, F. Xu, Z. Gabelica, C. Schick, *Energy Environ. Sci.* **2011**, *4*, 4522-4527.

[83] H. Yin, J. Wang, Z. Xie, J. Yang, J. Bai, J. Lu, Y. Zhang, D. Yin, J.Y.S. Lin, *Chem. Commun.* **2014**, *50*, 3699-3701.

[84] A. Ranft, F. Niekiel, I. Pavlichenko, N. Stock, B.V. Lotsch, *Chem. Mater.* **2015**, *27*, 1961-1970.

[85] T. Ahnfeldt, J. Moellmer, V. Guillerm, R. Staudt, C. Serre, N. Stock, *Chem. – Eur. J.* **2011**, *17*, 6462-6468.

[86] M. Haouas, C. Volkringer, T. Loiseau, G. Ferey, F. Taulelle, *Chem. Mater.* **2012**, *24*, 2462-2471.

[87] J. He, K.-K. Yee, Z. Xu, M. Zeller, A.D. Hunter, S.S.-Y. Chui, C.-M. Che, *Chem. Mater.* **2011**, *23*, 2940-2947.

[88] J.H. Cavka, S. Jakobsen, U. Olsbye, N. Guillou, C. Lamberti, S. Bordiga, K.P. Lillerud, *J. Am. Chem. Soc.* **2008**, *130*, 13850-13851.

[89] M. Zha, J. Liu, Y.-L. Wong, Z. Xu, *J. Mater. Chem. A* **2015**, *3*, 3928-3934.

[90] P. Xydias, I. Spanopoulos, E. Klontzas, G.E. Froudakis, P.N. Trikalitis, *Inorg. Chem.* **2014**, *53*, 679-681.

[91] B. Wang, H. Huang, X.-L. Lv, Y. Xie, M. Li, J.-R. Li, *Inorg. Chem.* **2014**, *53*, 9254–9259.

[92] D. Banerjee, Z. Zhang, A.M. Plonka, J. Li, J.B. Parise, *Cryst. Growth Des.* **2012**, *12*, 2162-2165.

[93] A.M. Plonka, D. Banerjee, W.R. Woerner, Z. Zhang, J. Li, J.B. Parise, *Chem. Commun.* **2013**, *49*, 7055-7057.

[94] G. Akiyama, R. Matsuda, H. Sato, A. Hori, M. Takata, S. Kitagawa, *Microporous Mesoporous Mater.* **2012**, *157*, 89-93.

[95] Y. Jin, J. Shi, F. Zhang, Y. Zhong, W. Zhu, *J. Molec. Catal. A* **2014**, *383–384*, 167-171.

[96] Y. Zang, J. Shi, F. Zhang, Y. Zhong, W. Zhu, *Catal. Sci. Technol.* **2013**, *3*, 2044-2049.

[97] Y.-X. Zhou, Y.-Z. Chen, Y. Hu, G. Huang, S.-H. Yu, H.-L. Jiang, *Chem. - Eur. J.* **2014**, *20*, 14976-14980.

[98] J. Chen, K. Li, L. Chen, R. Liu, X. Huang, D. Ye, *Green Chem.* **2014**, *16*, 2490-2499.

[99] M. Lin Foo, S. Horike, T. Fukushima, Y. Hijikata, Y. Kubota, M. Takata, S. Kitagawa, *Dalton Trans.* **2012**, *41*, 13791-13794.

[100] S. Biswas, J. Zhang, Z. Li, Y.-Y. Liu, M. Grzywa, L. Sun, D. Volkmer, P. Van Der Voort, *Dalton Trans.* **2013**, *42*, 4730-4737.

[101] Q. Yang, A.D. Wiersum, P.L. Llewellyn, V. Guillerm, C. Serre, G. Maurin, *Chem. Commun.* **2011**, *47*, 9603-9605.

[102] W.J. Phang, H. Jo, W.R. Lee, J.H. Song, K. Yoo, B. Kim, C.S. Hong, *Angew. Chem.* **2015**, DOI: 10.1002/ange.201411703.

[103] V. Bon, I. Senkovska, I.A. Baburin, S. Kaskel, *Cryst. Growth Des.* **2013**, *13*, 1231-1237.

[104] I.A. Ibarra, S. Yang, X. Lin, A.J. Blake, P.J. Rizkallah, H. Nowell, D.R. Allan, N.R. Champness, P. Hubberstey, M. Schröder, *Chem. Commun.* **2011**, *47*, 8304-8306.

[105] J. Yang, M. Lutz, A. Grzech, F.M. Mulder, T.J. Dingemans, *CrystEngComm* **2014**, *16*, 5121-5127.

[106] K.-K. Yee, N. Reimer, J. Liu, S.-Y. Cheng, S.-M. Yiu, J. Weber, N. Stock, Z. Xu, *J. Am. Chem. Soc.* **2013**, *135*, 7795-7798.

[107] N. Reimer, H. Reinsch, A.K. Inge, N. Stock, *Inorg. Chem.* **2014**, *54*, 492-501.

[108] C. Kiener, U. Müller, M. Schubert, US Pat (2012) 12/297, 2012, 666.

[109] B. Arstad, H. Fjellvag, K. Kongshaug, O. Swang, R. Blom, *Adsorption* **2008**, *14*, 755-762.

[110] K. Barthelet, D. Riou, M. Nogues, G. Férey, *Inorg. Chem.* **2003**, *42*, 1739-1743.

[111] S. Qing, W. Huang, D. Yan, *React. Funct. Polymers* **2006**, *66*, 219-227.

[112] D. Yuan, D. Zhao, D.J. Timmons, H.-C. Zhou, *Chem. Sci.* **2010**, *2*, 103-106.

[113] D. Yuan, R.B. Getman, Z. Wei, R.Q. Snurr, H.-C. Zhou, *Chem. Commun.* **2012**, *48*, 3297-3299.

Teil III.

Anhang

Supporting Information

Effective Mercury Sorption by Thiol-Laced Metal-organic Frameworks: in Strong Acids and the Vapor Phase

Ka-Kit Yee,[†] Nele Reimer,[‡] Jie Liu,[†] Sum-Yin Cheng,[†] Shek-Man Yiu,[†] Jens Weber,[§] Norbert Stock*[,‡] and Zhengtao Xu,*[, †]

[†]*Department of Biology and Chemistry, City University of Hong Kong, 83 Tat Chee Avenue, Kowloon, Hong Kong, China.* [‡]*Institut für Anorganische Chemie, Christian-Albrechts Universität, Max-Eyth-Str. 2, 24118 Kiel, Germany.* [§]*Max-Planck-Institute of Colloids and Interfaces, Department of Colloid Chemistry, Research Campus Golm, 14476 Golm, Germany.*

*Corresponding author.

E-mail address: stock@ac.uni-kiel.de; zhengtao@cityu.edu.hk (Z. Xu)

General Procedure. Starting materials, reagents, and solvents were purchased from commercial sources (Aldrich, Merck and Acros) and used without further purification. Elemental analysis was performed with a Vario Micro CUBE CHN elemental analyzer. FT-IR spectra were obtained using a Nicolet Avatar 360 FT-IR spectrophotometer. The ratios of the metal ions were determined by using a PerkinElmer Optima™ 2100 DV ICP optical emission spectrometer. Solution ^1H and ^{13}C NMR spectra were recorded on a 400 MHz Bruker superconducting magnet high-field NMR spectrometer at room temperature, with tetramethylsilane (TMS) as the internal standard. Thermogravimetric analyses (TG) were carried out in a nitrogen stream using PerkinElmer Thermal analysis equipment (STA 6000) with a heating rate of 10 °C/min. The 10 ppm Hg standard (10mg/L Mercury in 5% HNO_3) was purchased as a standard solution from PerkinElmer.

The porosity and surface area analysis was performed using a Quantachrome Autosorb iQ gas sorption analyzer. Each sample was outgassed at 0.03 torr with a 2 °C/min ramp to 150 °C and held at 150 °C for 36 hours. The sample was then held at vacuum until the analysis was run. Pore analysis was performed using N_2 at 77 K (P/P_0 range of 1×10^{-5} to 0.995). CO_2 and N_2 adsorption/desorption isotherms at 273 K and 283 K were performed on a Quantachrome Autosorb 1MP instrument. Initial data analysis was done using the AS1Win and QuadraWin 5.05 software (both of Quantachrome instruments). NLDFT analysis of the CO_2 adsorption isotherm (273 K) was done using a commercialized model (assuming carbon-CO_2 interaction parameters and slit-pore morphology). High purity gases were used throughout the analysis.

FT-Raman spectra were obtained using a FT-IR, NIR-FT-Raman Perkin–Elmer Spectrum 2000 instrument equipped with a diode pumped Nd:YAG laser PSU and using the standard Spectrum v2.0 software.

Powder X-ray diffraction data for the Zr-based MOF samples were collected in the reflection mode at room temperature on an Inel Equinox 1000 X-ray diffractometer (Inel, France) equipped with CPS 180 detector using monochromated Cu-Kα_1 (λ = 1.5406 Å) radiation. The X-ray tube operated at a voltage of 30 kV and a current of 30 mA.

High-resolution x-ray powder diffraction patterns (for the Al-based MOF samples) were collected in transmission mode using a STOE STADI P diffractometer equipped with a linear position sensitive detector using monochromated Cu-Kα_1 (λ = 1.5406 Å) radiation. Lattice parameters were determined and refined using TOPAS-Academic V4.1. All other powder data was recorded on a Stadi P Combi diffractometer with Cu-Kα_1 radiation equipped with an image-plate detector system and a xy-stage. Additional characterizations for the Al-based MOFs: Thermogravimetric (TG) measurements were carried out under a flow of air (75 cm^3/min) with a heating rate of 4 K min^{-1} using a Netzsch STA 409 CD analyzer; The contents of carbon, hydrogen and nitrogen were determined by elemental chemical analysis on an Eurovektor EuroEA Elemental Analyzer; IR-spectra were measured on a Bruker ALPHA-FT-IR A220/D-01 spectrometer equipped with an ATR-unit; FT-Raman spectra were recorded on a Bruker IFS 66 FRA 106 in the range of 0–3300 cm^{-1} using a Nd/YAG-Laser (1064 nm); Sorption measurements were carried out using a Belsorp-max instrument (BEL JAPAN INC.).

Preparation of Zr-DMBD crystalline samples. Syntheses of the Zr-DMBD framework were performed in 8 mL Teflon-capped glass vials, with different amount of acetic acid added as modulators for promoting the crystallization process. For example, $ZrCl_4$ (9.6 mg, 0.041 mmol) and a certain amount of acetic acid (i.e., we tested the following setups: 0, 30, 50, 70, 100, 160 equivalents to $ZrCl_4$) were dissolved in DMF (1.6 mL). The mixture was sonicated for about 30 min. The compound H_2DMBD (9.5 mg, 0.041 mmol) was added to the clear solution. For each setup (with different equivalents of acetic acid added), the vial was capped tightly and placed in a pre-heated oven at 120 ^{o}C for 24 hours. After 24 hours, the solution was cooled to room temperature and the precipitates were collected by centrifugation. The solid were suspended in DMF (10 mL) at 60 ^{o}C for 2 hours to remove unreacted substrate. The suspension was centrifuged and the solution was decanted. The obtained solid were washed with dichloromethane (10 mL) in the same way as described for the washing with DMF; and then dried in air to give the as-made product as a solid powder with a very light yellow tinge (16 mg, 79 % yield based on $ZrCl_4$ or H_2DMBD, see below for the composition of the as-made product; yields are similar for all the above setups). Examination by SEM reveals that the amount of acetic acid added significantly influenced the crystallite size of the Zr-DMBD product, i.e., with the acetic acid equivalents being incremented from 0 to 160 as stated above, one observes a development from intergrown aggregates of very small crystals to individual and octahedral nanocrystals of increasing sizes (Figure S1 below). Except mentioned specifically, all

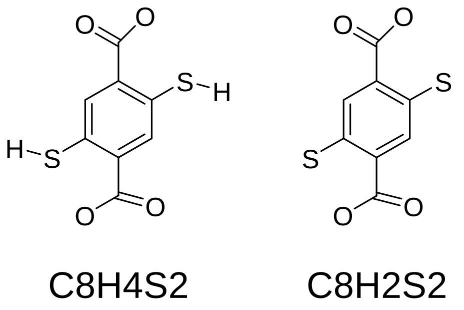

Scheme S1. Structure units of the pristine (left) and oxidized (right) DMBD dicarboxylate linker and the corresponding elemental compositions.

the Zr-DMBD samples used in this paper were prepared with 160 equivalents of acetic acid added, mainly because of the large, well-defined crystallites thus produced.

Elemental analyses and TGA on the as-made Zr-DMBD sample. Elemental analyses on the as-made sample (the one synthesized with 160 equivalents of acetic acid added) found [C (27.86%), H (3.88%), N (3.26%)]. For better characterizing the composition, thermogravimetirc (TG) data were also measured (see Figure S4 below for the TGA plot). The formula $Zr_6O_4(OH)_4{\cdot}(C_8H_4O_4S_2)_n{\cdot}(C_8H_2O_4S_2)_{n-x}{\cdot}(DMF)_m{\cdot}(H_2O)_y$ was used to fit the elemental analysis data and the TGA data, in which $C_8H_4O_4S_2$ and $C_8H_2O_4S_2$ stand for the pristine (with –SH groups intact) and the oxidized (i.e., the –SH becomes –S-S–) DMBD linker, respectively (see Scheme S1 for drawings of the two fragments). Because no quantitative data were obtained for the percentage of the thiol groups oxidized, the exact value of x remains unknown, but the variation of x does not largely alter the overall elemental composition profile. It was found that when n=6 (i.e., the linker sites are fully occupied), and m=7, both the elemental and TGA data can be readily fitted. For example, $Zr_6O_4(OH)_4{\cdot}(C_8H_4O_4S_2)_3{\cdot}(C_8H_2O_4S_2)_3{\cdot}(DMF)_7{\cdot}(H_2O)_{23}$ is calculated to give [C (27.91%), H (3.97%), N (3.30%)], matching closely the measured data [C (27.86%), H (3.88%), N (3.26%)]. The water content of 414/2967=14.0% is greater than that observed in the first step of weight loss in the TGA plot (10%), but precise water content is difficult to assess from the TGA, since the weight loss begins very early in the heating stage; also the water content could be affected by the moisture in the environment, and thus tend to be more variable. The DMF content calculated from the water-free formula $Zr_6O_4(OH)_4{\cdot}(C_8H_4O_4S_2)_3{\cdot}(C_8H_2O_4S_2)_3{\cdot}(DMF)_7$ equals 511/2554=20%, which is, by comparison, closely consistent with the second stage of weight loss in the TGA ((91-73)/0.91%=19.8%; see Figure S4). Moreover, the ZrO_2 content from $Zr_6O_4(OH)_4{\cdot}(C_8H_4O_4S_2)_3{\cdot}(C_8H_2O_4S_2)_3{\cdot}(DMF)_7$

equals 739/2554=28.9%, matching the residual weight percentage found in TGA (27/0.91% = 29.7%). Finally, we speculate that the slight weight loss starting at 620 °C in Figure S4 might be due to the transformation $Zr_6O_n(CO_3)_{12-n} \rightarrow ZrO_2 + CO_2$; but more experiments are needed for verification.

Activation of the Zr-DMBD sample. A thimble (e.g., made from folding filter paper) containing the as-made Zr-DMBD powder sample (150 mg) was loaded into the main chamber of a Soxhlet extractor. The Soxhlet extractor was connected onto a 250 mL round bottom flask containing 150 mL methanol, and then equipped with a condenser. The solvent is heated at 100 ^oC by an oil bath for 4 days. Afterwards a similar step of extraction—lasting also 4 days--was conducted by using dichloromethane (150 ml) in lieu of the methanol. The filter paper was then taken out and the solid was dried in air to give the activated Zr-DMBD sample (the original yellow tinge darkened somewhat to give a slight orange hue). Removal of the DMF guests was confirmed by elemental analysis (i.e., N content < 0.1%) and the absence of the DMF C=O stretching at 1650 cm^{-1} (see Figure S2). The powder XRD pattern of the bulk sample thus activated indicated a single crystalline phase, which was consistent with the as-made Zr-DMBD sample.

Elemental analyses of the $HgCl_2$-loaded sample (Zr-DMBD-$HgCl_2$). CHN analyses found [C (19.22%), H (2.53%), N (0.25%)]; ICP indicated a Zr/Hg ratio of 6:1.82. A fitting formula can be determined to be $Zr_6O_4(OH)_4{\cdot}(C_8H_2O_4S_2)_6{\cdot}(DMF)_{0.5}{\cdot}(H_2O)_{29}{\cdot}(HgCl_2)_{1.82}$, which gives a calculated profile as [C (19.24%), H (2.53%), N (0.23%)].

Elemental analyses of the Hg(0)-treated sample (Zr-DMBD-Hg). CHN analyses found [C (20.23%), H (3.03%), N (0.16%)]; ICP indicated a Zr/Hg ratio of 6:1.2. A fitting formula can be determined to be $Zr_6O_4(OH)_4{\cdot}(C_8H_2O_4S_2)_6{\cdot}(DMF)_{0.25}{\cdot}(H_2O)_{34}{\cdot}(Hg)_{1.2}$, which gives a calculated profile as [C (20.13%), H (2.97%), N (0.12%)].

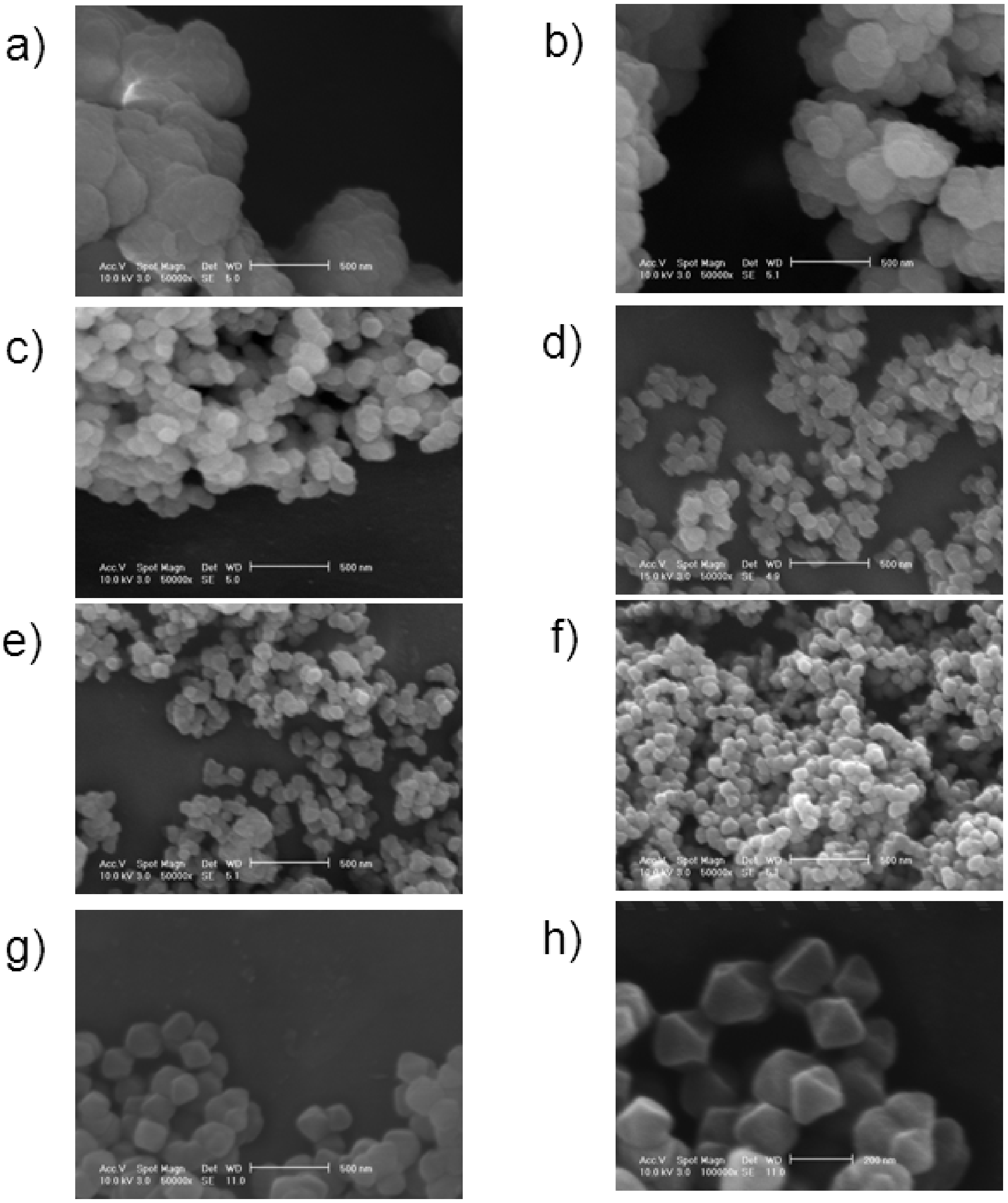

Figure S1 SEM images ($5x10^4$ magnification) of Zr-DMBD crystallites synthesized in the presence of a) 0, b) 10, c) 30, d) 50, e) 70, f) 100, g) 160 equivalents of acetic acid (scale bar: 500 nm); panel h is for the same sample as g, but of higher magnification (10^5; scale bar: 200 nm).

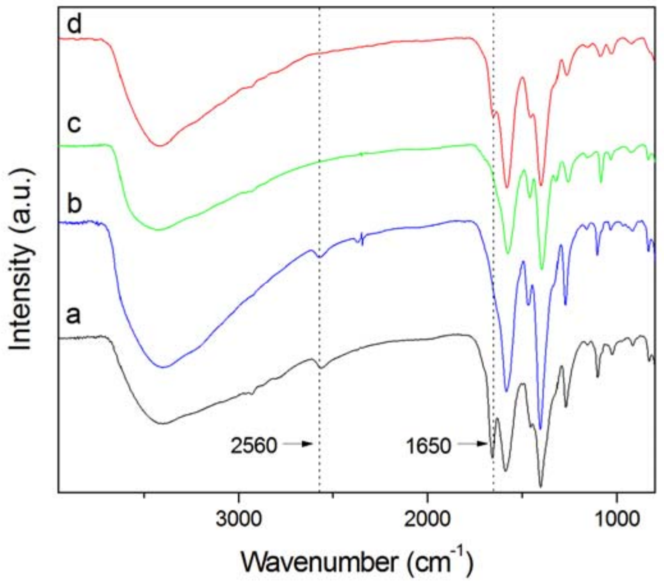

Figure S2. The IR spectra of (a) an as-made sample of Zr-DMBD, (b) activated sample of Zr-DMBD, and (c) $HgCl_2$ water solution treated Zr-DMBD sample and (d) Hg vapor treated Zr-DMBD sample. The 1650 peak in spectra of (a) and (d) arises from the C=O stretching of the DMF guests.

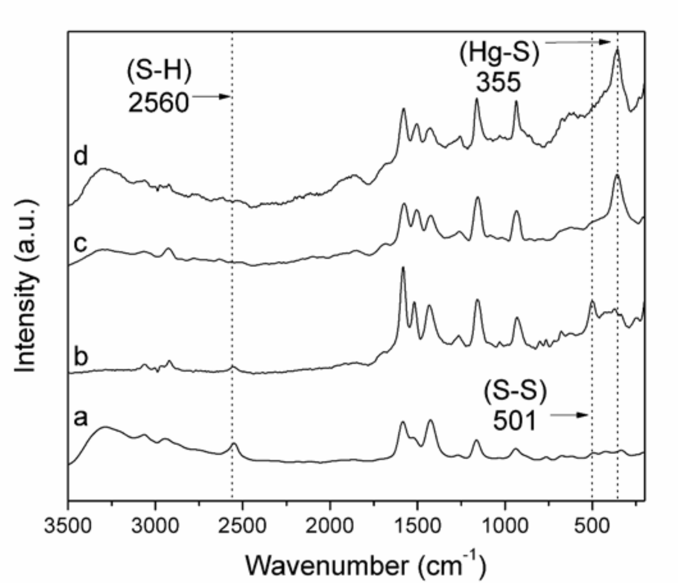

Figure S3. The Raman spectra of (a) an as-made sample of Zr-DMBD, (b) activated sample of Zr-DMBD, and (c) $HgCl_2$ water solution treated Zr-DMBD sample and (d) Hg vapor treated Zr-DMBD sample.

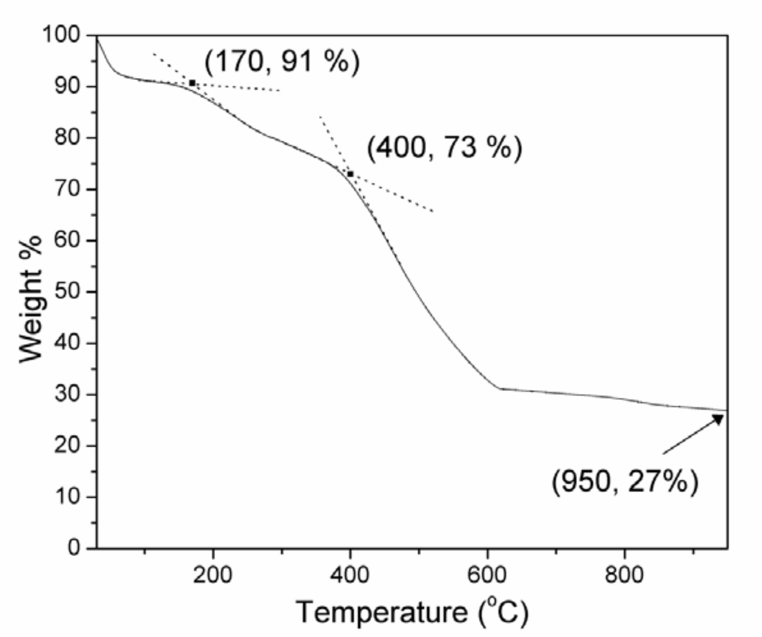

Figure S4. Thermogravimetric analysis (TGA) plot of an as-made Zr-DMBD sample. Heating rate: 2 °C/min.

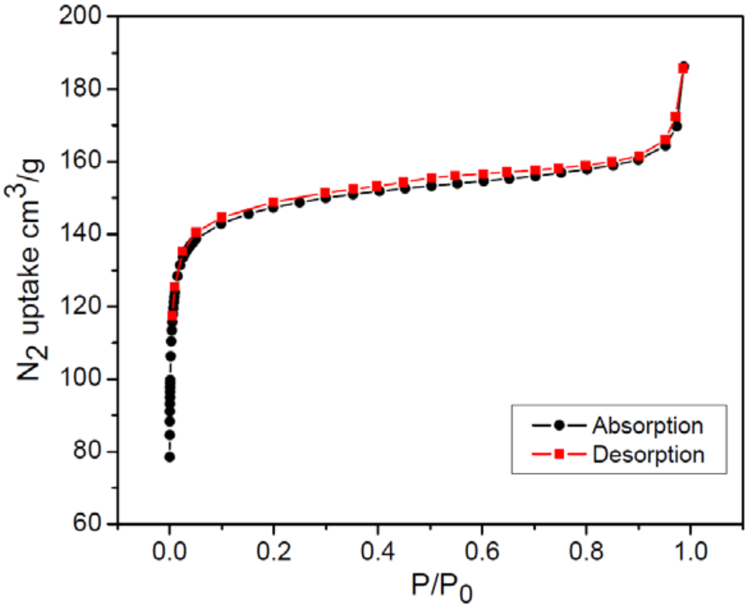

Figure S5. N_2 sorption isotherm at 77 K for an activated Zr-DMBD sample.

Gas adsorption fitting parameters, IAST modeling and heats of adsorption

Experimental CO_2 adsorption isotherms of Zr-DMBD were fitted using single-site and dual-site Langmuir models, yielding an expression for the adsorbed amount *q*. N_2 adsorption isotherms were fitted using a single-site Langmuir approach, as dual-site fitting gave a similar result.

$$q = \frac{(q_1 \cdot b_1 \cdot p)}{(1 + b_1 \cdot p)} + \frac{(q_2 \cdot b_2 \cdot p)}{(1 + b_2 \cdot p)}$$

p: pressure of the bulk gas at equilibrium with the adsorbed phase, *q*: adsorbed amount, q_1, q_2: saturation capacities of site 1 and 2, b_1 and b_2: affinity coefficients of sites 1 and 2.

For curve fitting of the measured data points the following fit equation was used.

$$y = \frac{(q_1 \cdot b_1 \cdot x)}{(1 + b_1 \cdot x)} + \frac{(q_2 \cdot b_2 \cdot x)}{(1 + b_2 \cdot x)}$$

Using the measured data of CO_2 and N_2 isotherms at 273 or 283 K and the fit equation, the calculated isotherms were obtained:

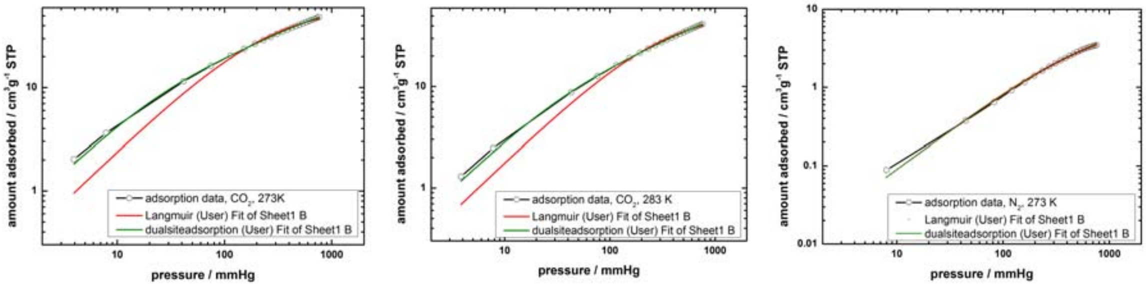

Figure S6. Dual-site (green solid lines) and single site fits (red solid lines) of CO_2 at 273 K, 283K and N_2 at 273 K plotted together with the experimental data (open circles).

Table S1: fit parameters

	CO_2 (273 K)	CO_2 (283 K)	CO_2 (273 K) (single site)	N_2 (273 K)
q_1	49.70720	49.57363	62.601002	7.2802
b_1	9.1E-4	6.6E-4	0.003930	0.0012
q_2	8.97920	8.24691	-	-
b_2	0.01049	0.0067	-	-
R^2	0.99998	0.99999		0.99914

Gas selectivity at 273 K was calculated using the common IAST equations using the single site Langmuir parameter as input. x_{CO2} was calculated using a MatLab ® (R2011a) script employing a Newton-Raphson methodology.[S1]

$$\alpha(CO_2 / N_2) = \frac{x_{CO2}/x_{N2}}{y_{CO2}/y_{N2}}$$

where α is the selectivity, *x* the adsorbed amount and *y* represents the gas phase composition.

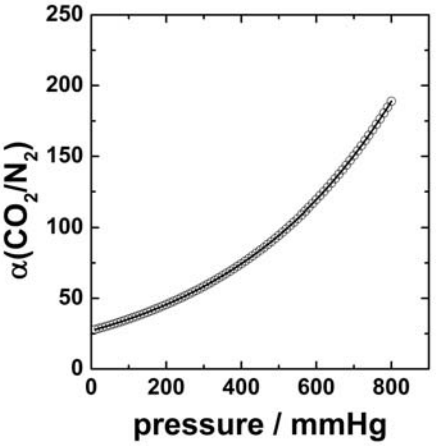

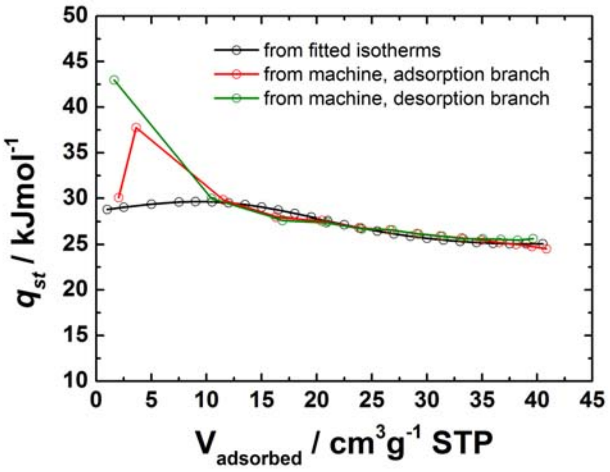

Figure S7. Left-hand side: IAST calculation of the gas selectivity for a gas composition of 0.15/0.85; right-hand side: isosteric heat of CO_2 adsorption, calculated using commercial Quantachrome software or using the fitted isotherms (Clausius-Clapeyron approach).

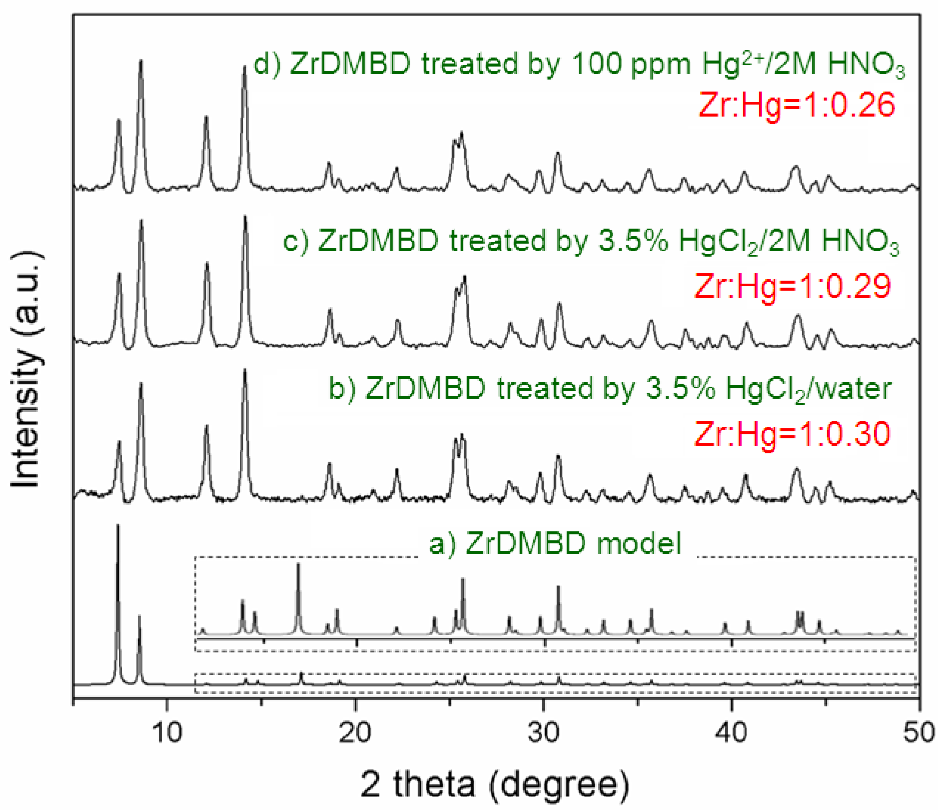

Figure S8. X-ray powder patterns (Cu Kα λ = 1.5418 Å) of $HgCl_2$-treated Zr-DMBD and related samples: (a) a simulation from a structure model of Zr-DMBD (see below for the file in res format; the inset above is an amplification of the higher angle region); (b) as-made Zr-DMBD sample after stirring with a water solution (4.0 ml, w/w 3.5%) of $HgCl_2$ (total amount of $HgCl_2$: 140 mg) at room temperature for 12 hrs (ICP analysis on the resultant sample indicated a Zr/Hg ratio of 1:0.3); (c) an as-made Zr-DMBD sample after stirring with a 2M HNO_3 solution (4.0 ml, w/w 3.5%) of $HgCl_2$ (total amount of $HgCl_2$: 140 mg) at room temperature for 12 hrs (ICP analysis on the resultant sample indicated a Zr/Hg ratio of 1:0.29); (d) an as-made Zr-DMBD sample after stirring with a 2M HNO_3 solution (26.0 ml, 100 ppm of Hg) of $HgCl_2$ (total amount of $HgCl_2$: 3.5 mg) at room temperature for 12 hrs (ICP analysis on the resultant sample indicated a Zr/Hg ratio of 1:0.26).

Information of the structure model of ZrDMBD in res format:

```
TITL ZrDMBD
CELL 0.71073 20.7004 20.7004 20.7004 90 90 90
ZERR 192 0.0002 0.0002 0.0002 0 0 0
LATT 4
SYMM -y,x,z
SYMM x,-y,-z
SYMM z,x,y
SYMM -x,-y,z
SYMM y,x,-z
SYMM -x,z,y
SYMM y,-x,z
SYMM -x,y,-z
SYMM -z,-x,y
SYMM -y,-x,-z
SYMM x,-z,y
SYMM z,-x,-y
SYMM -x,-z,-y
SYMM -z,x,-y
SYMM x,z,-y
SYMM y,z,x
SYMM z,-y,x
SYMM -z,y,x
SYMM z,y,-x
SYMM y,-z,-x
SYMM -z,-y,-x
SYMM -y,z,-x
SYMM -y,-z,x
SFAC C O S Zr
UNIT 192 128 96 24
FVAR 1.00
Zr1    4  1.119890  1.000000  0.000000  0.125000 0.05
```

```
O1     2  1.170470  1.000000  0.095300  0.500000 0.05
O2     2  1.056100  0.943900 -0.056100  0.166667 0.05
C1     1  1.153600  1.000000  0.153600  0.250000 0.05
C2     1  1.205000  1.000000  0.205000  0.250000 0.05
C3     1  1.267500  1.000000  0.184400  0.500000 0.05
S      3  0.712380  0.900195  0.000000  0.250000 0.05
END
```

Synthesis and characterization of CAU-1-SH.

The compound was synthesised using a 20 mL microwave glass vial capped with a silicon seal and a crimp cap. 355 mg (1.54 mmol) DMBD, 1250 mg (5.13 mmol) $AlCl_3 \cdot 6H_2O$ and 16.667 mL dry MeOH were heated for 4 hours at 125°C in a microwave oven with stirring (300 rpm). The formed yellow precipitate was centrifuged for 20 min with 15000 rpm, redispersed in water to remove Cl-ions and centrifuged again for 20 min with 15000 rpm. For the nitrogen sorption measurement the sample was then activated at 130°C for 3 h under vacuum.

The as-made sample of CAU-1-SH_H_2O thus obtained was subjected to thermogravimetric measurements (heating rate 4 $Kmin^{-1}$ under air; see Figure S9 for the TGA plot) and elemental analyses for characterizing the composition.

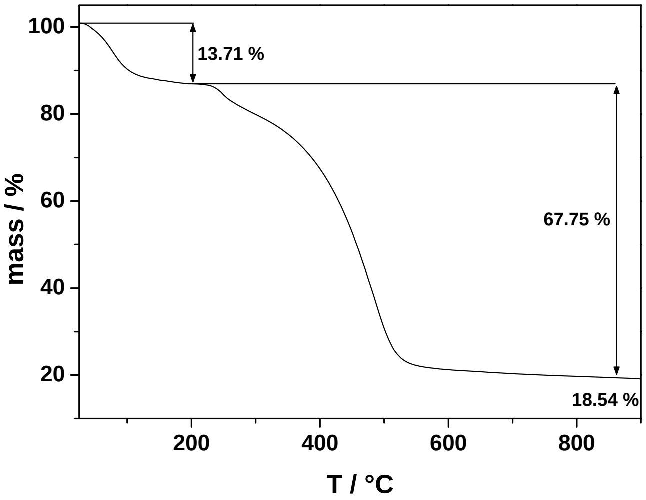

Figure S9. Thermogravimetric analysis (TGA) plot of the as-made sample of CAU-1-SH_H_2O.

The TG-curve of the water-washed sample of CAU-1-SH shows a two-step weight loss. The first step can be attributed to the removal of incorporated water molecules (obs. 13.71 %) and the second step is due to the decomposition of the framework (obs. 67.75 %) resulting in Al_2O_3 (obs. 18.54 %).

The values of the CHNS analysis are as follows: (obs. C: 29.902 %, H: 3.114 %, S: 18.051 %; calc. C: 32.608, H: 4.117 %, S:18.633 %).

The observed TGA and CHNS values were then first compared with the formula $[Al_4(OH)_2(OMe)_4(C_8H_4O_4S_2)_3]\cdot 8H_2O$, the calculated values for the carbon and hydrogen were found to be slightly higher than the observed data (see the listing below). The differences here could be attributed to the partial replacement of the –OMe group by –OH groups. For example, formula $[Al_4(OH)_4(OMe)_2(C_8H_4O_4S_2)_3]\cdot 8H_2O$ gives an overall better fit for the elemental compositions. However, a more rigorous characterization of the composition (e.g., by NMR-spectroscopy) would serve to further verify this suggestion.

Observed:

C, 29.90%; H, 3.11%; S, 18.05%; H_2O, 13.71%; Al_2O_3, 18.54%

$[Al_4(OH)_2(OMe)_4(C_8H_4O_4S_2)_3]\cdot 8H_2O$:

C, 30.71%; H, 3.87%, S: 17.57%; H_2O, 13.16%; Al_2O_3, 18.63%

$[Al_4(OH)_4(OMe)_2(C_8H_4O_4S_2)_3]\cdot 8H_2O$:

C, 29.27%; H, 3.59%, S: 18.03%; H_2O, 13.50%; Al_2O_3, 19.12%

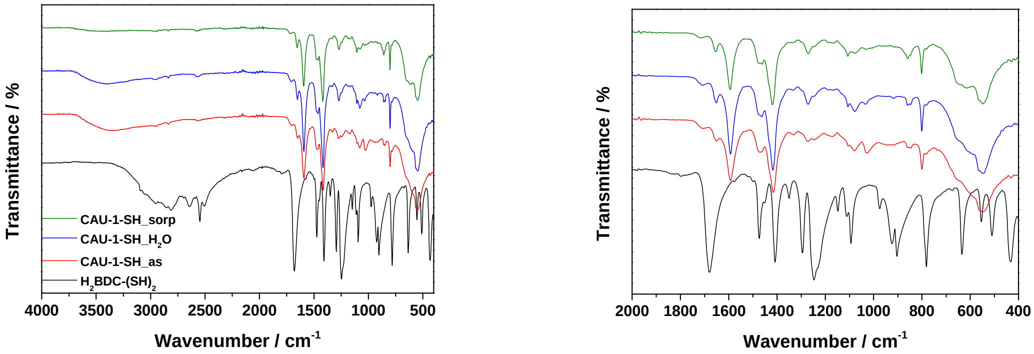

Figure S10. Left: The IR-spectra of the linker molecule [H_2DMBD, i.e., H_2BDC-$(SH)_2$, black], the as-made sample (red), the water-washed sample (blue) and the one after the sorption measurement (green) of CAU-1-SH. Right: an amplification to highlight a strong decrease of the band at 1680 cm^{-1} of the free acid group of the linker molecule due the coordination of that group resulting in a band at 1653 cm^{-1} for the CAU-1 compound. In addition a small band at 1712 cm^{-1} still occurs, probably due to small a residue of unreacted linker molecules.

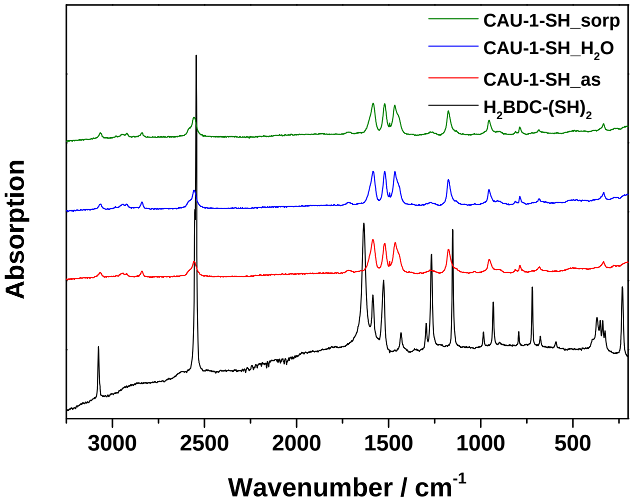

Figure S11. The Raman spectra of the linker molecule [H_2DMBD, i.e., H_2BDC-$(SH)_2$, black], the as-made sample (red), the water-washed sample (blue) and the one after the sorption measurement (green) of CAU-1-SH. The Raman-spectra of the different treated samples compared to the one of the linker molecule show a band at 2560 cm^{-1} which can be attributed to the SH-stretching vibration. Bands at 3065 cm^{-1} as well as 2940 and 2840cm^{-1} indicate the presence of aromatic and aliphatic CH-stretching (-OMe groups) vibrations. Also observed is the strong decrease of the band at 1635 cm^{-1} of the free carboxylic acid group in the spectrum of the linker compared to the ones of the CAU-1-SH samples due to the coordination of this group to the Al^{3+}-cation. In the region of about 450-550 cm-1 no significant band can be observed indicating that no disulfide-groups are present in the framework of the CAU-1-SH samples.

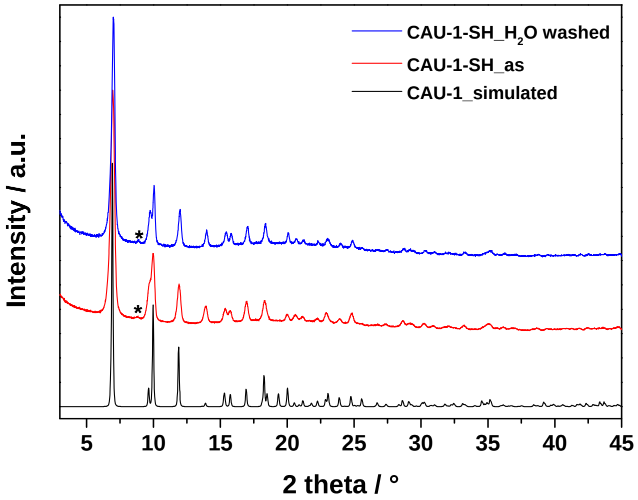

Figure S12. High-resolution powder patterns of the as-made (red) and the water-washed (blue) CAU-1-SH samples, as compared to a simulated one (black) of CAU-1. The asterisk is suggestive of a small impurity of Al-MIL-53-SH.

The powder pattern of the as-made sample was then indexed and the obtained cell parameters were refined by Pawley methods. The plot and the refined parameters are shown below.

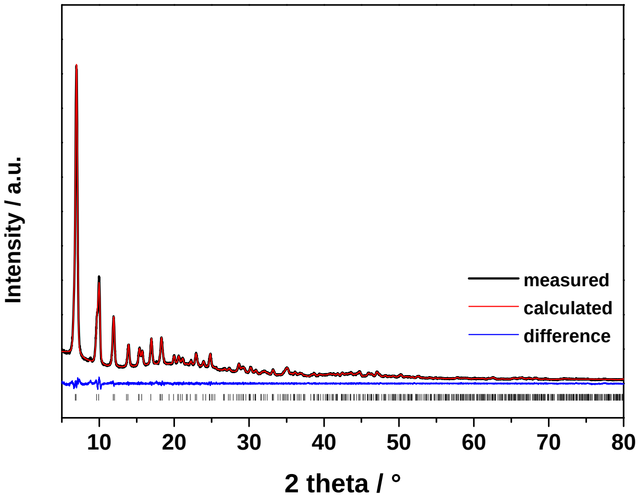

Figure S13. The plot for the Pawley refinement of the cell parameters of CAU-1-SH using the powder X-ray diffraction data obtained in Figure S10.

SG = *I4/mmm*

a = 18.361(22)Å

b = 18.361(22)Å

c = 17.827(23)Å

r_{wp} = 3.635

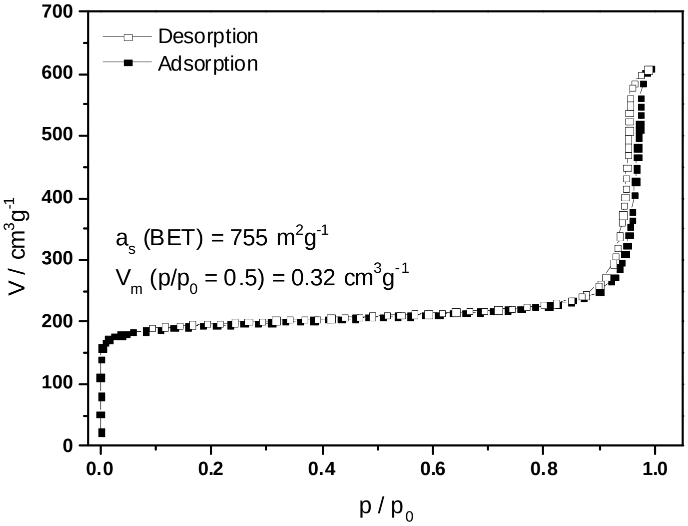

Figure S14. N_2 sorption isotherm at 77 K for an activated (3 h, 130°C under vacuum) CAU-1-SH_H_2O sample. The compound shows a type-1 isotherm characteristic of microporous compounds with a specific surface area of ca 750 m^2g^{-1} and a micropore volume of 0.32 cm^3g^{-1}.

Supplementary Data

Sulfonyl chlorides as an efficient tool for the postsynthetic modification of Cr-MIL-101-SO_3H and CAU-1-NH_2

Arne Klinkebiel, Nele Reimer, Martin Lammert, Norbert Stock and Ulrich Lüning

Otto-Diels Institut für Organische Chemie, Otto-Hahn-Platz 4, 24118 Kiel, Germany.
E-Mail: luening@oc.uni-kiel.de

Institut für Anorganische Chemie, Max-Eyth-Strasse 2, 24118 Kiel, Germany.
E-Mail: stock@ac.uni-kiel.de

Contents

1 General

1.1 Chemicals

Dimethylformamide, methylamine, ethylamine, sodium hypochlorite acid and 2-mercaptopyridine were bought from Sigma-Aldrich Chemicals Co. Propylamine, oxalylchloride, 2-aminotherephthalic acid and methyl sulfonylchloride were purchased from ABCR GmbH & Co. KG, dimethylamine from Alfa Aesar GmbH & Co. KG. Monosodium 2-sulfoterephthalic acid was recieved from TCI, methanol from Baker and aluminium chloride hexahydrate from Grüssing. Benzylamine, aniline, pyridine, aminopyridine, chromium trioxide and tetrahydrofuran were commercially available from Merck. Tetrahydrofuran was dried using lithiumalumnium hydride, pyridine was purified using basic aluminium oxide. All other chemicals were used without any further purification.

1.2 Characterization

NMR spectra were recorded on Bruker DRX 500 or AV 600 instruments. Assignments are supported by COSY, HSQC, and HMBC. Even when obtained by DEPT, the type of ^{13}C signal is always listed as singlet, doublet, etc. All chemical shifts are referenced to the residual proton or carbon signal of the solvent. Unless otherwise noted, deuterated sodium hydroxide was used as the solvent, so the carboxylic acids are deprotonated. Under this condition, all hydrogen atoms of the sulfonamides are exchanged by deuterium. Part of the amides may be deprotonated. However, in the drawings structures are drawn with N-H-groups.

Approximation of conversion degrees was determined by comparing the relative integrals in ^{1}H-NMR spectra of the digested material after synthesis and removal of chromium. In the spectra shown below, the unfunctionalized linker has been removed by aqueous extraction as described below.

IR spectra were recorded with a Perkin-Elmer 100 equipped with a MKII Golden Gate TM Single Reflection ATR unit.

Nitrogen sorption isotherms were recorded at 77 K with a BELSORP-max or if mentioned with a BELSORP-mini apparatus (BEL JAPAN INC.). Micropore volumes were calculated from the adsorption branch at $p/p_0 = 0.5$.

The initial characterization by means of PXRD methods was carried out on a STOE-Stadi-P Combi diffractometer (Cu $K_{\alpha 1}$ radiation) equipped with a xy stage and an image plate detector.

2 Post-Synthetic modification of Cr-MIL-101-SO_3H

2.1 Synthesis of Cr-MIL-101-SO_3H (1)

Cr-MIL-101-SO_3H was prepared according to a literatures procedure[1]. A 100 mL teflon reactor was loaded with 1.25 g (12.5 mmol) of chromium trioxide and 3.35 g (12.5 mmol) of monosodium 2-sulfoterephthalic acid. After the addition of 50 mL of demineralized water and 910 mg (25.0 mmol) concentrated hydrochloric acid, the reactor was sealed and heated to 180 °C within 1 h. The temperature was held for 144 h and the reactor was cooled to room temperature within 6 h. The green solid was collected by centrifugation and dispersed in 100 mL of demineralized water (this process was repeated two times with water and three times with ethanol). The resulting green solid was dried in air at 70°C.

2.2 Synthesis of Cr-MIL-101-SO_2Cl (2)

General procedure

A schlenck tube was loaded with 100 mg of Cr-MIL-101-SO_3H, sealed and evacuated for 2 h at room temperature. After flushing the tube with nitrogen, 2 mL of a 1.5 M solution of oxalylchloride in dry tetrahydrofuran was added followed by *N*,*N*-dimethylformamide (5-15 µL). After stirring the sample under nitrogen for 24 h at room temperature the precipitate was washed two times using tetrahydrofuran and separated by centrifugation. The sample was dried in vacuo.

2.3 Synthesis of Cr-MIL-101-SO_2NHR (3a-f)

General procedure

A Schlenck tube was loaded with 100 mg of Cr-MIL-101-SO_2Cl, sealed and evacuated for 2 h. After flushing the tube with nitrogen, a 2 M solution of amine in dry tetrahydrofuran was added. After stirring the sample under nitrogen for 24 h at room temperature the precipitate was separated by centrifugation and washed using tetrahydrofuran (2 x 2 mL, 2 x 15 min), methanol (4 x 2 mL, 3 x 15 min, 1 x 12 h), and water (4 x 2 mL, 3 x 15 min, 1 x 12 h). The sample was dried for 24 h at 60 °C in vacuo.

For ^1H-NMR analyses, the respective MOF was dissolved in 2 mL of 2 M sodium hydroxide solution. After a pH = 10 – 12 was reached by adding conc. hydrochloric acid, the precipitate was filtered off. The basic filtrate was washed three times using 5 mL of *tert*-butyl methyl ether, acidified and extracted using 5 mL of *tert*-butyl methyl ether. The organic phase was dried using magnesium sulfate, filtered and the solvent was removed in vacuo.

2.4 Characterisation of Cr-MIL-101-NHR

2.4.1 Cr-MIL-101-SO_2NHMe (3a)

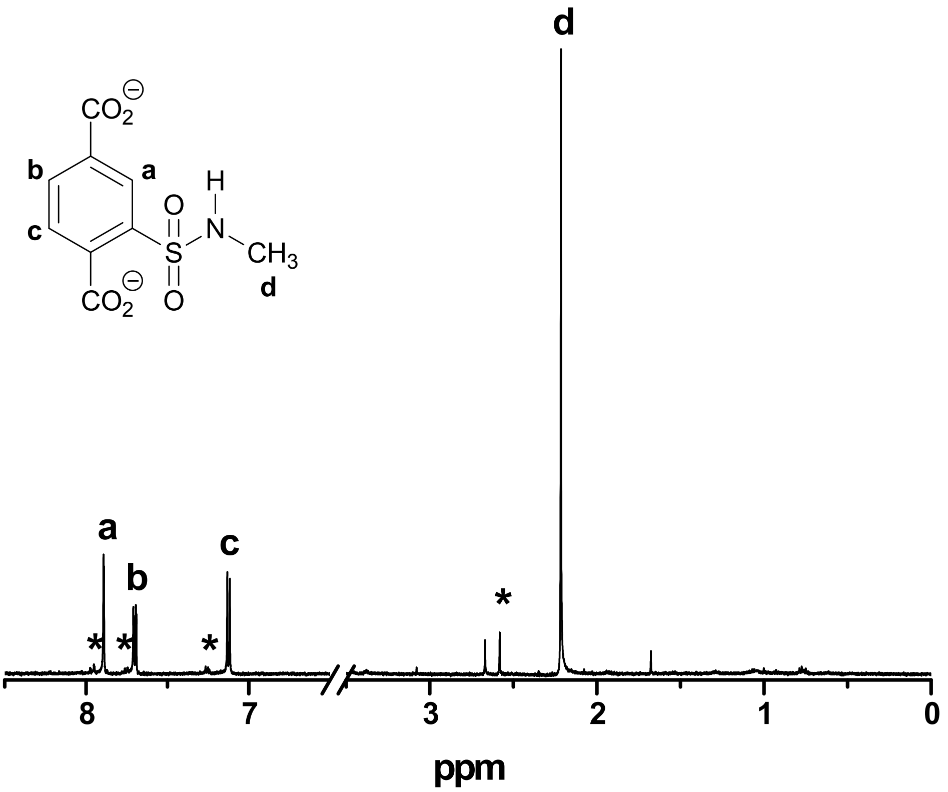

Fig. S1. ^1H-NMR spectrum of digested Cr-MIL-SO_2NHMe **3a** (500 MHz, 5 % NaOD in D_2O): (**a-c**) aromatic protons, (**d**) methyl group, (*) sideproduct *N*,*N*-dimethyl sulfonamide **3d** (< 2 %).

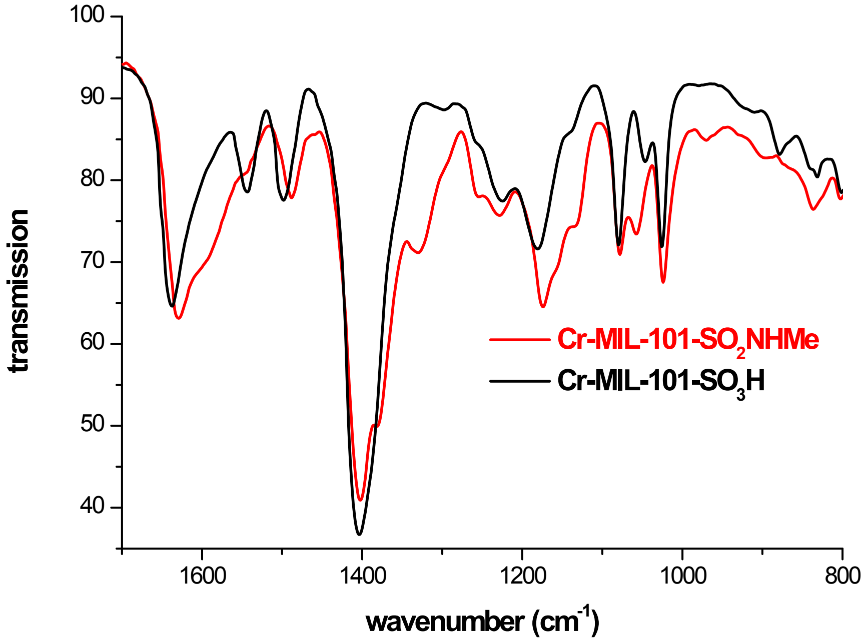

Fig. S2. FT-IR spectra of the starting material Cr-MIL-SO_3H **1** (**black**) and Cr-MIL-SO_2NHMe **3a** (**red**). Characteristical frequencies: 1380 cm^{-1} (SO_2NH), 1329 cm^{-1} (CH_3), 1057 cm^{-1} (S=O). No significant band between 3000 – 2800 cm^{-1} for CH_3 stretch were observed.

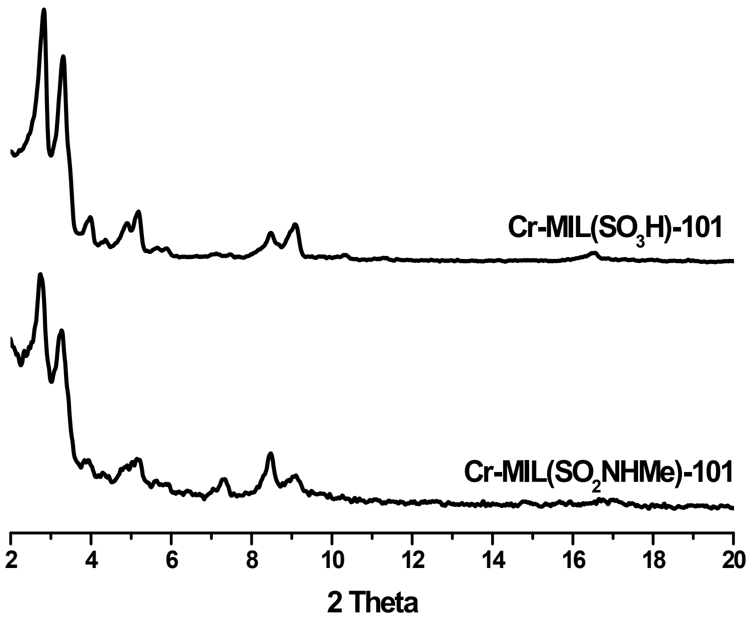

Fig. S3. PXRD pattern of the starting material Cr-MIL-SO_3H **1** (top) and Cr-MIL-SO_2NHMe **3a** (bottom).

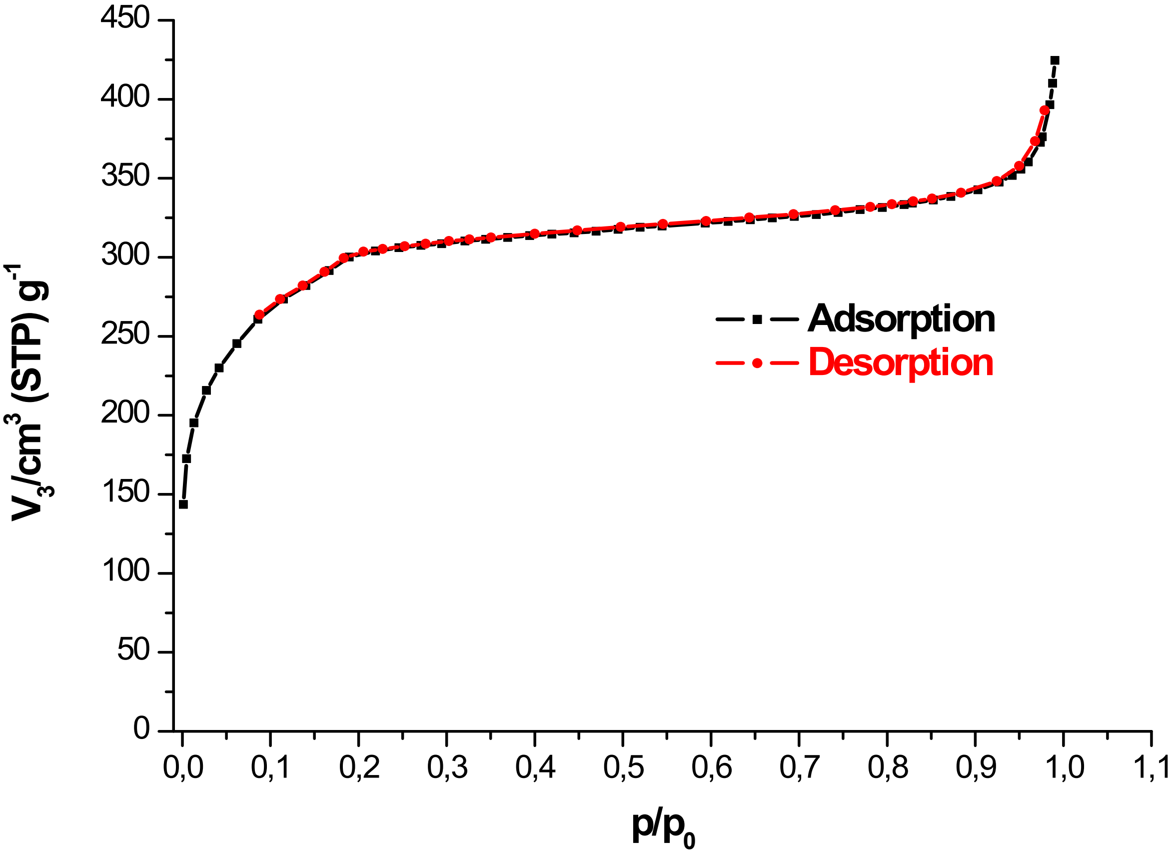

Fig. S4. N_2 adsorption isotherm (77 K) of Cr-MIL-SO_2NHMe **3a**: $a_{s,BET}$ = 1070 m^2/g, total pore volume = 0.443 cm^3/g (starting material **1**: $a_{s,BET}$ = 1350 m^2/g, total pore volume = 0.624 cm^3/g).

2.4.2 Cr-MIL-101-SO$_2$NHEt (3b)

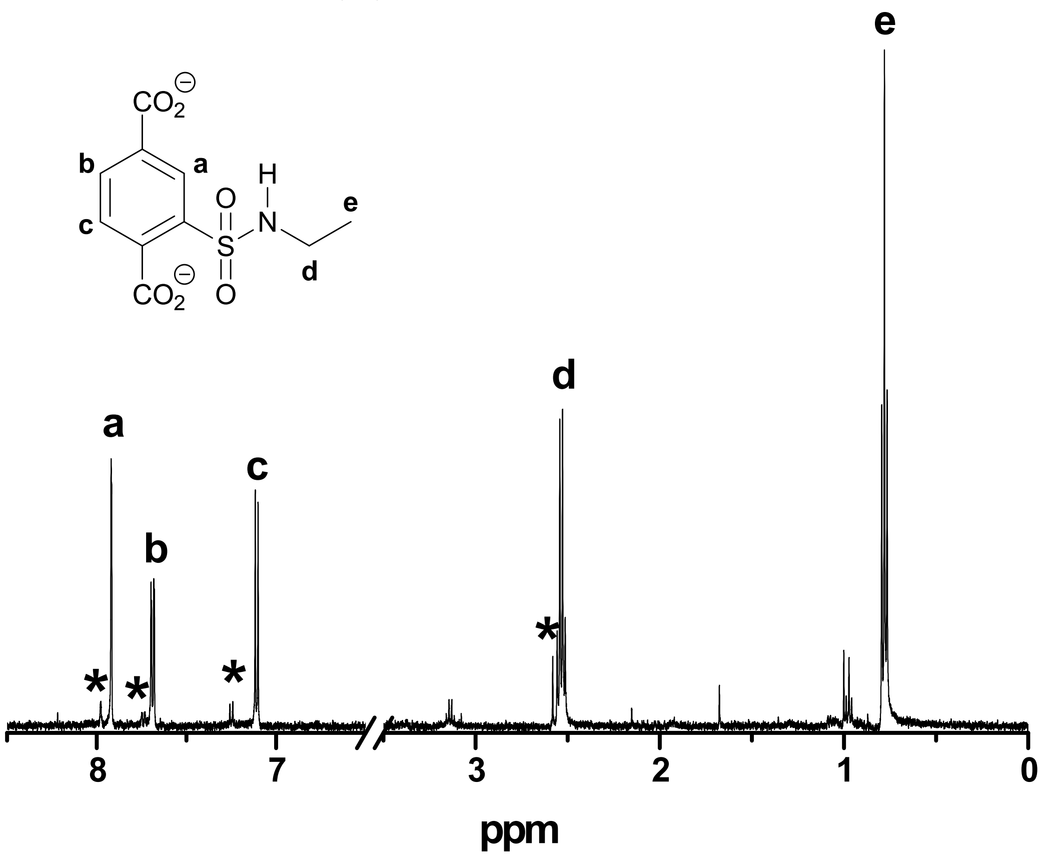

Fig. S5. ^{1}H-NMR spectrum of digested Cr-MIL-SO$_2$NHEt **3b** (500 MHz, 5 % NaOD in D$_2$O): (**a-c**) aromatic protons, (**d-e**) ethyl group, (*) sideproduct *N*,*N*-dimethyl sulfonamide **3d** (~ 2 %).

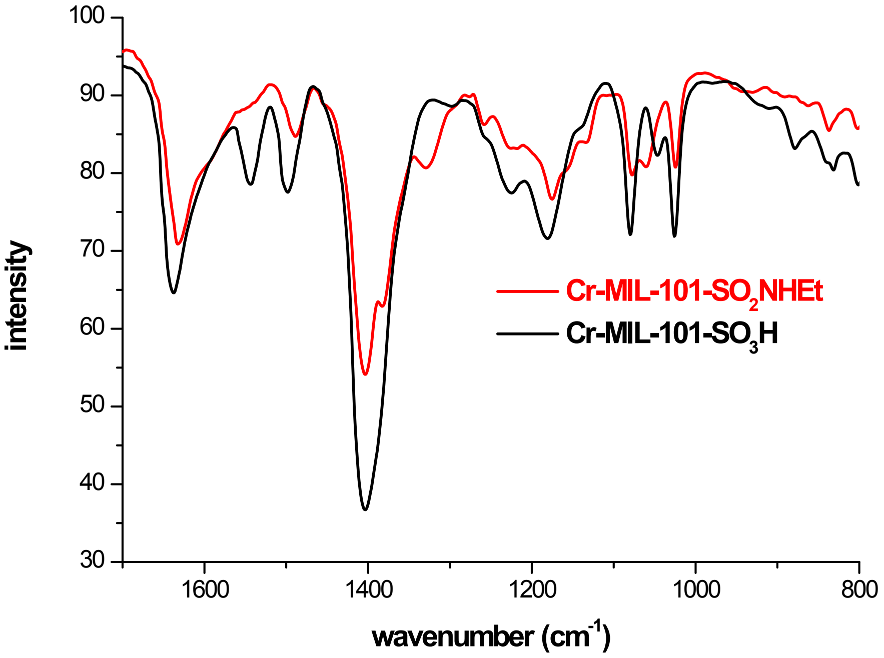

Fig. S6. FT-IR spectra of the starting material Cr-MIL-SO$_3$H **1** (**black**) and Cr-MIL-SO$_2$NHEt **3d** (**red**). Characteristical frequencies: 1383 cm^{-1} (SO$_2$NH), 1330 cm^{-1} (CH$_3$), 1060 cm^{-1} (S=O). No significant bands between 3000 – 2800 cm^{-1} for CH$_3$/CH$_2$ stretch were observed.

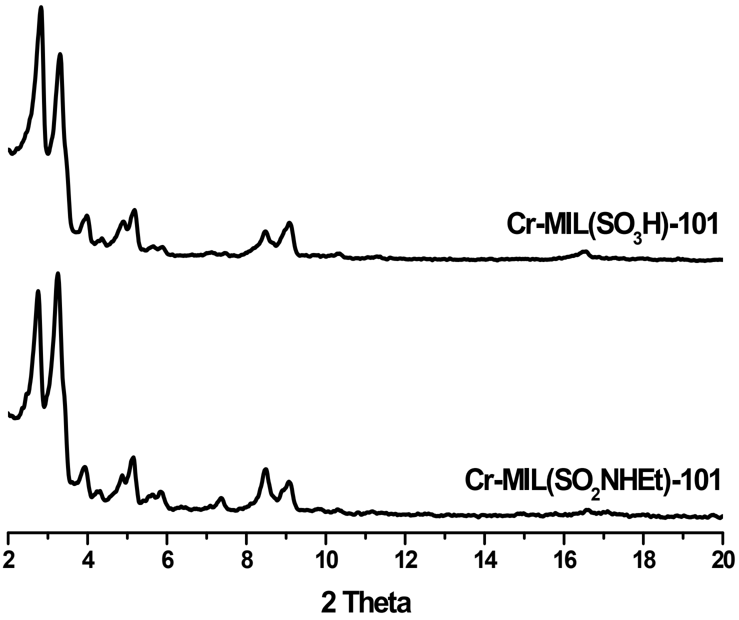

Fig. S7. PXRD pattern of the starting material Cr-MIL-SO$_3$H **1** (top) and Cr-MIL-SO$_2$NHEt **3b** (bottom).

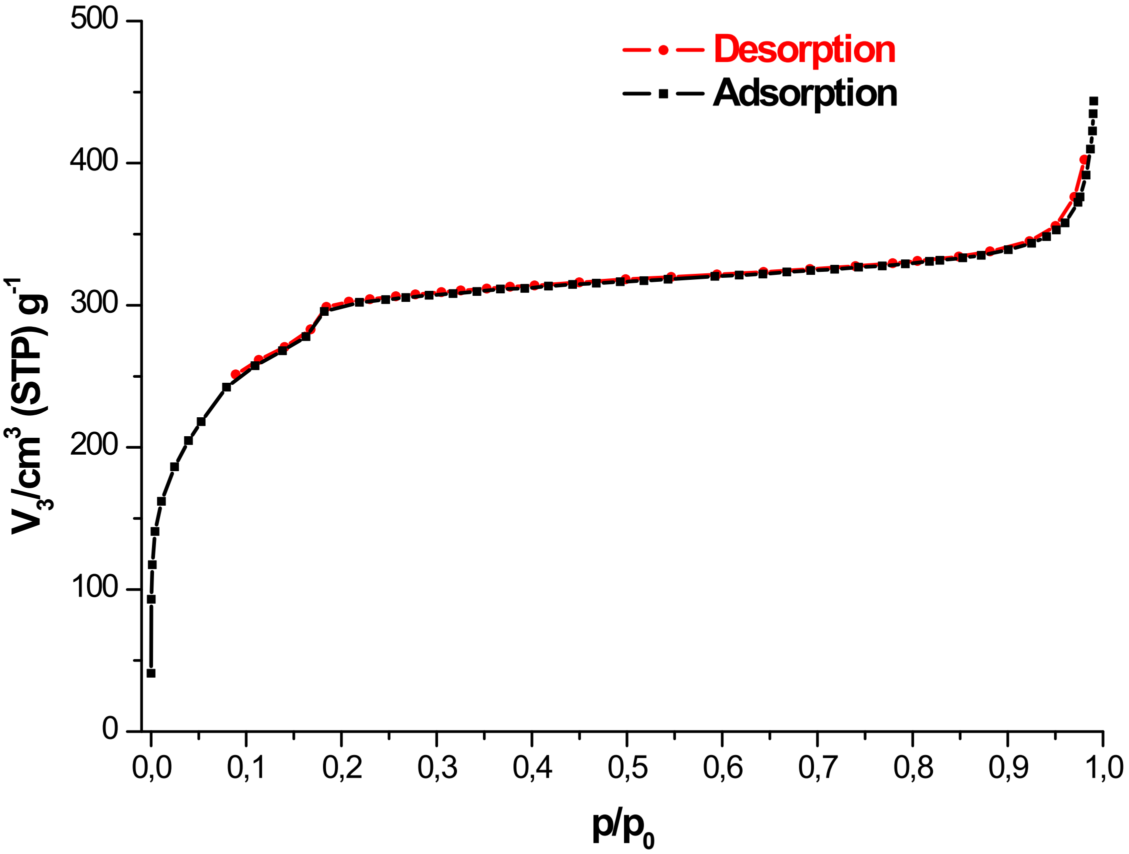

Fig. S8. N_2 adsorption isotherm (77 K) of Cr-MIL-SO$_2$NHEt **3b**: $a_{s,BET}$ = 1050 m^2/g, total pore volume = 0.490 cm^3/g (starting material **1**: $a_{s,BET}$ = 1350 m^2/g, total pore volume = 0.624 cm^3/g).

2.4.3 Cr-MIL-101-SO_2NHPr (3c)

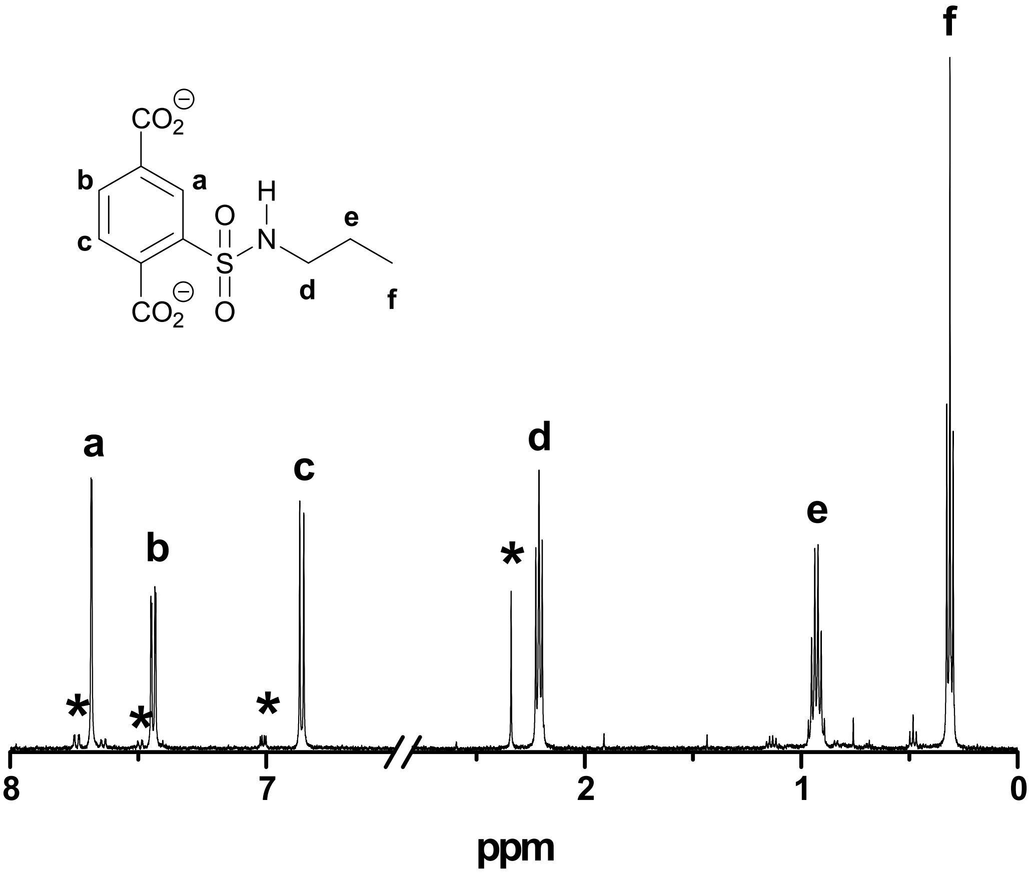

Fig. S9. ^{1}H-NMR spectrum of digested Cr-MIL-SO_2NHPr **3c** (500 MHz, 5 % NaOD in D_2O): (**a-c**) aromatic protons, (**d-f**) propyl group, (*) side product *N*,*N*-dimethyl sulfonamide **3d** (< 2 %)

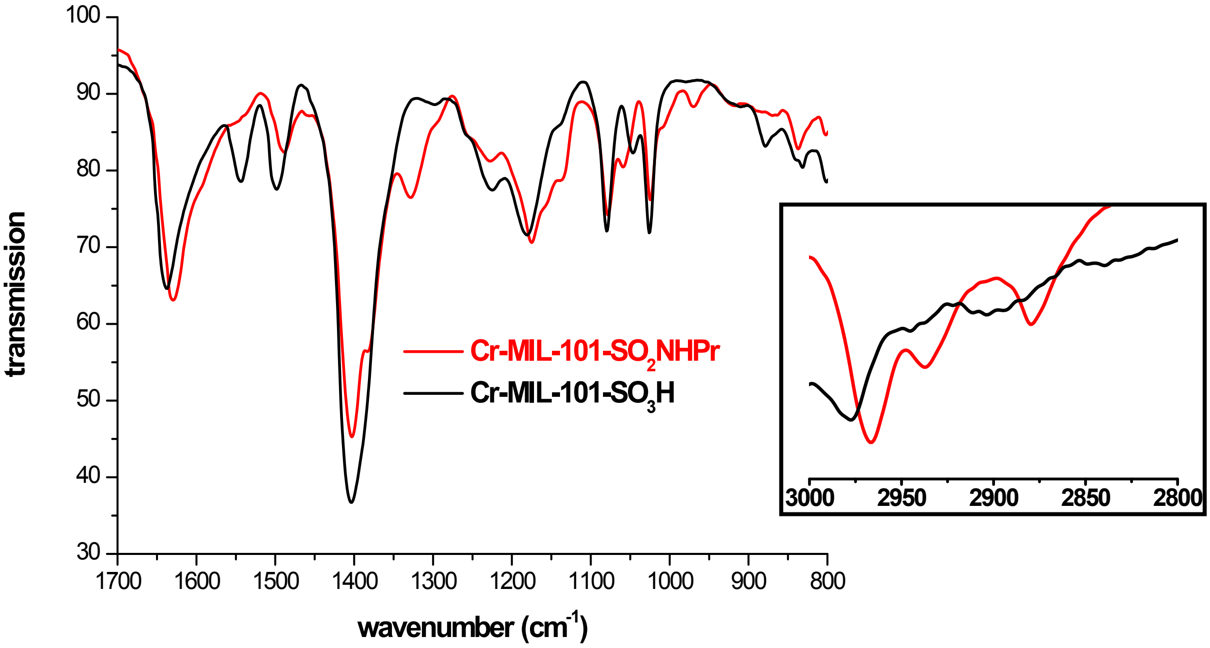

Fig. S10. FT-IR spectra of the starting material Cr-MIL-SO_3H **1** (**black**) and Cr-MIL-SO_2NHPr **3c** (**red**). Characteristical frequencies: 2976, 2937, 2880 cm^{-1} (CH_3/CH_2 stretch), 1383 cm^{-1} (SO_2NH), 1328 cm^{-1} (CH_3), 1059 cm^{-1} (S=O).

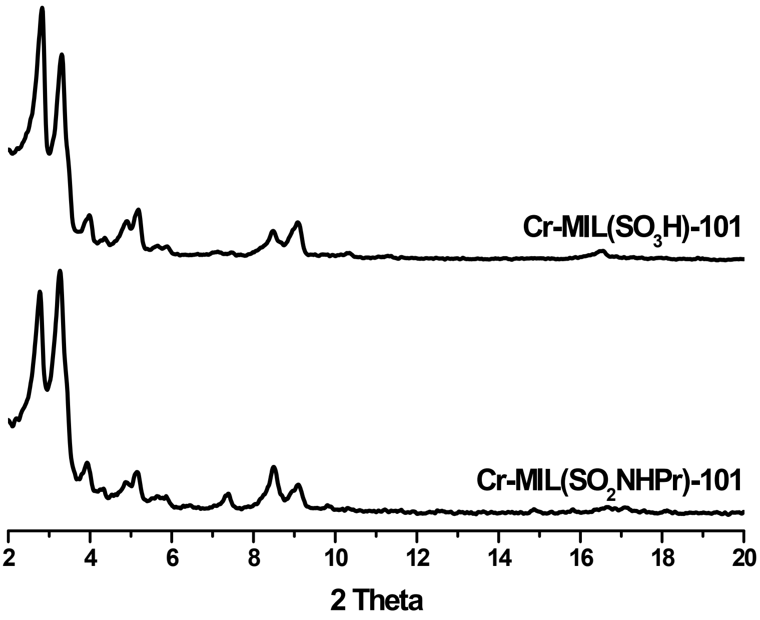

Fig. S11. PXRD pattern of the starting material Cr-MIL-SO$_3$H **1** (top) and Cr-MIL-SO$_2$NHPr **3c** (bottom).

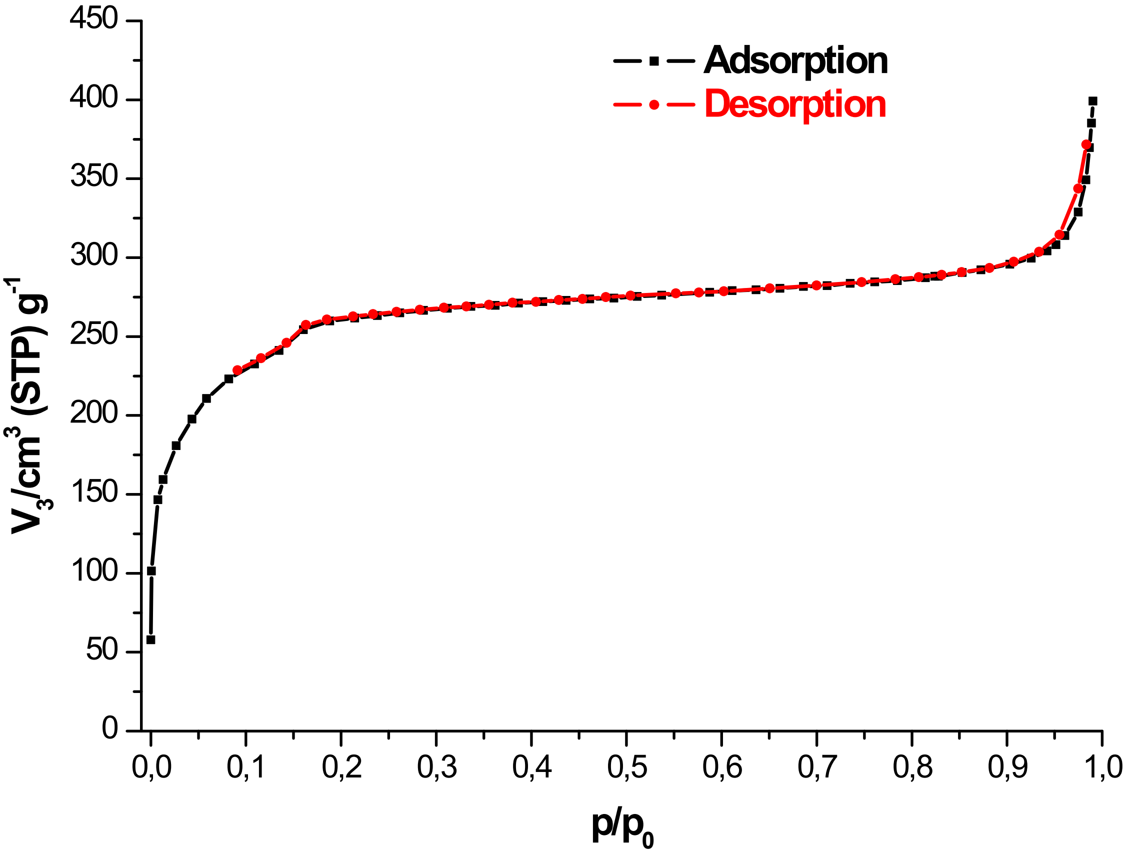

Fig. S12. N$_2$ adsorption isotherm (77 K) of Cr-MIL-SO$_2$NHPr **3c**: $a_{s,BET}$ = 940 m^2/g, total pore volume = 0.425 cm^3/g (starting material **1**: $a_{s,BET}$ = 1350 m^2/g, total pore volume = 0.624 cm^3/g).

2.4.4 Cr-MIL-101-SO_2NMe_2 (3d)

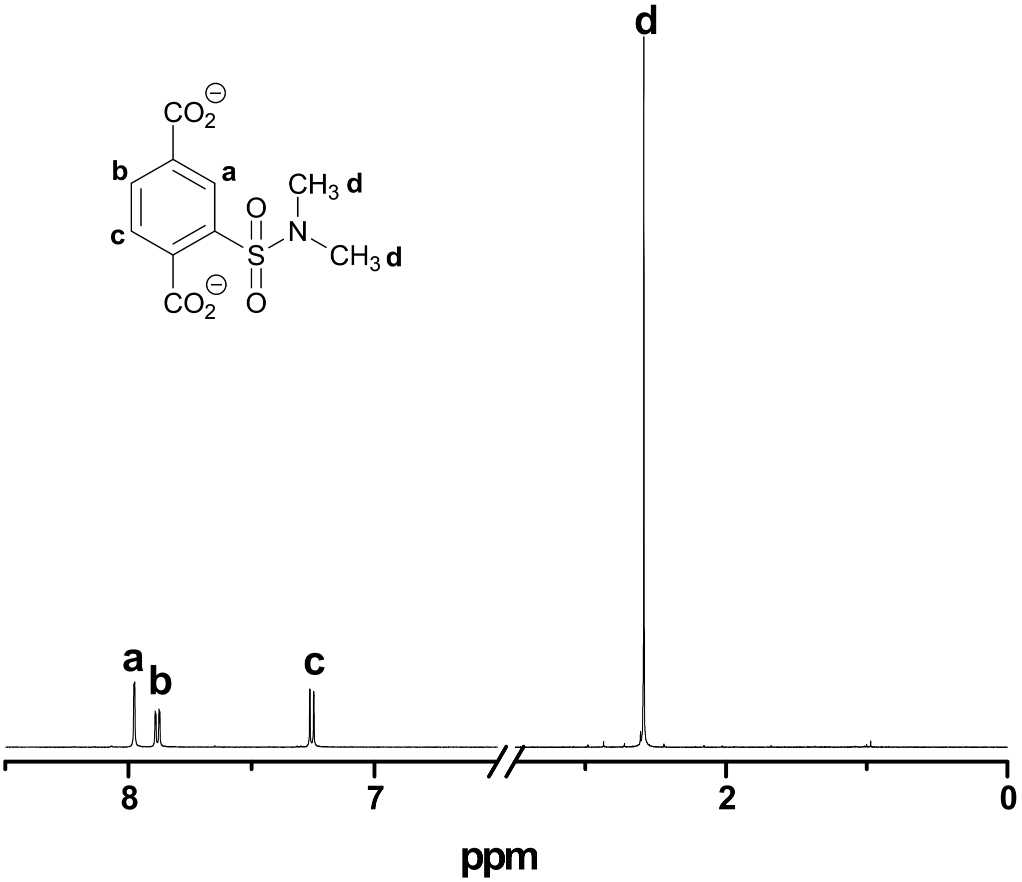

Fig. S13. ^{1}H-NMR spectrum of digested Cr-MIL-SO_2NMe_2 **3d** (500 MHz, 5 % NaOD in D_2O): (**a-c**) aromatic protons, (**d**) methyl groups.

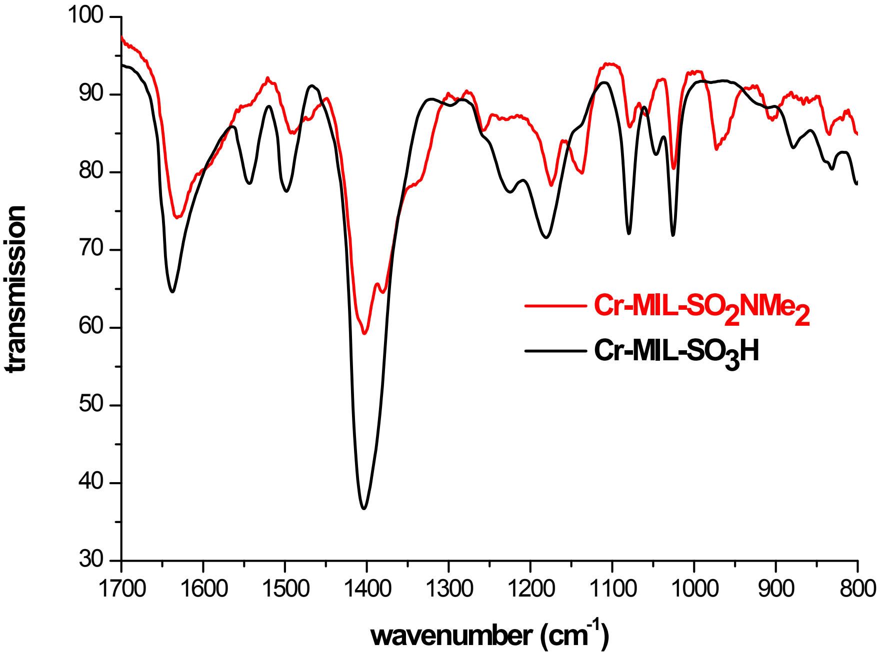

Fig. S14. FT-IR spectra of the starting material Cr-MIL-SO_3H **1** (**black**) and Cr-MIL-SO_2NHMe_2 **3d** (**red**). Characteristical frequencies: 1381 cm^{-1} (SO_2NH), 1338 cm^{-1} (CH_3), 1059 cm^{-1} (S=O). No significant bands between 3000 – 2800 cm^{-1} for CH_3 stretch were observed.

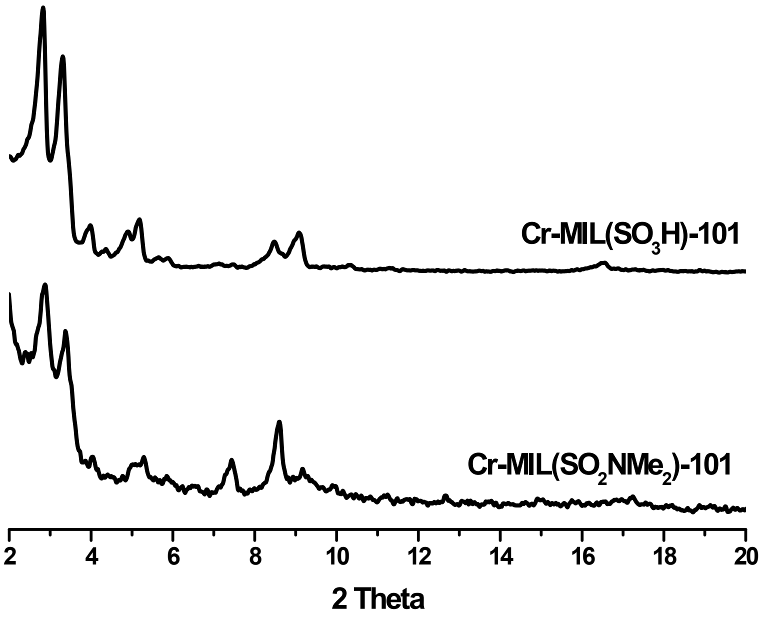

Fig. S15. PXRD pattern of the starting material Cr-MIL-SO$_3$H **1** (top) and Cr-MIL-SO$_2$NHMe$_2$ **3d** (bottom).

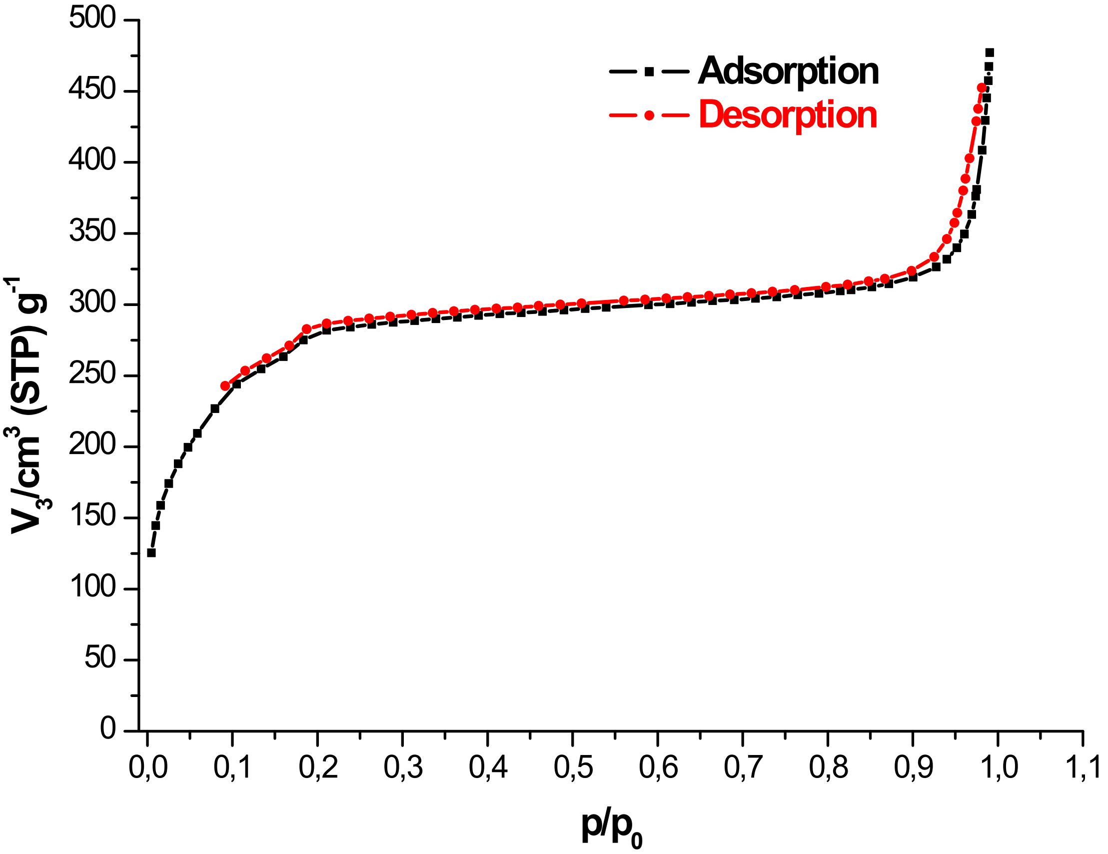

Fig. S16. N_2 adsorption isotherm (77 K) of Cr-MIL-SO$_2$NMe$_2$ **3d**: $a_{s,BET}$ = 1000 m^2/g, total pore volume = 0.459 cm^3/g (starting material **1**: $a_{s,BET}$ = 1350 m^2/g, total pore volume = 0.624 cm^3/g).

2.4.5 Cr-MIL-101-SO_2NHPh (3e)

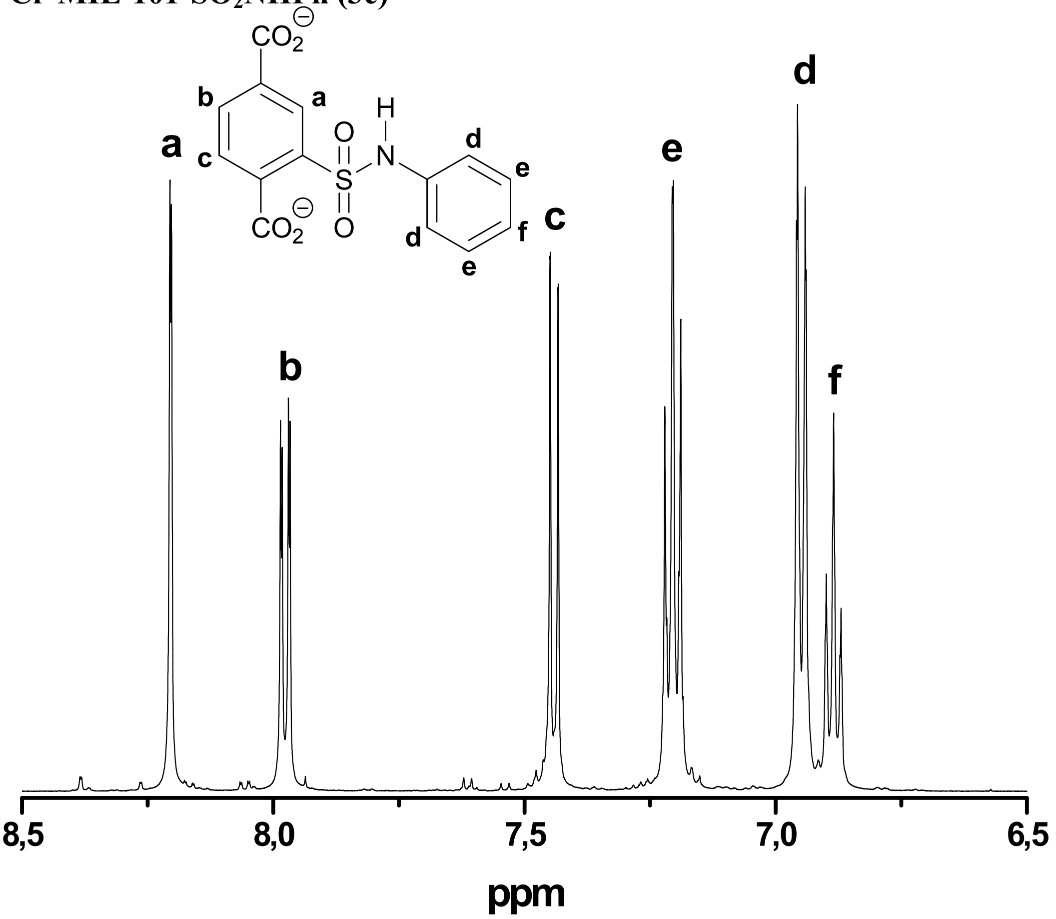

Fig. S17. ^{1}H-NMR spectrum of digested Cr-MIL-SO_2NHPh **3e** (500 MHz, 5 % NaOD in D_2O): (**a-c**) terephthalic protons, (**d-f**) phenyl protons.

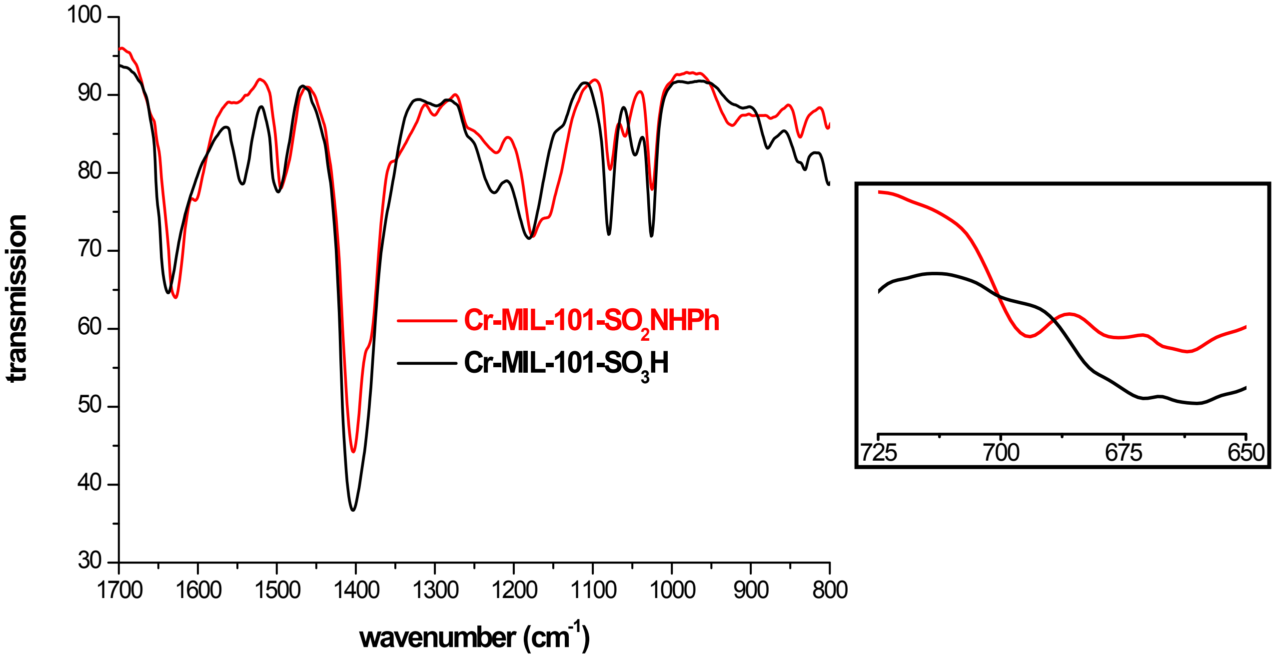

Fig. S18. FT-IR spectra of the starting material Cr-MIL-SO_3H **1** (**black**) and Cr-MIL-SO_2NHPh **3e** (**red**). Characteristical frequencies: 1383 cm^{-1} (SO_2NH), 1060 cm^{-1} (S=O), 695 cm^{-1} (mono substituted benzene).

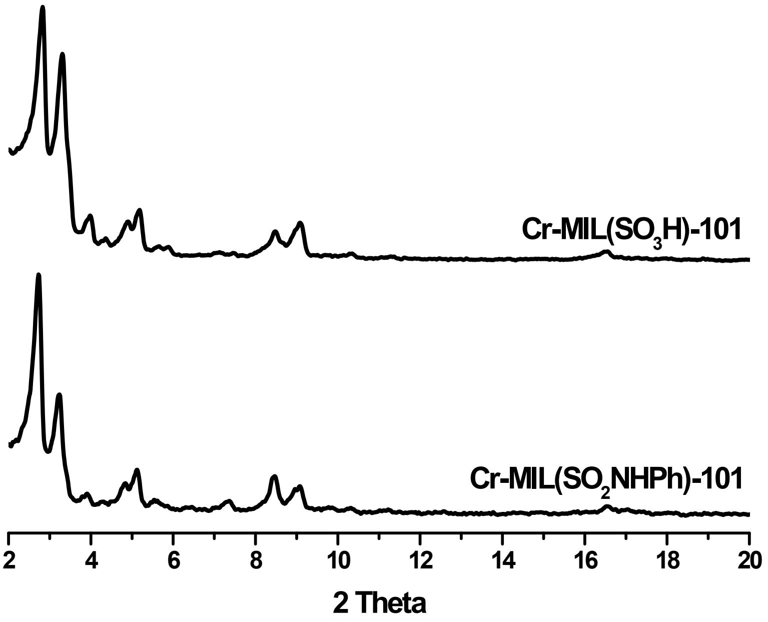

Fig. S19. PXRD pattern of the starting material Cr-MIL-SO$_3$H **1** (top) and Cr-MIL-SO$_2$NHPh **3e** (bottom).

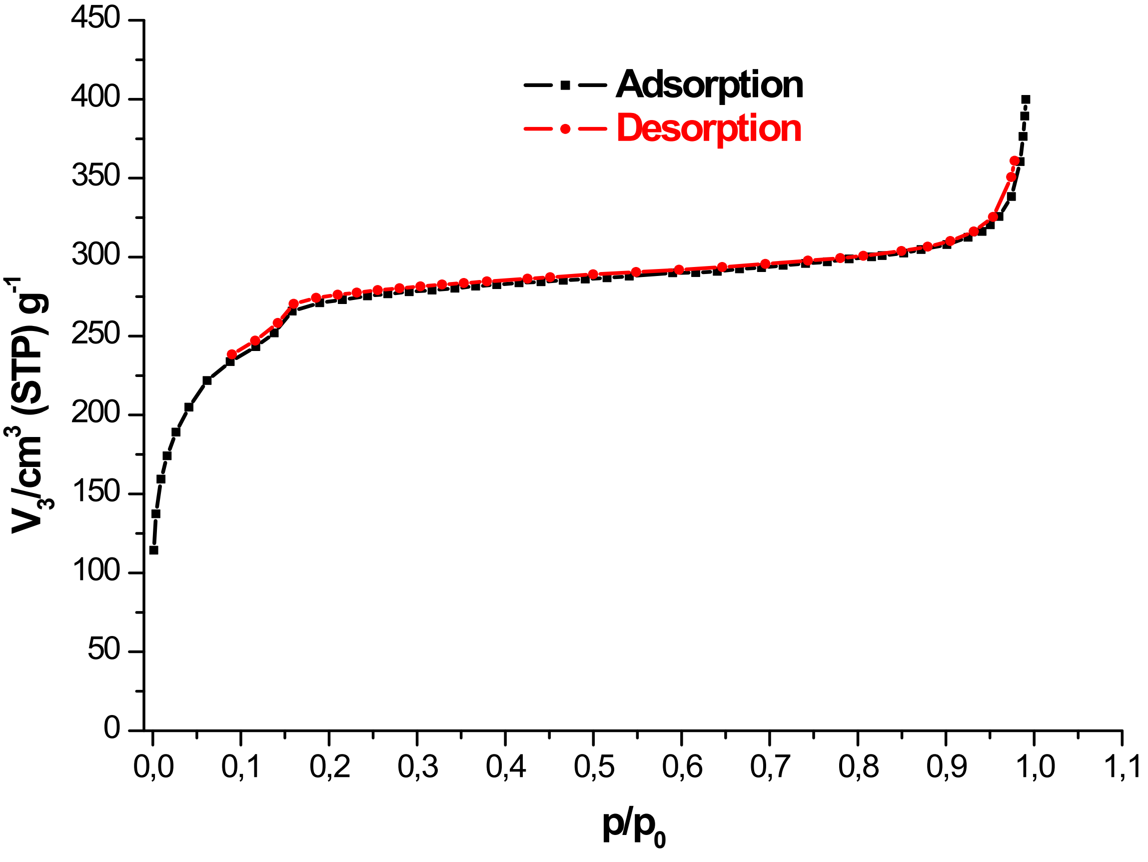

Fig. S20. N_2 adsorption isotherm (77 K) of Cr-MIL-SO$_2$NHPh **3e**: $a_{s,BET}$ = 980 m^2/g, total pore volume = 0.443 cm^3/g (starting material **1**: $a_{s,BET}$ = 1350 m^2/g, total pore volume = 0.624 cm^3/g).

2.4.6 Cr-MIL-101-SO_2NHCH_2Ph (3f)

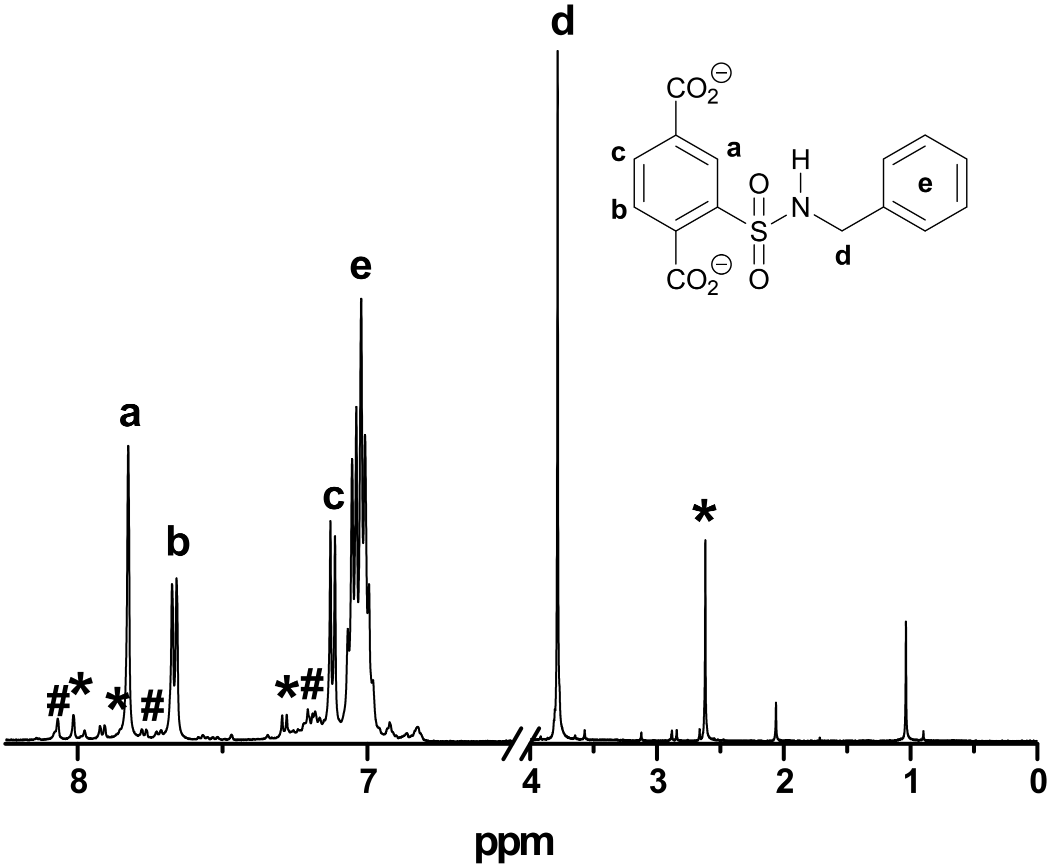

Fig. S21. ^{1}H-NMR spectrum of digested Cr-MIL-SO_2NHBn **3f** (500 MHz, 5 % NaOD in D_2O): (**a-c**) terephthalic protons, (**d**) methylene protons, (**e**) phenyl protons (*) side product *N*,*N*-dimethyl sulfonamide **3d** (< 5%), (#) residue of starting material **1**.

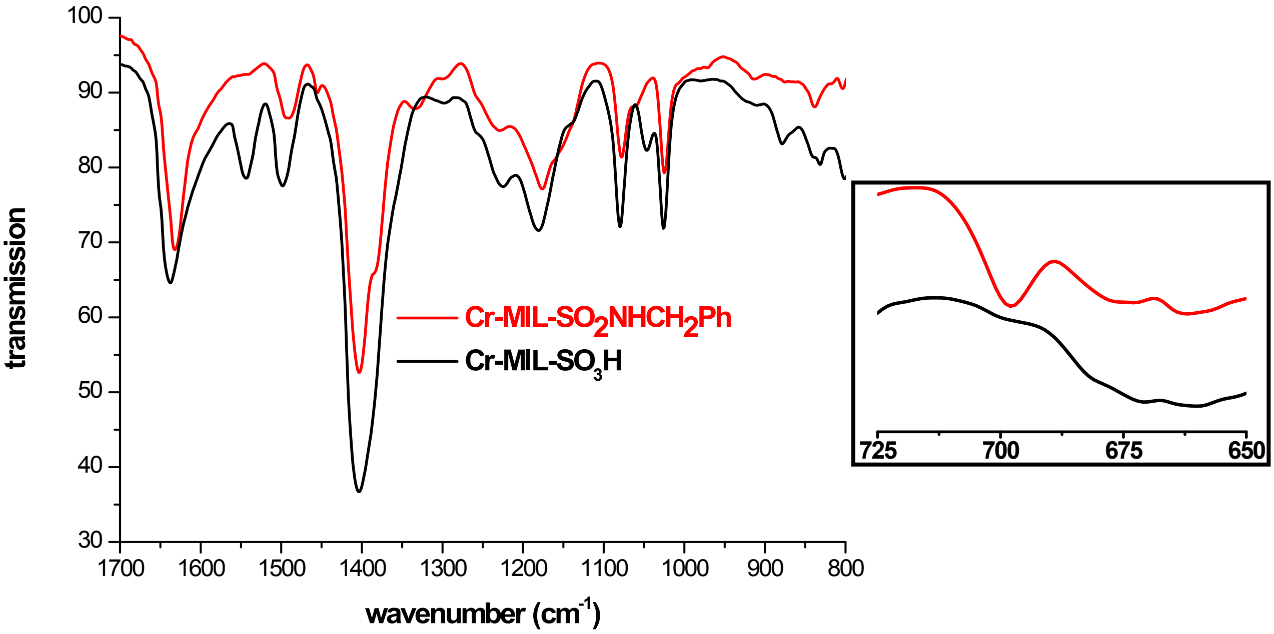

Fig. S22. FT-IR spectra of the starting material Cr-MIL-SO_3H **1** (**black**) and Cr-MIL-SO_2NHBn **3f** (**red**). Characteristical frequencies: 1383 cm^{-1} (SO_2NH), 1331 cm^{-1} (CH_3), 1060 cm^{-1} (S=O), 698 cm^{-1} (mono substituted benzene). No significant vibration between 3000 – 2800 cm^{-1} for CH_2 stretch.

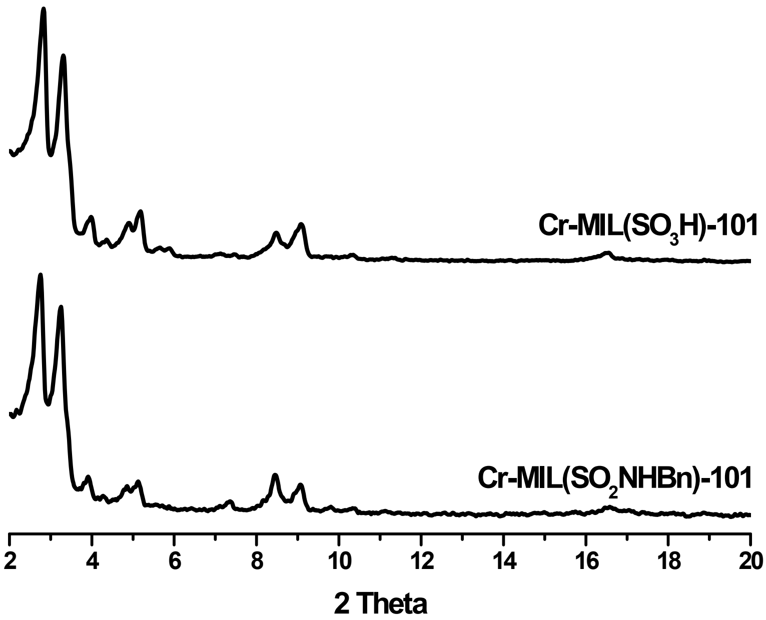

Fig. S23. PXRD PATTERN of the starting material Cr-MIL-SO_3H **1** (top) and Cr-MIL-SO_2NHBn **3f** (bottom).

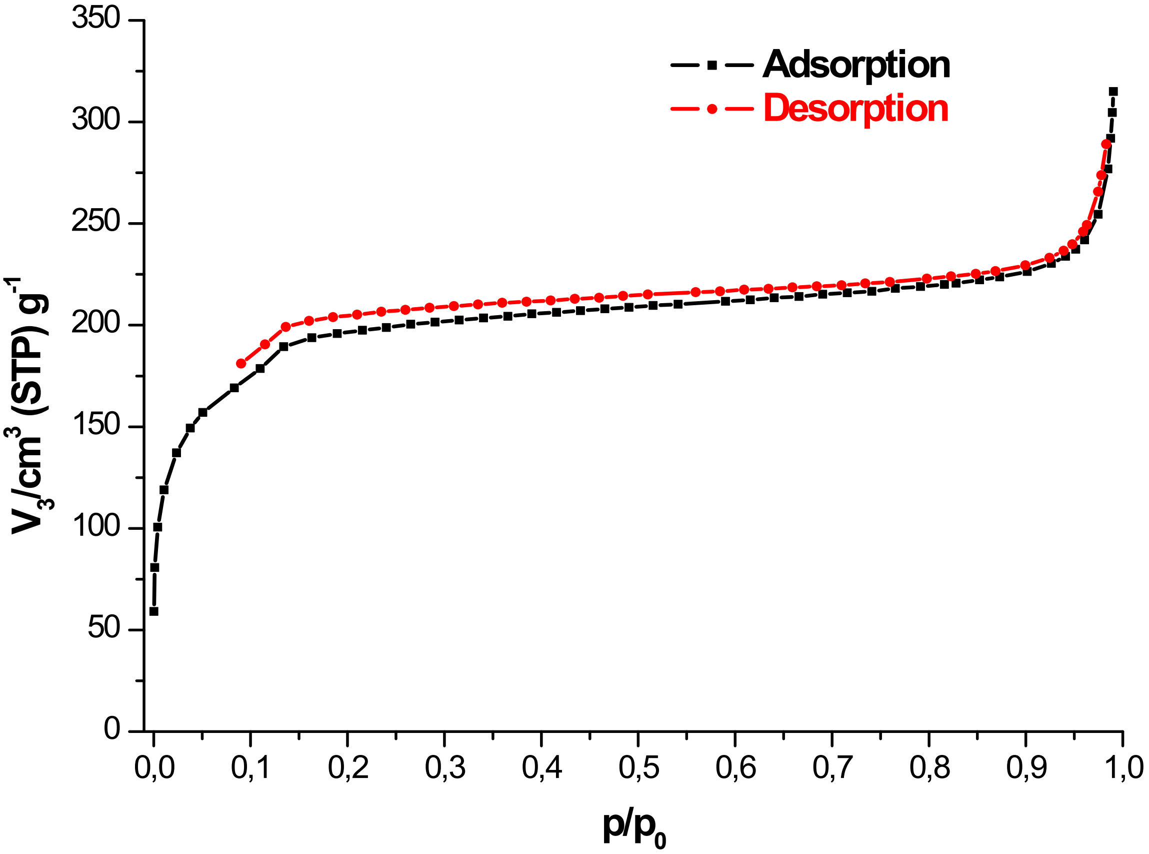

Fig. S24. N_2 adsorption isotherm (77 K) of Cr-MIL-SO_2NHBn **3f**: $a_{s,BET}$ = 720 m^2/g, total pore volume = 0.323 cm^3/g (starting material **1**: $a_{s,BET}$ = 1350 m^2/g, total pore volume = 0.624 cm^3/g).

2.4.7 Cr-MIL-101-SO_2NHPy (3g)

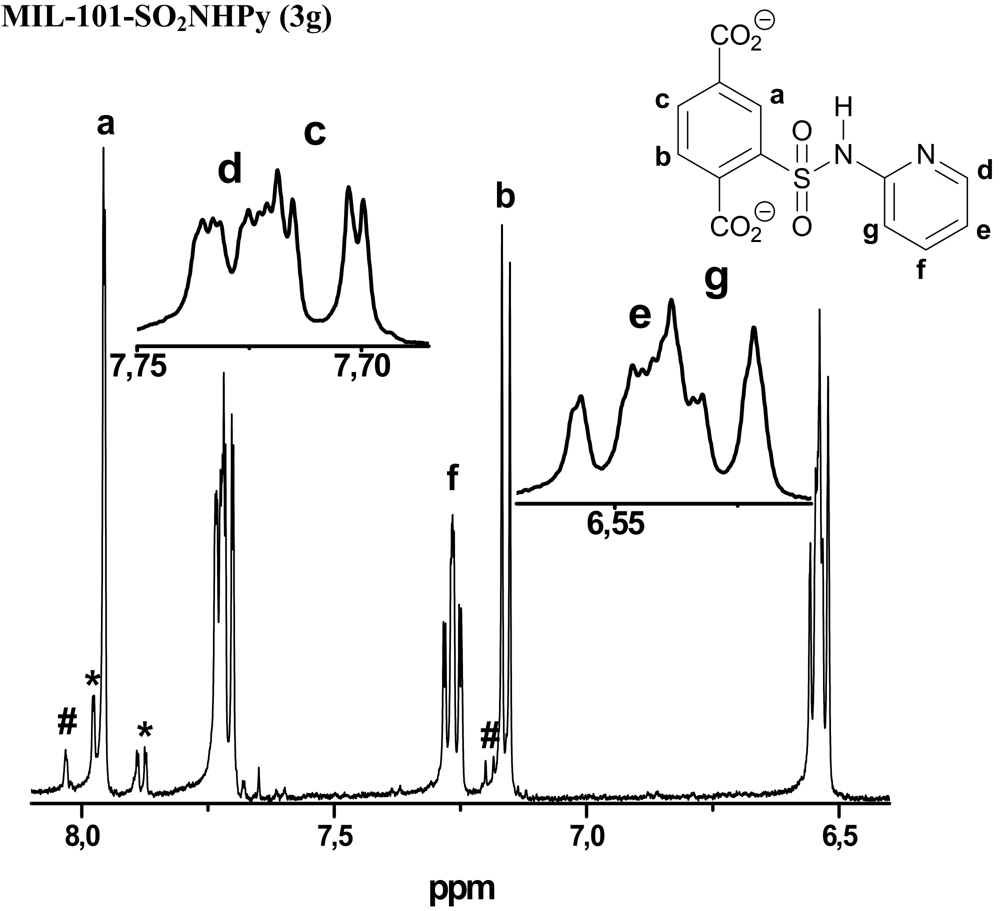

Fig. S25. ^{1}H-NMR spectrum of digested Cr-MIL-SO_2NHPy **3g** (500 MHz, 5 % NaOD in D_2O): (**a-c**) terephthalic protons, (**d-f**) pyridine protons (*) side product *N*,*N*-dimethyl sulfonamide **3d** (< 4 %), (#) residue of starting material **1**.

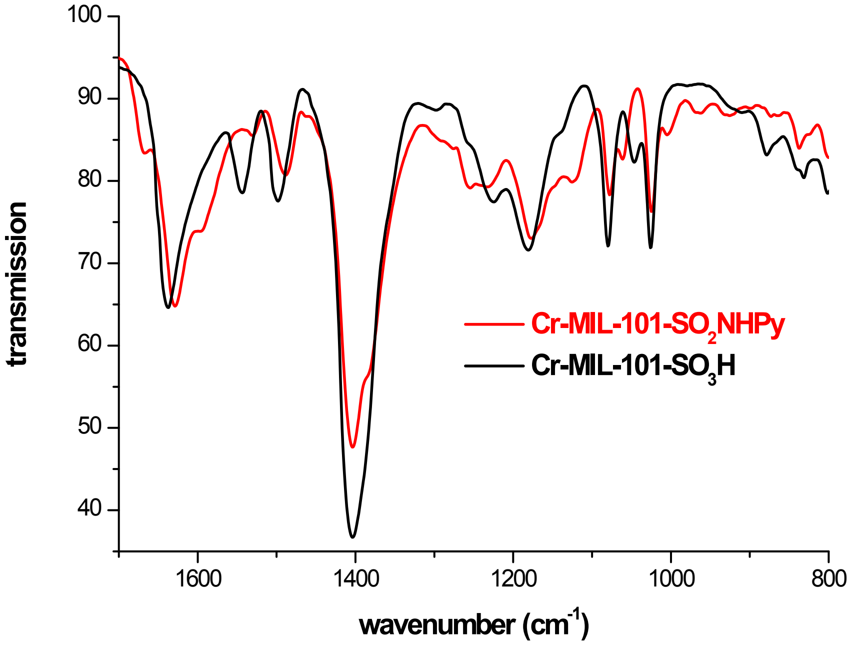

Fig. S26. FT-IR spectra of the starting material Cr-MIL-SO_3H **1** (**black**) and Cr-MIL-SO_2NHPy **3g** (**red**). Characteristical frequencies: 1385 cm^{-1} (SO_2NH), 1060 cm^{-1} (S=O).

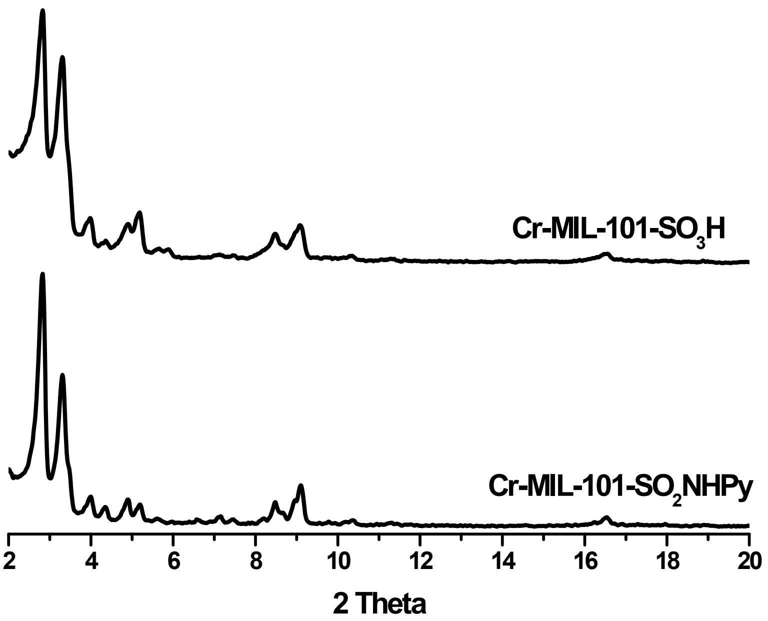

Fig. S27. PXRD PATTERN of the starting material Cr-MIL-SO$_3$H **1** (top) and Cr-MIL-SO$_2$NHPy **3g** (bottom).

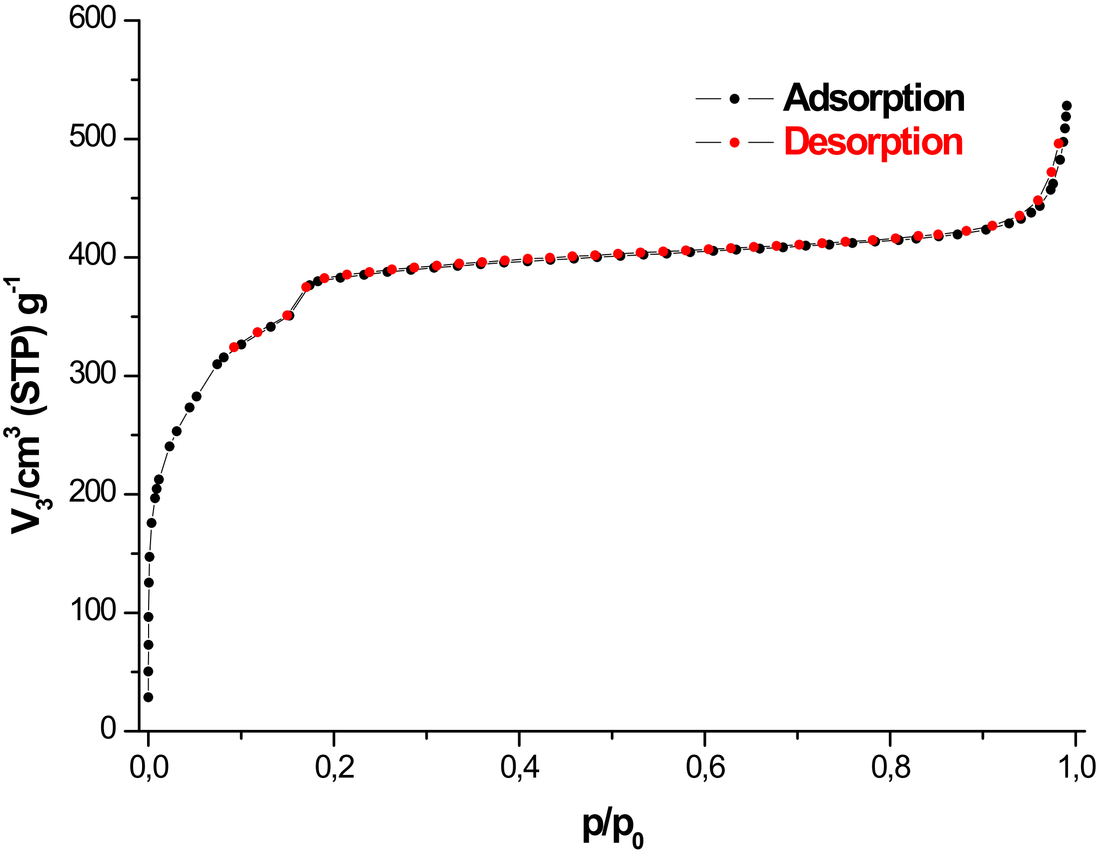

Fig. S28. N$_2$ adsorption isotherm (77 K) of Cr-MIL-SO$_2$NHPy **3g**: $a_{s,BET}$ = 1350 m^2/g, total pore volume = 0.620 cm^3/g (starting material **1**: $a_{s,BET}$ = 1860 m^2/g, total pore volume = 0.834 cm^3/g).

3 Postsynthetic modification of CAU-1-NH_2

3.1 Synthesis of CAU-1-NH_2 (5)

The synthesis of CAU-1-NH_2 was carried out in a microwave oven (Biotage Initiator) using 5 mL glass vials. A mixture of 232 mg (961 µmol) of aluminium trichloride hexahydrate, 58.0 mg (298 µmol) of 2-aminoterephthalic acid (BDC-NH_2) and 3.2 mL methanol was heated after 10 s of pre-stirring for 6 min to 145 °C. The reaction mixture was rapidly cooled to room temperature and a yellow microcrystalline dispersion was obtained. The dispersion was centrifuged and redispersed three times in water to remove chloride ions. The final product was dried in air resulting in CAU-1-NH_2 (**5**) with the molecular formula $[Al_4(OH)_2(OCH_3)_{1.69}(BDC\text{-}NH_2)_{2.89}(BDC\text{-}NHCH_3)_{0.11}]\cdot nH_2O$. The degrees of methoxy and aminomethyl groups were calculated from ^{1}H-NMR spectra of dissolved product **5**.

3.2 Synthesis and characterization of CAU-1-$NHSO_2Me$ (5)

3.2.1 Synthesis[2]

A 5 mL glass vial was loaded with 40 mg of CAU-1-NH_2, 2.0 mL of methyl sulfonyl chloride and 200 µL pyridine. The mixture was heated in a microwave oven after 1 min of pre-stirring tp 110 °C for 10 min. The precipitate was separated by centrifugation and washed using dichloromethane (2 mL, 2 x 15 min), methanol (2 mL, 3 x 15 min) and water (2 mL, 3 x 15 min). The sample was dried in vacuo at 60 °C for 12 h.

For ^{1}H-NMR analysis, the sample was digested in 5 % deuterated sodium hydroxide in deuterated water.

3.2.2 Characterization

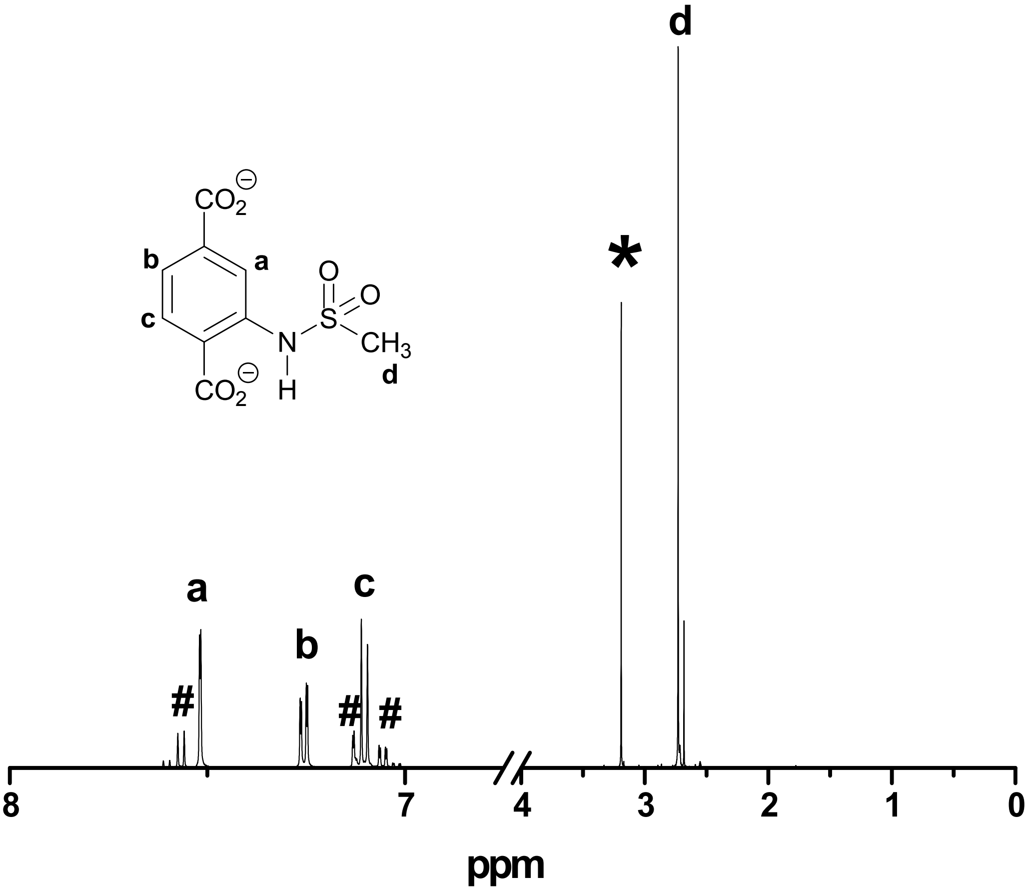

Fig. S29. ^{1}H-NMR spectrum of the digested CAU-1-NHSO$_2$Me **5** (500 MHz, 5 % NaOD in D$_2$O): (**a-c**) terephthalic protons, (**d**) methyl protons, (#) amino terephthalic acid from starting material **4**, (*) methanol.

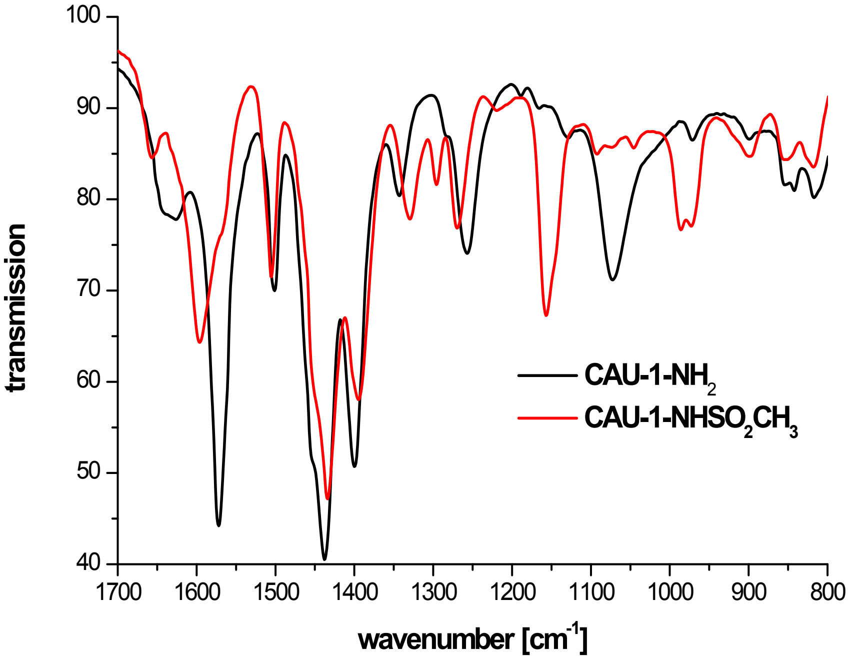

Fig. S30. FT-IR spectra of the starting material CAU-1-NH$_2$ **4** (**black**) and CAU-1-NHSO$_2$Me **5** (**red**). Characteristical frequencies: 1330 cm^{-1} (CH$_3$), 1296 cm^{-1}, 1157 cm^{-1}(sulfonamides).

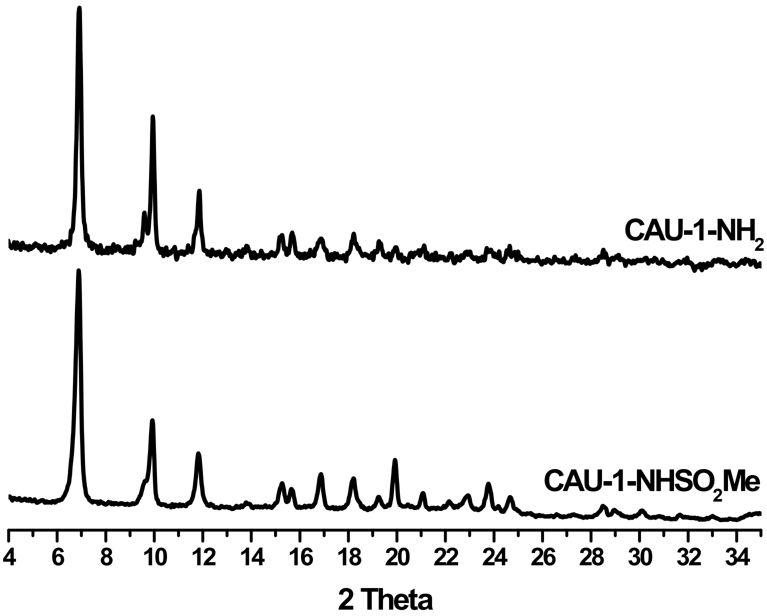

Fig. S31. PXRD PATTERN of the starting material CAU-1-NH$_2$ **4** (top) and CAU-1-NHSO$_2$Me **5** (bottom).

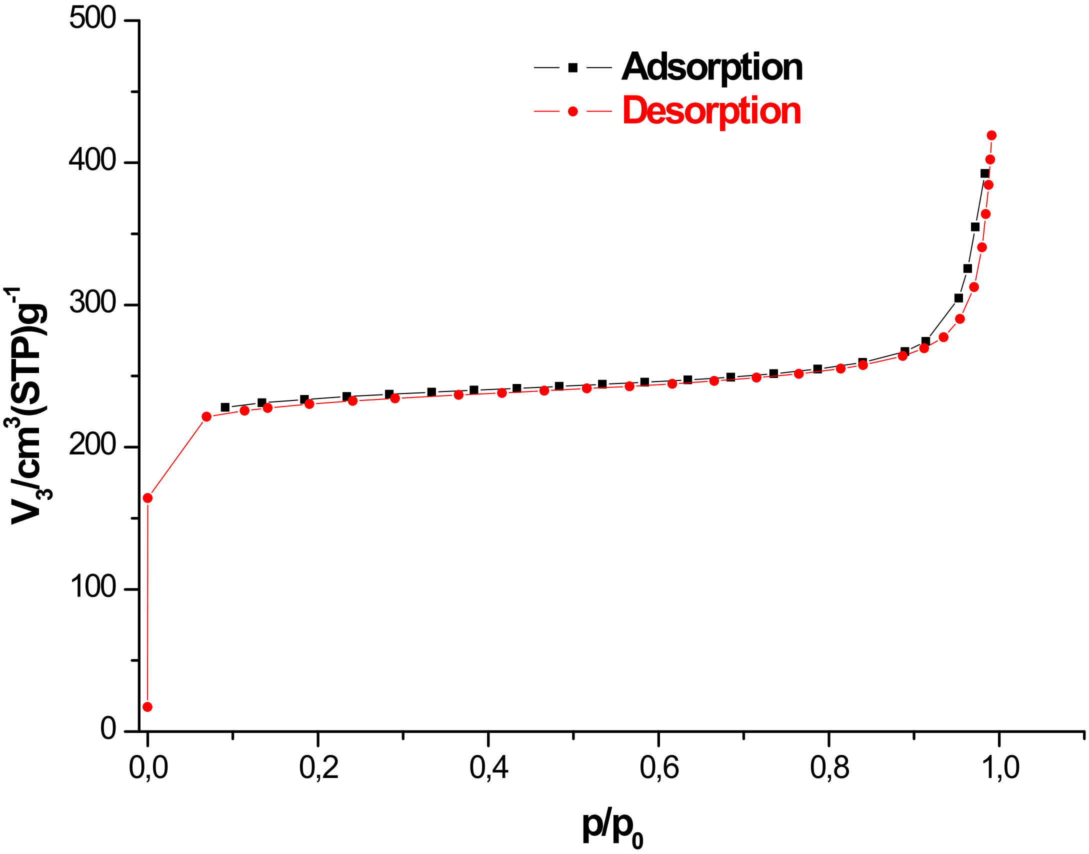

Fig. S32. N$_2$ adsorption isotherm (77 K) of CAU-1-NHSO$_2$Me **5**: $a_{s,BET}$ = 900 m^2/g, total pore volume = 0.372 cm^3/g (starting material **1**: $a_{s,BET}$ = 1480 m^2/g, total pore volume = 0.610 cm^3/g). Recorded with a BELSORP-mini apparatus (BEL JAPAN INC.).

3.3 Synthesis and characterization of CAU-1-NHSO$_2$Py (6)

3.3.1 Synthesis of pyridine-2-sulfonyl chloride[3]

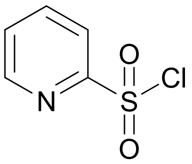

A solution of 1.00 g (9.00 mmol) of 2-mercaptopyridine in 25 mL of conc. sulfuric acid was cooled to 0 °C and treated carefully with 60 mL of sodium hypochlorite acid (10 - 15 % available chlorine). After stirring for additional 60 min at this temperature, the mixture was treated with 50 mL of ice cold water. The aqueous phase was extracted three times using 50 mL of ice cold dichloromethane. The organic phase was dried with magnesium sulfate and filtered. After removing the solvent in vacuo, a slightly yellow oil was obtained. Due to the instability of this compound, the crude product (1.12 g) was stored at – 18 °C and used without further purification.

^{1}H-NMR (600 MHz, CDCl$_3$): δ = 8.83 (d, 1H, ^3J = 4.6 Hz, Py-*H*-6), 8.12 (d, 1H, ^3J = 7.8 Hz, Py-*H*-3), 8.06 (td, 1H, ^3J = 7.8 Hz, Py-*H*-4), 7.70 (ddd, 1H, ^3J = 7.8 Hz, ^3J = 4.6 Hz, Py-*H*-5) ppm.

^{13}C-NMR (150 MHz, CDCl$_3$): δ = 159.21 (s, Py-*C*-2), 150.69 (d, Py-*C*-6), 139.02 (Py-*C*-4), 129.05 (d, Py-*C*-5), 121.91 (Py-*C*-3) ppm.

3.3.2 Synthesis of CAU-1-NHSO$_2$Py (6)

A Schlenck tube was loaded with 40 mg of CAU-1-NH$_2$ and cooled down to 0 °C. After addition of 1.0 mL of solution of pyridine-2-sulfonylchloride pyridine (crude product from the previous step, max. 2 mmol) in dry tetrahydrofurane, the sample was allowed to warm to room temperature and stirred overnight. The precipitate was collected by centrifugation and washed using dichloromethane (2 mL, 2 x 15 min), methanol (2 mL, 3 x 15 min) and water (2 mL, 3 x 15 min). The sample was dried in vacuo at 60 °C for 12 h.

For ^{1}H-NMR analysis, the sample was digested in 5 % deuterated sodium hydroxide in deuterated water.

3.3.2 Characterization

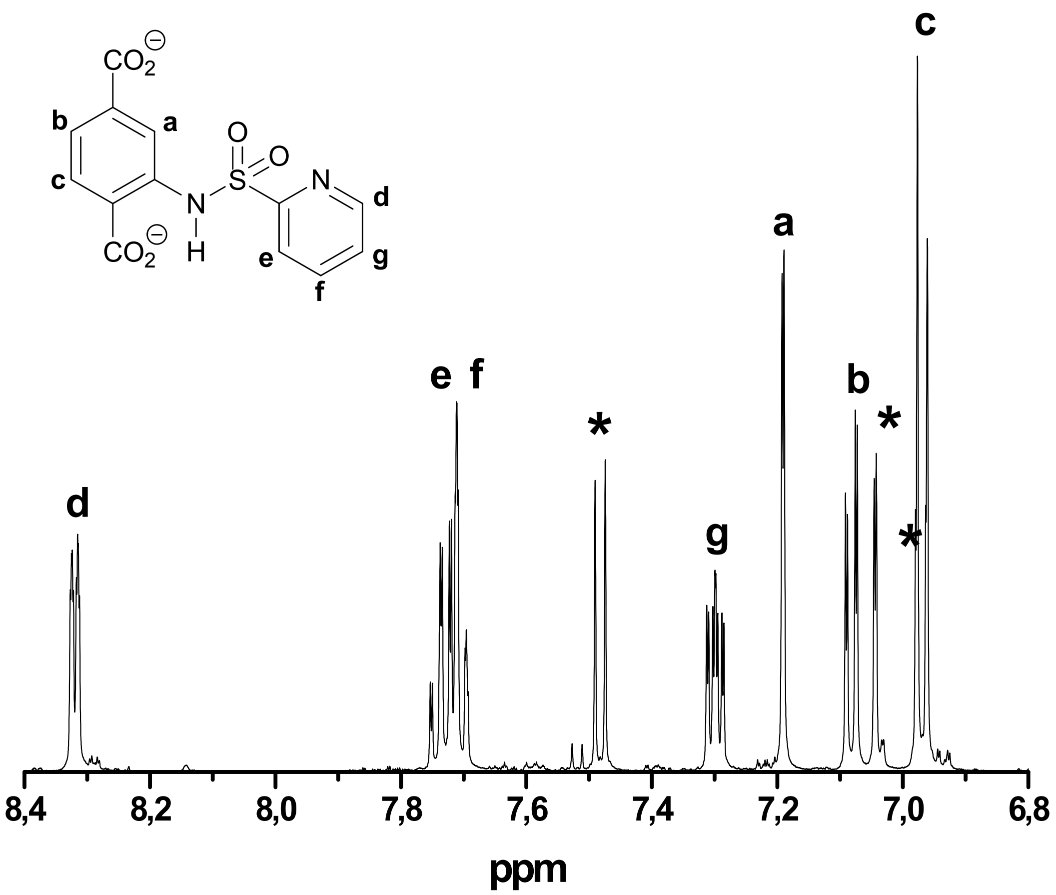

Fig. S33. ^{1}H-NMR spectrum of the digested CAU-1-NHSO$_2$Py **6** (500 MHz, 5 % NaOD in D$_2$O): (**a-c**) terephthalic protons, (**d-g**) pyridine protons, (*) amino terephthalic acid from starting material **4**.

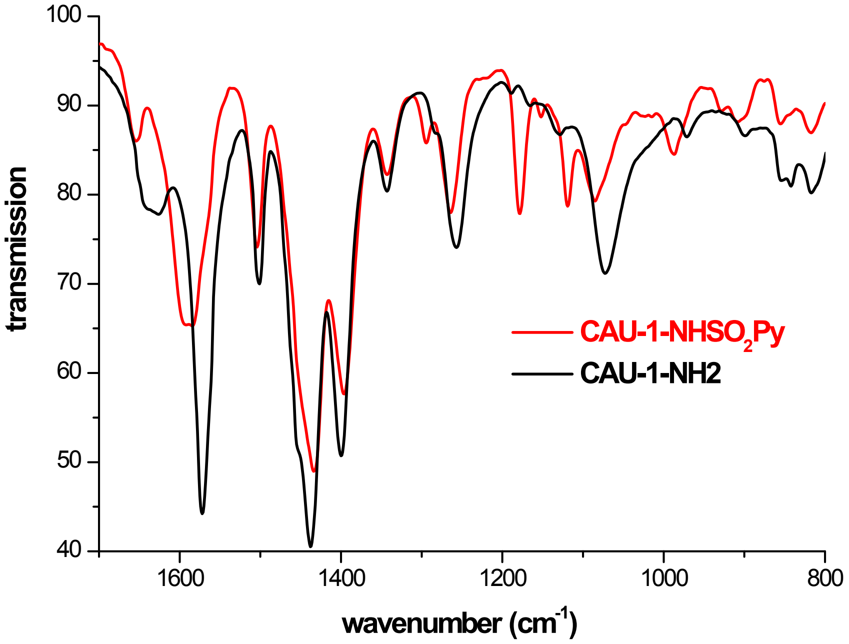

Fig. S34. FT-IR spectra of the starting material CAU-1-NH$_2$ **4** (**black**) and CAU-1-NHSO$_2$Py **5** (**red**). Characteristical frequencies: 1294 cm^{-1}, 1178 cm^{-1}(sulfonamides), 1119 cm^{-1} (S=O).

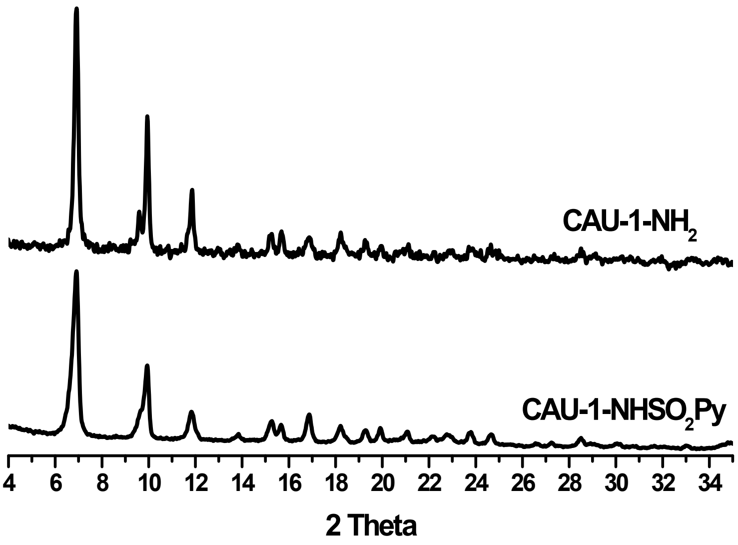

Fig. S35. PXRD PATTERN of the starting material CAU-1-NH$_2$ **4** (top) and CAU-1-NHSO$_2$Py **6** (bottom).

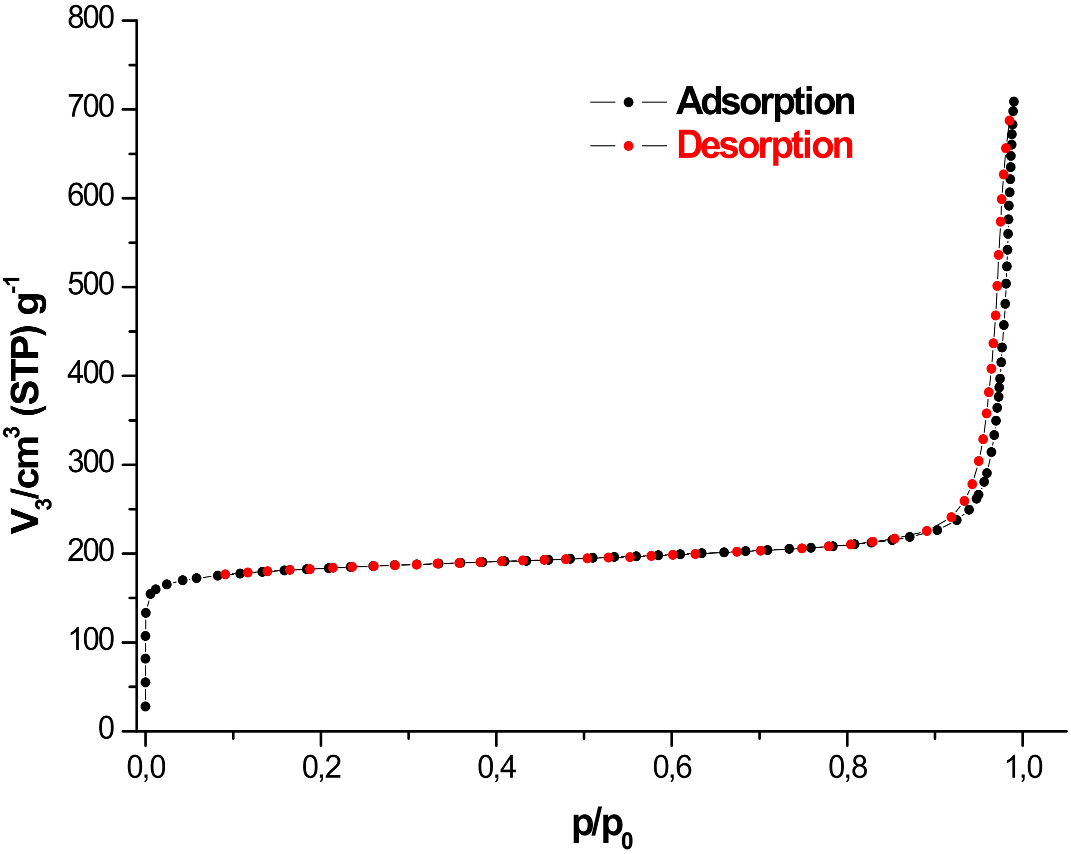

Fig. S36. N$_2$ adsorption isotherm (77 K) of CAU-1-NHSO$_2$Py **6**: $a_{s,BET}$ = 720 m^2/g, V_m = 0.294 cm^3/g (starting material **4**: $a_{s,BET}$ = 1480 m^2/g, total pore volume = 0.610 cm^3/g).

4. References

1. G. Akiyama, R. Matsuda, H. Sato, M. Takata, and S. Kitagawa, *Adv. Mater.*, 2011, **23**, 3294.

2. T. Ahnfeldt, N. Guillou, D. Gunzelmann, I. Margiolaki, T. Loiseau, G. Férey, J. Senker, and N. Stock, *Angew. Chem. Int. Ed.*, 2009, **48**, 5163; *Angew. Chem.*, 2009, **121**, 5265.

3. *US Pat.*, US2007/60623, 2007.

Supporting Information

New Al-MOFs based on sulfonyldibenzoate ions: A rare example of intralayer-porosity

Nele Reimer,[†] *Helge Reinsch,*[‡] *A. Ken Inge*[†] *and Norbert Stock**[†]

† Institut für Anorganische Chemie, Christian-Albrechts-Universität zu Kiel, Max-Eyth-Str. 2,
D-24118 Kiel, Germany

‡ INGAP Centre of Research-based Innovation, Department of Chemistry, University of
Oslo, Sem Saerlandsvei 26, N-0315 Oslo, Norway

* stock@ac.uni-kiel.de

Table of contents

HT-Syntheses

Crystal Structures

Thermal Analysis

IR spectroscopy

Sorption Measurements

Table S1. In the literature reported compounds based on 4,4’-sulfonyldicarboxylic acid.

Compound	Space group	Cell parameters	Structure motif	Lit.
$[Zn(SDBA)_2(DMF)_2]\cdot 5.5DMF$	*P*-1	a = 12.12(1) Å b = 13.108(8) Å c = 20.67(2) Å α = 70.83(4)° β = 78.80(5)° γ = 78.28(5)°	Zn-paddle-wheel units, 1D structure	[1]
$[K_2Pb(SDBA)_2(\mu_3\text{–}H_2O)]\cdot 3H_2O$	*Pmmn*	a = 13.5107(16) Å b = 23.380(3) Å c = 5.8727(7) Å	chains of aqua-lead di-potassium trihydrate units ladder-like Pb(II)/K(I)/$SDBA^{2-}$ motif, 3D structure; 1D rhombic channels 12x14 Å	[2]
$[Cs_2Pb_2(SDBA)_3(DMF)]\cdot DMF$	*P*2₁/*n*	a = 11.3401(5) Å b = 25.0935(10) Å c = 22.8740(11) Å β = 96.895(4)°	chains of $[Pb_2Cs_2O_{27}]$ rod-shaped Pb(II)/Cs(I)/$SDBA^{2-}$ motif, 3D structure	[2]
$[Zn(SDBA)(H_2O)_2]$	*P*2/*c*	a = 13.317(3) Å b = 5.0376(13) Å c = 12.120(3) Å β = 116.295(4)°	layers of $[Zn(SDBA)(H_2O)_2]$ chains	[3]
[Zn(SDBA)(DMF)]	*C*2/*m*	a = 22.151(7) Å b = 12.872(4) Å c = 9.993(3) Å β = 99.584(5)°	layered structure, Zn-paddle-wheel units	[4]
$[Ca(SDBA)]\cdot 0.45H_2O$	*P*2₁/*n*	a = 11.8301(5) Å b = 5.5761(2) Å c = 22.7922(9) Å β = 100.493(2)°	zigzag 1D chain of triangular edge-sharing CaO_7 monocapped trigonal prism, 3D structure; porous	[5]
$[Sr(SDBA)]\cdot 0.2H_2O$	*P*2₁/*n*	a = 11.7361(10) Å b = 5.5499(4) Å c = 22.8190(18) Å b = 100.999(4)°	zigzag 1D chain of triangular edge-sharing SrO_7 monocapped trigonal prism, 3D structure; porous	[5]
$[Cu(SDBA)(H2O)]_n\cdot 0.5n(i\text{-}C_3H_7OH)$	*Cmcm*	a = 22.073(5) Å b = 12.689(2) Å c = 11.592(2) Å	1D [Cu(SDBA)]n double-chains bearing Cu-paddlewheel units	[6]
$[Zn_2(SDBA)_2(DMF)_2]\cdot DMF$ (MOF-114)	*C*2/*c*	a = 22.241(2) Å b = 12.7034(12) Å c = 17.6543(16) Å β = 126.361(2)°	1D chains of Zn-paddlewheel units bridged by SDBA-ions	[7]
[Pb(SDBA)]	*Pnma*	a = 5.9527(3) Å b = 13.0441(6) Å	Chains of PbO_7-polyhedra, 3D structure	[8]

		c = 19.5781(10) Å		
$[PbCa(SDBA)_2(\mu_1\text{-}DMSO)_2]$	$C2/m$	a = 11.4429(14) Å b = 23.6717(14) Å c = 8.1660(9) Å β = 128.596(4)°	chains of edge sharing PbO_8 and CaO_6 polyhedra, 2D layer structure	9
$[Co_3(OH)_2(SDBA)_2(H_2O)_3(EtOH)]\cdot H_2O\cdot 0.5EtOH$	$P2/c$	a = 28.219(3) Å b = 6.3880(7) Å c = 24.928(3) Å β = 115.200(2)°	$[Co_3(\mu_3\text{-}OH)_2]$n chains, 3D structure; porous in case of solvent exchange	10
$[Ba(\mu_2\text{-}OH_2)(SDBA)(H_2O)_3]\cdot 0.5H_2O$ $[Ba(\mu_2\text{-}OH_2)(SDBA)(H_2O)_3]\cdot 0.5ben\cdot H_2O$ $[Ba(\mu_2\text{-}OH_2)(SDBA)(H_2O)_3]\cdot 0.5tolu\cdot H_2O$ $[Ba(\mu_2\text{-}OH_2)(SDBA)(H_2O)_3]\cdot 0.5bpy\cdot H_2O$ $[Ba(\mu_2OH_2)(SDBA)(H_2O)_3]\cdot 0.25bim\cdot H_2O$ $[Ba(\mu_2OH_2)(SDBA)(H_2O)_3]\cdot 0.5dfb\cdot 0.25H_2O$ $[Ba(\mu_2\text{-}OH_2)(SDBA)(H_2O)_3]\cdot 3.5H_2O$	P-1	a = 6.2064(12)-6.317(2) Å b = 12.8616(7)-14.130(5) Å c = 13.8616(8)-14.6389(4) Å α = 64.9800(10)-112.859(4)° β = 86.230(2)-91.748(4)° γ = 78.39(3)-93.0800(10)°	chains of edge-sharing BaO_9-polyhedra, 2d bilayer motif; porous in case of solvent exchange	11
$[Li_2(SDBA)]$	$P2_1/n$	a = 5.5480(11) Å b = 23.450(5) Å c = 10.320(2) Å β = 96.47(3)°	tetrameric clusters of tetrahedral lithium centers	12
$[Cd(SDBA)(H_2O)_2]_n$	$P2/c$	a = 13.293(3) Å b = 5.2742(12) Å c = 12.156(3) Å β = 116.145(2)°	zigzag chains of alternating $[Cd(H_2O)_2]^{2+}$ and sulfonyldibenzoate units, 2D structure	13
$[Mn_2(SDBA)_2(\mu\text{-}H_2O)(Py)_4]_n$	$P4_32_12$	a = 17.5506(4) Å c = 15.0396(5) Å	separated $Mn_2O_7N_4$ units	14
$[Mn_4(SDBA)_4(4\text{-}MePy)_2(H_2O)_4]_n2nH_2O$	P-1	a = 12.440(4) Å b = 12.707(4) Å c = 14.561(4) Å α = 91.081(1)° β = 111.994(2)° γ = 118.943(3)°	separated $Mn_2O_9N_2$ units	14
catena-(Di-sodium (μ_3-4,4'-sulfonyldibenzoato)-(μ_2-4,4'-sulfonyldibenzoato)-zinc dimethylformamide solvate)	$P2_1/c$	a = 24.704(5) Å b = 5.7098(11) Å c = 26.335(5) Å β = 114.87(3)°	separated Na_2ZnO_{10} units	15
$[Mn_5(SDBA)4(HSDBA)_2]\cdot 4.5H_2O$	P-1	a = 12.700(5) Å b = 12.714(5) Å c = 15.990(5) Å α = 72.773(5)° β = 88.047(5)° γ = 60.583(5)°	pentameric Mn_5 cluster	16
$[Mn_5K_2(H_2O)_2(SDBA)_6]$	P-1	a = 12.7407(3) Å b = 12.7787(3) Å	pentameric Mn_5 cluster	16

		c = 15.9960(4) Å α = 86.701(2)° β = 72.142(2)° γ = 60.438(3)°		
$[Mn_5Cs_2(SDBA)_6]$	P-1	a = 12.5500(6) Å b = 12.9301(6) Å c = 16.1279(7) Å α = 106.080(4)° β = 93.353(4)° γ = 118.627(5)°	pentameric Mn_5 cluster	[16]
$[Mn_5(NH_4)_2(SDBA)_6]\cdot 2H_2O$	P-1	a = 12.7609(6) Å b = 12.7682(6) Å c = 16.0315(7) Å α = 87.646(4)° β = 72.508(4)° γ = 60.477(5)°	pentameric Mn_5 cluster	[16]
$(Me_2NH_2)[CdLi(SDBA)_2]_3DMF_3CH_3OH$	Cc	a = 27.07(4) Å b = 6.347(2) Å c = 25.67(3) Å β = 107.930(3)°	monocapped pentagonal bipyramidal CdO_7 units connected by Li atoms to a chain and by the SDBA to a 2D layer structure	[17]
$(Me_2NH_2)[Cd_3(H_2O)_3(OH)(SDBA)_3]$	$P3$	a = 11.6534(3) Å c = 13.7499(5) Å	μ_3-OH-Cd_3O_{15} units	[17]
catena-[tris(μ_4-4,4'-Sulfonyldibenzoato-O,O',O'',O''')-dipyridine-tri-zinc(ii) pyridine solvate monohydrate]	$P2_1/n$	a = 16.033(4) Å b = 20.590(5) Å c = 17.404(4) Å β = 100.399(2)°	dense structure	[18]
catena-[bis(μ_4-4,4'-Sulfonyldibenzoato-O,O',O'',O''')-bis(μ_3-hydroxo)-tri-zinc(ii) dihydrate]	$P2_1/c$	a = 14.104(4) Å b = 6.1009(14) Å c = 23.341(5) Å β = 123.455(11)°	chains of ZnO_6 and ZnO_4 polyhedra	[18]
catena-[tris(μ_4-4,4'-Sulfonyldibenzoato-O,O',O'',O''')-bis(dimethylformamid e)-tri-zinc(ii) dimethylformamide solvate monohydrate]	$P2_1/n$	a = 16.615(5) Å b = 20.596(5) Å c = 17.252(4) Å β = 98.079(4)°	dense structure	[18]
$[Ca(SDBA)(DMF)_2]\cdot DMF$	$P2_1/c$	a = 8.7220(3) Å b = 27.5302(8) Å c = 11.2194(3) Å β = 107.284(3)°	chains of CaO_6 octahedra linked by μ_2 carboxylate groups,	[19]
$[Sr_5(SDBA)_4(HCOO)_2(DMF)_8]\cdot 2DMF$	P-1	a = 13.9492(9) Å b = 15.6692(13) Å c = 15.9071(13) Å α = 60.919(9)° β = 72.626(6)° γ = 88.389(6)°	pentanuclear Sr cluster linked by carboxylate groups of ligand	[19]
$[Ba_2(SBBA)_2]\cdot 4DEF$	P-1	a = 13.985(2) Å b = 14.614(3) Å c = 16.700(3) Å	chains of BaO_9 and BaO_{10} polyhedra linked by μ_2-carboxylate	[19]

		α = 68.406(3)° β = 84.457(3)° γ = 61.789(2)°	groups	
$[Cd(SDBA)(Py)_2(H_2O)]_n \cdot 2n(Py)$	*Pbcm*	a = 6.0417(10) Å b = 23.070(4) Å c = 24.165(4) Å	CdO_5N_2 polyhedra connected by carboxylate groups of linker to form chains	20
catena-((μ_8-4-((4-carboxyphenyl)sulfonyl)-1-benzenecarboxylato)-di-thallium (i))	*Pnma*	a = 8.7301(5) Å b = 28.4851(18) Å c = 5.8705(4) Å	dense structure	21
$[Cd(SDBA)(H_2O)]$	$P2_1/c$	a = 7.1616(14) Å b = 22.672(5) Å c = 9.7384(19) Å β = 104.99(3)°	twofold interpenetrating rutile network	22
catena-(bis(μ_4-Biphenyl sulfone-4,4-dicarboxylato)-(μ_2-biphenyl sulfone-4,4'-dicarboxylato)-tetrakis(dimethylformamide-O)-di-neodymium dimethylformamide methanol solvate)	*P*-1	a = 14.883(3) Å b = 16.795(4) Å c = 17.490(4) Å α = 93.192(4)° β = 114.063(3)° γ = 103.782(4)°	dense structure	23
catena-(bis(μ_4-Biphenyl sulfone-4,4'-dicarboxylato-O,O',O'',O''')-(μ_4-biphenyl sulfone-4,4'-dicarboxylato-O,O',O'',O''',O''')-diaqua-di-ytterbium sesquihydrate)	*P*-1	a = 12.5892(12) Å b = 12.7017(12) Å c = 17.5888(16) Å α = 101.382(1)° β = 94.941(1)° γ = 117.694(1)°	dense structure	23
catena-(bis(μ_4-Biphenyl sulfone-4,4'-dicarboxylato-O,O',O'',O''')-(μ_4-biphenyl sulfone-4,4'-dicarboxylato-O,O',O'',O''',O''')-diaqua-di-erbium hydrate)	*P*-1	a = 12.6140(11) Å b = 12.7074(11) Å c = 17.6356(17) Å α = 101.474(1)° β = 94.904(2)° γ = 117.645(1)°	dense structure	23
$[Cd(SDBA)(DMF)]\cdot 0.5H_2O$	*C2/m*	a = 11.700(3) Å b = 22.747(6) Å c = 7.664(2) Å β = 124.775(3)°	CdO_{10} polyhedra connected by linker molecules to form chains	24
$[Ca(SDBA)]$	$P2_1/n$	a = 11.8831(8) Å b = 5.5418(3) Å c = 22.6515(15) Å β = 101.607(7)°	chains of CaO_6 octahedra, connectes by linker to form diamond-shaped channels; porous	25
$[Zn_3(OH)_2(SDBA)_2]\cdot EtOH$ $[Mg_3(OH)_2(SDBA)_2(EtOH)(H_2O)_3]\cdot 3.5H_2O$ $[Ni_3(OH)_2(SDBA)_2(EtOH)(H_2O)_3]$	$P2_1/n$ *P2/c* *P2/c*	a = 14.0847(4) Å b = 5.9953(2) Å c = 19.3347(6) Å β = 93.729(2)° a = 28.1637(9) Å b = 6.4411(2) Å c = 24.8679(8) Å β = 115.445(2)° a = 27.051(7) Å	two-dimensional structures containing inorganic motifs with	26

$\cdot 3.5H_2O$		b = 6.2522(14) Å c = 24.945(8) Å β = 115.191(12)°	one-dimensional chains,	
$[Co_3(OH)_2(SDBA)_2(EtOH)(H_2O)_3]$ $\cdot 3.5H_2O$	$P2/c$	a = 28.1888(19) Å b = 6.3545(3) Å c = 24.9584(15) Å β = 115.737(4)°	porous upon thermal activation	
[Mn(SDBA)(EtOH)]	$P2_1/n$	a = 10.1610(5) Å b = 7.3197(3) Å c = 22.3295(10) Å β = 93.699(1)°		
$[Mn(SDBA)(H_2O)]$	P-1	a = 5.9980(2) Å b = 11.8959(4) Å c = 13.0287(7) Å α = 112.118(3)° β = 102.502(3)° γ = 99.816(2)°	dimers of trigonal prisms connected through SDBA linkers forming 2D neutral and porous channels	

HT-syntheses

Discovery of CAU-11

In Table S2 the synthesis parameters for the first high throughput experiment for the discovery of CAU-11 are shown. The over all concentration as well as the molar ratios of the starting materials were varied and NaOH was tested as additive in different ratios. 1 equivalent is 0.06 mmol.

Table S2. Molar ratios of the starting materials for the first high-throughput experiment for the discovery of CAU-11. The reaction was performed for 12 h at 120 °C under conventional heating.

SDBA_1	Composition			Salt		Linker		Additiv	solvent
	Salt	Linker	Additiv µL	$AlCl_3$ x 6 H_2O		H_2SDBA		NaOH in H_2O (2M)	H_2O
Nr	$AlCl_3$ x 6 H_2O	H_2SDBA	NaOH	mmol	mg	mmol	mg	mmol	µL
1	1	1	0	0.06	14.5	0.06	18.4	0	2000
2	2	2	0	0.12	29.0	0.12	36.8	0	2000
3	1	2	0	0.06	14.5	0.12	36.8	0	2000
4	1	3	0	0.06	14.5	0.18	55.1	0	2000
5	2	1	0	0.12	29.0	0.06	18.4	0	2000
6	3	1	0	0.18	43.5	0.06	18.4	0	2000
7	1	1	1	0.06	14.5	0.06	18.4	0.06	2000
8	2	2	1	0.12	29.0	0.12	36.8	0.06	2000
9	1	2	1	0.06	14.5	0.12	36.8	0.06	2000
10	1	3	1	0.06	14.5	0.18	55.1	0.06	2000
11	2	1	1	0.12	29.0	0.06	18.4	0.06	2000
12	3	1	1	0.18	43.5	0.06	18.4	0.06	2000
13	1	1	2	0.06	14.5	0.06	18.4	0.12	2000
14	2	2	2	0.12	29.0	0.12	36.8	0.12	2000
15	1	2	2	0.06	14.5	0.12	36.8	0.12	2000
16	1	3	2	0.06	14.5	0.18	55.1	0.12	2000
17	2	1	2	0.12	29.0	0.06	18.4	0.12	2000
18	3	1	2	0.18	43.5	0.06	18.4	0.12	2000
19	1	1	4	0.06	14.5	0.06	18.4	0.24	2000
20	2	2	4	0.12	29.0	0.12	36.8	0.24	2000
21	1	2	4	0.06	14.5	0.12	36.8	0.24	2000
22	1	3	4	0.06	14.5	0.18	55.1	0.24	2000
23	2	1	4	0.12	29.0	0.06	18.4	0.24	2000
24	3	1	4	0.18	43.5	0.06	18.4	0.24	2000

Discovery of CAU-11-COOH

In Table S3 the synthesis parameters for the first high throughput experiment for the discovery of CAU-11-COOH are shown. The over all concentration as well as the molar ratios of the starting materials were varied and NaOH was tested as additive in different ratios. After the isolation of the formed precipitates a product distribution as shown in Figure S1 could be obtained. 1 Equivalent is 0.05 mmol.

Table S3. Molar ratios of the starting materials for the first high-throughput experiment for the discovery of CAU-11-COOH. The reaction was performed for 3 h at 150 °C under microwave assisted heating.

DPST CDA_1	Composition			Salt		Linker		Additiv		solvent
	Salt	Linker	Additiv µL	$AlCl_3$ x $6H_2O$ in H_2O (1M)		DPSDA		NaOH in H_2O (2M)		H_2O
Nr	$AlCl_3$ x $6H_2O$	DPSDA	NaOH	mmol	µL	mmol	mg	mmol Soll	µL Soll	µL
1	1	1	0	0.05	25	0.05	17.9	0	0	1475
2	2	2	0	0.1	50	0.1	35.8	0	0	1450
3	1	2	0	0.05	25	0.1	35.8	0	0	1475
4	1	3	0	0.05	25	0.15	53.7	0	0	1475
5	2	1	0	0.1	50	0.05	17.9	0	0	1450
6	3	1	0	0.15	75	0.05	17.9	0	0	1425
7	4	2	0	0.2	100	0.1	35.8	0	0	1400
8	2	4	0	0.1	50	0.2	71.7	0	0	1450
9	1	1	2	0.05	25	0.05	17.9	0.1	50	1425
10	2	2	2	0.1	50	0.1	35.8	0.1	50	1400
11	1	2	2	0.05	25	0.1	35.8	0.1	50	1425
12	1	3	2	0.05	25	0.15	53.7	0.1	50	1425
13	2	1	2	0.1	50	0.05	17.9	0.1	50	1400
14	3	1	2	0.15	75	0.05	17.9	0.1	50	1375
15	4	2	2	0.2	100	0.1	35.8	0.1	50	1350
16	2	4	2	0.1	50	0.2	71.7	0.1	50	1400
17	1	1	4	0.05	25	0.05	17.9	0.2	100	1375
18	2	2	4	0.1	50	0.1	35.8	0.2	100	1350
19	1	2	4	0.05	25	0.1	35.8	0.2	100	1375
20	1	3	4	0.05	25	0.15	53.7	0.2	100	1375
21	2	1	4	0.1	50	0.05	17.9	0.2	100	1350
22	3	1	4	0.15	75	0.05	17.9	0.2	100	1325
23	4	2	4	0.2	100	0.1	35.8	0.2	100	1300
24	2	4	4	0.1	50	0.2	71.7	0.2	100	1350

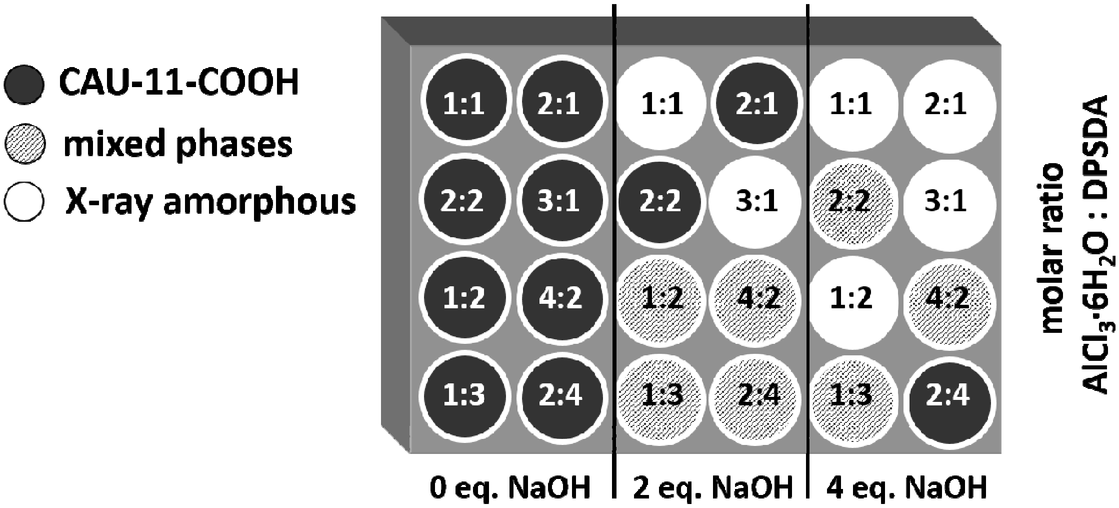

Figure S1. Product distribution of the first high-throughput experiment for the discovery of CAU-11-COOH.

Discovery of CAU-12

In Table S4 the synthesis parameters for the first high throughput experiment for the discovery of CAU-12 are shown. The over all concentration as well as the molar ratios of the starting materials were varied. After the isolation of the formed precipitates a product distribution as shown in Figure S2 could be obtained. 1 Equivalent is 0.05 mmol.

Table S4. Molar ratios of the starting materials for the first high-throughput experiment for the discovery of CAU-12. The reaction was performed for 160 min at 170°C under microwave assisted heating.

DPSTCDA_2	**Composition**		**Salt**		**Linker**		**Solvent**
	Salt	**Linker**	**$AlCl_3$ x 6 H_2O in H_2O (1M)**		**DPSDA**		**H_2O**
Nr	**$AlCl_3$ x 6 H_2O**	**DPSDA**	**mmol**	**µL**	**mmol**	**mg**	**µL**
1	2	1	0.1	50	0.05	17.9	1450
2	3	1	0.15	75	0.05	17.9	1425
3	4	1	0.2	100	0.05	17.9	1400
4	5	1	0.25	125	0.05	17.9	1375
5	7	1	0.35	175	0.05	17.9	1325
6	6	1	0.3	150	0.05	17.9	1350
7	8	1	0.4	200	0.05	17.9	1300
8	10	1	0.5	250	0.05	17.9	1250
9	3	2	0.15	75	0.1	35.8	1425
10	4	2	0.2	100	0.1	35.8	1400
11	5	2	0.25	125	0.1	35.8	1375
12	6	2	0.3	150	0.1	35.8	1350
13	7	2	0.35	175	0.1	35.8	1325
14	8	2	0.4	200	0.1	35.8	1300
15	10	2	0.5	250	0.1	35.8	1250
16	2	2	0.1	50	0.1	35.8	1450
17	3	3	0.15	75	0.15	53.7	1425

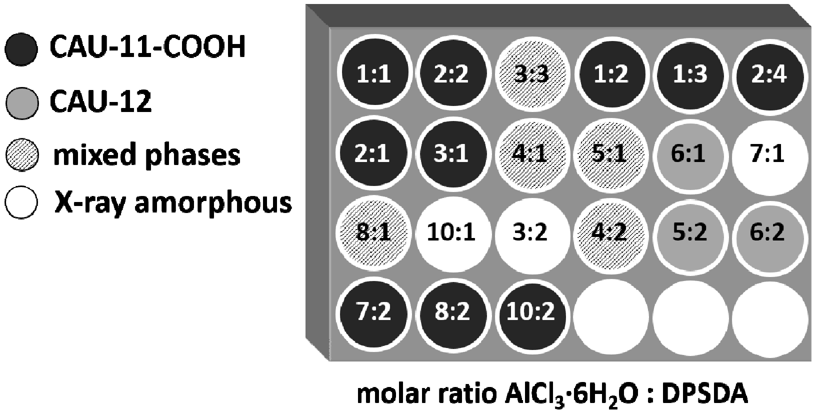

Figure S2. Product distribution of the first high-throughput experiment for the discovery of CAU-12.

Crystal Structures

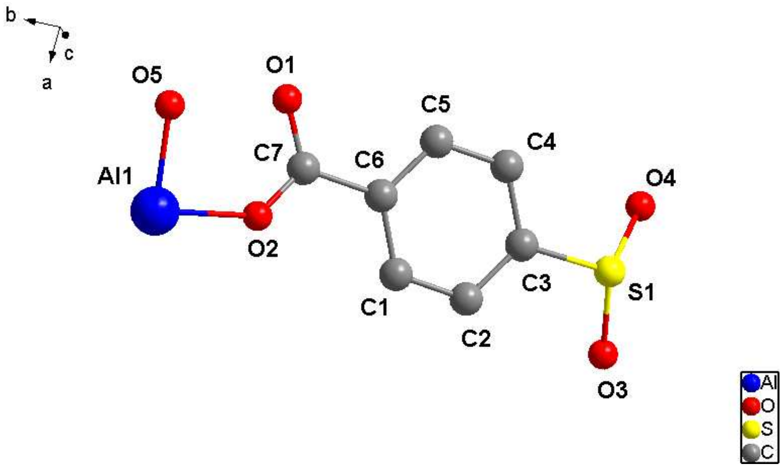

Figure S3. Asymmetric unit of CAU-11 with numbering scheme as used in Table S5.

Table S5. Bond lengths of CAU-11.

atom1	atom2	count	distance [Å]	atom1	atom2	count	distance [Å]
Al1	O5	1x	1.854(37)	C5	C4	1x	1.3562(1)
	O5	1x	1.882(37)		C6	1x	1.3562(1)
	O1	2x	1.931(11)		C1	1x	2.3490(2)
	O2	2x	1.974(10)		C3	1x	2.3490(1)
O5	Al1	1x	1.854(37)		C7	1x	2.4746(1)
	Al1	1x	1.882(37)	C6	C1	1x	1.3562(1)
S1	O3	1x	1.545(18)		C5	1x	1.3562(1)
	O4	1x	1.567(18)		C7	1x	1.5000(1)
	C3	2x	1.700(4)		O1	1x	2.3431(1)
O3	S1	1x	1.545(18)		O2	1x	2.3431(1)
O4	S1	1x	1.567(18)		C4	1x	2.3490(1)
C1	C2	1x	1.3562(1)		C2	1x	2.3490(1)
	C6	1x	1.3562(1)	C7	O1	1x	1.2000(1)
	C3	1x	2.3490(1)		O2	1x	1.2000(1)
	C5	1x	2.3490(2)		C6	1x	1.5000(1)
	C7	1x	2.4746(1)		C5	1x	2.4746(1)
C2	C1	1x	1.3562(1)		C1	1x	2.4746(1)
	C3	1x	1.3562(1)	O1	C7	1x	1.2000(1)
	C4	1x	2.3490(2)		Al1	1x	1.931(11)
	C6	1x	2.3490(1)		O2	1x	2.0785(2)
C3	C2	1x	1.3562(1)		C6	1x	2.3431(1)
	C4	1x	1.3562(1)	O2	C7	1x	1.2000(1)
	S1	1x	1.700(4)		Al1	1x	1.974(10)
	C1	1x	2.3490(1)		O1	1x	2.0785(2)
	C5	1x	2.3490(1)		C6	1x	2.3431(1)
C4	C5	1x	1.3562(1)				
	C3	1x	1.3562(1)				
	C2	1x	2.3490(2)				
	C6	1x	2.3490(1)				

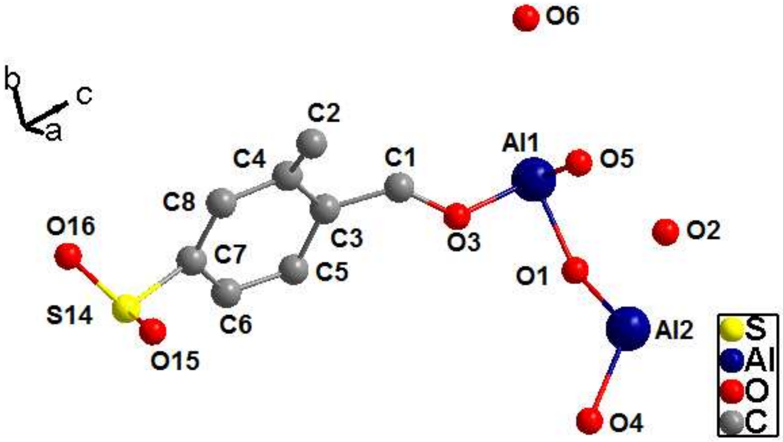

Figure S4. Asymmetric unit of CAU-12 with numbering scheme as used in Table S6.

Table S6. Bond lengths of CAU-12.

atom1	atom2	count	distance [Å]	atom1	atom2	count	distance [Å]
S14	O15	1x	1.494(10)	C3	C5	1x	1.412
	O16	1x	1.541(15)		C4	1x	1.422
	C6	1x	1.663(11)		C1	1x	1.460(8)
	C7	1x	1.736(11)	C4	C8	1x	1.3951
Al1	O5	2x	1.800(7)		C3	1x	1.4226
	O3	2x	1.807(6)		C2	1x	1.530(11)
	O1	2x	1.870(4)	C5	C6	1x	1.3995
Al2	O1	2x	1.840(5)		C3	1x	1.4112
	O6	2x	1.938(6)	C6	C7	1x	1.3389
	O4	2x	1.962(5)		C5	1x	1.3995
O1	Al2	1x	1.840(5)		S14	1x	1.663(11)
	Al1	1x	1.870(4)	C7	C6	1x	1.3389
O2	C2	1x	1.271(9)		C8	1x	1.3690
O3	C1	1x	1.245(9)		S14	1x	1.736(11)
	Al1	1x	1.807(6)	C8	C7	1x	1.3690
O4	C1	1x	1.247(8)		C4	1x	1.3951
	Al2	1x	1.962(5)				
O5	C2	1x	1.299(7)				
	Al1	1x	1.800(7)				
O6	Al2	1x	1.938(6)				
O15	S14	1x	1.494(10)				
O16	S14	1x	1.541(15)				
C1	O3	1x	1.245(9)				
	O4	1x	1.247(8)				
	C3	1x	1.460(8)				
C2	O2	1x	1.271(9)				
	O5	1x	1.299(7)				
	C4	1x	1.530(11)				

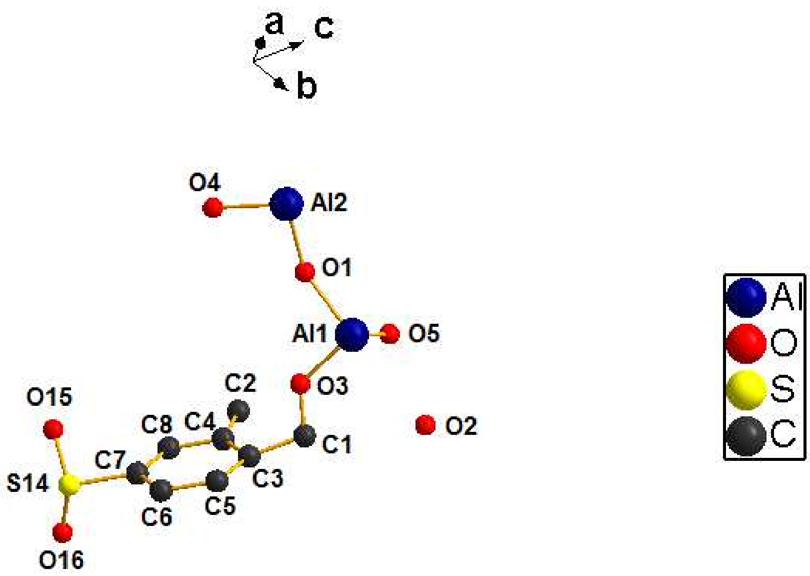

Figure S5. Asymmetric unit of CAU-12-dehy with numbering scheme as used in Table S7.

Table S7. Bond lengths of CAU-12-dehy.

atom1	atom2	count	distance [Å]	atom1	atom2	count	distance [Å]
Al1	O3	2x	1.871(5)	C2	O5	1x	1.275(7)
	O5	2x	1.925(5)		O2	1x	1.292(7)
	O1	2x	1.935(5)		C4	1x	1.469(9)
Al2	O2	2x	1.881(6)	C3	C4	1x	1.3945(1)
	O4	2x	1.884(6)		C5	1x	1.4031(2)
	O1	2x	1.917(3)		C1	1x	1.47(7)
O1	Al2	1x	1.917(3)	C4	C8	1x	1.3662(1)
	Al1	1x	1.935(5)		C3	1x	1.3945(1)
O2	C2	1x	1.292(7)		C2	1x	1.469(9)
	Al2	1x	1.881(6)	C5	C6	1x	1.3980(1)
O3	C1	1x	1.291(5)		C3	1x	1.4031(2)
	Al1	1x	1.871(5)	C6	C7	1x	1.3978(1)
O4	C1	1x	1.266(7)		C5	1x	1.3980(1)
	Al2	1x	1.884(7)		S14	1x	1.770(6)
O5	C2	1x	1.275(7)	C7	C8	1x	1.3607(2)
	Al1	1x	1.925(5)		C6	1x	1.3978(1)
S14	O16	1x	1.528(15)		S14	1x	1.697(7)
	O15	1x	1.597(11)	C8	C7	1x	1.3607(2)
	C7	1x	1.697(7)		C4	1x	1.3662(1)
	C6	1x	1.770(6)				
O15	S14	1x	1.597(11)				
O16	S14	1x	1.528(15)				
C1	O4	1x	1.266(7)				
	O3	1x	1.291(5)				
	C3	1x	1.447(7)				

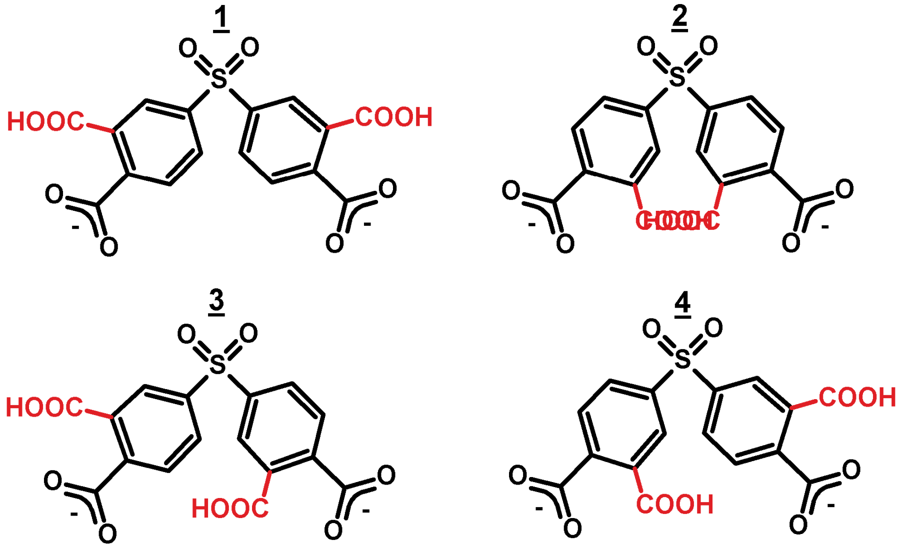

Figure S6. The four different possible conformation isomers in CAU-11-COOH.

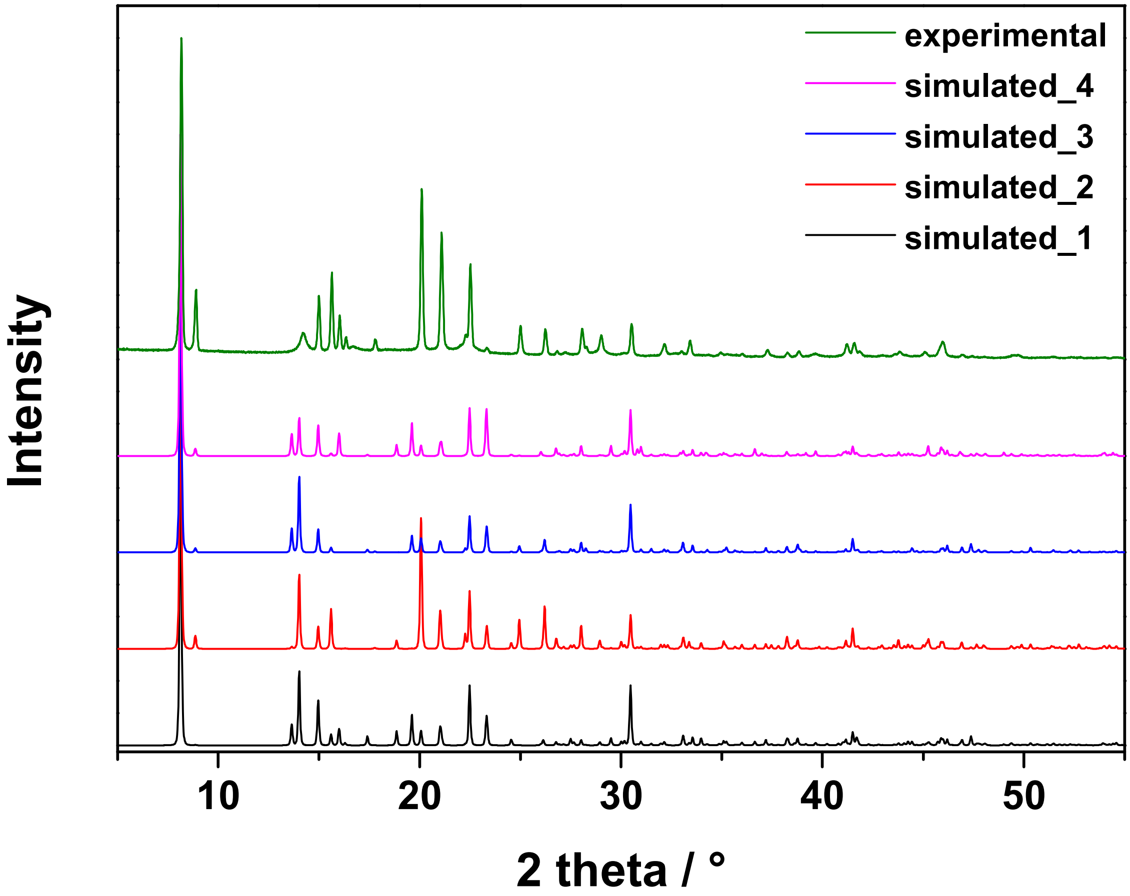

Figure S7. Simulated powder patterns for CAU-11-COOH for the four different positions of the non-coordinating carboxylate groups.

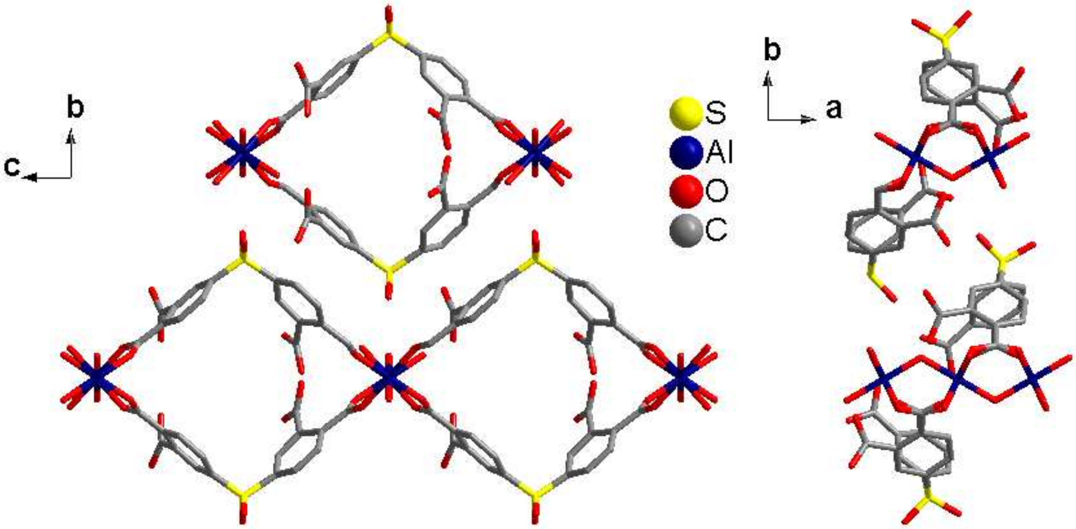

Figure S8. Simulated structure of CAU-11-COOH using the conformation **<u>1</u>** from Figure S6.

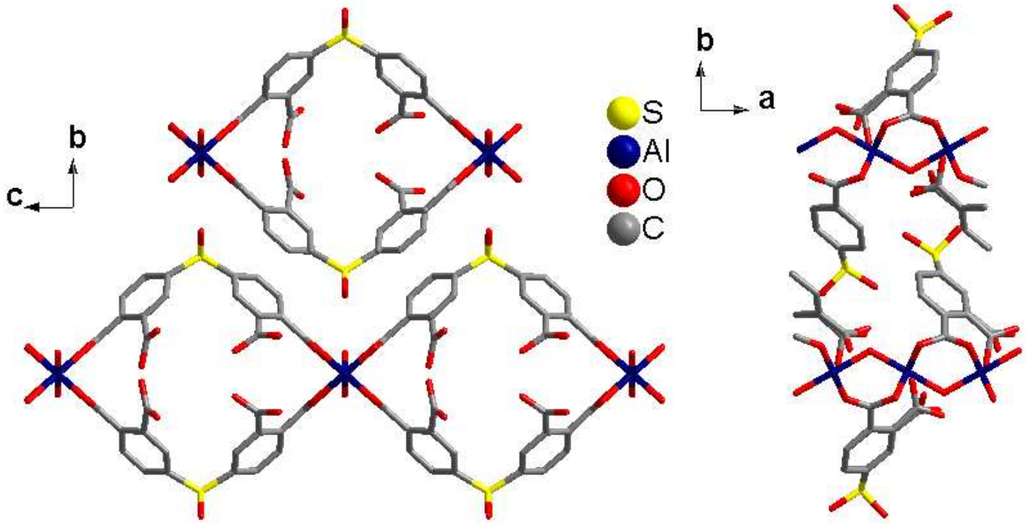

Figure S9. Simulated structure of CAU-11-COOH using the conformation **<u>2</u>** from Figure S6.

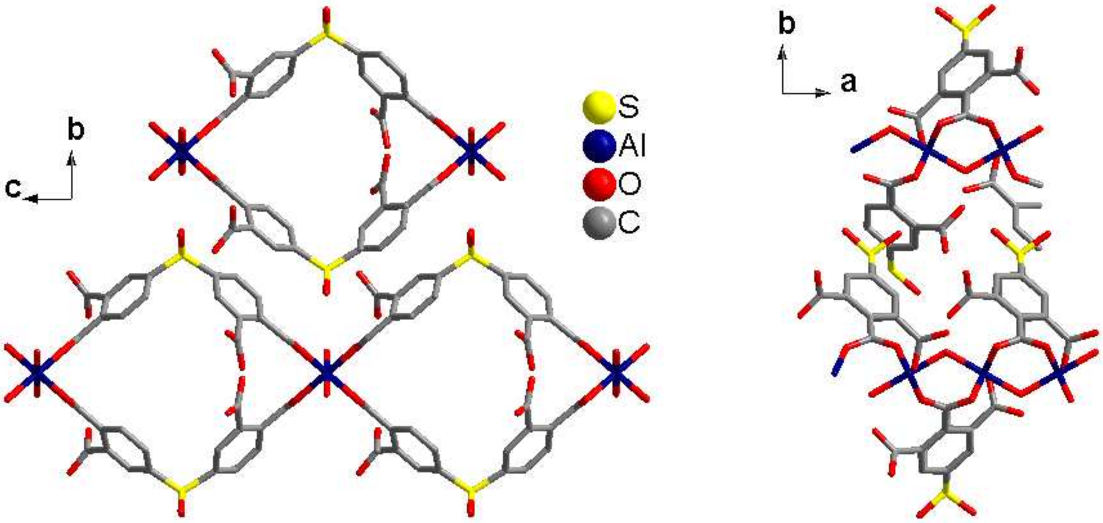

Figure S10. Simulated structure of CAU-11-COOH using the conformation **<u>3</u>** from Figure S6.

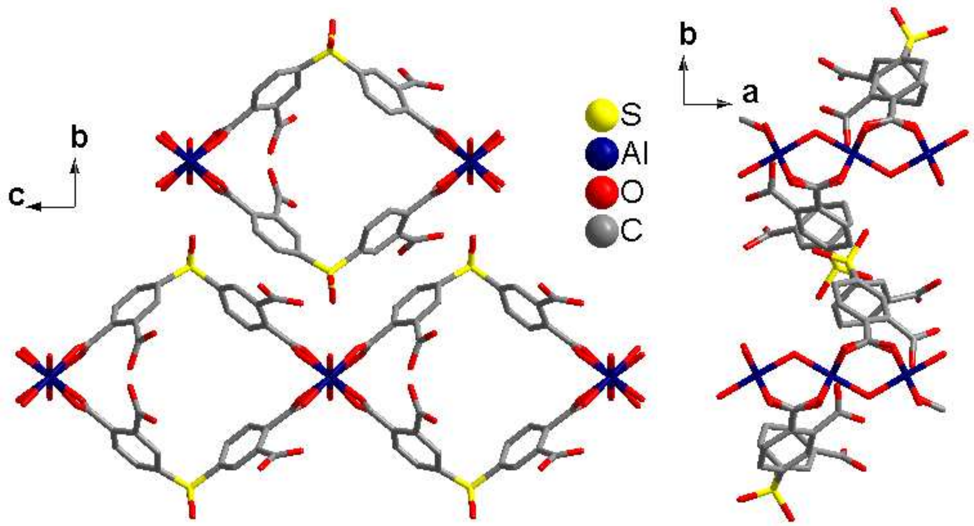

Figure S11. Simulated structure of CAU-11-COOH using the conformation **4** from Figure S6.

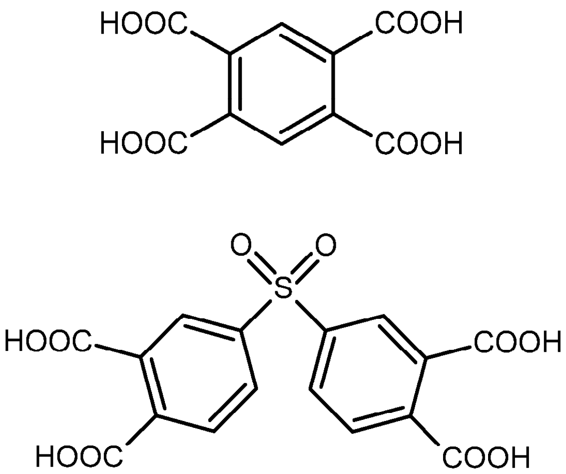

Figure S12. Linker molecule of MIL-60 (top) and linker molecule of CAU-12 (bottom).

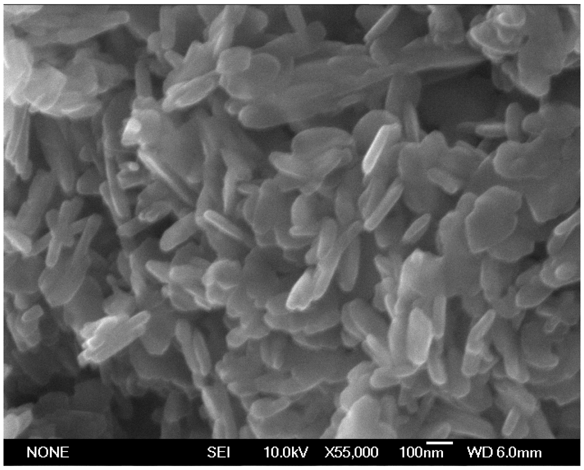

Figure S13. SEM picture of CAU-12.

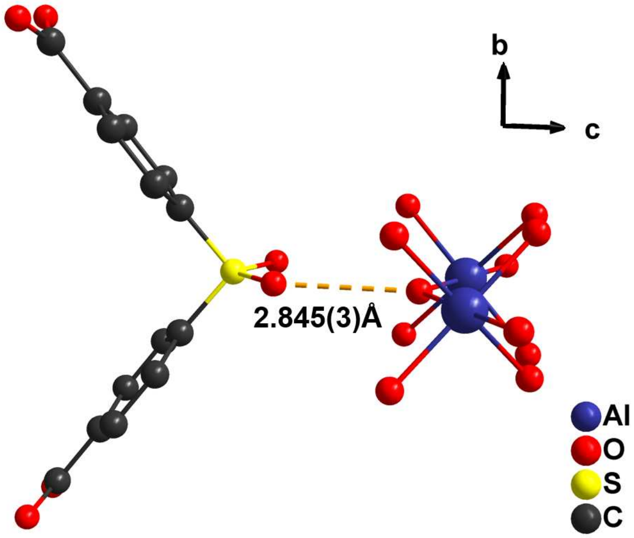

Figure S14. Section of the structure of CAU-11, demonstrating the orientation of and the distance between the sulfone group of the linker molecule and the bridging hydroxyl group of the inorganic building unit.

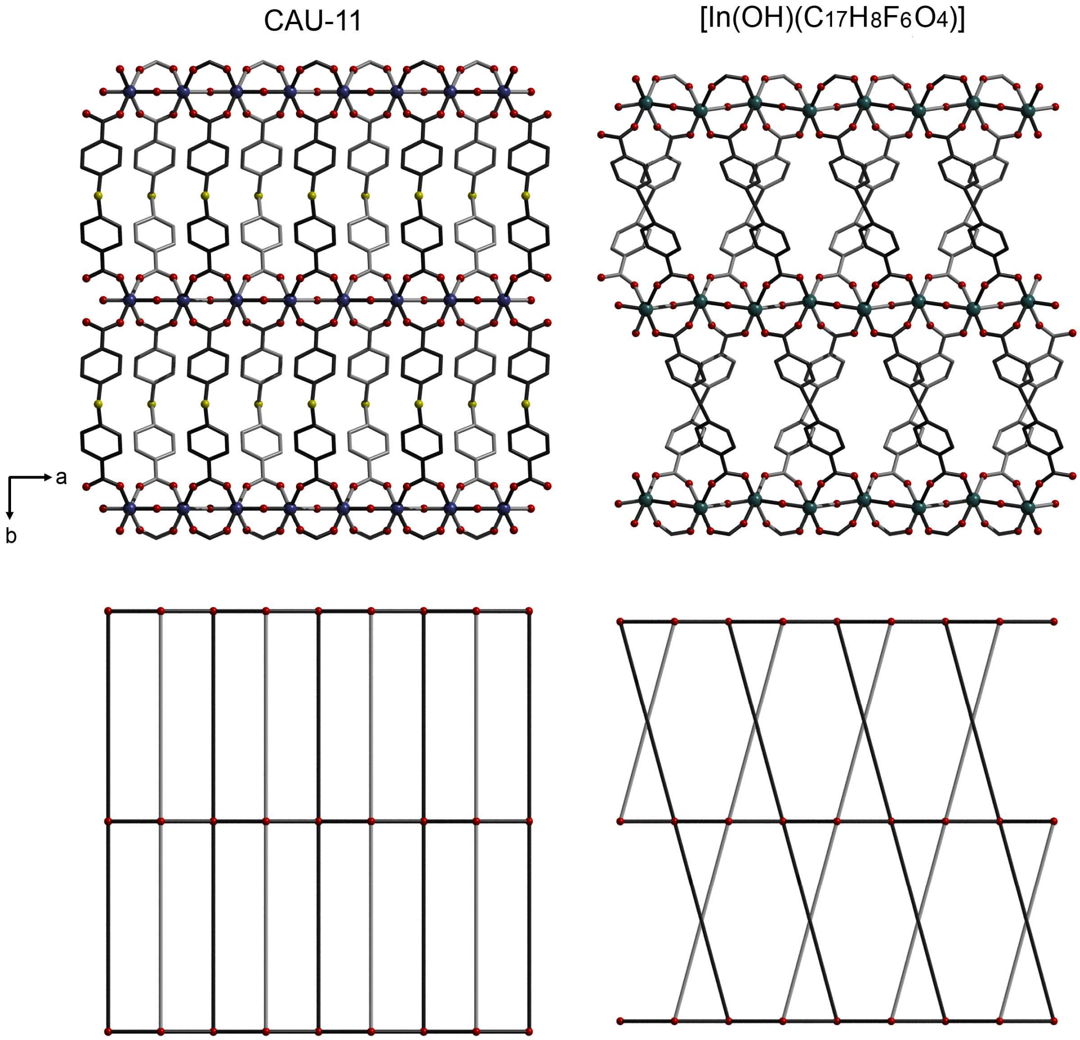

Figure S15. (Top) Comparison of the structures of CAU-11 and [In(OH)($C_{17}H_8F_6O_4$)] both with lozenge-shaped channels through layers. Oxygen atoms on the sulfone groups as well as the fluorine atoms have been removed for clarity. (Bottom) The underlining nets of the two structures. CAU-11 is simplified to a 4^4 square lattice and the net of [In(OH)($C_{17}H_8F_6O_4$)] has the Schläfli symbol ($4^2.6^3.8$). Unlike CAU-11 the net of [In(OH)($C_{17}H_8F_6O_4$)] must be described in three-dimensions as edges would cross if the net is flattened to a plane.

Thermal Analysis

The TG curve of CAU-11 shows a two-step weight loss (Figure S15). In accordance with the molecular formula [Al(OH)(SDBA)]·0.25DMF the first step (RT - 425 °C) can be attributed to the removal of incorporated DMF molecules (meas. 5.3 %, calc. 5.0 %) and the second (425°C – 600 °C) to the decomposition of the framework (meas. 80.6 %, calc. 81.1 %) resulting in an X-ray amorphous product, probably Al_2O_3 (meas. 14.1 %, calc. 13.9 %). The TD-PXRD measurement (Figure S16) shows that the compound is stable up to 420 °C, exhibiting a high crystallinity over the whole temperature range. Above 420 °C the sample starts to decompose and only an X-ray amorphous product is observed, which is in accordance with the results of the TG measurement X-ray amorphous Al_2O_3. The top view of the measurement shows no shift of any reflections revealing the rigidity of the framework (Figure S17).

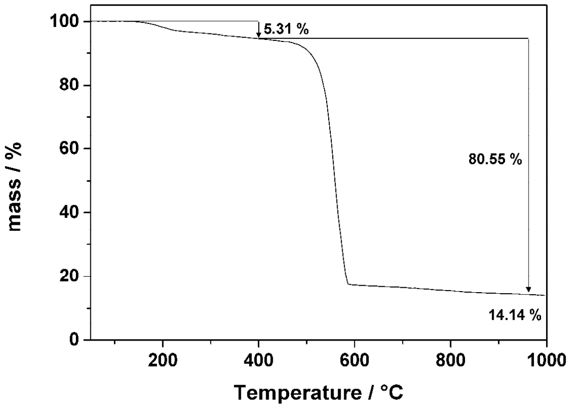

Figure S16. TG curve of CAU-11.

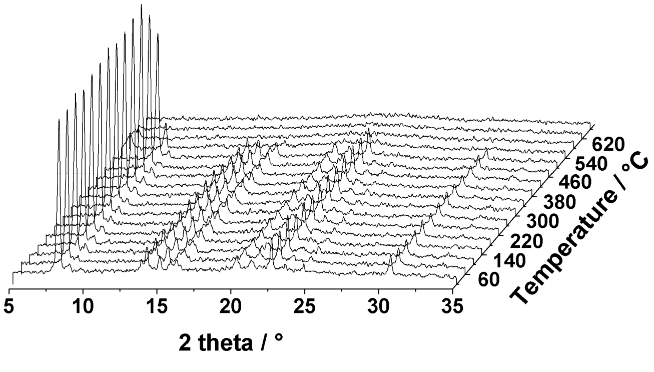

Figure S17. TD-PXRD of CAU-11 in steps of 40 °C from 20 °C up to 660 °C.

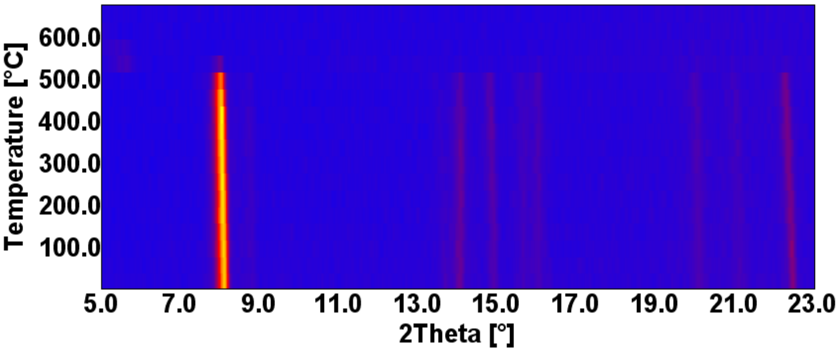

Figure S18. Top view of the TD-PXRD measurements of CAU-11.

The TG curve of CAU-11-COOH exhibits a two-step weight loss (Figure S18). The first step (RT - 280 °C) can be attributed to the removal of incorporated water molecules (meas. 2.2 %, calc. 2.1 %) and the second (350 °C - 650 °C) to the decomposition of the framework (meas. 86.0%, calc. 85.8 %) resulting in Al_2O_3 (meas. 11.8 %, calc. 12.1 %).

The stability of the framework is demonstrated by the TD-PXRD measurement (Figure S19). Up to a temperature of 380 °C no change in the crystallinity and no shift of the reflection positions is observed. Above 380 °C the intensity of the first reflection increases and also a shift to lower diffraction angles is observed (Figure S20). The remaining reflections do not change in intensity but slightly shift to higher diffraction angles. This data could be explained by interactions between neighboring non-coordinating carboxylic acid groups, which has earlier been reported for another Al-MOFs containing free carboxylic acid groups.[27] Unfortunately in the case of CAU-11-COOH, it wasn't possible to determine the formation of a specific functional group by in-situ IR-spectroscopy, due to the simultaneously decomposition of the framework during the formation of additional bands. In accordance with the TG-curve, the compound rapidly decomposes into X-ray amorphous Al_2O_3 above 460 °C.

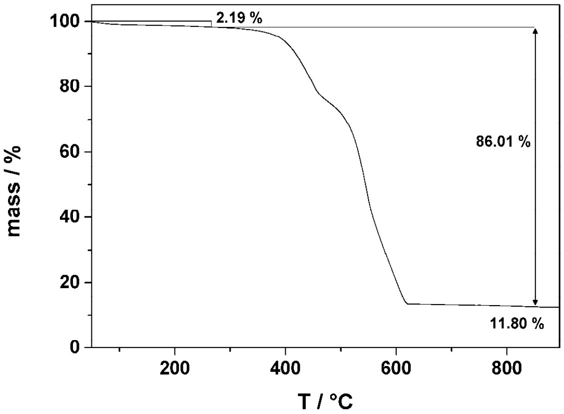

Figure S19. TG curve of CAU-11-COOH.

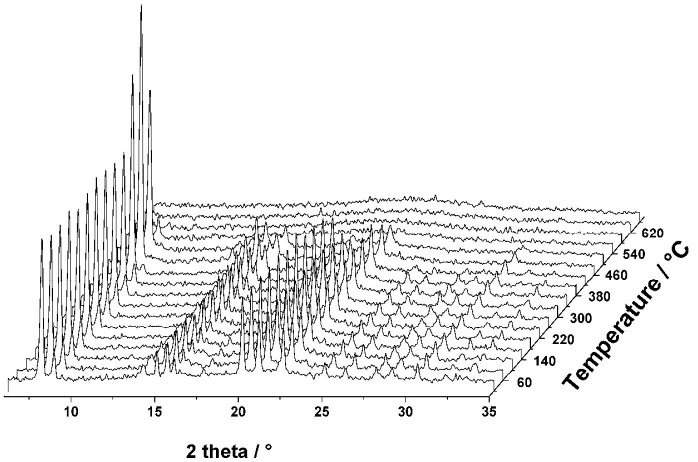

Figure S20. TD-PXRD of CAU-11-COOH in steps of 40°C from 20°C up to 660°C.

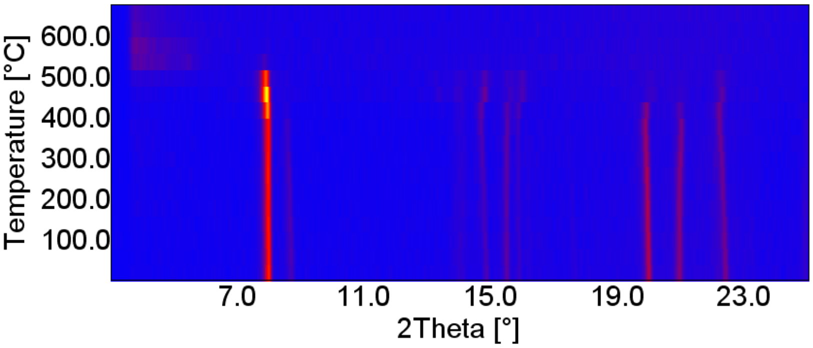

Figure S21. Top view of the TD-PXRD measurement of CAU-11-COOH.

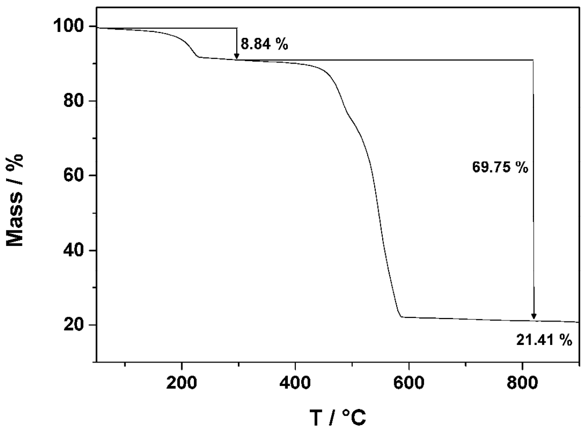

Figure S22. TG curve of CAU-12.

IR spectroscopy

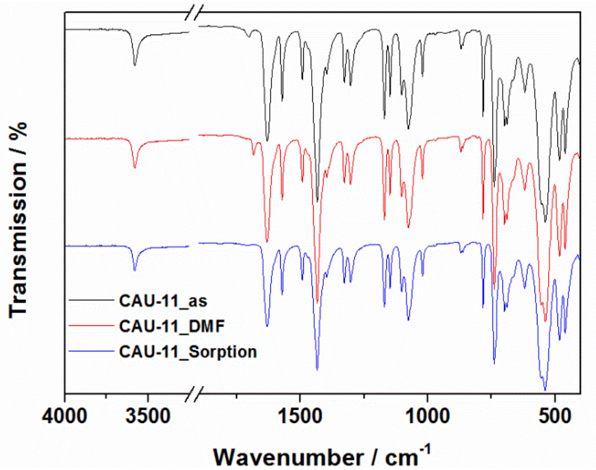

Figure S23. IR spectra of the compound CAU-11 as synthesized (black), CAU-11 solvothermally washed with DMF (red) and CAU-11 after nitrogen sorption measurement (blue).

Sorption measurements

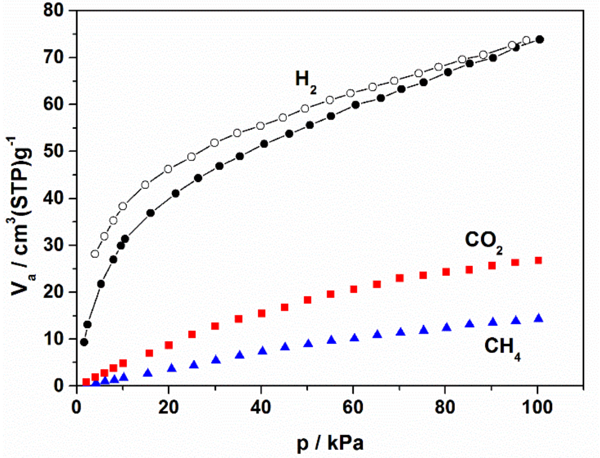

Figure S24. Hydrogen (77 K), carbon dioxide (298 K) and methane (298 K) sorption measurements of CAU-11- up to 100 kPa.

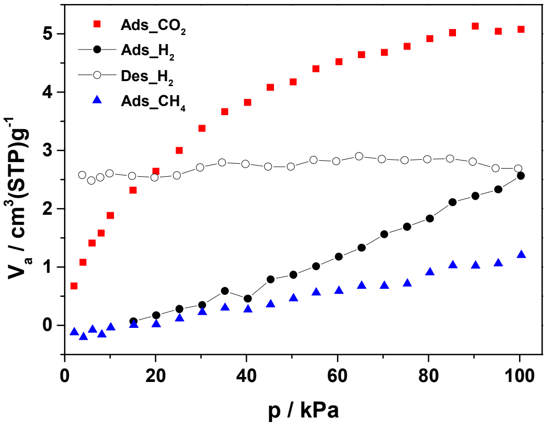

Figure S25. Hydrogen (77 K), carbon dioxide (298 K) and methane (298 K) sorption measurements of CAU-11-COOH up to 100 kPa.

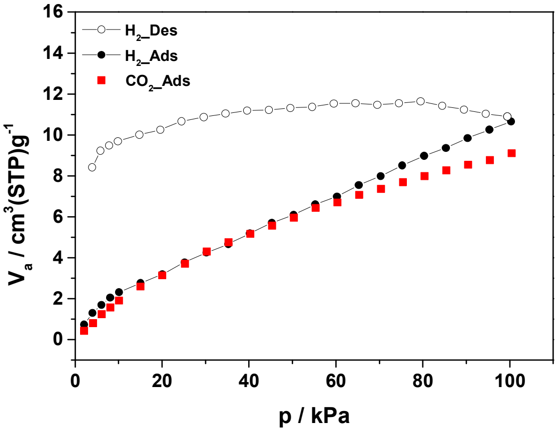

Figure S26. Hydrogen (77 K) and carbon dioxide (298 K) sorption measurements of CAU-12 up to 100 kPa.

Literature

(1) Miyazawa, M.; Irie, Y.; Kashimoto, K.; Nishina, N.; Kondo, M.; Yasue, S.; Maeda, K.; Uchida, F. *Inorg. Chem. Commun.* **2009**, *12*, 336-339.

(2) Li, X.-Q.; Zhang, H.-B.; Wu, S.-T.; Lin, J.-D.; Lin, P.; Li, Z.-H.; Du, S.-W. *CrystEngComm* **2012**, *14*, 936-944.

(3) Zhuang, W.-J.; Jin, L.-P. *Appl. Organom. Chem.* **2007**, *21*, 76-82.

(4) Zhuang, W.; Ma, S.; Wang, X.-S.; Yuan, D.; Li, J.-R.; Zhao, D.; Zhou, H.-C. *Chem. Commun.* **2010**, *46*, 5223-5225.

(5) Yeh, C.-T.; Lin, W.-C.; Lo, S.-H.; Kao, C.-C.; Lin, C.-H.; Yang, C.-C. *CrystEngComm* **2012**, *14*, 1219-1222.

(6) Zhuang, W.-J.; Sun, C.-Y.; Jin, L.-P. *Polyhedron* **2007**, *26*, 1123-1132.

(7) Furukawa, H.; Kim, J.; Ockwig, N. W.; O'Keeffe, M.; Yaghi, O. M. *J. Am. Chem. Soc.* **2008**, *130*, 11650-11661.

(8) Lin, J.-D.; Wu, S.-T.; Li, Z.-H.; Du, S.-W. *CrystEngComm* **2010**, *12*, 4252-4262.

(9) Ahnfeldt, T.; Gunzelmann, D.; Loiseau, T.; Hirsemann, D.; Senker, J.; Férey, G.; Stock, N. *Inorg. Chem.* **2009**, *48*, 3057-3064.

(10) Zhuang, W.; Sun, H.; Xu, H.; Wang, Z.; Gao, S.; Jin, L. *Chem. Commun.* **2010**, *46*, 4339-4341.

(11) Xiao, D.; Chen, H.; Sun, D.; He, J.; Yan, S.; Yang, J.; Wang, X.; Yuan, R.; Wang, E. *CrystEngComm* **2012**, *14*, 2849-2858.

(12) Banerjee, D.; Borkowski, L. A.; Kim, S. J.; Parise, J. B. *Cryst. Growth Des.* **2009**, *9*, 4922-4926.

(13) Jiao, C.-m. *Acta Crystallogr. E* **2010**, *66*, m1405.

(14) Li, N.; Chen, L.; Lian, F.; Jiang, F.; Hong, M. *Inorg. Chim. Acta* **2010**, *363*, 3291-3301.

(15) Liu, J.-Q.; Hu, W.-X.; Wu, T. *Synth. React. Inorg., Metal-Org., Nano-Metal Chem.* **2011**, *41*, 479-483.

(16) Bhattacharya, S.; Ramanujachary, K. V.; Lofland, S. E.; Magdaleno, T.; Natarajan, S. *CrystEngComm* **2012**, *14*, 4323-4334.

(17) Lin, J.-D.; Long, X.-F.; Lin, P.; Du, S.-W. *Cryst. Growth Des.* **2009**, *10*, 146-157.

(18) Li, N.; Chen, L.; Lian, F.-Y.; Jiang, F.-L.; Hong, M.-C.; Huaxue, J. *Chin. J. Struct. Chem.* **2009**, *28*, 1417-1426.

(19) Kundu, T.; Sahoo, S. C.; Banerjee, R. *Chem. Commun.* **2012**, *48*, 4998-5000.

(20) Lian, F.-Y.; Jiang, F.-L.; Yuan, D.-Q.; Chen, J.-T.; Wu, M.-Y.; Hong, M.-C. *CrystEngComm* **2008**, *10*, 905-914.

(21) Askarinejad, A.; Morsali, A. *J. Coord. Chem.* **2007**, *60*, 1903-1912.

(22) Xiao, D.; Chen, H.; Sun, D.; Zhang, G.; He, J.; Yuan, R.; Wang, E. *Solid State Sci.* **2011**, *13*, 1573-1578.

(23) Zhuang, W.-J.; Zheng, X.-J.; Sun, H.-L.; Jin, L.-P.; Xuebao, W. H. *Chin. J. Struct. Chem.* **2008**, *24*, 1305-1310.

(24) Liu, Z.; Stern, C. L.; Lambert, J. B. *Organometallics* **2008**, *28*, 84-93.

(25) Plonka, A. M.; Banerjee, D.; Woerner, W. R.; Zhang, Z.; Nijem, N.; Chabal, Y. J.; Li, J.; Parise, J. B. *Angew. Chem.* **2013**, *125*, 1736-1739.

(26) Wu, C.-Y.; Raja, D. S.; Yang, C.-C.; Yeh, C.-T.; Chen, Y.-R.; Li, C.-Y.; Ko, B.-T.; Lin, C.-H. *CrystEngComm* **2014**, *16*, 9308-9319.

(27) Reimer, N.; Gil, B.; Marszalek, B.; Stock, N. *CrystEngComm* **2012**, *14*, 4119-4125.

Supporting Information

Four new Al-based microporous metal-organic framework compounds with MIL-53-type structure using functionalized extended linker molecules

Selda Halis[a], Nele Reimer[a], Arne Klinkebiel[b], Ulrich Lüning[b] and Norbert Stock[a]

[a]Institut für Anorganische Chemie, Christian-Albrechts-Universität, Max-Eyth-Straße 2, D-24118 Kiel, Germany
[b]Otto Diels-Institut für Organische Chemie, Christian-Albrechts-Universität, Otto-Hahn-Platz 4, D-24098 Kiel, Germany

1. Synthesis of functionalized linker molecules

General

Dimethyl biphenyl-4,4`-dicarboxylate was purchased from Sigma-Aldrich Chemicals Co., palladium on activated charcoal was bought from Alfa Aesar GmbH & Co. KG.

NMR spectra were recorded on Bruker DRX 500 or AV 600 instruments. Assignments are supported by COSY, HSQC, and HMBC. Even when obtained by DEPT, the type of ^{13}C signal is always listed as singlet, doublet, etc. All chemical shifts are referenced to the residual proton or carbon signal of the solvent.

EI/CI mass spectra were recorded with a Finnigan MAT 8200 or MAT 8230.

Dimethyl 2-nitro-biphenyl-4,4'-dicarboxylate ($(CH_3)_2$BPDC-NO_2, 5)[1]

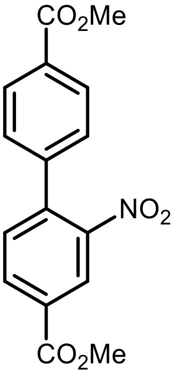

A solution of 5.00 g (18.5 mmol) of dimethyl biphenyl-4,4'-dicarboxylate in 50 mL of conc. sulfuric acid was cooled to 5 °C and carefully treated with a cold mixture of 3 mL of 55 % nitric acid and 4 mL of conc. sulfuric acid, so that the temperature did not exceed 10 °C. After complete addition, the mixture was stirred at room temp. for 24 h. The yellow solution was diluted with 150 mL of ice water and additional 50 mL of a sat. solution of sodium chloride, followed by extraction with 3 x 100 mL of chloroform. The extract was washed with 100 mL of a sat. solution of sodium hydrogen carbonate, dried over anhydrous magnesium sulfate, and the solvent was removed in vacuo. The crude product was purified by column chromatography (silica gel, cyclohexane/ethyl acetate, 2:1, R_f = 0.50) to separate the desired product from the dinitrated compound (R_f = 0.32). A colourless solid (4.67 g, 80 %) was obtained.

Melting point: 99 – 100 °C.

^{1}H-NMR (500 MHz, $CDCl_3$): δ = 8.56 (d, *J* = 1.7 Hz, 1H, Ar-*H*-3), 8.23 (dd, *J* = 1.7 Hz, *J* = 8.0 Hz,1H, Ar-*H*-5), 8.12 (m_c (d), *J* = 8.4 Hz, 2H, Ar'-*H*-2,6), 7.55 (d, J = 8.0 Hz, 1H, Ar-*H*-6), 7.41 (m_c (d), *J* = 8.4 Hz, 2H, Ar'-*H*-3,5), 4.00 (s, 3H, Ar-CO_2CH_3), 3.95 (s, 3H, Ar'-CO_2CH_3) ppm.

^{13}C-NMR (125 MHz, $CDCl_3$): δ = 166.45 (s, Ar'-CO_2Me), 164.71 (s, Ar-CO_2Me), 148.98 (s, Ar-*C*-NO_2), 141.07 (s, Ar'-*C*-1), 139.49 (s, Ar-*C*-1), 133.10 (d, Ar-*C*-5), 132.09 (d, Ar-*C*-6), 131.06 (Ar'-*C*-2,6), 130.52 (s, Ar-*C*-4), 130.05 (s, Ar'-*C*-4), 127.88 (d, Ar'-*C*-3,5), 125.49 (d, Ar-*C*-3), 52.86 (q, Ar'-CO_2CH_3), 52.32 (q, Ar-CO_2CH_3) ppm.

MS (EI, 70 eV): *m/z* (%) = 315 (27) $[M]^{+\cdot}$, 287 (100) $[M - 2CH_3 + 2H]^{+\cdot}$, 284 (74) $[M - CH_3O]^+$, 228 (59) $[M - C_4H_7O_2]^+$.

MS (CI, pos., isobutane): *m/z* (%) = 316 (100) $[M + H]^+$.

2-Nitrobiphenyl-4,4`-dicarboxylic acid (H_2BPDC-NO_2, 6)[2]

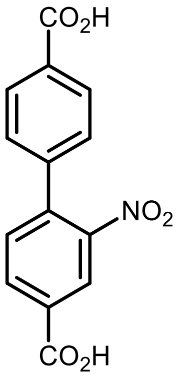

A suspension of 8.86 g (8.50 mmol) of dimethyl 2-nitrobiphenyl-4,4'-dicarboxylate (**5**) in 55 mL of dry THF and 55 mL of an aqueous solution of potassium hydroxide (1 M) was stirred at room temp. for 24 h. The THF was distilled off under reduced pressure and the aqueous residue was acidified with hydrochloric acid (6 M). The precipitate was filtered off and dried in high vacuum to give 2.34 g (8.15 mmol, 96 %) of a colourless solid.

Melting point: > 300 °C.

^{1}H-NMR (500 MHz, DMSO-d_6): δ = 13.41 (s, 2H, CO_2*H*), 8.47 (d, 1H, *J* = 1.6 Hz, Ar-*H*-3), 8.28 (dd, 1H, *J* = 1.6 Hz, *J* = 8.0 Hz, Ar-*H*-5), 8.03 (m_c (d), 2H, *J* = 8.1 Hz, Ar'-*H*-2,6), 7.72 (d, 1H, *J* = 8.0 Hz, Ar-*H*-6), 7.52 (m_c (d), 2H, *J* = 8.1 Hz, Ar'-*H*-3,5) ppm.

^{13}C-NMR (125 MHz, DMSO-d_6): δ = 167.30 (s, Ar'-*C*O_2H), 165.73 (s, Ar-*C*O_2H), 148.94 (s, Ar-*C*-NO_2), 141.13 (s, Ar'-*C*-1), 138.74 (s, Ar-*C*-1), 133.75 (d, Ar-*C*-5), 132.99 (d, Ar-*C*-6), 132.27 (s, Ar-*C*-4), 131.38 (s, Ar'-*C*-4), 130.13 (d, Ar'-*C*-2,6), 128.56 (d, Ar'-*C*-3,5), 125.49 (d, Ar-*C*-3) ppm.

MS (EI, 70 eV): *m/z* (%) = 287 (24) $[M]^{+\cdot}$, 259 (100) $[M - CO]^{+\cdot}$, 214 (56) $[M - CO - CO_2H]^{+\cdot}$, 151 (56) $[M - 2CO_2H - NO_2]^+$.

MS (CI, pos., isobutane): *m/z* (%) = 288 (100) $[M + H]^+$.

Dimethyl 2-aminobiphenyl-4,4`-dicarboxylate ((CH_3)$_2$BPDC-NH_2, 7)[1]

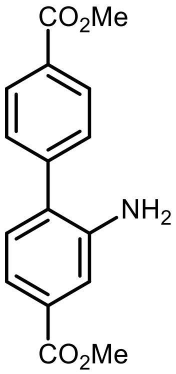

A solution of 500 mg (1.59 mmol) of dimethyl 2-nitrobiphenyl-4,4'-dicarboxylate (**5**) in 10 mL of dry THF was treated with 160 mg of palladium on activated charcoal (10 %) and stirred for 24 h at room temp. under a hydrogen atmosphere (1 bar, TLC-control, silica gel, cyclohexane/ethyl acetate, 1:1, R_f = 0.67). The catalyst was filtered off using celite and the solvent was removed in vacuo to give 446 mg (1.58 mmol, 99 %) of a colourless solid.

Melting point: 172 – 173 °C.

^{1}H-NMR (500 MHz, $CDCl_3$): δ = 8.12 (m_c (d), *J* = 8.5 Hz, 2H, Ar'-*H*-3,5), 7.55 (m_c (d), *J* = 8.5 Hz, 2H, Ar'-*H*-2,6), 7.48 (dd, *J* = 1.6 Hz, *J* = 7.9 Hz, 1H, Ar-*H*-5), 7.45 (d, *J* = 1.6 Hz, 1H, Ar-*H*-3), 7.18 (d, *J* = 7.9 Hz, 1H, Ar-*H*-6), 3.95 (s, 3H, Ar'-CO_2C*H_3*), 3.91 (s, 3H, Ar-CO_2C*H_3*), 3.88 (s, 2H, N*H_2*) ppm.

^{13}C-NMR (125 MHz, $CDCl_3$): δ = 166.99 (s, Ar-*C*O_2Me), 166.72 (s, Ar'-*C*O_2Me), 143.52 (s, Ar-*C*-NH_2), 143.36 (s, Ar'-*C*-1), 130.72 (s, Ar-*C*-4), 130.47 (s, Ar'-*C*-4), 130.32 (d, Ar-*C*-6), 130.21 (d, Ar'-*C*-2,6), 129.49 (s, Ar-*C*-1), 128.85 (d, Ar'-*C*-3,5), 119.69 (d, Ar-*C*-5), 116.66 (d, Ar-*C*-3), 52.20 (q, *C*H3, 52.11 (q, *C*H_3) ppm.

MS (EI, 70 eV): *m/z* (%) = 285 (100) $[M]^{+\cdot}$.

MS (CI, pos., Isobutan): *m/z* (%) = 286 (100) $[M + H]^+$.

2-Aminobiphenyl-4,4'-dicarboxylic acid (H_2BPDC-NH_2, 8)[3]

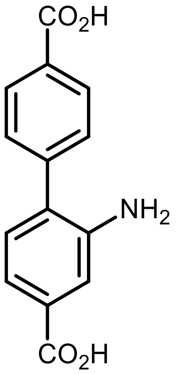

A suspension of 296 mg (1.04 mmol) of dimethyl 2-aminobiphenyl-4,4'-dicarboxylate (**7**) in 6.5 mL of dry THF and 5.6 mL of an aqueous solution of potassium hydroxide (1 M) was stirred at room temp. for 24 h. THF was distilled off under reduced pressure and the residue was acidified with hydrochloric acid (6 M). The precipitate was filtered off and dried in high vacuum to give 247 mg (1.02 mmol, 98 %) of a colourless solid.

Melting point: > 300 °C.

^{1}H-NMR (500 MHz, DMSO-d6): δ = 8.04 (m_c (d), 2H, *J* = 8.4 Hz, Ar'-*H*-3,5), 7.66 (s, 1H, Ar-*H*-3), 7.63 (m_c (d), 2H, *J* = 8.4 Hz, Ar'-*H*-2,6), 7.48 (d, 1H, *J* = 7.9 Hz, Ar-*H*-5), 7.28 (d, 1H, *J* = 7.9 Hz, Ar-*H*-6) ppm.

^{13}C-NMR (125 MHz, DMSO-d6): δ = 167.51 (s, Ar'-*C*O_2H), 167.48 (s, Ar-*C*O_2H), 142.74 (s, Ar-*C*-NH_2), 140.65 (s, Ar'-*C*-1), 132.40 (s, Ar-*C*-1), 131.67 (s, Ar-*C*-4), 131.20 (d, Ar-*C*-6), 130.41 (s, Ar'-*C*-4), 130.24 (d, Ar'-*C*-3,5), 129.41 (d, Ar'-*C*-2,6), 121.60 (d, Ar-*C*-5), 119.36 (d, Ar-*C*-3) ppm.

MS (EI, 70 eV): *m/z* (%) = 257 (100) $[M]^{+\cdot}$.

MS (CI, pos., isobutane): *m/z* (%) = 258 (100) $[M + H]^+$.

2. IR spectroscopy[4]

In the IR spectrum of [Al(OH)(NDC-$(NO_2)_2$)]·DMF **1** (black), the asymmetric and symmetric vibrations and of the coordinating carboxylate groups are observed at 1602 and 1439 cm^{-1} (Fig. S1, top). The asymmetric and symmetric N-O stretching vibrations of the NO_2 groups are located at 1530 and 1347 cm^{-1}; the C-N stretching vibration is of weak intensity and occurs at 896 cm^{-1}. The IR spectrum of the as-synthesized compound **1** (black) reveals a band at 1674 cm^{-1} which is assigned to the CO stretching vibration of the residual DMF molecules within the pores. After activation at 180 °C in vacuo, the bands that are due to the presence of DMF disappear (blue).

In the IR spectrum of the as-synthesized compound **2** (black), the asymmetric and symmetric stretching vibrations of the coordinating carboxylate groups are observed at 1605 and 1431 cm^{-1} (Fig. S1, bottom). The DMF containing compound **2** reveals a band at 1665 cm^{-1}, which can be attributed to the stretching vibration of the carbonyl groups of residual DMF molecules in the pores. The characteristic N-O stretching vibrations of the nitro groups are observed at 1535 and 1358 cm^{-1}; the weak C-N stretching vibration results in a band at 835 cm^{-1}. Furthermore, the as-synthesized compound **2** shows a small broad band at 3379 cm^{-1}, which indicates the presence of water molecules within the pores. After activation at 180 °C in vacuo, the activated compound (blue spectrum) exhibits no bands that can be assigned to DMF or water molecules. This proves the full removal of the guest molecules from the pores.

In the IR spectrum of the as-synthesized compound **3**, the bands at 1599 and 1496 cm^{-1} indicate the presence of coordinating carboxylate groups (Fig. S2, top). In addition, the as-synthesized compound **3** reveals a band at 1662 cm^{-1}, which can be attributed to the stretching vibration of the carbonyl groups of DMF molecules in the pores. Due to the presence of the NH_2 group and water molecules, broad bands are observed between 3671 and 3064 cm^{-1}. The weak signals at 1280 cm^{-1} and 1192 cm^{-1} can be attributed to the C-N stretching vibration. In the spectrum of the activated compound (blue), the characteristic bands of DMF disappear after removal of guest molecules by activation at 180 °C in vacuo.

The IR spectrum of the as-synthesized sample **4** shows the two characteristic bands at 1607 and 1478 cm^{-1} for the asymmetric and symmetric C-O stretching vibrations of the coordinating carboxylate groups (Fig. S2, bottom). The C=O stretching vibration of DMF is observed at 1667 cm^{-1}. The preservation of the sulfone groups is demonstrated by the bands at 1300 and 1137 cm^{-1}, which are due to the asymmetric and symmetric stretching vibrations. The band at 586 cm^{-1} can be assigned to the scissor vibration of the SO_2-group. The bands of the sulfone groups are still present in the spectrum of the activated compound and the band of the DMF is absent indicating a total removal of all DMF molecules during the activation process.

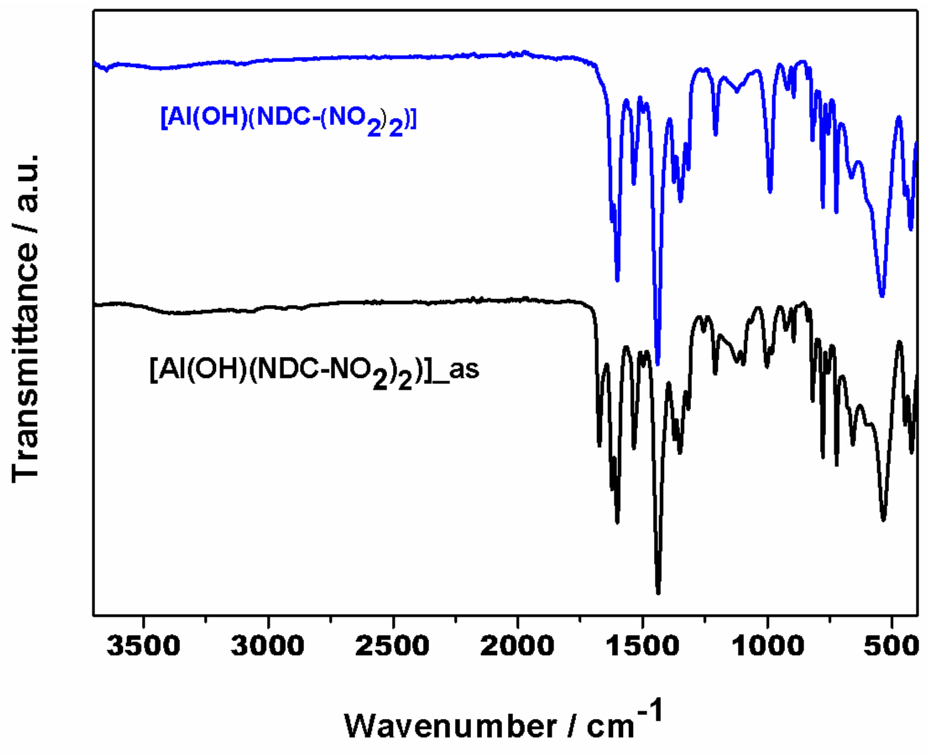

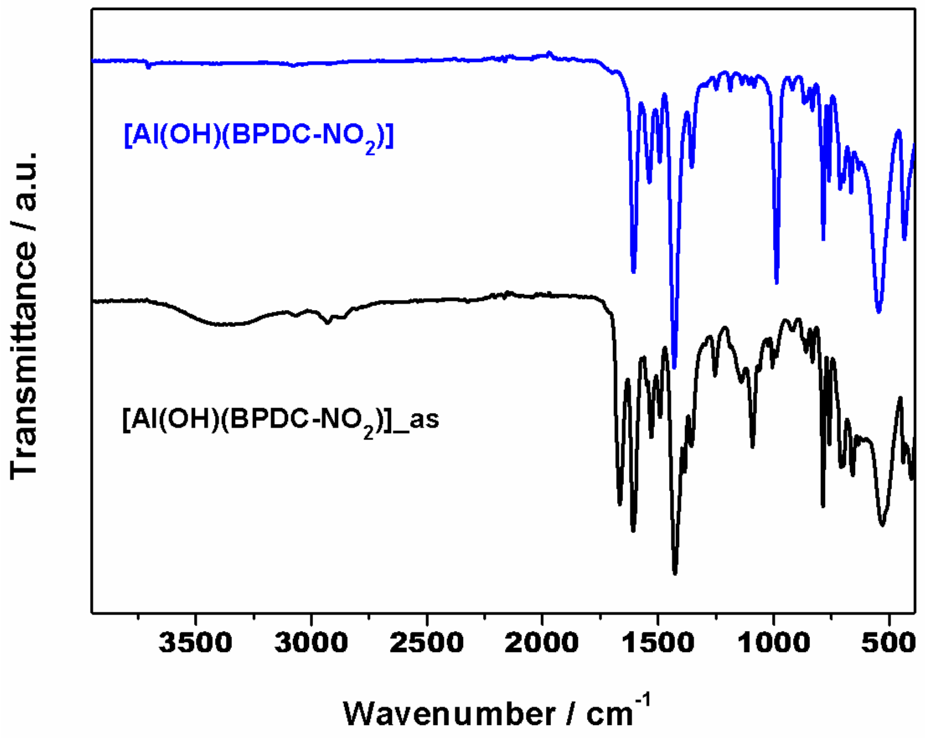

Fig. S1. Top: IR spectra of [Al(OH)(NDC-$(NO_2)_2$)]·DMF (**1**) (black) and activated [Al(OH)(NDC-$(NO_2)_2$)] (blue). Bottom: IR spectra of [Al(OH)(BPDC-NO_2)]·1.7DMF·0.8H_2O (**2**) (black) and activated [Al(OH)(BPDC-NO_2)] (blue).

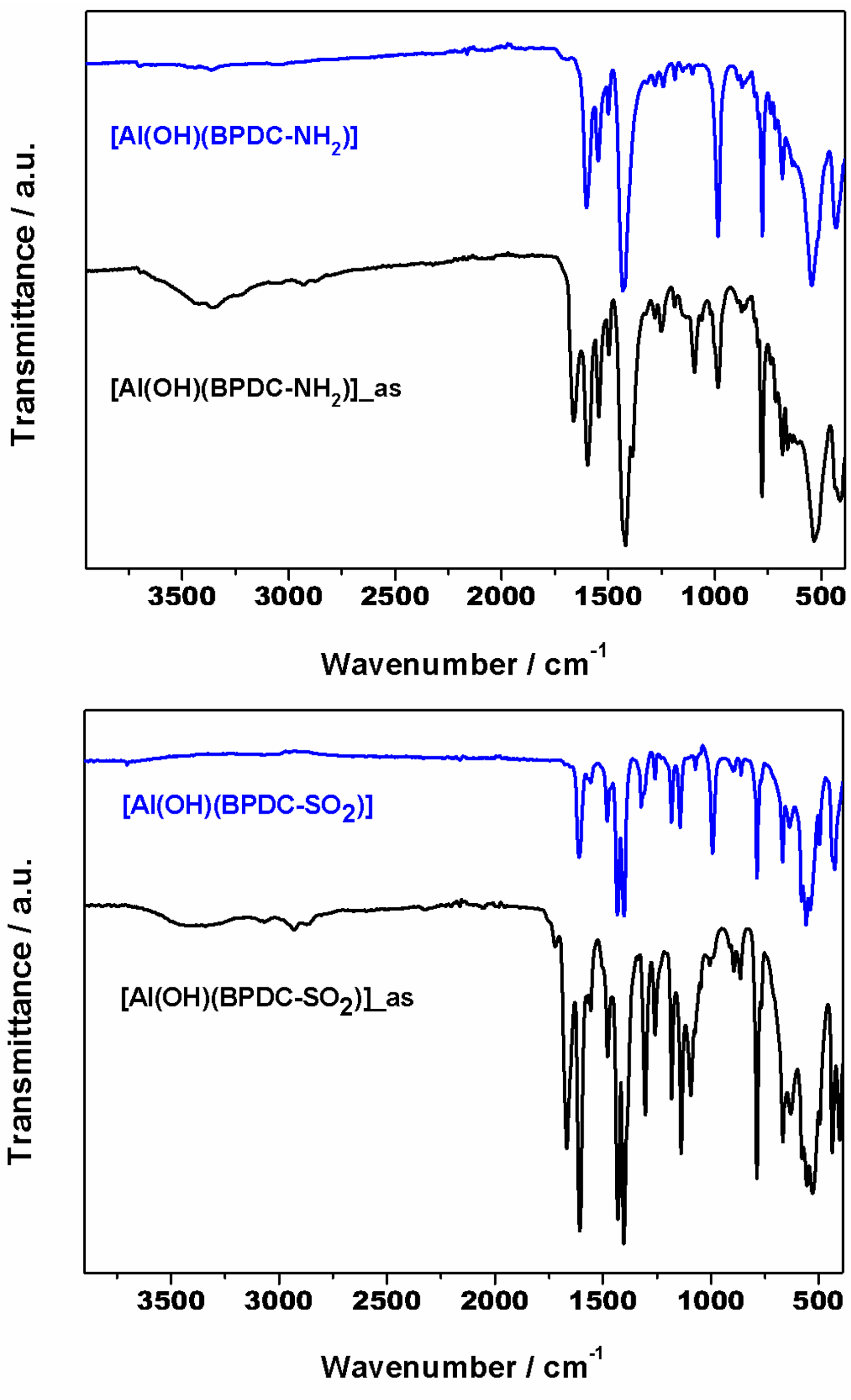

Fig. S2. Top: IR spectra of [Al(OH)(BPDC-NH_2)]·1.7DMF·H_2O (**3**) (red) and activated [Al(OH)(BPDC-NH_2)] (blue); Bottom: IR spectra of [Al(OH)(BPDC-SO_2)]·2.5DMF (**4**) (black) and activated [Al(OH)(BPDC-SO_2)] (blue).

3. Powder X-Ray diffraction patterns of compounds 1, 2, 3 and 4 after N_2-sorption measurements

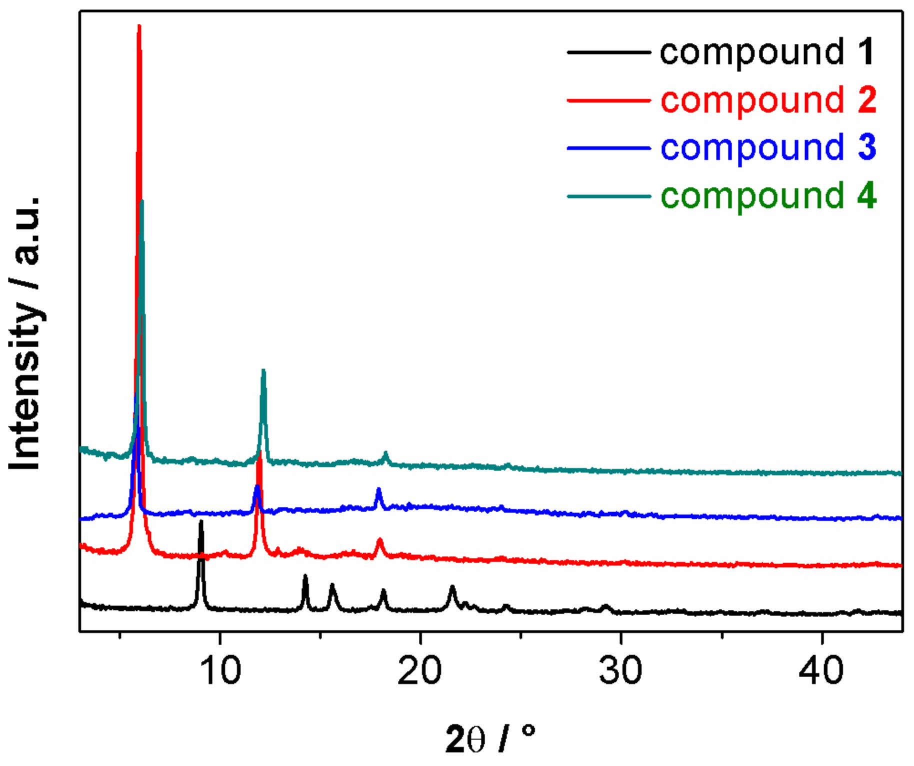

Fig. S3. PXRD patterns of [Al(OH)(NDC-$(NO_2)_2$)] (**1**) (black), [Al(OH)(BPDC-NO_2)] (**2**) (red), [Al(OH)(BPDC-NH_2)] (**3**) (blue) and [Al(OH)(BPDC-SO_2)] (**4**) (green) after N_2-sorption measurements.

4. CO_2-, H_2- and CH_4-sorption measurements of 1, 2, 3 and 4

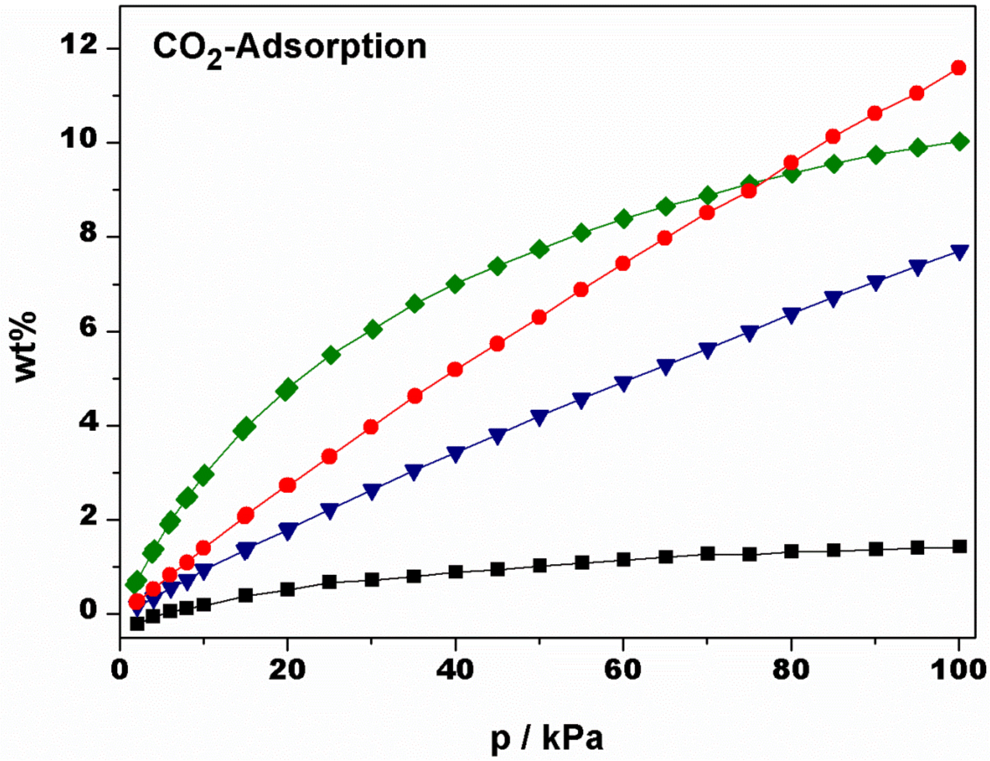

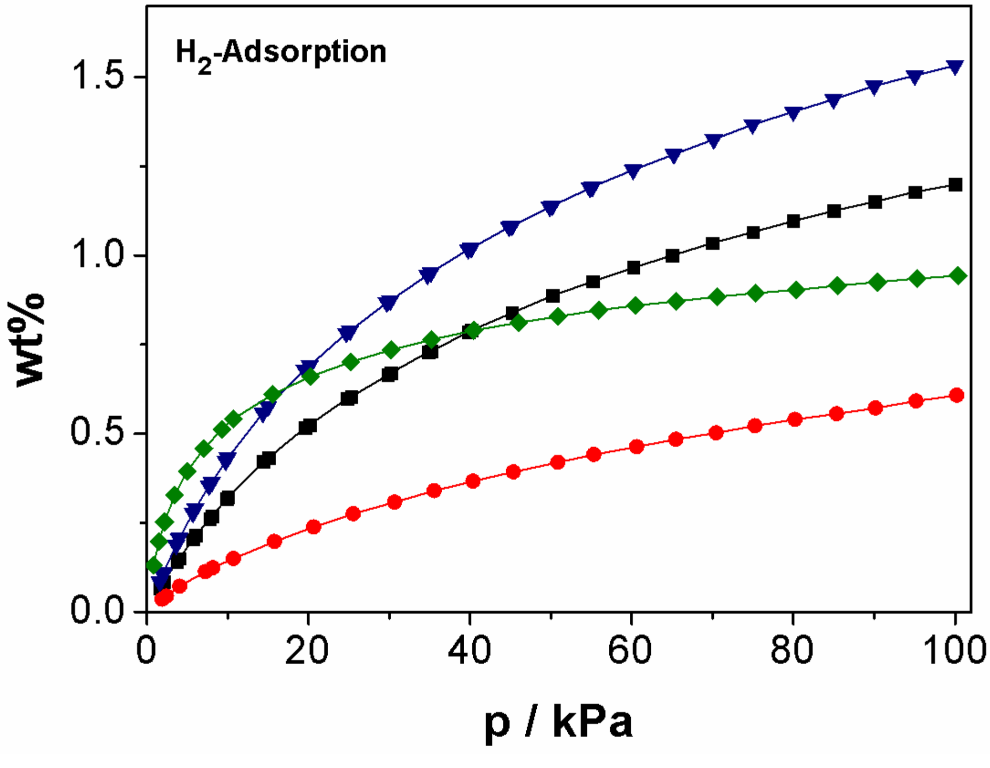

Fig. S4. Sorption isotherms of [Al(OH)(NDC-$(NO_2)_2$)] (**1**) (olive, diamonds), [Al(OH)(BPDC-NO_2)] (**2**) (blue, triangles), [Al(OH)(BPDC-NH_2)] (**3**) (black, squares) and [Al(OH)(BPDC-SO_2)] (**4**) (red, circles) towards CO_2 (top) and H_2 (bottom); compounds **2** (blue) and **3** (black) were activated at 180 °C for 16 h and **1** (olive) and **4** (red) at 250 °C for 16 h. The CO_2- and H_2-adsorption measurements were performed at 298 K and 77 K, respectively.

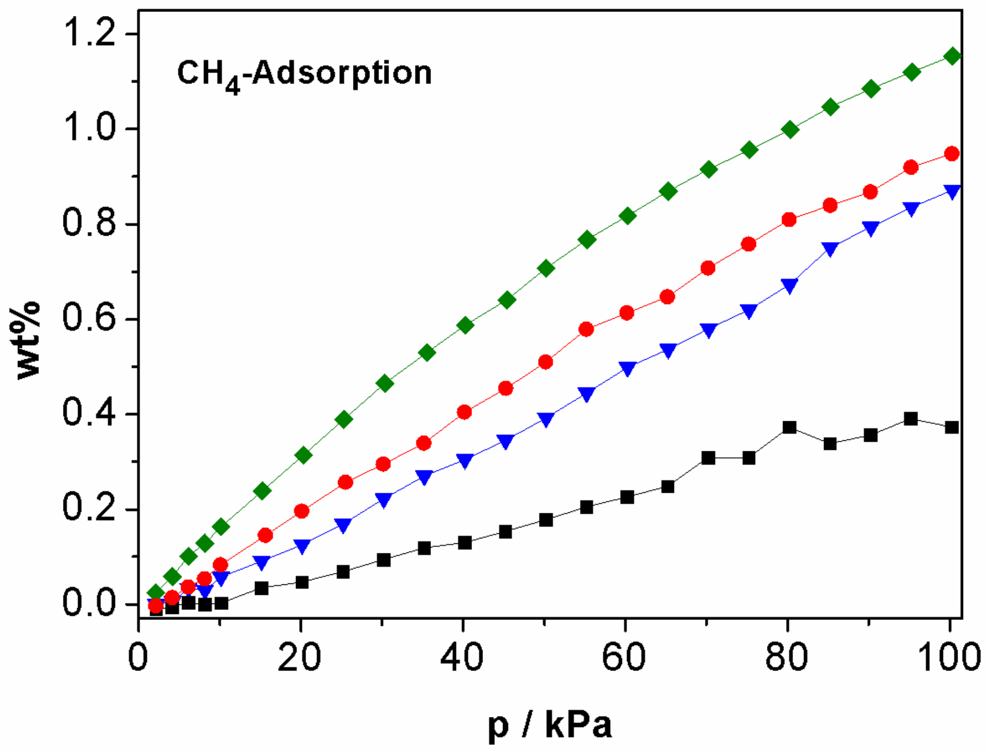

Fig. S5. CH_4-Sorption isotherms of [Al(OH)(NDC-$(NO_2)_2$)] (**1**) (olive, diamonds), [Al(OH)(BPDC-NO_2)] (**2**) (blue, triangles), [Al(OH)(BPDC-NH_2)] (**3**) (black, squares) and [Al(OH)(BPDC-SO_2)] (**4**) (red, circles); compounds **2** (blue), **3** (black) were activated at 180 °C for 16 h and **1** (olive), **4** (red) at 250 °C for 16 h. The CH_4-adsorption measurements were performed at 298 K.

5. CO_2-adsorption isotherms (at 298 K, 303 K, 308 K) of compounds 1 and 4

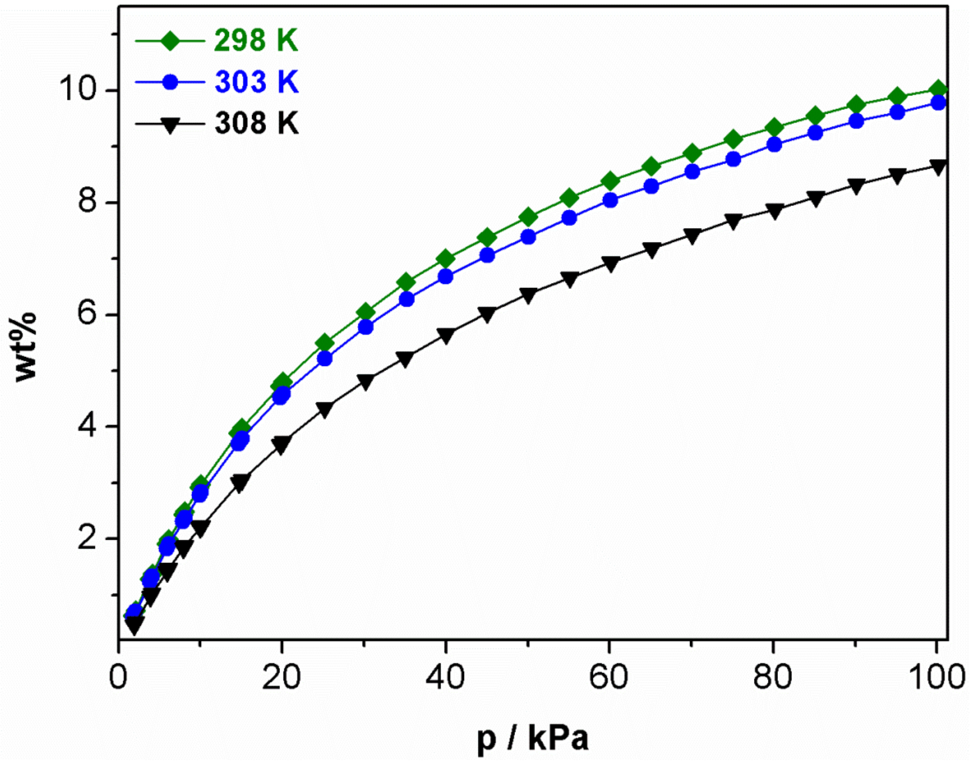

Fig. S6. CO_2-adsorption isotherms of [Al(OH)(NDC-(NO_2)$_2$)] (**1**) performed at 298 K (olive, diamonds), 303 K (blue, circles) and 308 K (black, triangles), respectively. The compound was activated at 250 °C for 16h.

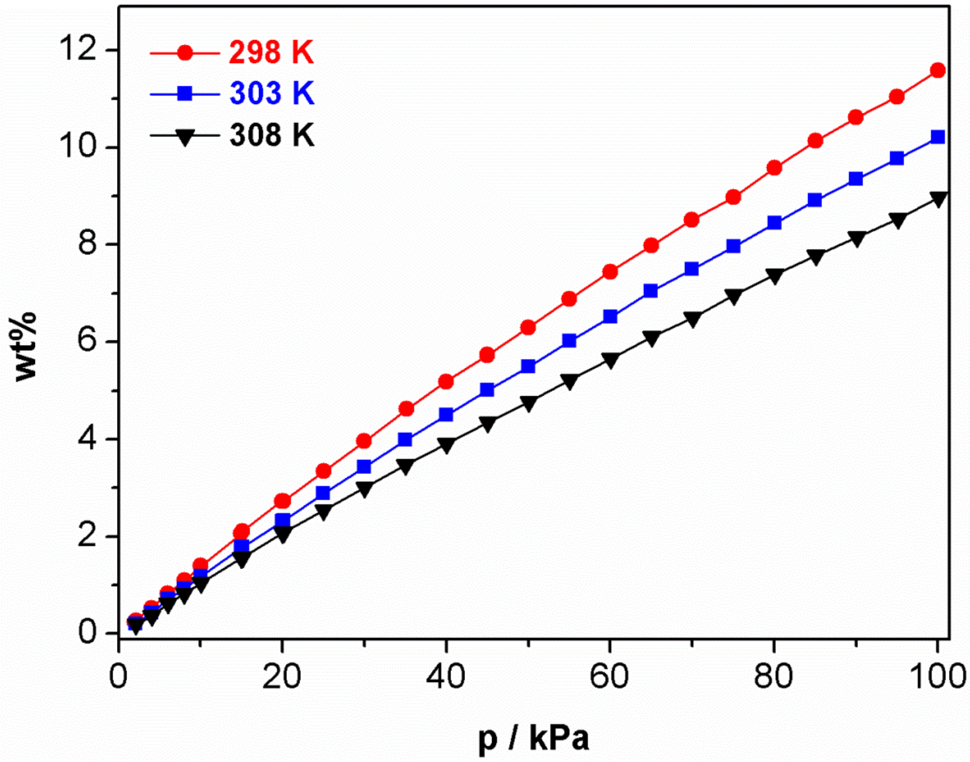

Fig. S7. CO_2-adsorption isotherms of [Al(OH)(BPDC-SO_2)] (**4**) measured at 298 K (red, circles), 303 K (blue, squares) and 308 K (black, triangles), respectively. The compound was activated at 250 °C for 16h.

6. Structural model of compounds 2, 3 and 4

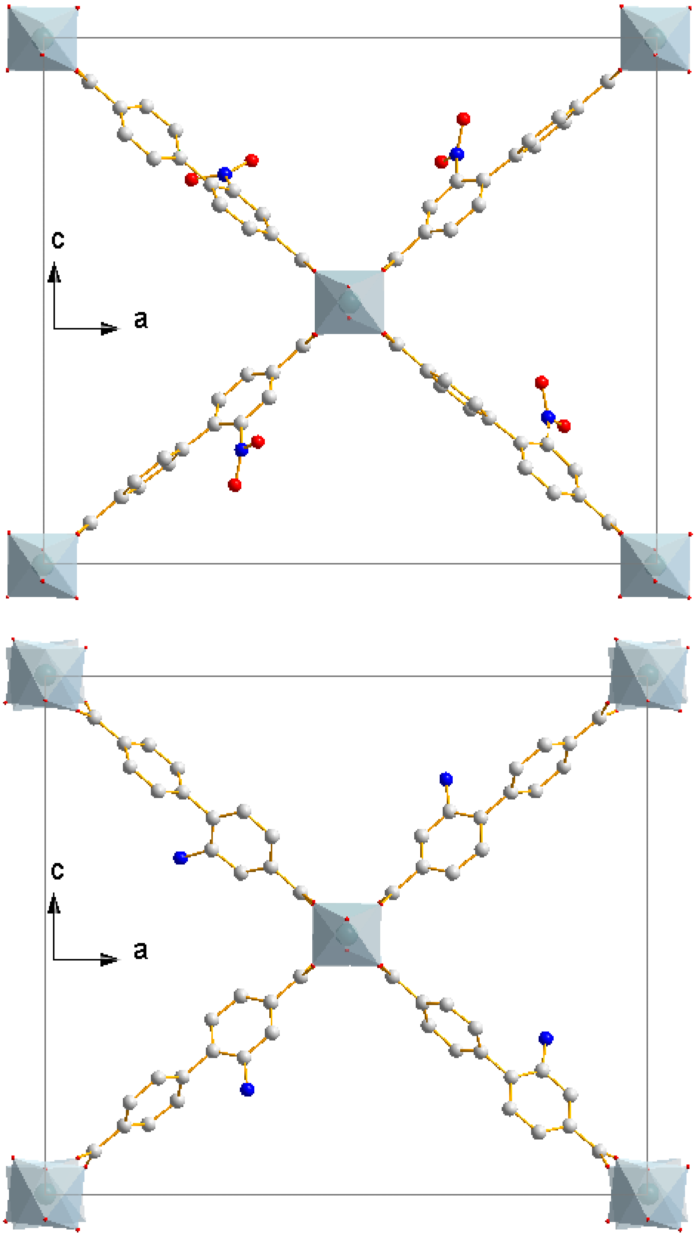

Fig. S8. Structural model of [Al(OH)(BPDC-NO_2)] (**2**) (top) and [Al(OH)(BPDC-NH_2)] (**3**) (bottom).

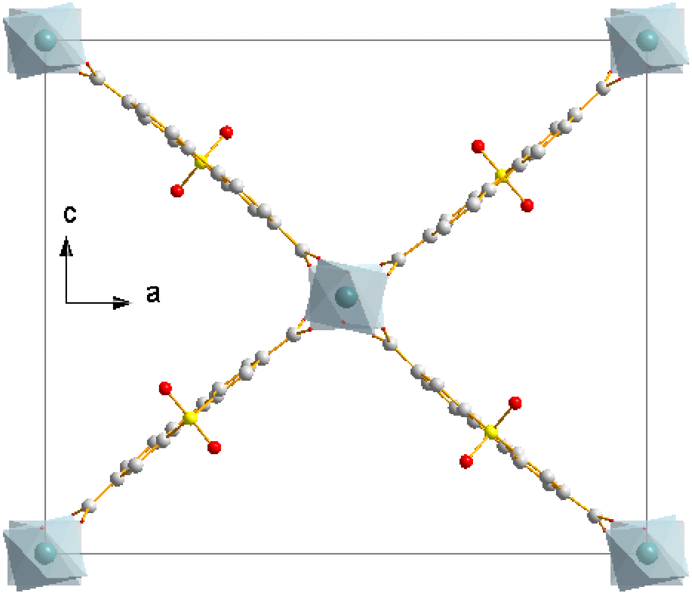

Fig. S9. Structural model of [Al(OH)(BPDC-SO$_2$)] (**4**).

7. PXRD pattern of the activated compound 4

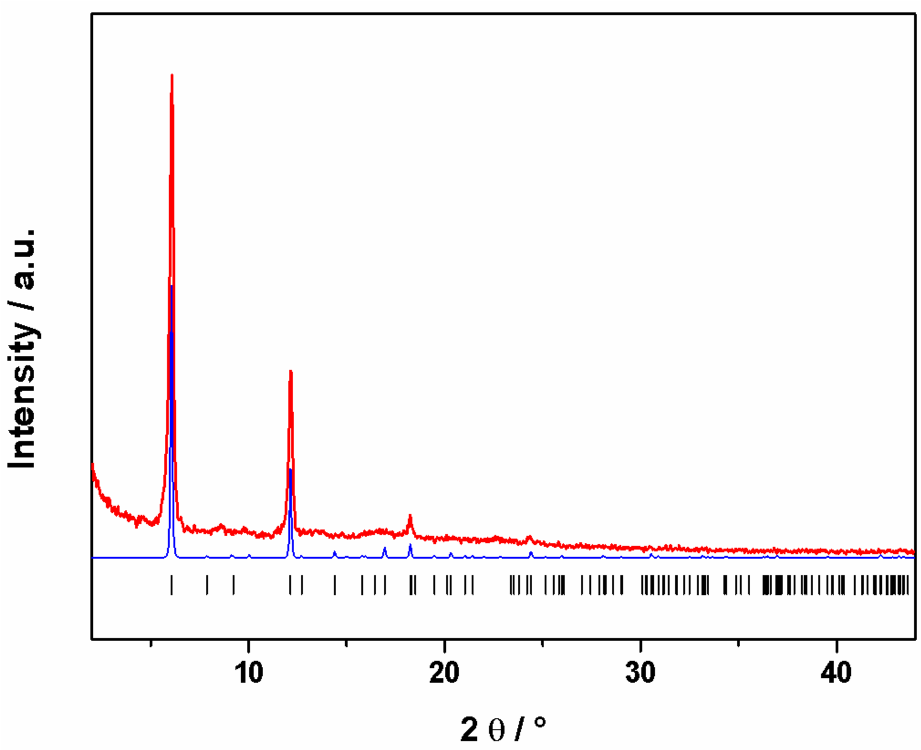

Fig. S10. PXRD pattern of the activated compound **4** ([Al(OH)(BPDC-SO_2)]) (red); calculated PXRD pattern of **4** (blue); with the tics marking the allowed Bragg positions (black).

8. Pawley-Fit of [Al(OH)(NDC-NO$_2$)$_2$)] after activation and the lattice parameters

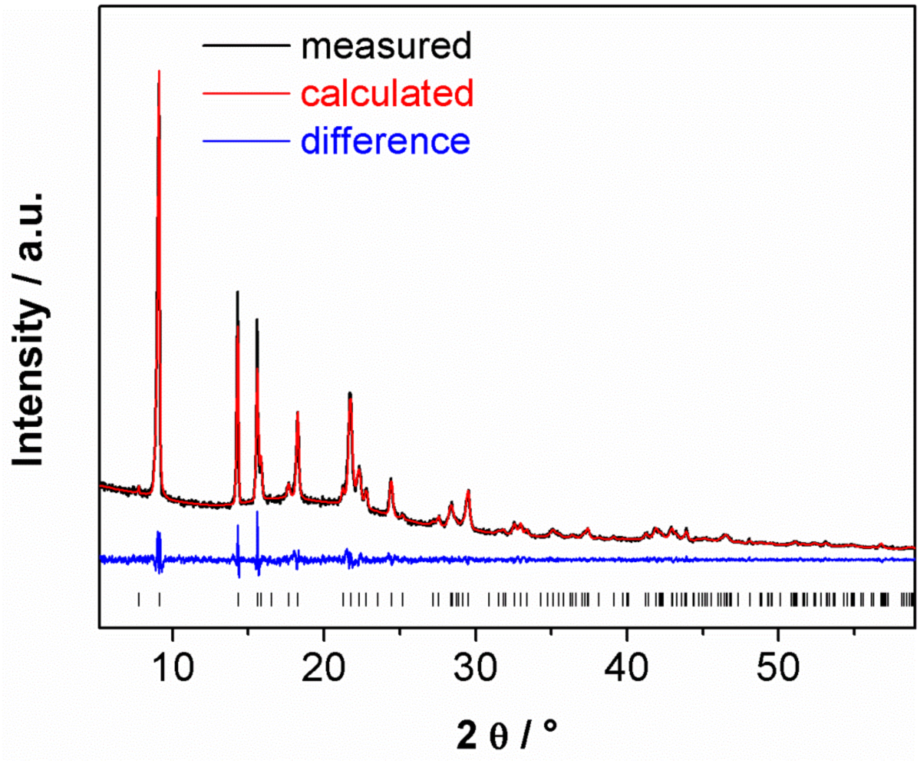

Fig. S11 Pawley-Fit of [Al(OH)(NDC-(NO$_2$)$_2$)] (**1**) after activation.

Table S1
Lattice parameters of the activated [Al(OH)(NDC-(NO$_2$)$_2$)] and the as synthesized compound **1** as obtained from the Pawley fit.

	[Al(OH)(NDC-(NO$_2$)$_2$)]	**activ. [Al(OH)(NDC-(NO$_2$)$_2$)]**
a/Å	23.654(3)	22.678(1)
b/Å	11.176(2)	10.727(1)
c/Å	6.592(1)	6.5481(7)
β / °	107.64(2)	90
V / Å^3	1660.8(5)	1593.0(2)
r_{wp}	4.0	4.2

9. Structural model of the activated [Al(OH)(NDC-NO$_2$)$_2$)]

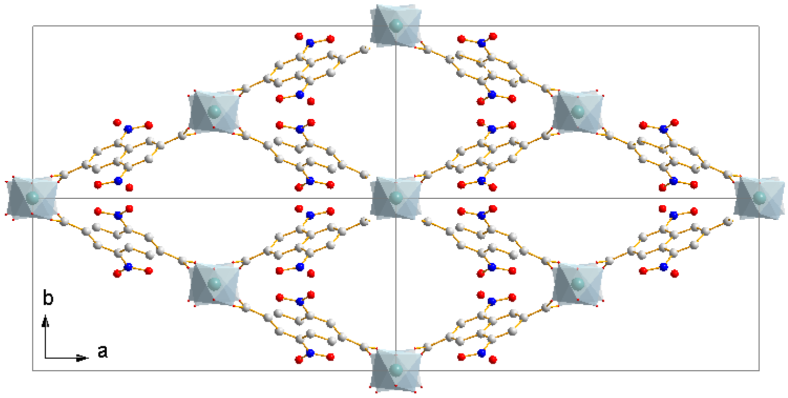

Fig. S12 Structural model of the activated compound **1**.

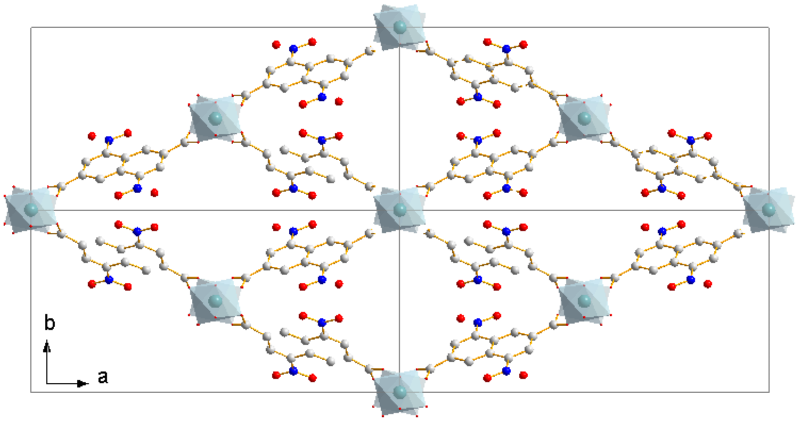

Fig. S13 Structural model of the as synthesized compound **1** for comparison.

Literature

---

[1] V. K. Olkhovik, A. A. Pap, V. A. Vasilevskii, N. A. Galinovskii, S. N. Tereshko, *Russ. J. Org. Chem.* **2008**, *44*, 1172–1179.

[2] B. Vercelli, G. Zotti, A. Berlin, M. Pasini, M. Natali, *J. Mater. Chem.* **2011**, *21*, 8645.

[3] R. K. Deshpande, J. L. Minnaar, S. G. Telfer, *Angew. Chem.* **2010**, *122*, 4702–4706; *Angew. Chem. Int. Ed.* **2010**, *49*, 4598–4602.

[4] G. Socrates, *Infrared and Raman Characteristic Group Frequencies: Tables and Charts*, 3rd ed.; Wiley & Sons: West Sussex, U.K., **2004**.

Table of content

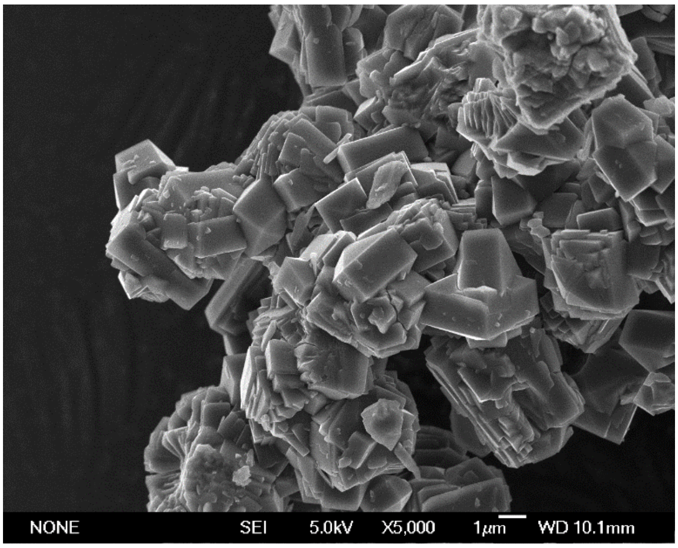

Figure S1. SEM image of CAU-H/S2.

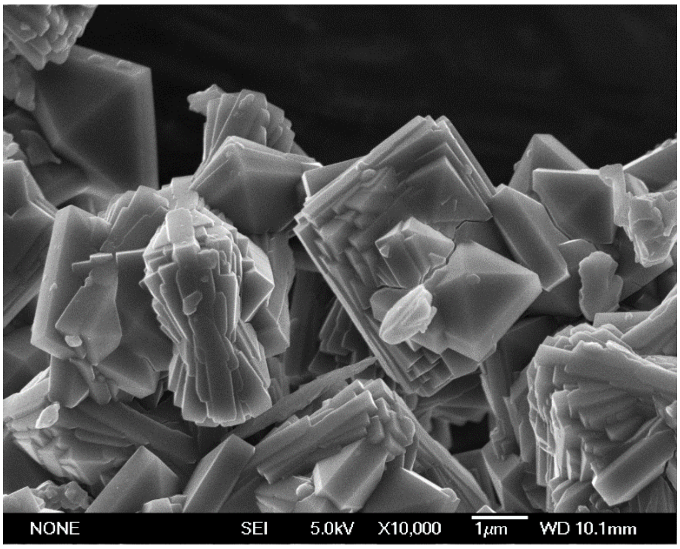

Figure S2. SEM image of CAU-H/S3.

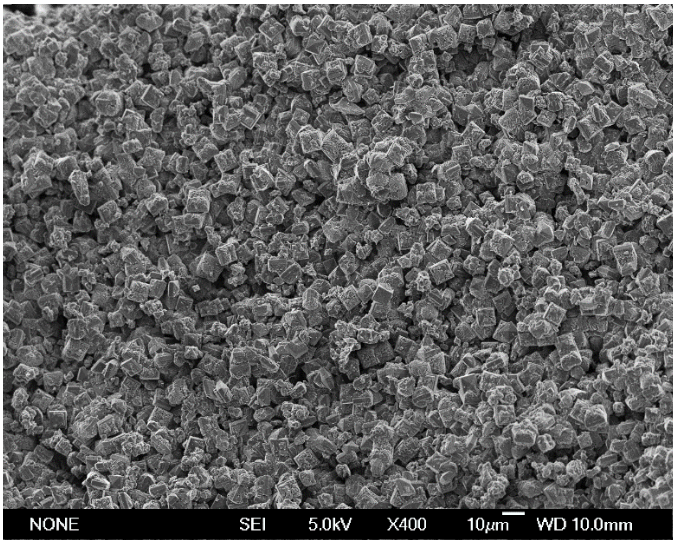

Figure S3. SEM image of CAU-H/S4.

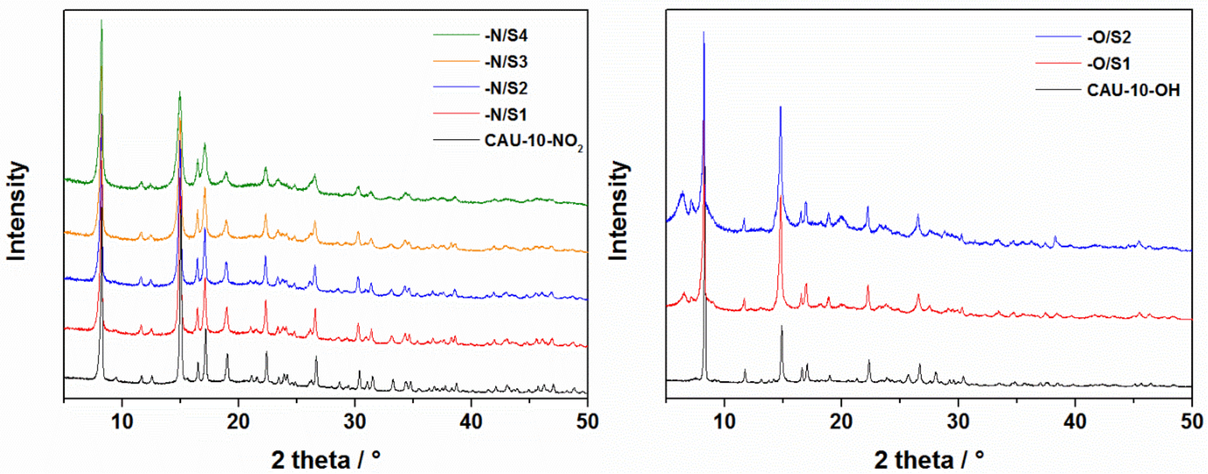

Figure S4. Powder patterns of CAU-10-N/Sx (left) and CAU-10-O/Sx (right) compared with the patterns of the parent compounds.

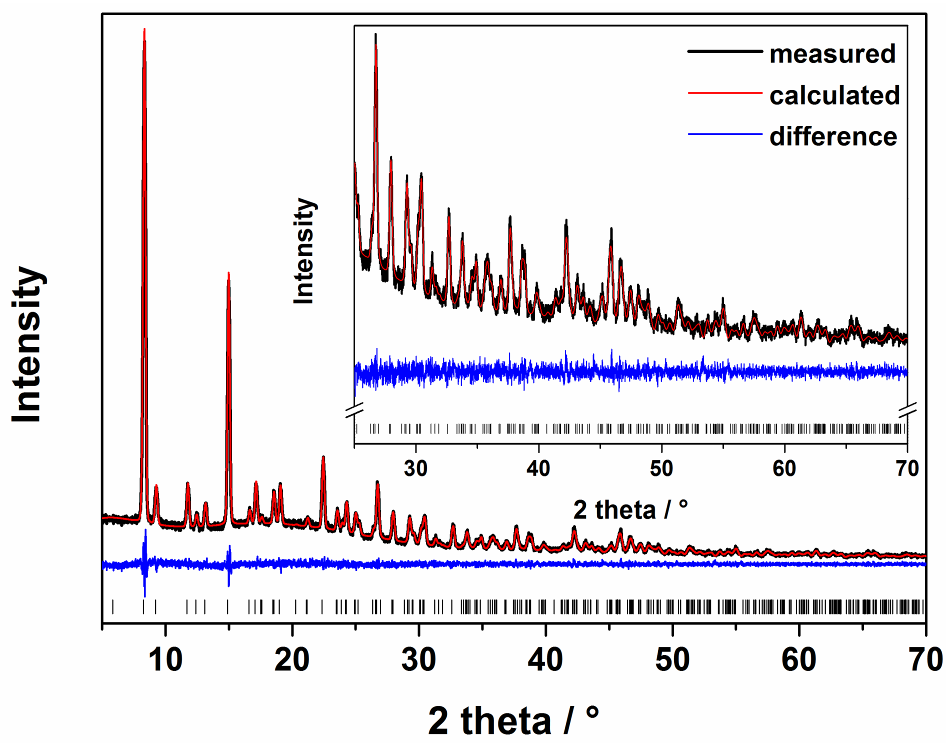

Figure S5. Pawley-Fit of CAU-10-H/S1.

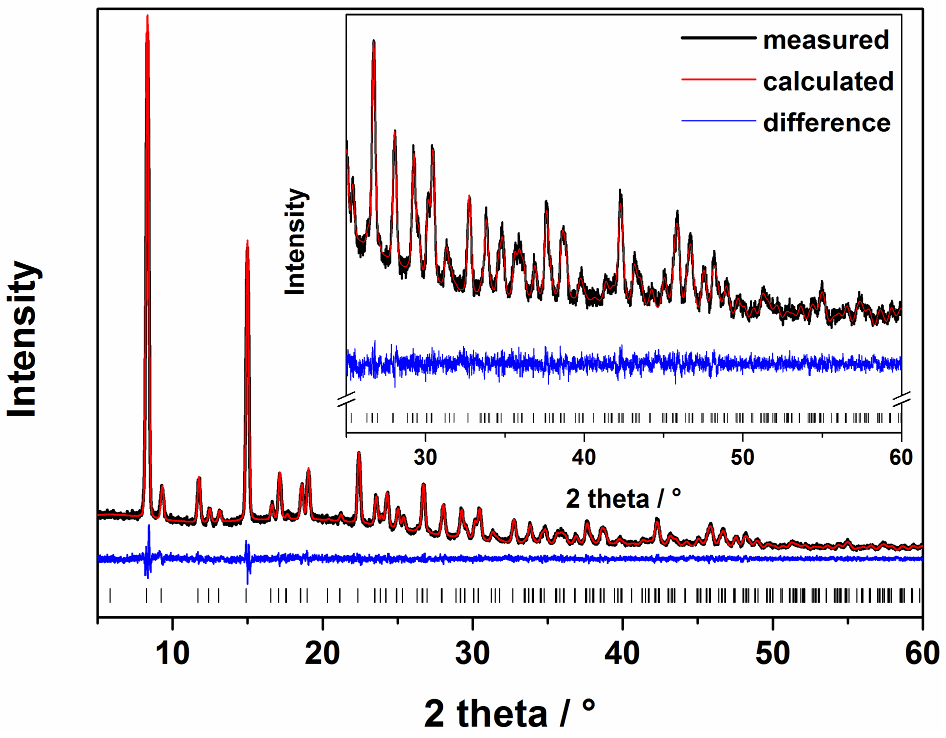

Figure S6. Pawley-Fit of CAU-10-H/S2.

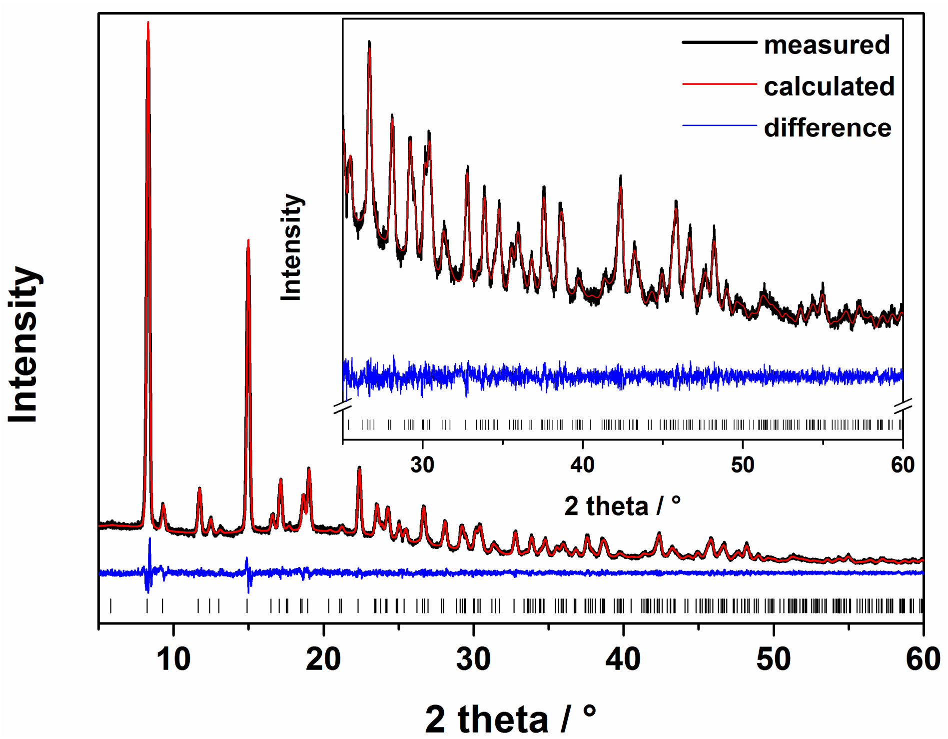

Figure S7. Pawley-Fit of CAU-10-H/S3.

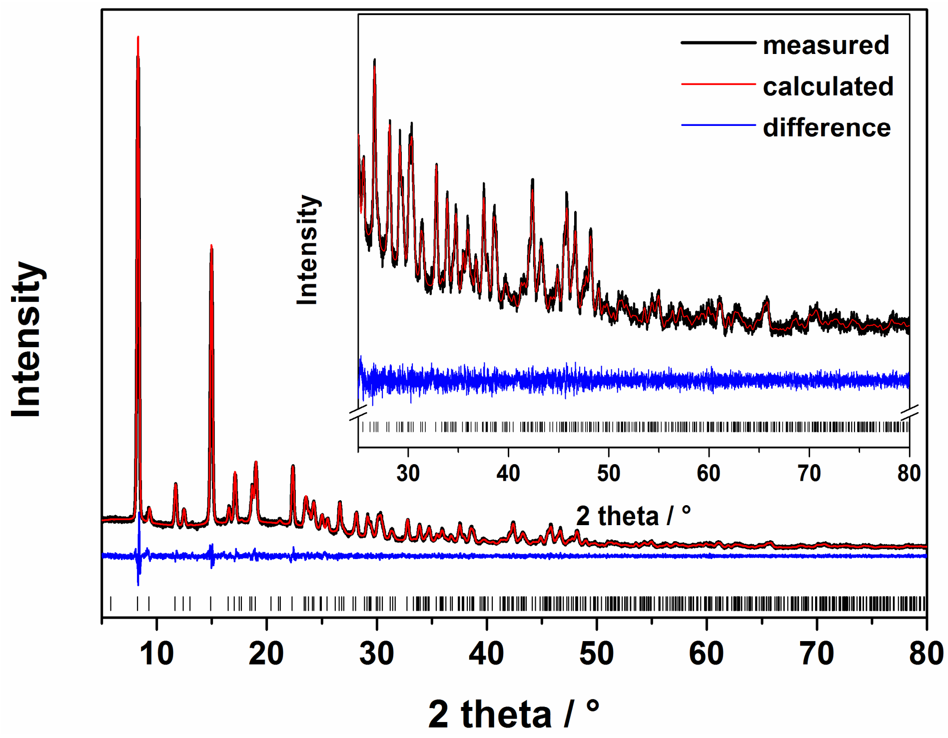

Figure S8. Pawley-Fit of CAU-10-H/S4.

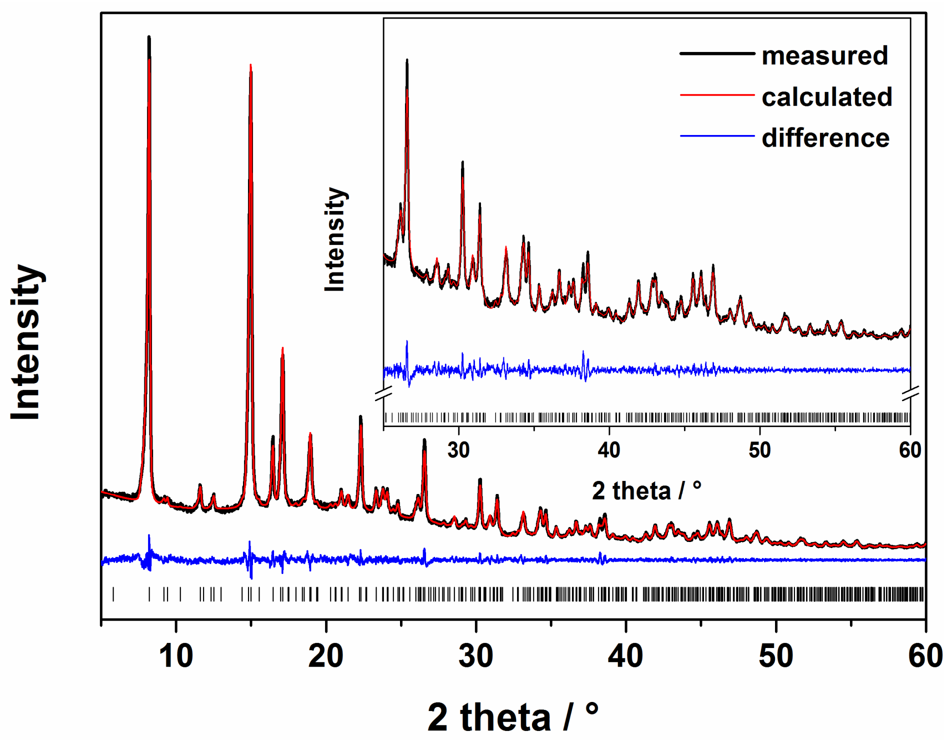

Figure S9. Pawley-Fit of CAU-10-N/S1.

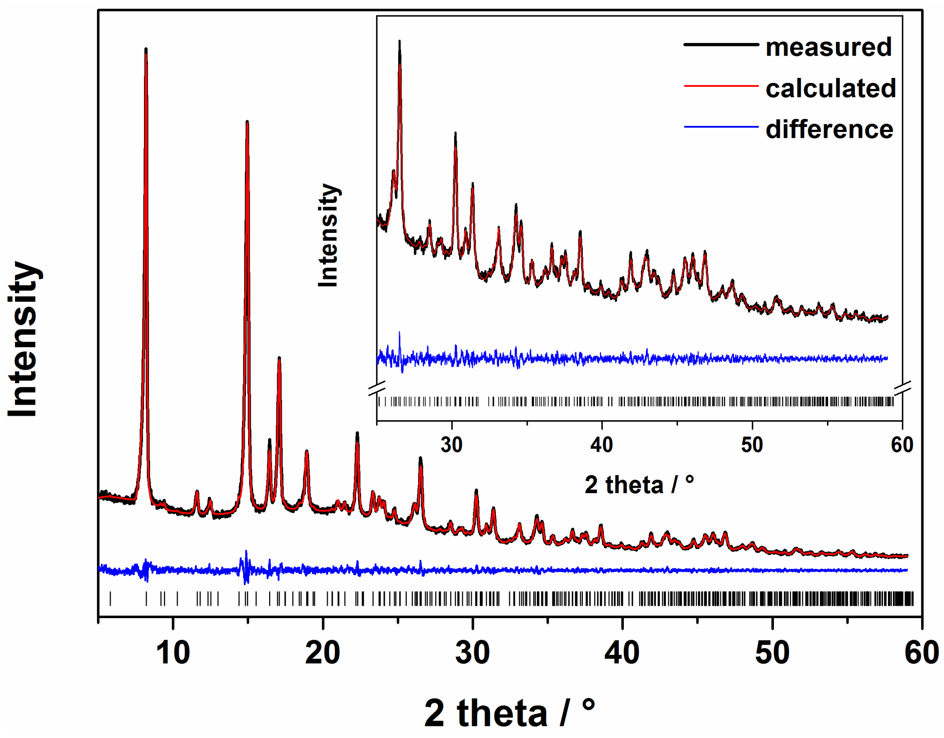

Figure S10. Pawley-Fit of CAU-10-N/S2.

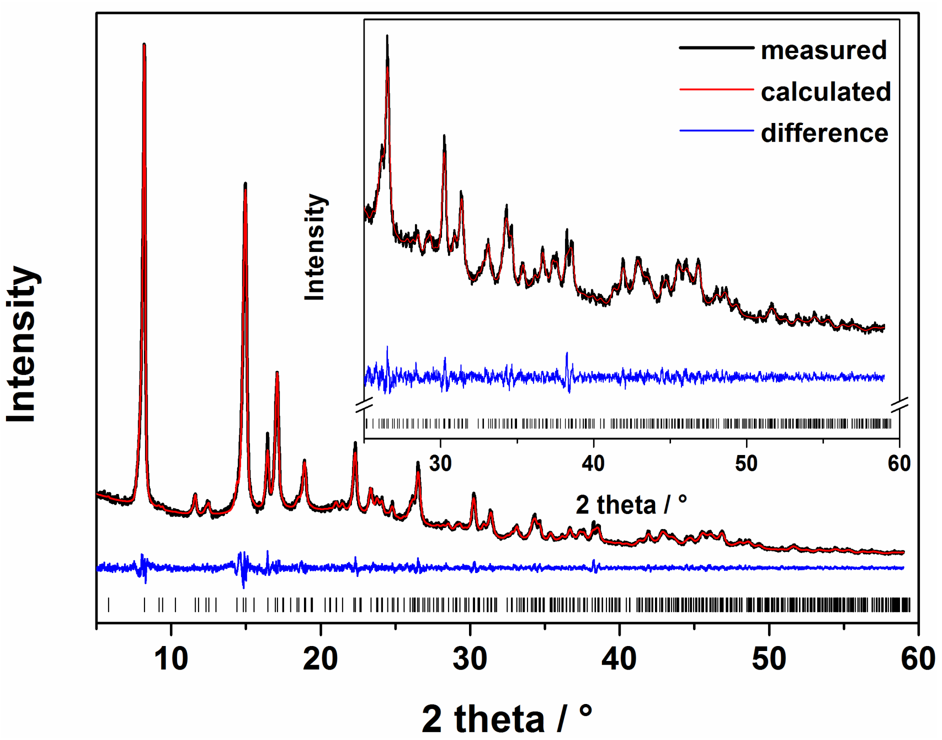

Figure S11. Pawley-Fit of CAU-10-N/S3.

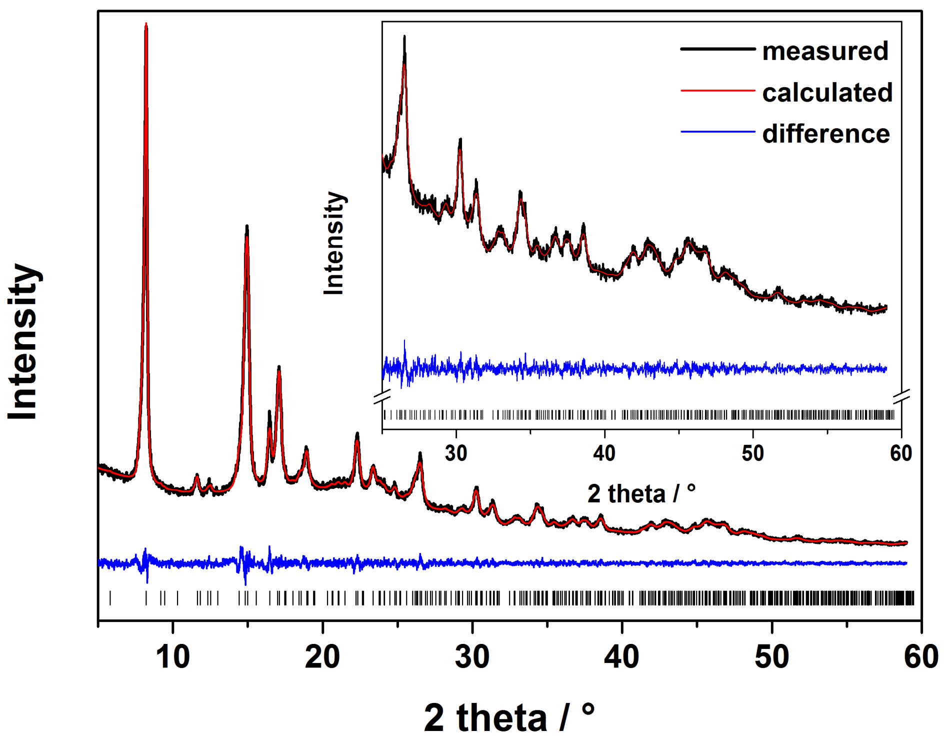

Figure S12. Pawley-Fit of CAU-10-N/S4.

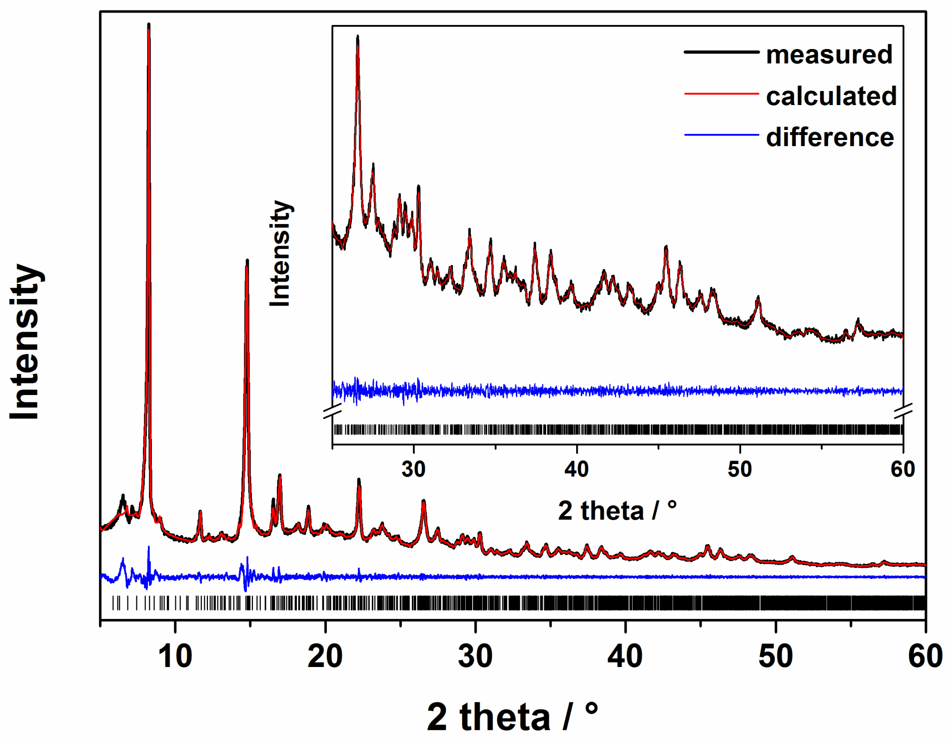

Figure S13. Pawley-Fit of CAU-10-O/S1.

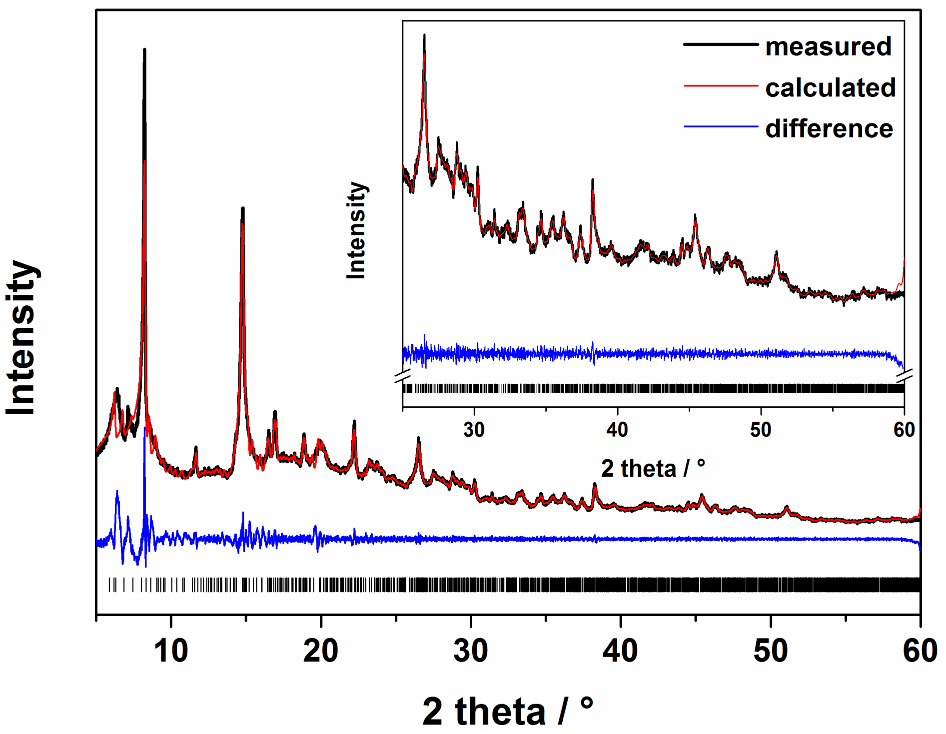

Figure S14. Pawley-Fit of CAU-10-O/S2.

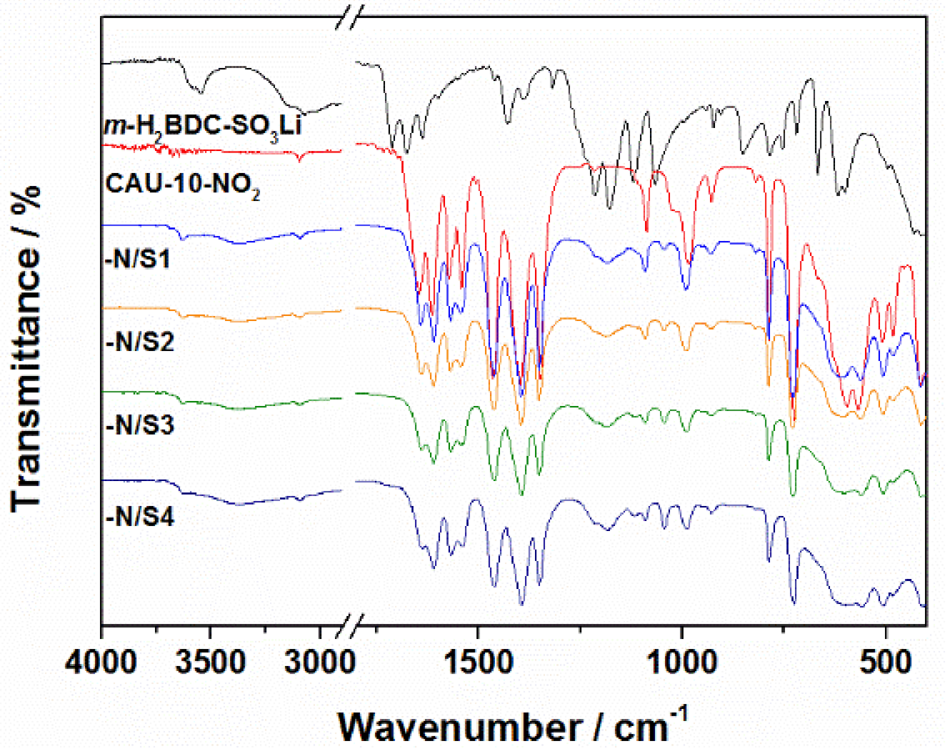

Figure S15. IR spectra of CAU-10-N/Sx compared to the linker and CAU-10-NO$_2$.

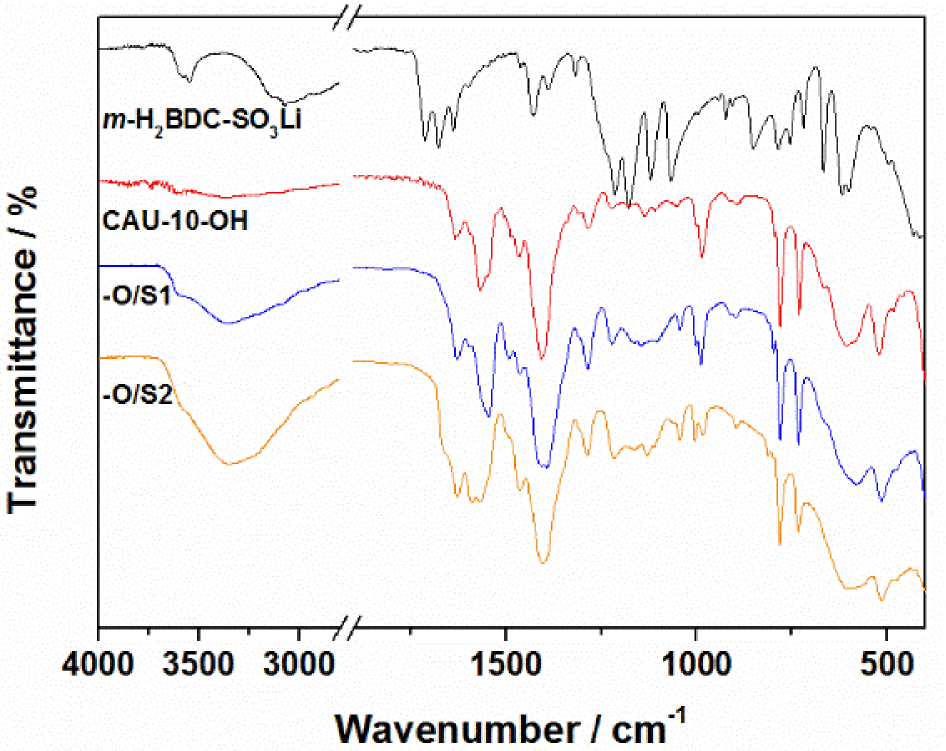

Figure S16. IR spectra of CAU-10-O/Sx compared to the linker and CAU-10-OH.

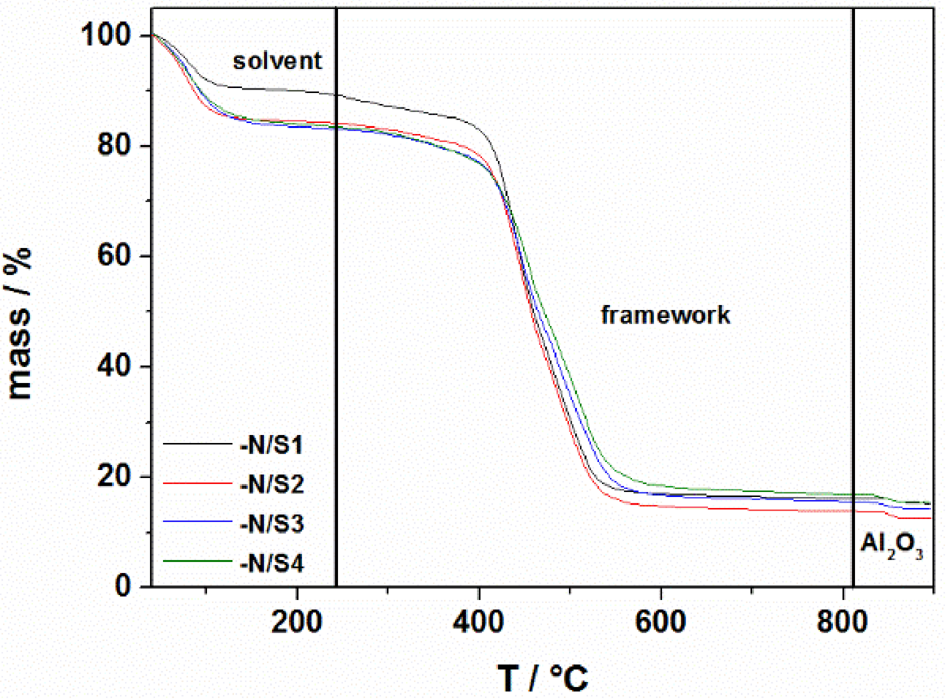

Figure S17. TG measurements of CAU-10-N/Sx.

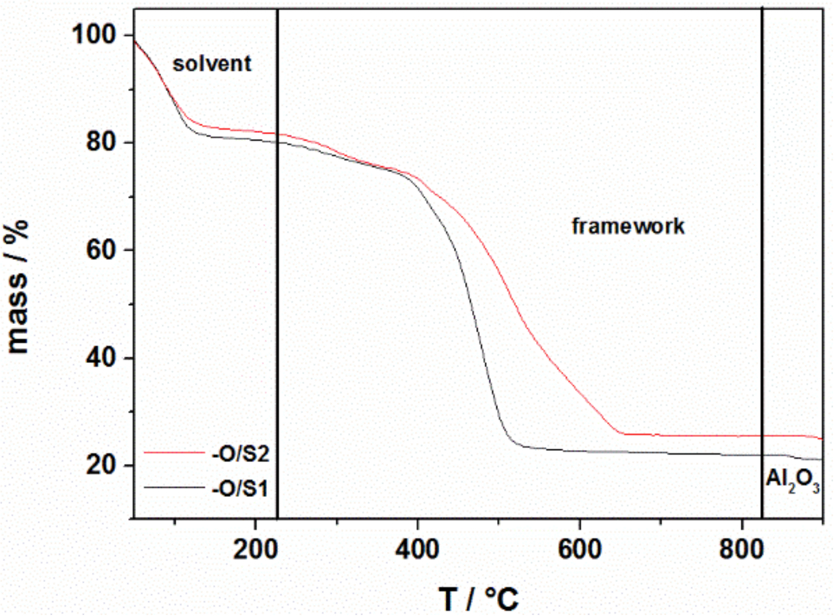

Figure S18: TG measurements of CAU-10-O/Sx.

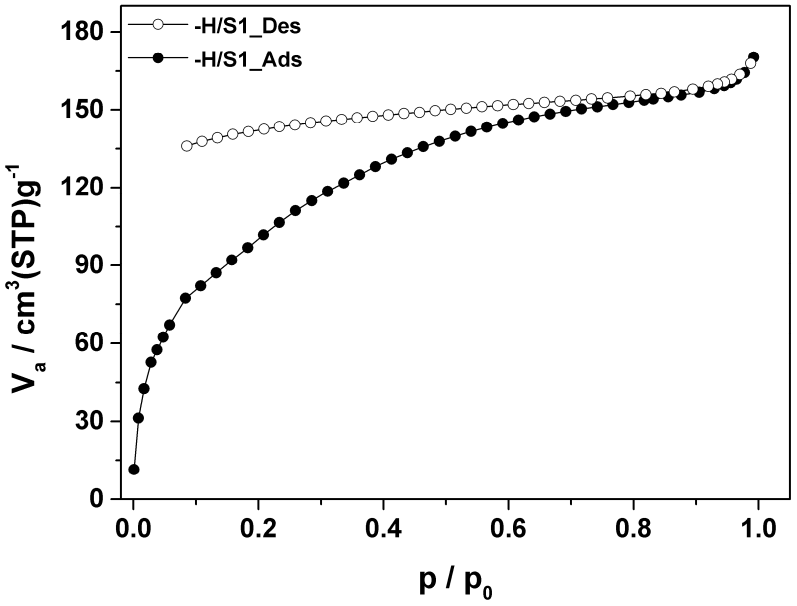

Figure S19. Nitrogen isotherm of CAU-10-H/S1 at 77 K.

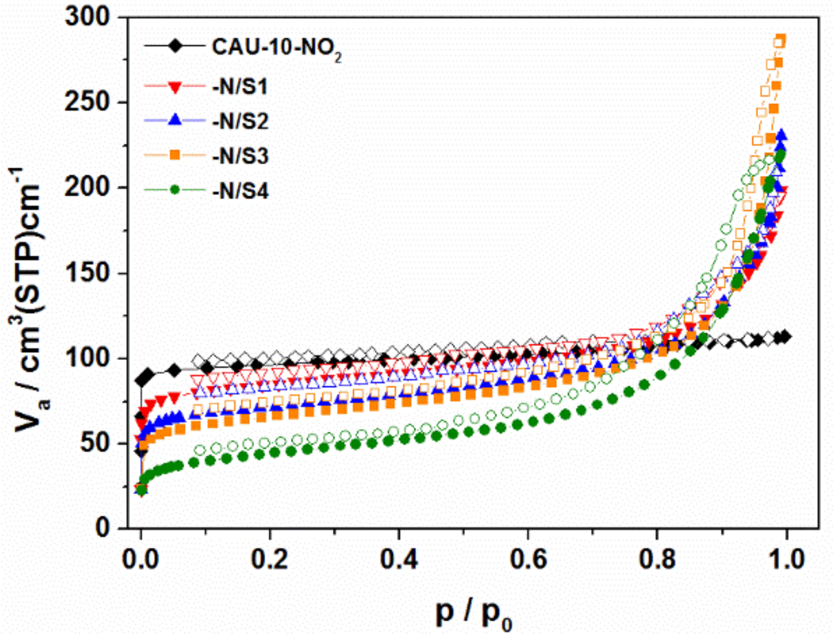

Figure S20. N_2 sorption isotherms of CAU-10-N/Sx compared to CAU10-NO_2 at 77 K.

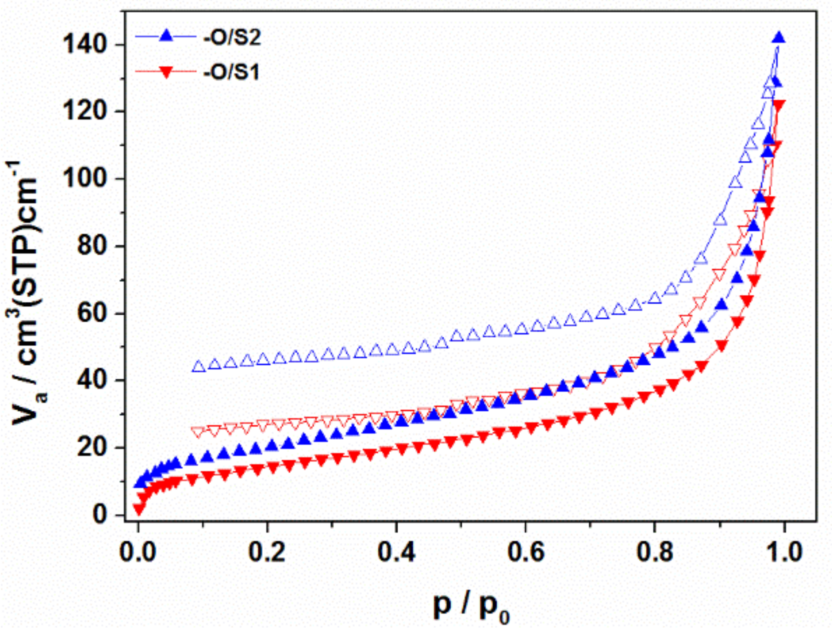

Figure S21. N_2 **sorption isotherms of CAU-10-O/Sx at 77 K.**

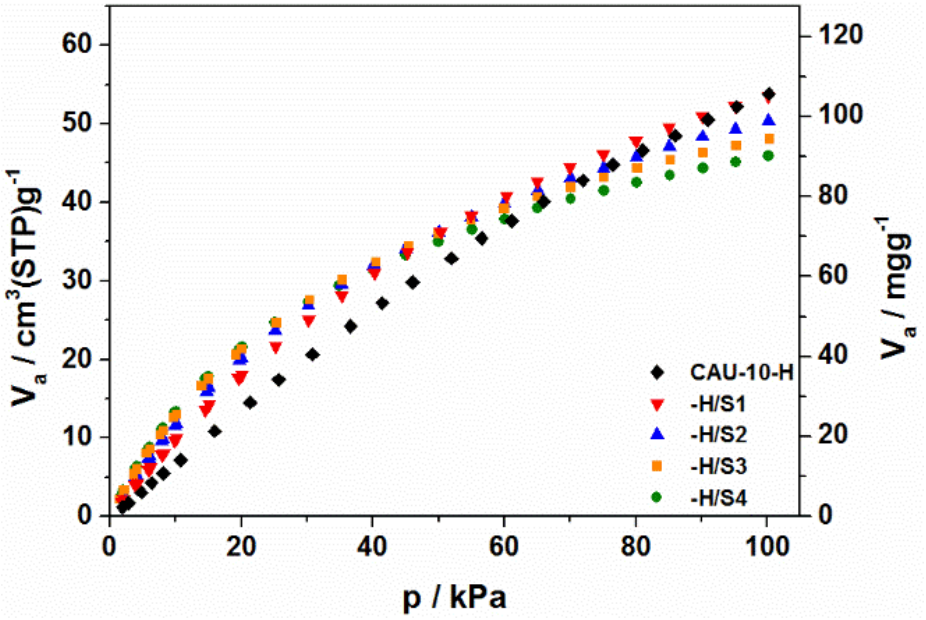

Figure S22. CO_2 **sorption measurements of CAU-10-H/Sx compared to CAU-10-H at 298 K.**

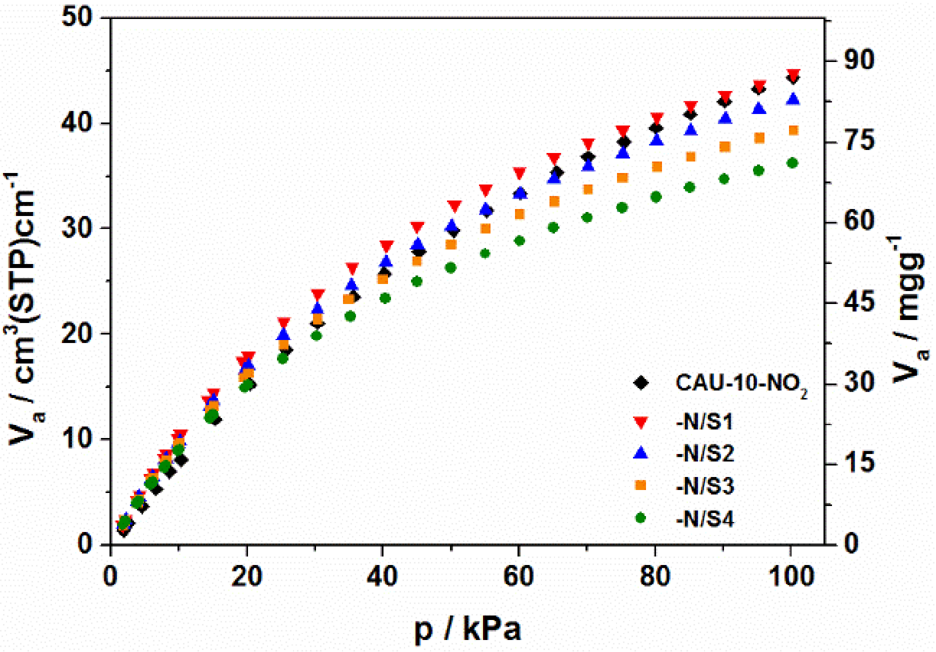

Figure S23. CO$_2$ sorption measurements of CAU-10-N/Sx compared to CAU-10-NO$_2$ at 298 K.

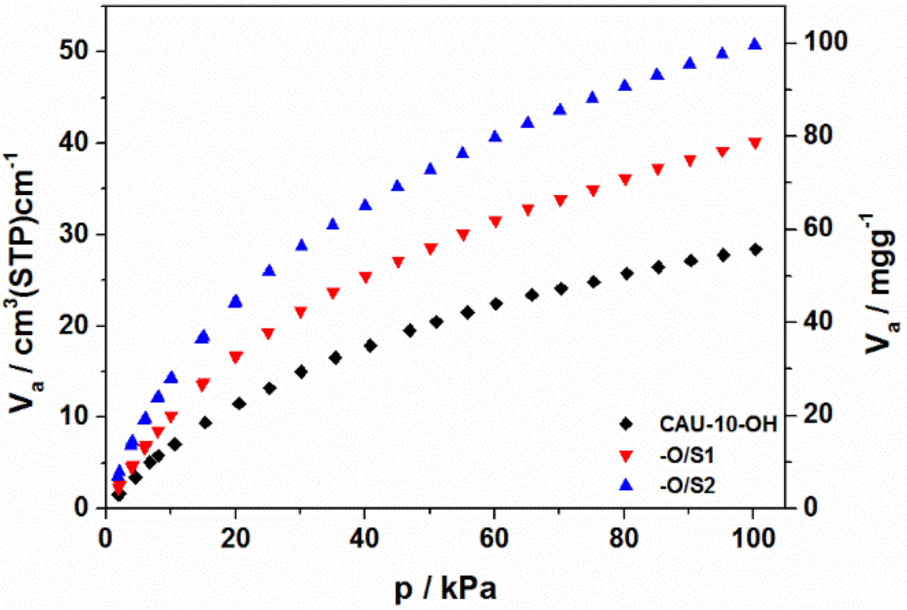

Figure S24. CO$_2$ sorption measurements of CAU-10-O/Sx compared to CAU-10-OH at 298 K.

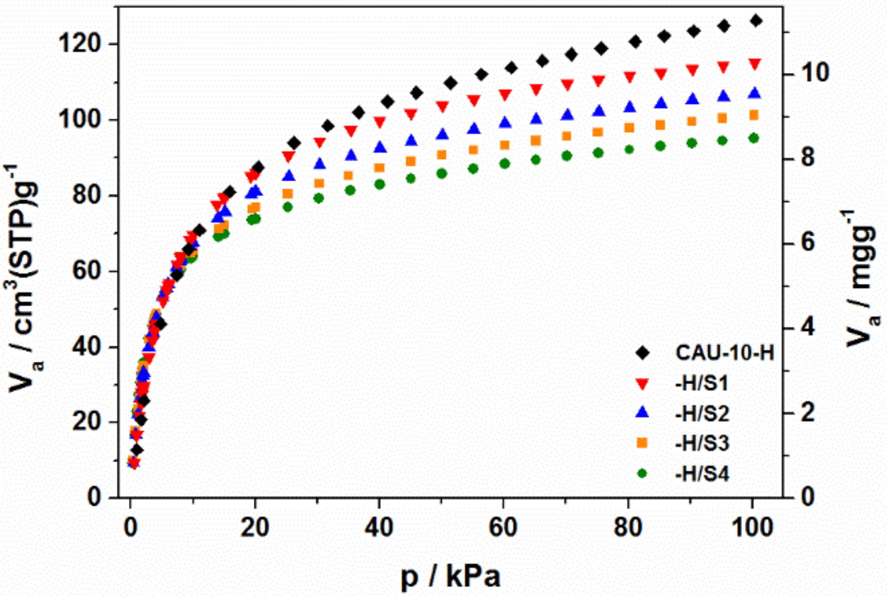

Figure S25. H_2 sorption measurements of CAU-10-H/Sx compared to CAU-10-H at 77 K up to 100 kPa.

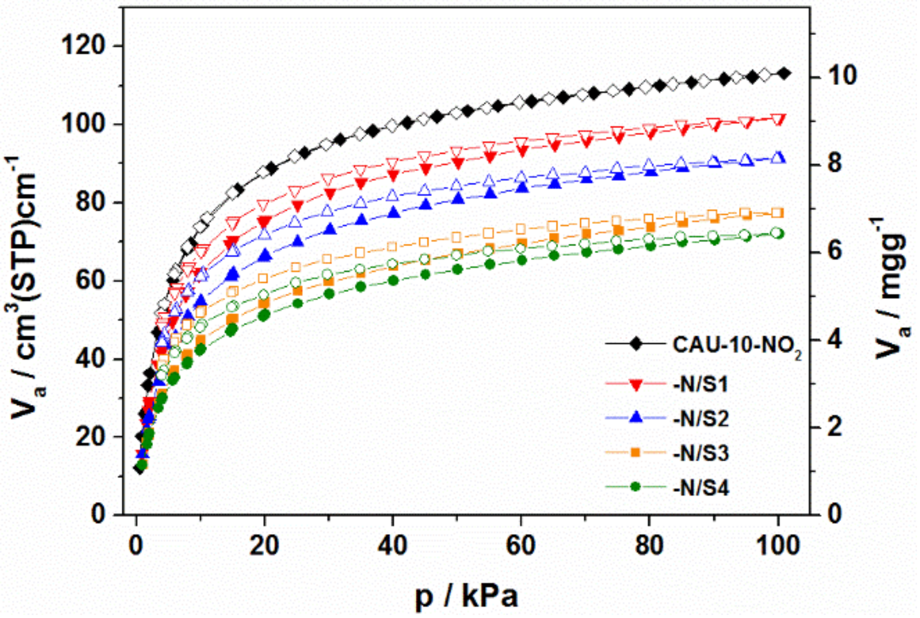

Figure S26. H_2 sorption measurements of CAU-10-N/Sx compared to CAU-10-NO_2 at 77 K up to 100 kPa.

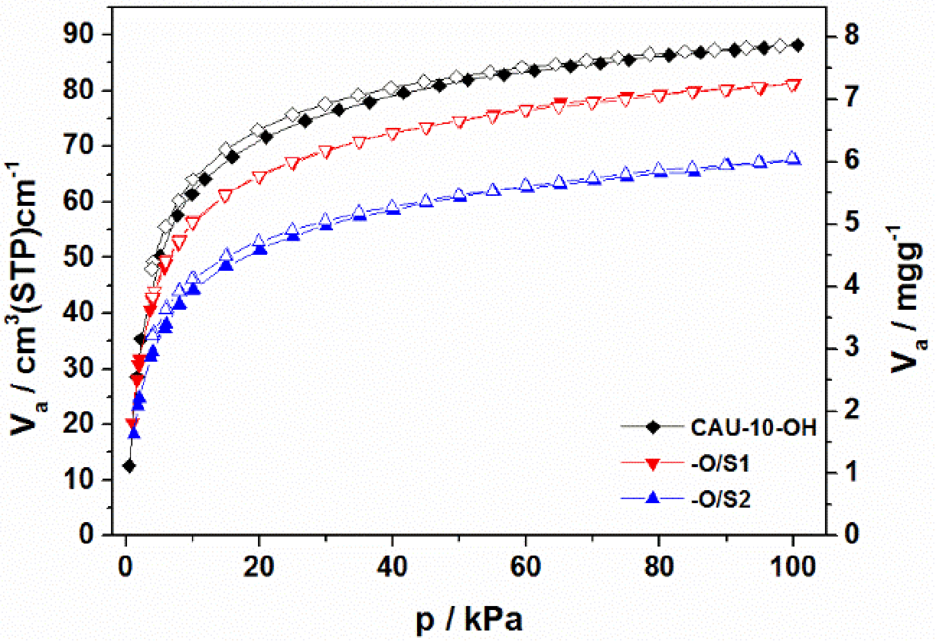

Figure S27. H_2 sorption measurements of CAU-10-O/Sx compared to CAU-10-OH at 77 K up to 100 kPa.

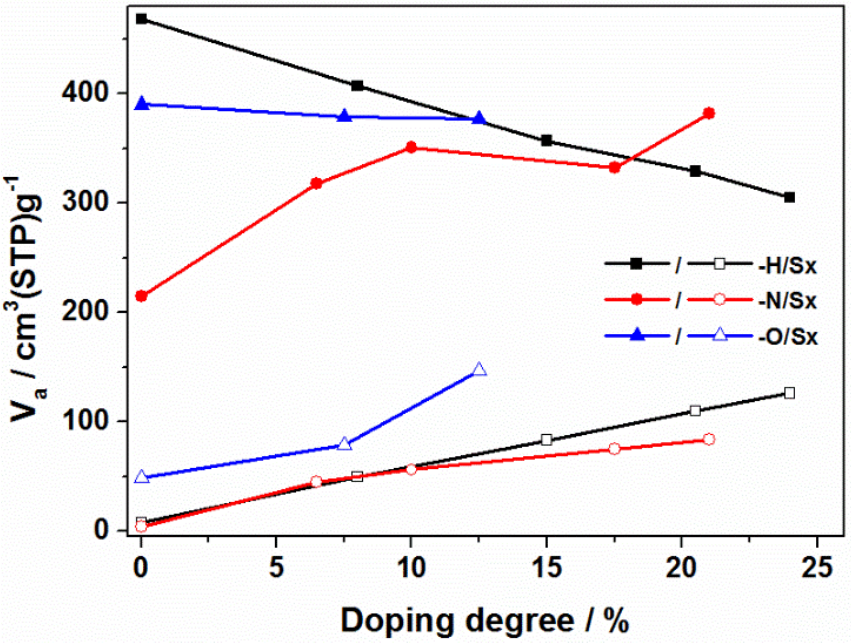

Figure S28. Capacities and affinities of all mixed linker samples compared to the single linker ones towards water vapor. Closed symbols display the maximum amount adsorbed, open symbols display the amount adsorbed at $p/p_0 = 0.1$. The maximum amount adsorbed for CAU-10-NO_2 was determined at $p/p_0 = 0.5$.

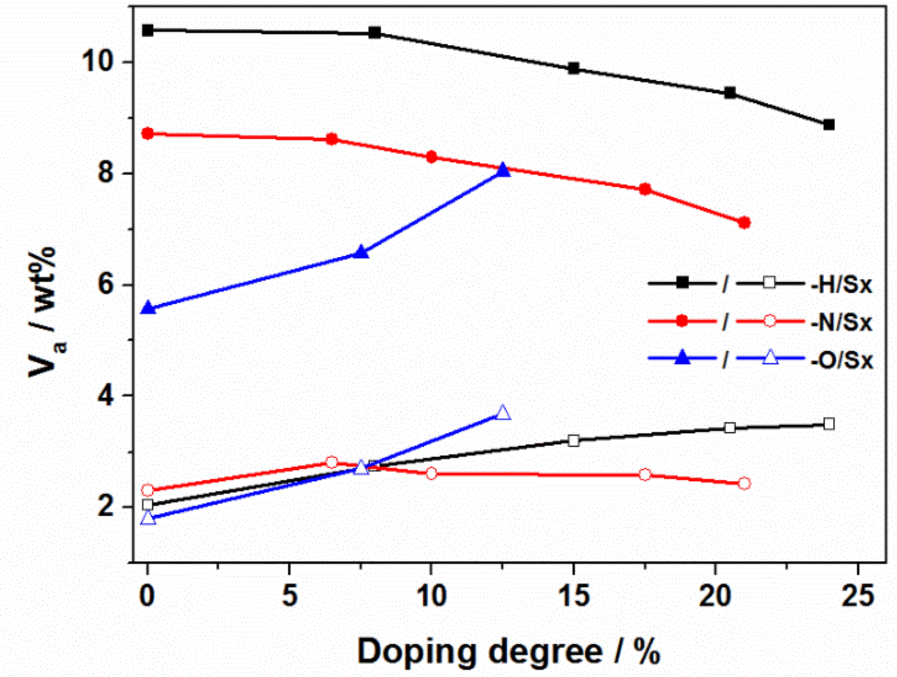

Figure S29. Capacities and affinities of all mixed linker samples compared to the single linker ones towards CO_2 gas. Closed symbols display the maximum amount adsorbed, open symbols display the amount adsorbed at p = 15 kPa.

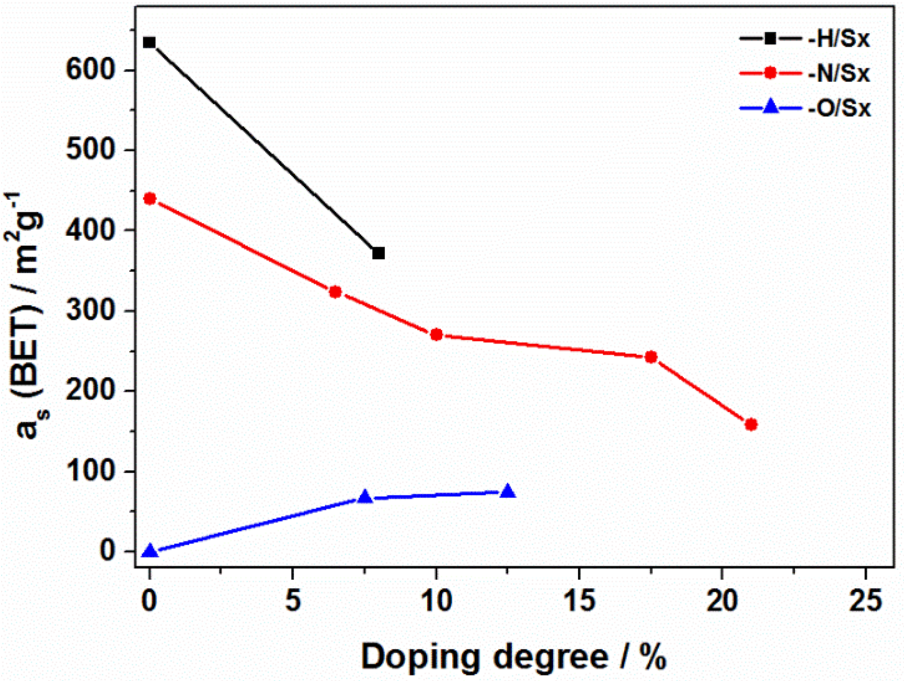

Figure S30. Calculated specific surface areas (BET) obtained from nitrogen sorption measurements of all compounds compared to each other.

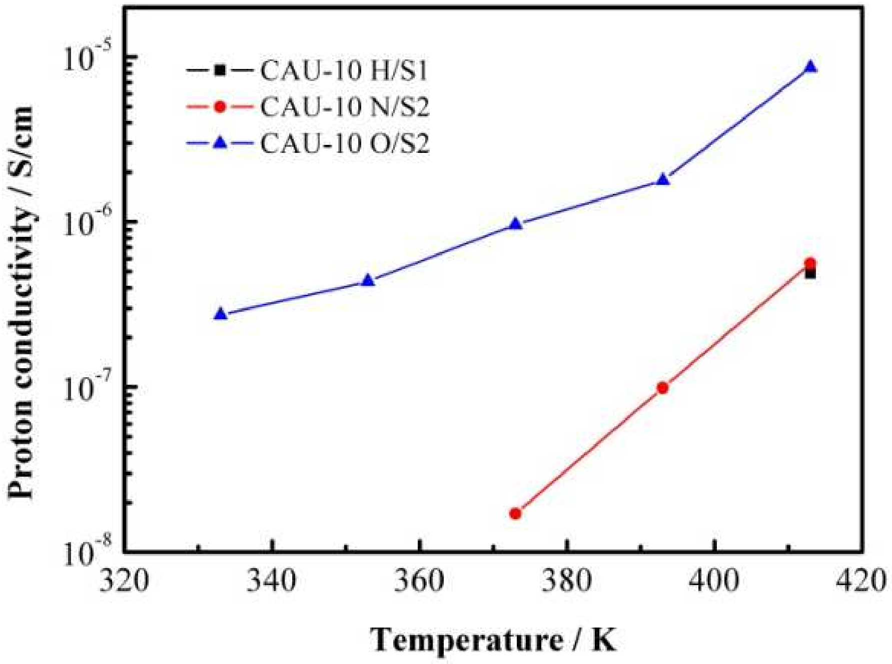

Figure S31: Proton conductivity of the three investigated CAU-10 (CAU-10-H/S1, CAU-10-N/S2 and CAU-10-O/S2) with approximately 10% sulfonic acid at different temperatures and 100% relative humidity.

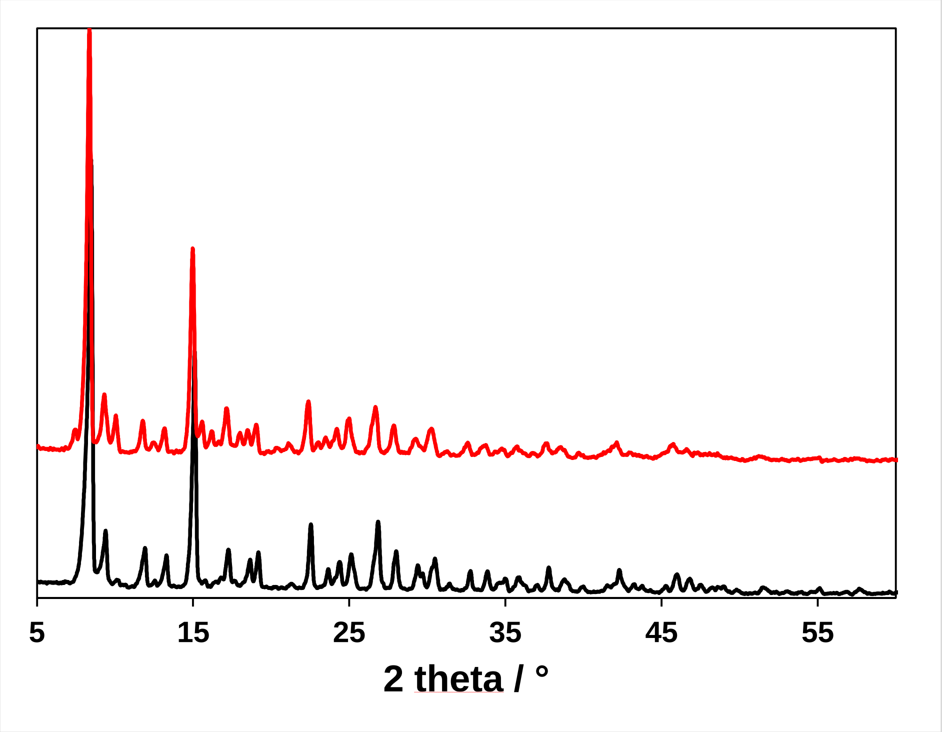

Figure S32. Powder X-ray diffraction pattern of CAU-10-H before (bottom) and after reaction (top).

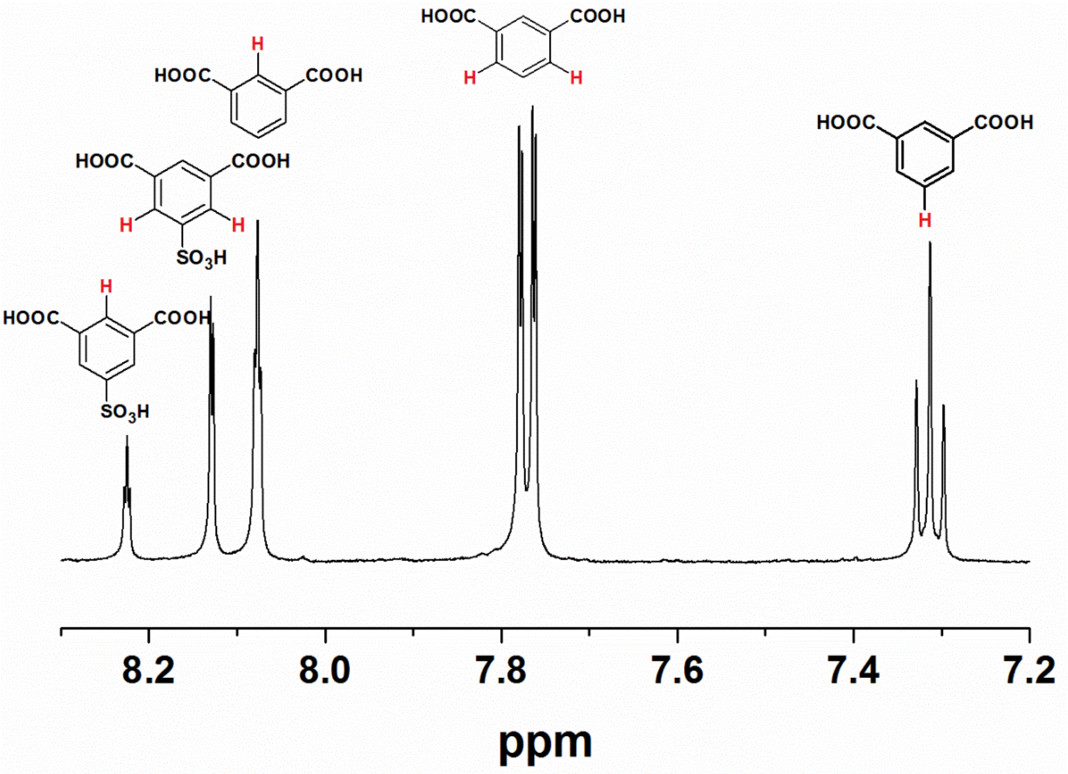

Figure S33. ^{1}**H-NMR spectrum of CAU-10-H/S4 after catalytic reaction. The fraction of sulfonic acid groups is 23.3 %.**

Proton conductivity

The proton conductivity was determined by electrochemical impedance spectroscopy (EIS).[1,2] EIS was performed with a 2 electrode cell setup using a Zahner Zennium workstation. Two stainless steel electrodes (diameter 8 mm) served as working and counter electrode. An AC voltage of 100 mV was applied between 1 Hz and 1 MHz. The measurements were performed using a custom made PTFE measuring cell consisting of two graphitic sheets each attached to one of the stainless steel electrodes. The powders were placed between the two electrodes and pressed with an angular moment of 30 cNm to obtain small sample pellets (diameter 8 mm, thickness 1.2 mm). The measuring cell was placed in a gastight, temperature-controlled stainless steel chamber with an attached water reservoir.[3] The relative humidity (RH) in the cell was determined by the Clausius-Clapeyron relation and controlled by heating of the water reservoir and the cell. Prior to each series of measurements, samples were dried at 413 K for 3 hours and equilibrated for 24 hours at 313K and at 50% RH. The samples were equilibrated for

1 hour at desired temperature and RH before measuring each data point. The measurements were performed at 100% RH in the range between 333 K to 413 K.

The proton conductivity (eq. 1)[1,2] was obtained by using the Ohmic resistance of the samples determined by EIS.

$$\sigma = \frac{L}{R\,A} \qquad (1)$$

σ: proton conductivity, R: Ohmic resistance,

L: sample thickness, A: sample cross-section area

The Ohmic resistance was taken from the Bode phase plot of the impedance. The impedance corresponding to the phase shift closest to zero is approximately equal to the Ohmic resistance of the sample.[1,2]

Each impedance value was measured three times, and the arithmetic mean was calculated and used in the analysis.

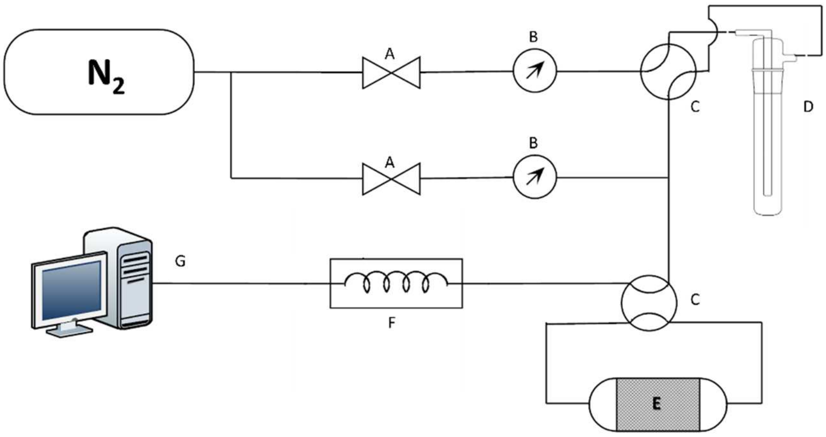

Figure S34. Schematic overview of the reactor setup. A: Two-way valve; B: Mass flow controller and pressure gauge; C: Four-way valve; D: Thermostatic bubbler containing pure ethanol; E: Plug flow reactor with heating mantle; F: On-line GC; G: Data acquisition and processing.

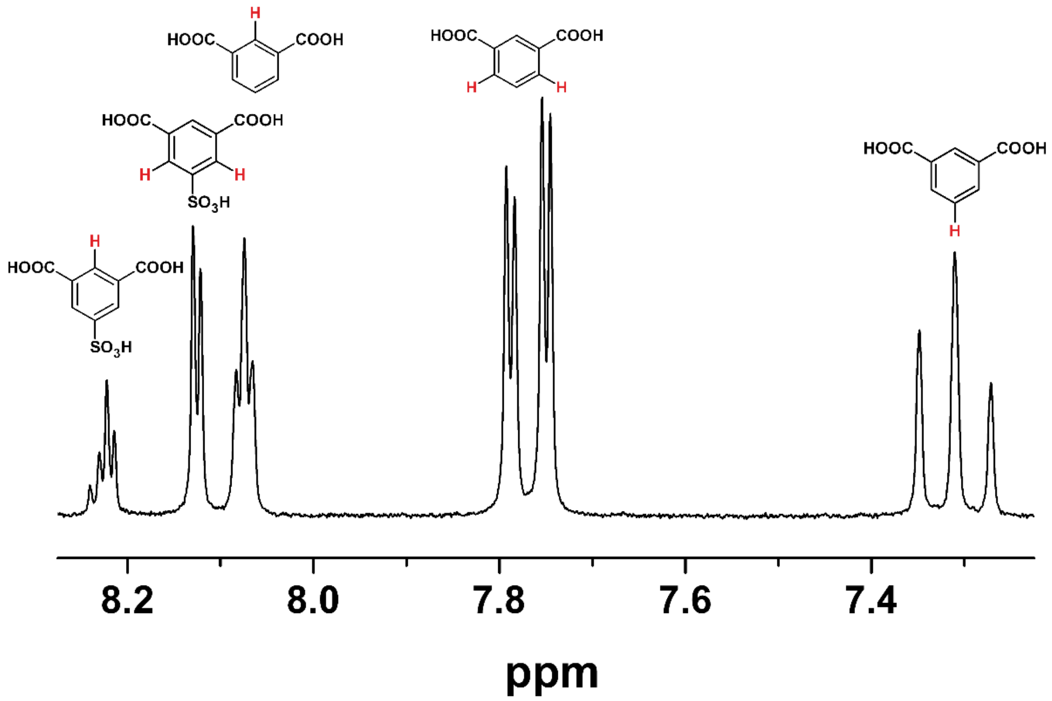

Figure S35. Section of the ^{1}H-NMR spectrum of CAU-10-H/S4.

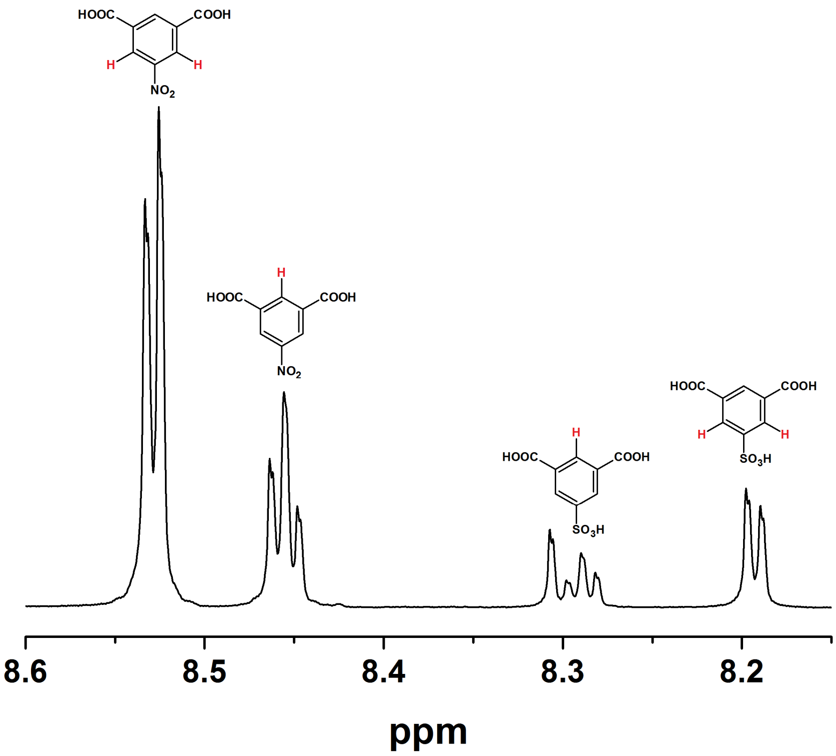

Figure S36. Section of the ^{1}H-NMR spectrum of CAU-10-N/S3.

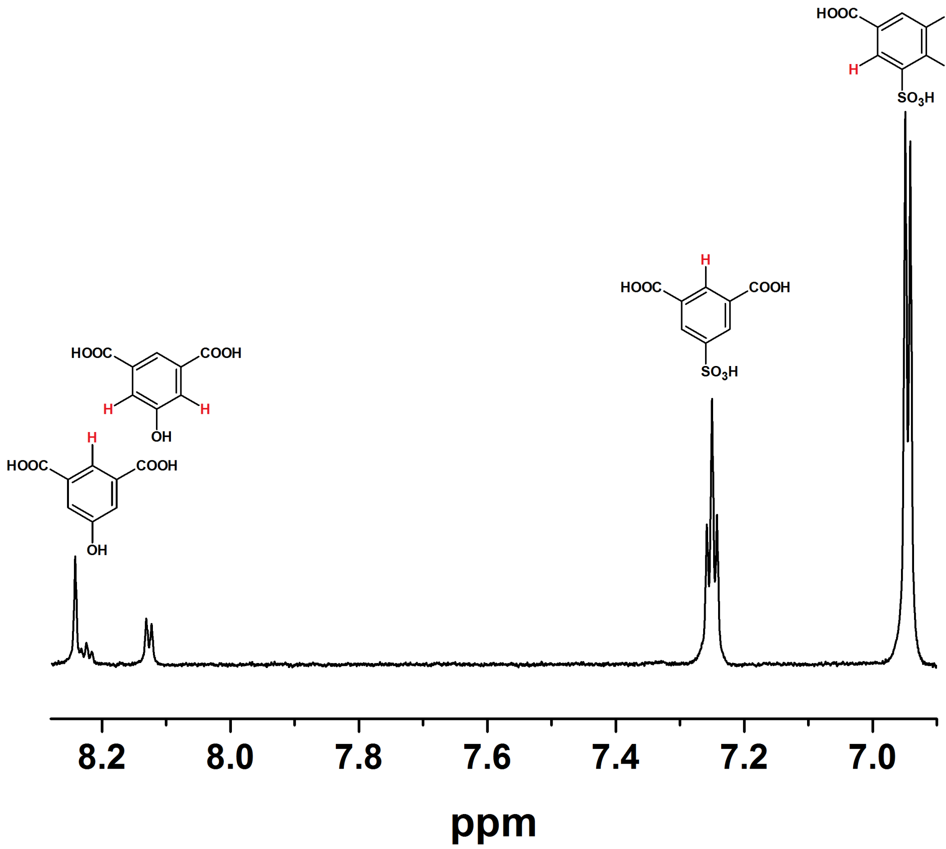

Figure S37. Section of the ^{1}H-NMR spectrum of CAU-10-O/S1.

Table S1: Exact amounts for the synthesis of the differently functionalized mixed-linker CAU-10 compounds.

Sample	Al-salt aq. Solution mmol(µL)	Linker ratio		Linker mmol (mg)		Solvent(µL)	
CAU-10-	$Al_2(SO_4)_3 \cdot 18H_2O$(1M)	*m*-H_2BDC-H	*m*-H_2BDC-SO_3Li	*m*- H_2BDC-H	*m*-H_2BDC-SO_3Li	DMF	H_2O
H/S1	1.38 (920)	0.825	0.125	1.21 (200.6)	0.172 (43.5)	1150	3680
H/S2	1.38 (920)	0.75	0.25	1.04 (171.9)	0.345 (87.0)	1150	3680
H/S3	1.38 (920)	0.625	0.375	0.863 (143.3)	0.518 (130.5)	1150	3680
H/S4	1.38 (920)	0.5	0.5	0.690 (114.6)	0.690 (174.0)	1150	3680
CAU-10-	$AlCl_3 \cdot 6H_2O$(2M)	*m*-H_2BDC-NO_2	*m*-H_2BDC-SO_3Li	*m*-H_2BDC-NO_2	*m*-H_2BDC-SO_3Li	DMF	H_2O
N/S1	6.8 (3400)	0.825	0.125	5.97 (1260)	0.853 (214.9)	4000	12600
N/S2	6.8 (3400)	0.75	0.25	5.12 (1080)	1.71 (429.9	4000	12600
N/S3	6.8 (3400)	0.625	0.375	4.26 (900.0)	2.56 (644.8)	4000	12600
N/S4	6.8 (3400)	0.5	0.5	3.41 (720.5)	3.41 (859.8)	4000	12600
CAU-10-	$AlCl_3 \cdot 6H_2O$(2M)	*m*-H_2BDC-OH	*m*-H_2BDC-SO_3Li	m-H_2BDC-OH	m-H_2BDC-SO_3Li	DMF	H_2O
O/S1	5.6 (2800)	0.825	0.125	4.80 (874.9)	0.686 (173.3)	4000	13200
O/S2	5.6 (2800)	0.75	0.25	4.12 (750.2)	1.37 (346.0)	4000	13200

Table S2: Results of the elemental analysis compared with the values calculated by the assumed molecular formulas.

CAU-10-		C (%)	H(%)	N(%)	S(%)
H/S1	calc.	34.9	4.3	0.5	0.9
	obs.	35.9	4.1	0.7	0.9
H/S2	calc.	35.4	4.0	0.5	1.8
	obs.	34.4	3.8	0.8	1.7
H/S3	calc.	35.1	3.6	1.0	2.4
	obs.	32.9	3.6	1.0	2.3
H/S4	calc.	35.9	3.3	1.0	2.9
	obs.	33.0	3.6	1.2	3.6
N/S1	calc.	32.4	2.9	4.4	0.7
	obs.	33.1	2.1	5.4	0.5
N/S2	calc.	30.8	3.3	4.0	1.1
	obs.	31.9	1.7	5.0	0.9
N/S3	calc.	30.7	3.3	3.7	1.8
	obs.	31.0	1.9	4.6	1.6
N/S4	calc.	30.7	3.2	3.5	2.2
	obs.	30.4	2.2	4.2	2.2
O/S1	calc.	30.6	4.6	0.0	0.8
	obs.	31.8	3.7	0.8	0.7
O/S2	calc.	30.4	4.6	0.0	1.3
	obs.	30.7	3.6	1.1	1.1

Figure S38. Indicator test using methyl red. From left to right: H_2O, H_2O+CAU-10-H/S1, H_2O+CAU-10-H/S2, H_2O+CAU-10-H/S3 and H_2O+CAU-10-H/S4.

---

1 Barsoukov, E.; MacDonald, J. R. *Impedance spectroscopy*; 2. ed.; Wiley&Sons: Hoboken, New Jersey, 2005.

2 Grehn, J.; Krause, J. *Metzler Physik*; 3. ed.; Schroedel Verlag: Hannover, 1998.

3 Alberti, G.; Casciola, M.; Massinelli, L.; Bauer, B. *J. Membr. Sci.* **2001**, *185*, 73-81.

Supporting Information

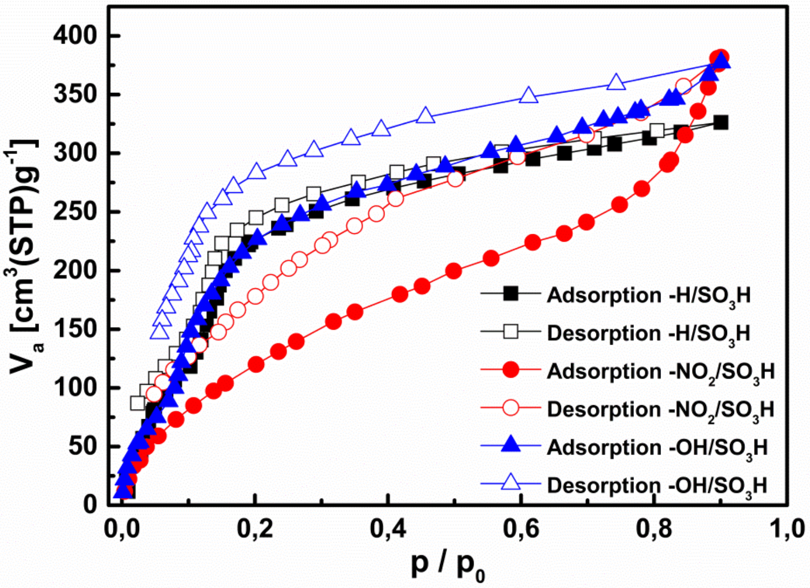

Figure S1. Water sorption isotherms at 298 K of the samples H-MOF (CAU-10-$H_{0.76}$/$(SO_3H)_{0.24}$), NO_2-MOF (CAU-10-$(NO_2)_{0.79}$/$(SO_3H)_{0.21}$) and OH-MOF (CAU-10-$(OH)_{0.89}$/$(SO_3H)_{0.11}$). Prior to each measurement the samples were activated at 200 °C over night under vacuum (10^{-2} kPa). [Weiss et al. 2015]

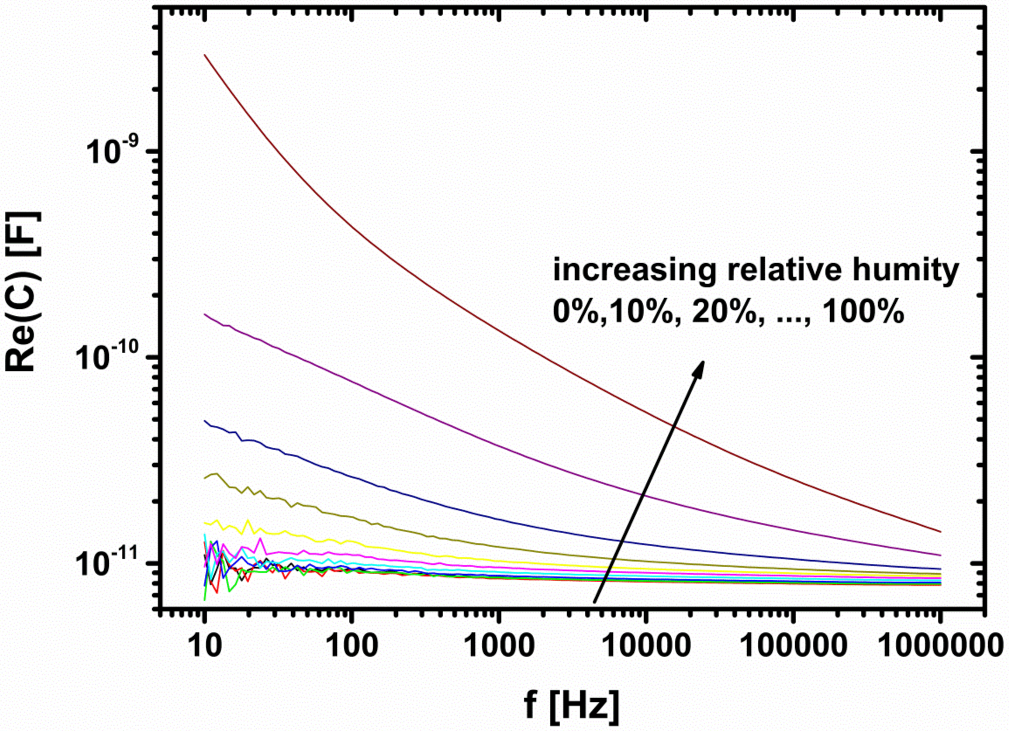

Figure S2. Screening using measurement setup (a) in the range from 10 Hz to 10^6 Hz. Exemplary plots of Re(C) over frequency for the H-MOF sample (CAU-10-$H_{0.76}$/$(SO_3H)_{0.24}$) at different relative humidity levels. Calculated according the the following equation: $Re(C) = \frac{-Im(Z)}{\omega(Re(Z)^2+Im(Z)^2)}$ [Weiss et al. 2015].

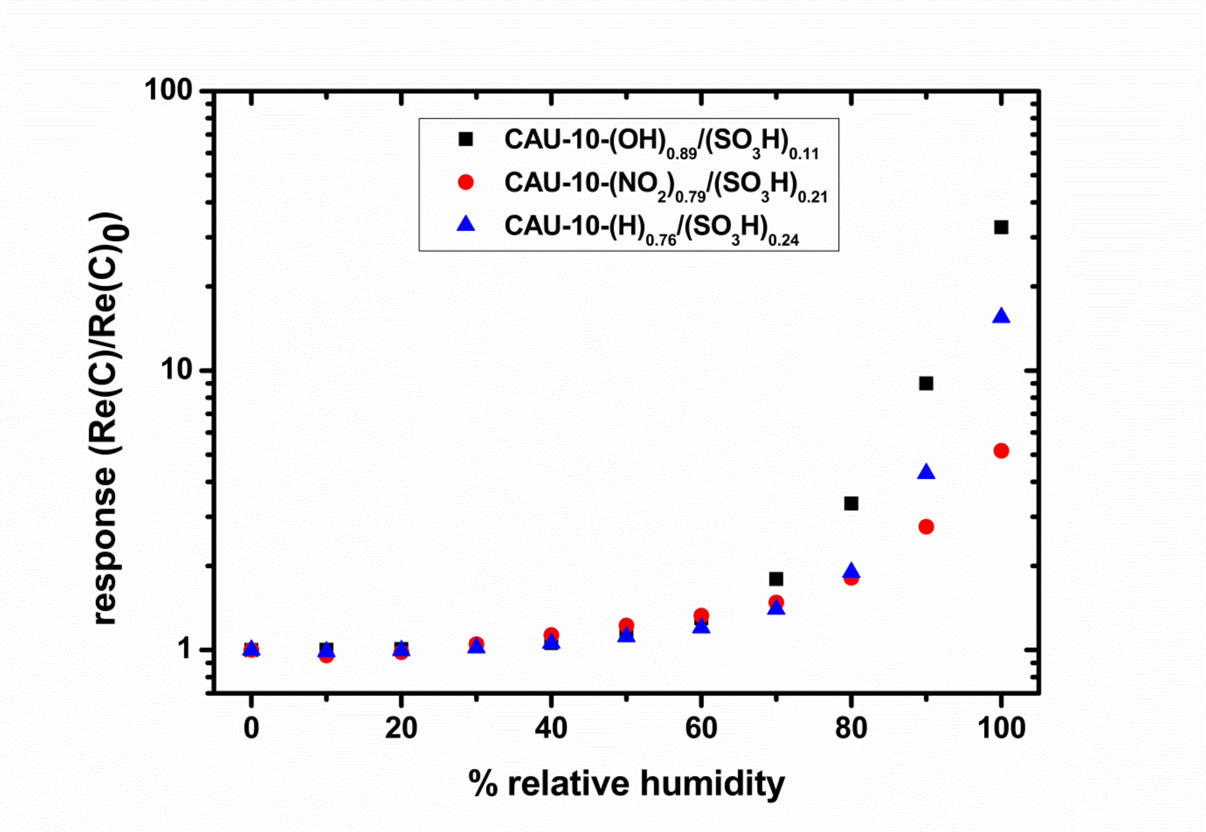

Figure S3. Response Re(C)/Re(C)$_0$ of the samples H-MOF (CAU-10-H$_{0.76}$/(SO$_3$H)$_{0.24}$), NO$_2$-MOF (CAU-10-(NO$_2$)$_{0.79}$/(SO$_3$H)$_{0.21}$) and OH-MOF (CAU-10-(OH)$_{0.89}$/(SO$_3$H)$_{0.11}$) when exposed to different humidity levels. Data points are calculated using the values at 1039 Hz from the frequency sweep. [Weiss et al. 2015]

Weiss et al. 2015	Weiss, A.; Reimer, N.; Stock, N.; Tiemann, M.; Wagner, T. Screening of Mixed-linker CAU-10 MOF Materials for humidity Sensing by Impedance Spectroscopy. Microporous and Mesoporous Materials, submitted 2015.

New group 13 MIL-53 derivatives based on 2,5-thiophenedicarboxylic acid

Nele Reimer[a], Ching-Wen Hsu[b], Helge Reinsch[a], Renée Siegel[c], Jiun-Jen Chen[d], Chia-Her Lin[b], Jürgen Senker[c], Norbert Stock[a]

[a] Institut für Anorganische Chemie, Christian-Albrechts-Universität zu Kiel, Max-Eyth-Straße 2, D-24118 Kiel, Germany

[b] Department of Chemistry, Professor Chung Yuan Christian University, Chung-Li 320, Taoyuan, Taiwan

[c] Department for Inorganic Chemistry III, University of Bayreuth, Universitätsstraße 30, D-95440 Bayreuth, Germany

[d] Green Energy & Environment Research Laboratories, Industrial Technology Research Institute, Hsinchu 310, Taiwan

[e] Institut Lavoisier de Versailles, UMR CNRS 8180, Université de Versailles St Quentin, 78035 Versailles, France

Corresponding author: Norbert Stock, Institut für Anorganische Chemie, Christian-Albrechts-Universität zu Kiel, Max-Eyth-Straße 2, D-24118 Kiel, Germany; E-mail address: stock@ac.uni-kiel.de; Tel.: +49 431 8801675

Table of Content

Table S1. Structures of coordination polymers containing on 2,5-thiophene-dicaboxylate ligand (CSD database, Dec. 2014).

Compound	SG	Cell parameters	Structural motifs	Lit.
$[Zr_6O_6(OH)_2(TDC)_4$ $(Ac)_2]\cdot6.5H_2O$ $\cdot4.7DMF$ [DUT-67(Zr)]	F*m*-3*m*	*a* = 39.120(5) Å	8-connected clusters reo topology porous	[1]
$[Hf_6O_6(OH)_2(TDC)_4$ $(Ac)_2]\cdot3.4H_2O$ $\cdot6.1DMF$ [DUT-67(Hf)]		*a* = 39.010(5) Å		
$[Zr_6O_6(OH)_2(TDC)_{4.5}(Ac)]\cdot7H_2O$ $\cdot7.75DMF$ DUT-68(Zr)	I*m*-3*m*	*a* = 53.680(6) Å	8-connected clusters; porous	
$Hf_6O_6(OH)_2(TDC)4.5(Ac)\cdot4.5H_2O$ $\cdot7.3DMF$ DUT-68(Hf)		*a* = 53.510(6) Å		
$[Zr_6O_4(OH)_4(TDC)_5(Ac)]_2\cdot11.7H_2O$ $\cdot4.1DMF$ DUT-69(Zr)	$P2_12_12_1$	*a* = 13.570(3) Å *b* = 19.800(4) Å *c* = 28.390(6) Å	uninodal 10-connected framework with the bct topolog; porous	
$[Hf_6O_4(OH)_4(TDC)_5$ $(Ac)_2[\cdot9.3H_2O$ $\cdot4.5DMF$ DUT-69(Hf)		*a* = 13.530(3) Å *b* = 19.710(4) Å *c* = 28.300(6) Å		
$[Sc(TDC)(OH)]\cdot2.6H_2O$ (NOTT-401)	$I4_1/amd$	*a* = *b* = 22.605(4) Å *c* = 12.474(2) Å	3D strucure based on binuclear $[Sc_2(l2\text{-}OH)(O_2CR)_4]$ building block	[2]
$[Zn_4O(TDC)_3(MeOH)]\cdot DMF\cdot4H_2O$	P*a*-3	*a* = 19.025(3) Å	$(Zn_4O)(O_2C)_6$ cluster, 3D network; twofold interpenetrated; porous	[3]
$(Me_2NH_2)[In(TDC)_2]\cdot nDMF$	$P4_122$	*a* = *b* = 13.5770(4) Å *c* = 15.5394(9) Å	2-fold interpenetrating diamond-type anionic framework; square channels; porous	[4]
$[Zn_{17}(TDC)_{14}(\mu4\text{-}O)_4(H_2O)(Me_2NH_2)]Me_2NH_2$ · guests	I4/*mmm*	*a* = 24.429(5) Å *c* = 45.411(11) Å	johnson-type cages with Zn_4O_{13} inorganic clusters, linkage via	[5]

			linker molecules to 3D structure; porous	
$C_9H_9CuNO_5S$	R-3*c*	*a* = *b* = 20.0402(6) Å *c* = 41.6541(13) Å	pallde-whel units, 2D layers, connection via H-bonds, porous	[6]
$[Ln(TDC)_{1.5}(H_2O)_2]$ (Ln = Pr, Nd)	C2/*c*	*a* = 25.553(4) / 25.617 Å *b* = 5.9007(9) / 5.8953(12) Å *c* = 19.174(3) / 19.210(4) Å *β* =24.132(2) / 124.22(3) °	1D rod-like chains connected by linker molecules to form rhombic channels	[7]
$[Ln(TDC)(Ac)(H_2O)]$ (Ln = Pr, Nd, Eu, Gd, Tb, Dy)	P2$_1$/*c*	*a* = 9.888(2)-9.9999(4) Å *b* = 14.1924(9)-14.6032(9) Å *c* = 7.7236(6)-8.0136(5) Å *β* = 103.017(5)-103.820(10) °	3D dense structure	
$[Ca_2(TDC)_2(DMF)_2]$	P2$_1$/*n*	*a* = 10.0704(3) Å *b* = 14.2521(3) Å *c* = 17.5644(6) Å *β* = 94.28(0) °	chains of Ca-O polyhedra; 1D channels	[8]
[Ca(TDC)]	P*bcm*	*a* = 5.3331(5) Å *b* = 6.8981(4) Å *c* = 18.1411(16) Å	chains of edge-linked calcium-centered, octahedra	
[Sr(TDC)(DMF)]	P2$_1$/*n*	*a* = 5.9795(3) Å *b* = 17.0583(10) Å *c* = 11.3592(6) Å *β* = 91.26(0) °	chains of strontium-oxygen polyhedra forming 1D channels	
[Mn(TDC)(DMA)]	C2/*c*	*a* = 11.8527(6) Å *b* = 18.2900(7) Å *c* = 11.4991(6) Å *β* = 99.02(0) °	Rod-packing pcu assembled with rod-shaped SBUs	[9]
[Mn(TDC)(NMP)]		*a* = 11.7729(2) Å *b* = 18.2439(4) Å *c* = 11.7165(2) Å *β* = 99.61(0) °		
[Mn(TDC)(DMSO)]		*a* = 11.2759(4) Å		

		b = 18.4795(4) Å c = 11.2782(4) Å β = 96.22(0) °		
$[Cu_2(TDC)_2(NH_3)_4]$	$C2/c$	a = 7.6170(6) Å b = 12.6984(8) Å c = 19.1943(14) Å β =100.37(1) °	dinuclear metal centres sql topology	
$[Zn_2(TDC)_2(DMA)_2]$	$P2_1/n$	a = 8.4866(2) Å b = 14.8476(4) Å c = 10.1406(3) Å β = 100.73(0) °		
$[Zn_2(TDC)_2(PY)_2]$	$P2_1/n$	a = 7.6939(2) Å b = 15.9643(4) Å c = 9.8577(3) Å β = 97.67(0) °		
$[Mn_2(TDC)_2(PYRO)_3]$	P-1	a = 9.4155(6) Å b = 9.9399(4) Å c = 15.3997(8) Å α = 82.24(1) ° β = 86.95(1) ° γ = 88.63(1) °	1D-rod-like chain consisting of pairs of corner-sharing MnO_6 polyhedra 2D-network with rhombic channels along the *a*-axis	[10]
$[Mn_3(TDC)_3(PYRO)_3]$	$P2_1/c$	a = 16.4733(12) Å b = 10.6596(6) Å c = 21.7791(13) Å β = 92.69(0) °	1D-rod-like chain, pairs of edge-sharing MnO_6 polyhedra alternating with isolated MnO_5 polyhedra, 3D structure	
$[Mn_2(TDC)_2(DMA)_2]$	$C2/c$	a = 11.857(9) Å b = 18.273(13) Å c = 11.496(11) Å β = 99.20(2) °	1D-chains of MnO_6 octahedra similar structure as MIL-47	
$[Mn_2(TDC)_2(CH_3COO)H_2N(CH_3)_2]$	$P4_2/nmc$	a = 22.7772(16) Å c = 12.8156(18) Å	1D-zigzag chains of corner-sharing MnO_6 octahedra, 3D structure	
$[Cu_2(TDC)_2(DEF)_2]\cdot(H_2O)\cdot(DEF)_3$ (MOF-107)	P-1	a = 11.0318 Å b = 18.0673 Å	2-D structure	[11]

		c = 18.4528Å *α* = 104.812 ° *β* = 97.075 ° *γ* = 95.206 °		
[Cu2(TDC)2(CH3OH)2]·(DBF)$_2$ (MOF-108)	$P2_1/c$	*a* = 15.474 Å *b* = 14.514 Å *c* = 14.031 Å *β* = 113.63 °	2-D structure	
$[Cu_2(TDC)_2(DMF)_2]\cdot(H_2O)$ ·(DMF)3.5 (MOF-110)	R-3*m*	*a* = *b* = 20.0468 Å *c* = 20.7484 Å	2-D structure	
$[Dy_2(TDC)_3(H_2O)_4]$	C2/*c*	*a* = 25.215(5) Å *b* = 5.7711(12) Å *c* = 18.858(4) Å *β* = 124.15(3)°	distorted triangular dodecahedral coordination polyhedra	[12]
$[Ho_2(TDC)_3(H_2O)_4]$	C2/*c*	*a* = 25.1320(7) Å *b* = 5.7534(2) Å *c* = 18.7976(5) Å *β* = 124.15(0) °		
$[Er_2(TDC)_3(H_2O)_4]$	C2/*c*	*a* = 25.158(2) Å *b* = 5.7475(5) Å *c* = 18.8033(17) Å *β* = 124.19(0) °		
$[Ln(TDC)_{1.5}(H_2O)_2]$ Ln=Dy, Gd	C2/*c*	*a* = 25.212(5)-25.341(5) Å *b* = 5.7646(12)-5.7895(12) Å *c* = 18.814(4) Å-18.900(4) Å *β* = 124.56(3)-124.64(3) °	3-D structure; 1D beltlike chain constructed by triangular $[Gd_3]$ motif	[13]
$[Li_4(TDC)_2(DMF)_2]$	P*bca*	*a* = 10.0216(18) Å *b* = 18.327(4) Å *c* = 24.871(5) Å	edge- and corner-sharing lithium-centered tetrahedral units giving tetrameric clusters; layered structure	[14]
$[Tb(TDC)(NO_3)(DMF)_2]$ (MOF-75)	P2/*n*	*a* = 10.6926(11) Å *b* = 10.6727(11) Å	linked TbO_8 polyhedra with the carboxyl carbon	[15]

		c = 15.7533(16) Å β = 95.865(2) °	atoms forming a twisted ladder; rhombic channels	
$[La_2(TDC)_3(DMF)_2]\cdot H_2O\cdot DMF$	$Pna2_1$	a = 17.434(4) Å b = 11.227(3) Å c = 17.980(4) Å	1D-chains of LaO_8 polyhedra; 3D structure; diamond shaped channels	[16]
$[Gd_2(TDC)_3(DMF)]\cdot 2H_2O$	$P2_1/n$	a = 17.5387(17) Å b = 10.8038(11) Å c = 17.7283(18) Å β = 104.793(2) °		
$[Ln(TDC)_2]\cdot(choline)$ (Ln = Gd, Nd, Eu, Er, Tb, Dy)	$P2_1/c$	a=11.5408(17)-11.6140(5) Å b=16.0888(7)-16.4488(5) Å c=12.0019(16)-12.0828(4) Å β=112.295(2)-112.733(6) °	dinuclear $Gd_2(COO)_4$ unit; large rhombic channels; uninodal 8-connected bcu network	[17]
$[Yb(TDC)_2(e\text{-}urea)]\cdot(choline)\cdot H_2O$	$P2_1/c$	a = 14.0214(2) Å b = 11.5047(2) Å c = 20.4346(3) Å β = 129.3750(10) °	layers connected by linker molecules to 3D structure, large rhombic channels	
$[Nd_2(TDC)_3(e\text{-}urea)_4]\cdot 3(e\text{-}urea)$	$P2/c$	a = 17.3413(5) Å b = 11.6871(3) Å c = 27.8924(10) Å β = 115.104(3)°	3D structure with helical substructures; small rectangle pores	
$[Eu_2(TDC)_3(MeOH)_2]\cdot(MeOH)$	$P2/n$	a = 17.219(5)) Å b = 10.692(3) Å c = 17.855(6) Å β = 104.85(1) °	1D rod-like chains connected by linker molecules to form rhombic channels	[18]
$[(Yb_2(TDC)_3(DMF)(H_2O))]\cdot(MeOH)]$	$P2/n$	a = 17.326(12) Å b = 11.492(8) Å c = 17.326(12) Å β = 106.05(1) °	1D rod-like chains connected by linker molecules to form rhombic channels	
$[(Tb_2(TDC)_3(H_2O)_4]$	$C2/c$	a = 25.181(2) Å b = 5.7808(5) Å c = 18.818(2) Å β = 124.05(1) °	1D chains connected by linker molecules to form 3D structure with three interpenetrated channels	
$[La_2(TDC)_2(NO_3)(H_2O)_4]\cdot(OH)\cdot 5H_2O$	$P2_1$	a = 12.827(3)Å b = 6.5366(13) Å c = 16.096(3) Å	1D inorganic chains connected by linker molecules to form 3D structure, porous	[19]

		β = 90.34(3) °		
$[Ln(TDC)(NO_3)(H_2O)]$ (Ln = Nd, Sm, Eu, Gd, Tb, Dy, Ho, Er, Yb)	$P2_1/c$	a = 9.8493(15)-9.971(3) Å b = 14.048(3)-14.420(5) Å c = 7.712(3)-7.971(2) Å β = 102.709(6)-104.119(3) °	left/right-handed helical chains forming a layer; layers connected by linker molecules to form 3D structure	
$[Emim][Ln_{1.5}(TDC)_2]\cdot Cl_{1.5}\cdot Br$ (Ln = Nd , Eu) (Emim = 1-methyl-3-ethylimidazolium)	$P2_12_12$	a = 16.3890(3) Å b = 12.0113(2) Å c = 12.2966(2) Å	trinuclear unit of $[Ln_3(TDC)_4Cl_2Br]_2$ forming 1D left-handed helical chains; 3D structure	[20]
$Emim][Ln(TDC)_2]$ (Ln = Nd, Eu) (Emim = 1-methyl-3-ethylimidazolium)	$P2_1/c$	a = 16.2850(5) Å b = 11.9314(3) Å c = 12.2099(4) Å	dinuclear inorganic units forming 8-connectes building blocks forming a 3D structure	
$[Cu_2(TDC)_2(MeOH)_2]_4\cdot$4naphthalene·8 MeOH	$C2/c$	a = 15.637(4) Å b = 15.430(4) Å c =13.332(3) Å β = 116.692(4) °	paddle-wheel units	[21]
$[Eu_2(TDC)_3(H_2O)_4]$	$C2/c$	a=25.366(8) Å b= 5.8326(14) Å c=19.008(6) Å β = 124.136(4) °	3D dense structure	[22]
[Sr(TDC)(DMF)]	$P2_1/c$	a = 6.0078(4) Å b = 16.9401(12) Å c = 13.0061(8) Å β = 116.158(3) °	SrO_8 polyhedra forming zigzag chains, 3D structure; rhombic channels	[23]
$[M_2(TDC)_2(H_2O)_3]$ (M=Co, Mn)	$C2/c$	a = 19.74(3) Å b = 7.506(11) Å c = 10.750(16) Å β = 103.65(2) °	1D-chains of CoO_6-octahedra, 3D structure	[24]
$[Co(TDC)(H_2O)_{1.5}]$	C2/c	a = 19.8280(5) Å b = 7.5130(2) Å c = 10.7300(3) Å β = 103.440(2) °	1D-chains of cobalt dimers, 3D structure	[25]
$[Ni_3(OH)_2(TDC)_2(H_2O)_4]$	$P2_1/c$	a = 6.3232(1) Å b = 19.1075(2) Å c = 7.9305(1) Å β = 96.373(1) °	1D chains of NiO_6 octahedra; 3D structure	[26]

$[In(TDC)(OH)(H_2O)]$	$P2_1/c$	a = 10.266(2) Å b = 7.6904(15) Å c = 11.138(2) Å β = 108.72(3) °	2D structure	[27]
$[Cd(TDC)(H_2O)_3]\cdot 4H_2O$	$P2/c$	a =10.283(2) Å b = 10.358(2) Å c = 6.7096(13) Å β = 107.45(3) °	1D structure	
$[Ln(TDC)_{1.5}(H_2O)_2]$ (La=Gd, Dy)	$C2/c$	a = 25.341(5) Å, b = 5.7895(12) Å c = 18.900(4) Å β = 124.64(3) ° a = 25.212(5) Å b = 5.7646(12) Å c =18.814(4) Å β = 124.56(3) °	1D-beltlike inorganic chains connected to 3D structure	[13]
$[Ln_2(TDC)_3(DMSO)_2]\cdot H_2O$ (Ln = Tb, Dy)	$Pna2_1$	a = 17.4400(4)/ 17.4356(5) Å b = 10.1537(3/ 10.1537(3) Å c = 17.6594(5) /17.6594(5) Å	3D nets with rhombic channels formed by chains of $Ln_2(COO)_6$ units	[28]
$[Mn_3(TDC)_4(H_2O)_4]\cdot(2,6\text{-lutidine})\cdot 2H_2O$	P-1	a = 11.351(3) Å b = 11.391(3) Å c = 11.480(3) Å α = 112.838(4) ° β = 90.696(4) ° γ = 99.328(4) °	2D structure	[29]
$[Mn_2(TDC)_2(DMF)_2]$	$P2_1/n$	a = 9.9415(2) Å b = 13.7273(2) Å c = 17.1781(2) Å β = 93.4404(14)°	1D-chains of MnO6 polyhedra forming a 3D structure with rhombic channels	[30]
$[Mn_3(TDC)_3(DMF)_3]$	$P2_1/c$	a = 17.9828(3) Å b = 19.8552(2) Å c = 21.3590(4) Å β = 103.9119(19) °	three corner-sharing polyhedra which are further bridged to the next subunit by a carboxyl to form a 1D rod, each rod is connected to six others, leading to a type 4 (hex) packing mode	
$[Mn(TDC)(H_2O)_2]$	$Pnma$	a = 7.349(1) Å b = 18.165(1) Å c = 6.721(1) Å	1D-chains of MnO_6 polyhedra connected by linker molecules to from 3D structure	[31]
$[Mg_3(TDC)_3(DMF)_3]$	$P2_1/c$	a = 17.747(4) Å b = 9.805(2) Å c = 21.359(4) Å	Mg^{2+} ions grouped into a corner-sharing trimeric unit;the polyhedral magnesium trimers form a secondary building unit, connected via a TDC2− carboxylate bridge, creating 1D	[32]

		β = 103.13(3) °	chains; 1D chains are further linked to form the 3D array.	
[Mg(TDC)(H$_2$O)$_2$]	P*nma*	a = 7.296(4) Å b = 17.760(4) Å c = 6.6631(3) Å	1D chains of magnesium ocatahedra connected by TDC-ligands to form the 3D coordination network	
[Nd(TDC)$_3$(EtOH)$_3$(H$_2$O)]·H2O	C*c*	a = 24.035(2) Å b = 10.063(1) Å c = 18.998(1) Å β = 132.41(1) °	1D-chains of individual 8-coordinate Nd polyhedra, diamond-like 3D network	[33]
[Tb(TDC)$_3$(EtOH)$_3$(H$_2$O)]·H$_2$O	P-1	a = 12.807(9) Å b = 14.557(1) Å c = 19.128(1) Å α = 106.66(2) ° β = 105.62(2) ° γ = 93.691(2)°	1D-chains of individual 8-coordinate Nd polyhedra , diamond-like 3D network	
[Dy(TDC)$_3$(EtOH)$_3$(H$_2$O)]·H$_2$O	P-1	a = 12.793(8) Å b = 14.682(1) Å c = 19.077(1) Å α = 107.12(1) ° β = 105.54(1) ° γ = 93.518(2) °	1D-chains of individual 8-coordinate Nd, diamond-like 3D network	

Al-MIL-53-TDC

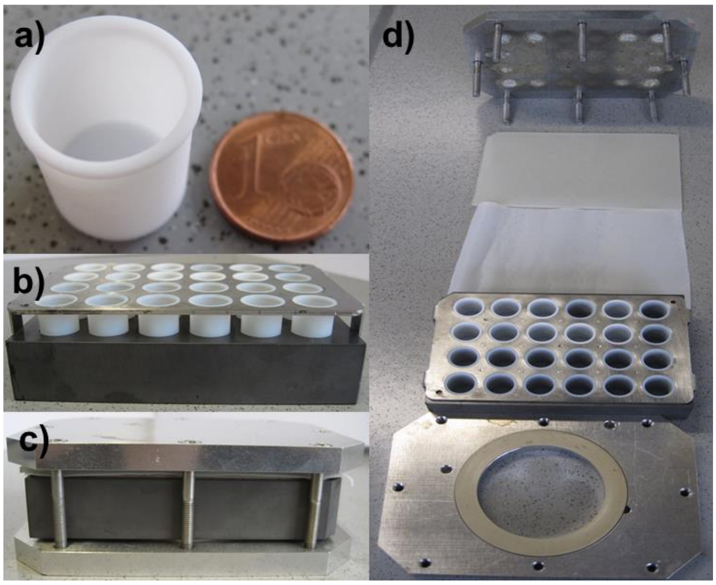

Fig. S1: a) Teflon inlet for the reaction in the HT-MW oven. b) SiC block with Teflon inlets. c) Complete synthesis set-up for the HT-MW oven. d) Single components of the set-up shown in c).

Structural characterization:

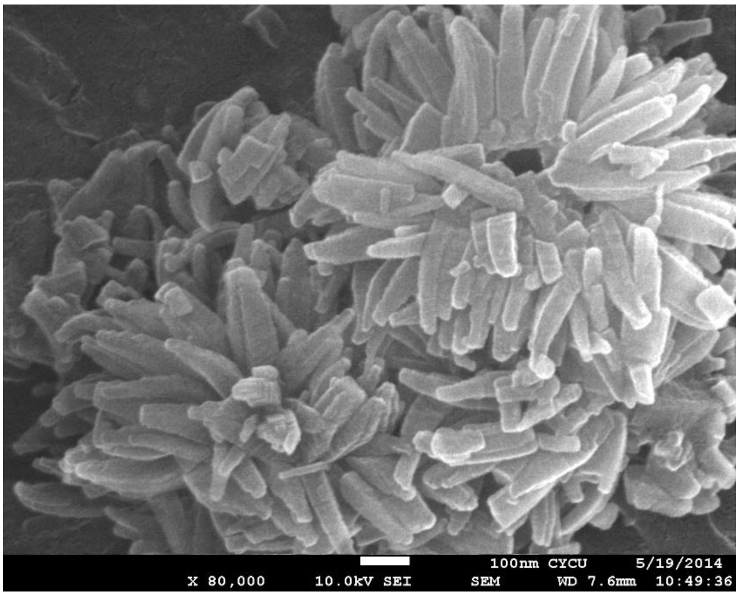

Fig. S2: SEM micrograph of Al-MIL-53-TDC.

Ga-MIL-53-TDC and In-MIL-53-TDC

Materials and Methods:

The characterization of Ga-MIL-53-TDC and In-MIL-53-TDC after sorption measurements by means of PXRD methods was carried out on a STOE-Stadi-P Kombi diffractometer (CuKα$_1$ radiation) equipped with an xy stage and an image plate detector. The high resolution PXRD data was collected on a STOE-Stadi-P diffractometer (CuKα$_1$ radiation) equipped with a mythen detector. Thermogravimetric analyses was performed using a DuPont TA Q50 analyser under owing N_2 with a heating rate of 10 Kmin^{-1}. Ga-MIL-53-TDC was measured after being washed with DMF. In-MIL-53-TDC was measured after being washed with MeOH. TD-PXRD meaurements were performed at BL01C2 beamline of the National Synchrotron Radiation Research Center (NSRRC) in Taiwan. The ring energy of NSRRC was operated at 12 keV with a typical current of 300 mA. The wavelength of the incident X-rays was 1.0332 Å, delivered from the superconducting wavelength shifting magnet, and a Si(111) double-crystal monochromator. SEM micrographs were collected on a JEOL JSM 7600F machine. For Ga-MIL-53-TDC the N_2, H_2 (both at 77 K) and CO_2 (298 K) measurements were performed on an ASAP 2020 system of Micromeritics. All gas sorption measurements for In-MIL-53-TDC as well as the CH_4 (298 K) measurement for Ga-MIL-53-TDC were performed on a Autosorp-iQ (Quantachrome Instruments). Prior to each measurement the samples were activated at 150°C for 1 d. The measurements using H_2O vapor at 298 K were performed using a BEL JAPAN INC. Belsorp$_{max}$ instrument. Prior to each measurement the samples were activated at 250 °C over night at 10^{-2} kPa.

Synthesis and Activation of Ga-MIL-53-TDC

A mixture of $Ga(NO_3)_3 \cdot xH_2O$ (0.1023 g), 2,5-thiophenedicarboxylic acid (H_2TDC, 0.4 mmol), and DMF (5 mL) sealed in a 20 mL glass vial, which was heated at 80 °C for 24 h. The resulting solid was filtered and washed with DMF (3x10 mL) leading to $[Ga(OH)(TDC)]\cdot 0.5H_2O\cdot DMF$ (elemental analysis: obs. C: 31.0 %, H: 2.9 %, N: 3.8 %, S: 9.7 %; calc. C: 31.9 %, H: 3.3 %, N: 4.1 %, S: 9.4 %).

After drying in an oven (120 °C), the samples were activated by heating to 150 °C under vacuum until a pressure of 100 mtorr was reached.

Synthesis and Activation of In-MIL-53-TDC

A mixture of $In(NO_3)_3 \cdot xH_2O$ (0.1203 g), 2,5-thiophenedicarboxylic acid (H_2TDC, 0.4 mmol), DMF (2.5 mL),and MeOH (2.5 mL) sealed in a 20 mL glass vial, which was heated at 80 °C for 24 h. The resulting solid was filtered, washed with MeOH (3x10 mL), and dried in an oven (50~60 °C) leading to $[In(OH)(TDC)]\cdot 0.25MeOH\cdot DMF$

(elemental analysis: obs. C: 28.8 %, H: 2.5 %, N: 3.3 %, S: 8.6 %; calc. C: 29.0 %, H: 2.9 %, N: 3.7 %, S: 8.4 %).

The samples were activated by heating to 150 °C under vacuum until a pressure of 100 mtorr was reached.

Both samples were obtained as microcrystalline powders. SEM images are shown in Fig. S3.

Fig. S3: SEM micrographs of Ga-MIL-53-TDC (left) and In-MIL-53-TDC (right).

Structural characterization:

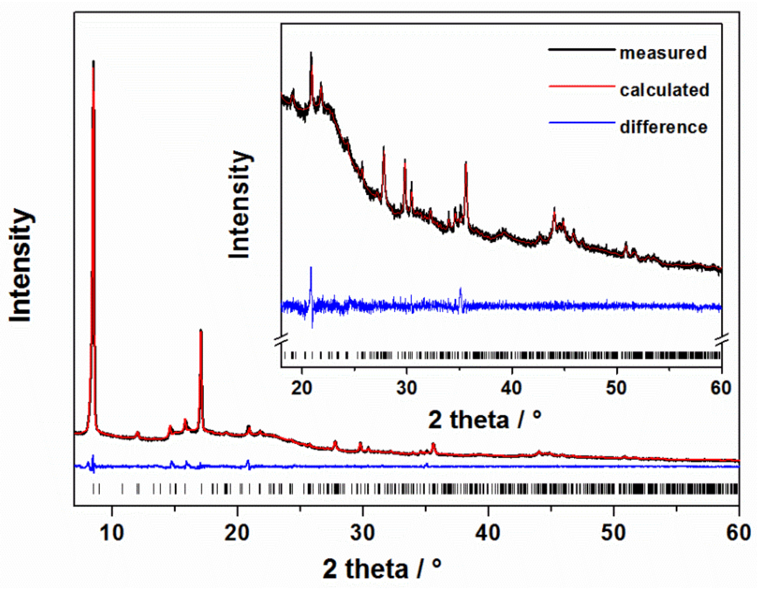

Fig. S4: Pawley-Fit of Al-MIL-53-TDC. The insert shows the area of 18-60 ° = 2 theta. Allowed Bragg positions are marked as black ticks.

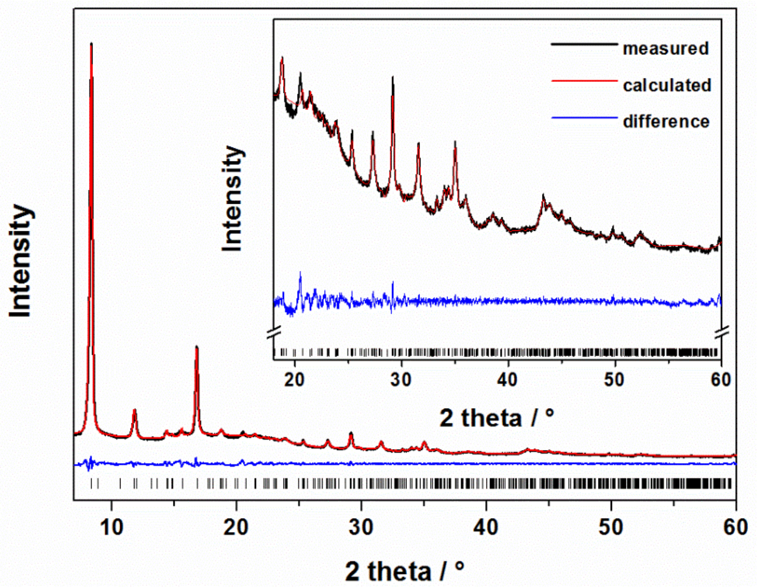

Fig. S5: Pawley-Fit of Ga-MIL-53-TDC. The insert shows the area of 18-60 ° = 2 theta. Allowed Bragg positions are marked as black ticks.

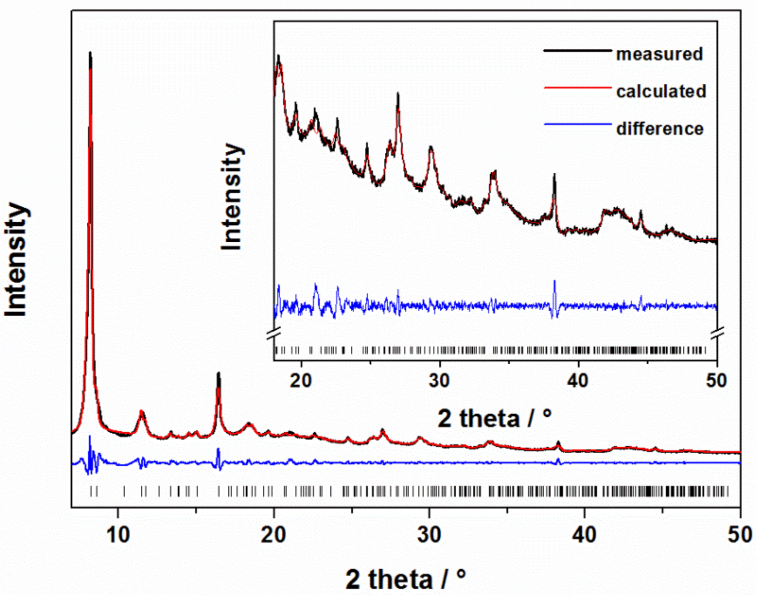

Fig. S6: Pawley-Fit of In-MIL-53-TDC. The insert shows the area of 18-50° 2 theta. Allowed Bragg positions are marked as black ticks.

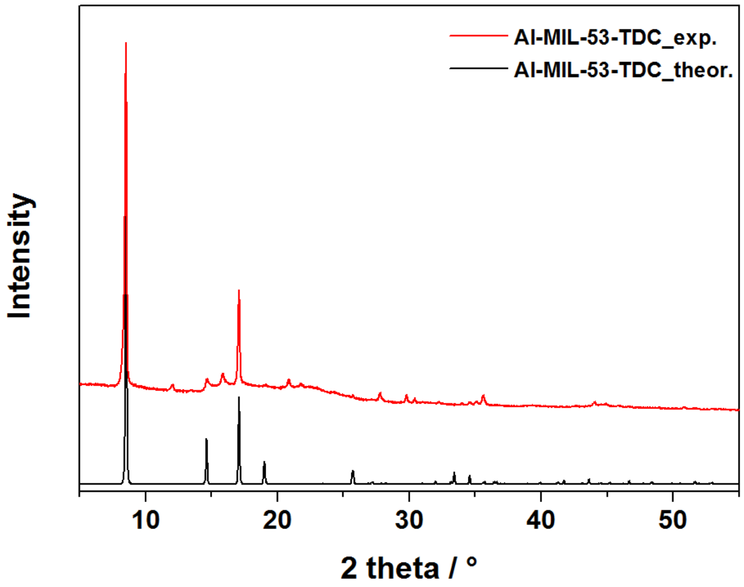

Fig. S7: Comparison of the theoretical and experimental powder patterns of Al-MIL-53-TDC.

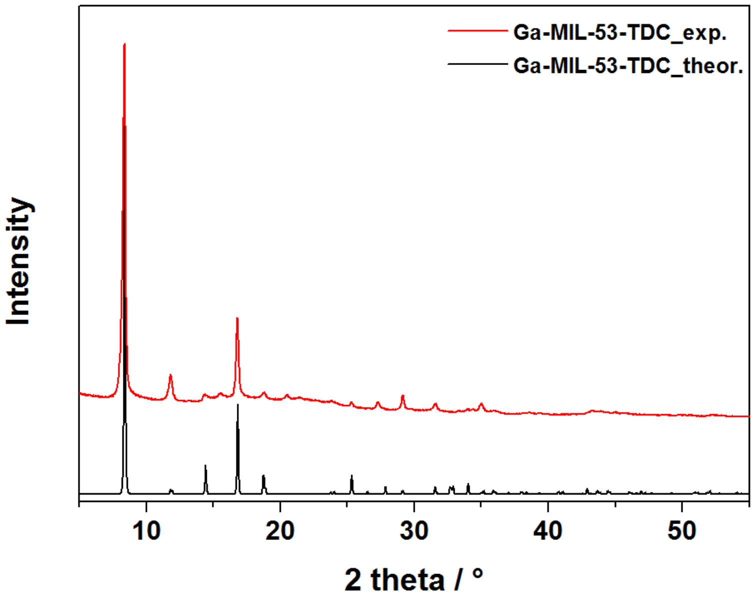

Fig. S8: Comparison of the theoretical and experimental powder patterns of Ga-MIL-53-TDC.

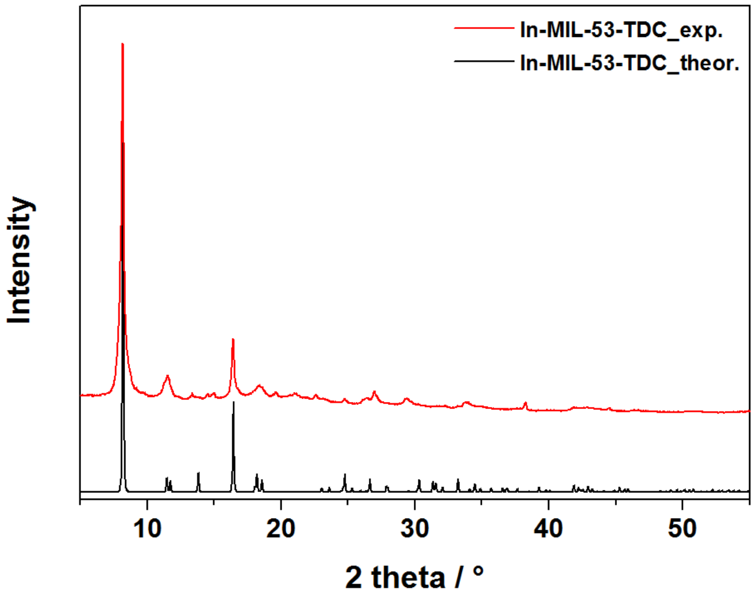

Fig. S9: Comparison of the theoretical and experimental powder patterns of In-MIL-53-TDC.

IR spectroscopy:

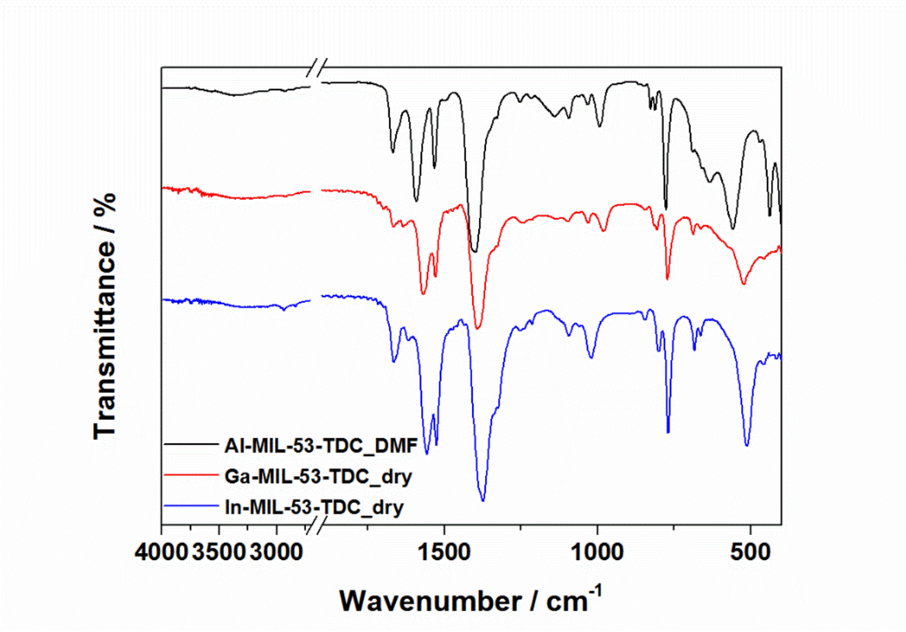

Fig. S10: IR spectra of the dry samples of Ga-MIL-53-TDC and In-MIL-53-TDC compares to the DMF washed sample of Al-MIL-53-TDC.

Thermal analysis:

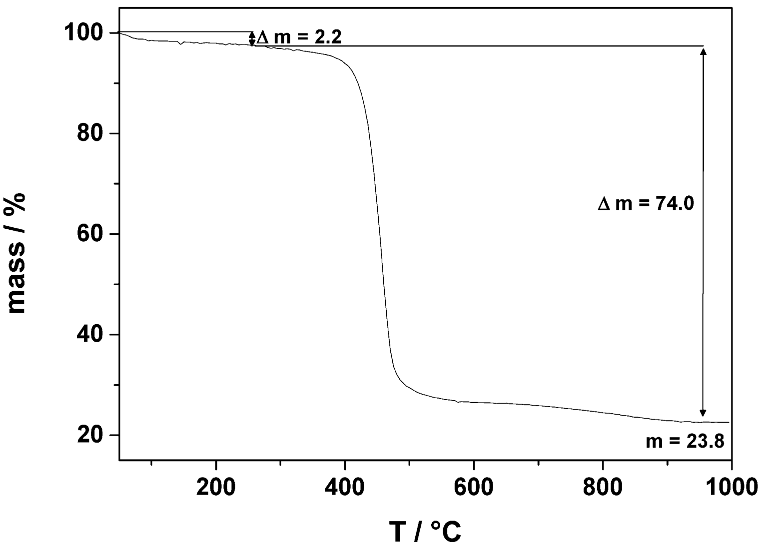

Fig. S11: Thermogravimetric measurement of activated Al-MIL-53-TDC.

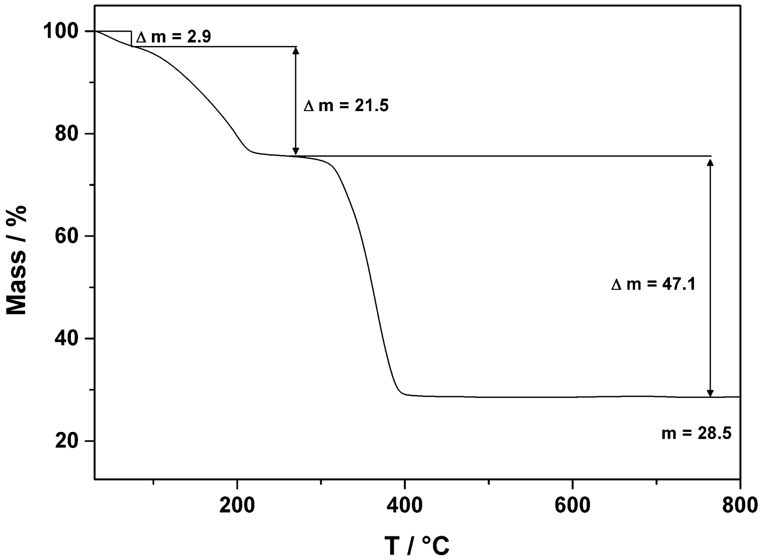

Fig. S12: Thermogravimetric measurement of [Ga(OH)(TDC)]·0.5H_2O·DMF.

The compound shows a three-step weight loss. The first two steps up to 250 °C can be attributed to the removal of incorporated solvent molecules. At temperatures above 300 °C the compound decomposes rapidly to form X-ray amorphous Ga_2O_3.

Table S2: Results of the TG measurement of Ga-MIL-53-TDC.

		Meas. %	Calc. %
1. Step	0.5 H_2O	2.9	2.7
2. Step	1 DMF	21.5	21.5
3. Step	Framework	47.1	47.8
Residue	Ga_2O_3	28.5	27.7

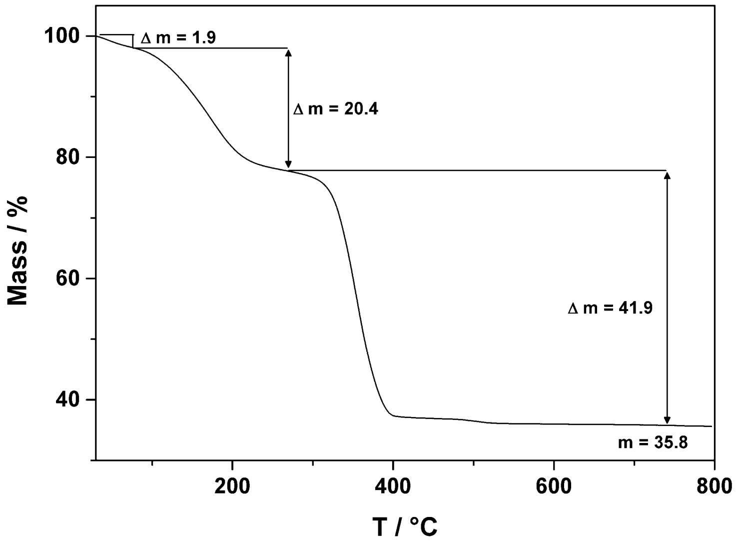

Fig. S13: Thermogravimetric measurement of [In(OH)(TDC)]·0.25MeOH·DMF.

The compound shows a three-step weight loss. The first two steps up to 250 °C can be attributed to the removal of incorporated solvent molecules. At temperatures above 300 °C the compound decomposes rapidly to form X-ray amorphous In_2O_3.

Table S3: Results of the TG measurement of In-MIL-53-TDC.

		Meas. %	Calc. %
1. Step	0.25 MeOH	1.9	2.1
2. Step	1 DMF	20.4	19.1
3. Step	Framework	41.9	42.3
Residue	In_2O_3	35.8	36.2

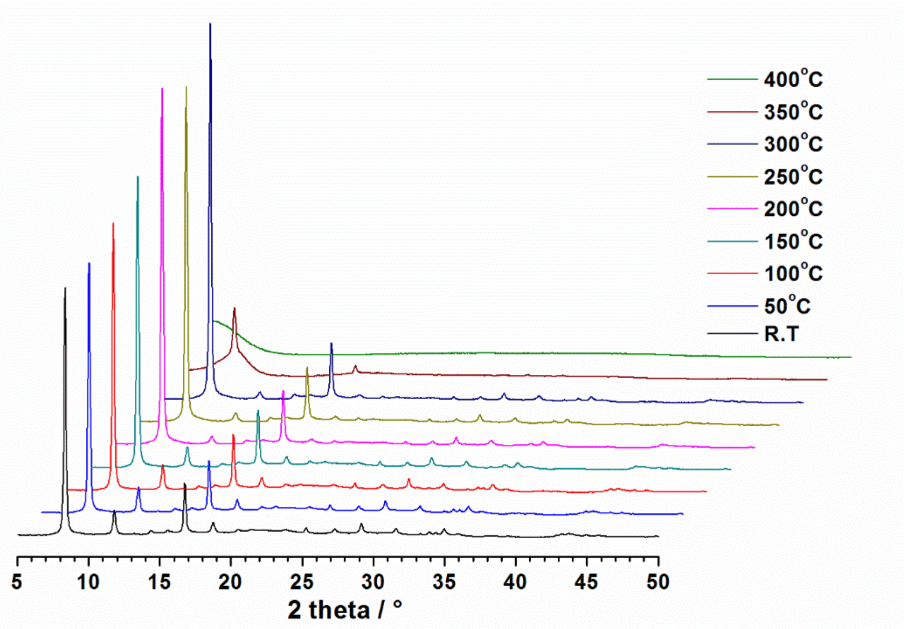

Fig. S14: Temperature-dependent PXRD measurements of Ga-MIL-53-TDC.

The results of the TD-XRPD measurements are in good agreement with the TG measurement. Above 150 °C a small increase in the intensity of the first reflection is observed, due to the removal of incorporated guest molecules. Above temperatures of 300 °C the compound rapidly decomposes to form amorphous Ga_2O_3.

Sorption properties:

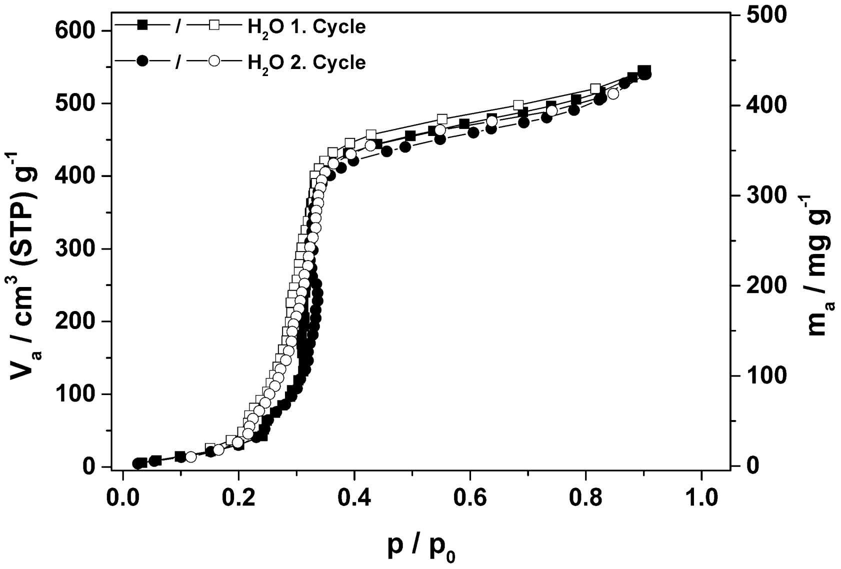

Fig. S15: Repeated H_2O sorption measurement at 298 K up to 1 bar of Al-MIL-53-TDC.

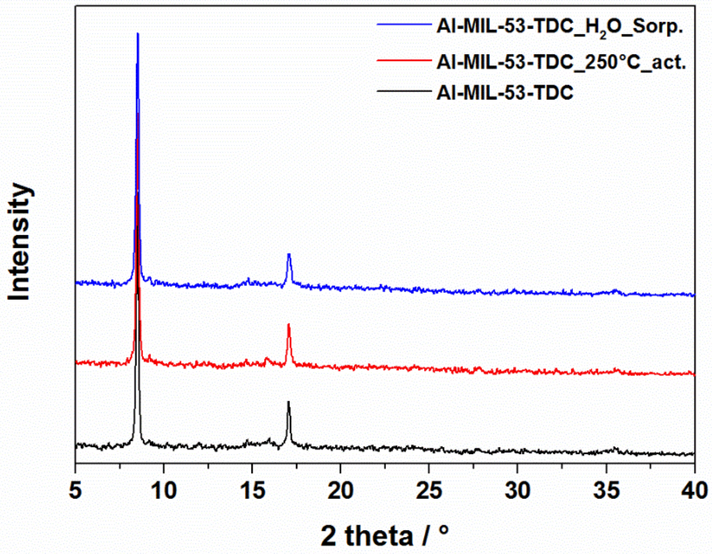

Fig. S16: PXRD patterns of Al-MIL-53-TDC after thermal activation in vacuum as well as after water vapor sorption measurements.

Table S4: Summary of the results of the sorption measurements for Al-MIL-53-TDC, Ga-MIL-53-TDC and In-MIL-53-TDC towards N_2, H_2 (each at 77 K), CO_2, CH_4 and H_2O (each at 298 K) vapor.

	Al-MIL-53-TDC	Ga-MIL-53-TDC	In-MIL-53-TDC
N_2, a_s (m^2g^{-1}) / V_{mic} (cm^3g^{-1})	1151 / 0.48	438 / 0.15	859 / 0.35
H_2 (wt%)	2.1	1.7	1.0
CO_2 (mmol g^{-1})	2.4	2.3	1.7
CH_4 (mmol g^{-1})	0.6	0.6	0.5
H_2O (mg g^{-1})	469	150	160

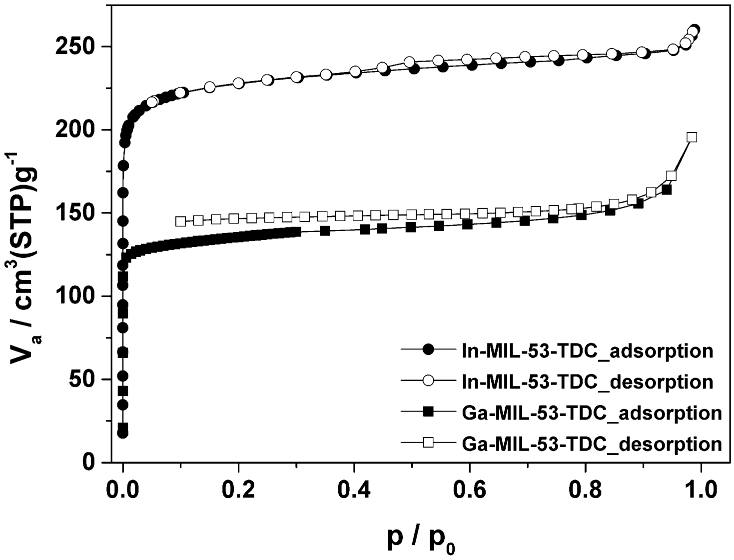

Fig. S17: N_2 sorption isotherms at 77 K of Ga-MIL-53-TDC (squares) and In-MIL-53-TDC (circles).

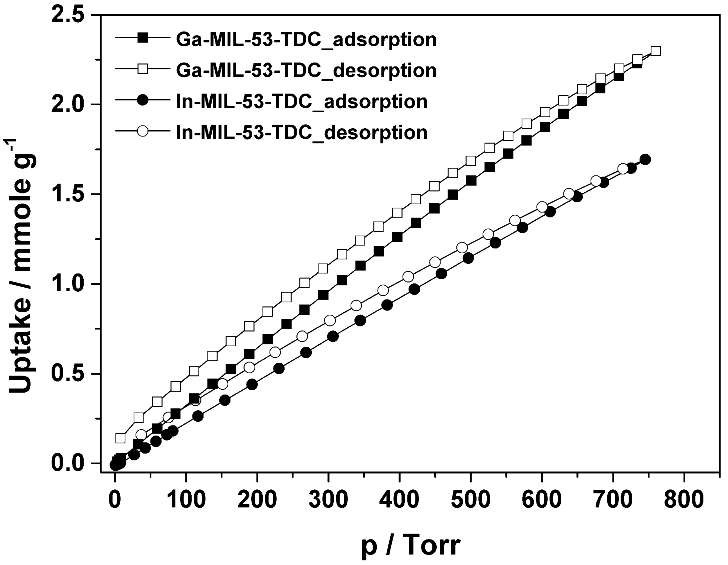

Fig. S18: CO_2 sorption measurements at 298 K up to 760 Torr of Ga-MIL-53-TDC (squares) and In-MIL-53-TDC (circles).

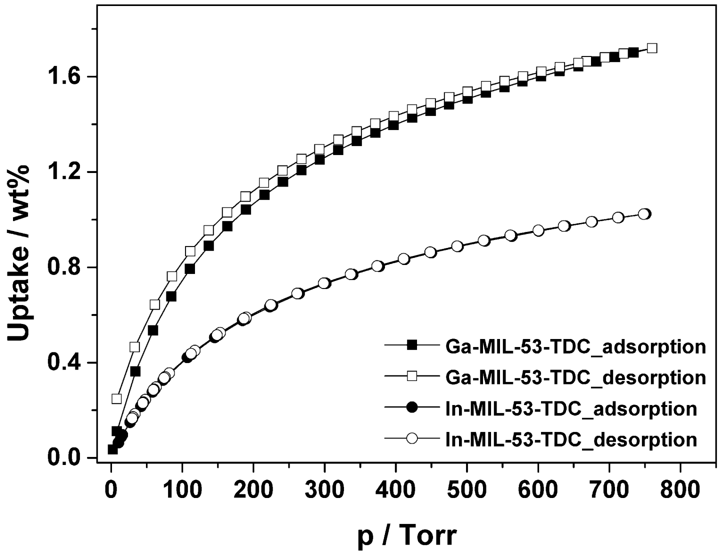

Fig. S19: H_2 sorption measurements at 77 K up to 760 Torr of Ga-MIL-53-TDC (squares) and In-MIL-53-TDC (circles).

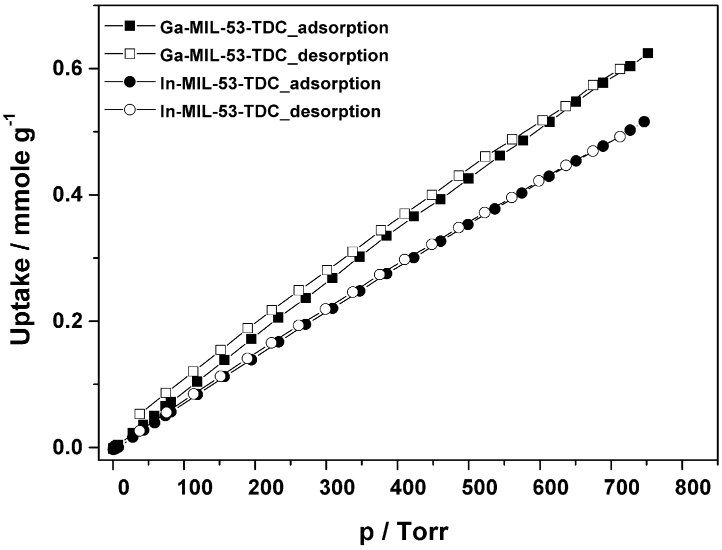

Fig. S20: CH_4 sorption measurements at 298 K up to 760 Torr of Ga-MIL-53-TDC (squares) and In-MIL-53-TDC (circles).

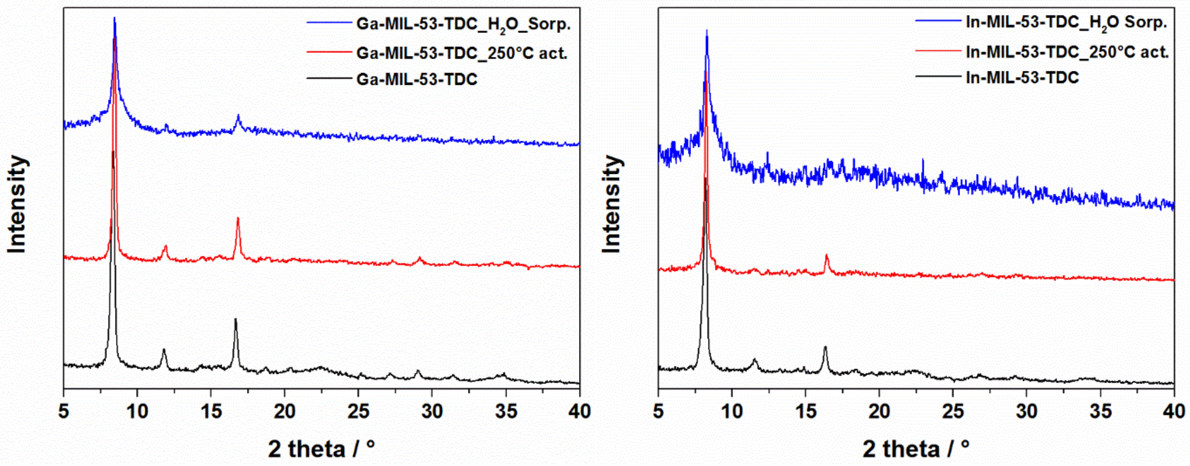

Fig. S21: PXRD patterns of Ga- (left) and In-MIL-53-TDC (right) after thermal activation in vacuum as well as after water vapor sorption measurements.

Literature

[1] V. Bon, I. Senkovska, I.A. Baburin, S. Kaskel, Cryst. Growth Des., 13 (2013) 1231-1237.
[2] I.A. Ibarra, S. Yang, X. Lin, A.J. Blake, P.J. Rizkallah, H. Nowell, D.R. Allan, N.R. Champness, P. Hubberstey, M. Schröder, Chem. Commun., 47 (2011) 8304-8306.
[3] Y. Takashima, C. Bonneau, S. Furukawa, M. Kondo, R. Matsuda, S. Kitagawa, Chem. Commun., 46 (2010) 4142-4144.
[4] J. Zhang, S. Chen, T. Wu, P. Feng, X. Bu, J. Am. Chem. Soc., 130 (2008) 12882-12883.
[5] Y.-X. Tan, Y.-P. He, J. Zhang, Chem. Commun., 50 (2014) 6153-6156.
[6] J. Yang, M. Lutz, A. Grzech, F.M. Mulder, T.J. Dingemans, CrystEngComm, 16 (2014) 5121-5127.
[7] J. Ren, Y. Liu, Z. Chen, G. Xiong, B. Zhao, Sci. China Chem., 55 (2012) 1073-1078.
[8] X. Chen, A.M. Plonka, D. Banerjee, J.B. Parise, Cryst. Growth Des., 13 (2012) 326-332.
[9] S.-Y. Yang, H.-B. Yuan, X.-B. Xu, R.-B. Huang, Inorg. Chim. Acta, 403 (2013) 53-62.
[10] Y.-X. Tan, Y.-P. He, Y. Zhang, Y.-J. Zheng, J. Zhang, CrystEngComm, 15 (2013) 6009-6014.
[11] M. Eddaoudi, J. Kim, D. Vodak, A. Sudik, J. Wachter, M. O'Keeffe, O.M. Yaghi, Proceedings of the National Academy of Sciences, 99 (2002) 4900-4904.
[12] J.-G. Wang, C.-C. Huang, X.-H. Huang, D.-S. Liu, Cryst. Growth Des., 8 (2008) 795-798.
[13] Z. Chen, B. Zhao, P. Cheng, X.-Q. Zhao, W. Shi, Y. Song, Inorg. Chem., 48 (2009) 3493-3495.
[14] R. El Osta, M. Frigoli, J. Marrot, M.E. Medina, R.I. Walton, F. Millange, Cryst. Growth Des., 12 (2012) 1531-1537.
[15] N.L. Rosi, J. Kim, M. Eddaoudi, B. Chen, M. O'Keeffe, O.M. Yaghi, J. Am. Chem. Soc., 127 (2005) 1504-1518.
[16] C. MacNeill, C. Day, S. Gamboa, A. Lachgar, R. Noftle, J Chem Crystallogr, 40 (2010) 222-230.
[17] C.-H. Zhan, F. Wang, Y. Kang, J. Zhang, Inorg. Chem., 51 (2011) 523-530.
[18] W. Huang, D. Wu, P. Zhou, W. Yan, D. Guo, C. Duan, Q. Meng, Cryst. Growth Des., 9 (2009) 1361-1369.
[19] Y.-g. Sun, B. Jiang, T.-f. Cui, G. Xiong, P.F. Smet, F. Ding, E.-j. Gao, T.-y. Lv, K. Van den Eeckhout, D. Poelman, F. Verpoort, Dalton Trans., 40 (2011) 11581-11590.
[20] M.-X. Wang, L.-S. Long, R.-B. Huang, L.-S. Zheng, Chem. Commun., 47 (2011) 9834-9836.
[21] H. Abourahma, G.J. Bodwell, J. Lu, B. Moulton, I.R. Pottie, R.B. Walsh, M.J. Zaworotko, Cryst. Growth Des., 3 (2003) 513-519.
[22] X.-G. Du, J. Zhang, J.-J. Li, Acta Crystallogr. E, 68 (2012) m1024.
[23] Q. Chen, P.-C. Guo, S.-P. Zhao, J.-L. Liu, X.-M. Ren, CrystEngComm, 15 (2013) 1264-1270.
[24] Y. Gong, T. Wang, M. Zhang, C.W. Hu, J. Mol. Struc., 833 (2007) 1-7.
[25] A. Demessence, G. Rogez, R. Welter, P. Rabu, Inorg. Chem., 46 (2007) 3423-3425.
[26] A. Demessence, A. Mesbah, M. François, G. Rogez, P. Rabu, Eur. J. Inorg. Chem., 2009 (2009) 3713-3720.
[27] Z. Chen, Y. Zuo, X.-H. Li, H. Wang, B. Zhao, W. Shi, P. Cheng, J. Mol. Struc., 888 (2008) 360-365.
[28] L.F. Marques, M.V. dos Santos, S.J.L. Ribeiro, E.E. Castellano, F.C. Machado, Polyhedron, 38 (2012) 149-156.
[29] B. Luisi, Z. Ma, B. Moulton, J Chem Crystallogr, 37 (2007) 743-747.
[30] H.-B. Yuan, S.-Y. Yang, Z.-X. Xie, R.-B. Huang, S.R. Batten, Inorg. Chem. Commun., 12 (2009) 755-757.
[31] B.-L. Chen, K.-F. Mok, S.-C. Ng, M. G. B. Drew, New J. Chem., 23 (1999) 877-883.
[32] P.J. Calderone, D. Banerjee, A.C. Santulli, S.S. Wong, J.B. Parise, Inorg. Chim. Acta, 378 (2011) 109-114.
[33] P.J. Calderone, A.M. Plonka, D. Banerjee, Q.A. Nizami, J.B. Parise, Solid State Sciences, 15 (2013) 36-41.

Eidesstattliche Erklärung

Hiermit versichere ich an Eides statt, dass ich die vorliegende Arbeit - mit Ausnahme der wissenschaftlichen Beratung durch meinen Betreuer Herrn Prof. Stock - selbstständig und nur unter Verwendung der angegebenen Hilfsmittel angefertigt habe. Sie hat weder in Auszügen noch als Ganzes einer anderen Stelle im Rahmen eines Prüfungsverfahrens vorgelegen. Teile der Arbeit wurden in den genannten Journalen als wissenschaftliche Beiträge veröffentlicht oder wurden bzw. werden in naher Zukunft zur Begutachtung eingereicht.

Hiermit erkläre ich, dass ich noch keinen Promotionsversuch unternommen habe und dass die Arbeit unter Einhaltung der Regeln guter wissenschaftlicher Praxis der Deutschen Forschungsgesellschaft entstanden ist.

Kiel, im Mai 2015 ________________________________

Nele Reimer

Curriculum Vitae

Nele Reimer

Persönliche Details

Geburtsdatum	16.05.1986
Geburtsort	Henstedt-Ulzburg
Staatsangehörigkeit	deutsch

Ausbildung

Okt. 2010 - Juni 2015	Promotion am Institut für Anorganische Chemie der Christian-Albrechts-Universität zu Kiel Thema der Dissertation: „*Synthese, Charakterisierung und Anwendung poröser Aluminium-MOFs auf Basis schwefelhaltiger Linkermoleküle*“
Okt. 2007 - Aug. 2010	Studium der Chemie an der Christian-Albrechts-Universität zu Kiel, Abschluss: Diplom Thema der Diplomarbeit: „*Säurefunktionalisierte Aluminiumhaltige Gerüstverbindungen auf Basis von MIL-53*“
Okt. 2005 - Okt. 2007	Studium der Wirtschaftschemie an der Christian-Albrechts-Universität zu Kiel
Aug. 1996 - Juni 2005	Gymnasium Harksheide, Norderstedt, Abschluss: Abitur

Tagungsbeiträge

Vorträge

27.02.2014	26. Deutsche Zeolith-Tagung Paderborn *Synthesis and Application of Sulfur-containing Aluminum-MOFs*
14.01.2014	AC Kolloquium Christian-Albrechts-Universität zu Kiel *Synthesis and Application of Sulfur-containing Aluminum-MOFs*
12.06.2013	MACADEMIA Abschluss-Workshop, Brüssel *Linear and V-shaped Functionalized Linker Molecules in the Synthesis of Al-based MOFs*
29.09.2011	14. Norddeutsches Doktorandenkolloquium, Walsrode *Al-MIL-53-COOH: A carboxylic acid functionalized metal-organic framework with MIL-53 topology*

Poster

26.-28.02.2014	26. Deutsche Zeolith-Tagung Paderborn *Surface modified CAU-10 MOF: influence on water uptake and application as capacitive humidity sensor*
11.-14.06.2012	MACADEMIA Jahresmeeting + Workshop, London *Al-MOFs based on sulphur-tagged ligands*
07.-09.03.2012	24. Deutsche Zeolith-Tagung Magdeburg *Al-MOFs based on sulphur-tagged ligands*
02.-04.03.2011	23. Deutsche Zeolith-Tagung Erlangen *Al-MIL-53-COOH: A carboxylate-functionalized MOF with MIL-53 topology*

Publikationen

N. Reimer, C.-W. Hsu, H. Reinsch, R. Siegel, J.-J. Chen, C.-H. Lin, A. Cadiau, C. Serre, J. Senker, N. Stock
New group 13 MIL-53 derivatives based on 2,5-thiophenedicarboxylic acid, *J. Mater Chem. A* **2015**, eingereicht.

N. Reimer, B. Bueken, S. Leubner, C. Seidler, M. Wark, D. De Vos, N. Stock
Three series of sulfonic acid functionalized mixed-linker CAU-10 analogues: Sorption properties, proton conductivity and catalytic activity, *Chem. - Eur. J.* **2015**, angenommen.

A. Weiss, N. Reimer, N. Stock, M. Tiemann, T. Wagner
Surface-modified CAU-10 MOF Materials as Humidity Sensors: Impedance Spectroscopic Study on Water Uptake, *Phys. Chem. Chem. Phys.* **2015**, eingereicht.

A. Weiss, N. Reimer, N.Stock, M. Tiemann, T. Wagner
Screening of Mixed-linker CAU-10 MOF Materials for Humidity Sensing by Impedance Spectroscopy, *Microporous Mesoporous Materials* **2015**, eingereicht.

S. Halis, N. Reimer, A. Klinkebiel, U. Lüning, N. Stock
Four new Al-based microporous metal-organic framework compounds with MIL-53-type structure containing functionalized extended linker molecules, *Microporous Mesoporous Materials*, **2015**, angenommen.

T. Wittmann, R. Siegel, N. Reimer, W. Milius, N. Stock, J. Senker
Enhancing the Water Stability of Al-MIL-101-NH_2 via Postsynthetic Modification, *Chem. - Eur. J*. **2015**, 21, 314.

N. Reimer, H. Reinsch, A. K. Inge, A. K., N. Stock
New Al-MOFs Based on Sulfonyldibenzoate Ions: A Rare Example of Intralayer Porosity, *Inorg. Chem.* **2014**, 54, 492.

M. Stöter, B. Biersack, N. Reimer, M. Herling, N. Stock, R. Schobert, J. Breu
Ordered Heterostructures of Two Strictly Alternating Types of Nanoreactors, *Chem. Mater.* **2014**, 26, 5412.

B. Bueken, H. Reinsch, N. Reimer, I. Stassen, F. Vermoortele, R. Ameloot, N. Stock, C. E. A. Kirschhock, D. De Vos
A zirconium squarate metal-organic framework with modulator-dependent molecular sieving properties, *Chem. Commun.* **2014**, 50, 10055.

Publikationen

A. Klinkebiel, N. Reimer, M. Lammert, N. Stock, U. Lüning
Sulfonyl chlorides as an efficient tool for the postsynthetic modification of Cr-MIL-101-SO_3H and CAU-1-NH_2, *Chem. Commun.* **2014**, 50, 9306.

K.-K. Yee, N. Reimer, J. Liu, S.-Y. Cheng, S.-M. Yiu, J. Weber, N. Stock, Z. Xu
Effective Mercury Sorption by Thiol-Laced Metal–Organic Frameworks: in Strong Acid and the Vapor Phase, *J. Am. Chem. Soc.* **2013**, 135, 7795.

N. Reimer, B. Gil, B. Marszalek, N. Stock
Thermal post-synthetic modification of Al-MIL-53-COOH: systematic investigation of the decarboxylation and condensation reaction, *CrystEngComm* **2012**, 14, 4119.